Optical Propagation in Linear Media:
Atmospheric Gases and Particles, Solid-State Components, and Water

Michael E. Thomas

OXFORD UNIVERSITY PRESS

Optical Propagation in Linear Media

THE JOHNS HOPKINS UNIVERSITY
APPLIED PHYSICS LABORATORY SERIES IN SCIENCE AND ENGINEERING

Previous Volumes

BRADLEY G. BOONE
Signal Processing Using Optics: Fundamentals, Devices, Architectures, and Applications

RICHARD A. HENLE AND BORIS W. KURSHINOFF
Desktop Computers: In Perspective

BRUCE I. BLUM
Beyond Programming: To a New Era of Design

R. M. FRISTROM
Flame Structure and Processes

WILLIAM H. AVERY AND WILLIAM H. CHIH WU
Renewable Energy from the Ocean: A Guide to OTEC

BRUCE I. BLUM
Software Engineering: A Holistic View

VINCENT L. PISACANE
Fundamentals of Space Systems, Second Edition

Optical Propagation in Linear Media

Atmospheric Gases and Particles, Solid-State Components, and Water

Michael E. Thomas

OXFORD
UNIVERSITY PRESS

To
my wife Martha,
and
my children
Daniel, Jane, Alissa, Rebecca, Joseph, and Christopher

This page intentionally left blank

Preface

In this text, the term *optical* represents the electromagnetic spectrum from microwaves to the ultraviolet. This is because the quantum nature of the field becomes important in light–matter interactions beginning with microwaves, and most propagation media are opaque beyond the vacuum ultraviolet (0.1 µm). (Transparency begins again with x-rays.) Also, the fundamental resonances of propagation media are rotational, vibrational, and electronic, which are all within the realm of optical frequencies. Electronic spectroscopy is complicated and, when possible, limiting our discussion to the onset of electronic absorption greatly simplifies the treatment of electromagnetic propagation. The importance of spectroscopy to the field of optical propagation cannot be overemphasized, and in many ways the central theme of Part I of this work is applied spectroscopy. This field, traditionally part of physics and chemistry, has matured to the point that it is now essential to many electro-optical and photonic engineering applications.

Three basic components: a source, a receiver, and a medium in which optical energy propagates (including windows on the source and detector) compose a typical optical system. Many textbooks cover sources and detectors, but very few cover propagation in a comprehensive way, incorporating the latest progress in theory and experiment concerning the propagation medium. Advances in source and detector technologies have resulted in greatly improved system performance. Frequently, the propagation medium limits performance and must be considered in any analysis of a complete optical system. It is the goal of this book to fulfill this need. The propagation medium can be atmospheric gases and particles, solid-state components (e.g., protective windows, devices, and fiber waveguides), or water (e.g., seawater and biomedical fluids). The application may be communication, remote sensing, photonic devices, imaging, or guidance. Physically based

models are developed and applied to diverse media. When the receiver and transmitter are well characterized, then knowledge of the propagation medium can be obtained. This is the important field of remote sensing. Remote sensing can be active (a source is used) or passive (the medium being probed is the source) and is usually noninvasive. Also, knowledge of the optical properties of semiconductors and insulators is essential to the design of optoelectronic devices. For these reasons, optical propagation is crucial to the fields of optical science and optical engineering.

This book can cover a full-year course on modern topics in optical propagation at the upper graduate level or a one-semester course if topics are appropriately selected (e.g., laser light propagation, solid-state optics, optical propagation in the atmosphere, etc.). It is based on a one-semester graduate-level course taught at The Johns Hopkins University, G.W.C. Whiting School of Engineering, which uses an introductory laser physics course as a prerequisite. A background in undergraduate electromagnetic theory and elementary quantum mechanics is essential. It is also helpful to have some background in Fourier optics or diffraction theory.

Material presentation is in a style appropriate for students in engineering and applied science, and for practicing scientists and engineers. Detailed derivations are used as needed, but not when a good reference exists or a simpler approach, utilizing basic concepts, is available. Extensive bibliographies and problem sets are listed at the end of each chapter. Problems are intended to reinforce and extend chapter material. Simple applications are given as example exercises within the text and stressed in homework problems as well. These aspects are important to those learning the field for the first time. Also, I have used the text, as it has developed, as a reference to solve real-world problems at the Applied Physics Laboratory. I believe the book contains enough detail and completeness in the models presented to be useful to practicing engineers and scientists.

The text is structured as two units. A basic background concerning definitions, theoretical fundamentals, and experimental aspects of the linear interaction of light and matter is presented in the first unit. Practical theoretical models should always lead to measurable quantities. Specific models and computer codes concerning propagation of optical energy in various media are covered in the second unit. The topics covered in this unit are also sufficiently comprehensive and contemporary for use as a reference source for practicing engineers and scientists. The presented material builds on other textbooks and does not attempt to rewrite the entire subject. The text strives to develop optical propagation in a variety of media from a general background in classical and quantum electrodynamics. This unifies the discussion of propagation, as opposed to other texts which treat solids and gases separately, for example. The result, I hope, is a fundamental and contemporary development of optical propagation in linear media.

Part I is based on Maxwell's equations as applied to optical frequencies, an introduction to spectroscopy of matter (gases, solids, and liquids), stationary-state quantum mechanics, and electrodynamics (classical and quantum) at optical frequencies. Electrodynamics covers the time-dependent interaction of light and matter. Emphasis is on linear absorption, refraction, and single scattering phenomena. (Turbulence is not covered here, since this requires additional background in the theory of random variables, and other excellent texts exist.) Time-domain and frequency-domain models are developed. Time-domain models of the electric susceptibility are required for high-bandwidth applications using finite-difference time-domain (FDTD) techniques.

Formulas derived in this part are fundamental to understanding many practical models of optical propagation. The main goal is to develop a theoretical foundation concerning the general properties of the complex index of refraction at a level that is reasonably complete but not too cumbersome. Also, measurement techniques are covered which allow verification of the theory and the determination of material specific optical constants for semiempirical models. In this way a general foundation is established to cover a variety of media and applications.

Part II develops practical models of the complex index of refraction, describing how light propagates through matter as a function of temperature, pressure, and frequency, with an emphasis on the similarities and differences between various media mentioned previously. These models are implemented by popular computer codes such as MODTRAN, FASCODE, and OPTIMATR. The material presented in this book previously existed in separate journal publications and reports and is therefore a unique and important feature of the text. Propagation in the atmosphere of the earth, and optical properties of solids and water-based media (e.g., seawater and biomedical fluids) are covered, emphasizing absorption and reflection, refraction, and scattering phenomena. Noise and background radiance in a propagation medium are also covered. Beam and pulse propagation are presented as the ultimate application of the prior chapters. Specific applications, such as remote sensing, optical coatings, lasers, waveguides, material property calculations, and design considerations, are presented to reinforce the topics covered.

The appendices address topics that would disrupt the flow of discussion in the main text. Appendix 1, on symbols and units, is intended to define all the variables and constants used in this text and list other symbols commonly used in the literature describing propagation in various media. The fields of absorption and scattering for various media have evolved independently, and the nomenclature is quite diverse. Appendix 2 lists special functions used in the text. Appendix 3 lists Hilbert and Fourier transform pairs and important relationships between them. Appendix 4 lists numerical values of model parameters for the complex index of refraction as developed in Part II of the text for a variety of optical media. This allows a fairly comprehensive characterization of optical properties. An extensive reference list is also given. Appendix 5 presents the quantization of the electromagnetic field. This appendix is intended for the more advanced student who seeks a more rigorous understanding of light–matter interaction.

An endeavor of this magnitude cannot be a singular effort. I have greatly benefited from the help of many people. First, I wish to acknowledge my students who, through their enthusiasm for the course material, have encouraged me to prepare this text. Also, the correctness and readability of the text has been improved by their comments. Second, the support to write the bulk of the text came from a Parsons and two Janney Fellowships, and a J.H. Fitzgerald Dunning Professorship granted by the Applied Physics Laboratory of the Johns Hopkins University. Much of the material in Part II of the book represents work accomplished at the Applied Physics Laboratory. Third, I gratefully recognize the help and inspiration of Professor Richard I. Joseph, who reviewed, with great thoroughness, the entire manuscript. His contributions have greatly improved the quality and organization of the text. Next, I wish to acknowledge Dr. William J. Tropf, my supervisor at the Applied Physics Laboratory for eleven years, for finding problems for me that I could solve and the necessary encouragement and support to complete the solution and its final publication. Also, many of my colleagues at the Applied Physics Laboratory and elsewhere deserve my thanks for their

It is said that we currently live in an information age. However, there is an important distinction between information and knowledge. Knowledge is the ability to process information. In the spirit of a recent book commemorating the 125th anniversary of the University entitled *Johns Hopkins Knowledge for the World*, it is my intention to write a book that provides insight and perspective in addition to information. Finally, it is my sincere hope that the deficiencies of this text are overcome by its utility.

Contents

PART II: PRACTICAL MODELS FOR VARIOUS MEDIA

This page intentionally left blank

BACKGROUND THEORY AND MEASUREMENT

This page intentionally left blank

1

Optical Electromagnetics I

In this chapter, the optical spectrum is defined and subdivided into many sub-bands, which are traditionally determined by transparency in various media. Propagation of the electromagnetic field in vacuum, as based on Maxwell's equations, and basic notions of geometrical and physical optics, are covered. The theoretical and conceptual foundation of the remaining chapters is established in this chapter and the next.

1.1 Introduction

Optical electromagnetic propagation is generally and often accurately described by classical geometrical optics or ray optics. When diffraction or wave interference is of concern, then the more complete field of physical optics is used. Geometrical optics requires precise knowledge of the spatial and spectral dependence of the index of refraction. This requires electrodynamics, which is most appropriately described by quantum optics. These topics are covered in the first five chapters. The definitions of the optical spectrum and the various models for describing propagation are introduced in the following.

1.1.1 The Electromagnetic Spectrum

The optical electromagnetic field covers the range of frequencies from microwaves to the ultraviolet (UV) or wavelengths from 10 cm to 100 nm. This is a very liberal definition covering six orders of magnitude, yet the description of propagation is very similar over this entire band, and distinct from radio-wave propagation and x-ray

Table 1.1 Definition of Spectral Regions

	Wavelength λ [μm]	Wave Number ν [cm^{-1}]	Frequency f [GHz]	Energy E [eV]
Soft x-ray	<0.01			>124
Extreme UV	0.01–0.1			124–12.4
Vacuum UV	0.1–0.185			12.4–6.7
Air cutoff	0.185			6.7
Solar blind UV	0.185–0.3			6.7–4.1
Near UV	0.2–0.4	50,000–25,000		6.2–3.1
Visible	0.4–0.7	25,000–14,286		3.1–1.8
Near-infrared	0.7–2.0	14,286–5000		1.8–0.62
Mid-infrared	2.0–10.0	5000–1000		
Far-infrared	10.0–100.0	1000–100		
Submillimeter	100–1000	100–10		
Millimeter waves	1000–10,000	10–1	300–30	
Microwaves	10,000–10^6		30–0.3	
Radio waves	>10^6		<0.3	

propagation. A listing of the nomenclature for the different spectral bands within the range of optical wavelengths is given in Table 1.1. Other commonly used units of spectral measure such as wave number, frequency, and energy are also listed in the table. These various quantities are related to wavelength by the following formulas:

$$c = \lambda f, \quad E = hf, \quad \text{and} \quad \nu = 1/\lambda = f/c \tag{1.1}$$

where c is the speed of light ($c = 2.99792458 \times 10^8$ m/sec), λ is wavelength, f is frequency in hertz, E is energy, h is Planck's constant ($h = 6.6260755(40) \times 10^{-34}$ J sec), and ν is frequency in wave numbers (the number of wavelengths per centimeter). Although wavelength is commonly used by applied scientists and engineers, frequency is the most appropriate unit for the theoretical description of light–matter interactions. Because of the importance of spectroscopy in the discussion of optical propagation, the spectroscopic unit of wave number will be consistently used.

The spectral nature of electromagnetic propagation in any medium is determined by the location of absorption bands and the type of scattering. Strong absorption characteristics of a medium define the window or transparency regions. Regardless of the medium, these absorption features generally involve transitions of electrons in atoms and vibrational motions of bound atoms within molecules. Weak absorption features and scattering determine the nature of propagation in the window region. The various bands in Table 1.1 are typically determined by absorption features in various media. The vacuum ultraviolet (VUV) cuts off at 0.1 μm because the transparency of typical ultraviolet window materials, MgF_2 and LiF, end at this wavelength. Thus the extreme ultraviolet (XUV) requires windowless operation and distinctly different sources. The vacuum ultraviolet begins at 0.185 μm because this is where molecular oxygen begins to absorb strongly, thus requiring high-vacuum spectrometers. The solar blind UV is the spectral region where sunlight is blocked by stratospheric ozone absorption and UV propagation is good in the troposphere. The visible spectrum is determined by the transparency of liquid water. The infrared (IR) is broken up into three different spectral

bands, the near-IR, mid-IR, and far-IR, based on the location of windows in water vapor. The far-IR is largely opaque in the atmosphere because of a major absorption band of water vapor. Transparency begins again at the submillimeter band and continues to improve at millimeter waves and on to microwaves. Microwaves are further subdivided into sub-bands based in part on water vapor and molecular oxygen absorption lines occurring in the atmosphere.

Two additional mechanisms affecting propagation in transparent regions are scattering and turbulence. Scattering results from small-scale, large-amplitude spatial and temporal fluctuations of density of the propagation medium. When the fluctuations are small compared with a wavelength, Rayleigh scatter results. This type of scatter falls off rapidly with decreasing frequency, thus emphasizing the blue end of a spectral region. When the fluctuations are on the order of a wavelength, Mie scatter results. This type of scatter has a relatively flat spectral response and results in the characteristic white color of clouds, for example. Turbulence results from large-scale, small-amplitude spatial and temporal variations of optical properties within the propagation medium.

The emphasis in this text will be on absorption and single scattering, since a similar background in electromagnetic theory can be used to describe these mechanisms. Turbulence is more appropriately covered in terms of statistical optics and excellent texts exist in this field (see references 1.10 and 1.11).

1.1.2 Classical and Quantum Concepts

The major distinction between optical and radar-/radio-frequency propagation is the need to include a quantum description of the field and medium. Based on Eq. 1.1, the energy is directly proportional to the frequency, so that at lower frequencies the energy of a single quantum of the field (the photon) is small and not easily detected. Many photons are required for detection and thus a field (classical) description is adequate. At optical wavelengths, single photon events and the discrete energy level structure within the medium match photon energies and are important in describing absorption and scattering mechanisms in detail. However, classical models are still very useful and instructive, because optical measurements are generally time averaged over many photon detections and a quantum description of the propagation media is not always necessary. Hence, both classical and quantum models will be used to describe optical propagation.

The most fundamental and practical description of optical propagation is given by nonrelativistic **quantum electrodynamics** or the subfield, **quantum optics** (which is quantum electrodynamics limited to low-energy optical frequencies). Quantum optics is a detailed microscopic theory of photons and molecules (atoms) in the gas, liquid, and solid phase, and their interactions involving quantum mechanics (Schrödinger's equation) and the quantized electromagnetic field. These combined theories lead to the quantum oscillator model. Because of the scope and level of detail of this theory, it is also the most complicated to present. The quantum-mechanical description of the energy structure of matter within the realm of quantum optics is called **spectroscopy**. This field considers the location, strength, and shape of spectral lines. Another fashionable subset of quantum electrodynamics is **quantum electronics**, which emphasizes optical devices such as lasers and nonlinear optics. Quantum electronics is often

presented within the context of **semiclassical radiation theory**. In this approach the propagation medium is treated quantum mechanically, but the field is treated classically. Thus, semiclassical radiation theory can be thought of as a bridge connecting spectroscopy with the classical version of Maxwell's equations. It allows the treatment of high field intensities interacting with matter. This is important in the description of laser phenomena.

When the quantum nature of the field and medium is not relevant, such as elastic scattering, refraction, or reflection, then **classical electrodynamics** or **classical optics** can be used. This allows a simpler and equally valid approach based solely on Maxwell's equations, Newtonian mechanics, and Lorentz force relation. This theoretical foundation leads to the commonly used classical oscillator model. Historically, the wave nature of light is the topic of **physical optics** or **wave optics**. The development of this field predates the unifying work of Maxwell and is based on solutions of the wave equation. Maxwell's equations include the wave equation and therefore form a more complete theory that describes the coupling of the field to the propagation media. As an example application, the fields of Fourier optics and particle scatter are based on physical optics. Furthermore, when wave interference of the field is not relevant and the frequency of the field is sufficiently high, then **geometrical optics** or **ray optics** can be employed. This field also predates the development of Maxwell's equations and is based on the particle interpretation of light. This approach is consistent with classical optics when based on a high-frequency asymptotic solution to the wave equation. It is the simplest description of optical field propagation and often a good place to begin a description of the propagation path. Optical engineers commonly use geometrical optics to design optical systems. The field of **radiometry** also should be mentioned in this introduction as a subfield to geometrical and physical optics.

Consequently, geometrical optics, as defined above, is a subset of physical optics, and physical optics is a subset of classical optics. Classical optics is a subset of quantum optics. This point is graphically illustrated in Fig. 1.1. Also, emphasis at the beginning will be on classical optics and, as background is developed, the more complete theories will be used. The first five chapters develop these important theories for practical use.

The inclusion of relativistic theory into our models is not necessary to meet the goals of this book. However, it is interesting to note that relativistic quantum mechanics (Dirac theory) includes the effect of particle spin. Photons have integer spin. This leads to polarization or the vector character of the electromagnetic field and will be handled by conventional classical methods.

The following sections in this chapter and the next describe electromagnetic field propagation based on Maxwell's equations in vacuum and in linear matter, respectively. In each section the classical aspects of the electromagnetic field and the propagation medium are discussed in detail. The quantum nature of the propagation medium is introduced in Chapter 3. Electrodynamics is then introduced in Chapters 4 and 5. Chapter 4 develops the classical version, covering the classical oscillator model for gases and solids, and elastic scattering for gases and particles. Chapter 5 presents applied quantum electrodynamics at optical frequencies or quantum optics. The quantum oscillator model is developed, which is the foundation for many of the practical models of Part II. The sixth chapter of this first part discusses experimental techniques to measure fundamental optical constants as dictated by the theory of the first
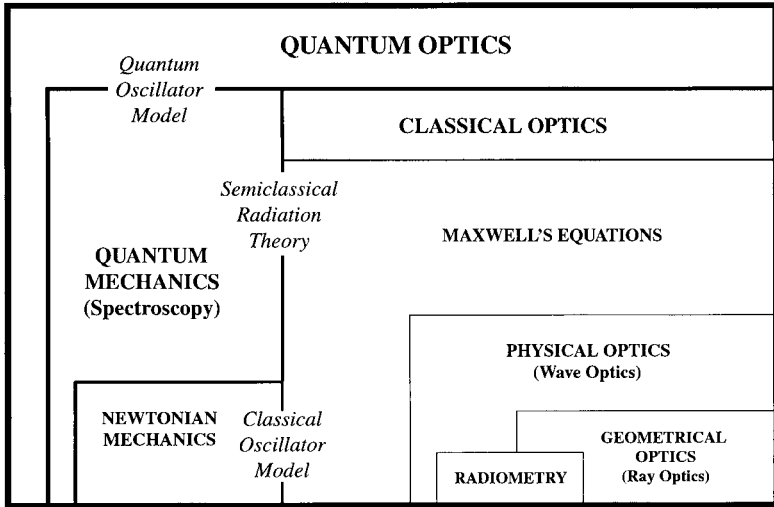
Fig. 1.1 Illustration of the relationship between and scope of the fields and subfields of quantum optics, spectroscopy, classical optics, semiclassical radiation theory, physical optics, and geometrical optics.

five chapters. The complementary interplay between theory and experiment is then more fully appreciated.

1.2 Macroscopic Properties in Vacuum

It is instructive and relevant to begin the development of optical electromagnetics with a discussion of plane-wave propagation in vacuum. The presence of matter greatly complicates the description of optical propagation and it is useful to distinguish between properties of the field and properties of the propagation medium. Furthermore, even though true plane waves cannot be physically realized, an understanding of plane-wave propagation allows a complete description of any function representing a realistic propagating electromagnetic wave via Fourier analysis. Plane-wave propagation is considered in unbounded and bounded vacuum.

1.2.1 Plane-Wave Propagation

The macroscopic properties of the electromagnetic field are represented by Maxwell's equations, which are founded in classical physics. Since plane waves form a complete basis set spanning a function space (an infinite-dimension vector space with monochromatic plane-wave functions as basis vectors), it is convenient and comprehensive to begin with a plane-wave solution of Maxwell's equations in unbounded vacuum or free space. Other function basis sets, such as spherical waves, are also useful and will be presented later. Solutions to Maxwell's equations in bounded vacuum are also examined in this section.

1.2.1.1 Maxwell's Equations in Free Space

Maxwell's equations in unbounded vacuum are:

$$\text{Faraday's law:} \quad \nabla \times \mathbf{e}(\mathbf{r},t) = -\frac{\partial \mathbf{b}(\mathbf{r},t)}{\partial t}, \tag{1.2}$$

$$\text{Ampere's law:} \quad \nabla \times \mathbf{h}(\mathbf{r},t) = \frac{\partial \mathbf{d}(\mathbf{r},t)}{\partial t} \tag{1.3}$$

and

$$\text{Gauss's law:} \quad \nabla \cdot \mathbf{d}(\mathbf{r},t) = \nabla \cdot \mathbf{e}(\mathbf{r},t) = 0, \tag{1.4}$$

$$\nabla \cdot \mathbf{b}(\mathbf{r},t) = \nabla \cdot \mathbf{h}(\mathbf{r},t) = 0, \tag{1.5}$$

with the free-space constitutive relations

$$\mathbf{d}(\mathbf{r},t) = \epsilon_0 \mathbf{e}(\mathbf{r},t) \quad \text{and} \quad \mathbf{b}(\mathbf{r},t) = \mu_0 \mathbf{h}(\mathbf{r},t), \tag{1.6}$$

where $\epsilon_0 (= 8.854188 \times 10^{-12} \, \text{F/m})$ is the free-space permittivity, $\mu_0 (= 4\pi \times 10^{-7} \, \text{H/m})$ is the free-space permeability, $\mathbf{e}$ is the electric field intensity in units of volts per meter, $\mathbf{d}$ is the electric flux density in units of coulombs per meter squared, $\mathbf{h}$ is the magnetic field intensity in units of amperes per meter, and $\mathbf{b}$ is the magnetic flux density in units of webers per meter squared. All lowercase vector symbols represent time-domain quantities. (An attempt to consistently use MKS units is made, but this is not always achieved because of the small size of optical wavelength and detectors; in this case cm is often used.) Taking the curl of Faraday's law and applying Gauss's law, a vector wave equation for $\mathbf{e}$ is obtained,

$$\nabla^2 \mathbf{e}(\mathbf{r},t) = \frac{1}{c^2} \frac{\partial^2 \mathbf{e}(\mathbf{r},t)}{\partial t^2}, \tag{1.7}$$

where

$$c^2 = \frac{1}{\epsilon_0 \mu_0}. \tag{1.8}$$

To solve this partial differential equation, the Fourier transform will be employed. It is defined for individual components of the field vector as[1]

$$\mathscr{F}\{e_i(\mathbf{r},t)\} = E_i(\mathbf{r},\omega) = \int_{-\infty}^{\infty} e_i(\mathbf{r},t) e^{-j\omega t} \, dt \tag{1.9}$$

and the corresponding inverse transform as

$$\mathscr{F}^{-1}\{E_i(\mathbf{r},\omega)\} = e_i(\mathbf{r},t) = \frac{1}{2\pi} \int_{-\infty}^{\infty} E_i(\mathbf{r},\omega) e^{-j\omega t} \, d\omega, \tag{1.10}$$

where, for Cartesian coordinates,

$$\mathbf{e} = e_x\hat{\mathbf{x}} + e_y\hat{\mathbf{y}} + e_z\hat{\mathbf{z}}, \qquad i = x, y, z, \quad \text{and} \quad \omega = 2\pi f.$$

Uppercase vector quantities are in the frequency domain with an amplitude that is constant over a unit bandwidth. The Fourier transform of Eq. 1.7 is given by

$$\nabla^2 E_i(\mathbf{r},\omega) = -\frac{\omega^2}{c^2} E_i(\mathbf{r},\omega). \tag{1.11a}$$

The electric field intensity is now in the frequency domain. The subscript i represents the two different directions of polarization of the E-field. Without loss of generality, since vacuum is isotropic, let E be polarized in the x-direction and propagate in the z-direction. An orthogonal polarization in the y-direction also exists but its representation, at this point, is analogous to x-direction field. (When accounting for the total field energy (both polarizations) a multiplication factor of two must be used for unpolarized light.) Thus, substituting $\mathbf{E} = E_x(z,\omega)\hat{\mathbf{x}}$ into Eq. 1.11a we obtain

$$\frac{\partial^2 E_x}{\partial z^2} + \frac{\omega^2}{c^2} E_x = 0. \tag{1.11b}$$

This is the standard one-dimensional scalar wave equation with the well-known solution describing a monochromatic plane-wave field, with the radiation boundary condition ($E_x(z \to \infty) \to e^{\pm j\omega z/c}$), as given by

$$E_x(z,\omega) = \frac{1}{2} E_{x0}^+ e^{-j\frac{\omega}{c}z} + \frac{1}{2} E_{x0}^- e^{j\frac{\omega}{c}z}. \tag{1.12a}$$

For arbitrary polarization and propagation direction, the solution is more generally written as

$$\mathbf{E}(\mathbf{r},\omega) = \frac{1}{2}\mathbf{E}_0^+ e^{-j\mathbf{k}'\cdot\mathbf{r}} + \frac{1}{2}\mathbf{E}_0^- e^{j\mathbf{k}'\cdot\mathbf{r}}, \tag{1.12b}$$

where $\mathbf{k}' = k_x'\hat{\mathbf{x}} + k_y'\hat{\mathbf{y}} + k_z'\hat{\mathbf{z}}$ is the wave vector with magnitude ω/c ($= 2\pi/\lambda$) and $\mathbf{r} = x\hat{\mathbf{x}} + y\hat{\mathbf{y}} + z\hat{\mathbf{z}}$ is the position vector. This describes a plane wave with both forward and backward (time-reversed) propagating components or, from a different perspective, positive and negative frequency components. This concept will be useful later. Also, observe that the plane-wave solution is not only time harmonic, but harmonic in space as well. It is required that e_x be real, thus

$$E_{x0}^- = \left(E_{x0}^+\right)^* \tag{1.13}$$

and Eq. 1.12a reduces to

$$E_x(z,\omega) = \text{Re}\left[E_{x0}e^{-j\frac{\omega}{c}z}\right]. \tag{1.14}$$

This, in effect, is phasor notation and, as is customary, the Re[·] symbol will almost always be suppressed in the notation from now on.[2]

The wave equation, as given by Eq. 1.11, can also be solved in a bounded rectangular region of free space with sides L_x, L_y, and L_z. The boundary condition for a metallic cavity, for example, is that the tangential **E**-field must vanish on the boundary. This leads to standing-wave solutions (see Problem 1.7) of the form

$$E_x(\mathbf{r},\omega) = E_{x0} \cos \frac{l\pi x}{L_x} \sin \frac{m\pi y}{L_y} \sin \frac{n\pi z}{L_z} \tag{1.15a}$$

$$E_y(\mathbf{r},\omega) = E_{y0} \sin \frac{l\pi x}{L_x} \cos \frac{m\pi y}{L_y} \sin \frac{n\pi z}{L_z} \tag{1.15b}$$

$$E_z(\mathbf{r},\omega) = E_{z0} \sin \frac{l\pi x}{L_x} \sin \frac{m\pi y}{L_y} \cos \frac{n\pi z}{L_z}, \tag{1.15c}$$

where Gauss's law requires

$$\frac{l}{L_x} E_{x0} + \frac{m}{L_y} E_{y0} + \frac{n}{L_z} E_{z0} = 0; \tag{1.15d}$$

l, m, and n are integers, and are related to the wave vector according to

$$k'^2 = \frac{\omega^2}{c^2} = \pi^2 \left(\frac{l^2}{L_x^2} + \frac{m^2}{L_y^2} + \frac{n^2}{L_z^2} \right). \tag{1.15e}$$

Such standing-wave fields are commonly discussed in textbooks on laser theory. For a finite cavity, only modes with discrete frequencies can be supported. The number of modes per unit volume with frequency less than f, ρ_{EM}, must be a finite value and, based on Eq. 1.15e, is given by (see Problem 1.5)

$$\rho_{EM} = \frac{8\pi f^3}{3c^3}. \tag{1.15f}$$

This is an important result that will be needed in Chapter 5.

1.2.1.2 Poynting Vector

The corresponding unbounded **H**-field solution comes from the solution of the frequency-domain version of Faraday's law, as given by

$$\nabla \times \mathbf{E}(\mathbf{r},\omega) = -j\omega\mu_0 \mathbf{H}(\mathbf{r}, \omega). \tag{1.16}$$

Substituting Eq. 1.14 for **E** in Eq. 1.16, the following is obtained

$$H_y(z,\omega) = \frac{1}{\eta_0} E_{x0} e^{-j\frac{\omega}{c}z}, \tag{1.17}$$

where $\eta_0 (= (\mu_0/\epsilon_0)^{1/2})$ is the intrinsic impedance of free space and equals 377Ω. At optical frequencies, field quantities are not directly measured. Instead, optical detectors typically measure time-average power density or radiance, L, in units of watts/ (cm^2 sr). In terms of field quantities this is the magnitude of the time-averaged time-domain Poynting vector, $\langle \mathscr{L}(t) \rangle_t$ $(= \langle \mathbf{e}(t) \times \mathbf{h}(t) \rangle_t)$, where $\langle \ \rangle_t$ is the time average as defined by

$$\langle a(t)b(t) \rangle_t = \frac{1}{2T} \int\limits_{-T}^{T} a(t)b(t)\, dt$$

where T is the observation time (usually much longer than an optical period). For a monochromatic field the time-averaged Poynting vector is given by (see Problem 1.3)

$$\langle \mathscr{L}(t) \rangle_t = \mathbf{L} = \frac{1}{2}\mathrm{Re}\left[\mathbf{E}(\omega) \times \mathbf{H}^*(\omega)\right] = \frac{|E_{x0}|^2}{2\eta_0}\hat{\mathbf{z}}. \tag{1.18}$$

The monochromatic Poynting vector is a good approximation for single-mode continous wave (CW) laser light, but does not represent common polychromatic sources (e.g., pulsed lasers and light bulbs). In that case, the individual electric and magnetic fields are represented by a sum of monochromatic fields possessing different frequencies, ω_m, and phases, ϕ_m,

$$\mathbf{E}(\omega) = \sum_m \mathbf{E_m}(\omega_m, \phi_m) \quad \text{and} \quad \mathbf{H}(\omega) = \sum_m \mathbf{H_m}(\omega_m, \phi_m),$$

and must be summed over all frequencies and phases. Substituting these expressions into Eq. 1.18 leads to the result for a polychromatic time-averaged Poynting vector:

$$\langle \mathscr{L}(t) \rangle_t = \frac{1}{2}\mathrm{Re}\left[\sum_m \mathbf{E_m}(\omega_m, \phi_m) \times \mathbf{H_m^*}(\omega_m, \phi_m) + \sum_{m \neq l} \mathbf{E_m}(\omega_m, \phi_m) \times \mathbf{H_l^*}(\omega_l, \phi_l) \right].$$

$$\tag{1.19a}$$

For a stationary random polychromatic field, each component in the second term of Eq. 1.19a is zero, and the sum is also zero. Thus, the time-averaged Poynting vector becomes a spectral distribution function, as given by

$$\langle \mathscr{L}(t) \rangle_t = \sum_m \frac{|E_{m0}|^2}{2\eta_0}\hat{\mathbf{z}} = \frac{c}{2}\epsilon_0 \sum_m |E_{m0}|^2\, \hat{\mathbf{z}}. \tag{1.19b}$$

The field polarization is arbitrarily chosen in the x-direction, consistent with the monochromatic case. Power flows in the z-direction, only.

A straight-line path is called rectilinear propagation and is consistent with the approximations of a lossless, homogeneous, isotropic unbounded region used thus far. Thus the electromagnetic field can be thought of as a light ray (ray optics), ignoring the details of the electric and magnetic fields composing the electromagnetic wave. The nonphysical condition of an unbounded medium containing rectilinear parallel rays results in a number of practical limitations on this particular solution of Maxwell's equations:

1. No restrictions on the extent of the field in the xy-plane exist. The field fills all space, requiring an infinite amount of energy.
2. Light does not always travel in a straight line, but can be bent.
3. Rays of light from other directions will intersect at some point in space (called a caustic) causing infinitely high power density to exist[3].

To resolve these limitations in this theory, finite boundaries and diffraction theory must be included. It is of interest to describe a beam of light that is finite in the transverse direction and not a plane wave over large distances. This increases the scope of the initial problem to consider solutions with finite sources.

1.2.2 Diffraction: Physical Optics

As previously noted, the solution to the wave equation in unbounded vacuum of the previous section has two serious problems. First, the field exists in all space as a plane wave propagating in the z-direction with no limitations in the xy-plane, requiring infinite energy. This cannot be a physical solution, since some limitation in the xy-plane must exist. Second, when geometrical rays come to a focus or caustic, it occupies a single point, requiring infinite energy density. This, also, is not a physical result. To overcome these limitations, diffraction theory must be addressed. The following development is more intuitive than rigorous but leads to meaningful results. More complete derivations are available in the bibliography.

1.2.2.1 Spherical-Wave Representation

Recall that the plane-wave solution, given by Eq. 1.14, represents an electromagnetic wave with planar wave fronts of infinite extent propagating in the positive z-direction, as illustrated in Fig. 1.2. The solid lines in the figure represent $z =$ constant planes, where phase repeats a certain arbitrary value (determined by the constant) every wavelength. This solution of the wave equation can be represented in other mathematical forms, which will prove useful for further analysis. The plane-wave representation resulted because of the choice of rectangular coordinates. Because sources of light can often be approximated by point sources, spherical waves are also a meaningful basis set, representing propagating fields.

Furthermore, an electromagnetic field generated by a finite source in the xy-plane can be represented by an integration of point sources over the xy-plane aperture. This statement is **Huygens' principle**, and allows the examination of the consequences of a finite source in a simple manner. (Point sources or impulse response functions are commonly used in science and engineering.) Consider the three-dimensional point source located at the origin of a spherical coordinate system in an unbounded medium,
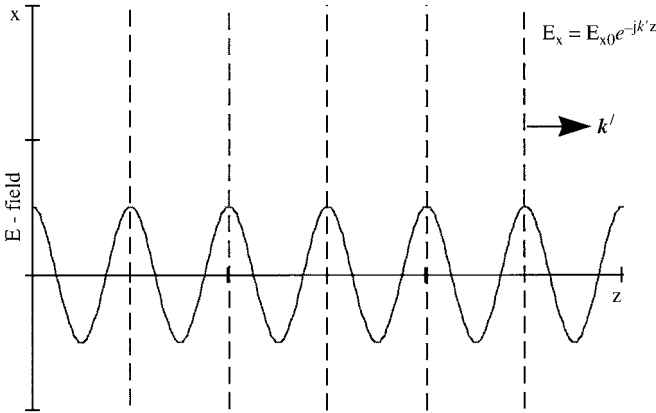
Fig. 1.2 Plane-wave propagation showing lines of constant phase in the xz-plane. The spacing between the lines is one wavelength.

$$dE_x(\mathbf{r}) = \text{const } E_{x0}\frac{e^{-jk'r}}{r}dS, \tag{1.20}$$

where "const" is a constant to be determined later, $r = |\mathbf{r}|$ and $dS(= dxdy)$ is a surface element in the xy-plane. This is a special function in applied mathematics and engineering called a free-space Green's function or impulse response function. Equation 1.20 is the three-dimensional free-space Green's function, and is the solution of the wave equation with a delta-function point source and the radiation boundary condition. Coulomb's law for point charges is an example of such a three-dimensional Green's function (for $k = 0$) and can be used to represent general charge distributions when integrated over a specified volume.

1.2.2.2 Fresnel and Fraunhofer Diffraction

The construction of optical fields in terms of spherical waves from a point source is an old concept originating with Fresnel, who in 1818, applied Huygens' principle and Young's concept of interference to explain diffraction phenomena. To see this, consider the spherical wave field such that $x \ll z$ and $y \ll z$, and that the observed field is determined by sources in the xy-plane directly behind it along the z-axis. This means the field is nearly a plane wave in the z-direction, this is known as the paraxial ray approximation. Based on this assumption and a binomial expansion, the observation point is given by

$$r = \sqrt{z^2 + x^2 + y^2} \underset{z \to \infty}{\sim} z + \frac{1}{2z}\left(x^2 + y^2\right) + O\left(\frac{1}{z^3}\right). \tag{1.21}$$

The analytical expression for an unbounded plane wave propagating in the positive z half-space, in terms of spherical waves, is obtained by integrating over all coherent

(identical phase) point sources in the xy-plane, as given by

$$E_x(z,\omega) = \frac{\text{const}}{z} \, e^{-jk'z} \int\limits_{-\infty}^{\infty} dx \int\limits_{-\infty}^{\infty} dy \, E_{x0} \, e^{-j\frac{k'}{2z}(x^2+y^2)}. \tag{1.22}$$

The approximation in Eq. 1.21 is used in the phase term because this adequately determines the locations of constructive and destructive interference, but a more relaxed approximation can be used in the denominator factor of the Green's function (e.g., $r \approx z$). The result of the above integration must have the same result as Eq. 1.14, thus the constant factor can be determined. The integrals are Gaussian, with well-known solutions. The result is

$$\text{const} = \frac{j}{\lambda}. \tag{1.23}$$

Now a representation of optical fields exist in the positive z-half-plane that can account for the effects of finite beam apertures by allowing E_x^0 to be nonzero only over the aperture.

Consider the double coordinate system in Fig. 1.3. A coordinate system is specified for the plane of the observer, such that the location of the field at a point is specified by

$$r = |\mathbf{r} - \mathbf{r}_o| = \sqrt{z^2 + (x - x_o)^2 + (y - y_o)^2}. \tag{1.24}$$

Again, applying the paraxial ray approximation, given by $|x - x_o| \ll z$ and $|y - y_o| \ll z$, and expanding r by a binomial expansion, one obtains

$$r \underset{z \to \infty}{\sim} z + \frac{(x - x_o)^2}{2z} + \frac{(y - y_o)^2}{2z} + O\left(\frac{1}{z^3}\right). \tag{1.25}$$
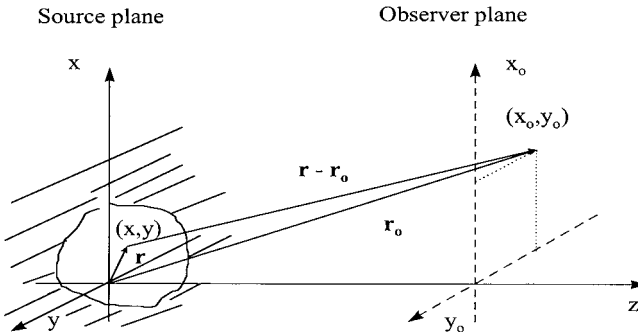
Fig. 1.3 Source and observer coordinates for electromagnetic field propagation, including diffraction by a limiting aperture.

Following the same procedure as before, an expression of the field in the $x_o y_o$-plane of the observer as a function of a source in the xy-plane is obtained. The result is the **Fresnel** formula of diffraction, as given by $(dS = dxdy)$

$$E_x(x_o,y_o,z,\omega) = \frac{j}{\lambda z}e^{-jk'z} \int\limits_{-\infty}^{\infty} \int\limits_{-\infty}^{\infty} dS\, E_{x0}(x,y)e^{-jk'\left(\frac{(x-x_o)^2}{2z} + \frac{(y-y_o)^2}{2z}\right)}, \qquad (1.26)$$

which is valid only within the paraxial ray approximation $(z^2 \gg [(x-x_o)^2+(y-y_o)^2]_{max})$ and where E_{x0} is an aperture function defining the extent of a beam in the xy-plane. The field expands and the spatial distribution changes beyond the xy-plane, thus losing uniform plane-wave properties.

To see this point more clearly, examine the integrand in the far field, where the approximation

$$z \gg \frac{k'}{4\pi} \left(x^2 + y^2\right)_{max} = z_R \qquad (1.27)$$

is valid. The parameter z_R is called the Rayleigh range. The phase factor in the integrand of Eq. 1.26 can be expanded to obtain

$$e^{-jk'\left(\frac{x_o^2}{2z} + \frac{y_o^2}{2z}\right)}e^{-jk'\left(\frac{x^2}{2z} + \frac{y^2}{2z}\right)}e^{jk'\left(\frac{xx_o}{z} + \frac{yy_o}{z}\right)}. \qquad (1.28)$$

Applying the far-field approximation, we obtain the **Fraunhofer** diffraction integral in the paraxial approximation[4], as given by

$$E_x(x_o,y_o,z,\omega) = \frac{j}{\lambda z}e^{-jk'z}e^{-jk'\frac{x_o^2+y_o^2}{2z}} \int\limits_{-\infty}^{\infty} \int\limits_{-\infty}^{\infty} dxdy\, E_{x0}(x,y)\, e^{jk'\frac{x_o}{z}x}e^{jk'\frac{y_o}{z}y}. \qquad (1.29)$$

The integral is of the form of a two-dimensional Fourier transform between a spatial distribution of a field in a plane at $z = 0$ and spatial frequencies, κ_x and κ_y in the far-field observation plane $(\kappa_x = k'x_o/z$ and $\kappa_y = k'y_o/z$ (see reference 1.5). The two-dimensional spatial Fourier transform is defined as

$$\mathbf{E}(\kappa_x, \kappa_y) = \mathscr{F}_{xy}[\mathbf{E}_0(x,y)] = \int\limits_{-\infty}^{\infty} \int\limits_{-\infty}^{\infty} dxdy\, \mathbf{E}_0(x,y)\, e^{j\kappa_x x}e^{j\kappa_y y}.$$

For visible wavelengths ($\lambda \approx 0.5$ μm) and 1 cm square aperture, and based on Eq. 1.27, the far-field distance or Rayleigh range is approximately 200 meters. For a uniformly illuminated aperture, the far-field pattern is composed of sinc functions (e.g., $\sin c(x) = \sin(x)/x$ in the x- and y-directions (see Problem 1.4). This field pattern will continue to widen as the wave propagates, completely changing the uniform field

distribution pattern in the $z = 0$ plane. The Fraunhofer diffraction pattern of the radiance is, based on Eq. 1.19,

$$L = \frac{\left|\mathbf{E}(x_o, y_o, z)\right|^2}{2\eta_0} = \frac{\left|\mathscr{F}_{xy}\left[\mathbf{E}_0(x, y)\right]\right|^2}{2(z\lambda)^2\eta_0},$$ (1.30)

where $\mathscr{F}_{xy}$ is the two-dimensional spatial Fourier transform.

Diffraction theory also limits the minimum size of a focus, thus solving the problem of caustics mentioned earlier. This is easily demonstrated using the Fraunhofer diffraction integral and the time–bandwidth product of Fourier transform theory ($\Delta x \Delta \kappa_x \geq 1/2$). Considering the far-field diffraction pattern of a large aperture lens, one obtains

$$\sin\alpha = \frac{\lambda}{4\pi D},$$

where $\sin\alpha = \Delta x_o/z$ and $D (= \Delta x)$ is the diameter of the focusing lens. For Δx_o to be zero (a point focus) requires an infinite-diameter lens, thus a finite field intensity at the focus is always the case.

1.3 Optical Propagation in Vacuum

In practice, optical engineers and scientists are concerned about the propagation of light in the form of CW or pulsed light beams. Applications for vacuum propagation include remote sensing and communication links in space. The following two sections apply the background obtained thus far to beam and pulse propagation in vacuum.

1.3.1 Beam Propagation

Generally, light-beam propagation is analyzed in terms of plane waves. This will be the approach taken in the remaining chapters. However, realistic beams of light can only be approximated by plane waves, and it is important to understand where this approximation is valid. Beams of light from the spherical sun, for example, are essentially plane waves to an observer on earth because of the great distance from the sun to the earth.

Laser beams are generated inside a resonant cavity. A stable spatial distribution of the output beam is desired, which requires the beam profile to remain the same as it propagates back and forth within the cavity. Furthermore, to minimize diffraction losses also requires maintaining the field pattern as the wave propagates. Thus, diffraction theory dictates that a field function which Fourier transforms into a function of the same form is desired. This is the Gaussian class of beams, commonly produced by lasers and customarily discussed in laser textbooks (see Bibliography). However, **Gaussian beams** continue to expand upon propagation because of diffraction. To see this, consider a circular beam in the xy-plane with a Gaussian distribution of the electric field polarized in the x-direction, as given by

$$E_{x0}(x, y, 0) = \frac{E_{x00}}{\pi w_0^2} e^{-(x^2 + y^2)/w_0^2},$$ (1.31)

where w_0 is the beam radius or waist at the $1/e$ field point, E_{x00} is a constant and the E-field is normalized such that

$$\int_{-\infty}^{\infty} \int_{-\infty}^{\infty} dx\,dy\,E_{x0} = E_{x00}.$$

It is assumed in this formulation that, in the region of the $z = 0$ plane, the beam is independent of z. Using Eq. 1.30 and the cosine Fourier transform, the far-field radiance becomes

$$L(x_o, y_o, z) = \frac{|E_{x00}|^2}{2(z\lambda)^2 \eta_0} e^{-2(x_o^2 + y_o^2)/W^2(z)}, \tag{1.32a}$$

where in the far-field limit

$$\lim_{z \to \infty} w(z) = \frac{2z}{k' w_0}. \tag{1.32b}$$

The angular divergence of the beam, θ_{beam}, can be determined from the beam radius and the distance z, as given by

$$\theta_{\text{beam}} = \tan^{-1}\left(\frac{w(z)}{z}\right) \simeq \frac{\lambda}{\pi w_0}. \tag{1.33}$$

As the beam propagates, the far-field intensity distribution is maintained, but the beam broadens and the radiance is attenuated. The beam divergence angle depends inversely on the beam waist in the $z = 0$ plane. Thus, as w_0 increases, the beam becomes more like a plane wave.

With this insight from the far-field case, a general expression for a Gaussian beam can be obtained, based on the Fresnel diffraction formula, in a straightforward manner. Substituting Eq. 1.31 into Eq. 1.26 and using Eq. 1.28, the following result is obtained:

$$E_x(x_o, y_o, z) = \frac{j}{\lambda z} e^{-jk'z}\, e^{-jk'\left(\frac{x_o^2}{2z} + \frac{y_o^2}{2z}\right)}\, \mathcal{F}_{xy}[E_{xGS}(x, y, z)], \tag{1.34a}$$

where

$$E_{xGS}(x, y, z) = \frac{E_{x00}}{\pi w_0^2} e^{-jk'\frac{(x^2 + y^2)}{2q(z)}}. \tag{1.34b}$$

The Fresnel diffraction integral becomes the spatial Fourier transform of a Gaussian spherical wave, E_{xGS}, with a complex radius of curvature, q, given by

$$\frac{1}{q} = \frac{1}{z} - j\frac{2}{k' w_0^2}. \tag{1.35}$$

Performing the spatial Fourier transform, a mathematical expression for a Gaussian beam is obtained:

$$E_x(x_o, y_o, z) = \frac{E_{x00}}{\pi w_0 w(z)} e^{-j(k'z - \psi(z))} e^{-jk' \frac{(x_o^2 + y_o^2)}{2\bar{q}(z)}}, \tag{1.36a}$$

where the following functions are defined as

$$w(z) = w_0 \left[1 + \left(\frac{2z}{k' w_0^2} \right)^2 \right]^{1/2}, \tag{1.36b}$$

$$\psi(z) = \tan^{-1} \left(\frac{2z}{k' w_0^2} \right), \tag{1.36c}$$

and

$$\bar{q}(z) = z + j \frac{k' w_0^2}{2}. \tag{1.36d}$$

Examining the real and imaginary parts of $q(z)$, we obtain the following more meaningful expression:

$$\frac{1}{\bar{q}(z)} = \frac{1}{R(z)} - j \frac{2}{k' w^2(z)}. \tag{1.37}$$

An explicit expression for $R(z)$ is the point of Problem 1.8. Now the Gaussian spherical-beam electric field becomes

$$E_x(x_o, y_o, z) = \frac{E_{x00}}{\pi w_0 w(z)} e^{-j(k'z - \psi(z))} e^{-jk' \frac{(x_o^2 + y_o^2)}{2R(z)}} e^{\frac{-(x_o^2 + y_o^2)}{w^2(z)}}. \tag{1.38}$$

$R(z)$ is the radius of curvature of the spherical wave and $w(z)$ is the beam waist as before. The Gaussian beam radiance is

$$L(x_o, y_o, z) = \frac{|E_x(x_o, y_o, z)|^2}{2\eta_0} = \frac{|E_{x00}|^2}{2\pi^2 w_0^2 w^2(z)\eta_0} e^{\frac{-2(x_o^2 + y_o^2)}{w^2(z)}}. \tag{1.39}$$

This describes a Gaussian beam from $z = 0$ to the far field. To see this, consider the far-field limit

$$w(z) \rightarrow \frac{2z}{k' w_0} = \frac{z\lambda}{\pi w_0},$$
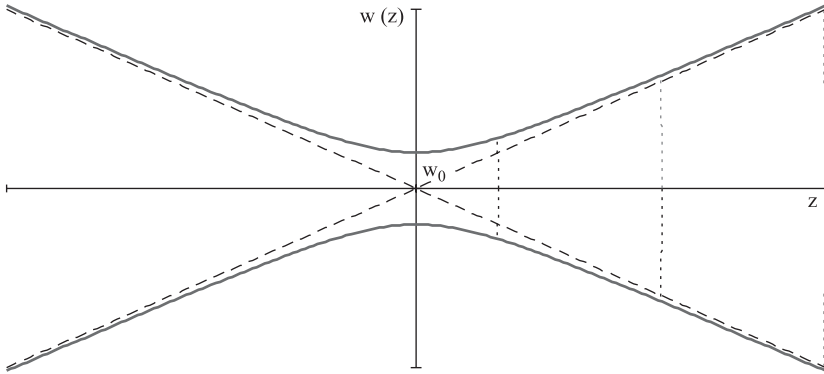
Fig. 1.4 Ray diagram of a Gaussian beam in two dimensions. Dotted lines indicate surfaces of constant phase.

and Eqs. 1.32a and 1.32b are obtained. A ray diagram of a Gaussian beam is illustrated in Fig. 1.4. The dashed curves represent the wavefronts. Notice at the beam waist $(w(z = 0) = w_0)$ the wavefronts are like a plane wave. Farther out, the wavefronts are spherical. The rays are perpendicular to the wavefronts and indicate the direction of the propagating Gaussian beam. Such beams are commonly produced by lasers.

A special beam profile represented by Bessel functions does not expand upon propagation over limited, but useful, distances, and is called a diffraction-free beam (see reference 1.7).

The lesson to be learned from this section is the importance of diffraction on propagation of realistic beams of light over long distances or originating from small apertures. The unbounded plane-wave solution of the previous section cannot be physically realized, although it can be closely approximated over practical distances. The intuitive development of diffraction theory used here is a good introduction, but does not replace more rigorous derivations based on Maxwell's equations (see references 1.2, 1.7, and 1.8). The formulas obtained are adequate for the needs of this text. It can be observed from Fig. 1.4 that the Gaussian beam can be represented by rectilinear rays and plane waves over meaningful regions of the beam. For this reason, most of the emphasis in this text will be on geometrical optics and the quantum nature of the medium and field.

1.3.2 Pulse Propagation

There is great interest today in high-speed pulse propagation. An electromagnetic pulse is composed of many frequencies. In fact, the narrower the pulse in the time domain, the broader it is in the frequency domain. The time–bandwidth product of Fourier transform theory states that

$$\Delta t \Delta f = 1,$$

where Δt is the temporal pulse width and Δf is the frequency bandwidth in hertz. Thus, monochromatic solutions to the wave equation are not appropriate in this case
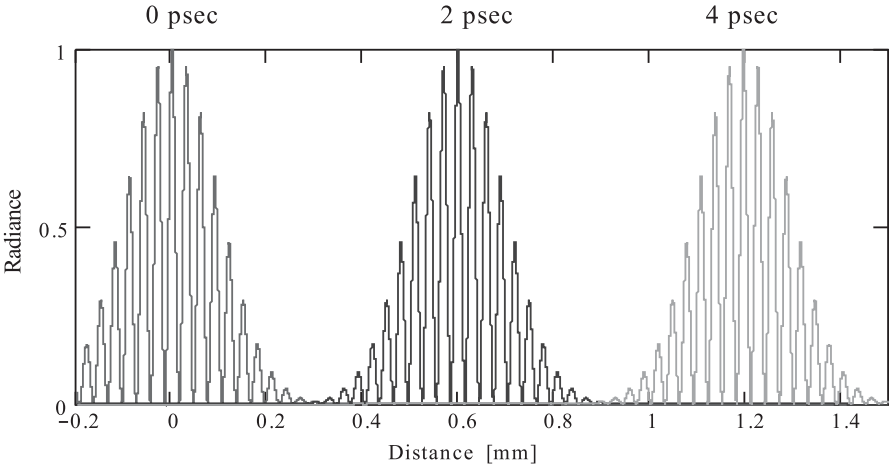
Fig. 1.5 An electromagnetic pulse propagating in free space at three different times.

and new solutions must be found. To this end, it is straightforward to show that a function of the general form

$$f(k'z - \omega t) = E(k'z - \omega t)\, e^{-j(k'z-\omega t)}$$

is a solution to the wave equation, as given by Eq. 1.11. Figure 1.5 plots such a function with an optical frequency carrier at discrete times. The pulse propagates forward in time with a velocity of $\omega/k' = c$, the speed of light in vacuum. Because the propagation medium is vacuum, the pulse propagates undistorted in time and space. Such a result will not be obtained when the propagation medium is matter, especially as the bandwidth increases. Further details can be found in reference 1.12.

Problems

1.1 A photon has an energy of 1 eV. Find the corresponding frequency in GHz, wavelength in μm and wave number in cm^{-1}.

1.2 Show that the free-space plane-wave solutions satisfy Gauss's laws ($\nabla \cdot \mathbf{B} = 0$ and $\nabla \cdot \mathbf{D} = 0$).

1.3 Show that the time average of the time-domain signals $a(t) = |A|\cos(\omega t + \alpha)$ and $b(t) = |B|\cos(\omega t + \beta)$ is given by

$$\langle a(t)b(t)\rangle_t = \frac{1}{2T}\int_{-T}^{T} a(t)b(t)\, dt = \frac{1}{2}\mathrm{Re}\,[AB^*]$$

where $A = |A|\, e^{j\alpha}$ and $B = |B|\, e^{j\beta}$ are the corresponding phasor quantities, respectively, and that the observation time, T, is long compared with the optical period.

1.4 Verify that Eqs. 1.15a–e satisfy Maxwell's equations.

1.5 Verify Eq. 1.15f for the mode density in a finite volume. (*Hint:* Convert the discrete sum to an integral in spherical coordinates. See Milonni and Eberly, reference 1.11, for details.)

1.6 Show that

$$\frac{e^{-jk'r}}{r}$$

is a solution of the wave equation.

1.7 What is the far-field (Fraunhofer) diffraction pattern of the uniformly illuminated rectangular aperture shown in Fig. P1.7.
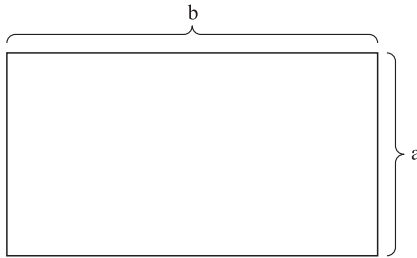
Fig. P1.7

1.8 Derive Eqs. 1.36 and 1.37 and show

$$R(z) = z + \frac{1}{z}\left(\frac{k'w_0^2}{2}\right)^2.$$

1.9 Show that Eq. 1.39 is consistent with the far-field formula given by Eq. 1.32a.

1.10 Verify that Eq. 1.40 is a solution to the wave equation as given by Eq. 1.7.

Notes

1 Engineers commonly choose $e^{-j\omega t}$ and physicists $e^{i\omega t}$. It is important to be consistent with the time harmonic choice of the field.

2 Phasor notation requires assuming a time-harmonic field

$$e_x(r,t) = \text{Re}\left[e_x(r)\,e^{hit}\right].$$

Using Eq. 1.10, over a finite bandwidth, and Eq. 1.14,

$$e_x(z,t) = \text{Re}\left[E_{x0}\,|\Delta f|\,e^{j\omega\left(t-\frac{z}{c}\right)}\right]$$

$$= e_{x0}\cos\omega\left(t - \frac{z}{c}\right).$$

In the following, a unit bandwidth is assumed. Therefore, the frequency-domain amplitude can be equated to the time-domain amplitude in size and dimension. Again this is consistent with phasor notation.

3 The problem with caustics.

At a focus, geometrical optics breaks down because it predicts an infinite field intensity at the focal point or curve (also called a caustic). To see this consider the figure below and the following equations:

$$dS_1 = (R_1 - d)(R_2 - d)\, d\theta d\phi$$

and

$$dS_2 = R_1 R_2 \, d\theta d\phi.$$

In geometrical optics the intensity is proportional to the ray density per unit area, thus the ratio of dS_2 to dS_1 is of interest. The ratio of intensities at surface A to surface B (see figure below) is proportional to

$$\frac{I_1}{I_2} = \left(1 - \frac{d}{R_1}\right)\left(1 - \frac{d}{R_2}\right).$$

At the focal line Q', $R_2 = 0$ and the intensity ratio goes to infinity, which is not physical. Diffraction theory is needed to resolve this limitation.
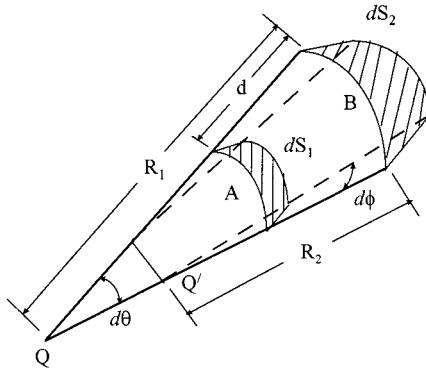
4 The paraxial ray approximation is not necessary for the Fraunhofer diffraction integral, but is useful for the description of beam propagation, the topic of the next section. A more general Fraunhofer diffraction integral is obtained by examining the distance from the source to the field point in three dimensions, as given by

$$r = |\mathbf{r} - \mathbf{r}_o| = \sqrt{(z - z_o)^2 + (x - x_o)^2 + (y - y_o)^2},$$

where $\mathbf{r}$ represents the source coordinates and $\mathbf{r}_o$ represents the field or observer coordinates. This expression can be rewritten, in general, as

$$r = |\mathbf{r}_o|\left(1 - 2\frac{\mathbf{r} \cdot \mathbf{r}_o}{|\mathbf{r}_o|^2} + \frac{|\mathbf{r}|^2}{|\mathbf{r}_o|^2}\right)^{1/2}.$$

It can be further simplified by a binomial expansion for $|\mathbf{r}_o|$ large to be

$$r \underset{z \to \infty}{\cong} |\mathbf{r}_o| - \frac{\mathbf{r} \cdot \mathbf{r}_o}{|\mathbf{r}_o|} + O\left(\frac{1}{|\mathbf{r}_o|^2}\right).$$

Because the dimensions of the source are much smaller than the observer distance in the far field, the last term in $|\mathbf{r}|^2$ can be dropped. The Fraunhofer diffraction integral, in general, then becomes (see reference 1.2)

$$E_x(\mathbf{r_o},\omega) = \frac{jz}{\lambda|\mathbf{r_o}|r} \mathrm{e}^{-jk'|r_o|} \int\limits_{-\infty}^{\infty} dx \int\limits_{-\infty}^{\infty} dy\, E_{x0}(\mathbf{r})\mathrm{e}^{jk'\frac{\mathbf{r}\cdot\mathbf{r_o}}{|\mathbf{r_o}|}}.$$

Applying the paraxial ray approximation to the above formula leads directly to Eq. 1.29.

Bibliography

1.1   W.H. Hayt, Jr., *Engineering Electromagnetics*, McGraw-Hill (1981), Ch. 11.

1.2   J.D. Jackson, *Classical Electrodynamics*, 2nd Ed., Wiley (1975).

1.3   R.F. Harrington, *Time-Harmonic Electromagnetic Fields*, McGraw-Hill (1961).

1.4   H.C. Van de Hulst, *Light Scattering by Small Particles*, Dover (1981).

1.5   J.W. Goodman, *Introduction to Fourier Optics*, McGraw-Hill (1968).

1.6   A.E. Siegman, *Lasers*, University Science Books (1986).

1.7   M. Nieto-Vesperinas, *Scattering and Diffraction in Physical Optics*, Wiley (1991) (see Ch. 2 for diffraction-free beams).

1.8   M. Born and E. Wolf, *Principles of Optics*, 6th Ed., Pergamon Press (1987).

1.9   B.E.A. Saleh and M.C. Teich, *Fundamentals of Photonics*, Wiley (1991).

1.10 J.W. Goodman, *Statistical Optics*, Wiley-Interscience (1985).

1.11 P.W. Milonni and J.H. Eberly, *Lasers*, Wiley (1988).

1.12 K.E. Oughstun and G.C. Sherman, *Electromagnetic Pulse propagation in Causal Dielectrics*, Springer-Verlag (1994).

This page intentionally left blank

2

Optical Electromagnetics II

In this chapter the same basic topics are addressed as in the previous chapter, but now in the presence of matter. This greatly complicates the description of optical propagation and continues to be the primary topic of the remaining chapters. A formal structure is developed to handle absorption and scattering phenomena in general. The modeling of optical propagation is reduced to having to know the complex index of refraction of the medium.

2.1 Macroscopic Properties in Matter

A macroscopic description represents the large-scale observable character of optical propagation. At this level, many models are phenomenological, but lead to important general properties, definitions, formulas, and the establishment of basic concepts. Because microscopic models to be presented in future chapters contain considerable detail, this section is an important prerequisite to the remaining text.

2.1.1 Plane-Wave Propagation and Linear Response Theory

Again, plane waves are a useful tool for the description of optical propagation. The Poynting vector, causality, and Poynting's theorem are used to develop and derive quantities and relationships concerning radiometry and the flow of electromagnetic power at optical frequencies.

2.1.1.1 Maxwell's Equations in an Unbounded Medium

Consider Maxwell's equations again, but in the presence of linear isotropic matter. Now the constitutive relations will play a more important role and are the foundation of

classical dispersion theory. Recall, Maxwell's equations in the time domain and in differential form:

$$\text{Faraday's law:} \quad \nabla \times \mathbf{e}(\mathbf{r},t) = -\frac{\partial \mathbf{b}(\mathbf{r},t)}{\partial t}, \tag{2.1}$$

$$\text{Ampere's law:} \quad \nabla \times \mathbf{h}(\mathbf{r},t) = \mathbf{j}(\mathbf{r},t) + \frac{\partial \mathbf{d}(\mathbf{r},t)}{\partial t}, \tag{2.2}$$

and

$$\nabla \cdot \mathbf{d}(\mathbf{r}, t) = \rho(r,t), \tag{2.3}$$

Gauss's laws:

$$\nabla \cdot \mathbf{b}(\mathbf{r},t) = 0 \tag{2.4}$$

with the time-domain constitutive relations given by

$$\mathbf{j}(\mathbf{r},t) = \sigma_t(\mathbf{r},t) * \mathbf{e}(\mathbf{r},t) = \int_{-\infty}^{\infty} dt' \sigma_t(\mathbf{r},t') \, \mathbf{e}\,(\mathbf{r},t - t'), \quad t > t', \tag{2.5}$$

$$\mathbf{b}(\mathbf{r},t) = \mu_t(\mathbf{r},t) * \mathbf{h}(\mathbf{r},t), \tag{2.6}$$

and

$$\mathbf{d}\,(\mathbf{r},t) = \epsilon_t(\mathbf{r},t) * \mathbf{e}(\mathbf{r},t)\,. \tag{2.7}$$

σ_t, μ_t, and ϵ_t are the phenomenological time-domain conductivity, permeability, and permittivity, respectively, and are scalars because the medium is assumed isotropic. Anisotropic media require σ_t, μ_t, and ϵ_t to be dyadic, and this issue is addressed in Chapter 4. The "*" operator signifies convolution as defined by Eq. 2.5. The relationships between the free-space constants μ_0 and ϵ_0, and μ_t and ϵ_t are given by

$$\mu_t(\mathbf{r},t) = \mu_0 \mu_r(\mathbf{r},t) \text{ [H/m sec]} \quad \text{and} \quad \epsilon_t(\mathbf{r},t) = \epsilon_0 \epsilon_r(\mathbf{r},t) \text{ [F/m sec]}, \tag{2.8}$$

where $\mu_r(\mathbf{r},t)$ and $\epsilon_r(\mathbf{r},t)$ are the relative causal time-domain permeability and relative causal time-domain permittivity, respectively, and have units of reciprocal time. σ_t has MKS units of mhos per meter second ($\mho$/(m sec)). For example, a material with an instantaneous response for the permittivity has the following approximate form:

$$\epsilon_t(\mathbf{r},t) \approx \epsilon_0 \left[\delta(t) - \chi(\mathbf{r}) \frac{d\delta(t)}{dt} h(t) \right],$$

where $\chi(\mathbf{r})$ is the electric susceptibility, $\delta(t)$ is the Dirac delta function, and $h(t)$ is the Heaviside step function. Since the constitutive parameters are driven by oscillating

fields, they also oscillate in time. Time-dependent properties of these quantities are addressed in the next section. Because of the complexity of the convolution relationship between fields, time-domain solutions of Maxwell's equations are not commonly attempted. For this reason, most of the analysis presented here will be in the frequency domain. However, high-speed and large-bandwidth systems can only be effectively handled in the time domain. For this reason, computational procedures, such as finite-difference–time-domain (FD-TD) technique, are emerging (see Ref. 2.3).

The Fourier transform of these time-domain constitutive parameters produces frequency-domain parameters as given by

$$\mathscr{F}\{\epsilon_t(\mathbf{r},t)\} = \epsilon(\mathbf{r}, \omega), \qquad \mathscr{F}\{\mu_t(\mathbf{r},t)\} = \mu(\mathbf{r},\omega), \qquad \mathscr{F}\{\sigma_t(\mathbf{r},t)\} = \sigma(\mathbf{r}, \omega).$$

The frequency-domain parameters have the time dimension removed, thus $\epsilon_r(\omega)$ and $\mu_r(\omega)$ are dimensionless quantities and $\sigma(\omega)$ has dimensions of mhos per meter. Only general macroscopic properties of these parameters will be examined at this time. A more detailed microscopic development is presented in Chapter 5.

The constitutive relations greatly complicate a time-domain solution of Maxwell's equations. For this reason, a frequency-domain solution is preferred because the convolution integrals are not needed. The Fourier transform of the above equations and the substitution of the constitutive relations into Maxwell's equations results in the following:

$$\nabla \times \mathbf{E}(\mathbf{r},\omega) = -j\omega\mu(\mathbf{r},\omega)\mathbf{H}(\mathbf{r},\omega), \tag{2.9}$$

$$\nabla \times \mathbf{H}(\mathbf{r},\omega) = \sigma(\mathbf{r},\omega)\mathbf{E}(\mathbf{r},\omega) + j\omega\,\epsilon(\mathbf{r},\omega)\mathbf{E}(\mathbf{r},\omega), \tag{2.10}$$

$$\nabla \cdot \epsilon(\mathbf{r},\omega)\mathbf{E}(\mathbf{r},\omega) = \rho(\mathbf{r},\omega), \tag{2.11}$$

and

$$\nabla \cdot \mu(\mathbf{r},\omega)\mathbf{H}(\mathbf{r},\omega) = 0. \tag{2.12}$$

Taking the curl of Faraday's law, one obtains the frequency-domain wave equation for the electric field, $\mathbf{E}$

$$\nabla \times \frac{1}{\mu}\nabla \times \mathbf{E}(\mathbf{r},\omega) = (-j\omega\sigma + \omega^2\epsilon)\mathbf{E}(\mathbf{r},\omega). \tag{2.13}$$

The following assumptions are now made:

1. ϵ, μ, and σ vary slowly with $\mathbf{r}$ such that spatial derivatives of ϵ, μ, and σ can be ignored.
2. $\rho = 0$, the medium contains no net volume charge.

Then, Eq. 2.13 reduces to the frequency-domain wave equation,

$$\nabla^2\mathbf{E}(\mathbf{r},\omega) = (j\omega\mu(\omega)\sigma(\omega) - \omega^2\mu(\omega)\,\epsilon(\omega))\mathbf{E}(\mathbf{r},\omega) = \gamma^2(\omega)\,\mathbf{E}(\mathbf{r},\omega), \tag{2.14}$$

where $\gamma(\omega)(= -jk'(\omega))$ is called the propagation constant. In complex form, it is given by

$$\gamma(\omega) = j\omega\sqrt{\mu(\omega)\epsilon(\omega)\left(1 - j\frac{\sigma(\omega)}{\omega\epsilon(\omega)}\right)} = \beta_{fa}(\omega) + j\alpha_{fp}(\omega) \tag{2.15}$$

where $\beta_{fa}(\omega)$ is the field absorption coefficient and $\alpha_{fp}(\omega)$ is the field phase coefficient. To simplify the notation, define

$$\epsilon_c(\omega) = \epsilon_r(\omega)\left(1 - j\frac{\sigma(\omega)}{\omega\epsilon(\omega)}\right). \tag{2.16}$$

$\epsilon_c(\omega)$ is a generalized permittivity, which includes contributions from free charges (via the conductivity, $\sigma(\omega)$) and bound charges (via the relative permittivity, $\epsilon_r(\omega)$). It is important to distinguish between these two very different processes. In the frequency domain, all the constitutive parameters are also complex quantities. Therefore, the propagation constant now becomes

$$\gamma(\omega) = j\frac{\omega}{c}\sqrt{\mu_r(\omega)\epsilon_c(\omega)}. \tag{2.17}$$

As in Chapter 1, let $\mathbf{E}(\mathbf{r},\omega)$ be polarized in the x-direction and propagate in the z-direction. Then a scalar wave equation is obtained:

$$\nabla^2 E_x(z,\omega) = \gamma^2(\omega)E_x(z,\omega). \tag{2.18}$$

The solution for monochromatic forward-propagating light is

$$E_x(z,\omega) = E_{x0}e^{-\gamma(\omega)z} = E_{x0}e^{-\beta_{fa}(\omega)z}e^{-j\alpha_{fp}(\omega)z} \tag{2.19a}$$

where $E_{x0} = E_x(z = 0)$. In the time domain, the steady-state solution becomes

$$e_x(z,t) = e_{x0}\,e^{-\beta_{fa}z}\cos(\omega t - \alpha_{fp}z).$$

This field is attenuated and delayed or phase shifted as it propagates and the meaning of $\beta_{fa}(\omega)$ and $\alpha_{fp}(\omega)$ is now more clear. For arbitrary polarization and propagation directions, the forward-propagating polychromatic electric field is expressed as

$$\mathbf{E}(\mathbf{r},\omega) = \sum_m \mathbf{E}_m(\omega_m)\,e^{-j\mathbf{k}'(\omega_m)\cdot\mathbf{r}}. \tag{2.19b}$$

Again, optical detectors measure the time-averaged power. Thus, the time-averaged Poynting vector is of interest, as defined by (recall Eq. 1.18)

$$\langle \mathfrak{L}(t)\rangle_t = \frac{1}{2}\mathrm{Re}\left[E_x(\omega)H_y^*(\omega)\right]\hat{\mathbf{z}} \quad \left[\text{watts}/(\text{m}^2\text{sr})\right]. \tag{2.20}$$

To derive H_y in terms of the electric field intensity, we use Faraday's law and obtain,

$$H_y = \sqrt{\frac{\epsilon_0 \epsilon_c}{\mu}} E_x = \frac{1}{\eta_c} E_x. \tag{2.21}$$

Using these results, the magnitude of the time-averaged Poynting vector is the frequency-domain radiance, $L(z,\omega)$, which, in terms of the electromagnetic field becomes

$$L(z,\omega) = |\langle \mathcal{L}(z,t) \rangle_t| = \frac{1}{2} \text{Re} \left[\frac{1}{\eta_c^*(\omega)} \right] |E_{x0}|^2 \, e^{-2\beta_{fa}(\omega)z}. \tag{2.22}$$

Most media in which light propagates are nonmagnetic, with $\mu = \mu_0$. Then, the intrinsic impedance simplifies to

$$\frac{1}{\eta_c} = \frac{1}{\eta_0} \sqrt{\epsilon_c}. \tag{2.23}$$

It is of interest to find the real and imaginary parts of the propagation constant, β_{fa} and α_{fp}, in terms of the generalized permittivity. Using Eq. 2.17, we have

$$\beta_{fa} = \text{Re} \left(j \frac{\omega}{c} \sqrt{\epsilon_c} \right) \quad \text{and} \quad \alpha_{fp} = \text{Im} \left(j \frac{\omega}{c} \sqrt{\epsilon_c} \right).$$

It is convenient to define a new parameter representing the dielectric properties of a medium, the complex index of refraction, n_c, by

$$\bar{n}_c = n - jk_a = \sqrt{\epsilon_c} = \sqrt{\epsilon_c' - j\epsilon_c''} \tag{2.24}$$

where n is the index of refraction, k_a is the index of absorption (also called the extinction coefficient in some publications), ϵ_c' is the real part of the relative permittivity and ϵ_c'' is the imaginary part of the relative permittivity. Now, the field absorption and phase coefficients become

$$\beta_{fa} = \frac{\omega}{c} k_a \quad \text{and} \quad \alpha_{fp} = \frac{\omega}{c} n. \tag{2.25}$$

The meaning of n and k_a is similar to α_{fp} and β_{fa}, respectively; n contributes to phase effects during propagation (e.g., time delay) and k_a contributes to attenuation of the propagating beam caused by absorption. The complex index of refraction affects refraction and reflection, as will be demonstrated later. Substituting these results into Eq. 2.22, the radiance now becomes

$$L(z,\omega) = n(\omega) \frac{|E_{x0}|^2}{2\eta_0} \exp \left(-\frac{2\omega k_a}{c} z \right). \tag{2.26}$$

The radiance at $z = 0$, $L(0,\omega)$, is

$$L(z = 0,\omega) = n(\omega)\frac{|E_{x0}|^2}{2\eta_0}. \tag{2.27}$$

The transmittance in an unbounded medium, $\tau_\infty(z,\omega)$, is therefore defined as

$$\tau_\infty(z,\omega) = \frac{L(z,\omega)}{L(0,\omega)} = e^{-2\beta_{fa}(\omega)z}. \tag{2.28}$$

The transmittance is dimensionless and always between zero and one. The power absorption coefficient, $\beta_{pa}(z, \omega)$, is defined as

$$\beta_{pa}(\omega) = 2\beta_{fa}(\omega) = 2\frac{\omega}{c}k_a(\omega) = \frac{\omega}{cn(\omega)}\epsilon_c''(\omega). \tag{2.29}$$

Normally β_{pa} is called the absorption coefficient and the subscript p will be dropped. It is a fundamental quantity concerning the description of optical propagation. Expressed in terms of wave numbers, $\beta_{abs}(\nu)$ becomes

$$\beta_{abs}(\nu) = 4\pi\nu k_a(\nu) = \frac{2\pi\nu}{n(\nu)}\epsilon_c''(\nu). \tag{2.30}$$

2.1.1.2 Temporal Dispersion and Causality

The fact that a medium cannot respond to the incident light field or power until after it has been illuminated is called causality. This fundamental requirement produces important symmetry properties and integral relationships between the real and imaginary parts of the complex permittivity and mathematical relationships between the real and imaginary parts of the complex index of refraction. These results will be of great use later.

Another definition of the complex relative permittivity, in terms of the complex electric susceptibility, χ, is given by

$$\epsilon_r(\omega) = 1 + \chi(\omega), \tag{2.31}$$

and

$$\epsilon_r'(\omega) - j\epsilon_r''(\omega) = 1 + \chi'(\omega) - j\chi''(\omega). \tag{2.32}$$

Also, the constitutive relation given by Eq. 2.7 is redefined using the polarization vector in the time domain, $\mathbf{p}(\mathbf{r},t)$,

$$\mathbf{d}(\mathbf{r},t) = \epsilon_0\mathbf{e}(\mathbf{r},t) + \mathbf{p}(\mathbf{r},t) \tag{2.33}$$

where

$$\mathbf{p}(\mathbf{r},t) = \epsilon_0\chi_t(\mathbf{r},t) * \mathbf{e}(\mathbf{r},t). \tag{2.34}$$

$\chi_t(\mathbf{r},t)$ represents the time-domain response of a passive medium to the electric field. Causality requires this response to come after the field excites the medium. Thus $\chi_t(t)$ (the spatial dependence of χ is suppressed, since it is not relevant to the remaining discussion) must contain a "turn on" function to account for causality. Therefore, for positive values of time

$$\chi_t(t) = h(t)\chi(t) \tag{2.35}$$

where $\chi(t)$ is the dimensionless time-domain susceptibility and is a real function. $h(t)$ is the Heaviside step-function in units of reciprocal time and is given by

$$h(t) = \frac{1}{2}(1 + \mathrm{sgn}(t)) = \begin{cases} 0 & t < 0 \\ \frac{1}{2} & t = 0 \\ 1 & t > 0. \end{cases} \tag{2.36}$$

The frequency-domain susceptibility is the Fourier transform of the time-domain susceptibility (Eq. 2.35) and becomes

$$\chi(\omega) = \mathscr{F}\{\chi_t(t)\} = \int_0^\infty dt\,\chi(t)\,e^{-j\omega t}. \tag{2.37}$$

This result leads to the following important properties:

1. The static susceptibility is the integral of the material response function over all positive time. That is,

$$\chi(\omega = 0) = \int_0^\infty dt\,\chi(t). \tag{2.38}$$

   Therefore, the true static susceptibility requires an infinite observation time.
2. Based on Eq. 2.37 and the fact that $\chi(t)$ is real, we obtain the following symmetry of the frequency-domain susceptibility about the origin of the frequency axis,

$$\chi(\omega) = \chi^*(\epsilon\omega), \quad \chi'(\omega) = \chi'(-\omega), \quad \text{and} \quad \chi''(\omega) = -\chi''(-\omega). \tag{2.39a}$$

The real part of the susceptibility is an even function of ω, and the imaginary part is an odd function. For the permittivity, based on Eq. 2.32, similar statements can be made:

$$\epsilon_r(\omega) = \epsilon_r^*(-\omega), \quad \epsilon_r'(\omega) = \epsilon_r'(-\omega), \quad \text{and} \quad \epsilon_r''(\omega) = -\epsilon_r''(-\omega). \tag{2.39b}$$

Based on these results the static susceptibility must be real. Furthermore, it similarly follows that the complex index of refraction must have the following symmetry relationships:

$$\bar{n}(\omega) = \bar{n}^*(-\omega), \quad n(\omega) = n(-\omega), \quad \text{and} \quad k_a(\omega) = -k_a(-\omega). \tag{2.39c}$$

These symmetry properties are illustrated in Fig. 2.1 for a medium with Debye, vibrational, and electronic transitions, and are fundamental to realistic models of
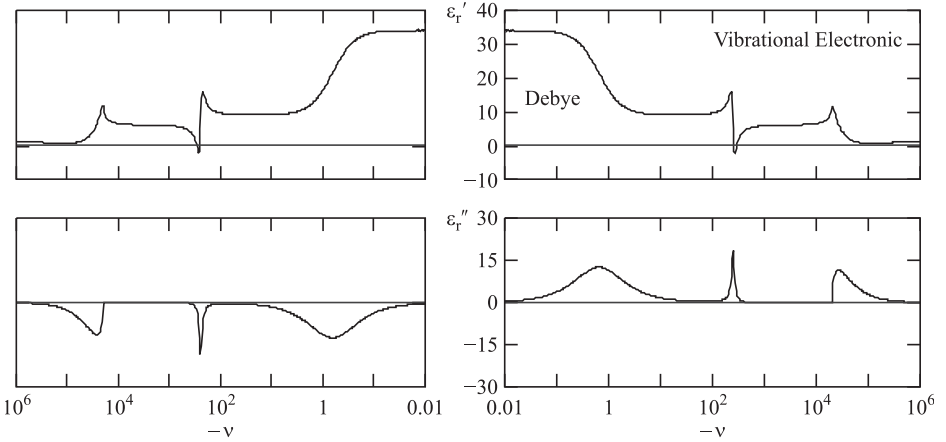
Fig. 2.1 The complex permittivity as a function of frequency representing various resonances in a medium.

the susceptibility. More details concerning these different transitions will be presented in Chapters 3 and 4. The symmetry of $\chi(\omega)$ forces the shape of absorption and emission (time-reversed) processes to be matched. This symmetry requirement is a part of what is called *detailed balance*.

The inverse transform of Eq. 2.37 can be expressed as the sum of a cosine transform and a sine transform, as given by

$$\chi_t(t) = \frac{1}{2\pi} \int\limits_{-\infty}^{\infty} d\omega \, \chi'(\omega) \cos(\omega t) + \frac{1}{2\pi} \int\limits_{-\infty}^{\infty} d\omega \, \chi''(\omega) \sin(\omega t). \qquad (2.40)$$

The cosine transform is even in t, and the sine transform is odd in t. That is, the time-domain susceptibility can be expressed as a sum of an even function, $\chi_{te}(t)$, and an odd function, $\chi_{to}(t)$, thus

$$\chi_t(t) = h(t)\chi(t) = \chi_{te}(t) + \chi_{to}(t).$$

Because the time-domain susceptibility is causal, it must be zero for $t < 0$. This means the even and odd susceptibility functions must be equal for positive time so that they cancel for negative time. This also implies that the noncausal susceptibility can be expressed as

$$\chi(t) = 2\chi_{to}(t) = 2\chi_{to}(t) \quad \text{for } t \geq 0. \qquad (2.41)$$

This result is useful because the time-domain susceptibility can now be determined from either the real or imaginary parts of the frequency-domain susceptibility.

The frequency-domain representation of $\chi(\omega)$ is also given by a convolution of the time-domain components given in Eq. 2.35,

$$\chi(\omega) = \mathcal{F}\{h(t)\} * \mathcal{F}\{\chi(t)\}. \qquad (2.42)$$

The Fourier transform of the Heaviside step function is a well-known result given by

$$\mathcal{F}\{h(t)\} = \frac{1}{2}\delta(\omega) - \frac{j}{2}\frac{P}{\pi\omega}. \tag{2.43}$$

P indicates the Cauchy principle value integral operator and $\delta(\omega)$ is the Dirac delta function. Substituting this result into Eq. 2.42 and recalling that $f(x) * \delta(x) = f(x)$, one obtains

$$\chi(\omega) = -P\left[\frac{1}{\pi\omega} * \frac{j}{2}\mathcal{F}\{\chi(t)\}\right] - j\left[\frac{j}{2}\mathcal{F}\{\chi(t)\}\right]. \tag{2.44}$$

The time symmetry of $\chi(t)$ is odd (i.e., $\chi(t) = -\chi(-t)$). This statement is supported by the following arguments. Negative time represents time reversal or, in this case, emission (time-reversed absorption). The negative sign indicates that population inversion exists in the medium and that the *gain coefficient* is the negative of the *absorption coefficient*. Emission is a source to the field. Thus, using the time-domain Maxwell's equations together with Eqs. 2.33 and 2.34, the following form of the wave equation in a nonconducting medium is obtained:

$$\nabla^2\mathbf{e} + \frac{1}{c^2}\frac{\partial^2\mathbf{e}}{\partial t^2} = \frac{1}{\epsilon_0 c^2}\frac{\partial^2\mathbf{p}_a}{\partial t^2} - \frac{1}{\epsilon_0 c^2}\frac{\partial^2\mathbf{p}_e}{\partial t^2}, \tag{2.45}$$

where the subscript a indicates absorption and the subscript e indicates emission. $\mathbf{p}_a$ is a sink to the field and $\mathbf{p}_e$ is a source to the field, and using Eq. 2.34, this justifies the symmetry relationship of $\chi(t)$. Causality must also be present for emission, but now the Heaviside step function is zero for positive time and unity for negative time. Therefore, the time reversal of the turn on function must be

$$h(-t) = [1 - h(t)].$$

Based on these arguments, the time-domain response function $\chi_t(t)$ in the time-reversed sense ($t < 0$) must be

$$\chi_t(t) = [1 - h(t)]\chi(t).$$

The odd symmetry of $\chi(t)$ now produces a negative $\chi_t(t)$ as desired.

The Fourier transform of $\chi(t)$ is pure imaginary and therefore only the sine transform exists, as given by

$$\mathcal{F}\{\chi(t)\} = -j\mathcal{F}_s\{\chi(t)\} \tag{2.46}$$

where the subscript s indicates a Fourier sine transform. Substitution of these results into Eq. 2.44 and equating real and imaginary parts, gives

$$\chi''(\omega) = \frac{1}{2}\mathcal{F}_s\{\chi(t)\} \tag{2.47a}$$

and

$$\chi'(\omega) = -P\left[\frac{1}{\pi\omega} * \chi''(\omega)\right]. \tag{2.47b}$$

Writing out the convolution integral leads to

$$\chi'(\omega) = \frac{1}{\pi}P\int_{-\infty}^{\infty} d\omega' \frac{\chi''(\omega')}{\omega' - \omega} = \mathrm{Hi}\left\{\chi''(\omega')\right\}. \tag{2.48a}$$

This integral relationship between the real and imaginary parts of the susceptibility is called a Hilbert transform, Hi{ }, or the Kramers–Krönig relation and is fundamental to realistic models. The inverse transform is given by

$$\chi''(\omega') = \frac{1}{\pi}P\int_{-\infty}^{\infty} d\omega \frac{\chi'(\omega)}{\omega' - \omega} = \mathrm{Hi}^{-1}\left\{\chi'(\omega)\right\}. \tag{2.48b}$$

These relations can also be applied to the permittivity, based on Eq. 2.31, to obtain

$$\epsilon_r'(\omega) - 1 = \mathrm{Hi}\left\{\epsilon_r''(\omega')\right\} \tag{2.49a}$$

and

$$\epsilon_r''(\omega') = \mathrm{Hi}^{-1}\{\epsilon_r'(\omega) - 1\}. \tag{2.49b}$$

This causal relationship must also hold between the components of the complex index of refraction, thus

$$n(\omega) - 1 = \mathrm{Hi}\left\{k_a(\omega')\right\} \tag{2.50a}$$

and

$$k_a(\omega') = \mathrm{Hi}^{-1}\{n(\omega) - 1\}. \tag{2.50b}$$

Using the symmetry properties of $\chi'(\omega)$ and $\chi''(\omega)$, the single-sided Hilbert transform becomes

$$\chi'(\omega) = \frac{2}{\pi}P\int_{0}^{\infty} d\omega' \frac{\omega'\chi''(\omega')}{\omega'^2 - \omega^2}, \tag{2.51a}$$

with the corresponding inverse transform given by

$$\chi''(\omega') = \frac{2}{\pi}\omega'P\int_{0}^{\infty} d\omega \frac{\chi'(\omega)}{\omega'^2 - \omega^2}. \tag{2.51b}$$

The single-sided Hilbert transform for the complex index of refraction follows similarly and is

$$n(\omega) - 1 = \frac{2}{\pi} P \int_0^\infty d\omega' \frac{\omega' k_a(\omega')}{\omega'^2 - \omega^2}, \tag{2.52a}$$

with the inverse transform given by

$$k_a(\omega') = \frac{2}{\pi} \omega' P \int_0^\infty d\omega \frac{n(\omega) - 1}{\omega'^2 - \omega^2}. \tag{2.52b}$$

These are fundamental relationships of any causal system.

Because of the odd symmetry of $\chi(t)$, it must equal zero at $t = 0$. Thus, $\chi_t(t = 0) = 0$, also. Using this result with the inverse transform of Eq. 2.40, we obtain the following integral relationship for $\chi'(\omega)$ and $\epsilon_r'(\omega)$:

$$\int_{-\infty}^\infty d\omega \, \chi'(\omega) = \int_0^\infty d\omega \, \chi'(\omega) = 0 = \int_0^\infty d\omega \left[\epsilon_r'(\omega) - 1 \right]. \tag{2.53a}$$

This is a practical test for any physical model of the refractive index. In a similar fashion, it can also be shown that for the real part of the index of refraction, the following is true:

$$\int_0^\infty [n(\omega) - 1] \, d\omega = 0. \tag{2.53b}$$

This is an interesting result that shows that the real part of the susceptibility and index of refraction has equal area above and below unity. Based on Fig.2.1, the permittivity above electronic transitions (x-ray region and above) is less than one, and asymptotically approaches one as ω goes to infinity.

Also, based on Eqs. 2.51a and 2.52a, the following relationships for the static susceptibility and for static index of refraction are obtained:

$$\chi'(\omega = 0) = \frac{2}{\pi} \int_0^\infty d\omega' \frac{\chi''(\omega')}{\omega'} \tag{2.54a}$$

and

$$n(\omega = 0) - 1 = \frac{2}{\pi} \int_0^\infty d\omega' \frac{k_a(\omega')}{\omega'}$$

$$= \frac{c}{\pi} \int_0^\infty d\omega' \frac{\beta_{abs}(\omega')}{\omega'^2}, \tag{2.54b}$$

where Eq. 2.29 was used to obtain the last equation.

Practical models, to be developed later, are required to satisfy these fundamental symmetry properties and integral relationships of temporal dispersion and linear response theory.

2.1.1.3 Poynting's Theorem and Conservation of Power Flow

Previous discussion concerned propagation in unbounded media and macroscopic properties of the media. Realistic theories must include the effect of boundaries, and this greatly complicates the problem of characterizing propagation.

Consider a bounded linear isotropic medium in the presence of an external optical source, as shown in Fig. 2.2. The flow of optical power through the medium must be conserved. A precise mathematical statement is obtained from Poynting's theorem. We begin with the time-domain Ampere's and Faraday's laws, and manipulate them in the following way:

$$\nabla \times \mathbf{e} \cdot \mathbf{h} = -\left(\frac{\partial \mathbf{b}}{\partial t}\right) \cdot \mathbf{h} \qquad (2.55a)$$

and

$$\mathbf{e} \cdot \nabla \times \mathbf{h} = \mathbf{e} \cdot \mathbf{j} + \mathbf{e} \cdot \left(\frac{\partial \mathbf{d}}{\partial t}\right). \qquad (2.55b)$$

Subtract Eq. 2.55b from 2.55a and apply the following identity:

$$\nabla \cdot (\mathbf{e} \times \mathbf{h}) = (\nabla \times \mathbf{e}) \cdot \mathbf{h} - \mathbf{e} \cdot \nabla \times \mathbf{h}$$

along with the definition of the time-domain radiance, to obtain Poynting's theorem in point form,
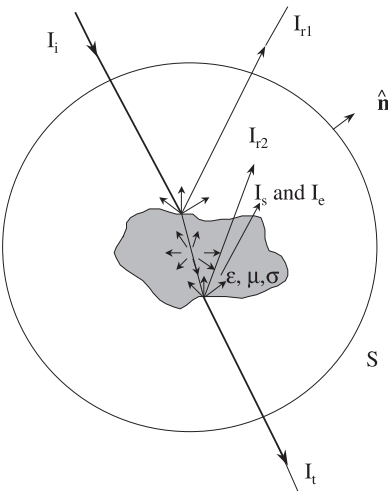
Fig. 2.2 Illuminated finite medium, where ϵ, μ, and σ are scalars. The medium is completely enclosed by a surface S with volume V. Upon propagation through the medium, the illuminating ray generates reflected rays, bulk scattered rays, absorbed rays (which are then emitted), and a transmitted ray.

$$\nabla \cdot \mathscr{L}(t) = -\frac{\partial \mathbf{b}}{\partial t} \cdot \mathbf{h} - \mathbf{e} \cdot \mathbf{j} - \mathbf{e} \cdot \frac{\partial \mathbf{d}}{\partial t}. \tag{2.56}$$

The time-domain version of Poynting's theorem, as given by Eq. 2.56, leads to a continuity equation for power flow, for $\mu = \mu_0$ and $\sigma = 0$ in a lossless medium,

$$\nabla \cdot \mathscr{L}(t) = -\frac{\partial u}{\partial t} = -\frac{n}{c}\frac{\partial |\mathscr{L}(t)|}{\partial t}.$$

where $u(= \frac{1}{2}[(\mathbf{e} \cdot \mathbf{d}) + (\mathbf{b} \cdot \mathbf{h})])$ is the stored energy density of the electromagnetic field. This result is useful when transient effects are important. A good example is the propagation of a laser pulse inside a lossy resonator.

The corresponding frequency-domain result of Poynting's theorem is obtained by beginning with Eqs. 2.9 and 2.10, and following the same mathematical procedure as above. Since the time-averaged Poynting vector is ultimately desired, we compute $\mathbf{E} \times \mathbf{H}^*$ and $\mathbf{E}^* \times \mathbf{H}$ and add the results, yielding

$$\nabla \cdot \text{Re}\,[\mathbf{E} \times \mathbf{H}^*] = -(\text{Re}\,[\sigma] + \omega\,\text{Im}\,[\epsilon])|\mathbf{E}|^2 - \omega\,\text{Im}\,[\mu]|\mathbf{H}|^2. \tag{2.57}$$

For a medium with no magnetic loss (i.e., $\text{Im}\,[\mu] = 0$) and using Eqs. 1.18, 2.27, and 2.29, Eq. 2.57 reduces to the following important result concerning electromagnetic propagation,

$$\nabla \cdot \text{Re}\,[\mathbf{E} \times \mathbf{H}^*] = \nabla \cdot \mathbf{L}(\omega, r) = -\frac{1}{2}\omega\epsilon_0\,\text{Im}\,[\epsilon_c(\omega, r)]\,|\mathbf{E}(\omega, r)|^2$$
$$= -\beta_{abs}(\omega, r)L(\omega, r), \tag{2.58}$$

where $\mathbf{L}(\omega)(= \frac{1}{2}\text{Re}\,[\mathbf{E} \times \mathbf{H}^*])$ is the frequency-domain time-averaged Poynting's vector or the spectral radiance vector. This is the frequency-domain continuity equation for time-averaged power flow. For propagation in the z-direction, Eq. 2.26 is a solution to the above equation when β_{abs} is independent of position. Based on Eq. 2.58, the vector radiance is solenoidal if β_{abs} is zero (i.e., there are no sinks). If we also consider a medium with gain and absorption, then a gain coefficient, β_{gain}, must be added as a source to the continuity equation, thus

$$\nabla \cdot \mathbf{L}(\omega, \mathbf{r}) = [-\beta_{abs}(\omega, \mathbf{r}) + \beta_{gain}(\omega, \mathbf{r})]L(\omega, \mathbf{r}). \tag{2.59}$$

Requiring thermal equilibrium, or that the medium is at constant temperature (steady state), means absorption loss and gain must be equal, and the field of rays is again solenoidal. Thus,

$$\nabla \cdot \mathbf{L}(\mathbf{r}, \omega) = 0. \tag{2.60}$$

Within the framework of geometrical optics, this means the number of rays of light entering a point equals the number leaving. This represents the time-averaged or steady-state flow of power through a source-free point. Then, Eq. 2.60 is a statement of conservation of power flow in the form of a source-free steady-state continuity equation in a lossless medium.

Further, consider a surface enclosing the medium and an incident ray upon the medium, as illustrated in Fig. 2.2. The incident ray is reflected at the first and second interface, as represented by $\mathbf{I}_{r1}$ and $\mathbf{I}_{r2}$, respectively. A series of reflected rays is produced with the intensity decreasing as the number of reflections increases. Also, surface roughness increases the angular spread of reflected rays. Scattered rays, $\mathbf{I}_s$, are produced within the medium, due to refractive index fluctuations. Light is also absorbed within the medium, as represented by $\mathbf{I}_a$. The remaining intensity, $\mathbf{I}_t$, is transmitted. The volume integration of Eq. 2.60 over the volume, V, contained within the surface, S, extends the conservation of power flow from a point to a realistic finite medium. Using the divergence theorem, convert the volume integration to a closed surface integration to obtain

$$\iiint_V \nabla \cdot \mathbf{L} \, dV = \oint_S \mathbf{L} \cdot \hat{\mathbf{n}} \, dS = 0. \tag{2.61}$$

The unit vector $\hat{\mathbf{n}}$ points outward perpendicular to the surface, so that incoming rays are negative and outward rays are positive. Let the surface S be a sphere so that $dS = r^2 \sin\theta \, d\theta d\phi = r^2 d\Omega$, where $d\Omega$ is a differential solid angle in units of steradians. Define the spectral radiant intensity vector, $\mathbf{I}(\Omega, \omega)$, as seen by an observer at a distance r from the source, to be

$$\mathbf{I}(\Omega, \omega) = \mathbf{L}(\Omega, \omega) r^2 \quad [\text{watts/(sr unit bandwidth)}]. \tag{2.62}$$

Eq. 2.61 becomes, with the substitution of Eq. 2.62 and conversion to solid-angle integration,

$$\oint_s \mathbf{I}(\Omega, \omega) \cdot \hat{\mathbf{n}} \, d\Omega = 0. \tag{2.63}$$

The net or integrated radiant intensity entering and exiting the surface, S, is the sum of the integrated incident, integrated reflected, integrated scattered, integrated emitted, and integrated transmitted radiant intensity of light, as given by

$$\oint_s \mathbf{I}(\Omega, \omega) \cdot \hat{\mathbf{n}} \, d\Omega = -\oint_s \mathbf{I}_i(\Omega_i, \omega) \cdot \hat{\mathbf{n}} \, d\Omega_i + \oint_s \mathbf{I}_r(\Omega_i, \Omega_r, \omega) \cdot \hat{\mathbf{n}} \, d\Omega_r$$

$$+ \oint_s \mathbf{I}_s(\Omega_i, \Omega_s, \omega) \cdot \hat{\mathbf{n}} \, d\Omega_s + \oint_s \mathbf{I}_e(\Omega_i, \Omega_e, \omega) \cdot \hat{\mathbf{n}} \, d\Omega_e$$

$$+ \oint_s \mathbf{I}_t(\Omega_i, \Omega_t, \omega) \cdot \hat{\mathbf{n}} \, d\Omega_t \tag{2.64}$$

$$= 0$$

where Ω_i is the solid angle of the incident beam, Ω_r is the solid angle of reflection, Ω_s is the solid angle of scatter, Ω_e is the solid angle of emission, and Ω_t is the solid angle of transmission. The magnitude of $\mathbf{I}(\Omega, \omega)$ is the radiometric quantity called the spectral radiant intensity, $I(\Omega, \omega)$ (e.g., $|\mathbf{I}(\Omega, \omega)| = I(\Omega, \omega)$). All unit vectors point in the

outward direction from the volume. The net absorbed intensity, I_a, is assumed to be reradiated, so that the medium does not change temperature (the assumption of thermal equilibrium). Thus, the net time-averaged absorbed power equals the time-averaged integrated emitted power. The reflected light represents surface effects. The scattered radiant intensity represents bulk scattering effects. These intensities are bidirectional frequency-domain quantities which depend on the solid angle of incidence, Ω_i, and the solid angle corresponding to the type of exiting light.

The closed surface integral over the spectral radiant intensity is the corresponding spectral flux, $\Phi(\omega)$, in units of watts per unit bandwidth. Flux is an especially important radiometric quantity because it is directly measurable by common optical detectors. Thus, based on Eq. 2.64, the following definitions are made:

$$\Phi_i(\omega) = \oint_s \mathbf{I}_i(\Omega_\mathbf{i}, \omega) \cdot \hat{\mathbf{n}} \, d\Omega_i \equiv \text{Net incident flux}, \tag{2.65a}$$

$$\Phi_r(\Omega_i, \omega) = \oint_s \mathbf{I}_r(\Omega_\mathbf{i}, \Omega_\mathbf{r}, \omega) \cdot \hat{\mathbf{n}} \, d\Omega_r \equiv \text{Net reflected flux}, \tag{2.65b}$$

$$\Phi_s(\Omega_i, \omega) = \oint_s \mathbf{I}_s(\Omega_\mathbf{i}, \Omega_\mathbf{s}, \omega) \cdot \hat{\mathbf{n}} \, d\Omega_s \equiv \text{Net scattered flux}, \tag{2.65c}$$

$$\Phi_e(\Omega_i, \omega) = \oint_s \mathbf{I}_e(\Omega_\mathbf{i}, \Omega_\mathbf{e}, \omega) \cdot \hat{\mathbf{n}} \, d\Omega_e \equiv \text{Net emitted flux}, \tag{2.65d}$$

and

$$\Phi_t(\Omega_i, \omega) = \oint_s \mathbf{I}_t(\Omega_i, \Omega_t, \omega) \cdot \hat{\mathbf{n}} \, d\Omega_t \equiv \text{Net transmitted flux}. \tag{2.65e}$$

Kirchhoff's radiation law states that the time-averaged power absorbed must equal the time-averaged power emitted for a medium at constant temperature and for no thermal conduction or convection losses. In general, the spectral emitted and absorbed flux must be integrated over all frequencies for this to be true:

$$\int_0^\infty \Phi_e(\Omega_i, \omega) \, d\omega = \int_0^\infty \Phi_a(\Omega_i, \omega) \, d\omega. \tag{2.66}$$

When the emitted and radiated power are in thermal equilibrium (e.g., like a blackbody), then integration over all frequencies is not necessary and the spectral power emitted equals the spectral power absorbed. This can also be true in the narrow spectral band field case if the absorption feature is also narrow band and uncoupled from its environment. Thus, in this case it also true that

$$\Phi_e(\Omega_i, \omega) = \Phi_a(\Omega_i, \omega). \tag{2.67}$$

Substituting these definitions into Eq. 2.64, we obtain

$$\Phi_i = \Phi_r + \Phi_s + \Phi_a + \Phi_t. \tag{2.68}$$

Normalizing this expression relative to the incident flux, the important statement of conservation of power flow is now obtained,

$$1 = \rho(\Omega_i,\omega) + \alpha_{sca}(\Omega_i,\omega) + \alpha_{abs}(\Omega_i,\omega) + \tau(\Omega_i,\omega) \tag{2.69}$$

where the following definitions have been made:

$$\rho(\Omega_i,\omega) = \frac{\Phi_r(\Omega_i,\omega)}{\Phi_i(\omega)} = \text{total integrated reflectance}, \tag{2.70a}$$

$$\alpha_{sca}(\Omega_i,\omega) = \frac{\Phi_s(\Omega_i,\omega)}{\Phi_i(\omega)} = \text{total integrated scatterance}, \tag{2.70b}$$

$$\alpha_{abs}(\Omega_i,\omega) = \frac{\Phi_a(\Omega_i,\omega)}{\Phi_i(\omega)} = \text{total integrated absorptance}, \tag{2.70c}$$

and finally

$$\tau(\Omega_i,\omega) = \frac{\Phi_t(\Omega_i,\omega)}{\Phi_i(\omega)} = \text{total integrated transmittance}. \tag{2.70d}$$

Notice that these quantities are functions of angles of incidence and frequency only. Equation 2.69 is also called the total power law. The sum of total integrated scatterance and total integrated absorptance is generally defined as the *total integrated extinctance*, α_{ext},

$$\alpha_{ext}(\Omega_i,\omega) = \alpha_{abs}(\Omega_i,\omega) + \alpha_{sca}(\Omega_i,\omega). \tag{2.71}$$

Using this result, the total power law becomes

$$1 = \rho(\Omega_i,\omega) + \alpha_{ext}(\Omega_i,\omega) + \tau(\Omega_i,\omega). \tag{2.72}$$

Another useful quantity is the spectral *directional emittance*, which is defined as

$$\epsilon(\Omega_i,\omega) = \frac{\Phi_e(\Omega_i,\omega)}{\Phi_{bb}(\omega)}, \tag{2.73}$$

where Φ_{bb} is the blackbody function representing the spectral emission of a medium which totally absorbs all light at all frequencies in thermal equilibrium (this function will be given explicitly in Chapter 5). When $\Phi_i(\omega) = \Phi_{bb}(\omega)$, and based on Eq. 2.67, the directional emittance equals the total integrated absorptance,

$$\epsilon(\Omega_i,\omega) = \alpha_{abs}(\Omega_i,\omega). \tag{2.74}$$

The above equation is another form of Kirchhoff's law of radiation.

This section has presented the effects of boundaries of finite media on optical propagation, and introduced the definition of several practical quantities. Further discussion of bidirectional quantities will come later.

2.1.1.4 Radiation Transfer Equation Along a Path

Another useful equation governing electromagnetic power flow is the radiation transfer equation (also called radiation transport equation), which is heuristically based on the point form of Poynting's theorem for time-averaged power flow in a homogeneous medium (see Eq. 2.60). In this case, the concept of the continuity equation is used. The radiance vector can be thought of as a current density of directed photons. Also, let the radiance vector in Eq. 2.60 represent only the incident and transmitted radiance. Then the field is no longer solenoidal and must include sinks, due to scattering and absorption along the path, and sources, due to path emission and scattering of external sources into the path. These concepts are illustrated in Fig. 2.3. Also, the point form of Poynting's theorem must be applied carefully, since only the integral form has physical meaning. Therefore, the propagation path is considered finite in size (macroscopic) and can be represented by a series of connected spheres along a specified path, as shown in Fig. 2.3. The point form is the limit of the spheres shrinking to a point, and therefore an approximation. Based on this discussion, consider the following form of Eq. 2.60:

$$\nabla \cdot \mathbf{L}(\omega, \mathbf{r}) = -\wp_-(\omega, \mathbf{r}) + \wp_+(\omega, \mathbf{r}). \tag{2.75}$$

This is a statement of the conservation of steady-state photon flow when sources and sinks exist. $\wp_+$ is related to the volume density of photon sources, and $\wp_-$ is related to the volume density of photon sinks. Equation 2.60 provides an explicit expression for $\wp_-$, as given by the following for multiple absorbers:

$$\wp_-(\omega, \mathbf{r}) = \left(\sum_i \beta_{abs,i}(\omega, \mathbf{r}) \right) \mathbf{L}(\omega, \mathbf{r}). \tag{2.76}$$

As discussed in the previous section, scattering also contributes to loss and, for the case of single scattering (which will be described in Section 2.1.2), a scattering coefficient, β_{sca}, is now defined, which is added to the absorption coefficient to obtain the net loss or extinction coefficient,

$$\beta_{ext} = \beta_{abs} + \beta_{sca}. \tag{2.77}$$
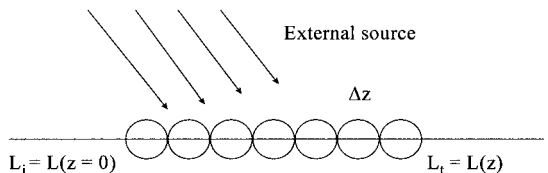
Fig. 2.3 Radiation transfer along a path in the z-direction.

Therefore, the sink term can be generalized to the form

$$\wp_-(\omega,\mathbf{r}) = \left(\sum_i \beta_{ext,i}(\omega,\mathbf{r})\right) L(\omega,\mathbf{r}), \tag{2.78}$$

where $\beta_{ext,i}$ is the extinction coefficient of the ith species, representing photon loss caused by absorption and single scattering. $\wp_+$ is a source function accounting for emission along the path and scattering along the path by external sources into the field of view of the receiver. Details of this function will be discussed later when background radiance is added to the signal, which is introduced in Chapter 11.

The magnitude of the radiance vector is the radiance, and this is the quantity commonly used in the radiation transfer equation. Based on Eq. 2.78, Eq. 2.75 is rewritten to obtain (suppressing for the moment ω)

$$\nabla \cdot \mathbf{L}(\mathbf{r}) = \nabla L(\mathbf{r}) \cdot \hat{\mathbf{s}} = -\left(\sum_i \beta_{ext,i}(\mathbf{r})\right) L(\mathbf{r}) + \wp_+(\mathbf{r}). \tag{2.79}$$

The position vector, $\mathbf{r}$, specifying the optical path, is made a function of the scalar parameter, s. The propagation path is now described along an arc, s, with direction $\hat{\mathbf{s}}$ (see Fig. 2.6), therefore the differential equation for the radiation transfer equation becomes

$$\nabla L[\mathbf{r}(s)] \cdot \hat{\mathbf{s}} = \frac{dL(s)}{ds} = -\left(\sum_i \beta_{ext,i}(s)\right) L(s) + \wp_+(s) \tag{2.80}$$

or in differential form

$$dL = -\left(\sum_i \beta_{ext,i}\right) L\, ds + \wp_+\, ds.$$

This is the radiation transfer equation (also called the radiation transport equation) for spectral radiance. In the literature on radiation transfer, the extinction coefficient is commonly replaced by the extinction cross-section, expressed as

$$\beta_{ext,i} = C_{ext,i}\rho_{p,i}, \tag{2.81}$$

where $C_{ext,i}$ is the extinction cross-section of the ith species with units of area and $\rho_{p,i}$ is the corresponding particle volume density with units of reciprocal volume. In some sense, the extinction cross-section can be visualized as an effective area blocking the beam, resulting in attenuation (see Section 2.1.2).

To solve Eq. 2.80, consider first the homogeneous portion of this differential equation, as given by

$$\frac{dL(s)}{ds} + \left(\sum_i \beta_{ext,i}(s)\right) L(s) = 0. \tag{2.82}$$

The solution is easily obtained to be

$$L(s) = L(0)\, e^{-\tau_{OD}(s)} \tag{2.83}$$

where $\tau_{OD}(s)$ is the optical depth as given by

$$\tau_{OD}(s) = \int_0^s \sum_i \beta_{ext,i}(s)\, ds'. \tag{2.84}$$

This result is a generalization of Eq. 2.28, since β_{ext} now depends on position.

The inhomogeneous differential equation, as given by Eq. 2.80, can now be solved by observing

$$\frac{d e^{\tau_{OD}(s)} L(s)}{ds} = e^{\tau_{OD}(s)} \left[\frac{dL(s)}{ds} + L(s)\left(\sum_i \beta_{ext,i}(s)\right) \right].$$

Since the factor in the brackets is equal to the source function, the solution to Eq. 2.80 is obtained in a straightforward manner to become the radiation transfer equation (reinserting ω),

$$L(\omega, s) = L(\omega, 0)e^{-\tau_{OD}(\omega,s)} + \int_0^s \wp_+(\omega,s')e^{(\tau_{OD}(\omega,s') - \tau_{OD}(\omega,s))}\, ds'. \tag{2.85a}$$

More details on β_{ext} and $\wp_+$ will be developed in Chapters 3, 4, 5, and 11. The radiation transfer equation is used when propagation within a medium is along a specified path. Boundaries can be included by incorporating reflection coefficients at the appropriate points along the path.

Equation 2.85a is valid for spectrally dependent radiation transfer. However, many practical electro-optical systems operate over a finite band of frequencies. For that case, the measured radiance is band averaged according to

$$\overline{L}(s) = \int_{\Delta\omega} d\omega\, L(\omega,s) = \int_{\Delta\omega} d\omega \left[L(\omega,0)\tau(\omega,s) + \int_0^s \rho_+(\omega,s')\frac{\tau(\omega,s)}{\tau(\omega,s')}\, ds' \right] \tag{2.85b}$$

where the internal transmittance is

$$\tau(\omega,s) = e^{-\tau_{OD}(\omega,s)}.$$

If we ignore sources along the path (e.g., path radiance and scatter) and the source radiance is constant over the spectral region of interest ($\Delta\omega$), then the band-averaged transmittance is obtained to be

$$\overline{\tau}(s) = \frac{\overline{L}(s)}{\overline{L}(0)} = \frac{1}{\Delta\omega} \int\limits_{\Delta\omega} d\omega\, \tau(\omega, s),$$

where the substitution $L(\omega, 0) = L(0) \cdot \Delta\omega$ has been made in Eq. 2.85b. $L(0)$ is the band-averaged radiance at the source.

Furthermore, in a real electro-optical system the spectral response of the detector must be included in Eq. 2.85a, so that the measured radiance can be modeled. This is accomplished by multiplying Eq. 2.85a by the detector spectral response or transfer function, tf(ω). The band integrated result is obtained by integrating over the band of interest, as given by

$$\overline{L}(s) = \int\limits_{\Delta\omega} d\omega\, \text{tf}(\omega) \left[L(\omega, 0)\tau(\omega, s) + \int\limits_0^s \rho_+(\omega, s') \frac{\tau(\omega, s)}{\tau(\omega, s')} \, ds' \right] \qquad (2.85c)$$

2.1.1.5 Total Power Law and Directional Dependence

Let us continue to examine, in more detail, the consequences of some of the defined quantities used in the total power law. This approach is most useful when the propagation medium of interest is finite in extent, such as a window or mirror, and can be enclosed by a surface. Consider, a finite slab of thickness d in thermal equilibrium with the surrounding environment, and a beam of incident optical energy on its surface that generates a reflected beam and an attenuated transmitted beam. The surface is not perfectly smooth, so that the reflected light will have an angular dependence, as indicated by the definition of the reflected intensity. Also, the bulk medium scatters light in all directions, as indicated by the definition of the scattered intensity. Thus, to completely characterize the angular effects of scatter, both the solid angle of incidence and the solid angle of the reflected or scattered light must be known. The quantities in Eqs. 2.69 and 2.70 depend only on the angles of incidence, so more general definitions are needed. The geometry is illustrated in Fig. 2.4a for reflectance measurements and 2.4b for scatterance measurements. Using the definitions of the flux (Eq. 2.65), a normalized differential flux is given by

$$\frac{d\Phi_r}{\Phi_i(\omega)} = \frac{I_r(\Omega_i, \Omega_r, \omega)\hat{\mathbf{\varepsilon}}_r \cdot \hat{\mathbf{n}}}{\Phi_i(\omega)} \, d\Omega_r = \frac{I_r(\Omega_i, \Omega_r, \omega)\cos\theta_r}{\Phi_i(\omega)} \, d\Omega_r \qquad (2.86)$$

where $\hat{\mathbf{\varepsilon}}_r$ is a unit vector that points in the direction of the reflected rays. Based on the above result, the following bidirectional reflection function is defined:

$$\frac{d\Phi_r}{d\Omega_r} = \rho(\Omega_i, \Omega_r, \omega)\Phi_i. \qquad (2.87)$$
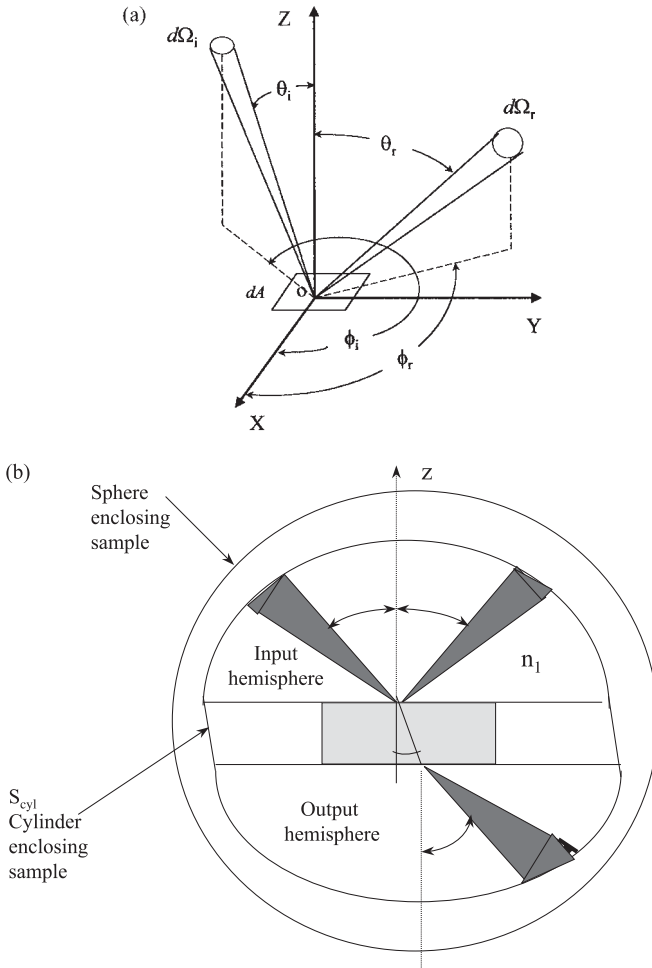
Fig. 2.4 (a) Three-dimensional geometry of focused incident light and the reflected beam defining a reflectance measurement. (b) Geometry of incident, reflected, and transmitted beams for a semitransparent slab of thickness d.

$\rho(\Omega_i, \Omega_r, \omega)$ is called the bidirectional reflectance distribution function (BRDF). For single-ray reflection, reciprocity requires the following symmetry relation:

$$\rho(\Omega_i, \Omega_r) = \rho(\Omega_r, \Omega_i).$$

Using the definition of scattered flux (Eq. 2.65c), a similar expression for $\alpha_{sca}(\Omega_i, \Omega_s, \omega)$, the bidirectional scatterance distribution function (BSDF), is also defined to be

$$\frac{d\Phi_s}{d\Omega_s} = \alpha_{sca}(\Omega_i, \Omega_s, \omega)\Phi_i = I_s(\Omega_i, \Omega_s, \omega)\cos\theta_s\,\Phi_i. \tag{2.88}$$

In these definitions of BRDF and BSDF, Ω_r covers the backward hemisphere and Ω_s represents the full sphere. (Also be aware that the $\cos\theta_{r,s}$ factor in Eqs. 2.86 and 2.88 is not always kept in the definition of the BRDF and BSDF.) BRDF measurements are for nontransmitting samples (e.g., mirrors, painted surfaces, etc.) and provide information about surface roughness. BSDF measurements are for transparent samples (e.g., windows) and provide information about the surface and bulk scattering. Also, in this development, the polarization state of the scattered optical fields has not been addressed. It is assumed that the observer is not sensitive to polarization. This topic will be further discussed later in the chapter. Furthermore, the details of scattering measurements are presented in Chapter 6.

Differentiating Eq. 2.88 with respect to area, leads to the definition of irradiance, as given by

$$L_s = \frac{d^2\Phi_s}{dAd\Omega_s} = \alpha_{sca}(\Omega_i, \Omega_s, \omega)\frac{d\Phi_i}{dA} = \alpha_{sca}(\Omega_i, \Omega_r)M_i, \tag{2.89}$$

where L_s is the scattered radiance and M_i is the incident irradiance.

Based on Eq. 2.86, the integral of the BRDF over Ω_r is the unidirectional reflectance, as defined in Eq. 2.70a, and is also called the total integrated reflectance (TIR). Similarly, the integral of the BSDF over Ω_s is the unidirectional scatterance or the total integrated scatter (TIS). The BRDF and BSDF are now broken down as a product of two factors, the total integrated quantity and a normalized solid-angle-dependent function called the phase function, $P_{r,s}(\Omega_i, \Omega_{r,s})$, for reflection and scatter, respectively. The normalization condition on the phase function is

$$\int\limits_{\Omega_{r,s}} P_{r,s}(\Omega_i, \Omega_{r,s}, \omega)\, d\Omega_{r,s} = 1. \tag{2.90}$$

The BRDF and BSDF are now written as

$$\rho(\Omega_i, \Omega_r) = \rho_{TIR}(\Omega_i)\, P_r(\Omega_i, \Omega_r) \tag{2.91a}$$

and

$$\alpha_{sca}(\Omega_i, \Omega_s) = \alpha_{sca,TIS}(\Omega_i)\, P_s(\Omega_i, \Omega_s), \tag{2.91b}$$

respectively.

It is instructive to further break the phase function into specular and diffuse components, separately representing the unscattered beam and the scattered light, respectively, as given by the following for reflection:

$$P_r(\Omega_i, \Omega_r, \omega) = P_{Sr}(\Omega_i, \Omega_r, \omega)\,\delta(\Omega_i + \Omega_r) + P_{Dr}(\Omega_i, \Omega_r, \omega) \tag{2.92}$$

and for scatter

$$\begin{aligned} P_s(\Omega_i, \Omega_s, \omega) =\, & P_{Ss}(\Omega_i, \Omega_s, \omega)[\delta(\Omega_i + \Omega_s) + \delta(\Omega_s - \Omega_t)] \\ & + P_{Ds}(\Omega_i, \Omega_s, \omega). \end{aligned} \tag{2.93}$$

Specular components (P_S) represent the contributions from the reflected and transmitted rays for a perfectly flat surface. Diffuse components (P_D) represent the effects of surface roughness. For a uniform surface with randomly oriented roughness there will be no dependence in the ϕ-direction. Thus, scatter from the sample is invariant under rotation by the angles ϕ_i and $\phi_{r,s}$, and the phase function is a function of θ_i and $\theta_{r,s}$ only. For diffuse reflectance, the phase function has the interpretation of a probability density function. It gives the probability of observing a reflected ray in a particular direction, given a specific incidence angle, which now leads to the realm of statistical optics.

For a passive medium with no surface roughness, no bulk scatter, and a collimated ray bundle with incidence angle θ_i, incident on the surface such that

$$\rho(\theta_i, \theta_r) = \rho_s(\theta_i)\delta(\theta_i + \theta_r)$$

and

$$\tau(\theta_i, \theta_t) = \tau_s(\theta_i)\delta(\theta_i - \theta_t).$$

Example 2.1 The diffuse component of a flat opaque medium with small-scale random roughness (see Fig. 2.4a) is called Lambertian. The phase function is

$$P_D(\theta_i, \theta_r) = (\cos \theta_r)/\pi, \tag{2.94}$$

and P_D is independent of the angle of incidence. The $\cos \theta_r$ factor accounts for the projected illuminated-surface area of the sample. In the case of a transparent sample with bulk and surface scatter, the phase function is $1/(2\pi)\,|\cos \theta_s|$. (Because an isotropic phase function is by definition a constant or equal in all directions, the $\cos \theta_{r,s}$ factor is sometimes put into the definition of BRDF/BSDF. But this change will alter the condition of normalization and is not adopted in this text.)

The subscript S denotes specular or flat surface terms where the reflected angle equals the negative of the incident angle and the transmitted angle approximately equals the incident angle (for nearly parallel surfaces, see Fig. 2.4). Then the generalized total power law reduces to the simple formula

$$\tau_s(\theta_i, \omega) + \rho_s(\theta_i, \omega) + \alpha_{abs}(\theta_i, \omega) = 1. \tag{2.95}$$

These deterministic specular terms are a function of the complex index of refraction for spectrally averaged (i.e., the bandwidth of the incident beam washes out interference effects) polarized light incident on a slab of thickness d, as given by (ignoring interference, fluorescence, and diffraction)

$$\tau_s(\theta_i, \omega) = \frac{[1 - R(\theta_i, \omega)]^2 \exp(-\beta_{abs}(\omega)d/\cos \theta_a)}{1 - R^2(\theta_i, \omega) \exp(-2\beta_{abs}(\omega)d/\cos \theta_a)}, \tag{2.96}$$

$$\rho_s(\theta_i,\omega) = \frac{R(\theta_i,\omega) + R(\theta_i,\omega)[1 - 2R(\theta_i,\omega)]\exp(-2\beta_{abs}(\omega)d/\cos\theta_a)}{1 - R^2(\theta_i,\omega)\exp(-2\beta_{abs}(\omega)d/\cos\theta_a)}, \qquad (2.97)$$

and

$$\alpha_{abs}(\theta_i,\omega) = \frac{[1 - R(\theta_i,\omega)][1 - \exp(-\beta_{abs}(\omega)d/\cos\theta_a)]}{(1 - R(\theta_i,\omega)\exp(-\beta_{abs}(\omega)d/\cos\theta_a))}. \qquad (2.98)$$

$R(\theta_i,\omega)$ is the single-surface Fresnel power reflection coefficient for polarized light as a function of the angle of incidence, θ_i, wave number, and complex index of refraction. For normal incidence, the above formulas can be applied for unpolarized light because the Fresnel power reflection coefficients for the two different polarizations are equal. Explicit formulas of R for unpolarized and polarized light will be presented in Chapter 4. In general, the specular transmittance for unpolarized light is given by

$$\tau_{\text{unpolarized}} = \frac{1}{2}(\tau_s + \tau_p),$$

where τ_s and τ_p are the transmittances for two orthogonal polarizations (see Section 2.1.2.2). Similar expressions for the unpolarized reflectance are also necessary. The factor $\exp(-\beta_{abs}(\omega)d/\cos\theta_a)$ is the internal transmittance. $\beta_{abs}(\omega)$ is the absorption coefficient, and also will be discussed in more detail in Chapters 4 and 5. θ_a is the refracted angle within the medium, as defined in Fig. 2.4, and is related to θ_i according to the well-known Snell's law of refraction,

$$\sin\theta_a = \frac{n_1}{n_2}\sin\theta_i. \qquad (2.99)$$

Equations 2.96–2.98 are derivable from geometrical optics approximations (see Problem 2.5a) or from a solution of Maxwell's equations for a uniform infinite slab. The denominator in Eqs. 2.96–2.98 represents contributions from multiple reflections within the slab. To find explicit formulas for transmittance, reflectance, and extinctance, including the effects of scattering, requires physical optics, and this is developed later in this chapter.

Including the effects of interference leads to the Airy formulas, which include the effects of phase of the field for a medium with parallel smooth surfaces (for a derivation, see Problem 2.5b and Born and Wolf, Ref. 2.1, and P. Yeh, Ref. 2.5 (lossless case). Again, ignoring contributions from fluorescence, scattering, and diffraction, the specular transmittance, reflectance, and absorptance, including interference, and for monochromatic light, now become

$$\tau_{SI}(\theta_i,\omega) = \frac{(1 - R)^2 K}{1 - 2RK\cos(2\omega n_2 d\cos\theta_a/c) + R^2 K^2}, \qquad (2.100)$$

$$\rho_{SI}(\theta_i,\omega) = \frac{R(1 - 2K\cos(2\omega n_2 d\cos\theta_a/c) + K^2)}{1 - 2RK\cos(2\omega n_2 d\cos\theta_a/c) + R^2 K^2}, \qquad (2.101)$$

and

$$\alpha_{abs}(\theta_i, \omega) = \frac{(1 + RK)(1 - R)(1 - K)}{1 - 2RK \cos\left(2\omega n_2 d \cos\theta_a/c\right) + R^2 K^2}, \quad (2.102)$$

where again the internal transmittance is

$$K = \exp\left(-\beta_{abs}(\omega)d/\cos\theta_a\right),$$

the field reflection coefficient for light from medium 1 reflecting off medium 2 is $r_{12} = -r_{21}$, and the field transmission coefficient is $t_{12} = t_{21}$ (see Chapter 4 for more information). The power reflection coefficient is $R = |r_{12}|^2$ and the power transmission coefficient is $T = t_{12}t_{21}$, where $T + R = 1$. These formulas are useful for Fabry–Perot interferometers and thin-film transmission calculations. Again, one needs to know the complex index of refraction of the media involved. The finite bandwidth Equations, 2.96–2.98, can be obtained from the monochromatic Equations 2.100–2.102, by performing a spectral average (or an angle average, see Problem 2.5c). At this point, the problem of modeling the propagation of light is reduced to knowing the geometry of the ray path and the complex index of refraction.

Thus far we have only considered conservation of power flow for integrated or unidirectional quantities. This is because Poynting's theorem and conservation of power flow only have meaning if integration of the propagation terms covers a completely enclosed surface. However, it is often necessary to consider a conservation law of power flow for bidirectional quantities.

The bidirectional reflectance can be equated to the bidirectional emittance based on the following arguments and Eq. 2.64. For a single incident ray propagating in a single direction, the incident intensity is described by

$$\mathbf{I}_i(\Omega, \omega) \cdot \hat{\mathbf{n}} = \Phi_i \delta(\Omega - \Omega_i),$$

where $\hat{\boldsymbol{\varepsilon}}_i \cdot \hat{\mathbf{n}} = 1$ and $\hat{\boldsymbol{\varepsilon}}_i$ is a unit vector pointing in the direction of Ω_i. For a single ray, only a single reflected ray, scattered ray, and so on, can exist. If we limit the solid-angle integrals to these specific directions, since otherwise it is zero, a conservation relation can be obtained for bidirectional quantities. In the limit of infinitesimal integration limits, the following is obtained:

$$\delta(\Omega - \Omega_i) = \frac{\mathbf{I}_r(\Omega_i, \Omega_r, \omega) \cdot \hat{\mathbf{n}}}{\Phi_i} + \frac{\mathbf{I}_s(\Omega_i, \Omega_s, \omega) \cdot \hat{\mathbf{n}}}{\Phi_i} + \frac{\mathbf{I}_e(\Omega_i, \Omega_e, \omega) \cdot \hat{\mathbf{n}}}{\Phi_i}$$
$$+ \frac{\mathbf{I}_t(\Omega_i, \Omega_t, \omega) \cdot \hat{\mathbf{n}}}{\Phi_i}.$$

Solid-angle integration is implied on each term in the above expression. That is, the incident ray can only result in single reflected, scattered, emitted, or transmitted ray. The delta function reminds us that integration is required to obtain a physically meaningful statement. Using the definitions of bidirectional functions, as given by Eqs. 2.87 and 2.88, the above equation becomes a statement of conservation of power flow, as given by
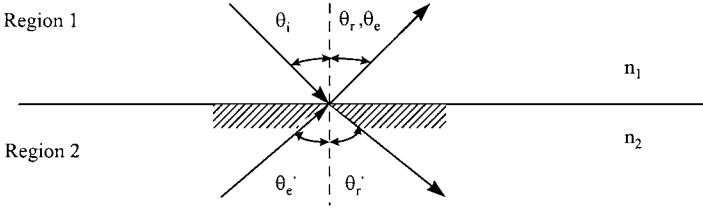
Fig. 2.5 Emission and reflection between two semi-infinite regions.

$$\delta(\Omega - \Omega_i) = \rho(\Omega_i, \Omega_r, \omega) + \alpha_{sca}(\Omega_i, \Omega_s, \omega) + \epsilon(\Omega_i, \Omega_e, \omega) + \tau(\Omega_i, \Omega_t, \omega).$$

Consider the geometry of Fig. 2.5, with rays of light being emitted from the surface at angle θ_e into region 1 and an incident ray (at θ_i) reflecting at angle $\theta_r (= \theta_e)$, also in region 1. In region 2, there are the corresponding refracted rays. These are semi-infinite regions, so no light is transmitted ($r = 0$). The total power law for radiation generated in region 2 and escaping from the surface into region 1 for a single ray is (now using solid angles and combining reflectance and scatter into one term)

$$\epsilon(\Omega'_e, \Omega_e, \omega) + \rho(\Omega'_e, \Omega'_r, \omega) = \delta(\Omega - \Omega'_e). \tag{2.103}$$

The total power law for incident blackbody radiation from region 1 with the same solid angle as the emitted light, onto region 2 is

$$\alpha_{abs}(\Omega_i, \Omega'_r, \omega) + \rho(\Omega_i, \Omega_r, \omega) = \delta(\Omega - \Omega_i). \tag{2.104}$$

The spectral bidirectional reflectance is the same for light rays in region 1 reflecting off the surface as for light rays in region 2 reflecting off the interface between the two regions. Thus, the following is true:

$$\rho(\Omega_i, \Omega_r, \omega) = \rho(\Omega'_e, \Omega'_r, \omega). \tag{2.105}$$

Substituting the above equation into Eq. 2.103 and subtracting Eq. 2.103 from Eq. 2.104, the desired result is obtained, relating internal emission to external bidirectional reflectance:

$$\epsilon(\Omega'_e, \Omega_e, \omega) + \delta(\Omega - \Omega_i) - \delta(\Omega - \Omega'_e) = \alpha_{abs}(\Omega_i, \Omega'_r, \omega)$$
$$= \delta(\Omega - \Omega_i) - \rho(\Omega_i, \Omega_r, \omega). \tag{2.106a}$$

The directional emissivity is obtained by integrating over all internal sources, Ω'_e. Using the principle of reciprocity, this is equivalent to integrating over all possible external sources, Ω_i. Thus, the following useful relationship is obtained:

$$\oint \epsilon(\Omega'_e, \Omega_e, \omega) \, d\Omega'_e = \epsilon(\Omega_e, \omega) = 1 - \oint \rho(\Omega_i, \Omega_r, \omega) \, d\Omega_i$$
$$= 1 - \rho(\Omega_e, \omega), \tag{2.106b}$$

where $\Omega_e = \Omega_r$. Equation 2.106b remains true for a finite semitransparent medium, when emitted light is observed at angles where no transmitted light from an external source exists. Also, using reciprocity, the integration over incidence angles can be changed to the reflected angles.

Example 2.2 Consider painted aluminum; the integrated transmittance must equal zero. Therefore, using Eqs. 2.69 and 2.74, a simple expression for the directional emittance is found, similar to the above result,

$$\epsilon(\Omega_i, \omega) = 1 - \rho(\Omega_i, \omega).$$

Near room temperature and below, it is much easier to measure the directional reflectance using a laser than the weak emitted radiance from a surface because of contaminating background radiance reflected from surrounding structures.

2.1.1.6 Formal Geometrical Optics

Thus far we have used the concept of the plane wave to incorporate loss and reflection along a propagation path. This restricts the description of the optical path to a straight line, which is seldom the case. The ability to specify the ray path in a medium of nonuniform index of refraction is necessary for the discussion of practical problems. This great need brings us to an introduction to geometrical optics.

Because of the importance of geometrical optics to optical propagation, a formal development is presented. In this way the approximations and realm of validity of geometrical optics can be precisely stated. The emphasis will be on obtaining a description of the optical path.

Geometrical optics is a high-frequency asymptotic solution of Maxwell's equations to the zeroth order. An asymptotic expression becomes increasingly accurate as a parameter in that expression becomes increasingly large. An asymptotic representation of the electromagnetic field with frequency as the large parameter and the leading term independent of frequency is desired. Such an expression is the Luneberg–Kline series for **E** and **H**, as given by (see Ref. 2.6)

$$\mathbf{E}(\mathbf{r}) \simeq e^{-jk_0'\psi(\mathbf{r})} \sum_{m=0}^{\infty} \frac{\mathbf{E}_m(\mathbf{r})}{(j\omega)^m} \tag{2.107a}$$

and

$$\mathbf{H}(\mathbf{r}) \simeq e^{-jk_0'\psi(\mathbf{r})} \sum_{m=0}^{\infty} \frac{\mathbf{H}_m(\mathbf{r})}{(j\omega)^m}. \tag{2.107b}$$

Substituting these asymptotic expressions into the frequency-domain Maxwell's equations (Eqs. 2.9–2.12) for the charge density $\rho = 0$, assuming that ϵ_r, μ_r, and σ are

constant in frequency, and using the relation $k_0' = \omega/c$, one obtains the following expansion:

$$\sum_m \nabla \psi(\mathbf{r}) \times \frac{\mathbf{E}_m(\mathbf{r})}{(j\omega)^m} = \sum_m \left(\frac{c\nabla \times \mathbf{E}_m(\mathbf{r})}{(j\omega)^{m+1}} + \frac{c\mu(\mathbf{r})\mathbf{H}_m(\mathbf{r})}{(j\omega)^m} \right), \tag{2.108a}$$

$$\sum_m \nabla \psi(\mathbf{r}) \times \frac{\mathbf{H}_m(\mathbf{r})}{(j\omega)^m} = \sum_m \left(\frac{c\nabla \times \mathbf{H}_m(\mathbf{r})}{(j\omega)^{m+1}} - \frac{c\epsilon(\mathbf{r})\mathbf{E}_m(\mathbf{r})}{(j\omega)^m} - \frac{c\sigma(\mathbf{r})\mathbf{E}_m(\mathbf{r})}{(j\omega)^{m+1}} \right), \tag{2.108b}$$

$$\sum_m \frac{\mathbf{E}_m(\mathbf{r})}{(j\omega)^m} \cdot \nabla \psi(\mathbf{r}) = \sum_m \left[\frac{c}{(j\omega)^{m+1}} \left(\mathbf{E}_m(\mathbf{r}) \cdot \frac{1}{\epsilon_r(\mathbf{r})} \nabla \epsilon_r(\mathbf{r}) + \nabla \cdot \mathbf{E}_m(\mathbf{r}) \right) \right], \tag{2.108c}$$

and

$$\sum_m \frac{\mathbf{H}_m(\mathbf{r})}{(j\omega)^m} \cdot \nabla \psi(\mathbf{r}) = \sum_m \left[\frac{c}{(j\omega)^{m+1}} \left(\mathbf{H}_m(\mathbf{r}) \cdot \frac{1}{\mu(\mathbf{r})} \nabla \mu(\mathbf{r}) + \nabla \cdot \mathbf{H}_m(\mathbf{r}) \right) \right]. \tag{2.108d}$$

Based on Fig. 2.1, the assumption that the permittivity, permeability, and conductivity are frequency independent means that ϵ_r, σ, and μ_r are constant in frequency and complex in general (although treated as real in the following). Grouping together terms of the same order in ω leads to the following sets of Maxwell's equations to various orders in ω:

Order 0:

$$\nabla \psi(\mathbf{r}) \times \mathbf{E}_0(\mathbf{r}) = c\mu(\mathbf{r})\mathbf{H}_0(\mathbf{r}), \tag{2.109a}$$

$$\nabla \psi(\mathbf{r}) \times \mathbf{H}_0(\mathbf{r}) = -c\epsilon_r(\mathbf{r})\mathbf{E}_0(\mathbf{r}), \tag{2.109b}$$

$$\mathbf{E}_0(\mathbf{r}) \cdot \nabla \psi(\mathbf{r}) = 0, \tag{2.109c}$$

and

$$\mathbf{H}_0(\mathbf{r}) \cdot \nabla \psi(\mathbf{r}) = 0. \tag{2.109d}$$

Equations 2.109c and 2.109d show that the **E**-field and **H**-field are perpendicular to the direction of ∇_ψ.

Order 1:

$$\nabla \psi(\mathbf{r}) \times \mathbf{E}_1(\mathbf{r}) = c\nabla \times \mathbf{E}_0(\mathbf{r}) + c\mu(\mathbf{r})\mathbf{H}_1(\mathbf{r}), \tag{2.110a}$$

$$\nabla \psi(\mathbf{r}) \times \mathbf{H}_1(\mathbf{r}) = c\nabla \times \mathbf{H}_0(\mathbf{r}) - c\epsilon_r(\mathbf{r})\mathbf{E}_1(\mathbf{r}) - \frac{c\sigma(\mathbf{r})}{\epsilon_0} \mathbf{E}_0(\mathbf{r}), \tag{2.110b}$$

$$\mathbf{E_1}(\mathbf{r}) \cdot \nabla \psi(\mathbf{r}) = \mathbf{E_0} \cdot \frac{c}{\epsilon_r(\mathbf{r})} \nabla \epsilon_r(\mathbf{r}) + c \nabla \cdot \mathbf{E_0}(\mathbf{r}), \qquad (2.110c)$$

and

$$\mathbf{H_1}(\mathbf{r}) \cdot \nabla \psi(\mathbf{r}) = \mathbf{H_0}(\mathbf{r}) \cdot \frac{c}{\mu(\mathbf{r})} \nabla \mu(\mathbf{r}) + c \nabla \cdot \mathbf{H_0}(\mathbf{r}). \qquad (2.110d)$$

and so on. For ω large, the zero-order equations are the most significant, and are the basis for geometrical optics. This is why geometrical optics is considered valid at high or optical frequencies. The higher order equations contribute to the geometrical theory of diffraction (GTD) and propagation in conductive media. GTD is commonly applied to microwave theory and is beyond the scope of this text. References on GTD are given in the Bibliography (see Refs. 2.6 and 2.7).

For a dielectric medium, the geometrical optic field is a transverse electromagnetic (TEM) wave, thus $\nabla \psi$ points in the direction of propagation. To see this for a simple case, consider the surface function of constant phase for a plane wave (see Eq. 2.19)

$$\psi = n \hat{\mathbf{s}} \cdot \mathbf{r} \qquad (2.111)$$

where $\hat{\mathbf{s}}$ is a unit vector pointing in the direction of propagation, and refractive index, n, is a constant in frequency and position. Then (this is true in general)

$$\nabla \psi = n \hat{\mathbf{s}}. \qquad (2.112)$$

Since the surfaces, specified by $\psi =$ constant, are the wavefronts, based on Eq. 2.112, the normal to these surfaces points in the direction of propagation. This concept is illustrated in Fig. 1.4 for regions were the plane-wave approximation is valid.

Following the same procedure for deriving the wave equation in a nonmagnetic medium, Eqs. 2.109a–d result in a more general expression valid for inhomogeneous media, called the eikonal equation, as given by

$$|\nabla \psi(\mathbf{r})|^2 = n^2(\mathbf{r}). \qquad (2.113)$$

This is a more general result than Eq. 2.112, because n is a function of position but is still independent of frequency. Again, it is of central interest to determine the time-averaged Poynting vector for the case of geometrical optics. Keeping only the leading terms in the Luneberg–Kline series leads to

$$\langle \mathscr{L}(t) \rangle_t = \frac{1}{2} \text{Re} \, [\mathbf{E_0} \times \mathbf{H_0^*}]. \qquad (2.114)$$

Using Eq. 2.109a for an expression of $\mathbf{H_0}$ in terms of $\mathbf{E_0}$ and substituting into the above equation results in

$$\langle \mathscr{L}(t) \rangle_t = \frac{|\mathbf{E_0}|^2}{2\eta_0} \nabla \psi. \qquad (2.115)$$

Based on the eikonal equation and the fact that the Poynting vector points in the direction of propagation, it follows that

$$\langle \mathscr{L}(\mathbf{r},t)\rangle_t = \frac{|\mathbf{E_0}|^2}{2\eta_0} n(\mathbf{r})\hat{\mathbf{s}} \qquad (2.116)$$

where $\hat{\mathbf{s}}$ is a unit vector pointing in the direction of propagation. This result is consistent with Eq. 2.27, which was obtained for the unbounded plane wave. The above equation is more general, since the index of refraction depends on position and a general path can be used. Based on this result the eikonal equation can be written in vector form as

$$\nabla \psi(\mathbf{r}) = n(\mathbf{r})\hat{\mathbf{s}}. \qquad (2.117)$$

Again this is a generalization of Eq. 2.112. The eikonal equation establishes a relationship between the complex index of refraction and the phase. This is a basic equation of geometrical optics, because it allows one to calculate the ray path. Consider an arc of length s with a position vector, $\mathbf{r}$, locating a point P on the arc as illustrated in Fig. 2.6, then in terms of differential arc lengths the unit vector, $\hat{s}$, is expressed as

$$\hat{\mathbf{s}} = \lim_{\Delta s \to 0} \frac{\Delta \mathbf{r}}{\Delta s} = \frac{d\mathbf{r}}{ds}. \qquad (2.118)$$

Using this result with the vector eikonal equation we obtain the following differential equation for the ray path in terms of the spatial variation of the real part of the refractive index,

$$\frac{d}{ds}\left(n(\mathbf{r})\frac{d\mathbf{r}}{ds}\right) = \nabla n(\mathbf{r}). \qquad (2.119)$$

Therefore, to completely specify a propagation problem within the context of geometrical optics, the spatial dependence and magnitude of the index of refraction must
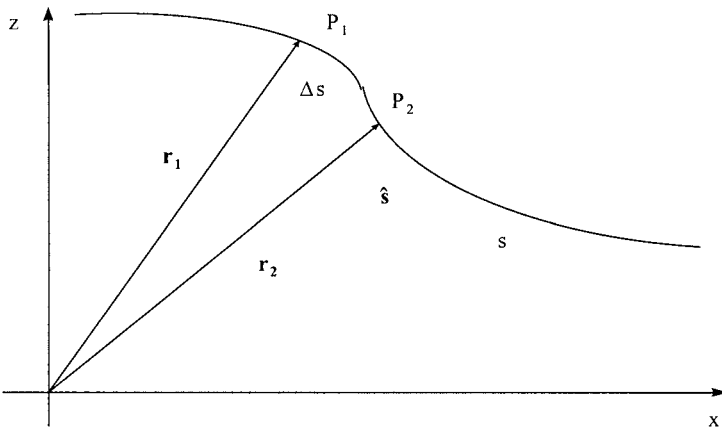
Fig. 2.6 Ray path geometry.

be known. Most practical problems concerning the propagation of light can be solved within the limits of geometrical optics. For this reason most of the remaining text will concentrate on understanding the complex index of refraction.

Spatial variations in the refractive index that are much larger than a wavelength lead to refraction for continuous variation and reflection for discontinuous variation. When the spatial variations of the index of refraction are on the order of the wavelength, then diffraction effects are important and the geometrical optics description of refraction breaks down. This becomes the topic of scattering, which is introduced in the next section.

Example 2.3 For $n =$ constant, Eq. 2.119 reduces to

$$\frac{d^2\mathbf{r}}{ds^2} = 0,$$

which leads to the following solution:

$$\mathbf{r} = s\mathbf{A} + \mathbf{B}.$$

This is an equation for a straight line path as expected, based on the plane-wave solutions obtained in the first section.

2.1.2 Elastic Scattering: Physical Optics

Scattering phenomena are of concern when refractive index (real part) spatial variations or fluctuations are on the order of a wavelength or less, and are categorized as either elastic or inelastic. Variations in the refractive index are caused by particles (molecules, aerosols, dust, fog, etc.), voids (bubbles in liquids or solids) or statistical fluctuations in the density. Media fluctuation effects, much larger than a wavelength, are covered in turbulence, which is outside the scope of this book. Elastic scattering refers to interactions with a medium where no energy is given or taken away from the incident field. Thus, the frequency of the incident light is unchanged by the interaction. Inelastic scattering, on the other hand, represents scattering where the frequency of the incident light has changed after the scattering interaction. Inelastic scattering involving vibrational and rotational transitions in the scattering medium is called Raman scatter. Inelastic scattering involving translational or acoustic transitions is called Brillouin scatter. To simplify this introductory section, only elastic scattering will be considered.

2.1.2.1 Particle Scattering

In the previous section we showed that the absorption coefficient, β_{abs}, and the index of refraction, n, affect the attenuation and phase of a propagating plane wave. These quantities are based on resonant phenomena of the medium. Now, we will examine the nonresonant process called particle scattering. This will lead to formulas for the scattering coefficient, β_{sca}. A few restrictions will be applied to the development:

1. *The scattered light has the same frequency as the incident light.* Raman and Brillouin scattering are ignored and only elastic scattering will be considered.

2. *The scattering particles are independent*. One particle can be studied to understand many particles.
3. *Single scattering dominates*, that is, the scattering by N particles is N times the scattering function of one particle. Essentially, the incident light ray is scattered by only one particle and sees no other. In the case of multiple scattering, more than one particle interacts with an incident ray before it exits the medium. Single scattering dominates when $\beta_{sca}z < 0.1$ or when $\beta_{sca}z$ scales with the path length, z.

Scattering can be treated either as classical or as quantum phenomena. However, a quantum approach is more important for molecular inelastic scatter, and practical scattering problems must, also, address larger scatters (clouds, fog, dust, etc. in the earth's atmosphere and grain boundaries in polycrystalline solids). For elastic scatter, quantum and classical models agree. Thus, scattering will be treated classically without any loss of generality. Molecular scattering will be treated classically via Rayleigh scattering.

Consider an unpolarized uniform plane wave, $\mathbf{E}_i (= \mathbf{E}_{i0} \exp(-jk'z + j\omega t))$, illuminating a single particle, as shown in Fig. 2.7. The scattered field can be represented by an unpolarized spherically outgoing wave (recall Eq. 1.20) given by

$$\mathbf{E}_s = S(\theta_s, \phi_s) \frac{\mathrm{e}^{-jk'r+j\omega t}}{jk'r} \mathbf{E}_{i0}. \tag{2.120}$$

$S(\theta_s, \phi_s)$ is called the amplitude function, much like an antenna pattern. (In general, the amplitude function is bidirectional and depends on the solid angle of incidence as well.) To simplify the following analysis the incident angle is fixed, forming a collimated beam, as specified in Fig. 2.7. In terms of the incident field, the scattered field becomes

$$\mathbf{E}_s = S(\theta_s, \phi_s) \frac{\mathrm{e}^{-jk'r+jk'z}}{jk'r} \mathbf{E}_i. \tag{2.121}$$

Again, in optics we are interested in the magnitude of the time-averaged Poynting vector of the scattered field, or the scattered radiance, L_{sca},

$$L_{sca}(\Omega_s) = \frac{|\mathbf{E}_s|^2}{2\eta_0} = \frac{|S(\theta_s, \phi_s)|^2}{k'^2 r^2} M_i, \tag{2.122}$$
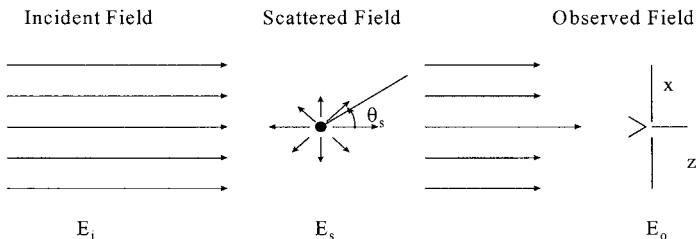
Fig. 2.7 Illustration of scattering phenomena.

where M_i is the incident irradiance (watts/cm^2) and the amplitude function magnitude squared takes on the unit 1/sr. Based on this formula and Eqs. 2.62 and 2.65c, the integrated scatter cross-section, C_{sca}, is defined as

$$C_{sca} = \oint d\Omega_s\, C_{sca}(\Omega_s) = \frac{\Phi_s}{M_i} = \oint d\Omega_s\, \frac{|S(\Omega_s)|^2}{k'^2}, \tag{2.123}$$

where $C_{sca}(\Omega_s)$ is the scattering cross-section with units of area/steradian for fixed angle of incidence, $\theta_i = 0$. For spherical particles, C_{sca} is independent of θ_i.

Since we are interested in attenuation or total extinction, the amplitude function in the forward direction, $S(\theta_s = 0)$, is of interest. This represents the scattered field that will be detected by the observer, and indistinguishable from the incident field. The forward and backward scattered fields are special cases because interference from the incident field must be included. Because of the small angles, it is a good approximation to state in the plane of the observer (recall Eq. 1.21), that

$$r = z + \frac{x^2 + y^2}{2z}.$$

Recall from Chapter 1 that this is the paraxial ray approximation. The total field at the observer is the sum of the incident and forward scattered (for $\theta_s = 0$) fields and becomes

$$\mathbf{E}_o = \mathbf{E}_i + \mathbf{E}_s = \mathbf{E}_i \left(1 + \frac{S(0)}{jk'z} e^{\frac{-jk'\left(x^2+y^2\right)}{2z}} \right) \tag{2.124}$$

where

$$\left| \frac{S(0)}{k'z} e^{\frac{-jk'\left(x^2+y^2\right)}{2z}} \right| \ll 1$$

in the far field for z large, which is consistent with the single scatter approximation. The observed radiance, to first order in $S(0)$, is

$$|\mathbf{E}_i + \mathbf{E}_s|^2 \approx \left(1 - \frac{2}{k'z} \mathrm{Re}\left[jS(0)\, e^{\frac{-jk'\left(x^2+y^2\right)}{2z}} \right] \right) |\mathbf{E}_i|^2. \tag{2.125}$$

The first term is the unattenuated radiance. The second term represents loss or light removed from the observer's aperture. Integration of the second over the xy-plane gives the general result for the forward direction extinction cross-section, C_{ext},

$$C_{ext}(\theta_s = 0) = \frac{4\pi}{k'^2} \mathrm{Re}[S(0)], \tag{2.126}$$

where $|\mathbf{E}_o|^2 = (1 - C_{ext})|\mathbf{E}_i|^2$. When the particle both absorbs and scatters, then the forward extinction cross-section is the sum of the absorption cross-section, C_{abs}, and the scatter cross-section caused by the presence of the particles, thus

$$C_{ext} = C_{sca} + C_{abs}. \tag{2.127}$$

Equation 2.126 is the fundamental forward extinction formula for scattering. Notice the similarity between this procedure for a blocking aperture and that for the transmitting aperture of Section 1.2.1.2 and diffraction theory. Thus, the mechanism of loss is more than a geometrical optics blocking of rays, but includes diffraction effects as well. Also, because scattered light rays are bent around the particle, care must be used in the measurement of C_{ext} to ensure that $\theta_s > 0$ rays are excluded from the field of view.

Now let us consider a cloud of scatterers, each independent and characterized by their amplitude function, $S_i(\theta_s, \phi_s)$. Again, we are interested in the intensities, but now must worry about cross-terms, $S_i(\theta_s, \phi_s)S_j(\theta_s, \phi_s)$, where $i \neq j$. However, the randomness of the phase means all the cross-terms average to zero. Thus, for single scattering,

$$L_s(\theta_s, \phi_s) = \sum_i L_{s,i}(\theta_s, \phi_s) \tag{2.128}$$

and it further follows (by integrating over all scatter directions, Ω_s)

$$C_{sca} = \sum_i C_{i,sca}. \tag{2.129}$$

The situation for $\theta_s (= \theta_i) = 0$ is different, the phase relationship between the incident and scattered fields is fixed and not random. In this case, the fields are added and

$$S(0) = \sum_i S_i(0) \tag{2.130}$$

and

$$C_{ext} = \sum_i C_{i,ext}. \tag{2.131}$$

Now, consider a slab with many scatters, as illustrated in Fig. 2.8. Assume all the particles have the same $S(\theta_s, \phi_s)$, are independent, and that there are N particles with a particle number density ρ_p. The field at the observer is influenced by scattering from all particles in the slab, but the observed forward traveling wave is coherently influenced only by the particles in the "active" volume of the slab, which coincides with a few central Fresnel zones, as seen by the observer. For r large enough ($r \approx z$) then

$$E_o = E_i \left(1 + S(0) \sum_N \frac{1}{jk'z} e^{\frac{-jk'(x^2+y^2)}{2z}} \right). \tag{2.132}$$

Converting the sum on N to a volume integration, we have

$$\sum_N \rightarrow \rho_p \int dV. \tag{2.133}$$
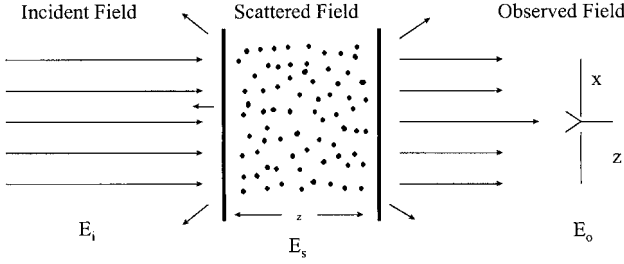
Fig. 2.8 Transmission through a slab of thickness z containing many particles.

Then, for $k' = k'_0 = 2\pi/\lambda$, in the vacuum outside the particles, Eq. 2.132 becomes

$$\mathbf{E}_o = \mathbf{E}_i \left(1 + S(0)\rho_p \int\limits_0^z dz' \int\limits_{-\infty}^{\infty} dx \int\limits_{-\infty}^{\infty} dy \, \frac{1}{jk'_0 z'} e^{\frac{-jk'_0(x^2+y^2)}{2z'}} \right).$$

Completing the integration yields

$$\mathbf{E}_o = \mathbf{E}_i \left(1 - \frac{2\pi}{k'^2_0} \rho_p z S(0) \right). \tag{2.134}$$

It is of great interest to relate this formalism for single scatter to the formalism developed for absorption in Section 2.1.1.1. Consider the $\mathbf{E}$-field at the observation point in terms of a plane wave, of the form

$$\mathbf{E}_o = \mathbf{E}_{o0} \, e^{-jk'_0 \overline{n} z},$$

just after propagation through a scattering medium with an effective index n. The change in the field relative to a particle-free vacuum with $n = 1$ is

$$\frac{e^{-jk'_0 \overline{n} z}}{e^{-jk'_0 z}} = e^{-jk'_0 z(\overline{n}-1)} \approx 1 - jk'_0 z(\overline{n} - 1) \tag{2.135}$$

for n close to 1. Then, recognizing that $\mathbf{E}_i = \mathbf{E}_{o0}$ and using Eq. 2.134 leads to

$$\frac{|\mathbf{E}_o|}{|\mathbf{E}_i|} = 1 - jk'_0 z(\overline{n} - 1) = 1 - \frac{2\pi}{k'^2_0} \rho_p z S(0). \tag{2.136}$$

Then, single scattering phenomena are represented by a new complex index of refraction,

$$(n_s - 1) - jk_s = \frac{2\pi}{k_0'^3}\rho_p\left(\text{Im}[S(0)] - j\frac{2\pi}{k_0'^3}\rho_p\text{Re}[S(0)]\right). \qquad (2.137)$$

$(n_s - 1)$ is the real part of the scattering index and is usually close to zero, thus very small compared with the normal index caused by absorption. k_s is the imaginary part of the scattering index, and includes the effects of particle scattering and absorption. A scattering coefficient for nonabsorbing particles can be defined analogously to the absorption coefficient using Eq. 2.29. Thus,

$$\beta_{sca} = 2k_0'k_s = \frac{4\pi}{k_0'^2}\rho_p\text{Re}[S(0)]. \qquad (2.138)$$

Comparing this result to Eq. 2.126 for a single particle, we obtain the following relation for the extinction coefficient,

$$\beta_{ext}(\theta_s = \theta_i) = \rho_p C_{ext}. \qquad (2.139)$$

In this way, single scatter and absorption by particles are handled by a familiar formalism through the complex index of refraction.

If the particles are embedded in a dielectric medium, then the background absorption and refraction can be included in a straightforward manner. The combination of background absorption and particle processes leads to the definition of the extinction coefficient, β_{ext}, in terms of β_{abs} and β_{sca},

$$\beta_{ext} = \beta_{abs} + \beta_{sca}(\theta_s = \theta_i). \qquad (2.140a)$$

The net index of refraction also becomes

$$n_{net} = n + (n_s - 1). \qquad (2.140b)$$

Now the total power law, as given by Eqs. 2.96–2.98, can be modified to include single scatter loss,

$$\tau_s(\theta_i, \omega) = \frac{[1 - R(\theta_i, \omega)]^2 \exp[-\beta_{ext}(\theta_i, \omega)\,d/\cos\theta_a]}{1 - R^2(\theta_i, \omega)\exp[-2\beta_{ext}(\theta_i, \omega)\,d/\cos\theta_a]}, \qquad (2.141)$$

$$\rho_s(\theta_i, \omega) = \frac{R(\theta_i, \omega) + R(\theta_i, \omega)[1 - 2R(\theta_i, \omega)]\exp[-2\beta_{ext}(\theta_i, \omega)\,d/\cos\theta_a]}{1 - R^2(\theta_i, \omega)\exp[-2\beta_{ext}(\theta_i, \omega)\,d/\cos\theta_a]} \qquad (2.142)$$

and

$$\alpha_{ext,s}(\theta_i, \omega) = \frac{[1 - R(\theta_i, \omega)]\{1 - \exp[-\beta_{ext}(\theta_i, \omega)d/\cos\theta_a]\}}{1 - R(\theta_i, \omega)\exp[-\beta_{ext}(\theta_i, \omega)d/\cos\theta_a]}. \qquad (2.143)$$

$\alpha_{ext,S}(\theta_i,\omega)$ is the total integrated extinctance. When $\beta_{sca} = 0$, the total integrated extinctance reduces to the absorptance (Eq. 2.98). When $\beta_{abs} = 0$ and the particles are nonabsorbing, the total integrated extinctance reduces to

$$\alpha_{ext,S}(\beta_{abs} = 0) = \beta_{sca}(\theta_i)d/\cos\theta_a = \alpha_{sca,S}(\theta_i), \tag{2.144}$$

where $\alpha_{sca,S}(\theta_a)$ is the total integrated scatterance, and related to the integrated scatter cross-section, as given by Eq. 2.123, according to

$$\alpha_{sca,S}(\theta_i) = C_{sca}(\theta_i)\rho_p d/\cos\theta_a = C_{ext}(\theta_i = \theta_s)\rho_p d/\cos\theta_a. \tag{2.145}$$

This result further develops the BSDF, as given in Eq. 2.91.

Since the transmittance, reflectance, and extinctance are integrated quantities, the extinction coefficient changes, depending on the angular extent of the integration. Transmittance and reflectance are specular and only considered in one direction. Based on Eqs. 2.144 and 2.145, the total integrated scatter, on the other hand, is integrated over all angles, which changes the functional form of the scatter coefficient to

$$\beta_{sca}(\theta_i) = C_{sca}(\theta_i)\rho_p. \tag{2.146}$$

This result is equivalent to Eq. 2.138, which considers the extinction in the transmitted direction only. This equivalence is the point of the optical theorem (see Bohren and Huffman, Ref. 2.9).

2.1.2.2 Polarization of Light

Thus far, the propagation medium has been linear and isotropic, and has not required a detailed discussion of polarization of the electromagnetic field. It was assumed that the polarization does not change during propagation. Because of the many different non-spherical shapes of particles, the scattered field can have different polarization properties from the incident field. A review of the characterization of light polarization is presented in this section to prepare for the introduction of this topic.

Two categories are used to characterize polarization, the state or type of polarization and the degree of polarization. Table 2.1 lists the various types of polarizations and the corresponding designations.

Linear polarization is usually designated relative to an interface of discontinuous indices of refraction and the plane of incidence, which includes both the incident and reflected rays. When the **E**-field is in the plane of incidence, the light is vertically polarized and parallel to the plane of incidence in the direction of the unit vector $\hat{\boldsymbol{\varepsilon}}_{\parallel}$. When the **E**-field is perpendicular to the plane of incidence the light is horizontally polarized and parallel to the surface in the direction of the unit vector $\hat{\boldsymbol{\varepsilon}}_{\perp}$. These concepts are illustrated in Fig. 2.9. The polarization vector has usually been assumed in the x-direction in past discussions, but can be any direction perpendicular to the propagation direction. Thus, to specify linear polarization in general requires a two-dimensional orthonormal vector basis set, as given by

$$\hat{\boldsymbol{\varepsilon}} = a\hat{\boldsymbol{\varepsilon}}_{\parallel} + b\hat{\boldsymbol{\varepsilon}}_{\perp}, \tag{2.147}$$

Table 2.1 States of Polarization

State	Designation
Linear	Horizontal, $\perp$, perpendicular, s, σ
	Vertical, $\parallel$, parallel, p, π
Circular	Right-handed
	Left-handed
Elliptical	Right-handed
	Left-handed

where

$$a^2 + b^2 = 1 = \hat{\boldsymbol{\varepsilon}} \cdot \hat{\boldsymbol{\varepsilon}} \quad \text{and} \quad \hat{\boldsymbol{\varepsilon}}_{\parallel} \cdot \hat{\boldsymbol{\varepsilon}}_{\perp} = 0$$

Orthonormal circular polarization basis vectors are complex, and given by

$$\hat{\boldsymbol{\varepsilon}}_R = \frac{1}{\sqrt{2}} \hat{\boldsymbol{\varepsilon}}_{\parallel} + j\hat{\boldsymbol{\varepsilon}}_{\perp} \quad \text{and} \quad \hat{\boldsymbol{\varepsilon}}_L = \frac{1}{\sqrt{2}}(\hat{\boldsymbol{\varepsilon}}_{\parallel} - j\hat{\boldsymbol{\varepsilon}}_{\perp}), \quad (2.148a)$$

for right and left circular polarization, respectively, where

$$\hat{\boldsymbol{\varepsilon}}_R \cdot \hat{\boldsymbol{\varepsilon}}_R^* = 1 = \hat{\boldsymbol{\varepsilon}}_L \cdot \hat{\boldsymbol{\varepsilon}}_L^* \quad \text{and} \quad \hat{\boldsymbol{\varepsilon}}_R \cdot \hat{\boldsymbol{\varepsilon}}_L^* = 0. \quad (2.148b)$$

Any polarization can be expressed in terms of this basis set as well. Thus it is not necessary to define a basis set for elliptical polarization.

The degree of polarization is an indication of the percentage of light that is polarized. Light may be polarized to a high degree, as is the case for some lasers. Light may be unpolarized, as is the case for blackbody radiation. Unpolarized light contains equal amounts of statistically independent horizontally and vertically polarized light. Light may also contain some levels of polarized and unpolarized light; this is referred to as partially polarized. It may also be of interest for polarized light, to determine the degree
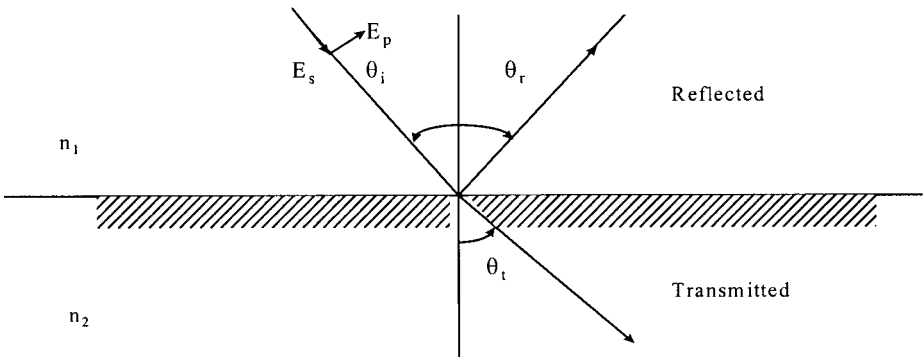
Fig. 2.9 Plane-wave reflection at a dielectric interface for parallel and perpendicular polarizations in the plane of incidence.

of linear or circular polarization within the polarized beam. This requires more sophistication than just specifying the polarization state.

The choice of polarization basis sets does not indicate the state and degree of polarization. To do this requires the four-component Stokes vector, as defined below and computed using Eq. 2.19a,

$$
\begin{pmatrix} I \\ Q \\ U \\ V \end{pmatrix} = \begin{pmatrix} \langle E_\| E_\|^* + E_\perp E_\perp^* \rangle_t \\ \langle E_\| E_\|^* - E_\perp E_\perp^* \rangle_t \\ \langle E_\| E_\perp^* + E_\perp E_\|^* \rangle_t \\ j \langle E_\| E_\perp^* - E_\perp E_\|^* \rangle_t \end{pmatrix} = \frac{1}{2} \begin{pmatrix} |E_{\|0}|^2 + |E_{\perp 0}|^2 \\ |E_{\|0}|^2 - |E_{\perp 0}|^2 \\ 2E_{\|0} E_{\perp 0}^* \cos[(\alpha_{\|fp} - \alpha_{\perp fp})z] \\ 2E_{\|0} E_{\perp 0}^* \sin[(\alpha_{\|fp} - \alpha_{\perp fp})z] \end{pmatrix}. \qquad (2.149)
$$

All the Stokes vector components are real and measurable. I is proportional to the total radiance of the light (by a factor of $1/(2\eta)$, see Eq. 1.19), the sum of all polarized and unpolarized light intensities. Q is a measure of the difference of horizontal and vertical light and can be experimentally determined by using linear polarizers. Also, the Stokes vector requires only three components when the light is completely polarized. The fourth component determines the degree of polarization (see Born and Wolf, Ref. 2.1, p. 30).

However, if unpolarized light is present in the beam then another measurement is required to uniquely determine the degree of polarization. The polarizer can be rotated $\pm 45°$ and the previous experiment repeated. Thus, the difference will change if the light is polarized, but will not change if the light is unpolarized. The rotation of the polarization basis vectors is accomplished by the following transformation

$$
\begin{pmatrix} \hat{\boldsymbol{\varepsilon}}_+ \\ \hat{\boldsymbol{\varepsilon}}_- \end{pmatrix} = \begin{pmatrix} \cos\theta & \sin\theta \\ -\sin\theta & \cos\theta \end{pmatrix} \begin{pmatrix} \hat{\boldsymbol{\varepsilon}}_\perp \\ \hat{\boldsymbol{\varepsilon}}_\| \end{pmatrix} \qquad (2.150)
$$

For $\theta = 45°$, the new orthonormal basis vectors, $\hat{\boldsymbol{\varepsilon}}_+$ and $\hat{\boldsymbol{\varepsilon}}_-$, become

$$
\hat{\boldsymbol{\varepsilon}}_- = \frac{1}{\sqrt{2}} \hat{\boldsymbol{\varepsilon}}_\| + \hat{\boldsymbol{\varepsilon}}_\perp \quad \text{and} \quad \hat{\boldsymbol{\varepsilon}}_+ = \frac{1}{\sqrt{2}} (\hat{\boldsymbol{\varepsilon}}_\| - \hat{\boldsymbol{\varepsilon}}_\perp), \qquad (2.151)
$$

as illustrated in Fig. 2.10. The corresponding **E**-field amplitudes in the $\hat{\boldsymbol{\varepsilon}}_+$ and $\hat{\boldsymbol{\varepsilon}}_-$ directions are

$$
\mathbf{E}_- = \frac{1}{\sqrt{2}} (\mathbf{E}_\| + \mathbf{E}_\perp) \quad \text{and} \quad \mathbf{E}_+ = \frac{1}{\sqrt{2}} (\mathbf{E}_\| + \mathbf{E}_\perp). \qquad (2.152)
$$

To repeat the previous experiment requires computation of the difference of the polarized intensities in the $\hat{\boldsymbol{\varepsilon}}_+$ and $\hat{\boldsymbol{\varepsilon}}_-$ reference frame. The result is

$$
E_+ E_+^* - E_- E_-^* = E_\| E_\perp^* + E_\perp E_\|^*. \qquad (2.153)
$$
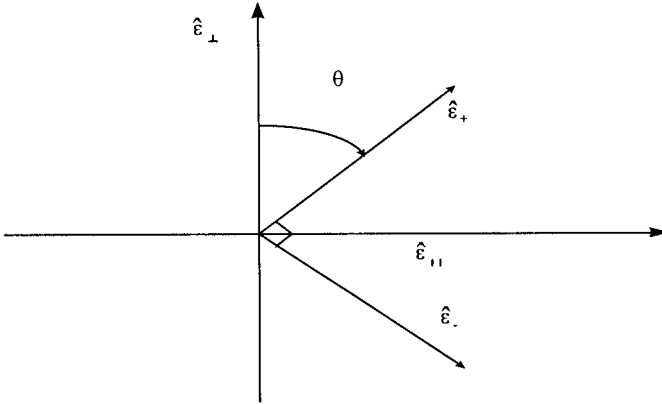
Fig. 2.10 Rotation of polarization unit vector basis set.

This is the U component of the Stokes vector. As a linear polarizer is rotated, it cannot distinguish between unpolarized and circularly polarized light. Thus the final test is to look at the difference of right and left circularly polarized light.

Using the basis vectors as defined in Eq. 2.148 the **E**-field components can be found by projection via the dot product,

$$\mathbf{E} \cdot \hat{\boldsymbol{\varepsilon}}_R^* = \mathbf{E}_R = \frac{1}{\sqrt{2}}(\mathbf{E}_\parallel - j\mathbf{E}_\perp), \tag{2.154a}$$

and

$$\mathbf{E} \cdot \hat{\boldsymbol{\varepsilon}}_L^* = \mathbf{E}_L = \frac{1}{\sqrt{2}}(\mathbf{E}_\parallel - j\mathbf{E}_\perp), \tag{2.154b}$$

The difference of the right circularly polarized and left circularly polarized light intensities becomes

$$E_R E_R^* - E_L E_L^* = j\left(E_\parallel E_\perp^* - E_\perp E_\parallel^*\right). \tag{2.155}$$

This represents the fourth component in the Stokes vector. From these measurements the degree of polarization can be found, using the following formula:

$$\text{Degree of polarization} = \frac{\sqrt{Q^2 + U^2 + V^2}}{I}. \tag{2.156}$$

When the degree of polarization is 0, the light is unpolarized. When it is 1, the light is competely polarized. Partial polarization occurs when the degree of polarization is

between 0 and 1. Also, the degree of polarization for linear and circular polarization can be obtained by the following formulas:

$$\text{Degree of linear polarization} = \frac{\sqrt{Q^2 + U^2}}{I} \tag{2.157}$$

and

$$\text{Degree of circular polarization} = \frac{V}{I}. \tag{2.158}$$

Based on Eqs. 2.149, 2.153, and 2.155, the Stokes parameters can be experimentally determined according to the following equation:

$$\begin{pmatrix} I \\ Q \\ U \\ V \end{pmatrix} = \eta_0 \begin{pmatrix} L \\ L_v - L_h \\ L_+ - L_- \\ L_R - L_L \end{pmatrix} = \eta_0 \begin{pmatrix} L \\ L - 2L_h \\ L - 2L_- \\ L - 2L_L \end{pmatrix} \tag{2.159a}$$

where (v = vertical, h = horizontal, $+$ = $+45°$, $-$ = $-45°$, etc., polarization), and

$$L = L_v + L_h = L_+ + L_- = L_R + L_L. \tag{2.159b}$$

Four independent radiance measurements are required to determine the four independent Stokes parameters. However, the results using seven radiance measurements lead to direct physical interpretation and will be used in following discussions. In matrix form, Eq. 2.159 becomes

$$\mathbf{s} = \begin{pmatrix} I \\ Q \\ U \\ V \end{pmatrix} = \eta_0 \begin{pmatrix} 1 & 0 & 0 & 0 & 0 & 0 & 0 \\ 0 & 1 & -1 & 0 & 0 & 0 & 0 \\ 0 & 0 & 0 & 1 & -1 & 0 & 0 \\ 0 & 0 & 0 & 0 & 0 & 1 & -1 \end{pmatrix} \begin{pmatrix} L \\ L_v \\ L_h \\ L_+ \\ L_- \\ L_R \\ L_L \end{pmatrix} \equiv \eta_0(T)\mathbf{L}. \tag{2.160}$$

(T) is the transformation matrix between the Stokes vector space and a vector space containing experimentally determined components based on radiance measurements with polarizers. Thus, the Stokes vector is a practical representation of polarization and allows the connection between theory (Eq. 2.149) and experiment (Eq. 2.159). The inverse transform is also useful, and is given by

$$\mathbf{L} = \frac{1}{\eta_0}(T)^{-1}\mathbf{s} \tag{2.161}$$

where

$$(T)^{-1} = \frac{1}{2}\begin{pmatrix} 2 & 0 & 0 & 0 \\ 1 & 1 & 0 & 0 \\ 1 & -1 & 0 & 0 \\ 1 & 0 & 1 & 0 \\ 1 & 0 & -1 & 0 \\ 1 & 0 & 0 & 1 \\ 1 & 0 & 0 & -1 \end{pmatrix}.$$

Based on Eq. 2.160, the Stokes vectors for standard states of polarization can be directly determined, and are listed in Table 2.2. The Stokes vectors are normalized so that $I = 1$ in the table.

2.1.2.3 Scattering and Polarization

When the scattering particle is spherical, the scattered light has the same state of polarization as the incident light field. However, very few particles and molecules are spherical in shape and, in general, the scattered field has a different polarization character relative to the incident field. Since the state and degree of polarization is completely specified by the Stokes vector, it is desirable to have a transformation matrix which produces the transmitted or scattered-field Stokes vector given the incident-field Stokes vector. Such a matrix is called the Mueller matrix, (M), as defined by

Table 2.2 Normalized Stokes Vectors for Various States of Polarization

Unpolarized

$$\begin{pmatrix} 1 \\ 0 \\ 0 \\ 0 \end{pmatrix}$$

Linearly polarized

$$\begin{pmatrix} 1 \\ 1 \\ 0 \\ 0 \end{pmatrix} \qquad \begin{pmatrix} 1 \\ -1 \\ 0 \\ 0 \end{pmatrix} \qquad \begin{pmatrix} 1 \\ 0 \\ 1 \\ 0 \end{pmatrix} \qquad \begin{pmatrix} 1 \\ 0 \\ -1 \\ 0 \end{pmatrix}$$

Vertical   Horizontal $+45°$ $+45°$

Circularly polarized

$$\begin{pmatrix} 1 \\ 0 \\ 0 \\ 1 \end{pmatrix} \qquad \begin{pmatrix} 1 \\ 0 \\ 0 \\ -1 \end{pmatrix}$$

Right   Left

$$\mathbf{s}_s = \begin{pmatrix} I_s \\ Q_s \\ U_s \\ V_s \end{pmatrix} = \begin{pmatrix} M_{11} & M_{12} & M_{13} & M_{14} \\ M_{21} & M_{22} & M_{23} & M_{24} \\ M_{31} & M_{32} & M_{33} & M_{34} \\ M_{41} & M_{42} & M_{43} & M_{44} \end{pmatrix} \begin{pmatrix} I_i \\ Q_i \\ U_i \\ V_i \end{pmatrix} = (M)\mathbf{s}_i. \quad (2.162)$$

The Mueller matrix elements can be determined both experimentally and theoretically. Each matrix element is a bidirectional function of Ω_i and Ω_s.

Experimental determination of the Mueller matrix elements is based on Eqs. 2.160 and 2.161, and the following transformation between the incident and scattered $\mathbf{L}$ vectors

$$\mathbf{L}_s = \begin{pmatrix} L_s \\ L_{vs} \\ L_{hs} \\ L_{+s} \\ L_{-s} \\ L_{Rs} \\ L_{Ls} \end{pmatrix} = \begin{pmatrix} X_{00} & X_{0v} & X_{0h} & X_{0+} & X_{0-} & X_{0R} & X_{0L} \\ X_{v0} & X_{vv} & X_{vh} & X_{v+} & X_{v-} & X_{vR} & X_{vL} \\ X_{h0} & X_{hv} & X_{hh} & X_{h+} & X_{h-} & X_{hR} & X_{hL} \\ X_{+0} & X_{+v} & X_{+h} & X_{++} & X_{+-} & X_{+R} & X_{+L} \\ X_{-0} & X_{-v} & X_{-h} & X_{-+} & X_{--} & X_{-R} & X_{-L} \\ X_{R0} & X_{Rv} & X_{Rh} & X_{R+} & X_{R-} & X_{RR} & X_{RL} \\ X_{L0} & X_{Lv} & X_{Lh} & X_{L+} & X_{L-} & X_{LR} & X_{LL} \end{pmatrix} \begin{pmatrix} L_i \\ L_{vi} \\ L_{hi} \\ L_{+i} \\ L_{-i} \\ L_{Ri} \\ L_{Li} \end{pmatrix} = (X)\mathbf{L}_i.$$

$$(2.163)$$

The (X) matrix represents 49 different but related experimental measurements involving various combinations of previously mentioned polarizers. The subscript 0 indicates unpolarized light, v, vertical polarization, h, horizontal polarization, $+$, 45° polarization, $-$, $-45°$ polarization, R, right circular polarization, and L, left circular polarization. The first subscript indicates the polarization of the incident light and the last subscript indicates the polarizer used on the scattered or transmitted light before the detector. These are more measurements than needed. However, this approach leads to Mueller matrix elements with direct interpretation. The experimental Mueller matrix is obtained by the following matrix transformation:

$$(M) = (T)(X)(T)^{-1}.$$

Performing the transformation, the experimentally determined Mueller matrix becomes

$(M)_0 =$

$$\frac{1}{2} \begin{pmatrix} 5X_{00} & (X_{0v} - X_{0h}) & (X_{0+} - X_{0-}) & (X_{0R} - X_{0L}) \\ 5(X_{v0} - X_{h0}) & (X_{vv} + X_{hh}) - (X_{vh} + X_{hv}) & (X_{v+} + X_{h-}) - (X_{h+} - X_{v-}) & (X_{vR} + X_{hL}) - (X_{hR} + X_{vL}) \\ 5(X_{+0} - X_{-0}) & (X_{+v} + X_{-h}) - (X_{-v} + X_{+h}) & (X_{++} + X_{--}) - (X_{-+} + X_{+-}) & (X_{+R} + X_{-L}) - (X_{-R} + X_{+L}) \\ 5(X_{R0} - X_{L0}) & (X_{Rv} + X_{Lh}) - (X_{Lv} + X_{Rh}) & (X_{R+} + X_{L-}) - (X_{L+} + X_{R-}) & (X_{RR} + X_{LL}) - (X_{LR} + X_{RL}) \end{pmatrix}.$$

$$(2.164)$$

To obtain this result the following relationships were used:

$$X_{00} = X_{0v} + X_{0h} = X_{0+} + X_{0-} = X_{0R} + X_{0L}.$$

In this formulation of the Mueller matrix, the M_{11} component is related to the BSDF or X_{00} when the incident and scattered fields, are properly defined (see Eq. 2.86). Thus, the Mueller matrix represents all combinations of polarization states of the incident and scattered fields, and each component is a bidirectional function of the solid angle of incidence and the solid angle of scatter. The BSDF concept now has been generalized to include polarization.

Theoretical determination of the Mueller matrix begins with the scattering matrix, (S), which is based on a generalization of Eq. 2.121 by representing the incident and scattered **E**-fields in terms of two orthogonal directions of polarization (vertical and horizontal in this case). Therefore,

$$\mathbf{E}_s = \begin{pmatrix} E_{vs} \\ E_{hs} \end{pmatrix} = \frac{e^{-jk'r+jk'z}}{jk'r} \begin{pmatrix} S_1(\Omega_i, \Omega_s) & S_2(\Omega_i, \Omega_s) \\ S_3(\Omega_i, \Omega_s) & S_4(\Omega_i, \Omega_s) \end{pmatrix} \begin{pmatrix} E_{vi} \\ E_{hi} \end{pmatrix} = \frac{e^{-jk'r+jk'z}}{jk'r}(S)\mathbf{E}_i.$$

(2.165)

Since we are interested in calculating optical field intensities and, ultimately, the Stokes vector, an intermediate step is necessary. This step begins with the definition of the coherency matrix, (C), defined as (see O'Neill, Ref. 2.10, Chapter 9)

$$(C) = \langle \mathbf{e}(t) \times \mathbf{e}^\dagger(t) \rangle_t = \begin{pmatrix} J_{xx} & J_{xy} \\ J_{yx} & J_{yy} \end{pmatrix}$$

(2.166)

where $\times$ represents a direct or Kronecker matrix product, $\mathbf{e}^\dagger$ is the Hermitian conjugate of $\mathbf{e}$ and

$$J_{ij} = \langle e_i e_j^\dagger \rangle_t = \frac{1}{2}\mathrm{Re}[E_i E_j^*].$$

Using Eq. 2.165 and the definition of the coherency matrix, a relation between the scattered and incident coherency matrices can be obtained, and is given by

$$(C)_s = \langle \mathbf{e}_s \times \mathbf{e}_s^\dagger \rangle_t = \frac{1}{k'^2r^2}\langle (S)E_i \times (S)^* E_i^* \rangle_t = \frac{[(S) \times (S)^*]}{k'^2r^2}(C)_i.$$

(2.167)

This result can be compared to Eq. 2.122. To express the above equation in matrix form requires reformatting the coherency matrix into a column vector, then

$$\mathbf{C}_s = \begin{pmatrix} J_{xxs} \\ J_{xys} \\ J_{yxs} \\ J_{yys} \end{pmatrix} = \frac{1}{k'^2r^2} \begin{pmatrix} S_{11} & S_{12} & S_{21} & S_{22} \\ S_{13} & S_{14} & S_{23} & S_{24} \\ S_{31} & S_{32} & S_{41} & S_{42} \\ S_{33} & S_{34} & S_{43} & S_{44} \end{pmatrix} \begin{pmatrix} J_{xxi} \\ J_{xyi} \\ J_{yxi} \\ J_{yyi} \end{pmatrix} \equiv \frac{(\overline{S})}{k'^2r^2}\mathbf{C}_i.$$

(2.168)

where

$$S_{ij} = S_i S_j^*.$$

The matrix transformation relationship between the coherency vector and the Stokes vector is straightforward to express,

$$
\mathbf{s} = \begin{pmatrix} J_{xx} + J_{yy} \\ J_{xx} - J_{yy} \\ J_{xy} + J_{yx} \\ j(J_{xy} - J_{yx}) \end{pmatrix} = \begin{pmatrix} 1 & 0 & 0 & 1 \\ 1 & 0 & 0 & -1 \\ 0 & 1 & 1 & 0 \\ 0 & j & -j & 0 \end{pmatrix} \begin{pmatrix} J_{xx} \\ J_{xy} \\ J_{yx} \\ J_{yy} \end{pmatrix} \equiv (\overline{T})\mathbf{C}. \qquad (2.169)
$$

The inverse transform is also needed and is given by

$$
\mathbf{C} = \frac{1}{2} \begin{pmatrix} 1 & 1 & 0 & 0 \\ 0 & 0 & 1 & -j \\ 0 & 0 & 1 & j \\ 1 & -1 & 0 & 0 \end{pmatrix} \begin{pmatrix} I \\ Q \\ U \\ V \end{pmatrix} \equiv (\overline{T})^{-1}\mathbf{s}. \qquad (2.170)
$$

Using Eqs. 2.162, 2.168, 2.169, and 2.170, the theoretical Mueller matrix can be obtained from the following formula:

$$(M)_{th} = \frac{1}{k'^2 r^2}(\overline{T})(\overline{S})(\overline{T})^{-1}. \qquad (2.171)$$

The solution is

$(M)_{th} = \frac{1}{2k'^2 r^2} \times$

$$
\begin{pmatrix}
(S_{11} + S_{22} + S_{33} + S_{44}) & (S_{11} + S_{33} - S_{22} - S_{44}) & (S_{12} + S_{34} + S_{21} + S_{43}) & j(S_{21} + S_{43} - S_{12} - S_{34}) \\
(S_{11} - S_{33} + S_{22} - S_{44}) & (S_{11} - S_{33} - S_{22} + S_{44}) & (S_{12} - S_{34} + S_{21} - S_{43}) & j(S_{21} - S_{43} - S_{12} + S_{34}) \\
(S_{13} + S_{31} + S_{24} + S_{42}) & (S_{13} + S_{31} - S_{24} - S_{42}) & (S_{14} + S_{32} + S_{23} + S_{41}) & j(S_{14} + S_{32} - S_{23} - S_{41}) \\
j(S_{13} - S_{31} + S_{24} - S_{42}) & j(S_{13} - S_{31} - S_{24} + S_{42}) & j(S_{14} - S_{32} + S_{23} - S_{41}) & (S_{14} - S_{32} - S_{23} + S_{41})
\end{pmatrix}.
$$

$$(2.172)$$

Again the M_{11} component is the BSDF when both the incident and scattered fields are unpolarized.

As an example, consider the characterization of a linear polarizer at an arbitrary angle, ξ, which is illuminated by a plane wave. The scattering matrix between the incident and transmitted fields is

$$
\begin{pmatrix} E_{vt} \\ E_{ht} \end{pmatrix} = \begin{pmatrix} \cos^2\xi & \sin\xi\cos\xi \\ \sin\xi\cos\xi & \sin^2\xi \end{pmatrix} \begin{pmatrix} E_{vi} \\ E_{hi} \end{pmatrix}. \qquad (2.173)
$$

Table 2.3. Mueller Matrices for Various Polarizers

Vertical polarizer, $\xi = 0°$

$$\frac{1}{2} \begin{pmatrix} 1 & 1 & 0 & 0 \\ 1 & 1 & 0 & 0 \\ 0 & 0 & 0 & 0 \\ 0 & 0 & 0 & 0 \end{pmatrix}$$

Horizontal polarizer, $\xi = 90°$

$$\frac{1}{2} \begin{pmatrix} 1 & -1 & 0 & 0 \\ -1 & 1 & 0 & 0 \\ 0 & 0 & 0 & 0 \\ 0 & 0 & 0 & 0 \end{pmatrix}$$

45° polarizer, $\xi = 45°$

$$\frac{1}{2} \begin{pmatrix} 1 & 0 & 1 & 0 \\ 0 & 0 & 0 & 0 \\ 1 & 0 & 1 & 0 \\ 0 & 0 & 0 & 0 \end{pmatrix}$$

−45° polarizer, $\xi = -45°$

$$\frac{1}{2} \begin{pmatrix} 1 & 0 & -1 & 0 \\ 0 & 0 & 0 & 0 \\ -1 & 0 & -1 & 0 \\ 0 & 0 & 0 & 0 \end{pmatrix}$$

Right circular polarizer

$$\frac{1}{2} \begin{pmatrix} 1 & 0 & 0 & 1 \\ 0 & 0 & 0 & 0 \\ 0 & 0 & 0 & 0 \\ 1 & 0 & 0 & 1 \end{pmatrix}$$

Left circular polarizer

$$\frac{1}{2} \begin{pmatrix} 1 & 0 & 0 & -1 \\ 0 & 0 & 0 & 0 \\ 0 & 0 & 0 & 0 \\ -1 & 0 & 0 & 1 \end{pmatrix}$$

This equation is for plane-wave transmission, thus the multiplicative factor of Eq. 2.165 for spherical-wave propagation is not appropriate.

Following the previously described procedure, the computed Mueller matrix becomes

$$(M)_{th} = \frac{1}{2} \begin{pmatrix} 1 & \cos 2\xi & \sin 2\xi & 0 \\ \cos 2\xi & \cos^2 2\xi & \cos 2\xi \sin 2\xi & 0 \\ \sin 2\xi & \sin 2\xi \cos 2\xi & \sin^2 2\xi & 0 \\ 0 & 0 & 0 & 0 \end{pmatrix}. \qquad (2.174)$$

Based on this result, the Mueller matrices for the linear polarizers needed to measure the Stokes vector components can be computed. The results are listed in Table 2.3, which also contain Mueller matrices for circular polarizers.

2.2 Optical Propagation in Matter

The propagation of beams and pulses of light in matter are now briefly considered. This section extends Section 1.3 for vacuum by updating previous equations for propagation in matter.

2.2.1 Beam Propagation

Equation 1.39 for a Gaussian beam is easily extended to propagation in matter. Consistent with the paraxial ray approximation, loss in the transverse directions can be ignored. Thus, the Gaussian beam radiance in a lossy medium becomes

$$L(x_o, y_o, z) = \frac{n \, |E_x(x_o, y_o, z)|^2}{2\eta_0} = \frac{n \, |E_{x00}|^2}{2\pi^2 w_0^2 w^2(z)\eta_0} e^{-2(x_o^2 + y_o^2)/w^2(z)} e^{-\beta_{ext} z}, \qquad (2.175)$$

where the substitution $k \rightarrow k_0' n$ $(k_0' = 2\pi/\lambda)$ is made, and the imaginary part of the complex index is kept only in factors that dictate the z-propagation dependence.

2.2.2 Pulse Propagation

The variation of the index of refraction with frequency is called dispersion. If dispersion can be ignored, then we need only change the speed of light in Eq. 1.40 to $c = c/n$ to obtain a valid solution. However, if dispersion cannot be ignored, then finding solutions to the wave equation is considerably more difficult. Furthermore, the frequency-domain wave equation given by Eq. 2.14 ignores the transient response of the medium to the electromagnetic field. To appreciate these points, let us examine the time-domain wave equation. Following the same procedure as in Section 2.1.1.1, we obtain

$$\nabla^2 \mathbf{e}(\mathbf{r}, t) = \frac{1}{c^2} \frac{\partial^2 \mathbf{e}(\mathbf{r}, t)}{\partial t^2} + \frac{1}{c^2} \frac{\partial^2}{\partial t^2} \int_{-\infty}^{\infty} dt' \chi(t') u(t') \, \mathbf{e}(\mathbf{r}, t - t'). \qquad (2.176a)$$

If a time-harmonic field is chosen, then the frequency-domain wave equation is obtained. However, pulses are inherently polychromatic, and time-harmonic solutions are not appropriate. Knowledge of the time-domain susceptibility now becomes important. If the time-domain electromagnetic pulse is slow compared with the dielectric response of the propagation medium, then the field can be brought outside the convolution integral, and frequency-domain solutions can be obtained. However, if the electromagnetic pulse is fast and comparable to the speed of the dielectric response, then it is best to solve the time-domain wave equation.

Equation 2.176a can be written more explicitly if we apply the step function in the convolution and require $t > t'$:

$$\nabla^2 \mathbf{e}(\mathbf{r}, t) = \frac{1}{c^2} \frac{\partial^2 \mathbf{e}(\mathbf{r}, t)}{\partial t^2} + \frac{1}{c^2} \frac{\partial^2}{\partial t^2} \int_{0}^{t} dt' \chi(t') \, \mathbf{e}(\mathbf{r}, t - t'). \qquad (2.176b)$$

This is an integrodifferential equation that is difficult to solve. Numerical techniques, such as finite-difference–time-domain (FD-TD), have been applied to obtain solutions for optoelectronic device design.

2.3 Microscopic Properties in Matter

Thus far, the problem of optical propagation has been reduced to requiring a knowledge of the spatial and spectral dependence of the complex index of refraction within the propagation medium, field polarization, and the path geometry. The most fundamental quantity is the complex index. This leads us to explore the microscopic nature of matter for the derivation of meaningful models of the complex refractive index.

2.3.1 The Dipole Moment

Most propagation media of interest are insulators with no net charge density. The number of positive and of negative charges is equal. However, the nature of the charge distribution determines the coupling of the incident electromagnetic field to the propagation medium. The charge distribution is affected by the arrangement and type of atoms composing the medium and field induced effects.

Consider the multipole expansion of an electric potential $V(r)$, given the charge density $\rho_c(r)$, as stated by (see Chapter 4 of Jackson, Ref. 2.13)

$$V(\mathbf{r}) = \int \frac{\rho_c(\mathbf{r}')}{|\mathbf{r} - \mathbf{r}'|} \, d^3 r'. \tag{2.177}$$

The Green's function can be expanded in terms of spherical harmonics, Y_{lm} (see Appendix 2), where for $r > r'$

$$\frac{1}{|\mathbf{r} - \mathbf{r}'|} = 4\pi \sum_{l=0}^{\infty} \sum_{m=-l}^{l} \frac{1}{2l+1} \frac{r'^l}{r^{l+1}} Y_{lm}^*(\theta', \phi') Y_{lm}(\theta, \phi). \tag{2.178}$$

This allows the potential to be expanded as a sum of multipole moments. By substituting Eq. 2.178 into Eq. 2.177, the following sum is obtained:

$$V(\mathbf{r}) = 4\pi \sum_{l,m} \frac{q_{lm}}{2l+1} \frac{Y_{lm}^*(\theta, \phi)}{r^{l+1}}, \tag{2.179}$$

where the q_{lm}s are the multipole moments, as given by

$$q_{lm} = \int Y_{lm}^*(\theta', \phi') r'^l \rho_c(\mathbf{r}') \, d^3 r'. \tag{2.180}$$

It is instructive to calculate the first few terms of q_{lm}. They are as follows:

$$q_{00} = \frac{1}{\sqrt{4\pi}} q, \tag{2.181}$$

$$q_{10} = \sqrt{\frac{3}{4\pi}} \mu_{dp,z}, \tag{2.182a}$$

and

$$q_{11} = -q_{1-1}^* = -\sqrt{\frac{3}{8\pi}} \left(\mu_{dp,x} - j\mu_{dp,y} \right) \tag{2.182b}$$

where q is the net charge of the medium and $\boldsymbol{\mu}_{dp}$ is the dipole moment, defined as

$$\boldsymbol{\mu}_{dp} = \int \mathbf{r}' \rho_c(\mathbf{r}') \, d^3 r'. \tag{2.183}$$

Higher order terms in the expansion include quadrupole moments, octupole moments, and so on. The strength of the potential decreases as the moments go to higher order. Thus, the leading nontrival term in the expansion is always the most important, and often the only one needed to represent the coupling of the electromagnetic field to the propagation medium.

The relevant microscopic element, for the coupling of the electromagnetic field to a neutral ($q = 0$) propagation medium, is the dipole moment. It is created by the separation of opposite charges, as illustrated below. The dipole moment strength, $\boldsymbol{\mu}_{dp}(t)$, is the product of the charge, q, and the charge separation, $\mathbf{x}(t)$,

$$\boldsymbol{\mu}_{dp}(t) = q\mathbf{x}(t). \tag{2.184}$$

For a neutral medium with no dipole moment, the quadrupole moment becomes the leading term; it is illustrated in Fig. 2.11. This is a very weak coupling term and is usually not an issue for most optical media and path lengths. A medium with permanent dipole moments is called polar. A medium with no permanent dipole moments is called nonpolar.

2.3.2 Polarizability

When an external electric field is present, the bound charge distribution of a medium is altered. The dominant effect is the induction of new dipole moments and alignment of permanent dipole moments by this external field. The degree to which this is done on a single molecule is a measure of the frequency-domain electric molecular polarizability, $\alpha_{e,mol}(\omega)$, defined as

$$\langle q\mathbf{X}(\omega)\rangle = \langle \boldsymbol{\mu}_{dp}(\omega)\rangle = \alpha_{e,mol}(\omega)\mathbf{E}. \tag{2.185}$$

$\langle \boldsymbol{\mu}_{dp}\rangle$ is the mean dipole moment vector and is proportional to the frequency-domain macroscopic polarization vector, $\mathbf{P}(\omega)$, as given by

$$\mathbf{P}(\omega) = \rho\langle \boldsymbol{\mu}_{dp}(\omega)\rangle = \epsilon_0\chi(\omega)\mathbf{E}(\omega), \tag{2.186}$$

where ρ is the number of dipoles per unit volume. Generally, the mean dipole moment, with no external field applied, is zero unless the material is an electret. Using the above
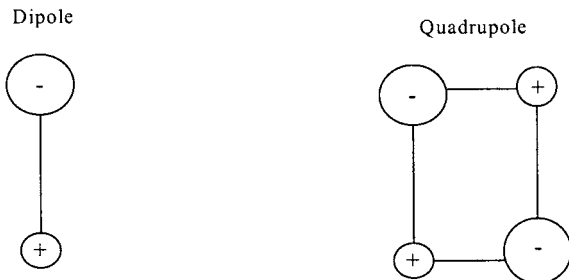
Fig. 2.11 Illustration of dipole and quadrupole moments.

results, the relation between the susceptibility and the molecular polarizability is obtained:

$$\chi(\omega) = \frac{\rho}{\epsilon_0} \alpha_{e,mol}(\omega). \tag{2.187}$$

In this manner, macroscopic quantities can be related to microscopic properties of a medium.

To further address the microscopic properties of the complex index of refraction requires the consideration of the quantum structure of matter and how light couples to that structure. This is the topic of the next three chapters.

Problems

2.1 For a nonmagnetic, nonconducting dielectric medium, show that the radiance, L, can be expressed as

$$L = \frac{1}{2} cn\epsilon_0 |\mathbf{E}|^2.$$

2.2 An absorption line in a medium is represented by the imaginary part of the relative permittivity $\epsilon_r''(v) = A\delta(v - v_0) - A\delta(v + v_0)$. Find the corresponding real part of the relative permittivity using the Kramers–Krönig relation. What is $\epsilon_r'(0)$ and $\epsilon_r'(\omega \gg \omega_0)$?

2.3 Derive Eqs. 2.51a, b from Eqs. 2.48a, b.

2.4 Derive Eq. 2.53a, using symmetry properties of the susceptibility.

2.5 Consider an infinite slab of thickness d, with a single-surface power reflection coefficient R, a single-surface power transmission coefficient $T = 1 - R$, and a one-pass loss factor $K = \exp(-\beta_{abs}d/\cos\theta_a)$.

  (a) The slab is illuminated by a rectilinear polychromatic ray bundle as illustrated in Fig. P2.5. Derive the specular transmittance, τ_S, the specular
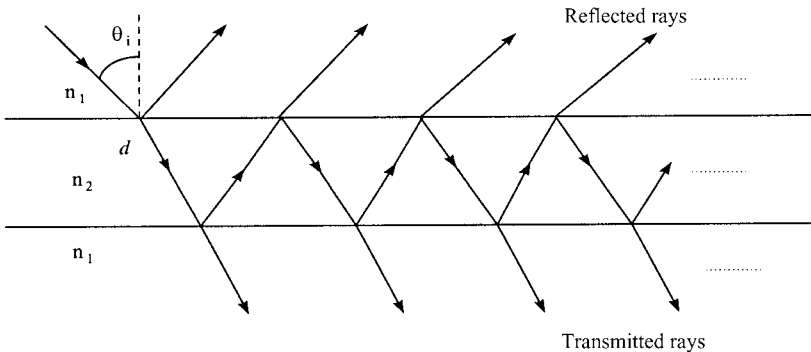
Fig. P2.5

reflectance, ρ_S, in terms of R and K, and verify Eqs. 2.96 and 2.97. According to the total power law,

$$\tau_S + \rho_S = 1 - \alpha_{abs,S}$$

where $\alpha_{abs,S}$ is the absorptance. Find the expression for $\alpha_{abs,S}$ in terms of R and K, as well, and show that for a lossless slab $\alpha_{abs,S}(K = 1) = 0$. (*Hint:* Use ray optics and obtain a series representation of the net transmitted power and reflected power rays.)

(b) Derive the corresponding formulas for transmittance, reflectance, and absorptance, and with monochromatic illumination, thus including the effects of interference. Now the rays represent field quantities. Let the field reflection coefficient, $r = |r| \exp(j\alpha_r)$, and field transmission coefficient, $t = |t| \exp(j\alpha_t)$, must be used. (*Note:* $R = |r|^2$ and $T = |t|^2$. The details of these coefficients in terms of the complex index of refraction are presented in Chapter 4.)

(c) Perform a spectral average on the transmittance of part (b) and show agreement with the transmittance of part (a). Thus, evaluate the following:

$$\tau_S = \langle \tau_{SI} \rangle = \frac{1}{\lambda_2 - \lambda_1} \int_{\lambda_1}^{\lambda_2} \tau_{SI}(\lambda) \, d\lambda = \frac{1}{2\pi} \int_0^{2\pi} \tau_{SI}(\phi) \, d\phi,$$

where $\phi = 2\omega n_2 (\cos\theta) \, d/c$. Then use contour integration to solve the integral on ϕ.

2.6 Based on Eqs. 2.74 and 2.98, show that a measurement of the emissivity is a direct measurement of the absorption coefficient when the internal transmittance is close to one ($K \geq 0.9$). Also, show that the emissivity is

$$1 - R,$$

when the absorption coefficient times the material thickness is large.

2.7 (a) Derive Eq. 2.119 from the eikonal equation. (b) Find the ray path in the xz-plane, given the spatial variation of the index of refraction is

$$n(z) = 1 + a + bz$$

for a ray initially directed in the x-direction and a and b small.

2.8 Verify Eq. 2.85.

2.9 Verify Eq. 2.126.

2.10 Start with Eq. 2.132 and derive Eq. 2.134. (*Hint:* This problem requires finding the solution to

$$\int_{-\infty}^{\infty} dt\, e^{-jat^2}.$$

Then let, $a = \lim_{b \to 0}(a - jb)$.

Then consult Gradshteyn and Ryzhik, Ref. 2.11.)

2.11 Show, for $\beta_{abs} = 0$ and $\theta_a = 0$, that Eq. 2.145 is true based on Eq. 2.143 in the single scatter limit.

2.12 For a spherical particle, the off-diagonal elements of the scattering matrix are zero. Obtain the Mueller matrix for this case.

Bibliography

General

2.1 M. Born and E. Wolf, *Principles of Optics*, 6th Ed., Pergamon Press (1980).

Section 2.1.1

2.2 F.K. Kneubühl, "Review on the Theory of Dielectric Dispersion of Insulators," *Infrared Physics*, **29**, pp. 925–942 (1989).

2.3 F.E. Nicodemus, J.C. Richmond, J.J. Hsia, I.W. Ginsberg, and T. Limperis, "Geometrical Considerations and Nomenclature for Reflectance," NBS Monograph 160 (1977).

2.4 W.L. Wolfe and G.J. Zissis (eds.), *The Infrared Handbook*, ERIM (1985).

2.5 P. Yeh, *Optical Waves in Layered Media*, Wiley-Interscience (1988).

2.6 M. Kline and I.W. Kay, *Electromagnetic Theory and Geometrical Optics*, Interscience Publishers (1965).

2.7 G.L. James, *Geometrical Theory of Diffraction for Electromagnetic Waves*, 2nd Ed., Peter Peregrinus (1980).

Section 2.1.2

2.8 H.C. Van de Hulst, *Light Scattering by Small Particles*, Dover (1981), Chs. 3 and 4.

2.9 C.F. Bohren and D.R. Huffman, *Absorption and Scattering of Light by Small Particles*, Wiley (1983).

2.10 E.L. O'Neill, *Introduction to Statistical Optics*, Addison-Wesley (1963).

2.11 I.S. Gradshteyn and I.M. Ryzhik, *Table of Integrals Series and Products*, 4th Ed., Academic Press (1965).

Section 2.2

2.12 A. Taflove, *Computational Electrodynamics: The Finite-Difference Time-Domain Method*, Artech House (1995).

Section 2.3

2.13 J.D. Jackson, *Classical Electrodynamics*, 2nd Ed., Wiley (1975).

3

Spectroscopy of Matter

It is critical to understand the nature of the propagation medium in terms of the available resonances which couple to the electromagnetic field. The detailed specification of the complex index of refraction as a function of frequency is the subject of spectroscopy. Since propagation media cover all phases of matter, the spectroscopy of gases, solids, and liquids is introduced in this chapter. Topics are not exhaustively covered, but rather with sufficient depth to support the practical applications that will come later.

The chapter begins with a formal review of topics covered in stationary-state quantum mechanics necessary for the development of spectroscopy. The next section develops models to calculate spectral line positions, which are necessary to characterize a spectral line. The full development of spectral line parameters is not only the goal of this chapter but the next two as well. The remaining sections address the essential elements of the spectroscopy of gases, solids and liquids. Both classical and quantum models are used.

3.1 Quantum Mechanics I

Time-independent quantum mechanics allows the description of the quantized energy level structure of matter. This is the central topic of this chapter. Time-dependent quantum mechanics is necessary for the development of a theory covering transitions between stationary-state energy levels and is the topic of Chapter 5.

3.1.1 Early Quantum Mechanics and Light

The classical concept of light is that of an oscillating continuous wave field, as presented in the first two chapters. This is consistent with the classical electrodynamics

based on Maxwell's equations. However, the work by Planck on blackbody radiation and Einstein on the photoelectric effect showed that optical fields also have a quantized or particle-like nature.

Planck, in 1900, suggested that the energy of light, E, be quantized according to

$$E = hf \text{ [J]} \tag{3.1}$$

where f is frequency (sec^{-1}) and h is Planck's constant ($h = 6.6260755(40) \times 10^{-34}$ J-sec). This allowed a theoretical description of blackbody radiation for the first time. However, it was Einstein, who, a few years later, made Eq. 3.1 more credible by applying it to explain the photoelectric effect.Only light of a certain frequency or greater, incident upon a material, can induce a current. A light field with the same radiance but lower frequency will not induce a current. This also required the energy of light to be quantized in packets or particle-like quantities. This notion of quantized light was further verified by the Compton effect (1923), which states that light will be deflected by an electron much like a particle–particle interaction. These wave packets or particles of light are called *photons*. The wave packet concept, as illustrated in Fig. 3.1, is commonly used to describe quantum-mechanical particles. The particle is contained within the packet, thus the precise position of the particle is uncertain.

This work showed that light has a particle nature, as well as the previously established wave nature (interference and diffraction of physical optics). This dual nature of light is naturally incorporated into quantum mechanics which requires all particles to have a characteristic wavelength or De Broglie wavelength, λ, expressed as

$$\lambda = \frac{h}{p}, \tag{3.2}$$

where p is the momentum. This equation, first expressed in 1924 by De Broglie, can also be written as

$$\hbar k' = p \tag{3.3}$$

where $\hbar = h/2\pi$ and $k' = 2\pi/\lambda$ and is called the magnitude of the wave-vector. Thus, electrons, protons etc., must also have a wave–particle duality just like the photon.
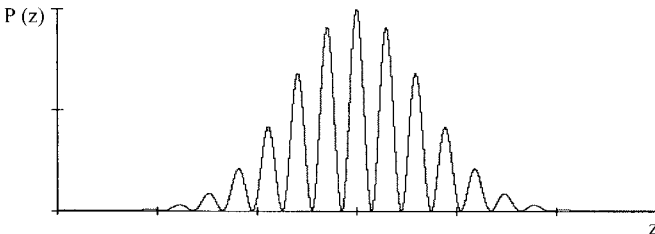
Fig. 3.1 The wave packet representation of a photon, indicating the probable location of the quantized particle.

The energy of a photon, because of its wave nature, cannot be precisely determined if anything is known about it in time. This statement can be intuitively made by using $E = hf$ and the time–bandwidth product of Fourier transform theory. Thus given

$$\Delta E = h \Delta f \quad \text{and} \quad \Delta f \Delta t \geq \frac{1}{4\pi},$$

then

$$\Delta E \Delta t \geq \frac{\hbar}{2}. \tag{3.4}$$

This statement is the Heisenberg uncertainty principle, which is fundamental to quantum physics. The uncertainty principle applies to Fourier transform or conjugate pairs, like time and energy or position and momentum. Simply put, the temporal and spectral character of the photon cannot be simultaneously stated with infinite precision.

The modern notion of the photon is based on the quantization of the electric and magnetic fields. These fields are assumed to be generated by harmonic oscillators. By quantizing these harmonic oscillators the electric and magnetic fields can be described in terms of raising and lowering operators which denote creation and annihilation of a photon with a particular frequency, direction, and polarization.

A vacuum state or field is one which contains no photons. However, the harmonic oscillator representation of the photon requires a zero point energy or a background fluctuation of the field. Photons are being created and annihilated by electron and positron pair creation and annihilation. This creates a fluctuation in the vacuum state. Thus, an excited atom in vacuum can be induced to emit a photon with energy equivalent to the energy difference between the excited and lower states of the atom by this fluctuating background field. This is called spontaneous emission.

Spontaneous emission is a noise source in many systems and is an example of quantum noise. In propagation problems one must consider the noise of a medium that will add to the noise of the source and detector. More details of the quantized electromagnetic field are presented in Appendix 5, after more background material is developed in Chapters 4 and 5.

3.1.2 Formal Introduction

We have already discussed the Heisenberg uncertainty principle in relation to the photon and its description in terms of a wavepacket. Again the uncertainty principle is stated as

$$(\Delta x)\,(\Delta p) \geq \frac{\hbar}{2}$$

or

$$(\Delta E)\,(\Delta t) \geq \frac{\hbar}{2}.$$

The language of quantum physics is not in terms of the exact location or momentum of a particle but rather in terms of a distribution function that represent the probability that it will have a certain location or momentum. The Heisenberg uncertainty principle also suggests this notion. This explanation is called the Copenhagen interpretation.

In general, a probability density function is normalized as

$$\int_{-\infty}^{\infty} P(x)\, dx = 1. \tag{3.5}$$

For example, $P(x)\, dx$ can represent the position of a particle between x and $x + dx$ with a certain probability. A general function of x, $f(x)$, has an expectation value, $\langle f(x) \rangle$, defined as

$$\langle f(x) \rangle = \int_{-\infty}^{\infty} f(x) p(x)\, dx. \tag{3.6}$$

Also of interest is the variance of the function, defined as

$$\langle f(x) - \langle f(x) \rangle \rangle^2 = \langle f^2(x) \rangle - \langle f(x) \rangle^2 = [\Delta f(x)]^2. \tag{3.7}$$

The standard deviation is the square root of the variance, $\Delta f(x)$. In this manner, observable quantities with corresponding uncertainties can be calculated.

Quantum mechanics, like any field of physics, can be formulated in terms of the following basic postulates:

1. Each particle in a physical system is described by a wave function, $\psi(\mathbf{r}, t)$. This function and its spatial derivative, $\nabla \psi$, are continuous, finite, and single valued.
2. In dealing with classical quantities such as position, r, energy, E, and momentum, p, we must relate these quantities with abstract quantum-mechanical operators defined in the following way:

	Classical Variable	Quantum Operator
Position	x, $\mathbf{r}$	$\hat{x}$, $\hat{\mathbf{r}}$
	$f(x)$, $f(\mathbf{r})$	$f(\hat{x})$, $f(\hat{\mathbf{r}})$
Momentum	$p(x)$, $p(\mathbf{r})$	$\frac{-\hbar}{j} \frac{\partial}{\partial x}$, $\frac{-\hbar}{j} \nabla$
Energy	E	$\frac{-\hbar}{j} \frac{\partial}{\partial t}$ or H

The hats (^) indicate an operator as opposed to a variable. H is the system Hamiltonian and equals the total system energy, thus

$$\hat{H} = \hat{T} + \hat{V}, \tag{3.8}$$

where T is the kinetic energy and V is the potential energy.

3. The probability of finding a particle with wave function ψ in the volume $dx\, dy\, dz$ is $\psi^* \psi\, dx\, dy\, dz$. The product $\psi^* \psi$ is normalized according to

$$\int_{-\infty}^{\infty} \psi^*(\mathbf{r})\, \psi(\mathbf{r})\, d\mathbf{r} = 1, \tag{3.9}$$

where $dr = dx\,dy\,dz$. The integration is over all space. Thus $\psi^*\psi(r)\left(=|\psi(r)|^2\right)$ is interpreted as a probability density function. The expectation value, $\langle Q \rangle$, of any variable Q is calculated from the wave function by using the operator Q_{op}, as defined in postulate 2, is given by

$$\langle Q \rangle = \int_{-\infty}^{\infty} \psi^* Q_{op}\psi\,dr. \tag{3.10}$$

4. Operators which commute produce observable quantities or expectation values that can be simultaneously determined with high accuracy. However, operators that do not commute produce observable quantities that cannot be determined simultaneously. This is the case for operators whose classical variable analogs are Fourier transform pairs, such as p and r. Because of its importance, commutation is designated by the commutation bracket, [ ]. For example,

$$\left(\hat{x}\hat{p}_x - \hat{p}_x\hat{x}\right)\psi(x) = \left[\hat{x},\,\hat{p}_x\right]\psi(x) = -j\hbar\psi(x).$$

The proof of this is left as an exercise in Problem 3.2.

5. Quantum mechanics must include classical mechanics in the appropriate limits, that is when:
   (a) The particles are large enough for wave motion to be neglected.
   (b) A continuum of energy levels exists.
   (c) $h \rightarrow 0$ approaches the "classical limit."

3.1.3 Wave and Matrix Mechanics

The total energy function for a particle is called its Hamiltonian. It is the kinetic plus potential energy $\left(\text{i.e., } H = T + V = 1/2\,mv^2 + V(\mathbf{r}) = p^2/(2m) + V(\mathbf{r})\right)$ The total energy and ψ are important parts of wave mechanics as represented by the Schrödinger wave equation, which determines the time and spatial evolution of these quantities. It is stated as

$$\hat{H}\psi(\mathbf{r},t) = -j\hbar\frac{\partial\psi(\mathbf{r},t)}{\partial t} \tag{3.11a}$$

or, expanding the Hamiltonian for a particle in a potential,

$$-\frac{\hbar^2\nabla^2}{2m}\psi(\mathbf{r},t) + V(\hat{\mathbf{r}},t)\,\psi(\mathbf{r},t) = -j\hbar\frac{\partial\psi(\mathbf{r},t)}{\partial t}. \tag{3.11b}$$

For a time-harmonic solution of the form

$$\psi(\mathbf{r},t) = \psi(\mathbf{r})\,e^{j\omega t}$$

and a time-independent potential, we obtain the stationary-state Schrödinger wave equation, the basis for wave mechanics, as given by

$$-\frac{\hbar^2 \nabla^2}{2m} \psi(\mathbf{r}) + V(\hat{\mathbf{r}}) \psi(\mathbf{r}) = \hbar \omega_n \psi(\mathbf{r}).$$

Based on Eq. 1.1, $\hbar \omega_n = E_n$ and the above equation reduces to

$$\hat{H} \psi_n(\mathbf{r}) = E_n \psi_n(\mathbf{r}). \tag{3.12}$$

Thus, stationary-state quantum mechanics is formulated as an eigenvalue problem with eigenfunctions, $\psi_n(\mathbf{r})$, eigenvalues, E_n, and quantum numbers, n (n can represent more than one number). The quantized energy structure of a system described by the Hamiltonian is the resulting energy eigenvalues. This approach, first proposed by Schrödinger in 1926, is commonly called "wave mechanics."

Another approach to describe quantum-mechanical phenomena was put forward by Heisenberg. It is called "matrix mechanics" and is mathematically isomorphic to wave mechanics. It offers a very useful, compact notation, called Dirac notation, emphasizing operators, eigenvalues, and quantum numbers. The statement of normalization of the probability density function is now defined by

$$\langle n|n \rangle = 1, \tag{3.13}$$

where $\langle n|$ is a "bra" vector and $|n\rangle$ is a "ket" vector (from the word "bracket"). The expectation value is $\langle Q \rangle = \langle n | Q_{op} | n \rangle$, where the operator is represented by a matrix. n represents the relevant quantum numbers of a system, and the spatial dependence is suppressed. The wave function, $\psi_n(\mathbf{r})$, is expressed as

$$\psi_n(\mathbf{r}) = \langle \mathbf{r}|n \rangle. \tag{3.14}$$

The corresponding stationary-state wave equation or eigenvalue equation is given as

$$\hat{H}|n\rangle = E_n|n\rangle, \tag{3.15}$$

similar to Eq. 3.12. The expectation value of the Hamiltonian operator becomes

$$\langle n|\hat{H}|n \rangle = E_n \langle n|n \rangle$$

and applying Eq. 3.13, the above equation reduces to

$$\langle H \rangle = E_n. \tag{3.16}$$

Generally, the ket vector $|n\rangle$ is denoted in terms of the set of system quantum numbers:

$$|n\rangle = |J, v\rangle,$$

for the case of molecular vibrating rotor. J is the rotational quantum number and v is the vibrational quantum number.

An operator is Hermitian or self-adjoint if it satisfies the following relation:

$$\langle n|\hat{H}|m \rangle = (\langle n|\hat{H})^*|m \rangle, \tag{3.17}$$

or in integral form

$$\int \psi_n(\hat{H}\psi_m)\, d\mathbf{r} = \int (\hat{H}\psi_n)^* \psi_m\, d\mathbf{r}. \qquad (3.18)$$

When the Hamiltonian of the system satisfies $H = H^*$, real energy eigenvalues are required, that is

$$\langle n|\hat{H}|n\rangle = E_n = \langle n|\hat{H}^*|n\rangle = E_n^*. \qquad (3.19)$$

Operators of physically observable quantities must be Hermitian and yield real eigenvalues.

The eigenstates, $|n\rangle$, form a basis set which spans the function space allowed by the governing differential equation, and are usually chosen to be orthonormal. An orthonormal basis set has the inner product property that

$$\langle n|n\rangle = \delta_{n'n}. \qquad (3.20)$$

The unit or identity operator, $\hat{1}$, is often useful and is defined as

$$\hat{1} = \int d\mathbf{r}|\mathbf{r}\rangle\langle\mathbf{r}| \quad \text{or} \quad \hat{1} = \sum_n |n\rangle\langle n| \qquad (3.21)$$

for either continuous or discrete systems, respectively. Using Eqs. 3.14, 3.20, and 3.21, it follows that the wave functions are orthonormal also, thus

$$\int d\mathbf{r}\psi_{n'}^*(\mathbf{r})\psi_n(\mathbf{r}) = \delta_{n'n}. \qquad (3.22)$$

In this manner the Dirac notation of matrix mechanics can be converted to the spatially dependent wave function of wave mechanics.

3.1.4 Single-Particle Propagation

As an example, consider the propagation of a free particle (e.g., $V(\mathbf{r}) = 0$) along the z-axis. The wave function solving the Schrödinger equation in this case is

$$\psi(z) = Ae^{-jk'z} + Be^{jk'z}, \qquad (3.23)$$

where $k' = (2m\omega/\hbar)$ based on Eq. 3.3 and $p^2/(2m) = E$. This solution is for the special case when the particle momentum is known precisely, which also means the particle position is completely unknown (see Problem 3.1). A more realistic solution can be represented by a linear combination of functions in the form of Eq. 3.23 for different values of momentum or k'. Now the momentum will have a nonzero uncertainty and the particle position will have a finite uncertainty based on the Heisenberg uncertainty principle. For propagation in the forward direction, a general solution of the wave function for free-particle propagation is

$$\psi(z,t) = \int_{-\infty}^{\infty} A(k')\, e^{j\omega(k')t}\, e^{-jk'z} dk'. \qquad (3.24)$$

Let the momentum uncertainty, $\Delta k'$, be 2ϵ centered about k_0', thus

$$k_0' - \epsilon \leq k' \leq k_0' + \epsilon. \tag{3.25}$$

Expand $\omega(k)$ about k_0' in the form of a Taylor series, to obtain

$$\omega(k') = \omega_0 + (k' - k_0')\left(\frac{d\omega}{dk'}\right)_{k_0'} + \cdots. \tag{3.26}$$

Substituting this result into Eq. 3.24, we obtain the following form for this particular free-particle wave function:

$$\psi(z,t) = e^{-j(k_0'z - \omega_0 t)} \int_{-\infty}^{\infty} A(k') e^{-j(k'-k_0')\left[z - \left(\frac{d\omega}{dk'}\right)_{k_0'} t\right]} dk'. \tag{3.27}$$

Therefore, general free-particle wave functions must be of the form

$$\psi(z,t) = A\left[z - \left(\frac{d\omega}{dk'}\right)_{k_0'} t\right] e^{-j(k_0'z - \omega_0 t)}. \tag{3.28}$$

This represents a traveling wave solution with an envelope function, defining the probable particle location in space. This wave function is called a wave packet. An illustration of the result in terms of the probability density function, $\psi^*\psi$, is shown in Fig. 3.1. This envelope function in Fig. 3.1 satisfies the realistic boundary condition that $\psi(\pm\infty) \to 0$. The velocity of the wave packet is called the group velocity and is given by

$$v_g = \left(\frac{d\omega}{dk'}\right)_{k_0'}. \tag{3.29}$$

The wave packet does not represent the size of the particle, but its probability of location and momentum. The particle is contained within the wave packet. These are fundamental concepts of quantum mechanics and are very different from our classical understanding of particle propagation.

3.2 Introduction to Spectroscopy

Spectroscopy is the field of study which characterizes the energy level structure of matter. In particular, it covers the location of spectral lines and the interaction of light and matter.

3.2.1 Line Position, Strength, and Shape

The energy structure of an atom or a molecule is composed of discrete or quantized energy levels. At optical frequencies, the quantum nature of molecular structure is important. This concept is illustrated in Fig. 3.2 for a two-level system. A photon has a
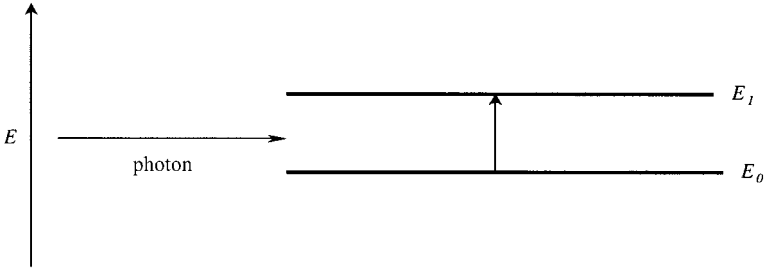
Fig. 3.2 Photon absorption in a two-level system.

characteristic frequency, f_0, which must be proportional to the final and initial energy level difference, such that $E_f - E_i = hf_0$, if the photon is to be absorbed by this two-level system. All other frequencies do not interact (to first order, e.g., scattering is excluded), and propagate beyond the molecule. Energy is removed from the photon field at precisely the frequency f_0. Thus a spectral line is observed at f_0 because of the absence of energy relative to the incident photon field.

A real spectral line has an integrated amplitude (or strength, S_i) and a half-width, γ_i, because the energy levels are not single valued, but instead have a distribution of energies caused by photon fluctuations, collisions from other molecules, electric fields, magnetic fields, and thermal motion. The resulting absorption feature is illustrated in Fig. 3.3.

The strength of the ith absorption line is defined as the entire area under the absorption curve, $\beta_{abs,i}(\nu)$. Thus,

$$S_i = \int_0^\infty \beta_{abs,i}\, d\nu. \tag{3.30}$$

Line strength is, therefore, independent of frequency. The profile or line shape function of the transition is defined as

$$g(\nu\,;\nu_0,\gamma_i)\,,$$
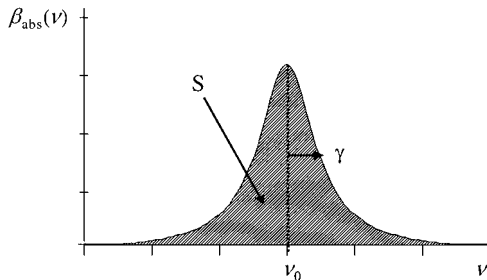
Fig. 3.3 Absorption coefficient of a spectral line, where $\nu_0 = (E_f - E_i)/hc = f_0/c$ where c is the speed of light.

where γ_i = half-width at half-maximum and ν_0 = line-center wave number (which is directly proportional to frequency). Thus the absorption coefficient of a single line can be broken down into two factors: the line strength and the line shape profile,

$$\beta_{abs,i}(\nu) = S_i g(\nu\,;\nu_0,\gamma_i) \tag{3.31a}$$

The definition of S_i as given by Eq. 3.30 requires the line shape profile to be normalized as

$$1 = \int\limits_0^\infty g\left(\nu;\nu_{0,}\gamma_i\right)d\nu. \tag{3.31b}$$

Also, as discussed in Section 2.1.1.2, the odd symmetry of the index of absorption requires the absorption coefficient to be even, based on Eq. 2.30. Based on Eq. 3.31 and the symmetry of the absorption coefficient, the line profile function must then have even symmetry (in classical theory only):

$$g(\nu) = g(-\nu). \tag{3.32}$$

This chapter shall be concerned with determining the position, ν_0, of an absorption line. In Chapters 4 and 5 the nature of the strength, S_i, and profile function, $g(\gamma)$, will be developed more completely. At infrared frequencies only molecules, not atoms, can strongly couple to the electromagnetic field. Atoms do not have rotational and vibrational spectra. Of course, no molecule has only one spectral line and a sum over all spectral lines must be made to compute the total absorption as a function of frequency. Therefore, replacing γ_0 with γ_i, the ith line position, and summing over all spectral lines, we have

$$\beta_{abs}(\nu) = \sum_i \beta_{abs,i}(\nu) = \sum_i S_i g\left(\nu\,;\nu_{i,}\gamma_i\right). \tag{3.33}$$

Substituting the above equation into Eq. 2.54b and converting to angular frequency ($\omega = 2\pi c\nu$), the following sum rule is obtained:

$$n(\omega) - 1 = \frac{c}{\pi}\sum_i S_i P \int\limits_0^\infty d\omega'\,\frac{g(\omega')}{\omega'^2 - \omega^2} \tag{3.34}$$

The Hilbert transform of $g(\omega)$ is now defined to be $d(\omega)$, the dispersion profile. Thus, the forward single-sided Hilbert transform is

$$d(\omega) = \frac{1}{\pi}P\int\limits_0^\infty d\omega'\,\frac{g(\omega')}{\omega'^2 - \omega^2} \tag{3.35a}$$

and the corresponding inverse transform is

$$g(\omega) = \frac{4}{\pi}\omega^2 P\int\limits_0^\infty d\omega'\,\frac{d(\omega')}{\omega^2 - \omega'^2}. \tag{3.35b}$$

Based on the symmetry of the spectral line profile function and Eq. 3.35a, the dispersion profile is an even function in frequency ($d(\omega) = d(-\omega)$). Using these results, Eq. 2.34 becomes

$$n(\omega) - 1 = c \sum_i S_i d(\omega; \omega_i).$$ (3.36a)

Again the sum is over all spectral lines. Based on Eq. 2.53b, the following condition on the dispersion profile is obtained:

$$\int_0^\infty d\omega\, d(\omega) = 0.$$ (3.36b)

These definitions and relationships are fundamental to realistic models of the complex index of refraction and to the discussion of optical propagation. They are applied to models in Part II of this text.

3.2.2 Dipole Moments and Selection Rules

Strength and line position of a molecular transition are influenced by the nature of the intramolecular bond, and by the configuration and mass of the atoms forming the molecule. A molecule with a **dipole moment** can couple to the photon field. The strength of the dipole moment partially determines the strength of the transition. The masses of the atoms, the relative positions, and the bond strengths determine the line positions of the transitions (for rotational and vibration–rotation spectra). Recall that the dipole moment is defined as

$$\mu_{dp} = qr.$$

It is illustrated in Fig. 3.4. An example of an ionically bonded gaseous molecule is HCl, and an ionically bonded solid is NaCl. The simplistic figure below is for a diatomic molecule. Molecules with dipole moment interactions will be emphasized because they are, by far, the strongest and therefore the most important in absorption spectroscopy. Infrared-active rotational spectra require molecules with permanent dipole moments (e.g., H_2O, O_3, and CO). Such molecules are called **polar** molecules.

In materials with proper structural symmetry and electron affinity (e.g., diamond, N_2, O_2, and CO_2) no dipole is formed, thus $\mu_{dp} = 0$. Such materials are called **nonpolar**. Nonpolar molecules typically have covalent bonds. Then quadrupole moments are most
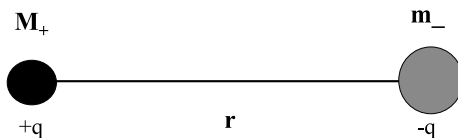
Fig. 3.4 Illustration of dipole moment for an ionic bond, where M_+ = mass of positive ion and m_- = mass of negative ion, and q is the charge magnitude.

important to the transition probability (the exception is a collision-induced dipole). These are very weak transitions, usually not important to optical propagation. Nonpolar molecules have no rotational spectra. Certain vibrational motions can break the symmetry, creating a temporary dipole moment and become infrared active.

Infrared-active vibrational spectra require molecules with only a change in the dipole moment caused by the asymmetric relative motions of the atoms within the molecule. Therefore, if the relative vibrational motion of the atoms within a nonpolar molecule is asymmetric, then a dipole moment may be produced and vibrational spectra can exist. This point can be stated mathematically by considering a Taylor series expansion of the dipole moment transition expectation value (explained in more detail in Chapter 5) about the equilibrium position, r_e, of a molecule. Thus,

$$\langle J_f v_f | \mu | J_i v_i \rangle = \langle J_f v_f | \mu_{dp0} | J_i v_i \rangle + \left\langle J_f v_f \left[\frac{\partial \mu_{dp}}{\partial r} \right]_{r=r_e} (r - r_e) | J_i v_i \right\rangle + \cdots, \quad (3.37)$$

where $\langle r | J v \rangle = \psi_{Jv}(r)$ represents the wave function of the molecule with the rotational quantum number, J, and the vibrational quantum numbers, v. (There are $3N - 5$ vibrational modes for linear molecules and $3N - 6$ otherwise; N is the number of atoms in the molecule. This is because every atom has three degrees of freedom for its motion, thus $3N$. As a molecule there are three translational degrees of freedom, thus $3N - 3$. A linear molecule has two degrees of freedom for rotation, otherwise there are three. Subtracting the rotational degrees of motion leaves only the vibrational modes of the system.) An illustration of vibrational motion in common molecules in the atmosphere of the earth is given in Fig. 3.5.

In the case of pure rotational transitions, the first term must exist for a molecule to be infrared active. The second term is unimportant. In the case of vibrational transitions,
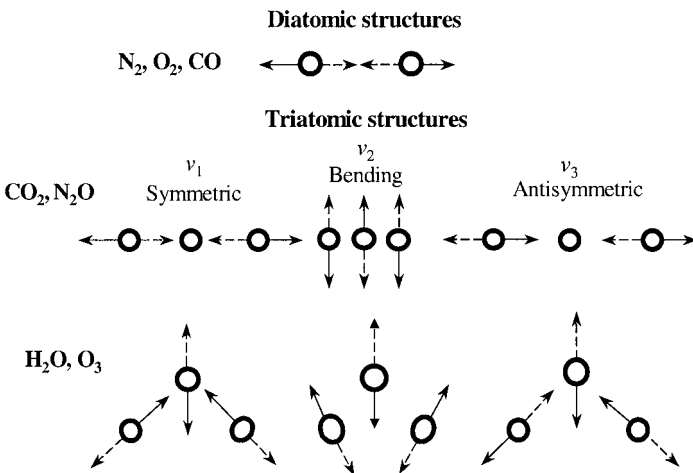
Fig. 3.5 Configurations and vibrational modes of diatomic and triatomic atmospheric molecules.

the second term must exist for a molecule to be infrared active. Polar molecules are typically strong absorbers of infrared radiation and have spectra from the far-infrared (pure rotational) to throughout the mid-infrared (vibration–rotation bands). Water vapor, for example, is the most important absorber of infrared radiation in the troposphere.

Based on Eq. 3.37, the selection rules are determined. For pure rotational transitions, $J_f - J_i = \Delta J = 1$. For vibration–rotation transitions, $v_f - v_i = \Delta v = 1$ and $\Delta J = \pm 1, 0$. The different rotational selection rules form distinct groups of lines or branches. $\Delta J = -1$ corresponds to the P-branch, $\Delta J = 0$ is the Q-branch, and $\Delta J = 1$ is the R-branch. These selection rules are discussed further in the following sections on line position.

A dipole moment can also be induced in molecules by an external electric field. Dipole moment strength is proportional to the external-field frequency and electronic polarizability, α_e, which results from electronic cloud distortion by the incident light field. This mechanism is important for Rayleigh and Raman scattering. Rayleigh scatter is elastic, thus the incident-field frequency equals the scattered-field frequency. Raman scatter is inelastic; the scattered-field frequency is shifted relative to the incident field, revealing internal rotational and vibrational structure. The selection rules change to $\Delta J = \pm 2, 0$, where $\Delta J = -2$ is called the O-branch and $\Delta J = 2$ is the S-branch, and $\Delta v = \pm 1$, forming the stokes ($\Delta v = -1$) and antistokes ($\Delta v = 1$) vibrational bands.

A special case of interest to tropospheric propagation is collision-induced absorption (CIA) of N_2 and O_2. Strong collisions by neighboring molecules induce a dipole moment that exists only during the duration of the collision. Because the collisions are very brief, the line widths are very broad, and individual transitions merge into a broad band structure. This type of featureless absorption is called continuum absorption. More will be said about this phenomenon in Chapter 7.

3.3 Spectroscopy of Gases

Fortunately, nature has greatly simplified the study of spectroscopy by sufficiently separating the fundamental energies of rotational, vibrational, and electronic transitions such that

$$E_{e1} \gg E_{vib} \gg E_{rot}.$$

The energy structure of each dynamics problem can be solved separately and treated independently in the zeroth order. Couplings between the different types of energy structures is then treated as a perturbation to the zeroth order system.

Rotational spectra typically occur in the far-infrared (0.1 to 100 cm^{-1}) and exist only for molecules with permanent dipole moments. Vibrational spectra typically occur in the mid-infrared and near-infrared (100 to 10,000 cm^{-1}) and only exist for molecules. Electronic spectra exist for atoms and molecules, and typically occur in the visible (weak bands) and ultraviolet (strong absorption bands which determine the end of optical transparency in a medium). Since the topics in this book are generally concerned with infrared and visible phenomena, electronic structure will not be covered in detail.

The development begins with rotation spectra in the vibrational and electronic ground state, then vibration–rotation spectra in the electronic ground state, and closes with a brief description of electronic spectra.

3.3.1 Rotational Spectroscopy

The weakest energy structures in molecules are purely rotational and are part of all other transitions. The simplest molecule is the diatomic molecule, which has only one unique axis of rotation and thus only one degree of rotation. For this reason, diatomic molecules are covered first. A polyatomic molecule requires, in general, three rotational degrees of freedom, and is more complicated to describe.

3.3.1.1 Diatomic Molecules

The simplest molecule is diatomic, and analytical models can be obtained in a straight-forward manner. In the following, it is assumed that the system is in the vibrational ground state (e.g., rigid rotor) and electronic ground state. Because of the importance of the quantized energy level structure in gas-phase spectroscopy, it is instructive to set up the rigid-rotor problem in quantum mechanics. Let us begin with the time-independent Schrödinger wave equation,

$$\hat{H}\psi(\mathbf{r}) = E\psi(\mathbf{r}).$$

The Hamiltonian for a rotating system is needed. In the case of a **rigid rotor**, the rotational kinetic energy is

$$T = \frac{1}{2}I\omega^2 = \frac{J^2}{2I}, \tag{3.38}$$

where I is the moment of inertia, as given by

$$I = \sum_i m_i r_i^2,$$

$J = I\omega$ is the angular momentum, and ω is the rotational frequency of the rotor.

The diatomic model can be simplified by using a center-of-mass coordinate system in the following way. The center of mass is defined to be at the origin and is determined by the following conditions:

$$\sum_i m_i\,\mathbf{r}_i = 0 \quad \text{and} \quad \mathbf{r}_1 + \mathbf{r}_2 = \mathbf{r}_e.$$

The equilibrium separation of the atoms is $\mathbf{r}_e$. This leads to the following result for the moment of inertia:

$$I = m_1 r_1^2 + m_2 r_2^2 = \mu' r_e^2, \tag{3.39}$$

where the following definitions are used,

$$r_1 = \frac{m_2}{m_1 + m_2}r_e, \quad r_2 = \frac{m_1}{m_1 + m_2}r_e, \tag{3.40a}$$

and μ' is the reduced mass, given by

$$\mu' = \frac{m_1 m_2}{m_1 + m_2}. \tag{3.40b}$$

r_1 and r_2 are distances from the atoms "one" and "two", respectively, to the center of mass (CoM) point of the system. The two-body diatomic model is then transformed into a single body of reduced mass, μ', rotating about an origin r_e away. This model is illustrated in Fig. 3.6. Thus, instead of considering the rotation of the dumbbell, we can equally well consider the rotation of a single particle of mass μ' at a fixed distance r_e from the axis of rotation. This reduces the two-body problem to the tractable single-body problem.

The Hamiltonian for a freely rotating body is composed of the rotational kinetic energy with no potential energy, thus based on Eqs. 3.38 and 3.39 the following operators are generated:

$$\hat{T} = \frac{\hat{p}^2}{2\mu'} = -\frac{\hbar^2 \nabla^2}{2\mu'} \quad \text{and} \quad V(\hat{\mathbf{r}}) = 0$$

where $\hat{J} = \hat{p} r_e$, $\hat{p}$ is the tangential momentum operator, and $V(\hat{\mathbf{r}})$ is the potential. The stationary-state Schrödinger wave equation now becomes

$$-\frac{\hbar^2 \nabla^2}{2\mu'} \psi(\mathbf{r}) = E\psi(\mathbf{r}). \tag{3.41}$$

Choosing spherical coordinates, the corresponding wave function is $\psi(r_e, \theta, \phi)$, where $r = \text{constant} \equiv r_e$ for a rigid rotor. Based on these results, let us solve the stationary-state
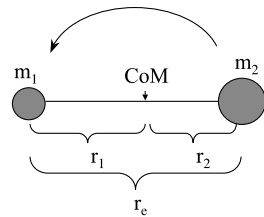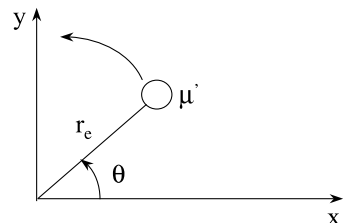
Fig. 3.6 Rigid-rotor model is illustrated in two steps: (a) two-body model and (b) the corresponding one-body model.

Schrödinger equation as given by

$$\frac{1}{\sin\theta}\frac{\partial}{\partial\theta}\left(\sin\theta\frac{\partial\psi(\theta,\phi)}{\partial\theta}\right) + \frac{1}{\sin^2\theta}\frac{\partial^2\psi(\theta,\phi)}{\partial\phi^2} = -\frac{2\mu'r_e^2 E}{\hbar^2}\psi(\theta,\phi). \qquad (3.42)$$

Assuming that the wave function is separable, the following substitutions are made: $\psi(\theta,\phi) = \Theta(\theta)\,\Phi(\phi)$, and $\mu'r_0^2 = I$. The wave equation now becomes

$$\frac{\sin\theta}{\Theta(\theta)}\frac{\partial}{\partial\theta}\left(\sin\theta\frac{\partial\Theta(\theta)}{\partial\theta}\right) + \left(\frac{2I}{\hbar^2}E\right)\sin^2\theta = -\frac{1}{\Phi(\phi)}\frac{\partial^2\Phi(\phi)}{\partial\phi^2}. \qquad (3.43)$$

The two sides of the above equation must equal a constant, M^2, independent of either θ or ϕ, because each side depends on a different variable. Therefore, a separate equation involving $\Phi(\phi)$ is obtained, thus

$$M^2 = -\frac{1}{\Phi(\phi)}\frac{d^2\Phi(\phi)}{d\phi^2} \qquad (3.44)$$

with the solution

$$\Phi(\phi) = Ae^{-jM\phi} + Be^{jM\phi}. \qquad (3.45)$$

The boundary condition for a periodic function requires $\Phi(\phi) = \Phi(\phi + 2\pi)$ because of the rotational nature of the problem, therefore

$$Ae^{-jM\phi} + Be^{jM\phi} = Ae^{-jM\phi}e^{-jM2\pi} + Be^{jM\phi}e^{jM2\pi}. \qquad (3.46)$$

The boundary condition will be satisfied if $e^{\pm jM2\pi} = 1$, where

$$M = 0, \pm1, \pm2, \pm3, \ldots. \qquad (3.47)$$

Now consider the right-hand side of Eq. 3.42 involving $\Theta(\theta)$,

$$\frac{\sin\theta}{\Theta(\theta)}\frac{d}{d\theta}\left(\sin\theta\frac{d\Theta(\theta)}{d\theta}\right) + \left(\frac{2I}{\hbar^2}E\right)\sin^2\theta = M^2. \qquad (3.48)$$

Letting $x = \cos\theta$, the above equation becomes

$$(1 - x^2)\frac{d^2\Theta(\theta)}{dx^2} - 2x\frac{d\Theta(\theta)}{dx} + \left(\frac{2I}{\hbar^2}E - \frac{M^2}{1 - x^2}\right)\Theta(\theta) = 0. \qquad (3.49)$$

This is a well-known differential equation with associated Legendre functions as solutions if

$$\frac{2I}{\hbar^2} E = J(J+1), \quad \text{where } |M| \le J = 0, 1, 2, 3, \ldots. \tag{3.50}$$

This condition requires the rotational energy levels to be quantized according to the following formula:

$$E_{Rot} = \frac{\hbar^2 J(J+1)}{2I}. \tag{3.51}$$

Writing the rotational frequency of a rigid rotor in units of wave numbers, we have

$$\nu_{Rot} = \frac{E_{Rot}}{hc} = \frac{h}{8\pi^2 Ic} J(J+1). \tag{3.52}$$

Spectroscopic notation expresses the rotational energy level in wave numbers by a term value, $F(J)$, where

$$\nu_{Rot} = F(J) = B_e J(J+1) \quad \text{and} \quad B_e = \frac{h}{8\pi^2 Ic}. \tag{3.53}$$

B_e is defined as the equilibrium rotational molecular constant valid for $r = r_e$. Notice that the energy of a rotational level depends only on J, not on M. There are $2J + 1$ values of M for each J and, therefore, $2J + 1$ unique wave functions, $\psi_{JM}(r_e, \theta, \phi)$, for a particular rotational energy level specified by J. For situations like this the energy level is called degenerate. In this case the degeneracy, g_J, is equal to $(2J + 1)$. A rotational energy level diagram is depicted in Fig. 3.7. Using the selection rule of $\Delta J = 1$, a series of spectral lines are formed with a regular interval between lines. The rotational constant determines the spacing between these lines. Thus light molecules have broad rotation bands and heavy molecules have narrow-band formation.

The resulting wave functions for the rigid rotor are spherical harmonics. A listing of these functions for various J and M values can be found in Appendix 2.

Example 3.1 Consider the diatomic molecule $^{12}C^{16}O$, given $r_e = 1.128$ Å, $m_1 = 12$ amu, and $m_2 = 16$ amu; what is the value of B_e?
The reduced mass is

$$\mu' = 6.857 \text{ amu} = 1.138 \times 10^{-23} \text{g}$$

where 1 amu $= 1.6604 \times 10^{-24}$ grams and the moment of inertia is

$$I = \mu' r_e^2 = 1.448 \times 10^{-39} \text{g cm}^2.$$

Therefore, based on Eq.3.53, the equilibrium rotational constant is

$$B_e = 1.931 \text{ cm}^{-1}.$$

The value $B_e = 1.9313$ cm^{-1} has been experimentally verified (see reference 3.4).

The location of a pure-rotation spectral line, representing a transition between two adjacent energy levels, is computed using the following formula:
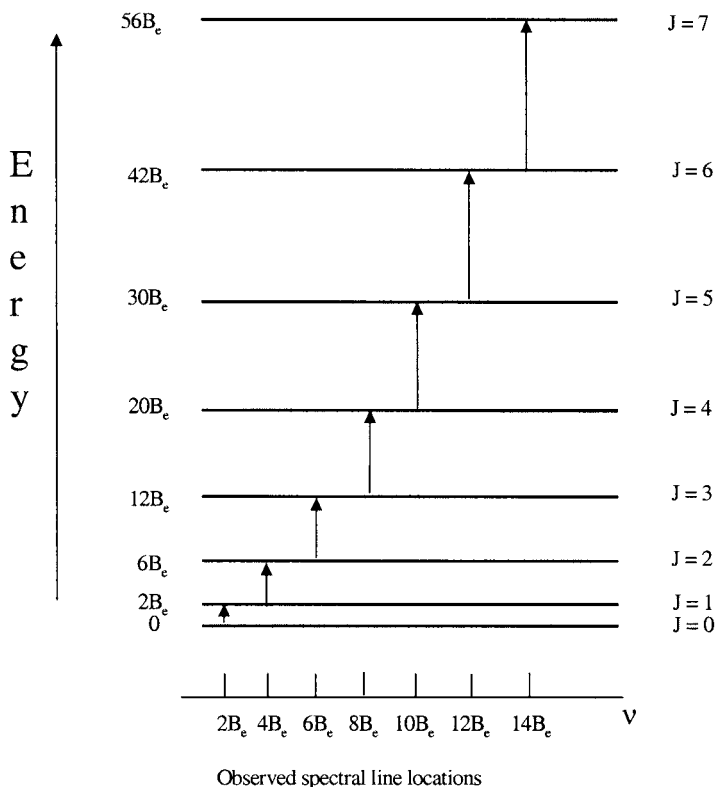
Fig. 3.7 Pure rotational energy structure and spectral line location of a diatomic molecule.

$$\frac{\Delta E_{Rot}}{hc} = F(J+1) - F(J) = 2B_e(J+1), \tag{3.54}$$

where J is the rotational quantum number of the *lower* state. The separation between adjacent spectral lines is $2B_e$. This regular spacing is characteristic of diatomic rotational spectra and is illustrated in Fig. 3.7. Notice that $\Delta J = 1$ was chosen for this computation. It is called a selection rule and is based on nonzero values of the transition matrix element of the dipole moment, as based on Eq. 3.37,

$$q\langle J_f|r|J_i\rangle \neq 0. \tag{3.55}$$

The verification of this selection rule is the point of Problem 3.5. The foundation for this rule requires examination of the time-dependent Schrödinger wave equation, which is discussed in Chapter 5.

3.3.1.2 Polyatomic Molecules

Pure rotational bands typically exist from millimeter waves to the far-infrared. The formulas for rotational spectral line positions vary for different types of molecules.

Molecules are classified as linear (e.g., N_2, O_2, H_2, CO, OH, CO_2, N_2O, OCS, HCN), spherical top (e.g., CH_4), symmetric top (e.g., NH_3, CH_3D, CH_3Cl, C_2H_6), and asymmetric top (e.g., H_2O, O_3, SO_2, NO_2, H_2O_2, H_2S). Energy level structure is specified by the term value, $F(J)(= E/(hc))$, and at most three rotational constants (A, B, and C; one for each direction), both in cm^{-1}. In general, there are three rotational degrees of freedom (J_a, J_b, and J_c) and three corresponding quantum numbers (J, K_a, and K_c), as illustrated in Fig. 3.8. However, symmetry of the molecular structure can reduce the number of independent quantum numbers. The rotational term value functions with the degeneracy factor g_J for the various types of molecules are as follows:

- Linear molecules (one independent rotational motion),

$$F(J) = BJ(J+1) \quad \text{and} \quad g_J = 2J + 1. \tag{3.56}$$

- Spherical-top molecules ($A = B = C$) (one independent rotational motion),

$$F(J) = BJ(J+1) \quad \text{and} \quad g_J = (2J+1)^2. \tag{3.57}$$

- Symmetric-top molecules (two independent rotational motions),
  - prolate ($A > B = C$),

$$F(J,K) = BJ(J+1) + (A-B)K^2 \quad \text{and} \quad g_J = \begin{cases} 2J+1 & K = 0, \\ 2(2J+1) & K \neq 0; \end{cases} \tag{3.58}$$

  - oblate ($A = B > C$),

$$F(J,K) = BJ(J+1) + (C-B)K^2 \quad \text{and} \quad g_J = \begin{cases} 2J+1 & K = 0, \\ 2(2J+1) & K \neq 0. \end{cases} \tag{3.59}$$

- Asymmetric-top molecules ($A > B > C$) (three independent rotational motions). $F(J, K_a, K_c)$ is treated as an intermediate state between oblate and prolate symmetric tops. Thus a precise statement depends on the molecule and the degree of asymmetry. For more information on this class of molecules see Herzberg Ref. 3.5.
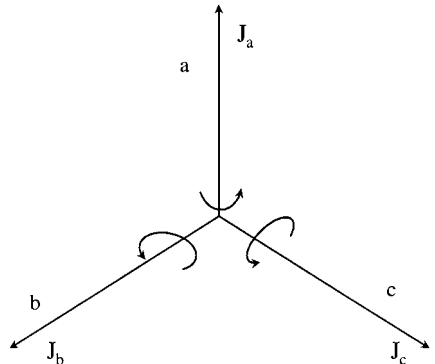
Fig. 3.8 Directions of angular momentum for a general polyatomic rotor.

The rotational constants are defined as

$$A = \frac{h}{8\pi^2 c I_a}, \quad B = \frac{h}{8\pi^2 c I_b}, \quad \text{and} \quad C = \frac{h}{8\pi^2 c I_c}, \tag{3.60}$$

where I_a, I_b, and I_c are the molecular moments of inertia. Values of rotational constants of atmospheric molecules are listed in Table 3.1. Line positions are calculated by using the selection rule $\Delta J = J_f - J_i = 1$ and Eqs. 3.8–3.11. For linear and symmetric top molecules the result is

$$\nu_{Rot} = F(J_f) - F(J_i) = 2BJ_f \text{ [cm}^{-1}]. \tag{3.61}$$

The purpose of this section is to develop insight into the nature of molecular rotational structure. For example, the rotational constants of water vapor are much larger than any other molecule listed of importance to atmospheric propagation. This means the rotational band structure of water vapor covers a much larger spectral range than the rotational structure of other molecules.

Also, water vapor is an asymmetric molecule requiring three quantum numbers. This produces a rich irregularly spaced spectrum, as depicted in Fig. 3.9. Because of this (and other properties), water vapor plays an important role in every infrared spectral region.

3.3.2 Vibrational Spectroscopy

Vibration bands of gases typically exist in the mid-infrared. Atmospheric infrared windows are defined by the locations of these vibrational frequencies. Again, this section will begin with a detailed presentation of vibrational motion in diatomic molecules.

Table 3.1 Rotational Constants of Common Atmospheric Gases*

Molecule	A [cm^{-1}]	B [cm^{-1}]	C [cm^{-1}]
H_2	—	60.853	—
OH	—	18.871	—
NO	—	1.7046	—
CO	—	1.9314	—
CO_2	—	0.3902	—
N_2O	—	0.4190	—
H_2O	27.877	14.512	9.285
O_3	3.553	0.445	0.395
CH_4	—	5.249	—
N_2	—	2.010	—
O_2	—	1.44566	—
NH_3	6.196	9.9444	—
SO_2	2.0274	0.3442	0.2935
NO_2	8.0012	0.4336	0.4104
H_2S	10.374	8.991	4.732

*From Herzberg (Refs. 3.4, 3.5).
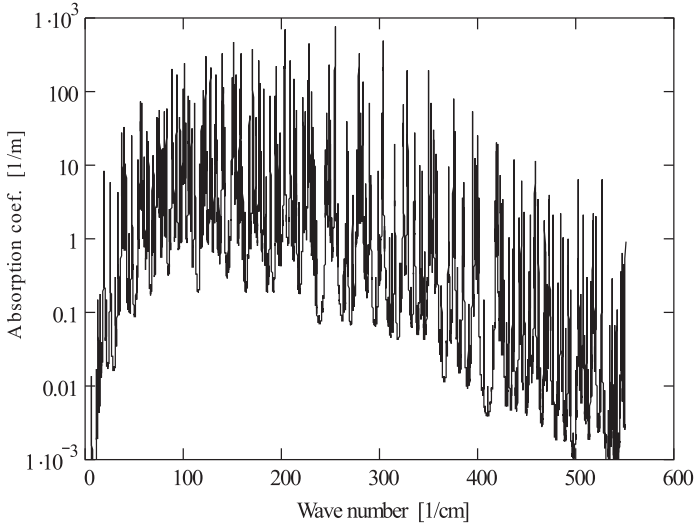
Fig. 3.9 Pure rotational band of nitrogen-broadened water vapor for $p_{H_2O} = 0.02$ atm, $p_{N_2} = 0.98$ atm, and $T = 296$ K.

3.3.2.1 Diatomic Molecules

At this point we recognize that not only will a diatomic molecule rotate, but it will also vibrate along the bond axis. To see this, consider the classical notion of two balls connected by a spring, with spring constant β_s, as shown in Fig. 3.10.

Using Newton's third law and reducing the two-body problem to a single-body problem, as in the case of the rigid rotor, the motion of the vibrating diatomic molecule can be described as

$$\mu' \frac{d^2 r(t)}{dt^2} = -\beta_s(r(t) - r_e), \qquad (3.62)$$

where μ' is the reduced mass, β_s is a spring constant, and $r(t)$ is the distance between the atoms. It is convenient to define the variable
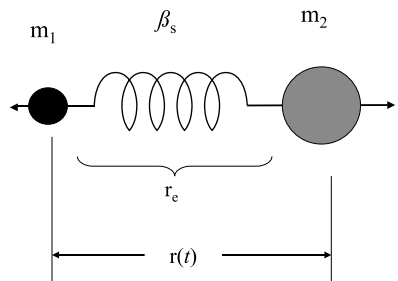
Fig. 3.10 Model for the vibrating diatomic molecule, where m_1 and m_2 are the masses of the atoms, β_s is the spring constant of the restoring force, and r_e is the equilibrium separation between the atoms.

$$q(t) = r(t) - r_e,$$ (3.63)

where r_e equals the time-independent equilibrium separation. Then, substituting Eq. 3.63 into Eq. 3.62, we obtain the homogeneous differential equation

$$\left(\frac{d^2}{dt^2} + \frac{\beta_s}{\mu} \right) q(t) = 0.$$ (3.64)

With the initial condition $q(t = 0) = 0$, the solution to this equation is

$$q(t) = q_0 \sin \omega_0 t, \quad \text{where } \omega_0 = \sqrt{\frac{\beta_s}{\mu'}}.$$ (3.65)

In quantum mechanics, we are interested in the potential energy as part of the system Hamiltonian, thus

$$F = -\nabla V(q) \quad \text{and} \quad V(\hat{q}) = \frac{1}{2} \beta_s \hat{q}^2.$$ (3.66)

Using the Hamiltonian for a particle in a harmonic potential as given above, the Schrödinger wave equation is

$$-\frac{\hbar^2}{2\mu'} \frac{d^2 \psi(q)}{dq^2} + \frac{1}{2} \beta_s q^2 \psi(q) = E \psi(q).$$ (3.67)

Making the substitution $\psi(q) = \exp\left(-aq^2\right) \Phi(q)$, we obtain

$$\Phi''(q) - 4aq\Phi'(q) + \left[\left(4a^2 - \frac{\mu'\beta_s}{\hbar^2} \right) q^2 + \frac{2\mu'E}{\hbar^2} - 2a \right] \Phi(q) = 0.$$ (3.68)

Hermite's differential equation can be obtained if the following substitutions are made:

$$a = \frac{\mu'\omega_0}{2\hbar} \quad \text{and} \quad x = \sqrt{\frac{\mu'\omega_0}{\hbar}} q.$$

Then, Eq. 3.68 reduces to

$$\Phi''(x) - 2x\Phi'(x) + \frac{\hbar}{\mu'\omega_0} \left[\frac{2\mu'E}{\hbar^2} - \frac{\mu'\omega_0}{\hbar} \right] \Phi(x) = 0.$$ (3.69)

Furthermore, impose the following quantization condition on the coefficient of the last term in the above equation:

$$\left[\frac{2\mu'E}{\hbar^2} - \frac{\mu'\omega_0}{\hbar}\right]\frac{\hbar}{\mu'\omega_0} = 2v, \quad \text{where } v = 0, 1, 2, 3, \ldots. \tag{3.70}$$

This leads to Hermite's differential equation, of the form

$$\Phi''(x) - 2x\Phi'(x) + 2v\Phi(x) = 0, \tag{3.71}$$

with the corresponding energy eigenvalues

$$E_{vib} = \hbar\omega_0\left(v + \frac{1}{2}\right). \tag{3.72}$$

The functions $\Phi(x)$ are the Hermite polynomials. The wave function then becomes

$$\psi(q) = \exp\left(-aq^2\right)\Phi\left(\sqrt{\frac{\mu'\omega_0}{\hbar}}q\right).$$

Converting Eq. 3.72 to wave numbers, the vibrational term value for a **harmonic oscillator** is defined to be

$$\frac{E_{vib}}{hc} = G(v) = \frac{\hbar\omega_0}{hc}\left(v + \frac{1}{2}\right) = \nu_{vib}\left(v + \frac{1}{2}\right). \tag{3.73}$$

The factor ν_{vib} is the vibrational resonant frequency. Notice that for $v = 0$, a nonzero vibrational energy still exists. It is called the zero-point energy and is a consequence of the Heisenberg uncertainty principle. Since p and q are contained in the system Hamiltonian and do not commute, the energy cannot be known with certainty. This is a nonclassical result, but it is not of concern in spectroscopy, since spectral lines are generated by energy level differences.

The selection rule for vibrational transitions is $\Delta v = 1$ or -1 for absorption or emission, respectively. The location of vibrational spectral lines is computed by taking the difference of the term values for the upper and lower levels,

$$G(v + 1) - G(v) = \nu_{vib}. \tag{3.74}$$

All vibrational transitions occur at the same wave number, since the above result is independent of v. This is a result of the harmonic approximation to the potential.

The solution of the harmonic oscillator is one of the most fundamental results of quantum mechanics. It allows the quantum-mechanical description of any oscillatory phenomena. To apply this formalism to some systems requires an algebraic solution within the formalism of matrix mechanics. This is accomplished in the following discussion.

The stationary-state Schrödinger equation in Dirac notation is given by

$$\hat{H}|v\rangle = E_v|v\rangle,$$

where for the harmonic oscillator

$$H(p,q) = \frac{1}{2}\left(\frac{p^2}{m} + \omega^2 m q^2\right).$$ (3.75)

The Hamiltonian can be simplified by reducing the momentum and position operators in the following way:

$$P = \frac{p}{\sqrt{m}} \quad \text{and} \quad Q = \sqrt{m}q, \quad \text{where } P = \dot{Q}.$$ (3.76)

Substituting the above definitions into Eq. 3.75, we obtain the following Hamiltonian:

$$H(P,Q) = \frac{1}{2}\left(P^2 + \omega^2 Q^2\right).$$ (3.77)

Also, based on Eq. 3.76 and $[p,q] = j\hbar$, the commutation relation between P and Q becomes

$$[P,Q] = j\hbar.$$ (3.78)

A useful perspective on the harmonic oscillator problem is obtained by defining new operators, as given by

$$\hat{a}^\dagger = \frac{1}{(2\hbar\omega)^{1/2}}(\omega Q + jP)$$ (3.79)

and

$$\hat{a} = \frac{1}{(2\hbar\omega)^{1/2}}(\omega Q - jP).$$ (3.80)

Then, based on these definitions and Eq. 3.78, the commutator bracket for the new operators becomes

$$\left[\hat{a}, \hat{a}^\dagger\right] = 1.$$ (3.81)

Substituting Eqs. 3.79 and 3.80 into Eq. 3.77, the system Hamiltonian can be expressed in terms of the a operators to be

$$H(P,Q) = \frac{1}{2}\left(P^2 + \omega^2 Q^2\right) = \hbar\omega\left(\hat{a}^\dagger\hat{a} + \frac{1}{2}\right).$$ (3.82)

Therefore, the energy eigenvalue equation is written as

$$\hbar\omega\left(\hat{a}^\dagger\hat{a} + \frac{1}{2}\right)|v\rangle = E_v|v\rangle$$ (3.83)

or in standard eigenvalue equation form

$$\hat{a}^\dagger\hat{a}|v\rangle = \left(\frac{E_v}{\hbar\omega} - \frac{1}{2}\right)|v\rangle.$$ (3.84)

Eigenvalue problems require that an operation on a function produces a number times the function, thus

$$\hat{a}^\dagger \hat{a} \, |v\rangle = \text{number} \, |v\rangle = v \, |v\rangle$$

Therefore, the numerical factor on the right-hand side of Eq. 3.84 must equal the number, v, and solving for E_v we obtain

$$E_v = \hbar\omega \left(v + \frac{1}{2} \right), \tag{3.85}$$

which is a result analogous to Eq. 3.72. Thus, v is the energy quantum number. The operator $\hat{a}^\dagger \hat{a}$ is called the number operator, because it yields the number of vibrational quanta a particular system has.

What do the operators $\hat{a}^\dagger$ and $\hat{a}$ represent? To answer this question, consider the following arguments. Let us find the eigenvalues of the operator $\hat{a}$, as defined by

$$\hat{a} \, |n\rangle = A_m | m\rangle, \tag{3.86}$$

where the numbers A_m and m need to be determined. The Hermitian conjugate form of this equation is given by

$$\langle n \, |\hat{a}^\dagger = \langle m| \, A_m^*. \tag{3.87}$$

Based on the previous two equations, it follows that the inner product of a state against the same state is

$$\langle n \, |\hat{a}^\dagger \hat{a}| \, n\rangle = \langle m \, |A_m^* A_m| \, m\rangle = |A_m|^2, \tag{3.88}$$

where it is assumed that the eigenvectors are orthonormal. Now, based on Eqs. 3.84 and 3.85, the following can be stated:

$$|A_m|^2 = \langle v \, |\hat{a}^\dagger \hat{a}| \, v\rangle = \langle v \, |v| \, v\rangle = v. \tag{3.89}$$

Therefore, the eigenvalue of the operator $\hat{a}$ can be expressed in terms of the energy quantum number, as

$$A_m = \sqrt{v}. \tag{3.90}$$

Further, the eigenvector can be determined by the following arguments. Consider the post operation of the operator $\hat{a}$ on an eigenvector with the number operator operating on the eigenstate, $|v\rangle$, as given by

$$\hat{a} \left(\hat{a}^\dagger \hat{a} \, |v\rangle \right) = v\hat{a} \, |v\rangle. \tag{3.91}$$

Rearranging the parentheses in the above equation, in the following manner,

$$\hat{a}\hat{a}^\dagger \left(\hat{a} \, |v\rangle \right) = v\hat{a} \, |v\rangle$$

and using the commutation relation, as given by

$$\hat{a}\hat{a}^{\dagger} = 1 + \hat{a}^{\dagger}\hat{a},$$

we obtain

$$\hat{a}^{\dagger}\hat{a}\,|m\rangle = (v - 1)|\,m\rangle. \tag{3.92}$$

The operator on the eigenvector, $|m\rangle$, is the number operator. Therefore, the quantum number of the eigenvector must be

$$|m\rangle = |v - 1\rangle.$$

The solution to Eq. 3.86 now becomes

$$\hat{a}|v\rangle = \sqrt{v}|v - 1\rangle. \tag{3.93}$$

The operator $\hat{a}$ lowers the quantum number of the eigenstate and, for this reason, it is called a lowering operator.

Also, let us examine the Hermitian conjugate of the lowering operator. Consider the following eigenvalue equation:

$$\hat{a}^{\dagger}\,|v\rangle = B_n|n\rangle, \tag{3.94}$$

where B_n and n are numbers to be determined. The Hermitian conjugate form of this equation is given by

$$\langle v\,|\hat{a} = B_n^{*}\langle n|\,. \tag{3.95}$$

In a similar fashion to the previous development, we compute the expectation value of the following operator, which also equals $|B_n|^2$:

$$|B_n|^2 = \langle v\,|\hat{a}\hat{a}^{\dagger}|\,v\rangle = \langle v\,|\left(1 + \hat{a}^{\dagger}\hat{a}\right)|\,v\rangle = 1 + v. \tag{3.96}$$

Therefore, the eigenvalue of the operator $\hat{a}^{\dagger}$ can be expressed in terms of the quantum number, v, as given by

$$B_n = \sqrt{1 + v}. \tag{3.97}$$

Furthermore, the eigenvector can be determined in a similar manner as before. Consider the number operator operating on Eq. 3.94, which becomes after simple algebraic manipulation

$$\hat{a}^{\dagger}\hat{a}\left(\hat{a}^{\dagger}|v\rangle\right) = (1 + v)\left(\hat{a}^{\dagger}\,|v\rangle\right). \tag{3.98}$$

Based on Eqs. 3.94 and 3.97, the above equation reduces to

$$\hat{a}^{\dagger}\hat{a}\,|n\rangle = (1 + v)\,|n\rangle. \tag{3.99}$$

This is the number operator operating on the state $|n\rangle$, which means

$$|n\rangle = |v + 1\rangle$$

must be true. Therefore, the solution to Eq. 3.94 is given by

$$\hat{a}^{\dagger}|v\rangle = \sqrt{v + 1}\,|v + 1\rangle. \tag{3.100}$$

$\hat{a}^{\dagger}$ is called a raising operator because it raises the quantum number of the eigenvector. (The raising and lowering operators are very useful tools when the electromagnetic field is quantized in Appendix 5.)

Note   The raising operator can be used to specify a state in general in the following way:

$$|v\rangle = \frac{(\hat{a}^{\dagger})^v}{\sqrt{v!}}|0\rangle$$

where $|0\rangle$ is the ground state.

The harmonic oscillator is only an approximation to a real potential function. It is valid only for systems in the lowest energy levels and even then does not give a detailed description of a system. A realistic potential is composed of attractive and repulsive potentials. The binding force in a polar molecule is the electrostatic attraction between unlike charges. The atoms can only get so close because the electronic clouds surrounding the nucleus begin to overlap and this is not allowed by the Pauli exclusion principle (see Merzbacher Ref. 3.2). Also, the repulsive force between the two (or more) positive nuclei will also have an effect when the atoms are close enough. The resulting potential is the sum of these components, forming a potential well with a minimum at the equilibrium separation between the atoms, r_e. This description is illustrated in Fig. 3.11.

Many intramolecular and intermolecular potential functions have been proposed; here are two popular examples:

Leonard–Jones potential (or Van der Waals, also called 6–12 potential):

$$V(r) = \frac{A}{r^{12}} - \frac{B}{r^6}. \tag{3.101a}$$

Morse potential:

$$V(r) = -D_0 + D_0 \left(1 - e^{-a(r-r_e)}\right)^2, \tag{3.101b}$$
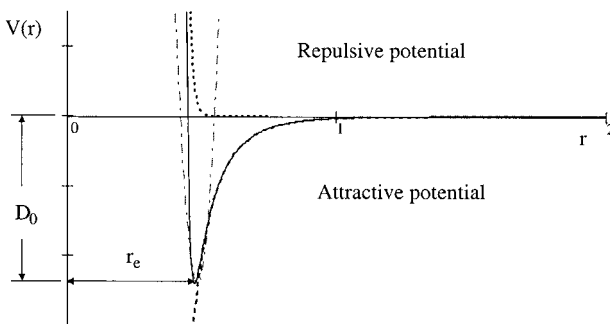
Fig. 3.11 Realistic intermolecular potential function between two atoms composing a molecule.

where D_0 is the dissociation energy and r_e is the equilibrium position as defined in Fig. 3.11. Near the bottom of a realistic potential well the function is harmonic (see Fig. 3.11). To see this, consider the Morse potential function, for $r - r_e$ small:

$$V(r) = -D_0 + D_0 \left\{ 1 - \left[1 - a\,(r - r_e) + \frac{a}{2}\,(r - r_e)^2 + \cdots \right] \right\}^2$$

$$\approx -D_0 + \frac{1}{2}\beta_s\,(r - r_e)^2 + \text{anharmonic terms.}$$

(3.102)

The Morse potential will be of interest later, mainly because it allows an exact solution to the Schrödinger equation. Thus, the anharmonicity is represented to all orders. The one-dimensional wave equation with the Morse potential is

$$-\frac{\hbar^2}{2\mu}\frac{d^2}{dx^2}\psi(x) + D_0\left\{1 - \exp\left[-a(x - x_e)\right]\right\}^2\psi(x) = (D_0 + E_v)\,\psi(x). \quad (3.103)$$

The corresponding energy eigenvalues are

$$E_v = \hbar\omega_0\left[\left(v + \frac{1}{2}\right) - \frac{1}{j'}\left(v + \frac{1}{2}\right)^2\right] - D_0 \quad (3.104)$$

where ω_0 is the fundamental vibrational frequency, $v = 0, 1, 2, 3, \ldots, v_{max} \leq (j' - 1)/2$ and

$$j' \equiv \left(\frac{4D_0}{\hbar\omega_0}\right). \quad (3.105)$$

The wave function in the rotational ground state is

$$\psi(x) = \frac{1}{\sqrt{4\pi}}\frac{\sqrt{a}}{\Gamma(k - v)}\left(\sum_{i=0}^{v}\frac{\Gamma(k - 2v - 1 + i)}{\Gamma(i + 1)}\right)^{\frac{1}{2}}e^{-\frac{z}{2}}z^{\frac{k-2v-1}{2}}e^{-j\pi(k-1)}L_v^{k-2v-1}(z)$$

where $k = (8\pi D_0)^{1/2}/a\hbar$, $z = ke^{a(x-x_e)}$ and $L_v^m(z)$ is the associated Laguerre polynomial. Another consequence of an anharmonic potential is that $\Delta v = \pm 1, \pm 2, \pm 3, \ldots$. Thus overtone bands are now allowed.

In general, the energy values of the one-dimensional anharmonic oscillator are given by

$$E_v = -D_0 + \hbar\omega_e\left(v + \frac{1}{2}\right) - \hbar\omega_e x_e\left(v + \frac{1}{2}\right)^2 + \hbar\omega_e y_e\left(v + \frac{1}{2}\right)^3 + \ldots, \quad (3.106)$$

where $\omega_e = \omega_0$, and x_e and y_e represent anharmonic corrections. Converting to wave numbers,

$$G(v) = \frac{E_v}{hc} = -\frac{D_0}{hc} + v_e\left(v + \frac{1}{2}\right) - v_e x_e\left(v + \frac{1}{2}\right)^2 + v_e y_e\left(v + \frac{1}{2}\right)^3 + \cdots \quad (3.107)$$

where $G(v)$ is the vibrational term value. Vibrational spectral line locations are computed by examining the differences between energy levels. To first order in the anharmonicity, this is

$$\nu_{vib} = G(v+1) - G(v) = \nu_e - \nu_e x_e \left[\left(v + \frac{3}{2} \right)^2 - \left(v + \frac{1}{2} \right)^2 \right]. \qquad (3.108a)$$

After some simple algebra, the result is

$$\nu_{vib} = \nu_e - 2\nu_e x_e (v+1). \qquad (3.108b)$$

Vibrational transitions which originate above the ground state are shifted to lower frequencies relative to the fundamental.

Now let us combine the rotational and vibrational motions, which we have thus far considered separately. As the nonrigid molecule rotates with increasing energy, it stretches until it ultimately flies apart. This is called centrifugal distortion, and it adds a correction term to the rotational term value of the form

$$F(J) = B_e J(J+1) - D_e J^2 (J+1)^2, \qquad (3.109)$$

where

$$D_e = \frac{4 B_e^3}{\omega_0^2}. \qquad (3.110)$$

The rotational constant B_e must also be modified, since r_e in the moment of inertia, I, is the equilibrium separation, which changes for anharmonic vibrations as a function of the vibrational level. Thus,

$$B_v = B_e - \alpha_e \left(v + \frac{1}{2} \right) + \cdots, \qquad (3.111)$$

where α_e is a correction factor listed as a molecular constant in tables (e.g., see Herzberg, Ref. 3.4). Further, a correction is also needed for the centrifugal distortion term,

$$D_v = D_e + \beta_e \left(v + \frac{1}{2} \right). \qquad (3.112)$$

Based on these results, it follows that

$$F_v(J) = B_v J(J+1) - D_v J^2 (J+1)^2 + \cdots \qquad (3.113)$$

(usually D_v is very small and can be neglected for J small). Now the energy levels of a vibrating rotator can be expressed as

$$\begin{aligned} T(v,J) &= G(v) + F_v(J) \\ &= \nu_e \left(v + \frac{1}{2} \right) - \nu_e x_e \left(v + \frac{1}{2} \right)^2 + \cdots + B_v J(J+1) - D_v J^2 (J+1)^2 + \cdots. \end{aligned} \qquad (3.114)$$
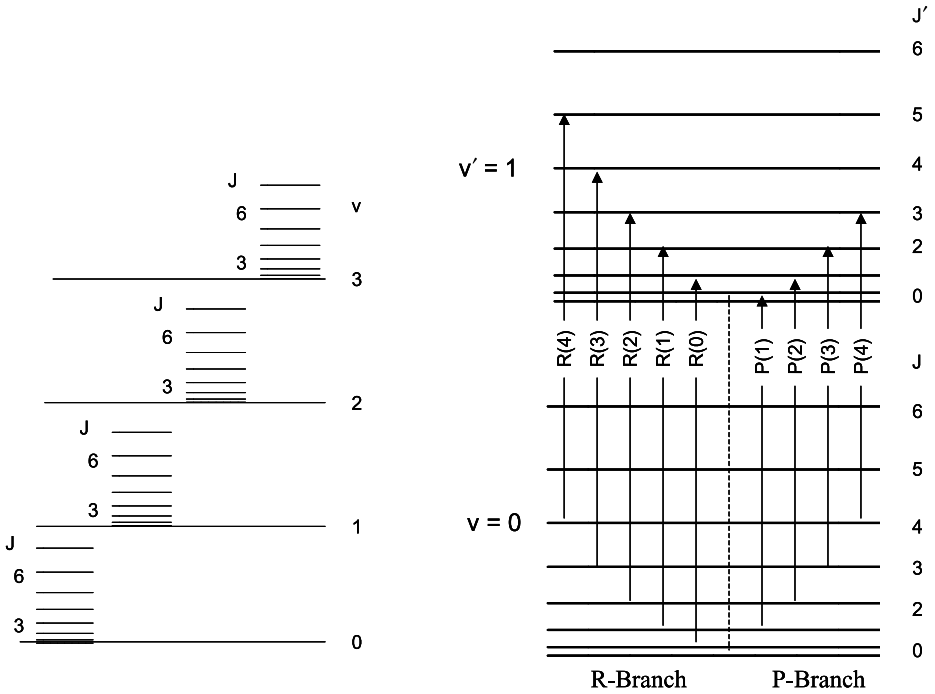
Fig. 3.12 Vibration-rotation energy level diagram (Herzberg, Ref. 3.4).

The corresponding energy level diagram is illustrated in Fig. 3.12.

We are now ready to compute the positions of infrared vibration–rotation bands. As before, $\Delta v = 1$, but now $\Delta J = \pm 1$ is possible. Thus for each vibrational transition there are two separate bands or *branches* of rotational lines that will exist. For $\Delta J = 1$, an R-branch is formed and for $\Delta J = -1$, a P-branch is formed. To see this, consider the energy level difference for $\Delta v = 1$ and $\Delta J = 1$,

$$\nu_R = G(v + 1) - G(v) + F_{v+1}(J + 1) - F_v(J). \tag{3.115a}$$

Substituting Eqs. 3.107 and 3.113 for the vibrational and rotational term values and ignoring the D rotational constant, the result for the R-branch line position is

$$\nu_R = \nu_e - 2\nu_e x_e(v + 1) + (B_{v+1} - B_v)J^2 + (3B_{v+1} - B_v)J + 2B_{v+1}. \tag{3.115b}$$

The corresponding energy level differences for the P-branch are computed in a similar manner according to

$$\nu_P = G(v + 1) - G(v) + F_{v+1}(J - 1) - F_v(J). \tag{3.116a}$$

The result for the P-branch line position is

$$\nu_P = \nu_e - 2\nu_e x_e(v + 1) + (B_{v+1} - B_v)J^2 - (B_{v+1} + B_v)J. \tag{3.116b}$$

Ignoring second-order effects in the rotational constant ($B_{v+1} \approx B_v = B_e$), we have the following simple formulas:

$$\nu_R = \nu_e - 2\nu_e x_e(v+1) + 2B_e J + 2B_e \tag{3.117}$$

for the R-branch lines with $\Delta J = 1$, and

$$\nu_P = \nu_e - 2\nu_e x_e(v+1) - 2B_e J \tag{3.118}$$

for the P-branch lines with $\Delta J = -1$. A particular transition is denoted as $P(J)$ or $R(J)$, where J is the lower-level quantum number. Note that the P-branch is below the vibrational transition frequency and the R-branch is above. An experimental vibrational spectrum of carbon monoxide is shown in Fig. 3.13.

Also in Fig. 3.13, secondary bands appear which are red shifted and weaker than the main band. These are isotopic bands in which one of the atoms in the molecule is an isotope. For example, in CO the main band is $^{12}C^{16}O$, and the red-shifted band is from the isotope $^{13}C^{16}O$. Since the ^{13}C atom is heavier, it is slower in vibration and rotation. The amount of the shift is determined by the ratio of the reduced masses (diatomic):

$$\frac{\nu_e^{isotope}}{\nu_e} = \sqrt{\frac{\mu'}{\mu'^{isotope}}} = \rho. \tag{3.119}$$

For the rotational constant B_e it can be shown that

$$B_e^{isotope} = \rho^2 B_e. \tag{3.120}$$
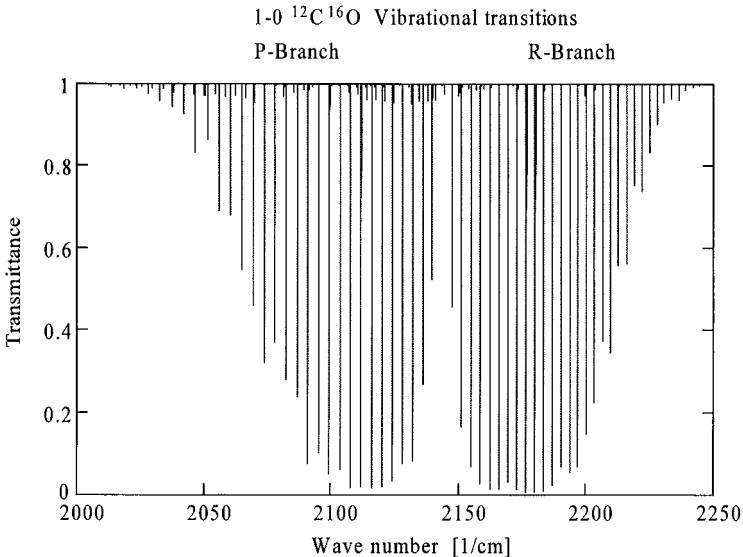
Fig. 3.13 Vibration–rotation bands of CO, showing the fundamental (1–0) of the main isotope $^{12}C^{16}O$ and the fundamental of $^{13}C^{16}O$.

This is very useful knowledge for problems in atmospheric propagation with CO_2 or CO lasers. Because these gases also exist in the atmosphere, the very transition that produces the laser radiation can also be an important absorber of that radiation in the atmosphere. Thus isotopic CO_2 and CO lasers will have improved propagation characteristics, because laser power will be unchanged but the atmospheric absorption will be greatly reduced. (CO_2 lasers are very popular for many electro-optic systems in the atmosphere and many companies offer isotopic CO_2 in the gain media.)

3.3.2.2 Polyatomic Molecules

A polyatomic molecule can have many more modes of vibration than the simple diatomic molecule. The number of possible vibrational modes is determined from the degrees of freedom of the particular system. Each atom can, in general, move in three directions. In a molecule with N atoms, there are $3N$ degrees of freedom describing the motion. Choosing a central coordinate system allows the description of motion of the molecule in three directions. Also the system can rotate in three different directions. Then the number of independent modes of vibration is $3N - 6$, where the "6" accounts for three degrees of rotation and three degrees of translation. In the case of a linear molecule (i.e., CO_2, diatomics, etc.) the number of vibrational modes is $3N - 5$, since only two independent rotational modes exist. The vibrational modes describe motion of the atoms relative to one another. When this motion is linear and with a fixed relative phase, a special set of vibrational modes are generated. Such vibrational modes are called the **normal modes of vibration**. Not all the modes will necessarily be infrared active. In a nonpolar molecule a dipole moment must be created by asymmetric vibrations of the atom, otherwise no dipole will exist and the modes are called "infrared inactive." The study of symmetry properties regarding the arrangement of atoms within a molecules is called group theory. Group theory can be used to determine the activity of a molecule but is beyond the scope of this text (see Herzberg, Ref. 3.4, and Burns, Ref. 3.8, for further references).

The vibrational term value function, $G(\ )$, for a polyatomic molecule with no degeneracy is

$$G(v_1, v_2, v_3, \ldots) = \sum_i v_i \left(v_i + \frac{1}{2} \right) + \sum_i \sum_{k \geq i} x_{ik} \left(v_i + \frac{1}{2} \right) \left(v_k + \frac{1}{2} \right), \quad (3.121)$$

where v_i is the vibrational quantum number of the ith mode, v_i is the ith harmonic vibrational mode frequency, and $x_{ik} (= x_{ki})$ accounts for an harmonic correction. Most vibrational bands observed in the atmosphere originate from the vibrational ground state (where $0 = v_1 = v_2 = \cdots$). The centers of such bands are calculated to be

$$G_0(v_1, v_2, v_3, \ldots) = G(v_1, v_2, v_3, \ldots) - G(0, 0, 0, \ldots)$$

$$= \sum_i v_{0i} v_i + \sum_i \sum_{k \geq i} x_{0ik} v_i v_k, \quad (3.122)$$

where

$$v_{0i} = v_i + x_{ii} + \frac{1}{2} \sum_{k \neq i} x_{ik}$$

and

$$x_{0ik} = x_{ik} \text{ (ignoring higher powers).}$$

If, for the ith mode, $v_i = 1$, then the transition is called fundamental. Fundamental normal-mode vibrational frequencies of atmospheric molecules are listed in Table 3.2. When $v_i > 1$, overtone bands result, which are harmonics of the fundamental. Combination bands involve transitions employing different vibrational modes. When the initial state of the molecule is not the ground state, hot bands result, with the following term value formula:

$$G(v_f, v_i) = G_0(v_{f1}, v_{f2}, v_{f3}, \ldots) - G_0(v_{i1}, v_{i2}, v_{i3}, \ldots), \qquad (3.123)$$

where $v_{f,i}$ represents the vibrational quantum number matrix of the final and initial states, respectively. Values of vibrational frequencies squared depend inversely on the reduced mass of the vibrating system and directly on the bond strength. Thus molecules with light atoms will have the highest vibration frequencies. Again, water vapor is such a molecule.

Rotational–vibrational spectra include the perturbation effect that rotational motion has on the vibrational energies. The allowed rotational transitions become $\Delta J = \pm 1, 0$ which results in P, Q, and R-branch structure (see Herzberg, Refs. 3.4 and 3.5). Net term value energies of the vibrating rotor become

$$T(v, J) = G(v) + F_v(J). \qquad (3.124)$$

Applying the selection rules leads to formulas predicting line position which can be found in Herzberg.

Table 3.2 Fundamental Vibrational Frequencies of Atmospheric Molecules[a]

Molecule	v_1 [cm^{-1}]	v_2 [cm^{-1}]	v_3 [cm^{-1}]	v_4 [cm^{-1}]	g_{v1}	g_{v2}	g_{v3}	g_{v4}
CO	2143				1			
H$_2$	4401.21[b]				1			
OH	3735.21				1			
NO	1904.0				1			
N$_2$	2359.6[b]				1			
O$_2$	1580.4[b]				1			
CO$_2$	1388.2[b]	667.4	2349.2		1	2	1	
N$_2$O	2223.8	588.8	1284.9		1	2	1	
H$_2$O	3652	1594.7	3755.7		1	1	1	
H$_2$S	2614.6	1182.7	2627.5		1	1	1	
NO$_2$	1319.7	749.8	1617.7		1	1	1	
O$_3$	1110	705	1042.1		1	1	1	
SO$_2$	1151.3	517.6	1361.7		1	1	1	
NH$_3$	3336.2	932.5	3443.6	1626.1	1	1	2	2
CH$_4$	2916.5[b]	1533.6	3019.5	1310.8	1	2	3	3

[a]From Herzberg (Refs. 3.4, 3.5).
[b]Infrared inactive.

As an example of this, let us consider the nonpolar linear molecule CO_2. It has three atoms, thus $3(3) - 5 = 4$ modes of vibration. They are illustrated below.

CO_2 *Normal Vibrational Mode Structure*

1. ν_1: Symmetric stretch mode
2 and 3. ν_2: Bending mode
(In the plane of the paper and perpendicular to the plane of this paper)
4. ν_3: Asymmetric stretch mode
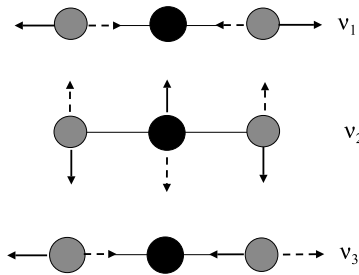
The ν_2 vibrational mode is twofold degenerate and requires two quantum numbers, as designated by ν_2^1. Thus four vibrational quantum numbers are necessary to describe vibrational motion in CO_2:

$$\nu_1 \, \nu_2^1 \, \nu_3.$$

The vibrational ground state is designated as $00^0 0$, the first ν_1 vibrational state is, $10^0 0$, and so on. Employing this notation with Table 3.2, we obtain

$$\nu_1 = 10^0 0 - 00^0 0 = 1388 \, \text{cm}^{-1},$$

$$\nu_2 = 01^0 0 - 00^0 0 = 667 \, \text{cm}^{-1},$$

$$\nu_3 = 00^0 1 - 00^0 0 = 2349 \, \text{cm}^{-1}.$$

Because of the symmetry of the ν_1 mode, it is infrared inactive. However, the other two vibrational modes are infrared active and are important absorption bands in the earth's atmosphere. (In fact, the ν_2 band contributes to the greenhouse effect in the atmosphere of the earth.) Each one of the bands will, of course, have rotational structure as well. The familiar P- and R-branches are present, and $\Delta J = 0$ also becomes possible (but not always), thus Q-branches may also appear. An example of the ν_3 vibrational band of CO_2 is shown in Fig. 3.14. Figure 3.15 also has a vibrational energy level diagram for CO_2.

Another example of great interest to us is H_2O because of its importance to atmospheric propagation and propagation in seawater (liquid phase). It has $3(3) - 6 = 3$ vibrational modes: the bending mode (ν_2), the symmetric stretch (ν_1), and the asymmetric stretch (ν_3). Because of the light hydrogen atoms in H_2O, high vibrational frequencies are possible, as opposed to other atmospheric gases.

Therefore, water vapor has strong absorption bands throughout the infrared. This fact, coupled with the large rotational constants of water vapor, explains why water vapor dominates attenuation of infrared photons by absorption in the lower atmosphere.
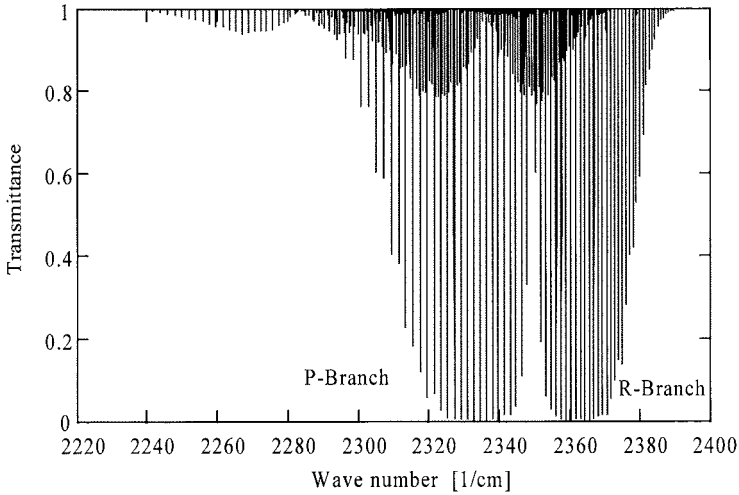
Fig. 3.14 CO_2 v_3 vibration–rotation band.

Also, the absorption spectrum of the gas and liquid phase of water has determined why, in evolution, natural selection has chosen the eye's visible spectrum.

3.3.3 Electronic Spectroscopy

Electronic absorption bands typically exist in the ultraviolet for atmospheric molecules and involve transitions of outermost orbital electrons within the molecule. These transitions mark the end of optical transparency in the atmosphere. Thus it is not necessary to present a detailed description of the entire band structure, but rather the beginning absorption edge. The most important molecules in this case are O_2 and O_3, since these molecules begin absorbing at lowest ultraviolet frequencies of the atmospheric gases. Also, electronic transitions of N_2 and O_2 contribute significantly to the real part of index of refraction throughout the infrared and visible.
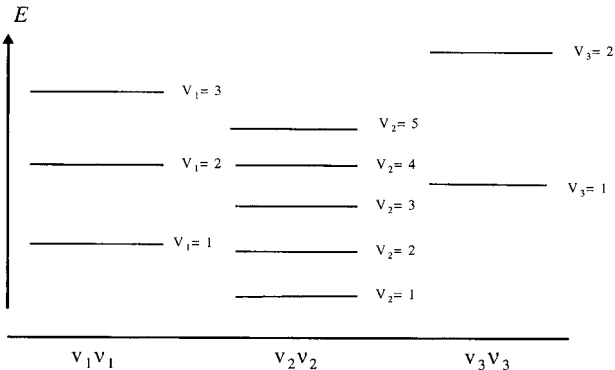
Fig. 3.15 Vibrational energy level diagram of CO_2.
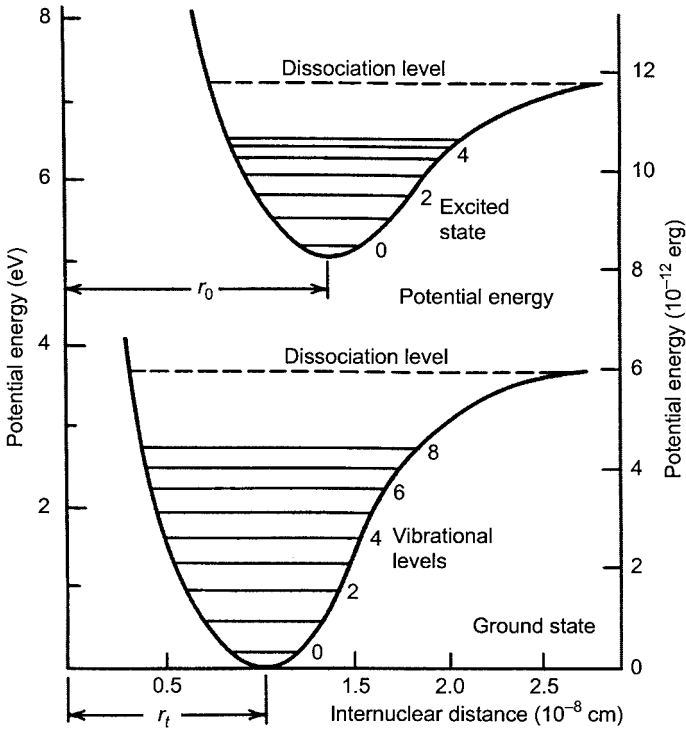
Fig. 3.16 Potential energy curves for two electronic states of a diatomic molecule (McCartney, Ref. 3.7, with permission).

Figure 3.16 illustrates a ground-state electronic level and an excited electronic level. Within these electronic states are vibrational energy structures and within the vibrational structures are rotational structures. The transition between these electronic energies contains many possible vibration–rotation bands, as Fig. 3.5 demonstrates. A series of absorption bands results, which characterizes the beginning of electronic band absorption. Oxygen begins strong absorption at 195 nm with the Schumann–Runge bands. Ozone, found primarily in the stratosphere, begins absorbing at 300 nm.

3.4 Spectroscopy of Solids

Solids do not have rotational spectra because the molecules are relatively fixed in position and cannot rotate, but they do have vibrational motion of the lattice sites and electronic transitions. The solid state adds a new look to these now familiar phenomena, especially the regular structure of crystals. Also, continuous bands, not discrete energy structures, are observed in solids, as opposed to gases. For this reason, a classical description of solid-state vibrational structure is used. Crystalline structure will be emphasized at this time and applied later to both single- and polycrystalline materials.

3.4.1 Lattice Vibrations and Phonons

When we discussed polyatomic molecules in the gas phase we stated that there are $3N - 6$ vibrational modes. The "6" corresponded to three rotational modes and three translational modes. N represented the number of atoms in the molecule. Now, since no rotational motion is allowed, the number of normal vibrational modes (which are also **optical modes**) becomes

$$3N - 3,$$

where the second term, "3", represents the number of translational modes. However, in a solid, the translational modes become **acoustic modes**, which are also vibrational in nature. Thus, there are actually $3N$ vibrational modes in a solid. The nonacoustic vibrational modes are called optical modes because they typically occur at infrared frequencies, which are higher frequencies than acoustic vibrations. Also, N now represents the number of atoms in a **primitive unit cell** or basis (which can be more than the number of atoms in the molecule). The primitive unit cell contains the basic configuration of the atoms, which is repeated in the crystal to form the macroscopic solid. Thus a solid can have many possible vibration modes. For example, NaCl has one molecule for each primitive unit cell, thus $N = 2$. The number of possible optical modes becomes three. Of course, not all of these are distinct infrared active modes. Because of symmetry, many modes will be degenerate or will have no dipole moment and, therefore, be optically inactive. Also, as is the case for NaCl, more optical modes are actually observed because of crystal defects and impurities.

3.4.1.1 One-Dimensional Diatomic Lattice

Let us begin the discussion of lattice vibration by considering the simple problem of a one-dimensional lattice with two atoms per unit cell. In this case, the number of optical modes is one ($= N - 1$). Therefore, one optical mode and one acoustic mode are expected. A diagram of this lattice is illustrated in Fig. 3.17. This will be a classical treatment, which will be very useful to us later, because the energy levels occur in bands and only broad spectral features can be observed.

Consider an infinite one-dimensional diatomic chain of a polar molecule. The negative atom has a mass M and the positive atom has a mass m. They are separated by the equilibrium distance a and held together by a Hooke's law force with spring constant β_s. This means, as before, we have assumed a harmonic potential. Now, let the atom have a small displacement from equilibrium, as shown in Fig. 3.18. v represents dis-
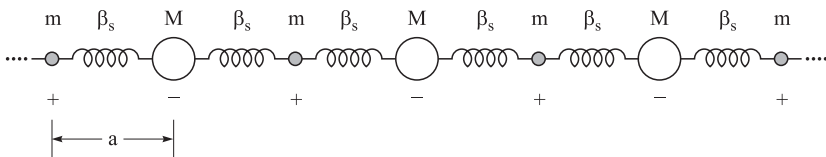
Fig. 3.17 The one-dimensional diatomic lattice. m is the positive ion, M is the negative ion, β_s is the spring constant representing the bond between atoms, and a is the equilibrium distance between atoms.
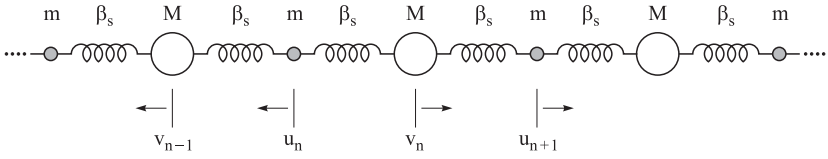
Fig. 3.18 Lattice site displacements.

placements of the negative atoms and u represents the displacements of the positive atoms. The subscripts locate the particular atom in the linear chain.

The lattice potential energy is (considering only nearest neighbors)

$$V_v(u,v) = \sum_{n=1}^{\infty} \left[\frac{\beta_s}{2}(u_n - v_n)^2 + \frac{\beta_s}{2}(v_n - u_{n+1})^2 \right] \text{ centered about } v_n \quad (3.125)$$

and

$$V_u(u,v) = \sum_{n=1}^{\infty} \left[\frac{\beta_s}{2}(v_n - u_n)^2 + \frac{\beta_s}{2}(u_n - v_{n-1})^2 \right] \text{ centered about } u_n. \quad (3.126)$$

Using, $F = -|\nabla V|$ and $F = m(d^2v/dt^2)$, we have the following coupled differential equations:

$$m \frac{d^2 u_n}{dt^2} = -\nabla_u V_u = -\frac{\partial}{\partial u_n} V_u = \beta_s(v_n + v_{n-1} - 2u_n) \quad (3.127)$$

and

$$M \frac{d^2 v_n}{dt^2} = -\nabla_v V_v = -\frac{\partial}{\partial v_n} V_v = \beta_s(u_{n+1} + u_n - 2v_n). \quad (3.128)$$

Assuming traveling wave solutions for u_n and v_n, we have

$$u_n = u\,e^{-j(2nk'a - \omega t)} \quad (3.129a)$$

and

$$v_n = v\,e^{-j[(2n+1)k'a - \omega t]}. \quad (3.129b)$$

Upon substitution into Eqs. 3.127 and 3.128, we find the following results:

$$-m\omega^2 u = \beta_s \left[v\left(e^{jk'a} + e^{-jk'a}\right) - 2u \right] \quad (3.130)$$

and

$$-M\omega^2 v = \beta_s \left[u(e^{jk'a} + e^{-jk'a}) - 2v \right]. \quad (3.131)$$

A solution will exist if the two equations are independent. Thus the determinant of the coefficient matrix must be zero:

$$\begin{vmatrix} m\omega^2 - 2\beta_s & \beta_s(e^{j'ka} + e^{-j'ka}) \\ \beta_s(e^{jk'a} + e^{-jk'a}) & M\omega^2 - 2\beta_s \end{vmatrix} = 0 \qquad (3.132)$$

Evaluating the determinant, we obtain the following **dispersion relation** between ω and k',

$$\omega^2 = \frac{\beta_s}{\mu'} \pm \beta_s \sqrt{\frac{1}{\mu'^2} - \frac{4\sin^2 k'a}{mM}} \qquad (3.133)$$

where $\mu' = [mM/(m + M)]$ is the reduced mass, just as in a diatomic gas.

A plot of $\omega(k')$ is shown in Fig. 3.19 for $k' > 0$ only, since the curve is symmetric about $k' = 0$ (i.e., $\omega(k') = \omega(-k')$). Also, the solution is periodic in k' with period π/a. This is a useful property, and the interval

$$\frac{-\pi}{2a} \le k' \le \frac{\pi}{2a}$$

is called the first Brillouin zone.

It is instructive to examine the dispersion relation for the simple case of the $k' \approx 0$ limit. Two solutions are possible,

$$\omega \approx \left(\frac{2\beta_s}{\mu'}\right)^{1/2}, \quad \text{and} \quad \frac{u}{v} \approx -\frac{M}{m} \text{ (optic branch)} \qquad (3.134)$$

and

$$\omega \approx \left(\frac{2\beta_s}{m + M}\right)^{1/2} k'a, \quad \text{and} \quad \frac{u}{v} \approx 1 \text{(acoustic branch).} \qquad (3.135)$$
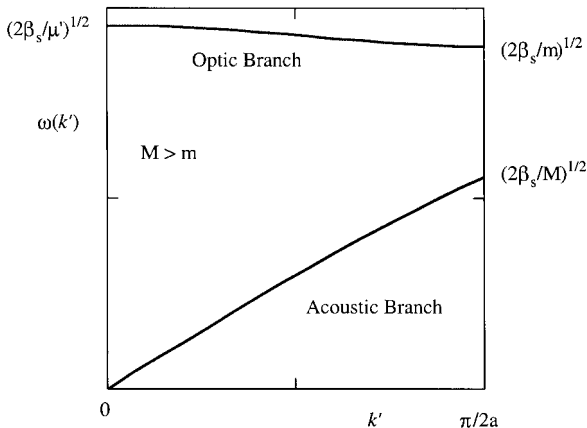
Fig. 3.19 The ω versus k' plot for a linear diatomic chain in the positive half of the first Brillouin zone.

One solution represents the optic branch, because it can be excited by high frequencies (infrared). The acoustic branch supports lower frequency modes. The solutions for $k' = \pi/(2a)$ are listed in Fig. 3.19. For this case, the lattice site position amplitude ratios are given by

$$\frac{u}{v} = \infty \text{ (i.e., } v = 0) \text{ (optic branch)},$$

and

$$\frac{u}{v} = 0 \text{ (i.e., } u = 0) \text{ (acoustic branch)}.$$

The corresponding motion of the atoms, as indicated by the ratio of the position components, is illustrated in Fig. 3.20 for both $k' = 0$ and $\pi/(2a)$. Note that the optic branch represents lattice motions consistent with an applied electric field (at optical frequencies) in the direction of the lattice and propagates perpendicular to the lattice. The acoustic branch represents compression waves or sound wave phenomena which propagate in the direction of the lattice.

From this model of the diatomic linear chain, the linear monatomic lattice can be directly understood. Setting $M = m$ reduces Eq. 3.133 to a single formula, from which the following dispersion relation is obtained:

$$\omega = 2\left(\frac{\beta_s}{m}\right)^{1/2} \left|\sin\left(k'\frac{a}{2}\right)\right|. \tag{3.136}$$

Now only one branch exists, the acoustic, as expected.
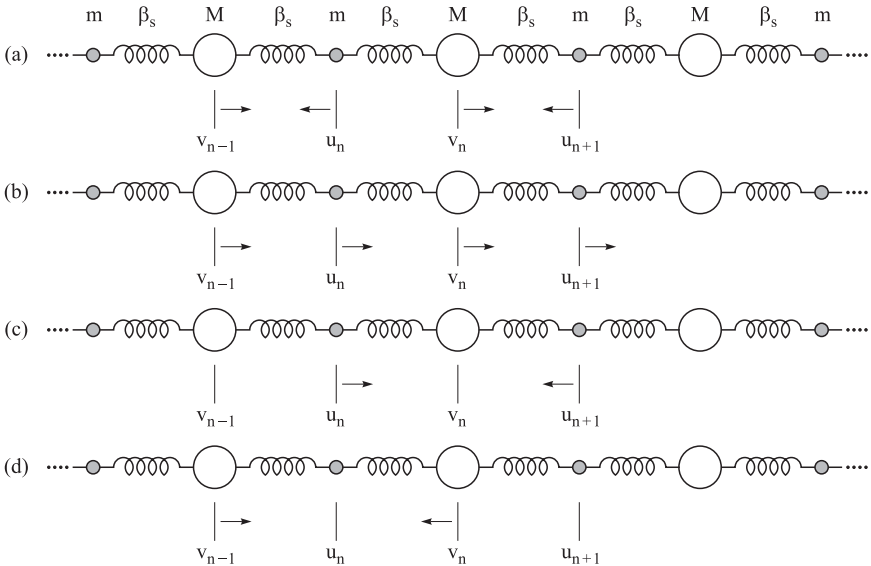
Fig. 3.20 Illustration of lattice motion for (a) $k' = 0$ optic branch, (b) $k' = 0$ acoustic branch, (c) $k' = \pi/2a$ optic branch, and (d) $k' = \pi/2a$ acoustic branch.

The group velocity, v_g, can be computed for each branch based on the dispersion relation and is defined as

$$v_g = \frac{d\omega}{dk'}.$$

For the optic branch at $k' \approx 0$ and $k' \approx \pi/(2a)$, the group velocity is

$$v_g^{OB} = 0.$$

For the acoustic branch, the group velocity is

$$v_g^{AB} = \left(\frac{2\beta_s}{m + M} \right)^{\frac{1}{2}} a = v_s \tag{3.137}$$

where v_s is the speed of sound in a diatomic crystal for $k' \approx 0$. Thus, the optic branch cannot support the transport of vibrational energy along the direction of the one-dimensional lattice for $k' \approx 0$, but the acoustic branch can. The optic branch supports a standing wave and the acoustic branch supports a traveling wave.

Also notice that the wavelength of optical radiation, λ (about 1000 to 0.1 μm), is much greater than the spacing between the lattice site, a (about 3 to 4 Å). Thus to match the wavelength of optical light the lattice has a very small value of k'. For this reason, many problems dealing with optical properties of solids are solved in the "long wavelength limit," that is, $k' \approx 0$.

3.4.1.2 Three-Dimensional Lattice

Many important points can be learned from the one-dimensional lattice problem, but it is too simplistic to represent other important issues of real materials. To complete this introduction to solid-state spectroscopy we must discuss the three-dimensional lattice.

Three-dimensional lattice structures can be represented by seven different crystal systems with 14 different unit cells. These systems are listed in Table 3.3 and the unit cell structures are illustrated in Fig. 3.21. The coordinate system used in their description is illustrated in Fig. 3.22. These different groupings represent three classes of importance to optical propagation in crystals. They are cubic, uniaxial, and biaxial, and are indicated in Table 3.3. Most optical crystals are either cubic or uniaxial; very few are biaxial. Cubic structures have the most symmetry, therefore fewer optical modes are expected and the material is more isotropic in character. Uniaxial structures have two directions of different symmetry and therefore two sets of vibrational modes, which depend on the crystal orientation. The properties of this class of material differ in the two directions. Biaxial structures differ in all three space directions and therefore have different vibrational modes and material properties in these directions as well. The importance of, and differences between, these classes concerning optical propagation is demonstrated in the next chapter.

Table 3.3 Organization of Crystal Systems

System	No. of Lattice Types	Axes and Angles	Optical Designation
Cubic	3	$a = b = c$ $\alpha = \beta = \gamma = 90°$	cubic
Hexagonal	1	$a = b \neq c$ $\alpha = \beta = 90°$ $\gamma = 120°$	uniaxial
Tetragonal	2	$a = b \neq c$ $\alpha = \beta = \gamma = 90°$	"
Trigonal	1	$a = b = c$ $\alpha = \beta = \gamma < 120°, \neq 90°$	"
Monoclinic	2	$a \neq b \neq c$ $\alpha = \beta = \gamma = 90° \neq \beta$	biaxial
Orthorhombic	4	$a \neq b \neq c$ $\alpha = \beta = \gamma = 90°$	"
Triclinic	1	$a \neq b \neq c$ $\alpha \neq \beta \neq \gamma$	"
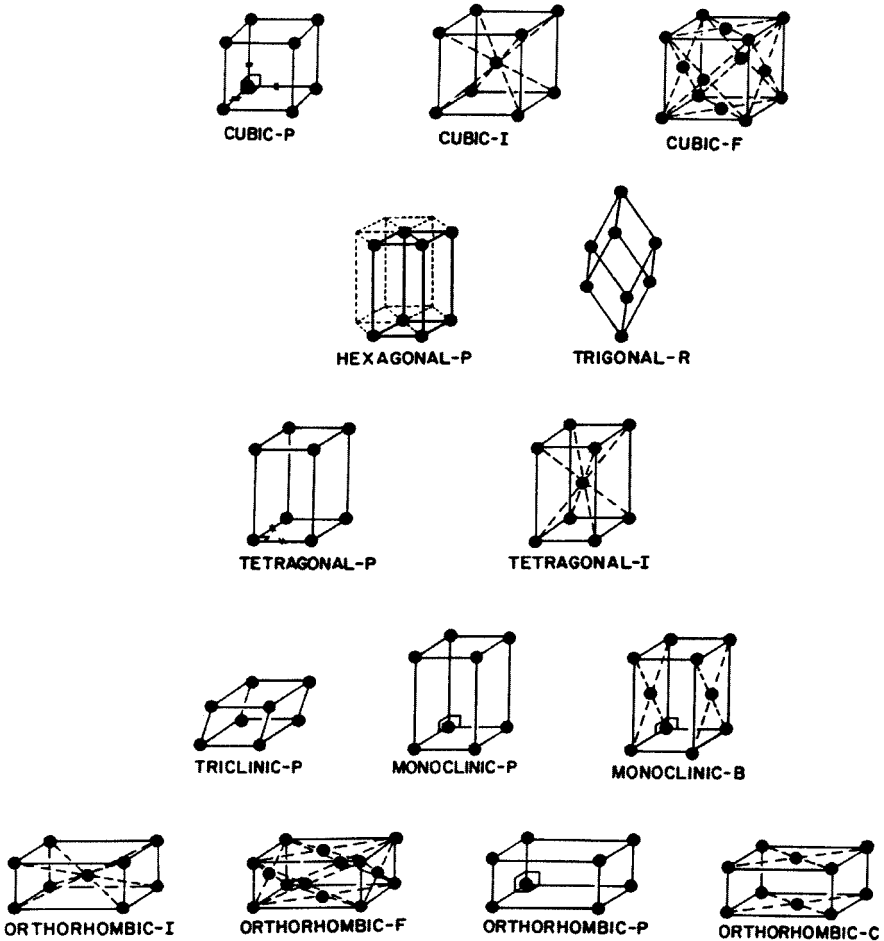
Fig. 3.21 The crystallographic systems and space lattices (Burns, Ref. 3.8, with permission).

Fig. 3.22 Crystal axes and angles.
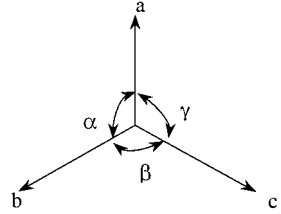
Each system structure has unique symmetry properties which determine mode degeneracy and infrared activity. This requires group theory of space structures and is not covered here, but can be found in the solid-state references at the end of this chapter (see Refs. 3.8 and 3.9).

Because of the additional dimensions, other vibration and acoustic modes are now possible. In one dimension only, modes in the direction of the lattice exist and are called longitudinal. For the case of the one-dimensional diatomic lattice, one mode is longitudinal acoustic (LA) and the other is longitudinal optical (LO). Now transverse modes are possible, where the lattice site oscillations are perpendicular to the direction of the bonds between the atoms, as illustrated in Fig. 3.23. Such modes can have an optic branch or an acoustic branch, and are called transverse optic (TO) and transverse acoustic (TA). For a crystal with one atom per unit cell, there are three acoustic modes, one longitudinal and two transverse. For a crystal with two atoms per unit cell, there are three acoustic modes (one LA and two TAs) and three optic modes (one LO and two TOs). Dispersion curves for various monatomic and diatomic crystals are shown in Fig. 3.24.

3.4.1.3 Vibrational Density-of-States

Many vibrational states can exist in a solid, and it is useful to define a density-of-states function, $\rho(\omega)$. It is the number of vibrational states between ω and $\omega + d\omega$ within a volume L^3, as defined by (see Kittel, Ref. 3.9)
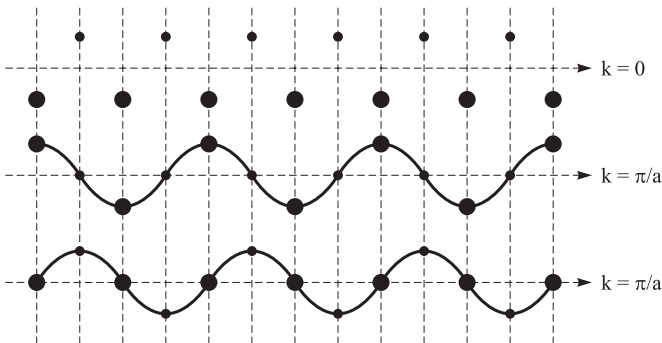
Fig. 3.23 Two-dimensional lattice showing transverse modes (Burns, Ref. 3.8, with permission).
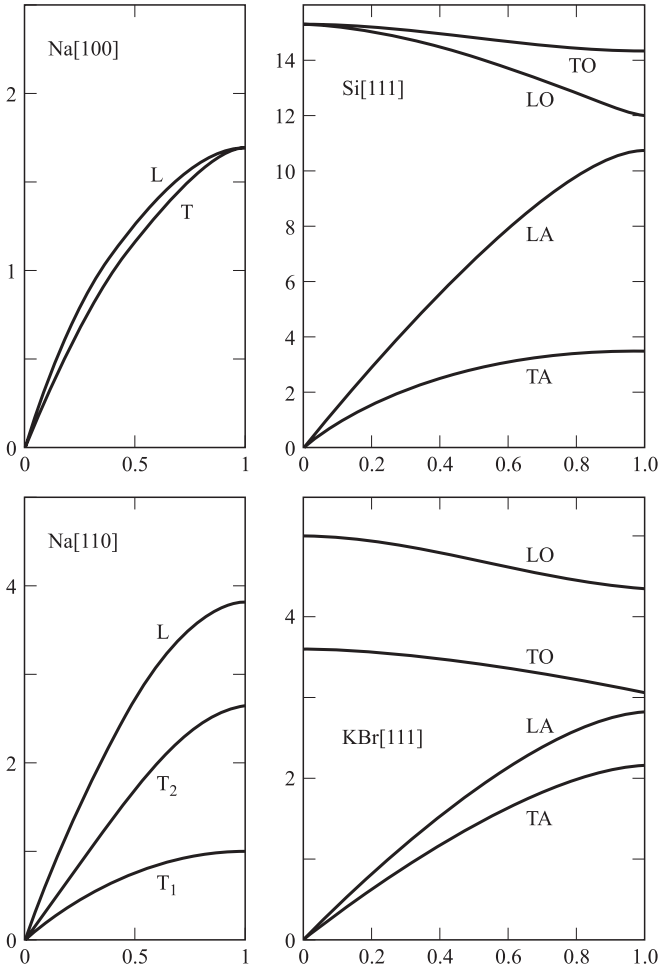
Fig. 3.24 Dispersion curves for Na, Si, and KBr (Burns, Ref. 3.8, with permission).

$$\rho(\omega)\, d\omega = dN = \left(\frac{L}{2\pi}\right)^3 \int\limits_{shell} d^3k', \tag{3.138}$$

where N is the number of modes and $\rho(\omega)$ is normlized according to

$$\int\limits_0^\infty \rho(\omega)\, d\omega = 1. \tag{3.139}$$

Based on Eq. 3.135, the frequency is directly proportional to the wave vector, k', for the acoustic branch. Thus, the number of acoustic vibrational modes less than k' is obtained by integrating Eq. 3.138 over the entire volume. The result is

$$N = \left(\frac{L}{2\pi}\right)^3 \frac{4\pi}{3} k'^3 = \frac{V\omega^3}{6\pi^2 v_s^3},$$

where the volume $V = L^3$. The vibrational density-of-states in the Debye approximation (considering only acoustic modes) is obtained by differentiating the above result with frequency. The normalized result is given by

$$\rho(\omega) = \begin{cases} \frac{3\omega^2}{\omega_{max}^3} & \omega \le \omega_{max} \\ 0 & \omega > \omega_{max} \end{cases}, \tag{3.140}$$

where ω_{max} is the maximum acoustic frequency the lattice will support. This is, in general, a crude approximation, good only for small ω (e.g., acoustic modes), but useful for many applications. An example of a real density-of-states function is shown Fig. 3.25 for a monatomic crystal. This model does give a relatively good representation of the acoustic density-of-states.

Optical-mode density-of-states structure is more complicated, and no generic model exists.

3.4.1.4 Phonons

In solid-state physics, lattice vibrations are often called **phonons**. A phonon is a quantized lattice vibration or a traveling wave packet with many similar characteristics of a photon (the particle of light). Thus the vibrational motion of a lattice can behave like a particle (wave packet).
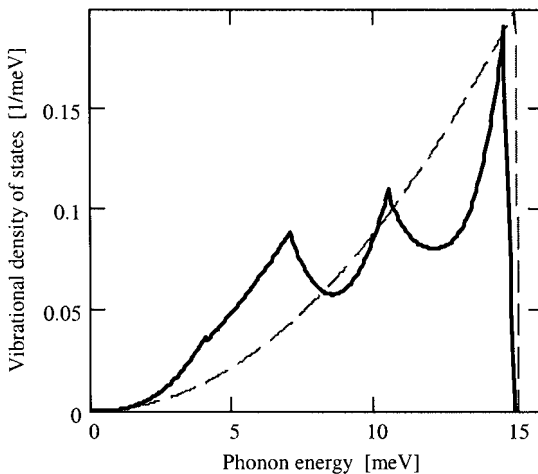
Fig. 3.25 An example of a real $\rho(\omega)$ for Na. Note the sharp cutoff near 15 meV. The dashed curve is the approximate Debye function.

3.4.2 Electronic Structure

Electronic transitions in a solid begin at the material's bandgap. This generally marks the end of a material's useful transparency. Above the bandgap, the material is reflective. Solid-state electronic spectroscopy is broad band, and is complicated by the many possible transitions. However, electronic structure is fundamental to understanding the nature of the bonds forming the solid and thus many of the material properties.

3.4.2.1 Band Structure

As in the case of vibrational structure, it is instructive to begin with a one-dimensional lattice. However, the problem will be posed within the formalism of quantum mechanics, because of the importance of energy level splitting in electronic band formation. This point is illustrated in Fig. 3.26 for diamond. Consider carbon atoms in the gas phase; the energy level structure is discrete and clearly defined. As the atoms come together to form the solid, the energy levels split N-fold, where N is the number of atoms. A covalent bond is formed by the new energy levels that are below the gas phase ground state levels because the system seeks the state of least energy.

Recall, the stationary-state Schrödinger equation in one-dimension,

$$\frac{d^2 \psi(x)}{dx^2} + \frac{2m}{\hbar}[E - V(x)]\psi(x) = 0.$$

Choose a periodic square potential such that $V(x + d) = V(x)$, as illustrated in Fig. 3.27. For an infinitely long one-dimensional solid, $V(x + nd) = V(x)$ also holds for any integer n. This arrangement approximates a lattice with the outermost electron in the atom at each lattice site trapped in the potential well between lattice sites.
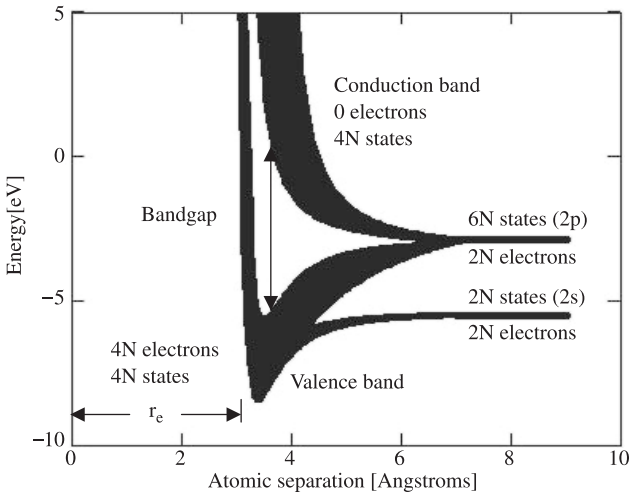
Fig. 3.26 The formation of energy bands as a function of atomic separation for diamond (Pankove, Ref. 3.10).
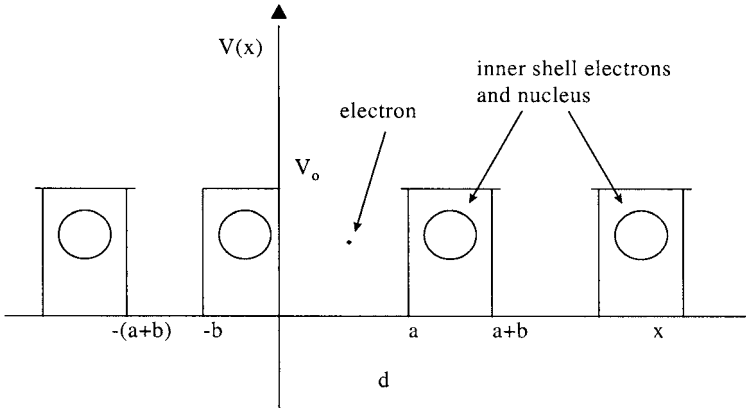
Fig. 3.27 Periodic potential of a one-dimensional linear monatomic lattice.

Based on the nature of the potential, choose a periodic solution of the form

$$\psi(x) = u(x)\,e^{jk'x}, \tag{3.141}$$

where u is periodic, as

$$u(x + nd) = u(x). \tag{3.142}$$

Solve separately for $\psi(x)$ in two regions: (1) for $V(x) = 0$ and (2) for $V(x) = V_o$.

1. For $V(x) = 0$ and $0 < x < a$, the Schrödinger equation reduces to

$$\left(D_x^2 + \frac{2mE}{\hbar^2}\right)\psi(x) = 0. \tag{3.143}$$

The solution is

$$\psi(x) = Ae^{j\alpha x} + Be^{-j\alpha x}, \tag{3.144}$$

where

$$\alpha = \left(\frac{2mE}{\hbar^2}\right)^{\frac{1}{2}}. \tag{3.145}$$

2. For $V(x) = V_o$ and $a < x < a + b$ (assuming $V_o > E$ (i.e., bound electrons)), the Schrödinger equation becomes ($D_x = d/dx$)

$$\left(D_x^2 - \frac{2m(V_o - E)}{\hbar^2}\right)\psi(x) = 0. \tag{3.146}$$

The solution in this region is

$$\psi(x) = Ce^{\beta x} + De^{-\beta x}, \tag{3.147}$$

where

$$\beta = \left(\frac{2m(V_o - E)}{\hbar^2}\right)^{\frac{1}{2}}. \tag{3.148}$$

Rearranging Eq. 3.141, we have

$$u(x) = \psi(x) e^{-jk'x}. \tag{3.149}$$

Then, substituting into the above equation the solutions for $\phi(x)$, the corresponding solutions for $u(x)$ in the two regions are as follows:

$$u_1(x) = Ae^{j(\alpha - k')x} + Be^{-j(\alpha + k')x} \quad \text{for } 0 < x < a \tag{3.150a}$$

and

$$u_2(x) = Ce^{(\beta - jk')x} + De^{-(\beta + jk')x} \quad \text{for } a < x < a + b. \tag{3.150b}$$

The boundary conditions in this case are that

$$\psi(x) \quad \text{and} \quad \frac{d\psi(x)}{dx}$$

are continuous functions everywhere. Thus u and u' must also be continuous everywhere. Therefore, at $x = 0$ we have $u(0) = u(d)$ and $u_1(0) = u_2(0)$, which results in the following conditions:

$$A + B = C + D \quad \text{(continuity of } u(x)\text{)}$$

and

$$j(\alpha - k')A - j(\alpha + k')B = (\beta - jk')C - (\beta + jk')D \qquad \text{(continuity of } u'(x)\text{)}.$$

Furthermore, since $u(x)$ must have the same periodicity of $V(x)$, then u must have the same values at $x = a$ and $x = -b$,

$$Ae^{j(\alpha - k')a} + Be^{-j(\alpha + k')a} = Ce^{-(\beta - jk')b} + De^{(\beta + j'k)b}$$
$$u_1(a) = u_2(-b) \tag{3.151a}$$

and similarly for u',

$$j(\alpha - k') Ae^{j(\alpha - k')a} - j(\alpha + k') Be^{-j(\alpha + k')a} = (\beta - jk') Ce^{-(\beta - jk')b}$$
$$- (\beta + jk') De^{(\beta + jk')b} u_1(a) = u_2(-b) \tag{3.151b}$$

For a solution of these four simultaneous homogeneous equations to exist, we require the determinant of the coefficients to vanish, which results in
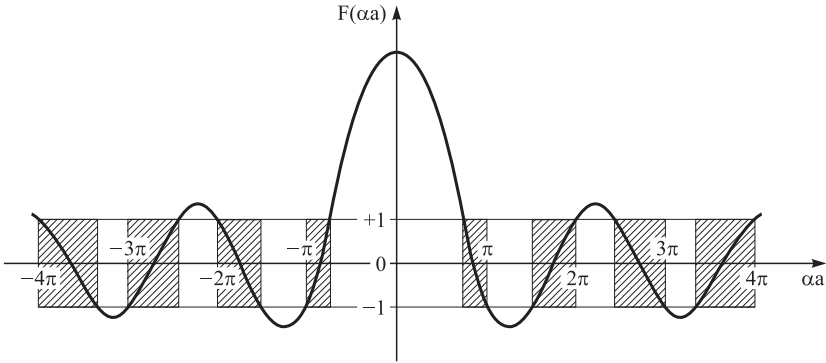
Fig. 3.28 Band structure of one-dimensional monatomic solid.

$$\frac{\beta^2 - \alpha^2}{2\alpha\beta} \sinh \beta b \sin \alpha a + \cosh \beta b \cos a\alpha = F(\alpha a) = \cos k'(a+b). \quad (3.152)$$

This equation is not tractable analytically and leads to the graphical solution shown in Fig. 3.28. Values of $F(\alpha a) \leq 1$ are valid solutions and define an energy band structure which we expect for solids. The lowest energy band is called the valance band and the first excited energy band is called the conduction band.

3.4.2.2 Electronic Density-of-States

In three dimensions, electronic band structure becomes more complicated, because it now varies with crystallographic direction, just as was the case for vibrational structure. This point is illustrated in Fig. 3.29 for the case of the electronic k'-space diagram for α-sapphire. At the bandgap, the energy structure of the valence and conduction bands is parabolic in nature. This is an important characteristic function near the bandgap for many optoelectronic devices. A brief development is presented below.

In a three-dimensional cubic box of length L, the wave function for a periodic potential takes the form

$$\psi(r) = u(r)e^{jk' \cdot r}, \qquad (3.153)$$

where the function u is periodic in three dimensions in a similar fashion to the one-dimensional case given by Eq. 3.142. The periodicity of the wave function requires the wave vector to be quantized according to

$$k_i' = \frac{2\pi m}{L_i},$$

where $i = x, y, z$ and $L = L_x = L_y = L_z$. In k'-space, the volume, V, per electronic state is

$$\frac{8\pi^3}{V}, \quad \text{where } V = L_x L_y L_z.$$
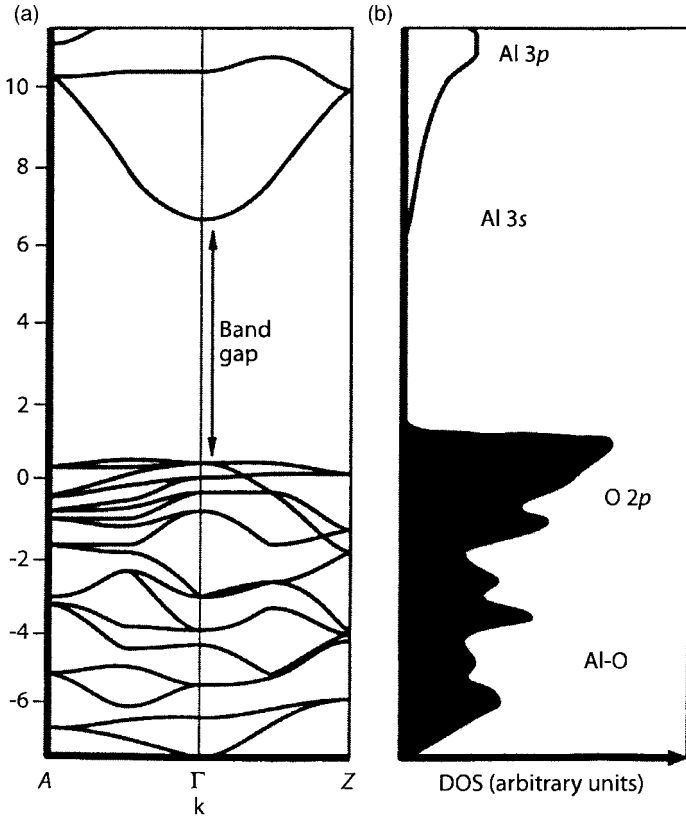
Fig. 3.29 (a) k'-space energy band structure for single-crystal sapphire. (b) The corresponding density-of-states (DOS) function for sapphire (French, Ref. 3.12a, with permission).

The electronic density-of-states, $\rho(k')$, is defined as the number of electronic states per band, with a value of k' between k' and $k' + dk'$. This is determined by computing the volume of states in a spherical shell times two, for the two different spin states, divided by the volume per electronic state, thus

$$\rho(k')\, dk' = 2 \frac{V}{8\pi^3} k'^2 \left(\int_{shell} \sin\theta\, d\theta\, d\phi \right) dk' = \frac{k'^2 V}{\pi^2}\, dk' \qquad (3.154)$$

For a given k', the associated kinetic energy of a conduction band electron is given by

$$E(k') = \frac{\hbar^2 k'^2}{2m_c}$$

where m_c is the effective mass of an electron in the conduction band. A similar formula is obtained for an electron in the valence band, where the effective mass becomes m_v. To convert the density-of-states to a function of energy, use

$$\rho(E)\, dE = \rho(k')\, dk'.$$

Using the above formulas, the following result for the electronic density-of-states is obtained:

$$\rho(E) = \frac{1}{2\pi^2} V \left(\frac{2m_{c,v}}{\hbar^2} \right)^{3/2} E^{1/2}, \tag{3.155}$$

where $m_{c,v}$ is either the mass of an electron in the conduction band or the valence band.

3.4.2.3 Excitons

An **exciton** is a bound electron–hole pair, formed by an electron in a conduction band with a hole (absence of an electron) in the valence band. It has many properties similar to that of a hydrogen atom. The spectrum of an exciton is similar to that of hydrogen and occurs near the bandgap of the host material. The bond length varies depending on the host medium. Long bond lengths are found in semiconductors and short bond lengths are found in insulating materials.

3.5 Spectroscopy of Liquids

Liquids can be thought of as a transition phase for matter between gases and solids. Thus we expect to see broad continuous spectral features, as is typical for condensed phase media at spectral locations similar to gas-phase spectra. This, it turns out, is basically true for vibrational structure but not for rotational structure. The rotational motion is hindered because of collisions with nearby neighboring molecules, and optically manifests as broad-band spectra, typically in the microwave.

From the point of view of the most important optical propagation media, one liquid stands out, water. The dielectric properties are needed for solving atmospheric scatter problems by fog, clouds, and sea spray, and absorption problems within seawater and biological fluids. Thus understanding the spectroscopy of water is fundamentally important to two common propagation media.

Liquid-phase spectroscopy is complicated and will only be surveyed here. The similarities with gases and solids are emphasized.

3.5.1 Orientational Polarizability

For the case of polar molecules in the liquid phase the molecules rotate to align themselves to an applied field. This produces what is called orientational polarizability. A relaxation time is given for a particular system to do the orientational process, it is called the Debye relaxation time. For water it is found to be $\tau_D \approx 10^{-11}$ sec.

The Debye relaxation process accounts for the damped rotation of the water molecule in the liquid state. The conductivity relaxation process accounts for the damped translational motion of the ionic charge carrier. Debye, in 1913 (Ref. 3.13), approximately determined the Debye relaxation time, τ_D, by considering Stoke's law converted for a rotating sphere and Brownian motion. The following formula was obtained:

$$\tau_D = \frac{8\pi \eta a^3}{k_B T},\qquad(3.156)$$

where η is the viscosity of water, a is the radius of water molecule and k_B is the Boltzmann's constant. Surprisingly, this formula predicts reasonably well the observed relaxation time of water, which is on the order of 1×10^{-11} sec. Figure 3.30 shows the Debye absorption band peaked at a wavelength of $\sim 10,000\,\mu m (= c\tau_D)$.

Microwave ovens use this absorption band to heat food. Infrared ovens (the common oven) use vibrational absorption bands for coupling energy into a medium. The amount
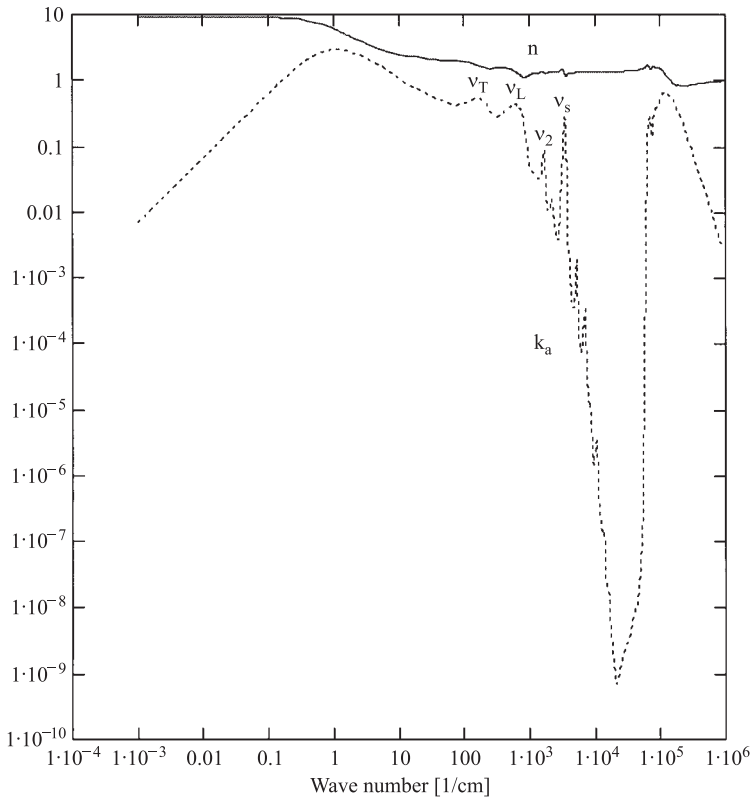
Fig. 3.30 The index of absorption, k_a, and index of refraction, n, as a function of wavelength for liquid water at room temperature and one atmosphere pressure.

of energy absorbed is proportional to the absorption coefficient and not the index of absorption. They are linearly related by frequency as given by Eq. 2.30.

Note   In the case of seawater, one must also consider the free-carrier contributions to the complex index of refraction. Intuitively, the relaxation time, τ_c, of the translational motion of the ionic charge carrier in water should be similar to the rotational relaxation of the water molecule. Following a similar approach to Debye, the conductivity relaxation time can be approximately found by examining the charge density and by applying Stoke's law and Brownian motion. The result is

$$\tau_c = \frac{6\pi \eta b x_0^2}{k_B T}, \tag{3.157}$$

where b is the radius of the charge carrier and x_0 is the $1/e$ point of the charge distribution. Substituting into the formula numbers for seawater and assuming that $a \approx b$ and x_0, one finds that $\tau_D \approx \tau_c$.

Thus, the microwave absorption coefficient is significantly lower than the infrared absorption coefficient. This is why microwave ovens heat a volume more uniformly and therefore quickly, and infrared ovens primarily couple to the surface and require more time to heat the entire medium.

3.5.2 Vibrational and Electronic Structure

Vibrational structure of the gas phase will also appear in the liquid phase; however, the location of the observed vibrational band will be shifted from the gas-phase location. Obviously, the intramolecular potentials have changed. Also, continuous band structures are observed. An example of this is the liquid H_2O spectrum in Fig. 3.30. The v_2 and v_s (v_1 and v_3 stretch bands combined) bands, as listed in Table 3.2 for the gas phase, are clearly present. Notice that no rotational structure is seen within the vibrational bands, only smooth bands. Also, new bands have appeared due to "intermolecular" potentials between molecules. v_T is the translation band caused by collisions by surrounding water molecules that hinder the translational motion of the absorbing molecule. v_L is the librational band caused by hindered rotations of two interacting molecules. The molecules rock about a hydrogen bond as they try to rotate. v_A is the association band caused by combinations of other bands ($v_2 + v_L$). Table 3.4 lists the location and identification of observed vibration bands of water. The strong absorption peak at 2.9 μm is commonly used for tissue ablation in biomedical applications.

The vibrational bands decrease in strength as the frequency increases. The minimum index of absorption occurs in the visible, which is a window region in water bordered by vibrational absorption bands to the low-frequency side and electronic absorption bands and scatter loss to the high-frequency side. This fact, plus the origin of life from seawater, is why we see in the visible spectrum. In fact, as discussed in Chapter 1, the visible spectrum is defined by liquid water absorption.

Pure water has reasonably good transparency out to 0.22 μm. Then electronic absorption bands rapidly increase in strength to end transmission at shorter wavelengths. More will be written about the optical properties of water in Chapter 9.

Table 3.4 Vibrational Bands of Water

Band Identification	Band Location	
	[cm⁻¹]	[μm]
ν_T	170	588
ν_L	590	16.95
ν_2	1640	6.097
ν_A	2130	4.695
ν_s	3390	2.950
$\nu_s + \nu_2$	5125	1.951
$2\nu_s$	6875	1.454
$\nu_2 + 2\nu_s$	8400	1.190
$3\nu_s$	10,250	0.975

Problems

3.1 (a) Verify that solution given by Eq. 3.23 satisfies the Schrödinger wave equation. (b) Show that this solution represents the momentum with no uncertainty and that the particle position is unknown for forward propagating particles ($B = 0$) in a finite region $[-L, L]$.

3.2 Show that $\hat{x}$ and $\hat{p}_x$ do not commute, that is, show that $[\hat{x}, \hat{p}_x]\psi(x) = (\hat{x}\hat{p}_x - \hat{p}_x\hat{x})\psi(x) = -j\hbar\psi(x)$.

3.3 A common line shape function is the Lorentz profile, given by

$$g(\nu - \nu_o; \gamma) = \frac{1}{\pi} \frac{\gamma}{(\nu - \nu_o)^2 + \gamma^2}.$$

Does this line shape function satisfy the normalization condition

$$\int_0^\infty g(\nu - \nu_o; \gamma)\, d\nu = 1?$$

Does the Lorentz line shape satisfy Eq. 3.32?

3.4 Compute B_e in cm⁻¹ for OH⁻, N_2, and CO_2, given $r_e = 0.97$ Å, 1.094 Å, and 1.15 Å, respectively (for CO_2, r_e is the distance from the O atom to the C atom). Which of these molecules have permanent dipole moments, thus observable rotational spectra?

3.5 Compute $\langle J_r|\mu_{dp}|J_i\rangle \neq 0$, thus show that the selection rule for rotational spectra is $\Delta J = \pm 1$.

3.6 Given the energy eigenvalues of the Morse potential,

$$\frac{E_\nu}{hc} = \nu_o\left[\left(\nu + \frac{1}{2}\right) - \frac{1}{j'}\left(\nu + \frac{1}{2}\right)^2\right],$$

plot the energy level structure for $j' = 10$ and $\nu_o = 1000$ cm⁻¹. What is the dissociation energy?

3.7 What is the *total* number of possible normal vibrational modes for CH_4 and SF_6?

3.8 (a) How do isotopes of the atoms affect rotational and vibrational spectra of molecules? Calculate the isotopic shift of $^{13}C^{16}O$ from the main isotope $^{12}C^{16}O$ vibrational band. (b) Show that $B_e^{isotope} = \rho^2 B_e$, where

$$\rho = \sqrt{\frac{\mu'}{\mu'^{isotope}}}.$$

(Consider diatomic molecules only.) (c) Why do molecules that contain light atoms have rotational and vibrational bands that are broad compared with those of molecules of all heavier atoms?

3.9 For the case of Raman bands and collision-induced bands (i.e., O_2 and N_2, which are important in atmospheric propagation), transitions for $\Delta v = 1$ and $\Delta J = \pm 2, 0$ are allowed. Compute the locations of the spectral line in terms of the quantum numbers and the molecular constants. Assume the vibrational motions are purely harmonic and $D_v \approx 0$. A S-branch is formed for $\Delta J = 2$, a Q-branch is formed for $\Delta J = 0$ and an O-branch is formed for $\Delta J = -2$, a Q-branch is formed for $\Delta j = 0$ and an O-branch is formed for $j = 2$. How does the spacing between spectral lines compare with pure rotational spectra and the R- and P-branch of vibration–rotation spectra?

3.10 Water vapor absorption bands determine the infrared windows of the atmosphere. Given that

$$v_2 = 1595 \text{ cm}^{-1},$$

$$v_1 = 3652 \text{ cm}^{-1},$$

and

$$v_3 = 3756 \text{ cm}^{-1}.$$

Plot the energy level diagram for H_2O and then compute the location of the combination overtone bands: $2v_2$, v_2+v_3, $2v_2 + v_3$, $v_1 + v_3$, $v_1 + v_2 + v_3$, and, $2v_1 + v_3$. Plot the location of these bands on a wave number axis and predict the location of atmospheric windows. (Ignore anharmonic corrections, but don't forget CO_2 to get a complete picture!)

3.11 A more realistic crystalline one-dimensional lattice is illustrated in Fig. P3.11 for $M > m$.
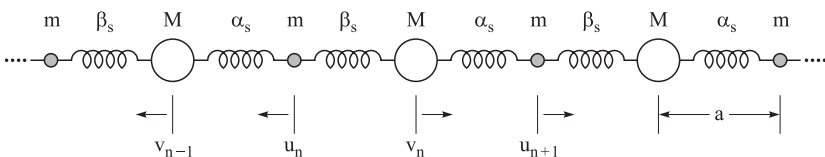
Fig. P3.11

Solve for the dispersion relation $\omega\left(k'\right) = ?$. This problem uses the molecular approximation, where $\beta_s > \alpha_s$. Thus the bonding within the molecule is greater than the bonding between molecules.

3.12 Derive the normalized Debye acoustic density-of-states distribution function as given by Eq. 3.140, knowing that $\rho\left(\omega\right) \propto \omega^2$ for $0 \leq \omega \leq \omega_{\max}$ and zero otherwise.

3.13 Compute the acoustic two-phonon density-of-states, $\rho_2(\omega)$, given that the one-phonon density-of-states function, $\rho_1(\omega)$, is the Debye function (see Eq. 3.140). The two-phonon density-of-states is computed by convolution as given by

$$\rho_2(\omega) = \rho_1(\omega) * \rho_1(\omega).$$

3.14 Derive the normalized electronic density-of-states function.

Bibliography

General

3.1 E. Goldin, *Waves and Photons: An Introduction to Quantum Optics*, Wiley (1982).

Section 3.1

3.2 E. Merzbacher, *Quantum Mechanics*, 2nd Ed., Wiley (1970).

Section 3.2

3.3 C.E. Dykstra, *Quantum Chemistry and Molecular Spectroscopy*, Prentice-Hall (1992).

Section 3.3

3.4 G. Herzberg, *Spectra of Diatomic Molecules*, 2nd Ed., Van Nostrand Reinhold (1950).
3.5 G. Herzberg, *Infrared and Raman Spectra*, Van Nostrand Reinhold (1945).
3.6 G. Herzberg, *Electronic Spectra and Electronic Structure of Polyatomic Molecules*, Van Nostrand Reinhold (1966).
3.7 E.J. McCartney, *Absorption and Emission by Atmospheric Gases*, Wiley-Interscience (1983).
3.8 C. Burns, *Solid State Physics*, Academic Press (1985).

Section 3.4

3.9 C. Kittel, *Introduction to Solid State Physics*, 4th Ed., Wiley (1971).
3.10 J.I. Pankove, *Optical Processes in Semiconductors*, Dover (1975).
3.11 E.D. Palik (ed.), *Handbook of Optical Constants of Solids*, Academic Press Handbook Series (1985).
3.12a R.H. French, "Electronic Band Structure of Al_2O_3 with Comparison to AlON and AlN," *J. Am. Ceram. Soc.* **73**, 477–489 (1990).
3.12b R.H. French, D.J. Jones, and S. Loughin, "Interband Electronic Structure of α-Alumina up to 2167 K," *J. Am. Ceram.* Soc. **77**, 412–422 (1994).
3.13 P. Debye, *Polar Molecules*, Dover (1945).

4

Electrodynamics I: Macroscopic Interaction of Light and Matter

Thus far, we have developed the properties of the electromagnetic field at optical frequencies, based on Maxwell's equations. These equations further give a classical macroscopic perspective on the coupling of the propagation media to the field, as presented in Chapter 2. The macroscopic properties of a medium are based on averaged microscopic properties. The microscopic energy structure of matter was presented in Chapter 3, covering gases, solids, and liquids by employing mostly quantum models. We now proceed to the next level of development, the dynamic description of the interaction between the optical field and the propagation medium as a function of the field frequency and propagation media variables (e.g., energy structure, temperature, and pressure). In this chapter, the classical electromagnetic field is coupled to discrete frequency oscillators via Newton's equation of motion. This approach leads to the popular classical oscillator model, often presented in introductory books on lasers. The classical oscillator model is an incomplete theory and can be only a semiempirical model. In the next chapter, a more detailed and comprehensive approach, which also includes statistical and quantum mechanics, is used leading to robust semiclassical and quantum oscillator models. This chapter and the next are the basis for the applied models presented in Part II of this book.

4.1 Classical Electrodynamics

Classical electrodynamics is based on Maxwell's equations, as given in Chapter 2 (Eqs. 2.1–2.6), and the Lorentz force relation, as given below:

$$\mathbf{F} = q[\mathbf{E} + (\mathbf{v} \times \mathbf{B})]. \tag{4.1}$$

These equations cover the classical description of the interaction of light and matter. The first term in Eq. 4.1 represents coupling of the electric field to the medium. As discussed in Chapter 2 (Section 2.2), the leading mechanism for this is the electric dipole moment. To see that this is the coupling mechanism in the first term, consider the potential function driving this force,

$$\mathbf{F} = -\nabla V(\mathbf{r}) = -\nabla(-q\mathbf{r} \cdot \mathbf{E}).$$

The above expression contains the dipole moment, as defined in Chapter 2. The second term in Eq. 4.1 represents coupling of the magnetic field to the medium. It is a weaker effect and will not be considered, since most propagation path lengths are too short for this coupling mechanism to be important.

In the classical limit, the electromagnetic field energy flow is considered continuous. When many photons compose the field, this is a good approximation and can often be applied. A good example of the success of this approximation is the fruitful field of physical optics.

Two approaches can be used to formulate this problem. One is a detailed microscopic theory and the other is a phenomenological macroscopic theory. It is instructive to consider the macroscopic approach first. This approach leads to simple phenomenological classical models, which demonstrate basic concepts and are surprisingly practical. Detailed classical microscopic models are not presented, since they will ultimately be replaced by more complete microscopic quantum models (see Chapter 5).

4.2 Classical Oscillator Model

The classical oscillator model (also called the Lorentz oscillator model) is largely phenomenological in nature but is commonly used to represent the real and imaginary parts of the complex index of refraction as a function of frequency for a wide variety of media. It is commonly presented in textbooks covering the topic of lasers.

4.2.1 Gases at Low Density

Assuming the medium is at low density (e.g., a gas), then the Newtonian equation of motion for an electron (or any other binary system), bound to a nucleus by a restoring force produced by a harmonic potential (recall Eqs. 3.65 and 3.66) and driven by an external electric field $\mathbf{e}(Z,t)$ propagating in the Z-direction, is given by

$$m\ddot{\mathbf{x}}(t) + m\Gamma\dot{\mathbf{x}}(t) + m\omega_0^2\mathbf{x}(t) = q\mathbf{e}(Z,t), \tag{4.2}$$

where m is the electron mass (or the reduced mass for diatomic vibrating or rotating nuclei, see Eq. 2.64), Γ is a phenomenological damping constant, q is the charge of the mass, and ω_0 is the system oscillation frequency. $\mathbf{R}(t)$ defines an external coordinate
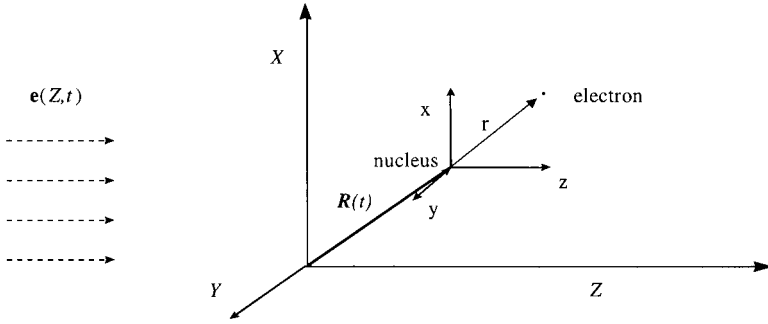
Fig. 4.1 Coordinate systems for the electromagnetic field (upper case italic) and atomic oscillator (lower case).

system that locates the nucleus of the moving atom and the spatial dependence of the incident electromagnetic field. The oscillator frequency, ω_0, is obtained from Chapter 3. Because the nucleus is much more massive than the electron, we assume the motion of the nucleus can be ignored. To simplify the problem, a system with only two energy levels or one transition frequency is considered. Later, a sum over all possible transitions will be performed. $\mathbf{x}(t)$ denotes the internal coordinate system of the oscillator and represents the relative motion between the opposite charges of the nucleus and the outermost electron. Figure 4.1 illustrates the geometry for an electron oscillating about a nucleus driven by an external electromagnetic wave. As previously argued, magnetic field effects are weak and therefore ignored. Also, the strength of the electric field is low, such that it does not distort the molecule to reveal anharmonic effects in the potential.

Then, assume time-harmonic (or monochromatic) behavior as $\mathbf{x}(t) = \mathbf{X}(\omega)\exp(j\omega t)$ and $\mathbf{e}(Z,t) = \mathbf{E}(Z,\omega)\exp(j\omega t)$. Making these substitutions, Eq. 4.2 is converted to the frequency domain and becomes

$$-m\omega^2\mathbf{X}(\omega) + jm\Gamma\omega\mathbf{X}(\omega) + m\omega_0^2\mathbf{X}(\omega) = q\mathbf{E}(Z,\omega). \tag{4.3a}$$

This is now an algebraic equation with the following solution for the electron position $\mathbf{X}(\omega)$:

$$\mathbf{X}(\omega) = \frac{q}{m}(\omega_0^2 - \omega^2 + j\omega\Gamma)^{-1}\mathbf{E}(Z,\omega). \tag{4.3b}$$

Now, based on Eq. 2.183, the frequency-domain dipole moment vector, $\boldsymbol{\mu}_{dp}(\omega)$, created by this oscillator model becomes

$$\boldsymbol{\mu}_{dp}(\omega) = q\mathbf{X}(\omega) = \frac{q^2}{m}\left(\omega_0^2 - \omega^2 + j\omega\Gamma\right)^{-1}\mathbf{E}(Z,\omega). \tag{4.4}$$

The direction of X is the same as the polarization direction of the $\mathbf{E}$-field. That is, the dipole moment of this system aligns with the field.

If there are N_a absorbing molecules per unit volume V with a number density $\rho_a\,(= N_a/V)$, and using Eqs. 2.31, 2.34, 2.184, and 2.185, then the

relationship between the applied electric field and the dipole moment of the medium is given by

$$\rho_a \langle \boldsymbol{\mu}_{dp}(\omega) \rangle = \mathbf{P}(Z,\omega) = \epsilon_0 \chi(\omega) \mathbf{E}(Z,\omega)$$

and

$$\epsilon(\omega) = \epsilon_r(\omega)\epsilon_0 = \epsilon_0 + \frac{|\mathbf{P}(Z,\omega)|}{|\mathbf{E}(Z,\omega)|} = (1+\chi(\omega))\epsilon_0. \tag{4.5}$$

$\mathbf{P}(Z,\omega)$ is the polarization vector, ϵ_0 is the free-space permittivity, $\epsilon_r(\omega)$ is the relative permittivity, and $\chi(\omega)$ is the electric susceptibility, as defined in Chapter 2. Further, based on these definitions and Eq 4.4, we sum over all allowed transitions to obtain

$$\mathbf{P}(Z,\omega) = \rho_a \sum_i \langle \boldsymbol{\mu}_{dp,i}(\omega) \rangle = \sum_i \frac{\rho_a (q^2/m)_i \mathbf{E}(Z,\omega)}{(\omega_i^2 - \omega^2 + j\omega\Gamma_i)} \tag{4.6}$$

Here ω_0 is replaced by ω_i representing multiple oscillators. The sum on i is over all allowed rotational, vibrational, and electronic transitions of the medium. Using Eqs. 4.5 and 4.6, the complex relative permittivity becomes

$$\epsilon_r(\omega) = 1 + \sum_i \frac{\rho_a \left(\frac{q^2}{\epsilon_0 m} \right)_i}{\omega_i^2 - \omega^2 + j\omega\Gamma_i}. \tag{4.7}$$

To somewhat reduce the notation, define

$$\Delta\epsilon_i = \rho_a \frac{q_i^2}{m_i \omega_i^2 \epsilon_0}. \tag{4.8a}$$

$\Delta\epsilon_i$ is related to the oscillator strength and is directly proportional to number density. For an ideal gas (noninteracting), the density is related to temperature and pressure according to

$$\rho_a = \frac{p_a}{k_B T}.$$

Thus, in general, $\Delta\epsilon_i$ is a function of temperature and pressure,

$$\Delta\epsilon_i = \Delta\epsilon_{i0} \frac{p_a T_0}{p_{a0} T}, \tag{4.8b}$$

where T_0 and p_{a0} are the reference temperature and reference pressure, respectively, and $\Delta\epsilon_{i0}$ is the value at the reference conditions. $\Delta\epsilon_{i0}$ is often listed for standard temperature and pressure (STP) (e.g., $T_0 = 273$ K and $p_{a0} = 1$ atm) conditions or for normal temperature and pressure (NTP) (e.g., $T_0 = 296$ K and $p_{a0} = 1$ atm) conditions. Equation 4.8b is needed when the permittivity at different conditions is desired.
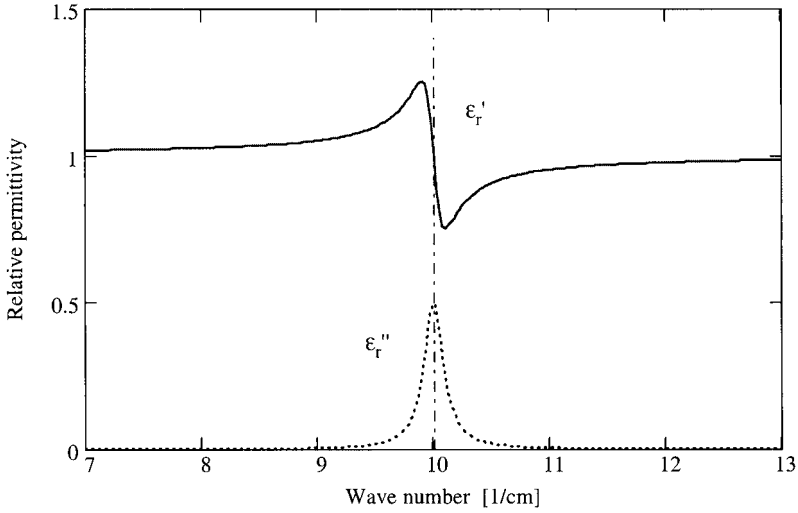
Fig. 4.2 The real, $\epsilon_r'(v)$, and imaginary, $\epsilon_r''(v)$, parts of the relative permittivity for a gas-phase oscillator centered at $v_0 = 10$ cm^{-1}, an oscillator strength of $\Delta\epsilon = 0.01$ and a full-width at half-maximum, $\Gamma = 0.2$ cm^{-1}.

With substitution of Eq. 4.8, the complex relative permittivity for a low-pressure ideal gas can be rewritten as

$$\epsilon_r'(\omega) - j\epsilon_r''(\omega) = 1 + \sum_i \frac{\omega_i^2 \Delta\epsilon_i}{\omega_i^2 - \omega^2 + j\omega\Gamma_i} \cdot \tag{4.9}$$

Solving the above equation for the real and imaginary parts of the complex relative permittivity, the following classical oscillator model for gaseous media is obtained:

$$\epsilon_r'(\omega) = 1 + \sum_i \frac{\omega_i^2 \Delta\epsilon_i (\omega_i^2 - \omega^2)}{(\omega_i^2 - \omega^2)^2 + (\omega\Gamma_i)^2} \tag{4.10a}$$

and

$$\epsilon_r''(\omega) = \sum_i \frac{\omega_i^2 \Delta\epsilon_i \omega\Gamma_i}{(\omega_i^2 - \omega^2)^2 + (\omega\Gamma_i)^2} \cdot \tag{4.10b}$$

Figure 4.2 illustrates these permittivity functions for a gaseous medium with a single oscillator as a function of wave number.

The permittivity of a noninteracting gaseous mixture is obtained by summing over each type of gas in the mixture, as given by

$$\epsilon_r'(\omega) = 1 + \sum_s \sum_i \frac{\omega_{s,i}^2 \Delta\epsilon_{s,i} (\omega_{s,i}^2 - \omega^2)}{(\omega_{s,i}^2 - \omega^2)^2 + (\omega\Gamma_{s,i})^2} \tag{4.11a}$$

and

$$\epsilon_r''(\omega) = \sum_s \sum_i \frac{\omega_{s,i}^2 \Delta\epsilon_{s,i}\omega\Gamma_{s,i}}{(\omega_{s,i}^2 - \omega^2)^2 + (\omega\Gamma_{s,i})^2}. \tag{4.11b}$$

The index s represents each type of molecule in the mixture. It is important to remember that $\Delta\epsilon_{s,i}$ depends on the number density of the s-type molecule that it represents.

At the resonance frequency, the real part of the relative permittivity exhibits anomalous dispersion, which connects the low- and high-frequency limits of the dielectric constant. These functions also satisfy the required symmetry properties established in Section 2.1.2. The classical oscillator model is useful because it satisfies these basic physical properties.

Further recall that, based on Eqs. 2.29 and 2.30, and assuming $n(\omega)$ is constant in the vicinity of the absorption feature, the absorption coefficient is obtained:

$$\beta_{abs}(\omega) = 4\pi\nu k_a(\omega) = 2\frac{\omega}{c}k_a(\omega) = \frac{\omega}{nc}\epsilon_r''(\omega).$$

Substituting Eq. 4.10b for $\epsilon_r''(\omega)$, we have the following result:

$$\beta_{abs}(\omega) = \frac{\omega^2}{nc}\sum_i \frac{\omega_i^2\Delta\epsilon_i\Gamma_i}{(\omega_i^2 - \omega^2)^2 + (\omega\Gamma_i)^2}. \tag{4.12}$$

This result can be broken down into the factors discussed in Chapter 2, the line strength and the line shape. First consider the near line center absorption coefficient ($\omega \approx \omega_i \pm \delta$), where Eq. 4.12 reduces to

$$\beta_{abs}(\omega) = \frac{\omega^2}{nc}\sum_i \frac{2\omega_i^2\Delta\epsilon_i\left(\frac{\Gamma_i}{2}\right)}{(2\omega_i \pm \delta)^2(\delta)^2 + 4\left(\frac{\omega_i\Gamma_i}{2}\right)^2} \tag{4.13}$$

Then, for δ small ($\omega_i \gg \delta$), and ignoring the mixing or coupling of adjacent absorption lines,

$$\beta_{abs}(\omega) = \sum_i \frac{\pi\omega_i^2\Delta\epsilon_i}{2nc}\left(\frac{\omega}{\omega_i}\right)^2 j_L(\omega) \text{ [L}^{-1}\text{]}, \tag{4.14}$$

where the dimension of β_{abs} is reciprocal length and

$$j_L(\omega) = \frac{1}{\pi}\frac{\gamma_i}{(\omega_i - \omega)^2 + \gamma_i^2} \tag{4.15}$$

is the Lorentz line shape (illustrated in Fig. 3.3), with $\gamma_i = \Gamma_i/2$ representing the half-width at half-maximum. Comparing Eq. 4.14 and Eq. 3.33, we obtain the line profile
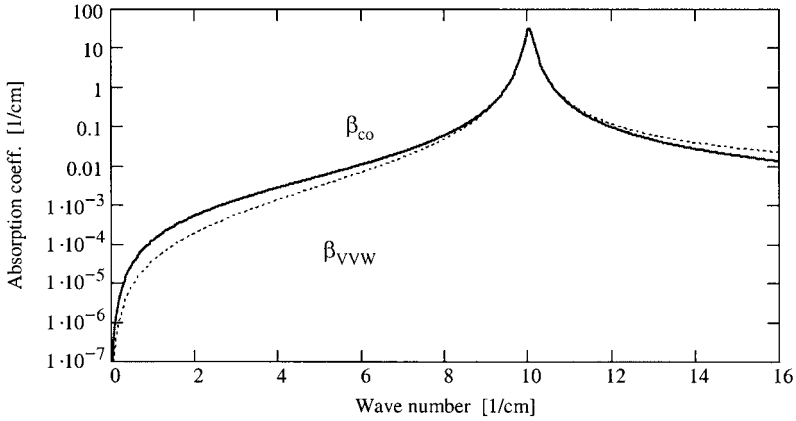
Fig. 4.3 Comparison of the absorption coefficient as given by the classical oscillator model (solid) to the Van Vleck–Weisskopf model in the near-line-center approximation (dotted). The same absorption line parameters are used as given in Fig. 4.2.

function for the near line center classical oscillator model:

$$g(\omega) = \left(\frac{\omega}{\omega_i}\right)^2 j_L(\omega) \quad \text{and} \quad S_i = \frac{\pi \omega_i^2 \Delta \epsilon_i}{2nc}.$$ (4.16)

Then, the absorption coefficient can be expressed in the familiar form, as defined in Chapter 3:

$$\beta_{abs}(\omega) = \sum_i S_i g(\omega) \quad \text{near line center}.$$

This equation agrees with the form stipulated in Section 3.2.1 (Eq. 3.33). The line profile function, $g(\omega)$, as defined above, is called the Van Vleck–Weisskopf line shape function. (At infrared and higher frequencies it simplifies to the Lorentz line shape.) Figure 4.3 compares the absorption coefficient as computed according to Eq. 4.12 with that as given by Eq. 4.14. The agreement at line center is very good, and the two functions disagree away from line center as expected.

The Van Vleck–Weisskopf and Lorentz line shapes are only valid near line center and cannot satisfy the normalization condition given by Eq. 3.31b. These line profile functions are not valid in the wing ($|\omega_i - \omega| \gg \gamma_i$) of an absorption line. A more complete line profile description is presented in Chapter 5. The description of the line wing is important in optical propagation, because systems are designed to operate away from strong absorption features and in the region of absorption line wings.

The real part of the permittivity, $\epsilon_r'(\omega)$, is related to the complex index of refraction by the expression

$$\epsilon_r'(\omega) = n^2(\omega) - k_a^2(\omega).$$ (4.17)

In the region of transparency (i.e., $n \gg k_a$ and $\omega_i^2 - \omega^2 \gg \omega\Gamma_i$), a simple expression for the real part of the index of refraction is obtained:

$$n^2(\omega) = 1 + \sum_i \frac{\omega_i^2 \Delta\epsilon_i}{\omega_i^2 - \omega^2}. \tag{4.18a}$$

This formula is known as Sellmeier's equation and is a convenient way of representing the index of refraction of gases (and also liquids and solids, as will be shown later) in spectral regions of transparency. Another common formula is a simplification of the Sellmeier equation when $\omega_i \gg \omega$, and is called the Cauchy model. It is given by

$$n(\omega) = 1 + \frac{1}{2} \sum_i \Delta\epsilon_i + \left(\frac{1}{2} \sum_i \frac{\Delta\epsilon_i}{\omega_i^2} \right) \omega^2. \tag{4.18b}$$

This model is appropriate when electronic oscillators dominate and infrared oscillators can be ignored. This is the case for atoms and nonpolar molecules, which have no vibrational spectra (e.g., Ar, N_2, O_2).

Although the classical oscillator model is simplistic, it has one very useful property: it satisfies the Hilbert transform or the Kramers–Krönig relation (see Appendix 3). From an experimental point of view, this is a very important fact. Reflectance measurements are easy to make, but only the reflectance magnitude is obtained. However, to determine the real and imaginary parts of the permittivity, phase information must also be obtained, and this is not as easy. The Kramers–Krönig relation provides the phase information given only the magnitude so that the complex permittivity can be determined in a meaningful way. Knowing the permittivity, the complex index of refraction can be found directly. Recall that

$$\bar{n}^2 = (n - jk_a)^2 = \epsilon_r = \epsilon_r' - j\epsilon_r'',$$

for $n > 0$ and real, and $k_a > 0$ and real; then

$$n^2 - k_a^2 - j2nk_a = \epsilon_r' - j\epsilon_r''. \tag{4.19}$$

Now, solving for n and k_a in terms of ϵ_r' and ϵ_r'', we obtain

$$n = \left(\frac{1}{2} \left(|\epsilon_r| + \epsilon_r' \right) \right)^{\frac{1}{2}} \tag{4.20}$$

and

$$k_a = \left(\frac{1}{2} \left(|\epsilon_r| - \epsilon_r' \right) \right)^{\frac{1}{2}} = \frac{\epsilon_r''}{2 \left(\frac{1}{2} \left(|\epsilon_r| + \epsilon_r' \right) \right)^{\frac{1}{2}}}. \tag{4.21}$$

The second solution for k_a is numerically more stable, since the imaginary part of the permittivity is often much smaller than the real part. The real and imaginary parts of the
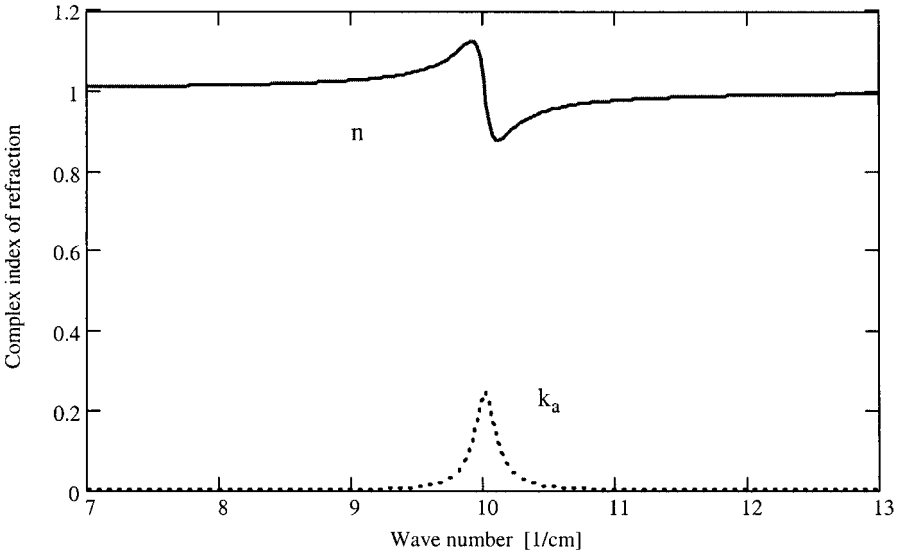
Fig. 4.4 The real and imaginary parts of the complex index of refraction. The same absorption line parameters are used as given in Fig. 4.2.

complex index of refraction are plotted in Fig. 4.4 for the same conditions used to generate Fig. 4.2. The same basic functional forms are observed as those for the complex permittivity. To apply this model to high densities, the effect of neighboring molecules must be considered and the Lorentz-Lorenz formula is needed.

4.2.2 Lorentz–Lorenz Formula

As the density of a gas increases, the molecules become closer together and the electric fields of local molecules must be considered. The polarization $\mathbf{P}$, in this case, is

$$\mathbf{P} = \rho_i \boldsymbol{\mu}_{dp} = \rho_i \alpha_e \mathbf{E}_{loc} \tag{4.22}$$

where ρ_i is the concentration of dipoles in number per unit volume, α_e is the mean polarizability, and $\mathbf{E}_{loc}$ is the local electric field. $\mathbf{E}_{loc}$ includes not only the externally applied field but also the internal field caused by neighboring dipoles. For a cubic geometry, the local polarization field is

$$\frac{\mathbf{P}}{3\epsilon_0}. \tag{4.23}$$

The net local field is now expressed as

$$\mathbf{E}_{loc} = \mathbf{E}_{ext} + \frac{\mathbf{P}}{3\epsilon_0}, \tag{4.24}$$

where $\mathbf{E}_{ext}$ is the external electric field imposed on the media. Therefore, substituting Eq. 4.24 into Eq. 4.22,

$$\mathbf{P} = (\rho_i \alpha_e) \left(\mathbf{E}_{ext} + \frac{\mathbf{P}}{3\epsilon_0} \right). \tag{4.25}$$

This leads to the susceptibility and permittivity,

$$\frac{|\mathbf{P}|}{|\epsilon_0 \mathbf{E}_{ext}|} = \chi = \frac{\rho_i \alpha_e}{\epsilon_0 - \frac{1}{3}\rho_i \alpha_e} = \epsilon_r - 1. \tag{4.26}$$

Solving for the mean polarizability, we have

$$\frac{\rho_i \alpha_e}{3\epsilon_0} = \frac{(\epsilon_r - 1)}{(\epsilon_r + 2)}, \tag{4.27}$$

the Clausius–Mossotti relation. This formula is commonly used at microwave frequencies, where $\epsilon_r(\omega \approx 0) \approx \epsilon_s$. Letting $n^2 = \epsilon_r$, and considering infrared and visible frequencies,

$$\left| \frac{n^2 - 1}{n^2 + 2} \right| = \frac{\rho_i \alpha_e}{3\epsilon_0}, \tag{4.28}$$

and the Lorentz–Lorenz relation is obtained. It accounts for the effect of internal-field-induced dipoles on the refractive index.

Collision-induced dipoles may also be of concern, and this adds more terms to the Lorentz–Lorenz expression, as given by

$$\frac{n^2 - 1}{n^2 + 2} = A_R \rho_i + B_R \rho_i^2 + C_R \rho_i^3 + \cdots, \tag{4.29}$$

where the coefficients A_R, B_R, and C_R are the first, second, and third refractive virial coefficients, respectively. B_R represents the contributions to the mean polarizability from interacting pairs of molecules or atoms. C_R represents contributions from three particle interactions. These coefficients become significantly weaker as the number of interacting particles increases; usually A_R and B_R are sufficient for most applications. This formula is very useful for modeling the refractive index of high-pressure gases. Parameters for the Lorentz–Lorenz formula are listed in Appendix 4 for specific gases.

4.2.3 Solids and the Classical Oscillator Model

Let us return to the discussion in Chapter 3 concerning the spectroscopy of lattice vibrations. Now, externally excite the lattice with an electromagnetic field and also recognize that the lattice motions are damped in a real crystal. This approach is often used to represent electronic transitions as well, but below the bandgap energy in the Sellmeier approximation.

The damping term accounts for coupling of the excited vibrational mode to other vibrational modes through anharmonicities in the potential energy and other effects thus far ignored. Now the system differential equations (see Eqs. 3.127 and 3.128) become

$$\frac{md^2\mathbf{u}_n}{dt^2} + m\Gamma\frac{d\mathbf{u}_n}{dt} + \beta_s\left[2\mathbf{u}_n - (\mathbf{v}_n + \mathbf{v}_{n-1})\right] = q\mathbf{E} \tag{4.30}$$

and

$$\frac{Md^2\mathbf{v}_n}{dt^2} + M\Gamma\frac{d\mathbf{v}_n}{dt} + \beta_s\left[2\mathbf{v}_n - (\mathbf{u}_n + \mathbf{u}_{n+1})\right] = -q\mathbf{E}, \tag{4.31}$$

where

$$m\Gamma\frac{d\mathbf{u}_n}{dt} \quad \text{and} \quad M\Gamma\frac{d\mathbf{v}_n}{dt} \tag{4.32}$$

are the damping terms. Let us again (see Chapter 3, Section 3.4.1.1) assume time-harmonic solutions for the diatomic lattice positions of the form

$$\mathbf{u}_n = \mathbf{u}\,e^{-j(2nk'a - \omega t)}, \quad \mathbf{E} = \mathbf{E_0}\,e^{j\omega t} \tag{4.33a}$$

and

$$\mathbf{v}_n = \mathbf{v}\,e^{-j[(2n+1)k'a - \omega t]}. \tag{4.33b}$$

Upon substitution of the above functional form into Eqs. 4.30 and 4.31, one finds the algebraic equations

$$-m\omega^2\mathbf{u} + jm\Gamma\omega\mathbf{u} + \beta_s\left[2\mathbf{u} - \left(e^{jk'a} + e^{-jk'a}\right)\mathbf{v}\right] = q\mathbf{E_0}\,e^{j2nk'a} \tag{4.34a}$$

and

$$-M\omega^2\mathbf{v} + jM\Gamma\omega\mathbf{v} + \beta_s\left[2\mathbf{v} - \left(e^{jk'a} + e^{-jk'a}\right)\mathbf{u}\right] = -q\mathbf{E_0}e^{j(2n+1)k'a}. \tag{4.34b}$$

For $k' \approx 0$ (long-wavelength condition), the solutions for $\mathbf{u}$ and $\mathbf{v}$ become

$$\mathbf{u} = \frac{(q/m)\mathbf{E_0}}{\omega_0^2 - \omega^2 + j\omega\Gamma} \quad \text{and} \quad \mathbf{v} = \frac{-(q/M)\mathbf{E_0}}{\omega_0^2 - \omega^2 + j\omega\Gamma}, \tag{4.35}$$

where

$$\omega_0^2 = \frac{2\beta_s}{\mu'}$$

for optic mode frequencies and μ' is the reduced mass as defined in Chapter 3. The dipole moment in this case must account for the motion of the opposing charges and hence

$$\mu_{dp} = q\,(\mathbf{u} - \mathbf{v})\,. \tag{4.36}$$

The total polarization is again

$$\mathbf{P} = \rho_a \langle \mathbf{\mu}_{dp} \rangle, \tag{4.37}$$

where ρ_a is the number density of dipoles. However, this accounts only for vibrational contributions, not electronic. Thus combining Eqs. 4.35–4.37 and Eq. 3.134, the relative permittivity becomes

$$\epsilon_r(\omega) = \epsilon_\infty + \frac{\omega_0^2(\epsilon_s - \epsilon_\infty)}{\omega_0^2 - \omega^2 + j\omega\Gamma}, \tag{4.38}$$

where $\epsilon_s = \epsilon_r(\omega = 0)$ is the static dielectric constant and ϵ_∞ is the high-frequency permittivity constant accounting for the low-frequency extrapolation of electronic transition contributions. Of course, most materials have more than one vibrational frequency, so that in general $\epsilon_r(\omega)$ becomes

$$\epsilon_r(\omega) = \epsilon_\infty + \sum_i \frac{\omega_i^2 \Delta\epsilon_i}{\omega_i^2 - \omega^2 + j\omega\Gamma_i}, \tag{4.39}$$

where

$$\epsilon_s = \epsilon_\infty + \sum_i \Delta\epsilon_i. \tag{4.40}$$

When $\epsilon_\infty > 1$, it accounts for high-frequency (usually vacuum and extreme ultraviolet) electronic contributions. A more complete model includes the frequency dependence of electronic transitions in an approximate manner by writing

$$\epsilon_\infty(\omega) = 1 + \sum_k \frac{\omega_k^2 \Delta\epsilon_k}{\omega_k^2 - \omega^2 + j\omega\Gamma_k}, \tag{4.41}$$

where the sum on k now includes electronic resonances. A simplification of this formula is often used to represent the index of refraction as a function of frequency in the transparent (window) regime of solids. For $\omega_i^2 - \omega^2 \gg \Gamma_i\omega$, we have

$$\epsilon_r(\omega) = n^2(\omega) = 1 + \sum_k^{Elec} \frac{\omega_k^2 \Delta\epsilon_k}{\omega_k^2 - \omega^2} + \sum_i^{Vibra} \frac{\omega_i^2 \Delta\epsilon_i}{\omega_i^2 - \omega^2}. \tag{4.42}$$

This is the Sellmeier equation, and is identical in form to the formula for gases. However, $\Delta\epsilon$ and Γ have somewhat different interpretations for solids. A table of coefficients for a variety of solid materials is available in Appendix 4 (Table A4.4). This is a very useful model for accurately characterizing the optical properties of solids at a constant temperature, and is commonly used to represent the real part of the complex index of refraction for solids in a semiempirical manner.

An example of this solid-state classical oscillator model is given for a typical solid in Fig. 4.5 for $\epsilon_\infty = 2$, a single oscillator with a strength of $\Delta\epsilon = 2$, a line center frequency of 250 cm^{-1}, and a width factor of $\Gamma = 10$ cm^{-1}. The real and imaginary

ν_{TO} ν_{LO}
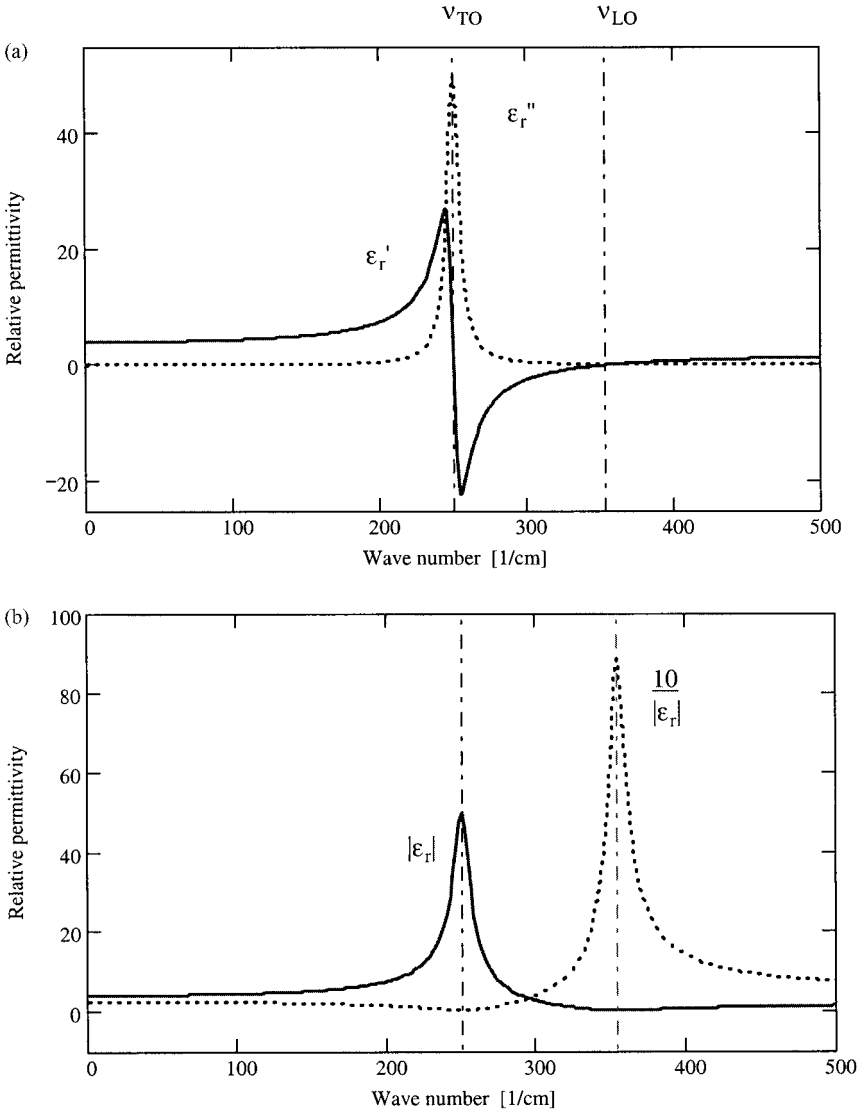
Fig. 4.5 The complex permittivity as a function of frequency. (a) The real (solid) and imaginary (dotted) parts with the following oscillator parameters: $\epsilon_\infty = 2$, $\Delta\epsilon = 2$, $\nu_0 = 250$ cm^{-1}, and $\Gamma/(2\pi c) = 10$ cm^{-1}. (b) The magnitude of the complex permittivity and the corresponding reciprocal scaled up by a factor of 10.

parts of the relative permittivity are illustrated as a function of frequency in part (a). Notice that the real part can be negative above the resonant frequency. The point where the real part becomes positive again is a special frequency and is designated ν_{LO}. The significance of this will be explored shortly. Also plotted in part (b) of this figure is the magnitude of the relative permittivity and the corresponding reciprocal. These functions peak at the oscillator frequencies, $\nu_0 (= \nu_{TO})$ and ν_{LO}, and provide a

(a)

(b)
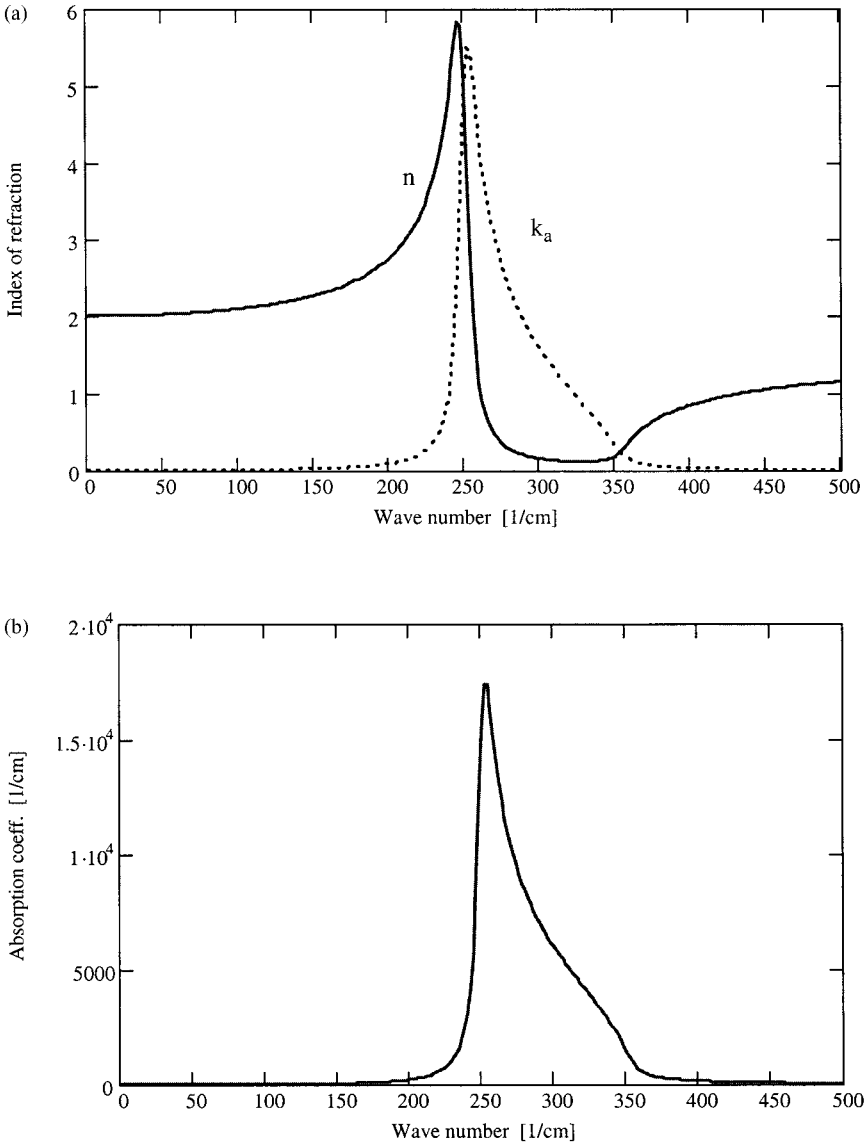
Fig. 4.6 The complex index of refraction as a function of frequency. (a) The real (solid) and imaginary (dotted) part using the same oscillator parameters as in Fig. 4.5. (b) The corresponding absorption coefficient.

useful means of determining these important frequencies. The real and imaginary parts of the complex index of refraction can be computed based on Eqs. 4.19–4.21, and are plotted in Fig. 4.6 along with the absorption coefficient. These functions have a differ-ent appearance from the relative permittivity function of Fig. 4.5. The absorption coefficient is broadened in the blue wing to account for the additional contributions of the longitudinal mode. This is a new aspect of the model, as opposed to the gas-phase

results, and will be characteristic also of noncrystalline solids and liquids that have similar oscillator parameters.

In Chapter 3, we discussed the existence of transverse and longitudinal optical modes. ω_i in the above model is the transverse optical mode frequency, or $\omega_{TO,i}$. To see the how ω_{LO} plays a part in this model, consider the case when $\epsilon_r' = 0$ and then solve Maxwell's equations for longitudinal excitation. (As Fig. 4.5 indicates, $\epsilon_r'(\omega_{LO}) = 0$.) In Chapters 1 and 2 we considered transverse (TEM) fields that satisfy $\nabla \cdot \mathbf{D} = 0$ (i.e., $\mathbf{D} = \epsilon E_x \hat{\mathbf{x}}$ and $\mathbf{k}' = k_z' \hat{\mathbf{z}}$). Thus

$$\nabla \cdot \mathbf{D} = \mathbf{k}' \cdot \mathbf{D} = \epsilon \mathbf{k}' \cdot \mathbf{E} = \epsilon k_z' E_x \hat{\mathbf{z}} \cdot \hat{\mathbf{x}} = 0. \tag{4.43}$$

However, another solution can occur when $\epsilon = 0$. Then $\mathbf{k}' = k_x' \hat{\mathbf{x}}$ becomes possible, or a longitudinal mode exists. This can happen near resonances in a crystal (or solids in general), as illustrated in Fig. 4.5. Thus, we must specify both ω_{TO} and ω_{LO} when discussing the vibrational structure of a solid. The longitudinal oscillation frequency can be found by plotting the reciprocal of the magnitude of $\epsilon_r(\omega)$ as illustrated in part (b) of Fig. 4.5.

For $\epsilon_r(\omega_{LO}) = 0$ and a single resonance with no damping, Eq. 4.39 becomes

$$\frac{\omega_{LO}^2}{\omega_{TO}^2} = \frac{\epsilon_s}{\epsilon_\infty}. \tag{4.44}$$

This is the Lyddane–Sachs–Teller (LST) relationship. Based on this relationship, ν_{LO}, as indicated in Fig. 4.5, equals 353.6 cm^{-1}. It is also straightforward to show that

$$\frac{\omega_{LO}^2 - \omega^2}{\omega_{TO}^2 - \omega^2} = \frac{\epsilon_r(\omega)}{\epsilon_\infty}. \tag{4.45}$$

This shows that ω_{TO} and ω_{LO} are related by the strength of the resonance. For example, when a mode is infrared inactive ($\Delta\epsilon = 0$), then ω_{TO} equals ω_{LO}. For multiple resonances, the LST relation becomes

$$\prod_i \frac{\omega_{LO,i}^2 - \omega^2}{\omega_{TO,i}^2 - \omega^2} = \frac{\epsilon_r(\omega)}{\epsilon_\infty}. \tag{4.46}$$

For $\Gamma = 0$, the ω_{TO}s are the poles and the ω_{LO}s are the zeroes of the permittivity function. All real materials have damping, and the above analysis suggests the following four-parameter model for the complex permittivity:

$$\epsilon_r(\omega) = \epsilon_\infty \prod_i \frac{\omega_{LO,i}^2 - \omega^2 + j\omega\Gamma_{LO,i}}{\omega_{TO,i}^2 - \omega^2 + j\omega\Gamma_{TO,i}}. \tag{4.47}$$

In this case, the ω_{TO}s are the maxima and the ω_{LO}s are the minima of the permittivity function. When $\Gamma_{TO} = \Gamma_{LO}$, this four-parameter oscillator model is identical to the three-parameter classical oscillator model. This is usually the case for cubic

materials and around room temperature for all solids. However, at high temperature in biaxial and uniaxial crystalline materials, $\Gamma_{TO} \neq \Gamma_{LO}$, the four-parameter model is needed for the best fit to experimental data.

4.2.3.1 Anharmonic Potential Considerations

In the discussion so far, we have used a harmonic potential. This can be seen by examining the restoring force in Eq. 4.2 and the potential expansion in Eq. 3.102. By taking the gradient of the leading harmonic term in the potential, we obtain a force in the form used in Eq. 4.2. To make our model more complete, let us consider anharmonic terms in the potential. Letting $\Gamma = 0$, Eq. 4.2 is rewritten as an undriven oscillator,

$$\ddot{x} + \omega_0^2 x + \lambda a x^2 + \lambda^2 b x^3 + \cdots = 0.$$

λ is a dummy parameter that helps to keep track of the order in the potential expansion. At the end of the analysis it will be set to one. Assume that x can be expanded in the following perturbation expansion:

$$x = x_0 + \lambda x_1 + \lambda^2 x_2 + \cdots$$

Substituting the expansion of x into the above differential equation and separating according to order, we obtain to the following set of equations:

Zeroth order, λ^0

$$\ddot{x}_0 + \omega_0^2 x_0 = 0 \Rightarrow x_0 = A e^{j\omega_0 t}.$$

First order, λ^1

$$\ddot{x}_1 + \omega_0^2 x_1 = -a x_0^2 = -a A^2 e^{j2\omega_0 t}.$$

Based on the source term in the above first-order differential equation, let the harmonic solution for $x_1(t)$ take the form of an oscillator at the second harmonic of $x_0(t)$, thus

$$x_1(t) = B e^{j2\omega_0 t}.$$

Substituting this solution into the first-order differential equation leads to the following condition on the coefficients:

$$3\omega_0^2 B = a A^2.$$

Second order, λ^2

$$\ddot{x}_2 + \omega_0^2 x_2 + 2a x_1 x_0 + b x_0^3 = 0.$$

The forms chosen for x_0 and x_1 suggest that

$$x_2(t) = C e^{j3\omega_0 t}.$$

Substituting the various orders of x into the second-order differential equations, we obtain following relationship:

$$8\omega_0^2 C = 2aAB + bA^3.$$

Now drive the lattice with an external electric field oscillating at the second-harmonic frequency of the fundamental lattice vibrations (i.e., at $\omega \approx 2\omega_0$). The first-order differential equation now becomes

$$\ddot{x}_1 + \omega_0^2 x_1 = -aA^2 e^{j\omega t} + \frac{q}{m} E e^{j\omega t}.$$

The solution of this equation leads to an oscillator amplitude resonating at the second harmonic lattice vibration frequency, as given by

$$B = \frac{qE/m}{(2\omega_0)^2 - \omega^2}.$$

This result leads to a second-harmonic response of the dielectric permittivity. As we shall see in Chapter 8, this is called two-phonon absorption or, in general, multiphonon absorption. All harmonics can be obtained by a similar procedure. The second-order differential equation driven by an external field at the third harmonic of the fundamental lattice vibration frequency is given by

$$\ddot{x}_2 + \omega^2 x_2 + 2ax_1 x_0 + bx_0^3 = \frac{q}{m} E e^{j\omega t}.$$

Solving this equation leads to a third-harmonic response of the lattice to the electromagnetic field, as given by

$$C = \frac{qE/m}{(3\omega_0)^2 - \omega^2}.$$

Multiphonon absorption is important in the optical properties of solids, because it determines the infrared edge of transparency and contributes to the infrared refractive index, as we shall see in more detail in Chapter 8. The lesson to this exercise is the importance of considering the anharmonic ramifications of a real potential.

4.2.4 Time-Domain Susceptibility for Lattice Vibrations

The classical oscillator model is particularly convenient in this case, because the time-domain susceptibility can be obtained in closed form by evaluating the inverse Fourier transform of the frequency-domain formula given by Eq. 4.9. Based on Eq. 2.37, the inverse Fourier transform is defined to be

$$\chi_{tv}(t) = \mathscr{F}^{-1}[\epsilon_{rv}(\omega) - 1] = \frac{1}{2\pi} \int\limits_{-\infty}^{\infty} [\epsilon_{rv}(\omega) - 1] e^{j\omega t} d\omega. \qquad (4.48)$$
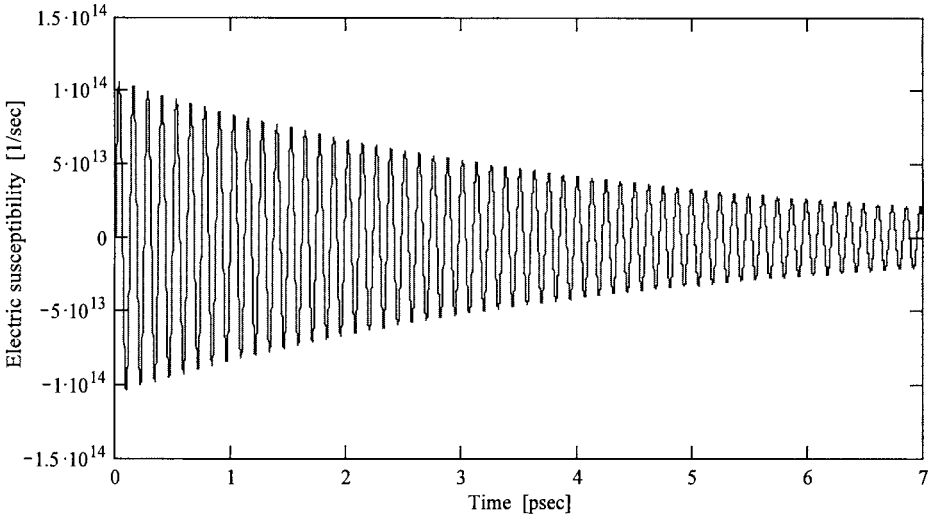
Fig. 4.7 Time-domain susceptibility for intrinsic GaAs at room temperature due only to the fundamental lattice vibration ($i = 0$, $\omega_0 = 5.054 \times 10^{13}$ rad sec^{-1}, $\Delta\epsilon_0 = 2.09$, and $\Gamma_0 = 4.679 \times 10^{11}$ rad sec^{-1}).

Evaluating the above equation, the time-domain electrical susceptibility due to lattice vibrations, $\chi_{tv}(t)$ (recall $\epsilon_{rv} = \epsilon_{tv} + \epsilon_\infty$) becomes

$$\chi_{tv}(t) = \sum_i \omega_i^2 \Delta\epsilon_i e^{-\Gamma_i t/2} \frac{\sin\left(\sqrt{\omega_i^2 - \left(\Gamma_i^2/4\right)}\,t\right)}{\sqrt{\omega_i^2 - \left(\Gamma_i^2/4\right)}} h(t) \qquad (4.49)$$

where $h(t)$ is the Heaviside step function, and $\omega = 2\pi c\nu$. Such information is needed in high-speed microwave device design using FD-TD techniques. A plot of this function for the single vibrational mode of intrinsic GaAs is given in Fig. 4.7. The figure demonstrates that the intrinsic impulse response of GaAs at microwave frequencies is that of a damped oscillator in the picosecond regime.

4.2.5 Free Carriers and Debye Relaxation

Both free-carrier effects and Debye relaxation are important in understanding the electrical (microwave to millimeter wave) properties of seawater and water. Free carrier effects dominate the infrared properties of metals and are important for many semiconductors as well. Debye relaxation is observed in some solids also, but at radio frequencies or lower. In metals, the charge carrier is the negatively charged electron. Holes and electrons exist in semiconductors and positive and negative hydrated ions exist in seawater.

A general and introductory understanding of the optical properties of metals, the microwave-infrared properties of semiconductors, and microwave properties of aqueous solutions (e.g., seawater) can be obtained from the development of

Drude's theory (1900). It is a limiting form of the classical oscillator model when the external field frequency, ω, is above all oscillator frequencies, ω_i.

To see how the properties of mobility influence the impedance of materials, consider the standard definition of conductivity for an electrically neutral medium

$$\sigma(\omega) = \sum_{i=1}^{N} \left[|e_{+i}| \rho_{+i} \mu_{+i}(\omega) + |e_{-i}| \rho_{-i} \mu_{-i}(\omega) \right], \tag{4.50a}$$

with the condition that

$$\sum_{i=1}^{N} (e_{+i} \rho_{+i} + e_{-i} \rho_{-i}) = 0, \tag{4.50b}$$

where $\rho_{\pm,i}$ is the number density per unit volume of the ith $\pm$ charge carrier, $e_{\pm,i}$ is the charge of the ith $\pm$ charge carrier, $\mu_{\pm,i}$ is the carrier mobility of the ith $\pm$ charge carrier, and N is the number of carrier types (solutes for an aqueous solution). Since most electrolytes composing the ocean, and holes and electrons in semiconductors, are 1:1 (i.e., the number of positive and negative particles generated is the same for an intrinsic material), it is assumed that

$$|e_{+i}| \rho_{+i} = |e_{-i}| \rho_{-i} = \rho_{c,i} \equiv \text{charge density.} \tag{4.51}$$

The conductivity for a single 1:1 charge carrier type simplifies to

$$\sigma = \rho_c (\mu_+ + \mu_-). \tag{4.52}$$

A simple expression for the carrier mobility can be obtained from the following equations:

$$\mu_\pm = \frac{\langle \mathbf{v}_\pm \rangle}{\mathbf{E}} \tag{4.53}$$

and

$$m_\pm \frac{d \langle \mathbf{v}_\pm \rangle}{dt} + m_\pm \Gamma_\pm \langle \mathbf{v}_\pm \rangle = |e| \mathbf{E}, \tag{4.54}$$

where $\langle \mathbf{v}_\pm \rangle$ is the mean velocity (or drift velocity) of the charge carrier, $m_\pm$ is the mass of the charge carrier, $\Gamma_\pm$ is the damping constant, $|e|$ is the charge of the charge carrier, and $\mathbf{E}$ is the applied electric field. Let $\langle \mathbf{v}_\pm \rangle$ and $\mathbf{E}$ be time harmonic as $e^{j\omega t}$. The solution of Eq. 4.54 results in the following relations for the mobility:

$$\mu_\pm(\omega) = \frac{\mu_{0,\pm}}{1 + j \frac{\omega}{\Gamma_\pm}}, \quad \text{where } \mu_{0,\pm} = \frac{|e|}{m_\pm \Gamma_\pm}. \tag{4.55}$$

Substituting this result into Eq. 4.52, the frequency-dependent conductivity becomes

$$\sigma(\omega) = \rho_c \left(\frac{\mu_{0,+}}{1 + j\frac{\omega}{\Gamma_+}} + \frac{\mu_{0,-}}{1 + j\frac{\omega}{\Gamma_-}} \right). \tag{4.56}$$

In a metal the only charge carrier is the electron. In electrolytic solutions, it can be assumed that the damping forces will be similar for both the positive and negative charge carriers. Therefore,

$$\Gamma_+ \approx \Gamma_- = \Gamma. \tag{4.57}$$

Γ is the reciprocal of the conductivity relaxation time. This interpretation is easily seen, based on Eq. 4.54. When the applied **E**-field is turned off, the charge carriers relax back to equilibrium and the mean velocity becomes

$$\langle \mathbf{v} \rangle = \langle \mathbf{v}(t = 0) \rangle e^{-t\Gamma}. \tag{4.58}$$

The conductivity relaxation time, $1/\Gamma_\pm$, is designated $\tau_{c,\pm}$. Thus, it follows that

$$\sigma(\omega) = \frac{\sigma_{0,+}}{1 + j\omega\tau_{c,+}} + \frac{\sigma_{0,-}}{1 + j\omega\tau_{c,-}} \tag{4.59a}$$

where the DC conductivity for each charge carrier is

$$\sigma_{0,+} = \rho_{c,+} \frac{|e_+|\tau_{c,+}}{m_+} \quad \text{and} \quad \sigma_{0,-} = \rho_{c,-} \frac{|e_-|\tau_{c,-}}{m_-}. \tag{4.59b}$$

This simple model breaks down when the mean free path of the charge carrier is greater than the skin depth, $\delta(\omega) (= 2/\beta_{abs}(\omega))$. This leads to the so-called anomalous skin effect, which is typically important at low temperatures for good metals.

Debye relaxation represents the orientational polarizability of a polar molecule to an applied electric field commonly observed in liquids (GHz frequencies) and solids (mHz frequencies). Essentially, it is hindered rotational motion converted to a vibrational mode. As was the case for electrical conduction, no restoring force exists, thus the differential equation describing this phenomenon is the same as Eq. 4.54. The complex relative permittivity for orientational polarizability is of a similar form to the free-carrier process and becomes (see Debye, Ref 4.2)

$$\epsilon_r(\omega) = 1 + \chi_D(\omega) = 1 + \frac{\Delta\epsilon_D}{1 + j\omega\tau_D}, \tag{4.60a}$$

where τ_D is the Debye relaxation time. Figure 4.8 illustrates the frequency-domain complex permittivity and the complex index of refraction for Debye relaxation with parameter values typical of a liquid. The Fourier transform of the frequency-domain

(a)

(b)
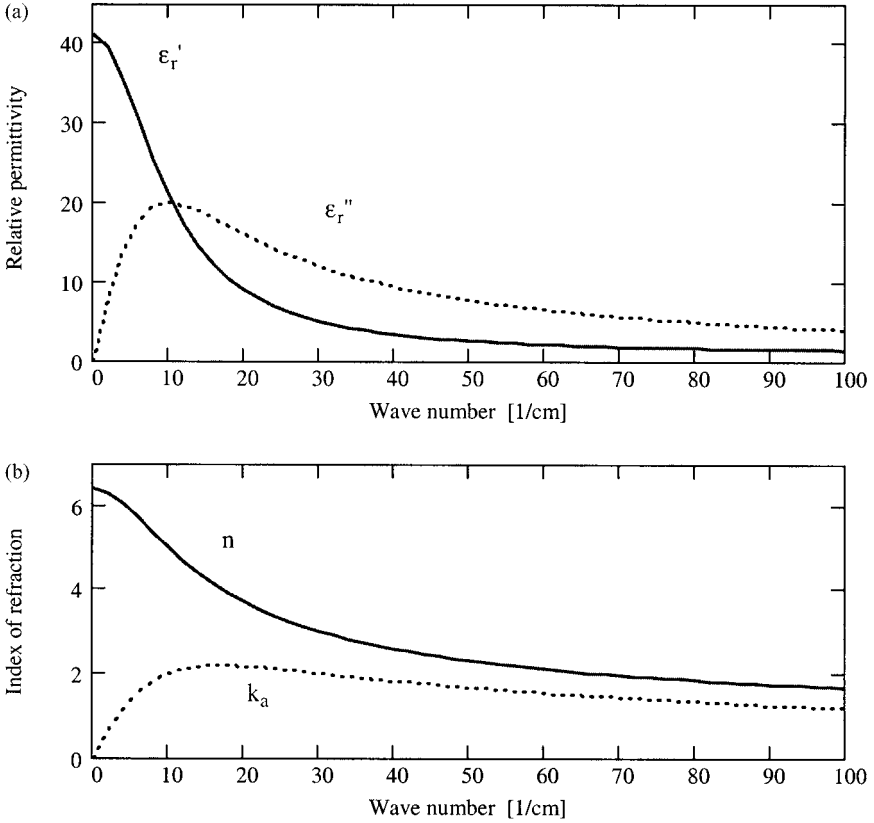
Fig. 4.8 (a) The complex permittivity due to Debye relaxation as a function wave number for $\Delta \epsilon_D = 40$ and $\Gamma_D/(2\pi c) = 0.1$ cm^{-1}. (b) The corresponding complex index of refraction as a function of wave number.

susceptibility leads to the time-domain susceptibility for Debye relaxation,

$$\chi_D(t) = \frac{\Delta \epsilon_D}{\tau_D} \exp\left(-t/\tau_D\right) h(t). \tag{4.60b}$$

Recall from Chapter 2 that the relative permittivity (bound-charge phenomena) can be redefined to include conductivity (free-carrier phenomena) in the following manner:

$$\epsilon_c(\omega) = \epsilon_r(\omega) + \chi_c(\omega) = \epsilon_r(\omega) - j\frac{\sigma(\omega)}{\omega \epsilon_0}. \tag{4.61}$$

Substituting Eq. 4.59b for a single carrier type ($N = 1$) into the above equation, we obtain

$$\epsilon_c(\omega) = \epsilon_r(\omega) - j\frac{\sigma_{0,+}/\epsilon_0}{\omega + j\omega^2 \tau_{c,+}} - j\frac{\sigma_{0,-}/\epsilon_0}{\omega + j\omega^2 \tau_{c,-}}. \tag{4.62}$$

To be consistent with the previously developed classical oscillator model for gases and solids, we use the conductivity damping parameter. Then the above term for free-carrier effects becomes

$$\epsilon_c(\omega) = \epsilon_r(\omega) - \frac{\omega_{p,+}^2}{\omega^2 - j\omega\Gamma_{c,+}} - \frac{\omega_{p,-}^2}{\omega^2 - j\omega\Gamma_{c,-}}, \tag{4.63a}$$

where $\omega_{p,\pm}$ is the plasma frequency, as defined by

$$\omega_{p,\pm}^2 = \frac{\rho_c|e|}{m_\pm\epsilon_0} = \frac{\rho e^2}{m_\pm\epsilon_0}. \tag{4.63b}$$

The plasma frequency marks the upper spectral limit of the free-carrier effect (see Fig. 4.8). Based on Eq. 4.59, for a single carrier, the DC conductivity is:

$$\sigma_{dc} = \frac{\omega_{p,+}^2\epsilon_0}{\Gamma_{c,+}} + \frac{\omega_{p,-}^2\epsilon_0}{\Gamma_{c,-}}. \tag{4.63c}$$

The corresponding time-domain susceptibility for free-carrier phenomena becomes

$$\mathscr{F}\{\chi_c(\omega)\} = \chi_c(t) = \frac{\omega_p^2}{\Gamma_c}(1 - \exp(-\Gamma_c t))h(t). \tag{4.63d}$$

Converting to wave numbers and writing out $\epsilon_r(\omega)$ for both Debye relaxation and resonant phenomena plus conductivity, the net complex permittivity is

$$\epsilon_c(\nu) = 1 + \frac{\Delta\epsilon_D}{1 + j\nu\frac{2\pi c}{\Gamma_D}} + \sum_i \frac{\nu_i^2\Delta\epsilon_i}{\nu_i^2 - \nu^2 + j\nu\frac{\Gamma_i}{2\pi c}} - \frac{\nu_{p,+}^2}{\nu^2 - j\nu\frac{\Gamma_{c,+}}{2\pi c}} - \frac{\nu_{p,-}^2}{\nu^2 - j\nu\frac{\Gamma_{c,-}}{2\pi c}}, \tag{4.64}$$

where $\Gamma_D = 1/\tau_D$. The real and imaginary parts of the general permittivity are

$$\epsilon_c'(\nu) = 1 + \frac{\Delta\epsilon_D}{1 + \nu^2\left(\frac{2\pi c}{\Gamma_D}\right)^2} + \sum_i \frac{\nu_i^2\Delta\epsilon_i(\nu_i^2 - \nu^2)}{(\nu_i^2 - \nu^2)^2 + \nu^2\left(\frac{\Gamma_i}{2\pi c}\right)^2} - \frac{\nu_p^2}{\nu^2 + \left(\frac{\Gamma_c}{2\pi c}\right)^2} \tag{4.65a}$$

and

$$\epsilon_c''(\nu) = \frac{\nu\Delta\epsilon_D\frac{2\pi c}{\Gamma_D}}{1 + \nu^2\left(\frac{2\pi c}{\Gamma_D}\right)^2} + \sum_i \frac{\nu_i^2\Delta\epsilon_i\nu\frac{\Gamma_i}{2\pi c}}{(\nu_i^2 - \nu^2)^2 + \nu^2\left(\frac{\Gamma_i}{2\pi c}\right)^2} + \frac{\nu_p^2\frac{\Gamma_c}{2\pi c}}{\nu^3 + \nu\left(\frac{\Gamma_c}{2\pi c}\right)^2}, \tag{4.65b}$$

respectively. This is the correct procedure to add together these three different phenomena. Debye relaxation, bound-charge resonances, and free-carrier processes are not

(a)

(b)
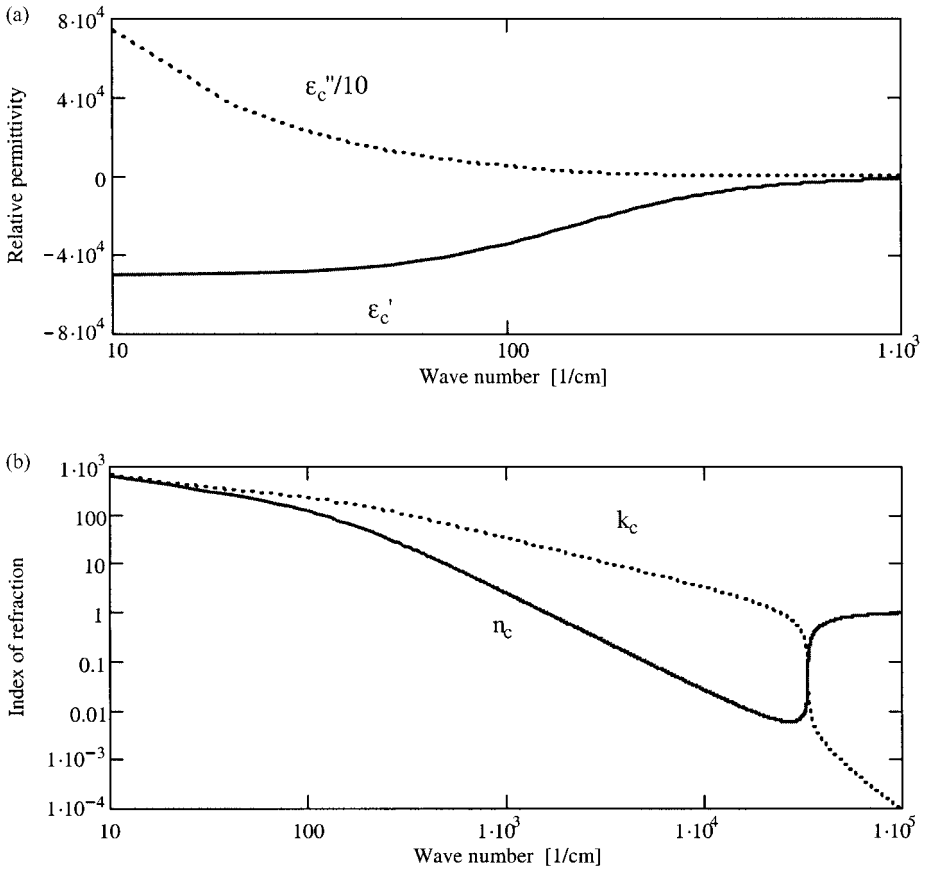
Fig. 4.9 (a) The complex permittivity due to free-carrier conduction in a typical metal as a function wave number for $v_p = 3.3 \times 10^4$ cm^{-1} and $\Gamma_c/(2\pi c) = 147$ cm^{-1}. (b) The corresponding complex index of refraction as a function of wave number.

always additive in terms of the complex index of refraction. Since at optical frequencies the complex index of refraction is commonly used, combining these phenomena must be approached with care.

Figure 4.9 illustrates the complex permittivity and the complex index of refraction for a typical conductive medium with a DC conductivity of 1.2×10^7 ℧/m. The intersection of the real and imaginary parts of the complex index of refraction occurs near the plasma frequency. Generally, this model works well at infrared frequencies but becomes less accurate at visible frequencies because interband transitions become important.

Figure 4.10 compares the absorption coefficient of a metal, as depicted in Fig. 4.9 with that of a moderate conductor with a DC conductivity of 1.2×10^3 ℧/m. The conductivity relaxation time is the same for both cases ($\Gamma_c/(2\pi c) = 147$ cm^{-1}). Notice the relative change in the shape of the functions in the two different cases. The large plasma frequency of the metal dominates the optical properties. However, as the plasma frequency becomes lower, charge carrier relaxation effects can be observed.
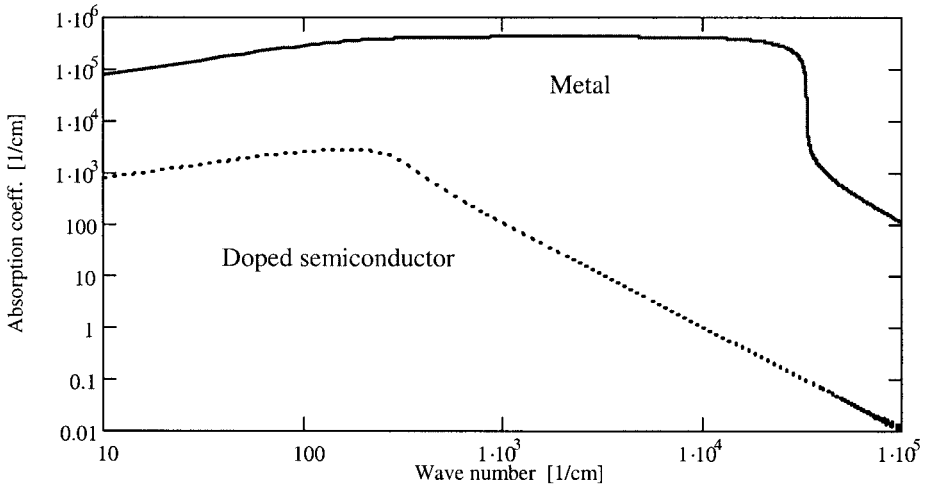
Fig. 4.10 The absorption coefficient as a function of wave number for a good ($\sigma_0 = 1.2 \times 10^7$ ʊ/m) and moderate conductor ($\nu_p = 330$ cm^{-1} and $\sigma_0 = 1.2 \times 10^3$ ʊ/m). The same conductivity relaxation time is used in both cases ($\Gamma_c/(2\pi c) = 147$ cm^{-1}).

The contribution from conductivity has the same form as the bound charge permittivity when ν is much greater than the maximum ν_i. Thus, when the photon energy is above the bandgap energy of a medium, valance band electrons are excited into the conduction band and free-carrier properties dominate, as expected.

Equation 4.65 provides a comprehensive model as a function of frequency (wave number), combining the effects of conductivity, orientational polarizability, rotation, vibration, and electronic transitions, that matches experimental data fairly well for many cases. This classical model satisfies the symmetry relations given by Eq. 2.39b and the Hilbert transform given by Eq. 2.49a, which in part explains the model's utility. However, this model has a number of serious limitations, which require corrections beyond the classical approach used here.

A list is given below:

1. No temperature dependence beyond density is specified.
2. The model only predicts loss; *no gain is allowed*, preventing thermal equilibrium and lasers.
3. Line strength and line width cannot be computed with this model.

The classical oscillator model does not explain all observations. Despite the limitations of such classical macroscopic models, they are successfully used within the regions of validity, in the solid-state optical properties code OPTIMATR, which is described in Chapter 8. Important corrections to this classical model will be introduced at that point.

4.2.6 Dyadic Permittivity

Thus far, we have considered only isotropic media. However, many important window materials are anisotropic (i.e., Al_2O_3, SiO_2, MgF_2 etc., see Appendix 4). In particular

they can be uniaxial. To understand how this affects the optical properties, it is necessary to develop the concept of the dyadic complex permittivity. In general, for a Cartesian coordinate system, XYZ, the relationship between $\mathbf{D}$ and $\mathbf{E}$ is

$$\mathbf{D} = \begin{pmatrix} D_X \\ D_Y \\ D_Z \end{pmatrix} = \begin{pmatrix} \epsilon_{XX} & \epsilon_{XY} & \epsilon_{XZ} \\ \epsilon_{YX} & \epsilon_{YY} & \epsilon_{YZ} \\ \epsilon_{ZX} & \epsilon_{ZY} & \epsilon_{ZZ} \end{pmatrix} \begin{pmatrix} E_X \\ E_Y \\ E_Z \end{pmatrix} = (\boldsymbol{\varepsilon}) : \mathbf{E}. \tag{4.66}$$

The corresponding susceptibility and complex index of refraction are also dyadic. The dyadic permittivity represents the effect the electric field has on the medium in other directions in addition to the direction of polarization. Transforming into a coordinate system that matches the geometry of the unit cell, xyz, the permittivity matrix (dyad) can be made diagonal, thus

$$\begin{pmatrix} D_x \\ D_y \\ D_z \end{pmatrix} = \begin{pmatrix} \epsilon_{xx} & 0 & 0 \\ 0 & \epsilon_{yy} & 0 \\ 0 & 0 & \epsilon_{zz} \end{pmatrix} \begin{pmatrix} E_x \\ E_y \\ E_z \end{pmatrix}. \tag{4.67}$$

The values of the diagonal elements are called the principal values, and they determine the type of optical material, that is, whether it is cubic, uniaxial, or biaxial:

$$\text{cubic} \quad \Rightarrow \quad \epsilon_{xx} = \epsilon_{yy} = \epsilon_{zz},$$
$$\text{uniaxial} \quad \Rightarrow \quad \epsilon_{xx} = \epsilon_{yy} \neq \epsilon_{zz},$$

and

$$\text{biaxial} \quad \Rightarrow \quad \epsilon_{xx} \neq \epsilon_{yy} \neq \epsilon_{zz} \quad \text{and} \quad \epsilon_{xx} \neq \epsilon_{zz}.$$

For cubic materials, the optical properties are called isotropic, and the dyad can be replaced by a single scalar value, as was done in Chapter 2. For uniaxial materials, the z-axis is aligned with the crystallographic c-axis. Light that propagates in this direction only experiences ϵ_{xx} and ϵ_{yy} and the medium appears isotropic. For this reason, the light ray that enters along the c-axis is called the ordinary ray. Light that enters along the a- or b-axis will experience different permittivities, depending on the polarization, and is called the extraordinary ray. Crystals that satisfy the condition $\epsilon_{zz} > \epsilon_{xx}$ are called positive uniaxial, and for $\epsilon_{zz} < \epsilon_{xx}$ are called negative uniaxial. Because of the variation with direction of the biaxial type materials, they are seldom used in optical systems.

4.3 Reflection and Refraction at a Plane Boundary

For TEM waves, two polarizations completely describe the $\mathbf{E}$-field orientation, as discussed in Chapter 2. The geometry was also presented in Fig. 2.9. The Fresnel formulas on reflection and transmission at an interface are commonly derived in textbooks on electromagnetic theory (see Jackson, Ref. 4.4, p. 281, for example). It is assumed the reader is familiar with this derivation, and therefore only the results are

presented here. Two cases are considered. The first is for cubic materials, and the second is for uniaxial materials that have the crystallographic c-axis in the direction of the normal to the interface surface. Unfortunately, very little published literature exists on solutions for the reflection coefficients of uniaxial materials.

When the **E**-field is in the plane of incidence, it is called ***p*-polarization** or **vertical polarization**. When the **E**-field is perpendicular to the plane of incidence it is called ***s*-polarization** or **horizontal polarization**. This notation is used in the following.

4.3.1 Cubic Media

For cubic media:

$$\epsilon_{xx} = \epsilon_{yy} = \epsilon_{zz} = \epsilon_0 \bar{n}^2.$$

The field reflection, r_{12}, and transmission, t_{12}, Fresnel formulas for propagation from medium 1 to medium 2 are given as follows (see Ref. 4.1):

p-Polarization

$$r_{p12} = \frac{\bar{n}_2 \cos\theta_i - \bar{n}_1 \cos\theta_t}{\bar{n}_1 \cos\theta_t + \bar{n}_2 \cos\theta_i} = \frac{\bar{n}^2 \cos\theta_i - \sqrt{\bar{n}^2 - \sin^2\theta_i}}{\bar{n}^2 \cos\theta_i + \sqrt{\bar{n}^2 - \sin^2\theta_i}} = -r_{p21}, \qquad (4.68)$$

where $\bar{n} = \bar{n}_2/\bar{n}_1$ for n_1 real and

$$t_{p12} = \frac{2\bar{n}_1 \cos\theta_i}{\bar{n}_1 \cos\theta_t + \bar{n}_2 \cos\theta_i} = \frac{\bar{n}_1 \cos\theta_i}{\bar{n}_2 \cos\theta_t} t_{p21}. \qquad (4.69)$$

s-Polarization

$$r_{s12} = \frac{\bar{n}_1 \cos\theta_i - \bar{n}_2 \cos\theta_t}{\bar{n}_1 \cos\theta_i + \bar{n}_2 \cos\theta_t} = \frac{\cos\theta_i - \sqrt{\bar{n}^2 - \sin^2\theta_i}}{\cos\theta_i + \sqrt{\bar{n}^2 - \sin^2\theta_i}} = -r_{s21}, \qquad (4.70)$$

where $\bar{n} = \bar{n}_2/\bar{n}_1$ for n_1 real and

$$t_{s12} = \frac{2\bar{n}_1 \cos\theta_i}{\bar{n}_1 \cos\theta_i + \bar{n}_2 \cos\theta_t} = \frac{\bar{n}_1 \cos\theta_i}{\bar{n}_2 \cos\theta_t} t_{s21}. \qquad (4.71)$$

Recall that Snell's law is given by

$$n_1 \sin\theta_i = \bar{n}_2 \sin\theta_t, \qquad (4.72)$$

where the refracted angle, θ_t, is complex and the angle of incidence, θ_i, is real. r_{21} and t_{21} are the field reflection and transmission coefficients for propagation from medium 2 to medium 1, respectively. The relationship between r_{12} and r_{21}, and t_{12} and

t_{21} is called the principle of reversibility. The single-surface Fresnel power coefficients for reflection (R) and transmission (T) are directly obtained according to the following formulas for p- and s-polarization,

$$R_{p,s} = |r_{p,s}|^2 \tag{4.73}$$

and

$$T_{p,s} = \frac{\bar{n}_2 \cos \theta_t}{\bar{n}_1 \cos \theta_i} |t_{p,s}|^2. \tag{4.74}$$

Based on these formulas, and substituting the complex index of refraction of medium 2 when medium 1 is vacuum, we have the following useful results:

$$R_s = \frac{(a - \cos \theta_i)^2 + b^2}{(a + \cos \theta_i)^2 + b^2} \tag{4.75a}$$

and

$$R_p = R_s \left(\frac{(a - \sin \theta_i \tan \theta_i)^2 + b^2}{(a + \sin \theta_i \tan \theta_i)^2 + b^2} \right) \tag{4.75b}$$

where the terms a and b are defined as

$$a^2 = \frac{1}{2} \left\{ [(n^2 - k_a^2 - \sin^2 \theta_i)^2 + 4n^2 k_a^2]^{\frac{1}{2}} + (n^2 - k_a^2 - \sin^2 \theta_i) \right\} \tag{4.76a}$$

and

$$b^2 = \frac{1}{2} \left\{ [(n^2 - k_a^2 - \sin^2 \theta_i)^2 + 4n^2 k_a^2]^{\frac{1}{2}} - (n^2 - k_a^2 - \sin^2 \theta_i) \right\}. \tag{4.76b}$$

The principle of reversibility and Snell's law require that

$$R_{12} = R_{21} \quad \text{and} \quad T_{12} = T_{21}. \tag{4.77}$$

Also, it can be shown by simple algebra that

$$R_{s,p} + T_{s,p} = 1. \tag{4.78}$$

For unpolarized light, the single-surface power reflection coefficient becomes

$$R_{unpol} = \frac{1}{2}(R_s + R_p). \tag{4.79}$$

For partially polarized light, the single-surface power reflection coefficient becomes

$$R_{pp} = (1 - \text{DoP})R_{unpol} + [x R_s + (1 - x)R_p]\text{DoP}$$

where DoP is the degree of polarization as defined in Chapter 2 and x is the fraction of polarized light in the R_s direction. Other basis sets for the type and direction of
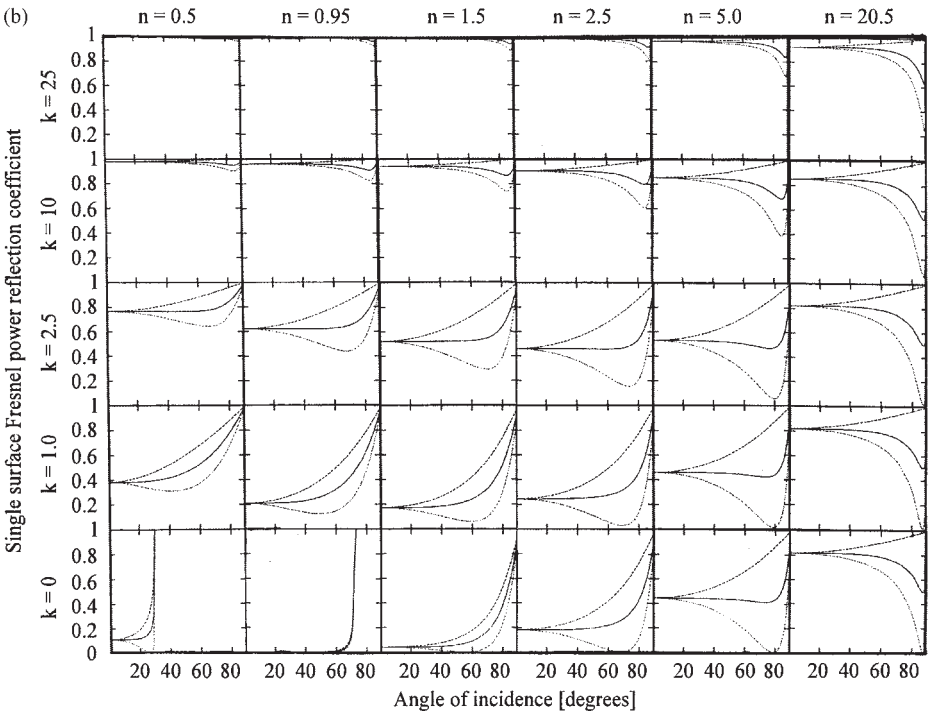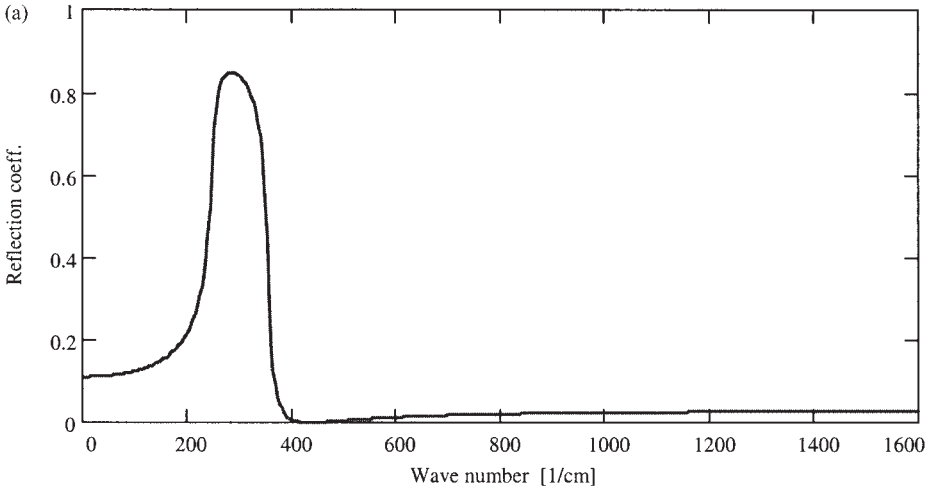
Fig. 4.11 (a) Spectral dependence of the reflection coefficient for an insulator. (b) The single-surface power reflection coefficient for R_s (upper curve), R_p (lower curve), and R_{unpol} (middle curve).

polarization can be used. The spectral dependence of the reflection coefficient is shown in Fig. 4.11a for an insulator modeled by the classical oscillator model using the parameters listed in Fig. 4.5. Note that above the one-phonon region the reflection is very low. In fact there is a spectral point where the reflection coefficient comes very close to zero, called the Christiansen frequency. Example plots of R_s, R_p, and R_{unpol} as a function of the illumination angle are illustrated in Fig. 4.11b for different values of n_2/n_1 and k_{a2} for $k_{a1} = 0$.

4.3.2 Biaxial and Uniaxial Media

For uniaxial media

$$\epsilon_{xx} = \epsilon_{yy} = \epsilon_0 \bar{n}_o^2 \quad \text{and} \quad \epsilon_{zz} = \epsilon_0 \bar{n}_e^2.$$

The general solution for the uniaxial reflection coefficients is very complicated (see Lekner, Ref. 4.6). However, solutions for special cases have been obtained. Let the z-axis be the crystallographic c-axis and the surface normal, then, R_p and R_s become

$$R_p = \left| \frac{n_o n_e \cos \theta_i - \left(n_e^2 - \sin^2 \theta_i \right)^{1/2}}{n_o n_e \cos \theta_i + \left(n_e^2 - \sin^2 \theta_i \right)^{1/2}} \right|^2 \tag{4.80a}$$

and

$$R_s = \left| \frac{\cos \theta_i - (n_o^2 - \sin^2 \theta_i)^{1/2}}{\cos \theta_i + (n_o^2 - \sin^2 \theta_i)^{1/2}} \right|^2. \tag{4.80b}$$

Obviously, if $n_o = n_e$, then the cubic results are obtained.

The near-normal transmittance for a plane-parallel uniaxial dielectric slab of thickness d with the c-axis on the surface (90° material), illuminated by unpolarized light and including the effects of interference, is given by

$$\tau = \frac{1}{2}(\tau_o + \tau_e), \tag{4.81}$$

where

$$\tau_{o,e} = \frac{\exp(-4\pi \nu d k_{o,e})(1 - R_{o,e})}{1 - 2\exp(-4\pi \nu d k_{o,e})R_{o,e}\cos(4\pi \nu d n_{o,e}) + \exp(-8\pi \nu d k_{o,e})R_{o,e}^2} \tag{4.82}$$

and

$$R_{o,e} = \left(\frac{1 - n_{o,e}}{1 + n_{o,e}} \right)^2.$$

This is a useful result, because the e-ray absorption coefficient can be obtained knowing the e-ray index of refraction and the o-ray complex index of refraction.

In general, when dealing with polarized light the transmittance, reflectance, and soon, must be broken down into components that distinguish polarization as well. Thus,

$$\tau_o = \tau_{so} + \tau_{po} \quad \text{and} \quad \tau_e = \tau_{so} + \tau_{po}.$$

For biaxial media:

$$\epsilon_{xx} = \epsilon_0 \bar{n}_x^2, \quad \epsilon_{yy} = \epsilon_0 \bar{n}_y^2, \quad \text{and} \quad \epsilon_{zz} = \epsilon_0 \bar{n}_z^2.$$

Uniaxial and biaxial materials are birefringent, that is, light linearly polarized in one direction experiences a different refractive index than light polarized in a different direction. The description of the effective index is best handled by the well-known index ellipsoid, as given by

$$\frac{x^2}{n_x^2} + \frac{y^2}{n_y^2} + \frac{z^2}{n_z^2} = 1. \tag{4.83}$$

This formula is commonly applied to phase matching that involves second-harmonic generation in nonlinear optical materials. When $n_x = n_y$ the uniaxial case is obtained.

4.4 Single Scattering

The definition of, and introduction to, single scattering was presented in Chapter 2. Now specific formulas will be derived for the complex index of refraction for scatter that depend on frequency, temperature, and media composition. Two general models are presented, Rayleigh scatter for gases and small-scale structures and Mie scatter for particles.

4.4.1 Rayleigh Scattering

A general solution for particles of arbitrary shape can be obtained if the size, a, of the particle is much smaller than the wavelength, λ, of the incident light. A good example is the scattering of visible light ($\lambda \approx 5000$ Å) by atoms and molecules ($a \approx 1$–5 Å). The mechanism of this scattering is through the mean electronic polarizability, α_e. The electrons or dipoles in the molecule try to orient to the $\mathbf{E}$-field of the incident light. No absorption takes place because this is not a resonant condition; however, the molecule does respond to incident fields with frequencies below the resonance frequency. A dipole is induced in the illuminated molecule, which then quickly radiates in all directions. We will consider elastic reactions (collisions) (recall that an inelastic collision produces Raman scattering); thus the molecule radiates, because of this stimulation, at the frequency of the incident field. This is Rayleigh scattering.

For an isotropic polarizability ($\langle \boldsymbol{\mu}_{dp} \rangle = \alpha_e \mathbf{E}_i$, where $\mathbf{E}_i$ is the incident field), the scattered electric field radiating from a single particle with an electric dipole moment in the far field limit is (see Jackson, Ref. 4.4, p. 395)

$$\mathbf{E}_s = \frac{k'^2 \langle \boldsymbol{\mu}_{dp} \rangle \sin \theta_d}{4\pi \epsilon_0 r} \, \mathrm{e}^{-jk'r} = \frac{k'^2 \alpha_e \mathbf{E}_i \sin \theta_d}{4\pi \epsilon_0 r} \, \mathrm{e}^{-jk'r}. \tag{4.84}$$
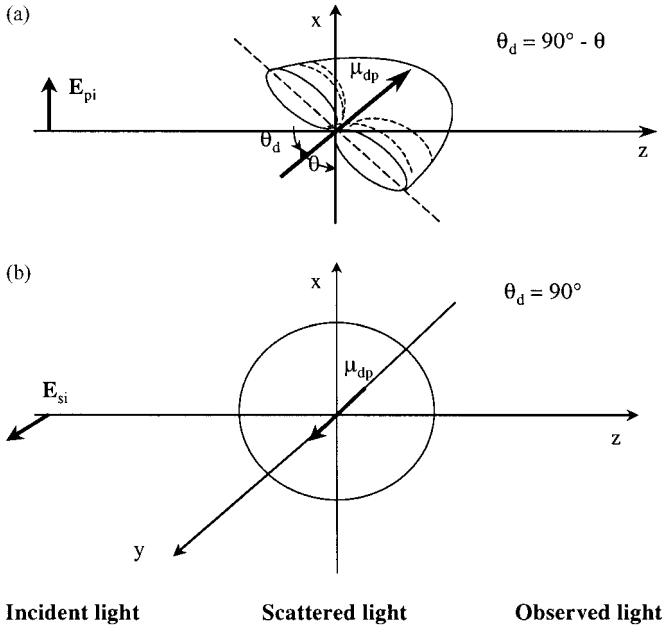
Fig. 4.12 Geometry of scattering pattern in the xz-plane by a dipole for (a) p-polarization (vertical polarization) with the dipole in the xz-plane and (b) s-polarization (horizontal polarization) with the dipole in the y-direction.

The angle θ_d is the angle between the dipole moment direction and the direction of propagation, as illustrated in Fig. 4.12. The scattered irradiance is obtained, using Eqs. 2.19b, 2.20, and 4.84, as

$$L_s(\omega) = \frac{\omega^4 |\alpha_e|^2 \sin^2 \theta_d}{32\pi^2 c^3 \epsilon_0 r^2} |\mathbf{E}_{i0}|^2. \tag{4.85}$$

This result shows the characteristic ω^4 frequency dependence of Rayleigh scattering. Because of the strong decrease in the scatter strength as the frequency decreases, molecular Rayleigh scatter is important at visible and ultraviolet frequencies and not at infrared and lower frequencies.

An observer in the xz-plane at an angle θ from the x-axis sees a different scattering pattern depending on the incident light polarization. For s-polarization in the xz scattering plane (see Fig. 4.12), $\theta_d = 90°$, and no θ-dependence is observed. For p-polarization, $\theta_d = 90° - \theta$ in the xz scattering plane. In terms of the scattering matrix and incident light fields, the observed scattered field for s- and p-polarizations, becomes

$$\begin{pmatrix} E_{ps} \\ E_{ss} \end{pmatrix} = \left\{ \frac{jk'^3 \alpha_e}{4\pi \epsilon_0} \begin{pmatrix} \cos\theta & 0 \\ 0 & 1 \end{pmatrix} \right\} \frac{e^{-jk'r}e^{jk'z}}{jk'r} \begin{pmatrix} E_{0pi} \\ E_{0si} \end{pmatrix}. \tag{4.86}$$
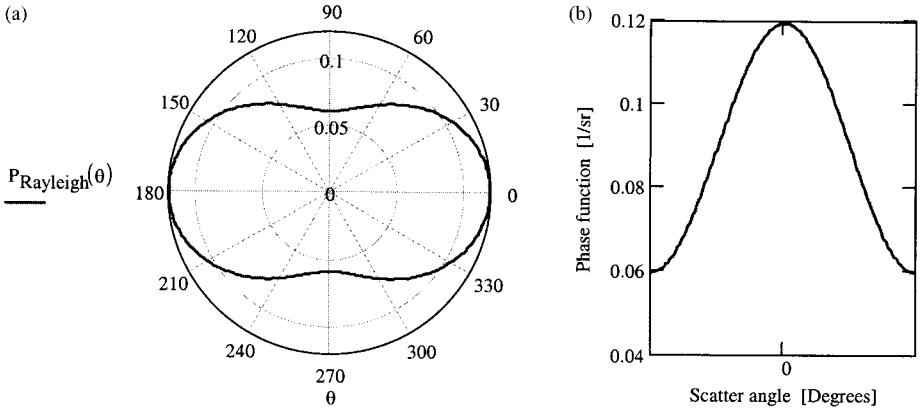
Fig. 4.13 The phase function for Rayleigh scatter as a function of scatter angles: (a) polar plot, (b) rectangular plot.

Notice that the scattering matrix is diagonal, which is the case for spherical particles. In the far field of a small particle, the nonspherical shape does not contribute to the radiation pattern or the amplitude function. Thus, for the wavelength much greater than the particle size, the scattered field is insensitive to the particle shape. Also, note that Rayleigh scatter emphasizes s-polarized light.

Based on the definitions of Chapter 2 (Eqs. 2.62, 2.66, 2.123, and 2.145), the angular scattering cross-section $C_{sca}(\theta)$ for unpolarized incident light is one-half the sum of the s- and p-polarized scatter intensities, thus

$$C_{sca}(\theta) = \frac{I_s(\theta)}{M_i} = \frac{(1 + \cos^2\theta)k'^4|\alpha_e|^2}{32\pi^2\epsilon_0^2}. \tag{4.87}$$

Based on Eqs. 2.89, 2.91, and 4.87, the phase function for Rayleigh scatter is:

$$P_s(\theta) = \frac{3}{16\pi}(\cos^2\theta + 1). \tag{4.88}$$

A plot of this phase function is displayed in Fig. 4.13.

Based on the development of Chapter 2 for nonabsorbing particles (molecules), the net extinction cross-section equals the integration of the angular scatter cross-section over all solid angles. Thus,

$$C_{ext} = 2\pi \int_0^\pi \sin\theta \, d\theta C_{sca}(\theta).$$

Evaluating the integral for Eq. 4.87, the following result is obtained:

$$C_{ext} = \frac{k'^4|\alpha_e|^2}{6\pi\epsilon_0^2}. \tag{4.89}$$

Recalling the relation between the extinction cross-section and the scattering coefficient (Eq. 2.139), we obtain a useful result for the Rayleigh scatter coefficient in gases as a function of frequency and gas density:

$$\beta_{sca}(\omega, \rho_p) = \rho_p C_{ext}(\omega, \rho_p) = \frac{1}{6\pi}\left(\frac{\omega}{c}\right)^4 \frac{\rho_p |\alpha_e(\omega)|^2}{\epsilon_0^2}. \tag{4.90}$$

Substituting the Lorentz–Lorenz formula (Eq. 4.28) for the polarizability of a gas, the scattering coefficient becomes

$$\beta_{sca}(\omega) = \frac{3\omega^4}{2\pi c^4 \rho_p}\left(\frac{n^2(\omega) - 1}{n^2(\omega) + 2}\right)^2, \tag{4.91}$$

representing the net attenuation caused by scatter. This is the scattering coefficient commonly used for molecular Rayleigh scattering with unpolarized light, and n is the index of refraction of the medium. For normal temperature and pressure (NTP, $T = 298\,\text{K}$ and $P = 1$ atm) gases, the index of refraction is approximately unity. Based on this result and using the ideal gas law, we obtain

$$\beta_{sca}(\omega, P, T) = \frac{\omega^4 \left[n^2(\omega, P, T) - 1\right]^2 k_B T}{6\pi c^4 P}, \tag{4.92}$$

where P is the total pressure, T is temperature, and k_B is Boltzmann's constant. Multiplying this result by the path length yields the total integrated scatter, α_{sca}. The Rayleigh scatter coefficient for gases is further developed in Chapter 7 and applied to optical propagation in the atmosphere of the earth. This formula can be used to explain the blue sky and the changing colors of the sun at sunset and sunrise, as illustrated in Fig. 4.14. When polarization is important, the Mueller matrix formalism can be used as introduced in Chapter 2. The development of the Mueller matrix for Rayleigh scattering is left to the reader (see Problem 4.13).

4.4.2 Mie Scattering

Mie scattering describes a general solution to Maxwell's equations for particles of arbitrary size and refractive index but limited to spherical shape. This is a very useful model commonly applied to particle scattering. Nonspherical and noncylindrical particle geometries are very difficult to solve and the Mie model is generally the only option for interpretation of measurements. Also, because particles are often randomly oriented, nonspherical particles average out to have spherical-particle scattering properties.

We begin with Eqs. 2.9–2.12 for a nonmagnetic lossy medium with no net charge. The vector wave equation is obtained directly for both the electric and magnetic fields. These fields are solenoidal and related to one another by the curl (Faraday's and Ampere's laws). It can be shown that the vector wave equation of fields with these
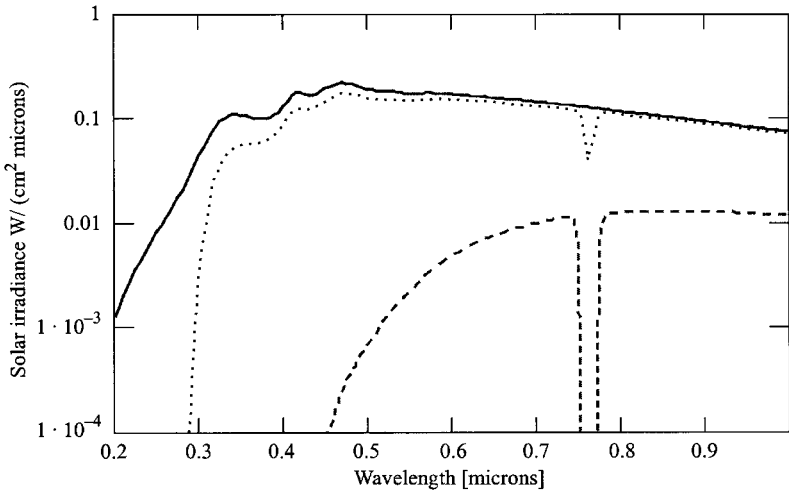
Fig. 4.14 Spectral power output of the sun above the atmosphere (solid line). Solar output at the surface of the earth for $0°$ zenith angle (dotted line). Solar output of the sun at the surface of the earth for the sun at the horizon (dashed line).

characteristics can be reduced to a scalar wave equation (see Bohren and Huffman, Ref 4.9, Chapter 4, and Stratton, Ref. 4.1, Chapter 6). This procedure is outlined below.

Begin with the following vector wave equation:

$$\nabla^2 \mathbf{M}(\mathbf{r}) - \gamma^2 \mathbf{M}(\mathbf{r}) = 0, \tag{4.93}$$

where $\mathbf{M}$ is solenoidal. It can represented by a the curl of a constant radial vector and a scalar function, as given by

$$\mathbf{M}(\mathbf{r}) = \nabla \times \mathbf{a}\psi(\mathbf{r}). \tag{4.94}$$

In this way, the vector field is guaranteed to be solenoidal. Substituting this definition of $\mathbf{M}$ into the vector wave equation, we obtain a scalar wave equation in ψ,

$$\nabla^2 \psi(\mathbf{r}) - \gamma^2 \psi(\mathbf{r}) = 0. \tag{4.95}$$

Thus, solving for ψ also leads to solutions to $\mathbf{M}$. Another vector, orthogonal to $\mathbf{M}$, is also generated by ψ (or $\mathbf{M}$) and is defined by

$$\mathbf{N}(\mathbf{r}) = \frac{\nabla \times \mathbf{M}(\mathbf{r})}{j\gamma}. \tag{4.96}$$

This vector field is also solenoidal. The electromagnetic fields $\mathbf{E}$ and $\mathbf{H}$ can be represented as a linear combination of the vector fields $\mathbf{M}$ and $\mathbf{N}$.
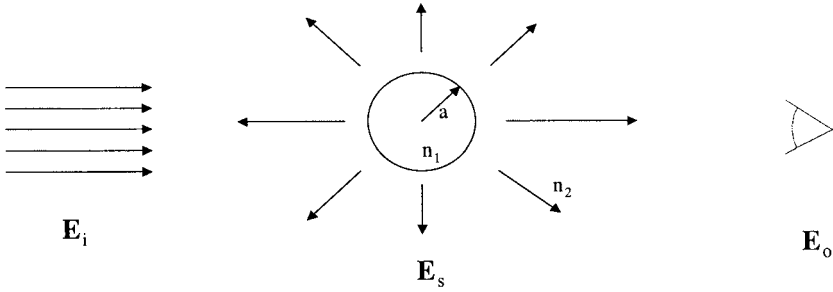
Fig. 4.15 Geometry of a plane-wave illuminated spherical particle of radius a and complex index of refraction $\bar{n}_1$.

The solution of Eq. 4.95 in spherical coordinates with the appropriate boundary conditions is a long and tedious story that has been told in many other texts (see Bohren and Huffman, Ref. 4.9, Chapter 4, and Stratton, Ref. 4.1, Chapter 6). The geometry is illustrated in Fig. 4.15. Parts of the problem have been solved in Chapter 3 (Section 3.3.1.1). We shall emphasize the results in the form of the scattering matrix (Eq. 2.165), given by the following equations:

$$S_1(\theta_s) = \sum_m \frac{2m+1}{m(m+1)} [a_m(x)\tau_m(\theta_s) + b_m(x)\pi_m(\theta_s)] \tag{4.97a}$$

and

$$S_2(\theta_s) = \sum_m \frac{2m+1}{m(m+1)} [a_m(x)\pi_m(\theta_s) + b_m(x)\tau_m(\theta_s)], \tag{4.97b}$$

where $x = k'a = 2\pi a n_1/\lambda$, $a = |\mathbf{a}|$ is the particle radius and is a constant,

$$a_m(x) = \frac{\bar{n}\psi_m(\bar{n}x)\psi_m'(x) - \psi_m(x)\psi_m'(\bar{n}x)}{\bar{n}\psi_m(\bar{n}x)\xi_m'(x) - \xi_m(x)\psi_m'(\bar{n}x)} \tag{4.98a}$$

and

$$b_m(x) = \frac{\psi_m(\bar{n}x)\psi_m'(x) - \bar{n}\psi_m(x)\psi_m'(\bar{n}x)}{\psi_m(\bar{n}x)\xi_m'(x) - \bar{n}\xi_m(x)\psi_m'(\bar{n}x)}, \tag{4.98b}$$

where $\bar{n} = \bar{n}_1/n_2$ is the complex index of refraction ratio and the Riccati–Bessel functions are

$$\psi_m(x) = xj_m(x) \quad \text{and} \quad \xi_m(x) = xh_m^{(1)}(x)$$

and $j_m(x)$ is the spherical Bessel function and $h_m^{(1)}(x)$ is the spherical Hankel function of the first kind, and

$$\pi_m(\theta_s) = \frac{P_m^l(\cos\theta_s)}{\sin\theta_s} \tag{4.99a}$$

and

$$\tau_m(\theta_s) = \frac{dP_m^l(\cos\theta_s)}{d\theta_s}, \tag{4.99b}$$

where P_m^l (where $l = 1$) are the associated Legendre functions. These special functions are listed in Appendix 2.

Based on Eq. 2.123, the scatter cross-section for spherical particles illuminated by unpolarized light is

$$C_{sca} = \frac{1}{2k'^2} \int\limits_{4\pi} d\Omega_s \left(|S_1(\theta_s)|^2 + |S_2(\theta_s)|^2 \right). \tag{4.100}$$

Figure 4.16a illustrates the angular dependence of the scatter cross-section for spherical particles with $n = 1.33$ and $k = 1 \times 10^{-5}$ in the Rayleigh limit, when the radius and wavelength are comparable and for large particles. The angular dependence can be considerably different, from Rayleigh scatter to when the particle size and wavelength become comparable. The figure shows the angular pattern for the size parameter $x = 0.1$, 1, and 10. As x increases above one, the angular structure greatly increases. Of particular note, as x increases, the forward-scattered and back-scattered amplitudes become very different. This is a major indicator of the relative particle size, knowing the wavelength. In Fig. 4.16b, the M_{11} component of the Mueller matrix is plotted. This plot shows the relative amplitudes of the scatter in the different regimes of x.

The corresponding extinction cross-section for spherical particles illuminated by unpolarized light is

$$C_{ext}(k') = \frac{2\pi}{k'^2} \text{Re}[S_1(\theta_s = 0) + S_2(\theta_s = 0)]. \tag{4.101}$$

In the real world, particles within any group are not identical and can cover a wide range of sizes and shapes. Assuming that randomly oriented particles scatter as spheres, then shape is not an important parameter. However, any extinction coefficient requires the consideration of spherical particles of different radii. Thus, the particle density must be a function of the particle radius. The extinction coefficient for Mie scatter now becomes

$$\beta_{ext} = \int\limits_0^\infty dr\, C_{ext}(r)\rho_p(r). \tag{4.102}$$
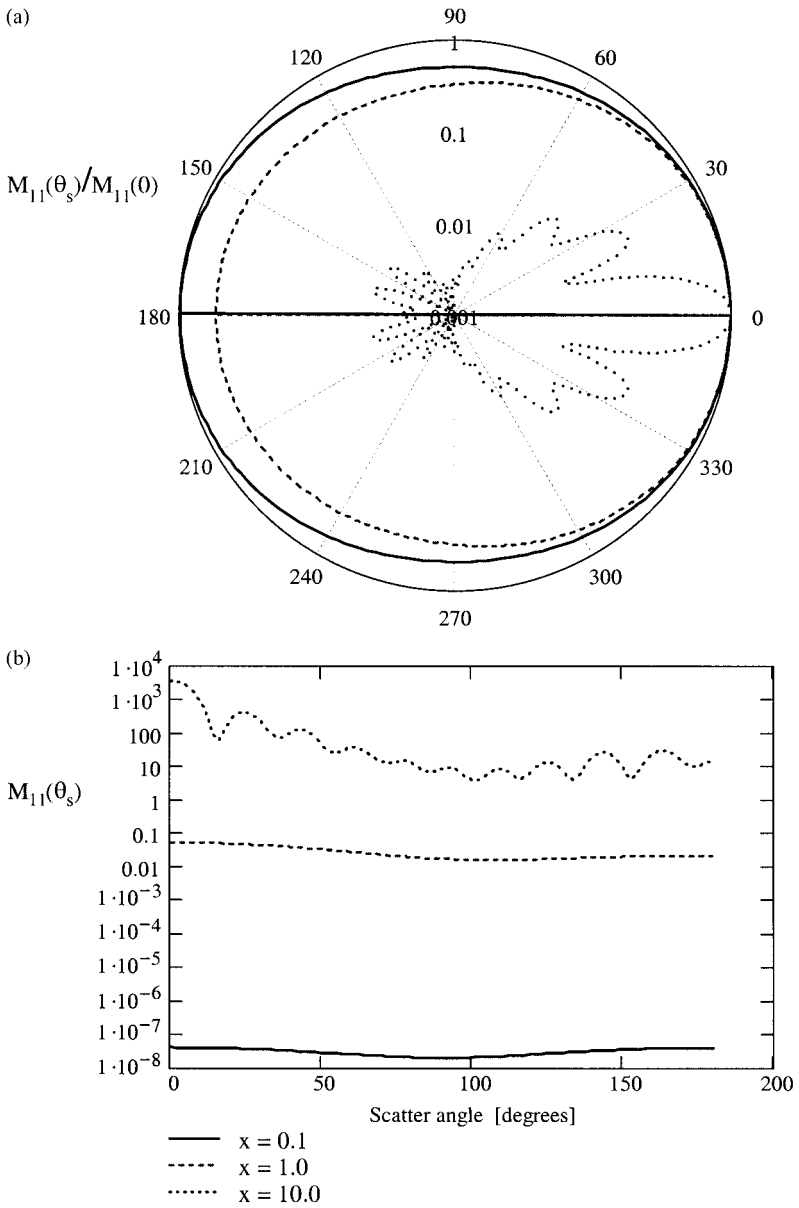
Fig. 4.16 Angular dependence of the scatter cross-section for Mie scatter for $x = 0.1$, 1 and 10, $n = 1.33$, and $k = 1 \times 10^{-5}$, and an unpolarized incident light field. (a) Log-polar plot with all plots normalized to one at $\theta = 0$. (b) Log-linear plot of the M_{11} Mueller matrix element.

Specific particle distribution functions depend on the medium and are most appropriately discussed in Part II of this text.

In the Rayleigh limit ($x \ll 1$), the Mie equations are greatly simplified and are very useful at infrared and microwave wavelengths. The resulting scattering field amplitudes for scattering and absorbing particles of uniform radius, a, $n_1 = 1$, are (see Bohren and Huffman, Ref. 4.9)

$$S_1 = jx^3 \frac{\bar{n}^2 - 1}{\bar{n}^2 + 1} \quad \text{and} \quad S_2(\theta_s) = S_1 \cos(\theta_s). \tag{4.103}$$

The corresponding extinction coefficient illuminated by unpolarized light is

$$\beta_{ext}(\lambda) = -\frac{8\pi^2 a^3 \rho_p}{\lambda} \text{Im} \left[\frac{\bar{n}^2 - 1}{\bar{n}^2 + 2} \left(1 + \frac{2\pi a}{\lambda} \left(\frac{\bar{n}^2 - 1}{\bar{n}^2 + 2} \right) \frac{\bar{n}^4 + 27\bar{n}^2 + 38}{2\bar{n}^2 + 3} \right) \right]$$
$$+ \frac{128\pi^5 a^6 \rho_p}{3\lambda^4} \text{Re} \left[\left(\frac{\bar{n}^2 - 1}{\bar{n}^2 + 2} \right)^2 \right]. \tag{4.104}$$

Absorption is a higher order process over scatter and dominates the extinction coefficient. However, in many cases, the imaginary part of the complex index of refraction is very small, and absorption and scatter loss are comparable in magnitude. The corresponding scattering coefficient is

$$\beta_{sca} = \frac{128\pi^5 a^6 \rho_p}{3\lambda^4} \left| \frac{\bar{n}^2 - 1}{\bar{n}^2 + 2} \right|^2. \tag{4.105}$$

This compares closely to the result given for molecular scatter in Eq. 4.91, but now the dependance of the particle radius explicitly appears. When the particle is nonabsorbing (e.g., $\bar{n}$ is real), then the extinction and scattering coefficients are equal. A plot of the extinction coefficient and the scatter coefficient as a function of the imaginary part of the particle complex index of refraction is shown in Fig. 4.17. For k_a of the particle below 1×10^{-4}, β_{ext} and β_{sca} are equal. Thus only the real part of the refractive index is relevant and the particle is effectively nonabsorbing in this case. This is also the case for the plot of Fig. 4.16b. The large change in the scatter amplitude from $x = 0.1$ to 1 is indicative of the a^6 dependence in Eq. 4.104. For x much greater than one, the M_{11} component or the scatter coefficient basically depends on the area of the particle. This is a much weaker dependence on the particle size than in the Rayleigh limit and explains the reduced rate of increase from $x = 1$ to 10 in Fig. 4.16b.

4.4.3 Rayleigh–Gans Scattering

Rayleigh–Gans scattering considers particles of arbitrary size but with small changes in the index of refraction relative to the surrounding medium. This is a common situation in solids and liquids.
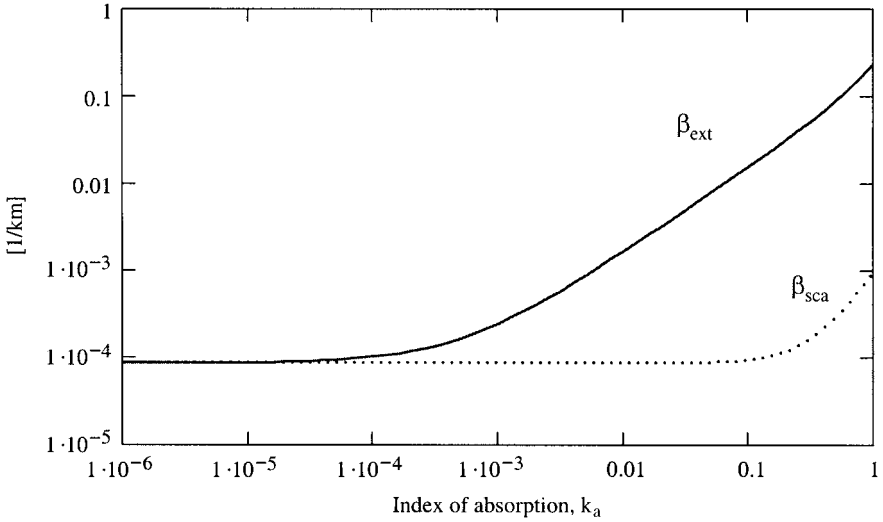
Fig. 4.17 A comparison between the extinction coefficient and the scatter coefficient as a function of k_a for a particle with $a = 0.05\ \mu m$, $\lambda = 1\ \mu m$, $n = 1.33$, and $\rho_p = 10^4\ cm^{-3}$ for Mie scatter in the Rayleigh limit.

The Rayleigh–Gans model is valid when

$$|\bar{n} - 1| \ll 1, \tag{4.106}$$

where $\bar{n} = \bar{n}_1/n_2$, as in Mie theory. In this limit, it can be shown that the scattered field is independent of the scattering particle size. To see this, recall that, in the limit, Eq. 4.106 is true:

$$\bar{n} - 1 \propto \frac{N}{V},$$

where N is the number of dipoles per unit volume, V. Consider a coherent sum of small volume elements, dV, over the total volume of a particle in the single scatter limit (e.g., $2k'a\,|\bar{n} - 1| \ll 1$). The Mie formulas in the Rayleigh limit (Eqs. 4.103) can be applied to the small volume elements. The net result is obtained by integrating the scatter matrix elements over all volume elements. (The details of this procedure are given in Bohren and Huffman, Ref. 4.9, Chapter 6.) The results are given in the following, consistent with the definition of the scatter matrix as given by Eq. 2.165,

$$S_1(\theta, \phi) = \frac{jk'^3}{2\pi}(\bar{n} - 1)Vf(\theta,\phi), \tag{4.107a}$$

$$S_2(\theta, \phi) = \frac{jk'^3}{2\pi}(\bar{n} - 1)Vf(\theta, \phi)\cos(\theta), \tag{4.107b}$$
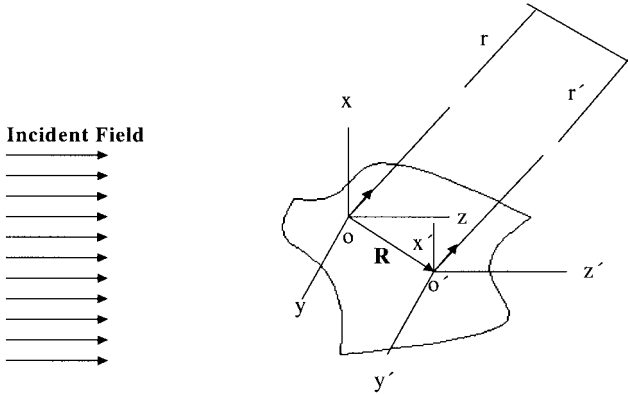
Fig. 4.18 Rayleigh–Gans scattering geometry for an arbitrary particle (Bohren and Huffman, Ref. 4.9).

where

$$f(\theta, \phi) = \frac{1}{V} \int_V e^{-jk'\mathbf{R}\cdot(\hat{\mathbf{e}}_z - \hat{\mathbf{e}}_r)} \tag{4.107c}$$

is called the form factor. The geometry is illustrated in Fig 4.18.

Problems

4.1 Obtain a Cauchy model for the index of refraction of dry air at NTP (normal temperature and pressure, 296 K and 1 atm) using the parameters listed in Appendix 4 and the fact that dry air is composed of 79% N_2, 20% O_2, and 1% Ar.

4.2 Starting with the classical oscillator model for solids ($\epsilon_\infty = 1$),

$$\epsilon_r(\omega) = 1 + \sum_i \frac{\omega_i^2 \Delta\epsilon_i}{\omega_i^2 - \omega^2 + j\Gamma_i\omega},$$

obtain the Sellmeier model ($\Gamma_i = 0$) in the common form

$$n^2 - 1 = \sum_i \frac{\lambda^2 \Delta\epsilon_i}{\lambda^2 - \lambda_i^2}.$$

Now compute the index of refraction of CaF_2 at $\lambda = 5\,\mu m$, given $\Delta\epsilon_1 = 0.5675888$, $\lambda_1 = 0.050263605\,\mu m$; $\Delta\epsilon_2 = 0.4710914$, $\lambda_2 = 0.1003909\,\mu m$; $\Delta\epsilon_3 = 3.8484723$, $\lambda_3 = 34.649040\,\mu m$.

4.3 Using the index of refraction computed above for CaF_2 at $\lambda = 5\ \mu m$. Compute both R_p and R_s for an angle of incidence of 54.4°. Comment on the transmission characteristics at that angle.

4.4 Compute the transmittance, reflectance, and emittance of a dielectric slab of thickness $L = 1$ cm, given that the complex index of refraction of the slab is

$\bar{n} = 1.727 - j3.8 \times 10^{-5}$ for $\nu = 1000 \text{ cm}^{-1}$, $T = 295$ K, and $\theta = 0°$ (i.e., normal incidence). The medium outside the slab is vacuum.

4.5 (a) Convert the classical oscillator model (Eq. 4.9) from angular frequency to wave numbers [cm^{-1}]. For $\nu_1 = 400 \text{ cm}^{-1}$, $\Delta\epsilon_1 = 3$, $\epsilon_\infty = 2$, and $\Gamma_1/(2\pi c\nu_1) = 0.01$, plot $\epsilon_r'(\nu)$, $\epsilon_r''(\nu)$, and $1/|\epsilon_r(\nu)|$ from $\nu = 0$ to 1000 cm^{-1}. Also, plot R for $\theta = 0°$ over the same spectral range. What mathematical formulas can be used to explain the relationship between all these curves?

(b) Show that the classical oscillator model, in general, satisfies

$$\int_0^\infty (\epsilon_r'(\omega) - 1)\, d\omega = 0.$$

(c) Also evaluate the integral

$$\int_0^\infty d\omega \beta_{abs}(\omega)$$

for the classical oscillator model given by Eq. 4.12 for a single mode. Then construct the line strength and line shape function for the classical oscillator model. (*Hint*: For parts (b) and (c), apply contour integration, as demonstrated in Appendix 3.)

4.6 Using the Hilbert transform (or Kramers–Krönig relation) show that

$$n(\nu) = 1 + \frac{1}{2\pi^2} \sum_i \frac{S_i}{\nu_i^2 - \nu^2}$$

given

$$\beta_a(\nu) = \sum_i S_i \delta(\nu - \nu_i)$$

where $\delta(\nu)$ is a Dirac delta function. How does the index of refraction vary with density? Why is the index of refraction often greater in the RF than in the visible? How does the index of refraction vary with the line position and line strength?

4.7 A dielectric slab waveguide can be used for optical propagation. The reflectivity at the boundary of the slab will determine loss of a geometrical optics ray. For the geometry and refractivity shown in Fig. P4.7, determine $|R_p|$ and $|R_s|$. Is this a good waveguide?

$n_1 = 1$

$n_2 = 1.7$

$\theta_i = 67°$

$n_1 = 1$
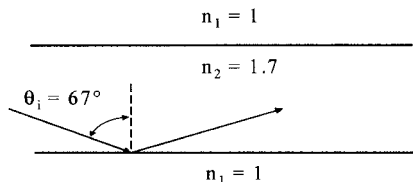
Fig. P4.7

4.8 At low number density (i.e., atmospheric densities), N, the ideal gas law ($pV = nR_{GC}T$) can be used to express density in terms of pressure and temperature. Find that expression and compute the NTP ($T = 296$ K and $P = 1$ atm) number density of an ideal gas.

4.9 Show that the conductive permittivity is obtained from the dielectric permittivity (classical oscillator model) when ω is much greater than the bandgap frequency. Explain why this occurs (or why Ge appears metallic).

4.10 Show that the Debye and free-carrier models satisfy a Hilbert transform.

4.11 Verify Eqs. 4.75a and b based on Eqs. 4.73, 4.68, and 4.70.

4.12 Using the concepts of Rayleigh scattering, explain why the sky is blue and sunsets are yellow to red even though the sun appears white. The wavelength of blue light (sky blue that is) $i_s \sim 0.48$ μm, yellow light is 0.61 μm and red light is 0.65 μm. Give numerical evidence to support your explanation. (*Note*: It will take more than Rayleigh scattering to completely explain the blue sky; think about the nature of the source and the receiver, also.)

4.13 (a) What is the ratio of forward scatter ($\theta = 0$) to back scatter ($\theta = \pi$) for Rayleigh scattering?
(b) Determine the Mueller matrix for Rayleigh scatter. Then compute the scattered Stokes vector for unpolarized incident light. Comment on the angular dependence of the polarization of scattered light.

4.14 For a particle with $n = 1.33$, $k = 1 \times 10^{-5}$, $x = 0.1$ (Rayleigh limit), $\lambda = 0.5$ μm, and $\rho_p = 100$ cm^{-3}, compute the extinction coefficient in km^{-1}. What is the corresponding extinction cross-section?

Bibliography

General

4.1 J.A. Stratton, *Electromagnetic Theory*, McGraw-Hill (1941).

Section 4.2

4.2 P. Debye, *Polar Molecules*, Dover (1957).
4.3 P.W. Milonni and J.H. Eberly, *Lasers*, Wiley-InterScience (1988).
4.4 J.D. Jackson, *Classical Electrodynamics*, 2nd Ed., Wiley (1975).

Section 4.3

4.5 P. Yeh, *Optical Waves in Layered Media*, Wiley-InterScience (1988).
4.6 J. Lekner, "Reflection and Refraction by Uniaxial Crystals," *J. Phys. Condens. Matter* **3**, 6121–6133 (1991). J. Lekner, *Theory of Reflection*, Martinus Nijhoff (1987).
4.7 A. Yariv, *Introduction to Optical Electronics*, Holt, Rinehart and Winston (1971).

Section 4.4

4.8 H.C. Van de Hulst, *Light Scattering by Small Particles*, Dover (1981).
4.9 C.F. Bohren and D.R. Huffman, *Absorption and Scattering of Light by Small Particles*, Wiley-InterScience (1983).

5

Electrodynamics II: Microscopic Interaction of Light and Matter

Although the primarily phenomenological theory of absorption and refraction of light by matter, based on classical models as presented in Chapter 4, is very useful, it is incomplete and often inadequate. A more complete and accurate picture of electrodynamics is given by the theory of quantum optics, and that is the topic of this chapter. The models developed in this chapter are more detailed and therefore more complicated than the phenomenological models of Chapter 4. The most robust models, which are applied in Part II, are presented in this chapter. The quantum models accurately represent experimental data and allow extrapolation and interpolation of such data. Many practical computer based models concerning optical propagation are based on this theory.

The theory of elastic scatter as presented in Chapter 4 is consistent with quantum optics and is not presented again. (However, inelastic scatter must address the quantum nature of the scattering medium.)

5.1 Quantum Optics

Quantum optics is not completely covered in this chapter. Entire textbooks are devoted to this diverse and comprehensive topic covering optics (see Refs. 5.1–5.3). The emphasis of this book is on absorption and reflection spectroscopy. Now details of internal structure of the medium impacting light–matter interaction are examined. The classical oscillator

model is upgraded by semiclassical radiation theory and a quantum oscillator model is developed. Semiclassical radiation theory is based on a quantized medium coupled to a classical field. It is often applied to laser theory, where near-line-center stimulated emission dominates. The quantum oscillator model again utilizes the quantized medium and classical field, but with more attention to detailed balance between absorption and emission. It satisfies causality and the fundamental symmetry relationships established in Chapter 2. These quantum optics models are more complete formalisms and provide solutions to the shortcomings of classical electrodynamics.

Of particular interest to propagation in gaseous media is the line shape in the far wing. To achieve long path lengths, propagation near line center of a resonance must be avoided. Line shape models in quantum optics accurately represent much of the frequency and temperature dependence observed in experimental data. For this reason a full discussion of line shapes has been postponed until this chapter.

In Part II of this book, the quantum oscillator model is used to represent the complex index of refraction of a variety of media with good success. The semiclassical model is also useful because it allows upgrades (i.e., temperature dependence and population distributions) to parameters in the commonly used classical oscillator model. Part II is a testimony to the great utility of quantum optics and applied spectroscopy. The optical scientist and engineer of today must be aware of these powerful tools.

5.2 Statistical Distribution Functions

This section is intended to provide the necessary background for Sections 5.4 and 5.6. We will begin with a brief discussion of energy distribution functions for various types of many body systems in thermal equilibrium. The models presented here are founded in statistical mechanics and the reader is referred to the bibliography for a deeper understanding.

5.2.1 Maxwell–Boltzmann Statistics

For a medium or single particle in thermal equilibrium with its environment at temperature T, the distribution of energy E_i within the system is given by

$$f_{MB}(E_i) = \frac{g_i e^{-E_i/(k_B T)}}{Q(T)}, \tag{5.1}$$

where k_B is Boltzmann's constant (1.380622×10^{-16} erg/K) and g_i is the degeneracy of energy level E_i. $Q(T)$ is the partition function, such that

$$\sum_{E_i} f_{MB}(E_i) = 1. \tag{5.2}$$

Thus, the partition function normalizes the distribution function to satisfy the above condition. Therefore, it is given by

$$Q(T) = \sum_{E_i} g_i e^{-E_i/(k_B T)}. \tag{5.3}$$

In an ensemble of N particles, the number of particles with energy E_i becomes

$$N_i = N f_{MB}(E_i) = N g_i \frac{\mathrm{e}^{-E_i/(k_B T)}}{Q(T)}.$$

(5.4)

Note that the sum of N_i over all energies must equal the total number of particles in the system, thus

$$\sum_i N_i = N \frac{\sum_i g_i \mathrm{e}^{-E_i/(k_B T)}}{Q(T)} = N.$$

Particles that satisfy this distribution law are called **boltzons** (like fermions and bosons). Molecules and atoms are examples of boltzons. The internal energy distribution at thermal equilibrium of rotational, vibrational, and electronic motion follows $f_{MB}(E)$.

In general, the net internal energy of a molecule is the sum of the rotational, vibrational, and electronic energies. However, because of the large differences between these different types of energies in molecules, the partition function can be approximately expressed by the following product:

$$Q_{Tot}(T) \approx Q_{E1}(T)\, Q_{Vib}(T)\, Q_{Rot}(T)$$

$$= \sum g_n \exp\left(\frac{-E_{E1}(n)}{k_B T}\right) \sum g_v \exp\left(\frac{-E_{Vib}(v)}{k_B T}\right) \sum g_J \exp\left(\frac{-E_{Rot}(J)}{k_B T}\right).$$

(5.5)

This ignores interactions between the different types of molecular energies. Over the range of typically encountered temperatures, $Q_{El} = 1$ and $Q_{Vib} \approx 1$ are good approximations. Knowledge of the rotational partition function is always important. A listing is given, according to the class of molecule (see Chapter 3), in the following section.

5.2.1.1 Diatomic Molecules

Because the rotational energy levels are often closely spaced, the sum is converted to an integral (see Example 5.1 below). The general rotational partition function for a diatomic molecule becomes

$$Q_{Rot}(T) = \frac{8\pi^2 I_e k_B T}{\sigma h^2} = \frac{1}{\sigma} \frac{T}{1.4388 B_e},$$

(5.6)

where σ is a symmetry number with $\sigma = 2$ when homonuclear molecules are considered (for N_2, O_2, etc.) and $\sigma = 1$ otherwise (for CO, HF, etc.). B_e can be found in Table 3.1 for various diatomic molecules.

Example 5.1 The rigid rotor for AB (non-homonuclear) molecules has the following formula for its rotational energy levels:

$$E_J = hcB_eJ(J+1), \quad \text{where} \quad g_J = (2J+1)$$

and the rotational quantum number is $J = 0,1,2,3....$. The partition function for a system in the electronic and vibrational ground state is

$$Q_{Rot}(T) = \sum_{J=0}^{\infty} (2J+1)\exp\left(-\frac{hc}{k_BT}B_eJ(J+1)\right).$$

Because of the closeness of rotational energy levels (e.g., B_e is small), we will convert the sum to an integral. Thus

$$Q_{Rot}(T) = \int_0^{\infty} dJ(2J+1)e^{-y(J^2+J)},$$

where the following substitution is made:

$$y = \frac{hc}{k_BT}B_e.$$

This is a good approximation for most atmospheric molecules of interest. The resulting rotational partition function is

$$Q_{Rot}(T) = \frac{1}{y} = \frac{k_BT}{hcB_e}.$$

The diatomic molecule has only one vibrational mode. Thus the vibrational partition function for a purely harmonic potential becomes (see Chapter 3)

$$Q_{Vib}(T) = \sum_{v=0}^{\infty} \exp\left(-\frac{hcv_0}{k_BT}v\right) = \left[1 - \exp\left(\frac{-hcv_0}{k_BT}\right)\right]^{-1}. \tag{5.7}$$

The ground-state energy is set to zero, since it is not relevant to population calculations. The electronic partition function, $Q_{El}(T) \approx 1$ for most temperatures of interest (e.g., near room temperature).

5.2.1.2 Polyatomic Molecules

The rotational energies for the various polyatomic molecules are listed in Section 3.3.1.2 and applied using Eq. 5.3 to obtain the partition function.

Linear Molecules   Based on Eq. 3.56 the same energy eigenvalues are obtained for linear polyatomic molecules as for diatomic molecules, thus the partition functions are also the same.

Symmetric-Top Molecules   Based on Eqs. 3.58 and 3.59, the partition function becomes

$$Q_{Rot} = \frac{1}{\sigma} \sum_{K=-\infty}^{K=\infty} \exp\left(-\frac{hc}{k_B T}(A - B)K^2\right) \sum_{J=|K|}^{\infty} (2J + 1) \exp\left(-\frac{hc}{k_B T}BJ(J + 1)\right).$$

(5.8)

As before, $hcB/k_B T$ and $hc(A - B)/(k_B T)$ are small and the sums can be replaced by integrals, thus for prolate symmetric tops

$$Q_{Rot} = \frac{\sqrt{\pi}}{\sigma}\left(\frac{8\pi^2 I_a k_B T}{h^2}\right)^{1/2}\left(\frac{8\pi^2 I_b k_B T}{h^2}\right)$$

$$= \frac{\sqrt{\pi}}{\sigma}\left(\frac{T}{1.4388A}\right)^{1/2}\left(\frac{T}{1.4388B}\right).$$

(5.9)

Spherical-top molecules are a special case of the prolate symmetric top where $A = B$ or $I_a = I_b$. This substitution into the above formulas produces the rotational partition function for the spherical top.

Similarly, the rotational partition function for the oblate case (σ is a symmetry number as previously defined) is

$$Q_{Rot} = \frac{\sqrt{\pi}}{\sigma}\left(\frac{T}{1.4388C}\right)^{1/2}\left(\frac{T}{1.4388B}\right).$$

(5.10)

Asymmetric Top   The rotational partition function for the asymmetric top is

$$Q_{Rot} = \frac{\sqrt{\pi}}{\sigma}\left(\frac{8\pi^2 I_a k_B T}{h^2}\right)^{1/2}\left(\frac{8\pi^2 I_b k_B T}{h^2}\right)^{1/2}\left(\frac{8\pi^2 I_c k_B T}{h^2}\right)^{1/2}.$$

(5.11)

The vibrational partition function for polyatomic molecules within the unperturbed harmonic oscillator approximation, and ignoring the zero point energy, becomes

$$Q_{Vib}(T) = \sum_{v_1, v_2, \cdots v_n=0}^{\infty} \exp\left(-\left[\frac{hcv_1}{k_B T}v_1 + \frac{hcv_2}{k_B T}v_2 + \cdots + \frac{hcv_n}{k_B T}v_n\right]\right)$$

$$= \left[1 - \exp\left(\frac{-hcv_1}{k_B T}\right)\right]^{-1}\left[1 - \exp\left(\frac{-hcv_2}{k_B T}\right)\right]^{-1}\cdots\left[1 - \exp\left(\frac{-hcv_n}{k_B T}\right)\right]^{-1}, \quad (5.12)$$

where n is the number of normal vibrational modes of the molecule.

5.2.2 Fermi–Dirac Statistics

Two states per orbital are available to fermions (half-integer spin particles, e.g., electrons). Thus the occupancy number, N, must equal 1 or 0. The thermally averaged value of the occupancy of an orbital is the ratio of the term in the grand sum with $N = 1$ to the sum of the terms with $N = 0$ ($E = 0$) and $N = 1$ ($E = E$). The average number of fermions in an energy level E is

$$\langle N(E) \rangle = \frac{e^{-E/k_B T}}{1 + e^{-E/k_B T}} = \frac{1}{e^{E/k_B T} + 1} = f_{FD}(E). \tag{5.13}$$

This is the Fermi–Dirac distribution function for fermions at thermal equilibrium.

5.2.3 Bose–Einstein Statistics

Any number of bosons (integer spin particles) can occupy a single state with energy E. The ensemble average of the occupancy number, N, must consider all available states and is given by

$$\langle N(E) \rangle = \frac{\sum_{N=0}^{\infty} N e^{-NE/k_B T}}{\sum_{N=0}^{\infty} e^{-NE/k_B T}} = \frac{\sum_{N=0}^{\infty} N x^N}{\sum_{N=0}^{\infty} x^N}; \quad x = e^{-E/k_B T}. \tag{5.14}$$

The geometric series in the above expression contains the following closed form sums:

$$\sum_{n=0}^{\infty} x^n = \frac{1}{1-x} \quad \text{and} \quad \sum_{n=0}^{\infty} n x^n = x \frac{d}{dx} \sum_{n=0}^{\infty} x^n = \frac{x}{(1-x)^2}.$$

The average boson occupation number for a system of bosons in thermal equilibrium with a particular energy, E, becomes

$$\langle N(E) \rangle = \frac{e^{-E/k_B T}}{1 - e^{-E/k_B T}} = \frac{1}{e^{E/k_B T} - 1} = f_{BE}(E). \tag{5.15}$$

This is the Bose–Einstein distribution function, f_{BE}. Photons are bosons and must satisfy the Bose–Einstein distribution function.

A good example is the blackbody radiance and irradiance functions, $L_{BB}(v)$ and $M_{BB}(v)$, respectively, given $E = hcv$ is the photon energy. It describes the total energy density or spectral distribution of radiation from a medium in thermal equilibrium that is a perfect absorber at all frequencies. The radiated energy per unit volume and unit bandwidth is the photon energy times the number density of modes per unit bandwidth (see Eq. 1.15f) times the Bose–Einstein distribution function, $f_{BE}(hcv)$, as given by

$$u_{BB}(v) = hcv \frac{d\rho_{EM}}{dv} f_{BE}(hcv) = \frac{8\pi h v^3 c}{e^{hcv/(k_B T)} - 1} \quad [\text{J cm}^{-3}\,\text{cm}], \tag{5.16a}$$

where $hc/k_B = 1.43879$ [cm K]. To obtain the power per unit area-bandwidth integrated over all directions, u_{BB} is multiplied by the speed of light (see Chapter 2),

$$cu_{BB}(\nu) = \frac{8\pi h \nu^3 c^2}{e^{hc\nu/k_B T} - 1} \quad [\text{W cm}^{-2}\text{ cm}]. \tag{5.16b}$$

This is the total spectral radiated power per area-unit bandwidth for a perfect blackbody radiating in all directions. The blackbody radiance, $L_{BB}(\nu)$, is obtained by dividing by 4π steradians,

$$L_{BB}(\nu) = \frac{2hc^2\nu^3}{e^{hc\nu/k_B T} - 1} \quad [\text{W}/(\text{cm}^2 \text{ sr cm}^{-1})]. \tag{5.17a}$$

Because the blackbody radiance is also used as a function of wavelength, it is of interest to convert $L_{BB}(\nu)$ to $L_{BB}(\lambda)$. Remember radiance is per unit bandwidth, thus the equality between $L_{BB}(\nu)$ to $L_{BB}(\lambda)$ is given by

$$L_{BB}(\nu)|d\nu| = L_{BB}(\lambda)|d\lambda|.$$

Using this relation, the blackbody radiance as a function of wavelength becomes

$$L_{BB}(\lambda) = \frac{2hc^2}{\lambda^5} \frac{1}{e^{hc/k_B T} - 1}. \tag{5.17b}$$

The blackbody irradiance from a surface is obtained by integrating the radiance times $\cos\theta$ over all solid angles within a hemisphere. The result is

$$M_{BB}(\nu) = \pi L_{BB}(\nu). \tag{5.18a}$$

$M_{BB}(\nu)$ is illustrated in Fig. 5.1 for typical temperatures of the surface of the earth and solar photosphere.

It is often of interest to obtain the integrated irradiance over all frequencies. A closed-form solution results, as given by

$$\int_0^\infty d\nu M_{BB}(\nu) = \frac{2\pi^5 k_B^4}{15c^2 h^3} T^4 = \sigma_{SB} T^4. \tag{5.18b}$$

where $\sigma_{SB} = 5.671 \times 10^{-8}$ W/(m^{2}K^4) is called the Stefan–Boltzmann constant. Another related result of common interest is a band limited integration of the blackbody irradiance. For an integration between the spectral points λ_1 and λ_2 the result is

$$\int_{\lambda_1}^{\lambda_2} d\lambda M_{bb}(\lambda) = \sigma_{SB} T^4 \left[F\left(\frac{hc}{k_B \lambda_2 T}\right) - F\left(\frac{hc}{k_B \lambda_1 T}\right) \right], \tag{5.18c}$$
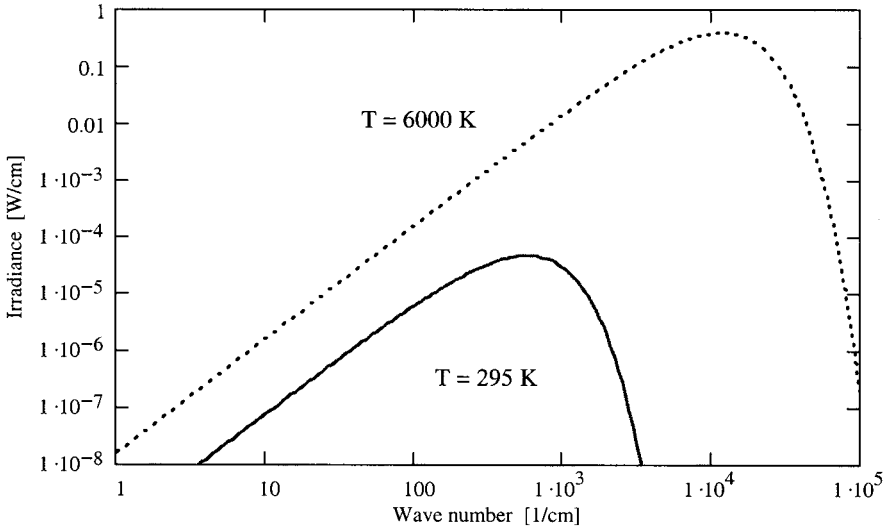
Fig. 5.1 Spectral distribution of blackbody irradiance function at two different temperatures.

where

$$F(x) = \frac{15}{\pi^4} \sum_{n=1}^{\infty} e^{-nx} \left(\frac{x^3}{n} + \frac{3x^2}{n^2} + \frac{6x}{n^3} + \frac{6}{n^4} \right).$$

In summary, molecules are boltzons and must satisfy the Maxwell–Boltzmann distribution function, $f_{MB}(E)$. Electrons are fermions and must satisfy the Fermi–Dirac distribution function, $f_{FD}(E)$. Integer spin particles, such as photons and phonons, are bosons and must satisfy the Bose–Einstein distribution, $f_{BE}(E)$. These are all energy distribution functions for systems in thermal equilibrium.

5.3 Quantum Mechanics II

This section presents the time-dependent perturbation expansion of the Schrödinger wave equation. Also, the density matrix formalism is developed and applied to the semi-classical oscillator model. This provides the necessary tools to model the interaction of light and matter in a more complete manner, including the temperature dependence of the complex index of refraction. The development is not intended to be rigorous, but to provide the insight to properly apply the theory.

5.3.1 Time-Dependent Perturbation Theory

In quantum mechanics, only a few problems can be solved exactly. Thus techniques are used that allow approximate solutions based on exact solutions. This is called

perturbation theory. Examples of stationary-state perturbation theory are suggested in Chapter 3 (i.e., rotational motion added to vibrational motion, and anharmonicity corrections to the harmonic oscillator). Now we are interested in dynamic solutions to the time-dependent Schrödinger equation. Consider a system Hamiltonian of the form

$$H(t) = H_0 + H_{int}(t),\qquad(5.19)$$

where H_0 has an exact solution to the time-independent Schrödinger equation and $H_{int}(t)$ is a time-dependent interaction Hamiltonian and represents a perturbation to the stationary-state system.

The probability that a system will change from an initial state $|s^i(t)\rangle$ to some final state $\langle s^f(t)|$ is

$$P_{i \to f} = |\langle s^f(t)|s^i(t)\rangle|^2.\qquad(5.20)$$

$|s^i(t)\rangle$ and $\langle s^f(t)|$ are describable in terms of time-independent eigenfunctions of $\hat{H}_0$. This leads to the time development operator, $\hat{S}(t)$, as defined by

$$|s^i(t)\rangle = \hat{S}_{Tot}(t)|i\rangle\qquad(5.21a)$$

for initial states before and during the interaction, and after the interaction

$$\langle s^f(t)| = \langle f|\hat{S}_0^\dagger(t),\qquad(5.21b)$$

for final states. $|i\rangle$ and $|f\rangle$ are stationary-state eigenfunctions generated by $\hat{H}_0$. Based on the general solution to the time-dependent Schrödinger equation, as given by Eq. 3.11, the form of the time development operator becomes

$$\hat{S}_{Tot}(t) = \exp\left(\frac{j}{\hbar}\int_0^t \left[\hat{H}_0 + \hat{H}_{int}(t')\right]dt'\right)\qquad(5.22a)$$

and for the Hermitian conjugate operator

$$\hat{S}_0^\dagger(t) = \exp\left(\frac{-j}{\hbar}\int_0^t \hat{H}_0\, dt'\right) = \hat{S}_0^{-1}(t).\qquad(5.22b)$$

Thus, $\hat{S}_0(t)$ is unitary. $\hat{S}_0^\dagger(t)$ lacks the interaction Hamiltonian because the perturbation comes before the final state. (This will not always be true when steady-state collisions by other molecules [or systems] are considered.) The time dependence is now contained in the operator and not in the wave function. This approach is called the Heisenberg picture.

Now, the transition probability becomes

$$\begin{aligned} P_{i \to f} &= |\langle f|\,\hat{S}_0^\dagger(t)\,\hat{S}_{Tot}(t)\,|i\rangle|^2 \\ &= |\langle f|\,\hat{S}_0^{-1}(t)\,\hat{S}_{Tot}(t)\,|i\rangle|^2. \end{aligned}\qquad(5.23)$$

Let the time development operator product be expressed as a single operator,

$$\hat{V}(t) = \hat{S}_0^{-1}(t)\hat{S}_{Tot}(t). \tag{5.24}$$

Based on the time-dependent Schrödinger equation, the equation of motion for this operator becomes

$$-j\hbar \frac{\partial \hat{V}(t)}{\partial t} = \hat{S}_0^{-1}(t)\hat{H}_{int}(t)\hat{S}_0(t)\hat{V}(t), \tag{5.25}$$

where the unit operator,

$$\hat{S}_0\hat{S}_0^{-1} = \hat{1}$$

is used. Solving the differential equation, we obtain

$$\hat{V}(t) = \exp\left(\frac{j}{\hbar}\int_0^t \hat{S}_0^{-1}(t')\hat{H}_{int}(t')\hat{S}_0(t')\,dt'\right); \quad \text{where } \hat{V}(t=0) = \hat{1}. \tag{5.26}$$

The expansion of this operator in terms of the integral over time must be performed carefully so that correct operator sequence is maintained. The time ordered perturbation expansion of $\hat{V}(t)$ is

$$\hat{V}(t) = \hat{1} + \sum_{n=1}^{\infty}\left(\frac{j}{\hbar}\right)^n \int_0^t dt' \int_0^{t'} dt'' \cdots \int_0^{t^{(n-1)}} dt^{(n)} \left[\hat{S}_0^{-1}(t')\hat{H}_{int}(t')\hat{S}_0(t')\right]$$

$$\times \left[\hat{S}_0^{-1}(t'')\hat{H}_{int}(t'')\hat{S}_0(t'')\right]\cdots\left[\hat{S}_0^{-1}(t^{(n)})\hat{H}_{int}(t^{(n)})\hat{S}_0(t^{(n)})\right]. \tag{5.27}$$

To first order in this expansion, $\hat{V}(t)$ becomes (the higher order terms in Eq. 5.27 lead to phenomena in nonlinear optics)

$$\hat{V}(t) = \hat{1} + \frac{j}{\hbar}\int_0^t dt' \left[\hat{S}_0^{-1}(t')\hat{H}_{int}(t')\hat{S}_0(t')\right]. \tag{5.28}$$

Now, to first order the transition probability becomes (recall the orthogonality requirement on the stationary eigenstates, $\langle f|i\rangle = \delta_{if} = 0$ for $i \neq f$, as presented in Section 3.1.3),

$$P_{i\to f} = \left|\frac{j}{\hbar}\int_0^t dt'\langle f|\hat{S}_0^{-1}(t')\hat{H}_{int}(t')\hat{S}_0(t')|i\rangle\right|^2. \tag{5.29}$$

Furthermore, recognizing that $\hat{S}_0$ contains the zero-order Hamiltonian and that the eigenstates are determined by this Hamiltonian, the operation on the initial state by the time development operator simplifies to

$$\hat{S}_0(t)|i\rangle = \exp\left(\frac{j}{\hbar}\int_0^t dt' \hat{H}_0\right)|i\rangle = e^{\frac{j}{\hbar}E_i t}|i\rangle. \tag{5.30}$$

Similarly, $\hat{S}_0^{-1}$ operating on the final state, simplifies to

$$\langle f|\hat{S}_0^{-1}(t) = \langle f|\exp\left(-\frac{j}{\hbar}E_f t\right). \tag{5.31}$$

Therefore, based on the above results, the transition probability between two stationary eigenstates to first order reduces to

$$P_{i\to f} = \frac{1}{\hbar^2}\left|\int_0^t dt' e^{-j\omega_0 t}\langle f|\hat{H}_{int}(t')|i\rangle\right|^2, \tag{5.32}$$

where $E_f - E_i = \hbar\omega_0$.

5.3.2 Fermi's Golden Rule

Assume the interaction Hamiltonian, $\hat{H}_{int}(t)$, is time harmonic, that is,

$$\hat{H}_{int}(t) = \hat{H}_{int}\, e^{j\omega t} \tag{5.33}$$

Substituting the above form of the interaction Hamiltonian into the transition probability yields

$$P_{i\to f} = \frac{1}{\hbar^2}\left|\langle f|\hat{H}_{int}|i\rangle\int_0^t dt' e^{j(\omega-\omega_0)t'}\right|^2. \tag{5.34}$$

Evaluating the above integral, we obtain

$$P_{i\to f} = \frac{1}{\hbar^2}\left|\langle f|\hat{H}_{int}|i\rangle\left(\frac{e^{j\Delta\omega t}}{j\Delta\omega} - \frac{1}{j\Delta\omega}\right)\right|^2. \tag{5.35}$$

where $\Delta\omega = \omega - \omega_0$. With some simple manipulation, this reduces to

$$P_{i\to f} = \frac{1}{\hbar^2}\left|\frac{\sin\Delta\omega t/2}{\Delta\omega/2}\right|^2 |\langle f|\hat{H}_{int}|i\rangle|^2. \tag{5.36}$$
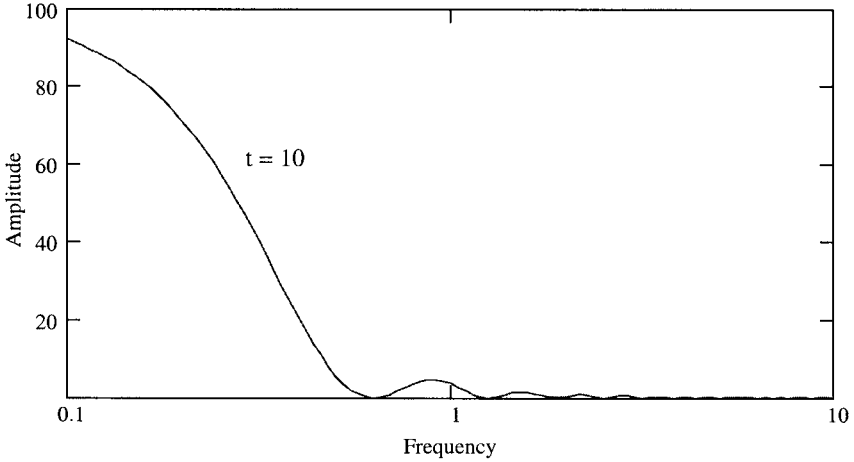
Fig. 5.2 A plot of Eq. 5.37 for $t = 10$ sec. As t increases the function narrows and peaks at $\Delta\omega = 0$. The integral on $\Delta\omega$ of this function is $2\pi t$.

The time-dependent factor of the above result represents strong transient behavior of the system due to the instantaneous turn on of the perturbation. Real systems cannot do this, and we are interested in the result at long time. In the limit of $t \to \infty$, the transient effects decay away and this function goes into the form of a delta function, thus

$$\lim_{t \to \infty} \left| \frac{\sin \Delta\omega t/2}{\Delta\omega/2} \right|^2 = 2\pi t \delta(\Delta\omega) \,. \tag{5.37}$$

This point is illustrated in Fig. 5.2. Therefore in the limit, the transition probability becomes

$$P_{i \to f} = \frac{2\pi}{\hbar^2} t |\langle f | \hat{H}_{int} | i \rangle|^2 \delta(\Delta\omega) \,. \tag{5.38}$$

The transition rate, Γ, is defined as the transition probability per unit time. Based on the above result for $P_{i \to f}$ and dividing by t, we obtain Fermi's golden rule for harmonic perturbations,

$$\Gamma_{i \to f} = \frac{2\pi}{\hbar^2} |\langle f | \hat{H}_{int} | i \rangle|^2 \delta(\Delta\omega) \,, \tag{5.39}$$

or converting the argument of the delta function to energy,

$$\Gamma_{i \to f} = \frac{2\pi}{\hbar} |\langle f | \hat{H}_{int} | i \rangle|^2 \delta(E_f - E_i - \hbar\omega) \,. \tag{5.40}$$

This formula is fundamental to the description of linear absorption and emission phenomena. The importance is further emphasized by the choice of name given by Enrico Fermi.

5.3.3 Density Matrix Formalism

The density matrix formalism allows the combination of the probability and statistics of *quantum* and *statistical* mechanics in a straightforward manner. Since we are interested in characterizing large numbers of molecules, this approach makes a lot of sense. Now, macroscopic models can be obtained with a microscopic basis. Therefore, more complete and useful models result from this practical formalism.

Consider a time-dependent wave function expanded in terms of a time-independent stationary-state basis set $|n\rangle$,

$$|\psi(t)\rangle = \sum_{n=0}^{\infty} c_n(t)|n\rangle. \tag{5.41}$$

The coefficients, $c_n(t)$, are the time-dependent portion of the time-dependent wavefunction. The expectation value of some observable parameter, A, is of vital interest and is given by

$$\langle\psi|\hat{A}|\psi\rangle = \sum_{\substack{n=0 \\ m=0}}^{\infty} c_n c_m^* \langle m|\hat{A}|n\rangle.$$

The averaged (i.e., over time or ensemble average over molecules) expectation value is denoted with an overbar, thus

$$\langle\overline{A}\rangle = \sum_{\substack{n=0 \\ m=0}}^{\infty} \overline{c_n c_m^*} \langle m|\hat{A}|n\rangle. \tag{5.42}$$

At this point the microscopic expectation value becomes a macroscopic quantity as desired. Now, define the density matrix element and the expectation value matrix element as

$$\rho_{nm}(t) = \overline{c_n(t)c_m^*(t)} \quad \text{and} \quad A_{mn} = \langle m|\hat{A}|n\rangle, \tag{5.43}$$

respectively. Since $\rho_{nm} = \rho_{mn}^*$, ρ is a Hermitian matrix. The averaged expectation value is now expressed as a matrix product,

$$\langle\overline{A}\rangle = \sum_{\substack{n=0 \\ m=0}}^{\infty} \rho_{nm} A_{mn}. \tag{5.44}$$

In matrix notation the averaged expectation value can be written in a more compact form as

$$\langle \overline{A} \rangle = \sum_{n=0} \left(\sum_{m=0} \rho_{nm} A_{mn} \right) = \sum_{n=0} (\rho A)_{nn}$$
$$= \mathrm{Tr}\,(\rho A),$$
(5.45)

where $\mathrm{Tr}\,()$ is a trace operator, which produces the sum of the diagonal elements. Thus, the trace is written out as

$$\mathrm{Tr}\,(\rho) = \rho_{11} + \rho_{22} + \rho_{33} + \cdots$$
(5.46)

Furthermore,

$$\mathrm{Tr}\,(\rho) = |\overline{c}_1|^2 + |\overline{c}_2|^2 + |\overline{c}_3|^2 + \cdots = 1$$

since the wave function inner product is normalized to one (i.e., $\langle \psi | \psi \rangle = 1$). Thus, the $|c_n|^2$ coefficients are interpreted as the probability that the nth state is occupied. In a thermally averaged system, the density matrix elements become constant in time and form a diagonal matrix with the diagonal elements equal to Boltzmann factors in a Maxwell–Boltzmann distribution. Thus, based on Eq. 5.1, it follows that

$$\rho_{ii} = \frac{g_i e^{-E_i/k_B T}}{Q(T)}.$$

Also, density matrix elements can be generated by the following operator:

$$\rho_{nm} = \overline{c_n c_m^*} = \overline{\langle n | \psi \rangle \langle \psi | m \rangle} = \langle n | \hat{\rho} | m \rangle .$$
(5.47)

Thus, the density matrix operator is defined as

$$\hat{\rho} = |\psi\rangle\langle\psi| .$$
(5.48)

Based on the time-dependent Schrödinger equation, the equation of motion for the density matrix operator can be obtained in the following manner. For the bra version of the wave function defined by Eq. 5.41, the Schrödinger wave equation is written

$$j\hbar \frac{\partial \langle \psi | m \rangle}{\partial t} = \sum_{k=0} \langle \psi | k \rangle H_{km} .$$

(Note that $\langle \psi | m \rangle = c_m^*(t)$.) In a similar fashion the ket wave function produces the following wave equation:

$$-j\hbar \frac{\partial \langle n | \psi \rangle}{\partial t} = \sum_{k=0} H_{nk} \langle k | \psi \rangle .$$

Now differentiating the density matrix with respect to time and using the above results, we obtain the following equation of motion:

$$j\hbar\dot{\rho}_{nm} = \sum_k (\rho_{nk}H_{km} - H_{nk}\rho_{km}),$$ (5.49a)

or in more compact notation using commutator brackets,

$$j\hbar\frac{d\hat{\rho}}{dt} = \hat{\rho}\hat{H} - \hat{H}\hat{\rho} = [\hat{\rho},\hat{H}].$$ (5.49b)

5.4 Semiclassical Oscillator Model

The quantized propagation medium is limited to two energy levels and interacts with a classical field, producing a semiclassical oscillator model. This approach leads to a tractable solution without use of perturbation theory. This means the semiclassical oscillator model can be applied to interactions with high-intensity fields, such as inside laser resonators.

To obtain a semiclassical oscillator model, consider a two-level quantum system with states $|1\rangle$ and $|2\rangle$. As previously described in Chapter 4, consider the following Hamiltonian for dipole moment coupling of the electromagnetic field with a medium:

$$H(t) = H_0 + \boldsymbol{\mu_{dp}} \cdot \mathbf{e}(Z,t).$$ (5.50)

The differential equations describing time evolution of the density matrix are derivable from the equation of motion (Eq. 5.49), and become

$$j\hbar\dot{\rho}_{mn} = \rho_{mn}E_n - E_m\rho_{mn} + \sum_k (\rho_{mk}\boldsymbol{\mu_{kn}} - \boldsymbol{\mu_{mk}}\rho_{kn}) \cdot \mathbf{e}(Z,t).$$ (5.51)

Considering a two-level system (e.g., $n, m, k = 1,2$), using Eq. 1.12 for the electric field and converting energy to frequency, the above equation becomes

$$j\hbar\dot{\rho}_{mn} = \hbar\omega_{nm}\rho_{mn} + \frac{1}{2}\sum_k (\rho_{mk}\boldsymbol{\mu_{kn}} - \boldsymbol{\mu_{mk}}\rho_{kn}) \cdot (\mathbf{E}e^{j\omega t} + \mathbf{E}^*e^{-j\omega t}),$$ (5.52)

where $\omega_{nm} = E_n - E_m$. The time-harmonic nature of the wave function, as stated in Section 3.1.3, is contained in the c-coefficients. The lower energy level can be defined as a reference state against which the upper state frequency is measured. Thus, the time-harmonic factor ($e^{j\omega t}$) exists only in the $c_2(t)$ coefficient. Based on this convention, the time-harmonic factor only exists in the off-diagonal density matrix elements, as given by

$$\rho_{21}(t) \rightarrow \rho_{21}(t)e^{j\omega t} \quad \text{and} \quad \rho_{12}(t) \rightarrow \rho_{12}(t)e^{-j\omega t}.$$

Example 5.2 The interaction Hamiltonian, as stated in Eq. 5.50, is the same coupling mechanism used in Chapter 4, which applies the Lorentz force relation. This can be understood by converting the force equation of Eq. 4.1 to work or energy on a negative charge in the electric dipole approximation, as follows:

$$-\nabla H_{int}(\mathbf{r}, t) = \mathbf{F}(t) = q\mathbf{e}(Z, t).$$

Solving for the interaction Hamiltonian, one obtains

$$H_{int}(\mathbf{r}, t) = -q\mathbf{r} \cdot \mathbf{e}(Z, t) = \boldsymbol{\mu}_{dp} \cdot \mathbf{e}(Z, t),$$

which agrees wi}th Eq. 5.50. However, it is important to realize that this Hamiltonian is, in general, incomplete, and represents linear coupling only.

Making this substitution into Eq. 5.52, we obtain to the following set of differential equations

$$j\hbar\dot{\rho}_{11} = \frac{1}{2}(\rho_{12}\boldsymbol{\mu}_{21} \cdot \mathbf{E} + \rho_{12}\boldsymbol{\mu}_{21} \cdot \mathbf{E}^*e^{-2j\omega t} - \boldsymbol{\mu}_{12}\rho_{21} \cdot \mathbf{E}e^{2j\omega t} - \boldsymbol{\mu}_{12}\rho_{21} \cdot \mathbf{E}^*) \quad (5.53a)$$

$$j\hbar\dot{\rho}_{22} = \frac{1}{2}(\rho_{21}\boldsymbol{\mu}_{12} \cdot \mathbf{E}e^{2j\omega t} + \rho_{21}\boldsymbol{\mu}_{12} \cdot \mathbf{E}^* - \boldsymbol{\mu}_{21}\rho_{12} \cdot \mathbf{E} - \boldsymbol{\mu}_{21}\rho_{12} \cdot \mathbf{E}^*e^{-2j\omega t}) \quad (5.53b)$$

and

$$j\hbar\dot{\rho}_{21} = \hbar(\omega - \omega_{21})\rho_{21} + \frac{1}{2}(\rho_{22}\boldsymbol{\mu}_{21} - \boldsymbol{\mu}_{21}\rho_{11}) \cdot (\mathbf{E} + \mathbf{E}^*e^{-j2\omega t}) = -j\hbar\dot{\rho}_{12}^*. \quad (5.53c)$$

The high-frequency terms cannot be detected and essentially average to zero over typical observation times. These terms can be dropped in the so-called rotating wave approximation. Eqs. 5.53a–c now become

$$\dot{\rho}_{11} = -\frac{j}{2}\left(\rho_{12}\frac{\boldsymbol{\mu}_{21} \cdot \mathbf{E}}{\hbar} - \frac{\boldsymbol{\mu}_{21}^* \cdot \mathbf{E}^*}{\hbar}\rho_{21}\right) \quad (5.54a)$$

where for a Hermitian operator $\mu_{ij} = \mu_{ji}^*$ and

$$\dot{\rho}_{22} = -\frac{j}{2}\left(\rho_{21}\frac{\boldsymbol{\mu}_{21}^* \cdot \mathbf{E}^*}{\hbar} - \frac{\boldsymbol{\mu}_{21} \cdot \mathbf{E}}{\hbar}\rho_{12}\right) \quad (5.54b)$$

$$\dot{\rho}_{21} = \dot{\rho}_{12}^* = -j(\omega - \omega_{21})\rho_{21} - \frac{j}{2}(\dot{\rho}_{22} - \rho_{11})\frac{\boldsymbol{\mu}_{21} \cdot \mathbf{E}}{\hbar}. \quad (5.54c)$$

Relaxation processes, such as adiabatic collisions, must also be included in this model. This type of collision will not affect the population distribution, therefore only Eq. 5.54c needs to be modified. It is

$$\dot{\rho}_{21} = [-\gamma - j(\omega - \omega_{21})]\,\rho_{21} + \frac{j}{2}(\rho_{11} - \rho_{22})\frac{\boldsymbol{\mu}_{21} \cdot \mathbf{E}}{\hbar}, \qquad (5.55)$$

where γ represents collisional relaxation processes. It is assumed that the transition probability (ρ_{21}) will not change rapidly. In the quasi-steady state $\dot{\rho}_{21} \approx 0$, an expression for ρ_{21} is obtained to be

$$\rho_{21}(\omega) = \frac{(\rho_{11} - \rho_{22})\frac{\boldsymbol{\mu}_{21}\cdot\mathbf{E}}{2\hbar}}{(\omega - \omega_{21}) - j\gamma} = \rho_{12}^{*}(\omega). \qquad (5.56)$$

The equation set given by Eq. 5.54 can now be reduced to two equations in $\rho_{11}(\omega)$ and $\rho_{22}(\omega)$. This is accomplished by substituting the steady-state solution of $\rho_{21}(\omega)$ and $\rho_{12}(\omega)$ into Eqs. 5.54a and 5.54b. The result is

$$\dot{\rho}_{11}(t) = -\frac{|\boldsymbol{\mu}_{21} \cdot \mathbf{E}|^{2}}{2\hbar^{2}}(\rho_{11} - \rho_{22})\frac{\gamma}{(\omega_{21} - \omega)^{2} + \gamma^{2}} = -\dot{\rho}_{22}(t). \qquad (5.57)$$

The ρ_{ii} density matrix element times the total population, N, is the population of the ith state, N_i. That is, the rate of change of the upper state population must be equal and of opposite sign to the rate of change of the lower level population. This is true for a closed system in thermal equilibrium. After multiplying through by the number of absorbing molecules, N, Eq. 5.57 becomes,

$$\dot{N}_{1} = -\frac{\pi\,|\boldsymbol{\mu}_{21} \cdot \mathbf{E}|^{2}}{2\hbar^{2}}(N_{1} - N_{2})\,j_{L}(\omega) = -\dot{N}_{2}, \qquad (5.58)$$

where $j_L(\omega)$ is the Lorentz line shape as defined by Eq. 4.15. The quantity between the equal signs in the above equation can also be thought of as a photon absorption rate. This quantity is also the negative of stimulated emission rate. Spontaneous emission is missing in this model. The semiclassical theory of radiation used in laser theory adds spontaneous emission in a heuristic manner (see Milonni and Eberly, Ref. 5.8).

A model for the absorption coefficient can be obtained based on Eq. 5.58, because the absorption process is dominantly a stimulated process. Also, based on Eq. 2.80 for no external sources and no scatter loss, the absorption coefficient is

$$\beta_{abs} = -\frac{(dL/ds)}{L}.$$

Furthermore, the change in incremental radiance per incremental path is the photon energy times the incremental number of photons absorbed, N_p, per incremental time divided by the volume, thus

$$\frac{dL}{ds} = \frac{\hbar\omega\dot{N}_p}{V}.$$

The rate of change of the number of photons absorbed must equal the rate of change of the population of the lower energy level, that is,

$$\dot{N}_p = \dot{N}_i$$

Combining these results yields the formula for the absorption coefficient,

$$\beta_{abs}(\omega) = \frac{-\hbar\omega\dot{N}_1(\omega)}{\frac{1}{2}cn\epsilon_0 V |\mathbf{E}|^2} = \frac{\pi\omega}{\hbar cn V \epsilon_0} |\boldsymbol{\mu}_{21} \cdot \hat{\boldsymbol{\epsilon}}|^2 (N_1 - N_2) j_L(\omega). \qquad (5.59)$$

$\hat{\boldsymbol{\epsilon}}$ is the unit vector pointing in the direction of polarization. In a gas or for randomly polarized light, an orientational average is needed on the dot product between the direction of the dipole moment and the electric field. The details of the calculation are left as an exercise (see Problem 5.13). The absorption coefficient, as a function of wave number and including orientational averaging, becomes

$$\beta_{abs}(\nu) = \frac{8\pi^3\nu}{3h\epsilon_0 n} |\boldsymbol{\mu}_{ul}|^2 (\rho_l - \rho_u) j_L(\nu), \qquad (5.60)$$

where the substitution $\rho = N/V$ is made, and the subscripts 1 and 2 are changed to l (lower state) and u (upper state), respectively. The population densities are dependent on the energy level and therefore the frequency. This can be seen by using Eq. 5.4 to obtain the following:

$$\beta_{abs}(\nu, T) = \frac{8\pi^3\nu_0}{3hn\epsilon_0} |\boldsymbol{\mu}_{ul}|^2 \rho_a (f_{MB}(E_l) - f_{MB}(E_l + \nu)) \frac{\nu}{\nu_0} j_L(\nu). \qquad (5.61)$$

Substituting the explicit formulas for the Maxwell–Boltzmann distribution, ignoring degeneracy, the absorption coefficient becomes

$$\beta_{abs}(\nu, T) = \frac{8\pi^3\nu_0}{3hn\epsilon_0} |\boldsymbol{\mu}_{ul}|^2 \rho_a \frac{e^{-E_l/k_B T}}{Q(T)} (1 - e^{-hc\nu/k_B T}) \frac{\nu}{\nu_0} j_L(\nu). \qquad (5.62)$$

This result can be broken down into the standard form of line strength and line shape functions. The line strength is

$$S_{lu}(T) = \frac{8\pi^3\nu_0}{3hn\epsilon_0} |\boldsymbol{\mu}_{ul}|^2 \rho_a \frac{e^{-E_l/k_B T}}{Q(T)} (1 - e^{-hc\nu_0/k_B T}) \qquad (5.63a)$$

and the line shape profile is

$$g(\nu) = \frac{(1 - e^{-hc\nu/(k_B T)})}{(1 - e^{-hc\nu_0/(k_B T)})} \frac{\nu}{\nu_0} j_L(\nu). \tag{5.63b}$$

It is interesting to compare this result with the classical oscillator model. First, the population difference factor now appears in the line strength. This is an important improvement. The line profile functions agree when $hc\nu/(k_B T) \ll 1$ and $hc\nu_0/(k_B T) \ll 1$. Typically this will be the microwave region.

Although great progress has been made with the semiclassical oscillator model, it is still incomplete. This is easily demonstrated by realizing that Eq. 5.63b does not satisfy the symmetry condition of Eq. 3.32. Section 5.6 presents a new development which addresses this important point. Furthermore, the description of spontaneous emission is missing in this model. Spontaneous emission represents the majority of light sources in use today (i.e., incandescent and fluorescent light bulbs). The next section addresses this important topic.

5.5 The Einstein Relation and Spontaneous Emission

We begin by considering a medium in thermal equilibrium (constant temperature or steady state) in which the rate of the number of photons absorbed equals the rate of the number of photons emitted. Otherwise, the internal energy in the medium would be increased or decreased and the net temperature will change. Thus,

$$\left(\frac{dN_{m\sigma}}{dt}\right)_{abs} = \left(\frac{dN_{m\sigma}}{dt}\right)_{em} \tag{5.64}$$

where $N_{m\sigma}$ is the photon occupation number with mode number m and polarization σ. These time derivatives are related to the transition rate, Γ, by

$$\left(\frac{dN_{m\sigma}}{dt}\right)_{abs} = N_{al}\Gamma_{l \to u} \equiv \text{rate of photons absorbed} \tag{5.65a}$$

and

$$\left(\frac{dN_{m\sigma}}{dt}\right)_{em} = N_{au}\Gamma_{u \to l} \equiv \text{rate of photons emitted}, \tag{5.65b}$$

where N_{al} and N_{au} are the number of absorbing molecules in the lower (l) and upper (u) transition levels, respectively. $\Gamma_{l \to u}$ is the transition rate from the lower energy level to the upper energy level, and conversely for $\Gamma_{u \to l}$.

For stimulated processes the transition rate is proportional to electromagnetic field radiance. This can be seen by examining Fermi's golden rule in Eq. 5.40, given the interaction Hamiltonian in Eq. 5.50. For a system in thermal equilibrium, the field radiance must obey the blackbody formula and satisfy a Bose–Einstein distribution. Given this fact and the fact the upper and lower populations must satisfy a Maxwell–Boltzmann distribution, Eq. 5.64 cannot be satisfied. Thus, thermal equilibrium cannot be satisfied, and we know from experience that this is not true.

In 1917, Albert Einstein realized this dilemma and proposed the following solution. There must be two types of emission, stimulated and spontaneous. Spontaneous emission does not require illumination by an external field to occur. Thus the upper to lower transition rate is modified in the following way:

$$\Gamma_{u \to l} = u_{BB}(\nu) B_{ul} + A_{ul} \tag{5.66a}$$

and in a consistent fashion the lower to upper transition rate is

$$\Gamma_{l \to u} = u_{BB}(\nu) B_{lu}. \tag{5.66b}$$

A_{ul} is called the Einstein A-coefficient, and B_{ul} and B_{lu} are called the Einstein B-coefficients. Substituting the above transition rates into Eqs. 5.65 and 5.64, using Eq. 5.4, and solving for the field energy density, we obtain the following expression:

$$u_{BB}(\nu) = \frac{A_{ul}}{B_{ul}} \frac{1}{\dfrac{g_l B_{lu}}{g_u B_{ul}} \exp\left(\dfrac{hc\nu}{k_B T}\right) - 1}.$$

$u_{BB}(\nu)$ is the blackbody spectral energy density formula (Eq. 5.16a) when

$$g_l B_{lu} = g_u B_{ul} \quad \text{and} \quad \frac{A_{ul}}{B_{ul}} = 8\pi hc\nu^3. \tag{5.67}$$

Thus, the requirement of the existence of spontaneous emission allows thermal equilibrium between bosons and boltzons to be satisfied.

The Einstein relation for an interaction system of photons and molecular oscillators in thermal equilibrium is obtained by substituting Eqs. 5.65 and 5.66 into Eq. 5.64, to obtain

$$N_{al} u_{BB}(\nu) B_{lu} = N_{au}[u_{BB}(\nu) B_{ul} + A_{ul}]. \tag{5.68}$$

The result is important because it describes a distinction between stimulated processes by direct illumination and nonstimulated processes.

If no stimulating field is present (i.e., $u(\nu) = 0$), then spontaneous emission is the only radiative process that occurs. Since the time rate of change of photons emitted must equal the negative of the time rate of change of the upper population level, we have

$$\dot{N}_u = -\dot{N}_{m\sigma} = -N_u A_{ul}. \tag{5.69}$$

Solving the differential equation, we obtain a description of an exponentially decaying population:

$$N_u(t) = N_u(0) \exp(-A_{ul} t). \tag{5.70}$$

Thus, the reciprocal of the Einstein A-coefficient is the lifetime, τ_{ul}, of the upper level for transitions between levels u and l. The net lifetime, τ_u, of the upper level is the sum of all allowed transitions from the upper level, thus

$$\frac{1}{\tau_u} = \sum_l A_{ul}. \qquad (5.71)$$

Finally, spontaneous emission is not spontaneous, but a causal phenomenon. The correct interpretation comes from electromagnetic field quantization, as presented in Appendix 5. Spontaneous emission by an oscillator is caused by collisions with other molecules or when in vacuum by background field fluctuations that occur randomly all the time. Furthermore, field quantization rigorously describes stimulated emission, and absorption. Stimulated emission duplicates the frequency, polarization, and direction of the incident photon, thus explaining why lasers have unique coherence properties over conventional sources. The details are beyond the scope and purpose of this book, but it is important to be aware of the correct cause of this phenomenon.

5.6 Quantum Optics of Low-Density Gases

Quantum electrodynamics is one of the most successful theories ever developed by mankind. The name is often associated with high-energy physics. However, this fundamental theory contains a comprehensive description of the electromagnetic field and molecular systems, and can be applied to many topics at much lower energies. Quantum electrodynamics at optical frequencies is often referred to as quantum electronics (which emphasizes optical devices, usually solid state) or quantum optics (which emphasizes the electromagnetic field, but includes light–matter interactions). Since the emphasis of this section is on light–matter interaction with gases, the name quantum optics is preferred.

The main objective of this section is to provide the fundamental line shape and line strength formulas for optical propagation models concerning the atmosphere of the earth (e.g., those used in commercially available computer codes such as FASCODE and MODTRAN). In particular, the complete description of the line shape function away from line center is addressed. This is a practical consideration because long-path propagation does not occur when the frequency of the field matches the line center frequency of an absorption line.

The HITRAN database is used in conjunction with FASCODE and MODTRAN, and provides absorption line parameters of atmospheric molecules. A theoretical model of the absorption coefficient is developed, which utilizes this database and is consistent with current models. The description and application of these models are the topics of Part II of this book.

5.6.1 Formal Development

As in prior sections, the first-order light–matter interaction Hamiltonian is the dipole moment operator coupled to a classical electromagnetic field, as given by (suppressing the spatial dependence of the field)

$$H_{int}(t) = \boldsymbol{\mu}_{dp}(t) \cdot \mathbf{e}(t) = \boldsymbol{\mu}_{dp}(t) \cdot \frac{1}{2}(\mathbf{E}e^{j\omega t} + \mathbf{E}^*e^{-j\omega t})$$

This interaction Hamiltonian will be assumed weak, since our applications concern propagation in window regions where absorption line wings are important. The use of a classical field is valid when stimulated emission and absorption processes dominate. Such an approximation ignores spontaneous emission, which is the process of conventional light sources (i.e., blackbody radiation and fluorescence). As the previous section shows, spontaneous emission is required to satisfy thermal equilibrium. A propagating field within a medium in thermal equilibrium that does not saturate the medium presents a minor perturbation to thermal equilibrium, and spontaneous emission can be ignored.

Fermi's golden rule for the above interaction Hamiltonian, initially assuming that μ_{dp} is time independent, is

$$\Gamma_{i \to f} = \frac{2\pi}{4\hbar^2}\big[|\langle f|\hat{\boldsymbol{\mu}}_{dp}\cdot\mathbf{E}\,|i\rangle|^2\delta(\omega_{if} - \omega) + |\langle f|\hat{\boldsymbol{\mu}}_{dp}\cdot\mathbf{E}^*|i\rangle|^2\delta(\omega_{if} + \omega)\big]. \quad (5.72)$$

The first term represents absorption and the second term represents the time reversed process of emission. Recall the integral representation of the Dirac delta function,

$$\delta(\omega_{if} - \omega) = \frac{1}{2\pi}\int\limits_{-\infty}^{\infty} dt\, e^{j\omega t}e^{-j\omega_{if}t}.$$

Then, knowing $\hbar\omega_{if} = E_f - E_i$ and using Eqs. 5.30 and 5.31, Fermi's golden rule can be modified to include the time-dependent dipole moment operator in the following intuitive manner:

$$\Gamma_{i \to f} = \frac{\pi}{2\hbar^2}\bigg[\frac{1}{2\pi}\int\limits_{-\infty}^{\infty} dt e^{j\omega t}\,\langle i|\hat{\boldsymbol{\mu}}_{dp}(0)\cdot\mathbf{E}^*|f\rangle\langle f|e^{-j\hat{H}_0 t/\hbar}\hat{\boldsymbol{\mu}}_{dp}(0)e^{j\hat{H}_0 t/\hbar}\cdot\mathbf{E}\,|i\rangle$$

$$+ \frac{1}{2\pi}\int\limits_{-\infty}^{\infty} dt e^{-j\omega t}\,\langle i|e^{-j\hat{H}_0 t/\hbar}\hat{\boldsymbol{\mu}}_{dp}(0)e^{j\hat{H}_0 t/\hbar}\cdot\mathbf{E}\,|f\rangle\langle f|\hat{\boldsymbol{\mu}}_{dp}(0)\cdot\mathbf{E}^*|i\rangle\bigg] \quad (5.73)$$

Notice that the pre- and post-operators on the dipole moment are of the form of time development operators. Using the Heisenberg representation for the time-dependent dipole moment operator we obtain

$$\hat{\boldsymbol{\mu}}_{dp}(t) = e^{-j\hat{H}_0 t/\hbar}\hat{\boldsymbol{\mu}}_{dp}(0)e^{j\hat{H}_0 t/\hbar}. \quad (5.74a)$$

Furthermore, the effect of collisions by external molecules can now be handled by the addition to the zero-order system Hamiltonian of a collision Hamiltonian, $H_c(t)$. Thus,

$$H(t) = H_0 + H_c(t). \quad (5.75)$$

Applying the above Hamiltonian, the time-dependent dipole moment operator now includes the dynamics of collisions, and the transition rate becomes

$$\Gamma_{i \to f} = \frac{\pi}{2\hbar^2} \left[\frac{1}{2\pi} \int_{-\infty}^{\infty} dt \, e^{j\omega t} \langle i | \hat{\boldsymbol{\mu}}_{dp}(0) \cdot \mathbf{E}^* | f \rangle \langle f | \hat{\boldsymbol{\mu}}_{dp}(t) \cdot \mathbf{E} | i \rangle \right.$$

$$\left. + \frac{1}{2\pi} \int_{-\infty}^{\infty} dt \, e^{j\omega t} \langle i | \hat{\boldsymbol{\mu}}_{dp}(t) \cdot \mathbf{E} | f \rangle \langle f | \hat{\boldsymbol{\mu}}_{dp}(0) \cdot \mathbf{E}^* | i \rangle \right], \tag{5.76}$$

where

$$\hat{\boldsymbol{\mu}}_{dp}(t) = e^{-j\hat{H}t/\hbar} \hat{\boldsymbol{\mu}}_{dp}(0) e^{j\hat{H}t/\hbar}. \tag{5.74b}$$

As discussed in Chapter 2, the susceptibility is a causal function and directly proportional to the dipole moment. Thus, the dipole moment is causal as well. After removing the turn-on function, it is an odd function in time (i.e., $\mu_{dp}(t) = -\mu_{dp}(-t)$), just like the susceptibility. With this insight, and realizing that the first matrix element product represents absorption, we have

$$i \to l \quad \text{and} \quad f \to u$$

and the second term represents stimulated emission, thus

$$i \to u \quad \text{and} \quad f \to l,$$

where l indicates the lower state and u indicates the upper state, Equation 5.76 becomes

$$\Gamma_{l \to u} = \frac{\pi}{2\hbar^2} \left[\frac{1}{2\pi} \int_{-\infty}^{\infty} dt \, e^{j\omega t} \langle l | \hat{\boldsymbol{\mu}}_{dp}(0) \cdot \mathbf{E}^* | u \rangle \langle u | \hat{\boldsymbol{\mu}}_{dp}(t) \cdot \mathbf{E} | l \rangle \right.$$

$$\left. - \langle l | \hat{\boldsymbol{\mu}}_{dp}(0) \cdot \mathbf{E} | u \rangle \langle u | \hat{\boldsymbol{\mu}}_{dp}(-t) \cdot \mathbf{E}^* | l \rangle \right]. \tag{5.77}$$

Now examine the dipole moment matrix element product in the above equation,

$$\langle l | \hat{\boldsymbol{\mu}}_{dp}(0) \cdot \mathbf{E}^* | u \rangle \langle u | \hat{\boldsymbol{\mu}}_{dp}(t) \cdot \mathbf{E} | l \rangle.$$

Expanding the Heisenberg dipole moment operator, we obtain

$$\hat{\boldsymbol{\mu}}_{dp}(t) = e^{-j\hat{H}_c t/\hbar} e^{-j\hat{H}_0 t/\hbar} \hat{\boldsymbol{\mu}}_{dp}(0) e^{j\hat{H}_c t/\hbar} e^{j\hat{H}_0 t/\hbar}$$

$$= \hat{S}_c^{-1}(t) \hat{\boldsymbol{\mu}}_{dp}(0) \hat{S}_c(t) e^{-j\omega_{ul} t}.$$

Using this expanded form of the dipole moment operator and then inserting unit operators between the time-independent dipole moment operator and the time development operators, the matrix element becomes

$$\sum_{u',l'} \langle l|\hat{\boldsymbol{\mu}}_{dp}(0)\cdot\mathbf{E}^*|u\rangle\langle u|S_c^{-1}(t)|u'\rangle\langle u'|\boldsymbol{\mu}_{dp}(0)\cdot\mathbf{E}|l'\rangle\langle l'|S_c(t)|l\rangle e^{-j\omega_{ul}t}$$

$$= |\langle u|\hat{\boldsymbol{\mu}}_{dp}(0)\cdot\mathbf{E}^*|l\rangle|^2 \sum_{u',l'}\langle u'|S_c^{-1}(t)|u'\rangle\langle l'|S_c(t)|l'\rangle e^{-j\omega_{ul}t}$$

$$= |\langle u|\hat{\boldsymbol{\mu}}_{dp}(0)\cdot\mathbf{E}^*|l\rangle|^2 C(t)e^{-j\omega_{ul}t}$$

where $C(t)$ is an autocorrelation function. Substituting this result into the transition rate and using the Fourier transform defined by Eq. 1.9, we obtain

$$\Gamma_{l\to u} = \frac{\pi}{2\hbar^2}|\langle u|\hat{\boldsymbol{\mu}}_{dp}\cdot\mathbf{E}|l\rangle|^2 \frac{1}{2\pi}\ \mathfrak{F}\left\{e^{-j\omega_{ul}t}C(t) - e^{-j\omega_{ul}t}C(-t)\right\}.$$

The principle of detailed balance or microscopic reversibility requires the following relation between the two correlation functions (see Milonni and Eberly, Ref. 5.8)

$$\exp\left(\frac{-\hbar\omega_{ul}}{k_BT}\right)e^{-j\omega_{ul}t}C(t) = e^{j\omega_{ul}t}C(-t). \qquad (5.78a)$$

Defining the variable $\tau = t - j\hbar/(2k_BT)$, the above relation can also be rewritten as

$$e^{j\omega_{ul}\tau}C\left(\tau + j\frac{\hbar}{2k_BT}\right) = e^{-j\omega_{ul}\tau}C\left(-\tau + j\frac{\hbar}{2k_BT}\right). \qquad (5.78b)$$

Suppressing the frequency shift factors, the more commonly stated result is obtained

$$C\left(\tau + j\frac{\hbar}{2k_BT}\right) = C\left(-\tau + j\frac{\hbar}{2k_BT}\right). \qquad (5.78c)$$

The time-reversed variable is written as $-\tau = -t - j\hbar/(2k_BT)$, because the Boltzmann factor cannot change sign, since it is time independent. Thus the complex time variable must exist in the upper half-plane. Any complete theory of spectral line shapes must satisfy this fundamental relation. Using Eq. 5.78a, the transition rate becomes

$$\Gamma_{l\to u} = \frac{\pi}{2\hbar^2}|\langle u|\hat{\boldsymbol{\mu}}_{dp}\cdot\mathbf{E}|l\rangle|^2\left[1 - \exp\left(\frac{-\hbar\omega}{k_BT}\right)\right]\frac{1}{2\pi}\ \mathfrak{F}\{e^{j\omega_{ul}\tau}C(\tau)\}. \qquad (5.79)$$

The Fourier transform of an autocorrelation function is the power spectral density function, $j(\omega)$, according to the Wiener–Khintchine theorem. The power spectral density function is an important part of the line shape function. To ensure that the resulting line shape function will satisfy the symmetry properties, the following reconfiguration is performed:

$$\left(1 - e^{-\hbar\omega/k_BT}\right)\frac{(1 + e^{-\hbar\omega/k_BT})}{(1 + e^{-\hbar\omega/k_BT})}\frac{1}{2\pi}\ \mathfrak{F}\left\{e^{j\omega_{fi}\tau}C(\tau)\right\}$$

$$= \tanh\left(\frac{\hbar\omega}{2k_BT}\right)[j(\omega) + j(-\omega)].$$

Based on Eq. 5.69, the rate of change of population in the time of the state $|i\rangle$ with energy E_l is

$$\dot{N}_l = -N_l\,\Gamma_{l\to u}.$$

Substituting this population rate into Eq. 59 for the absorption coefficient, we obtain

$$\beta_{abs} = \frac{-\hbar\omega\dot{N}_l}{\frac{1}{2}cn\epsilon_0\,|E_0|^2\,V} = \frac{2\hbar\omega N_l\Gamma_{l\to u}}{cn\epsilon_0 V\,|E_0|^2}. \tag{5.80}$$

Substituting Eq. 5.79 for $\Gamma_{l\to u}$ produces the following fundamental result:

$$\beta_{abs}(\omega) = \frac{\pi\omega}{cn\epsilon_0\hbar}\frac{N_1}{V}\,|\langle u|\hat{\pmb{\mu}}_{dp}\cdot\hat{\pmb{\varepsilon}}|l\rangle|^2\,\tanh\left(\frac{\hbar\omega}{2k_BT}\right)[j(\omega)+j(-\omega)], \tag{5.81}$$

where $\mathbf{E} = E_0\hat{\pmb{\varepsilon}}$ and $\hat{\pmb{\varepsilon}}$ is a unit vector pointing in the direction of polarization. For gases and amorphous materials, the dipoles are randomly oriented relative to the field polarization. An orientational average removes the dot product in the matrix element and produces a multiplicative factor of one-third (see Problem 5.13). Also, the above result accounts for only one polarization direction and there are two. Therefore, we must also multiply the above result by a factor of two. Finally, the derivation thus far considers only one transition and many overlapping absorption lines are often present. Thus, we sum over all initial states to obtain the following result:

$$\beta_{abs}(\omega) = \sum_l \frac{2\pi\omega}{3cn\epsilon_0\hbar}\rho_{al}\frac{1}{g_l}\,|\pmb{\mu}_{dp,ul}|^2\,\tanh\left(\frac{\hbar\omega}{2k_BT}\right)[j(\omega)+j(-\omega)], \tag{5.82}$$

where $\rho_{al} = N_l/V$.

Using the Maxwell–Boltzmann distribution for ρ_{al}/g_l and converting to wave numbers, we obtain the quantum oscillator model for the absorption coefficient,

$$\beta_{abs}(\nu) = \frac{8\pi^3\nu}{3cn\epsilon_0 h}\rho_a\sum_l\frac{e^{-E_l/k_BT}}{Q(T)}\,|\pmb{\mu}_{dp,ul}|^2\,\tanh\left(\frac{hc\nu}{2k_BT}\right)[j(\nu)+j(-\nu)]$$

$$= \sum_l S_{lu}g(\nu) \tag{5.83}$$

where the line strength and line shape functions are given by

$$S_{lu} = \frac{8\pi^3\nu_l}{3cn\epsilon_0 h}\frac{e^{-E_l/k_BT}}{Q(T)}\rho_a\,|\pmb{\mu}_{dp,ul}|^2\,\tanh\left(\frac{hc\nu_l}{2k_BT}\right), \tag{5.84}$$

and

$$g(\nu) = \frac{\nu}{\nu_l}\frac{\tanh\left(\frac{hc\nu}{2k_BT}\right)}{\tanh\left(\frac{hc\nu_l}{2k_BT}\right)}[j(\nu)+j(-\nu)]. \tag{5.85a}$$

$j(\nu)$ is the power spectral density function or the Fourier transform of the time dependent autocorrelation function, $C(\tau)$, which describes the time evolution of the state of the absorbing molecule, and is expressed by

$$j(\nu) = \frac{1}{2\pi} \int\limits_{-\infty}^{\infty} d\tau \; e^{-j2\pi c\nu\tau} e^{j2\pi c\nu_0\tau} C(\tau), \qquad (5.85b)$$

where the autocorrelation function for a gas mixture is given by the product of individual autocorrelation functions,

$$C(\tau) = C_a(\tau)C_b(\tau)\cdots C_m(\tau), \quad \text{and} \quad g(\nu) = g(-\nu).$$

The subscripts designate the different types of molecules composing the gas. The normalization condition on $j(\nu)$ is

$$\int\limits_{0}^{\infty} d\nu \, j(\nu) = 1 \; \text{ for } \; C(0) = 1.$$

Note that $j(\nu)$ is a real and even function. More details on the autocorrelation function will be given in Section 5.6.3.

5.6.2 Line Strength

To complete the line strength expression requires specifying the partition function, $Q(T)$, the lower energy level E_l and the matrix elements $|\mu_{dp}|^2$. The partition functions are given for each class of molecule in Section 5.2.1. A polynomial representation of the partition function is often used to include coupling of rotational and vibrational motion. The lower energy levels are computed by the formulas of Chapter 3.

The matrix elements can be found by evaluation of $|\mu_{dp}|^2$. This has been done for certain molecules. Some analytical results are given below.

For rotational transitions in diatomic molecules in the electronic ground state, the matrix elements for the R- and P-branches are (see Herzberg, Ref. 5.15)

$$\left|\mu_{dp}\right|^2 \propto J + 1 \quad \text{for} \quad \Delta J = 1 \qquad (5.86a)$$

and

$$\left|\mu_{dp}\right|^2 \propto J \quad \text{for} \quad \Delta J = -1. \qquad (5.86b)$$

For vibrational transitions with the Morse anharmonic potential as given by Eq. 3.101b, the matrix element is (see Scholz, Ref. 5.38)

$$|\mu_{dp,nm}|^2 = \frac{q^2 h}{8\pi^2 c\nu_0 \mu'} \frac{\Gamma(m+n+1)}{n^2 \Gamma(m+1)}$$

$$\times \frac{j'(j'-1-2m)\,[j'-1-2(m+n)]\,\Gamma\left(j'-m-n\right)}{(j'-1-2m-n)^2 \Gamma(j'-m)}, \quad (5.87)$$

where n represents the number of vibrational quanta or the number of phonons in the transition and cannot exceed m_{max}. The transitions originate from the initial state m. $\Gamma()$ is a gamma function.

Also, matrix elements and lower energy levels for many gases are provided by the HITRAN database (see Section 7.2.2).

5.6.3 Line Shape Profiles

The most general classification of line shapes is either as homogeneous or inhomogeneous broadening. Homogeneous broadening means that all molecules have the same basic line shape characteristics. That is, if a line shape is observed for a collection of molecules, the same line shape will be observed for each molecule. Examples are natural broadening (radiation damping) and collision broadening. Inhomogeneously broadened lines represent a collection of shifted homogeneously broadened lines. Thus, each molecule's line shape may be completely different from the total line shape of a collection of molecules. Examples are Doppler broadening, nonuniform electric and magnetic fields in Stark and Zeeman effects, and inhomogeneities in a medium (such as crystalline strains and defects in solids). These concepts should become more clear when Doppler broadening is thoroughly treated.

5.6.3.1 Homogeneous Line Shapes

Two related cases will be considered. These are radiation damping (natural broadening) and collision broadening. Consider a perturbation to a quantum system, whether it be an incident photon or colliding molecule that will smear the energy level structure. Due to this probabilistic nature, an uncertainty results in observing the effects of the perturbation. This is manifested by the Heisenberg uncertainty principle,

$$\Delta x \Delta p = \Delta t \Delta E \approx \hbar.$$

Using $\Delta E = h \Delta f$, where Δf is the change in frequency,

$$\Delta t \Delta f \approx \frac{1}{2\pi} \rightarrow \Delta f = \frac{1}{\Delta t \, 2\pi} = \frac{\gamma}{2\pi}, \tag{5.88}$$

where γ is the reciprocal lifetime. A transition between two energy levels of a quantum system, which results in the emission or absorption of a photon, will have an uncertainty in the separation of the levels and therefore an uncertainty in the emitted photon frequency. Therefore,

$$\Delta f_{ul} = \Delta f_{lu} = \frac{1}{h} (\Delta E_u + \Delta E_l) = \frac{1}{2\pi} (\gamma_u + \gamma_l). \tag{5.89}$$

These concepts are illustrated in Fig. 5.3. A spread in frequency about line center of the transition results, which is the same for every molecule. The amount of spreading depends on the nature of the interaction: small shifts for radiation damping and large shifts for molecular-collision-driven conditions of the lower troposphere. A brief discussion of these different mechanisms will follow.

Natural Line Shape   The natural line shape, $g_N(\nu - \nu_o)$, is caused by fluctuations of the background electromagnetic field (see Appendix 5). The effect is small but is important in determining lifetimes of energy levels and astrophysical problems.

The line shape function, $j_N(\nu)$, is based on an exponential autocorrelation function (i.e., $C_N(\tau) = \exp(-\gamma_N \tau)$) and is a Lorentzian function,
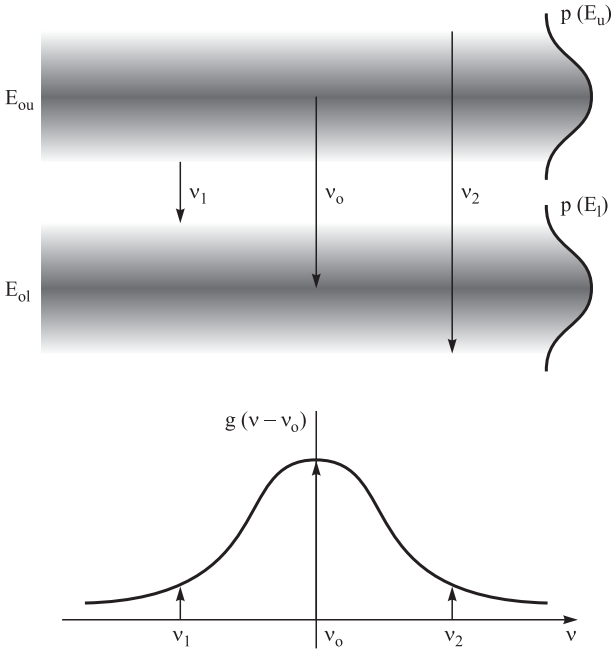
Fig. 5.3 Smearing of energy levels caused by external perturbations and the resulting line shape.

$$j_N(v - v_0) = \frac{1}{\pi} \left(\frac{\gamma_N}{(v - v_0)^2 + \gamma_N^2} \right). \tag{5.90}$$

γ_N is the half-width at half-intensity and related to the Einstein spontaneous emission coefficient by (Ref. 5.10)

$$\gamma_N = \frac{A_{ul}}{2\pi c} = \frac{1}{2\pi c t_{spontaneous}} \tag{5.91}$$

$t_{spontaneous}$ is the lifetime of the upper level and A_{ul} is the Einstein A-coefficient. Further, the line profile function becomes

$$g_N(v; v_0) = \frac{v}{v_0} \frac{\tanh[hcv/(2k_BT)]}{\tanh[hcv_0/(2k_BT)]} [j_N(v) + j_N(-v)]. \tag{5.92}$$

Near line center ($v \approx v_0$) and $v_0 \gg \gamma_N$,

$$g_N(v; v_0) = j_N(v \approx v_0). \tag{5.93}$$

Natural line widths are very narrow, making this an excellent approximation. Further, the line profile function, $g(\nu)$, is normalized as required by Eq. 3.31b within this approximation.

Collision-Broadened Line Shape   The collision-broadened line shape is essential for accurate atmospheric propagation models. Long-path propagation simulations require characterization of the line profiles far from line center, and the commonly used Lorentz line profile function is not adequate. This point is readily made by observing that the normalization condition of Eq. 3.31b cannot be satisfied by the simple Lorentz formula. Thus, a more complete theory must be applied, and the work of Birnbaum and Cohen will be followed because it leads to a simple, practical, and versatile line shape function (see Ref. 5.22). Other formalisms are also possible, but lead to complicated numerical techniques for a complete line profile representation. The Birnbaum–Cohen autocorrelation function for a binary mixture is semiempirically chosen to satisfy detailed balance (Eq. 5.78c) and is given by

$$
\begin{aligned}
C(\tau) &= C_a(\tau)\, C_b(\tau) \\
&= \exp\left\{\left[\tau_{a2} - \left(\tau_{a2}^2 + \tau^2 - j2\tau_0\tau\right)^{1/2}\right]/\tau_{a1}\right\} \\
&\quad \times \exp\left\{\left[\tau_{b2} - \left(\tau_{b2}^2 + \tau^2 - j2\tau_0\tau\right)^{1/2}\right]/\tau_{b1}\right\}.
\end{aligned}
\tag{5.94}
$$

$C_a(\tau)$ is the autocorrelation function for absorber–absorber and $C_b(\tau)$ is the autocorrelation function for absorber–broadener interactions. The relaxation times τ_1 and τ_2 represent the long-time and short-time behavior of the autocorrelation function. τ_o is a thermal time defined by

$$
\tau_0 = \frac{h}{4\pi k_B T}.
\tag{5.95}
$$

(For $T = 298\,\text{K}$, $\tau_o = 1.29 \times 10^{-14}$ sec.) The resulting line profile function and the Lorentz line shape is illustrated in Fig. 5.4.

The long-time behavior of the autocorrelation function becomes

$$
C(\tau \to \infty) = \exp\left(-|\tau|/\tau_1\right),
\tag{5.96}
$$

where the reciprocal of the relaxation time, τ_1, is

$$
\tau_1^{-1} = \tau_{a1}^{-1} + \tau_{b1}^{-1} = \gamma_c = \gamma_{ca} + \gamma_{cb}
$$

for a binary mixture and γ_c is the usual collision-broadened half-width at half-intensity. Based on the kinetic theory of gases, the temperature and pressure dependence of the collision–broadened half-width is

$$
\gamma_c = \gamma_{cbo}\left[\rho_b + (\gamma_{cao}/\gamma_{cbo})\,\rho_a\right]\sqrt{T},
\tag{5.97}
$$

$$
= \gamma_{cbo}\,(p_b + Bp_a)/T^{1/2},
$$
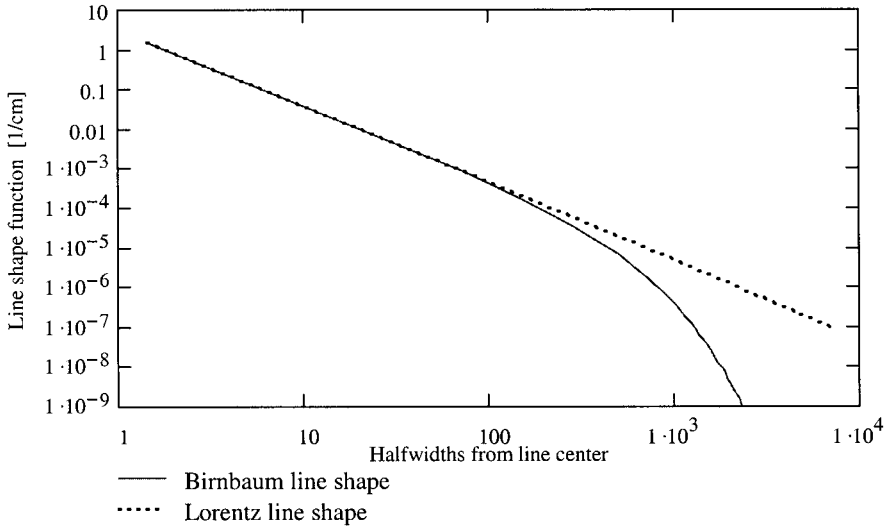
Fig. 5.4 Birnbaum line shape as function of frequency compared to the Lorentz line shape.

where $\rho = p/(k_B T)$ and the ratio $\gamma_{cao}/\gamma_{cbo}$ is the dimensionless self-broadening coefficient, B. Table 5.1 lists B-values for various atmospheric absorbing gases relative to nitrogen. The exponent of the temperature can vary between 0.5 and 1.0, based on experimental results and more complete theories. The predicted pressure dependence agrees very well with experimental data. This point is illustrated in Fig. 5.5. The curve becomes linear when collisions dominate and the pressure is high enough. The low-pressure half-width approaches the Doppler half-width, which will be covered in the next section. Collision-broadened half-widths do vary with the rotational quantum number, but only weakly with the vibrational quantum number.

The long-time autocorrelation function results in the near-line-center line shape function. Substituting Eq. 5.94 into Eqs. 5.85 and 5.79 results in the following near-line-center profile:

$$g_{NLC}(\nu; \nu_i) = \frac{\nu}{\nu_i} \frac{\tanh[hc\nu/(2k_B T)]}{\tanh[hc\nu_i/(2k_B T)]} [j_{NLC}(\nu) + j_{NLC}(-\nu)] \tag{5.98}$$

Table 5.1 Dimensionless Self-Broadening Coefficient, B, Relative to Nitrogen and Near Line Center

Molecule	B
H_2O	5
CH_4	1.3
N_2O	1.24
CO	1.02
CO_2	1.3
O_3	1.0
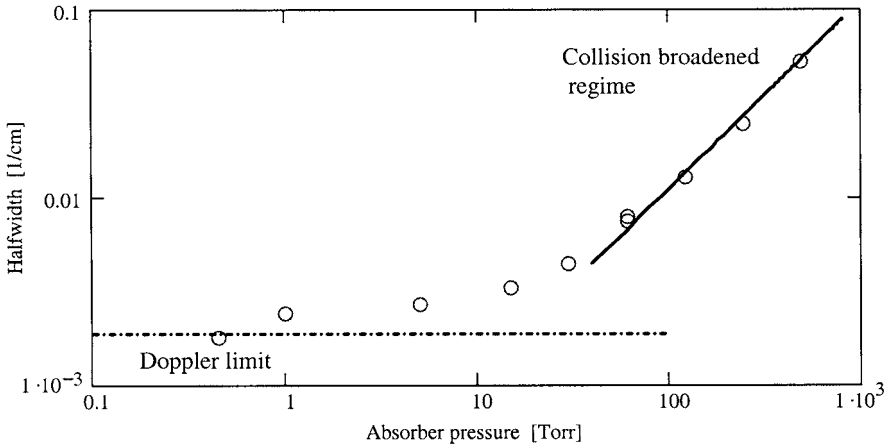
Fig. 5.5 The half-width versus absorbing gas pressure for the 11^10-00^00 $R(24)$ line of CO_2 located in the 5 μm region.

and

$$j_{NLC}(\nu) = \frac{1}{\pi} \left(\frac{\gamma_c}{\left(\nu - \nu_i - \gamma_{c,i}\right)^2 + \gamma_c^2} \right) \tag{5.99}$$

where the conversion to wave numbers has been made ($\gamma_c \rightarrow 2\pi c\gamma_c$). This result is consistent with the FASCODE model (see Section 7.4) and, for $hc\nu/k_B T$ small, the MPM model (see Section 7.4). Equation 5.99 includes a pressure shift term, $\gamma_{c,i}$, which occurs in more general theories, producing a complex γ_c ($\gamma_{c,i} = \text{Im}[\gamma_c]$). Pressure shift contributions are roughly 10–100 times smaller than $\text{Re}[\gamma_c]$ and for this reason usually are ignored. However, it can be important for laser or narrow-band system propagation (e.g., atmospheric lidar) when operating near a spectral absorption line. The pressure and temperature dependence is similar to the half-width as given by kinetic theory model,

$$\gamma_{c,i} = \left(\gamma_{cbo,i}\rho_b + \gamma_{cao,i}\rho_a\right)\sqrt{T}. \tag{5.100}$$

The pressure shift is usually negative, depends on the quantum numbers of the absorption line, and is on the order of a few milli-wave numbers per atmosphere.

Many of the popular line shapes can be obtained from these formulas by using various approximations. It should be noted that most of these approximations are not always appropriate for the RF–millimeter region. Thus, when in doubt about the correct line shape for a particular application, use the most general model.

One important shortcoming of this near-line-center model is that it does not include line-mixing effects. That is, the coupling of neighboring lines, which results in the alteration of the near-line-center line shape. This is important for O_2 absorption of the 60 GHz band (see Ref. 5.28 and 5.29) and for CO_2 (see Ref. 5.30 and 5.31), but greatly complicates absorption line modeling. A relatively simple modified Lorentz line shape, as given by Rosenkranz and applied to O_2, is given by

$$j_{NLC}(v) = \frac{1}{\pi} \left(\frac{\gamma_c + (v - v_i) y_i}{(v - v_i - \gamma_{c,i})^2 + \gamma_c^2} \right), \tag{5.101}$$

where y_i is the coupling constant, representing the effects of neighboring energy levels on the levels involved in the transition.

The leading factor in the line shape profile, as given by

$$\frac{v}{v_0} \frac{\tanh[hcv/(2k_B T)]}{\tanh[hcv_0/(2k_B T)]} = H(v, T; v_0), \tag{5.102}$$

is an important part of this model and makes $g(v)$ more general than other shape functions, such as developed in Chapter 4 and Section 5.3.3. Furthermore, $g(v)$ reduces to other models in appropriate limits. The following examples illustrate this point.

Classical limit ($h \to 0$)

$$g_{NLC}(v; v_0) \quad \xrightarrow[h \to 0]{} \quad \left(\frac{v}{v_0} \right)^2 [j_{NLC}(v; v_0) + j_{NLC}(-v; v_0)].$$

This result is consistent with the classical oscillator model of Eq. 4.33 for $v_0 \gg 0$.

$v \to 0$

$$g_{NLC}(v; v_0) \quad \xrightarrow[h \to 0]{} \quad \frac{bv^2/T}{v_0 \tanh(bv_0/T)} [j_{NLC}(v) + j_{NLC}(v)],$$

where $b = hc/(2k_B)$. The frequency-squared dependence is commonly observed at microwave and millimetre-wave frequencies.

$v = v_0$

$$g_{NLC}(v_0; v_0) = [j_{NLC}(v_0) + j_{NLC}(-v_0)],$$

Thus, at line center the profile is Lorentzian.

$bv \gg T$ and $bv_0 \gg T$ (infrared approximation)

$$g_{NLC}(v; v_0) \quad \xrightarrow[\substack{bv \gg T \\ bv_0 \gg T}]{} \quad \frac{v}{v_0} [j_{NLC}(v) + j_{NLC}(-v)]$$

A plot of $H(v; v_0)$ is given in Fig. 5.6 as a function of v for $T = 296$ K, showing the low-frequency and high-frequency limiting forms of this function.

The short-time behavior of the autocorrelation function leads to the far-wing character of the profile. The real part short-time behavior ($\tau \to 0$) of Eq. 5.94 becomes (ignoring foreign gas effects)

$H(\nu, 296, 100)$

$$\frac{\nu}{100} \cdot \frac{1}{\tanh\left(\dfrac{h\cdot c\cdot 100}{2\cdot k_B\cdot 296}\right)}$$

$$\frac{(\nu)^2}{100} \cdot \frac{\dfrac{h\cdot c}{2\cdot k_B\cdot 296}}{\tanh\left(\dfrac{h\cdot c\cdot 100}{2\cdot k_B\cdot 296}\right)}$$
- - - -
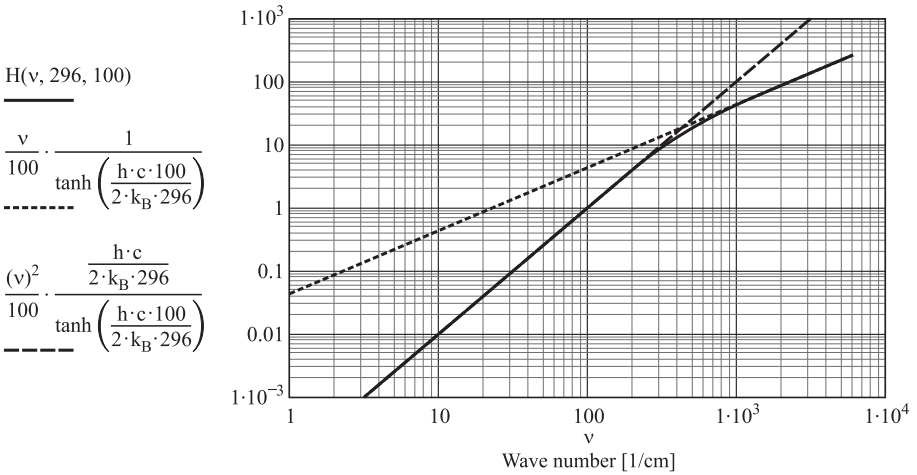
Wave number [1/cm]

Fig. 5.6 H-function versus wave number for a line-center position of 100 cm^{-1} and $T = 296$ K.

$$C(\tau) \underset{\tau \to 0}{\longrightarrow} e^{-\tau^2/(2\tau_{a1}\tau_{a2})}. \tag{5.103}$$

The Gaussian form is consistent with theoretical models of the autocorrelation function (Davies et al., Ref. 5.12). Thus a complete line shape is specified from line center to the far wing. The far wing result has been obtained for the case of a single absorbing molecule (i.e., $C(\tau) = C_a(\tau)$) and is given by (Birnbaum, Ref. 5.23)

$$g_{FW}(\nu; \nu_i) = \frac{\nu}{\nu_i} \frac{\tanh\left[hc\nu/(2k_B T)\right]}{\tanh\left[hc\nu_i/(2k_B T)\right]} j_{FW}(\nu) \tag{5.104}$$

and

$$j_{FW}(\nu) = \left(\frac{\tau_{a2}}{2\pi}\right)^{1/2} \frac{1}{\tau_{a1}} \frac{\exp\left(-2\pi c \left|\nu - \nu_i\right| \tau_{a2}\right)}{4\pi^2 \left|\nu - \nu_i\right|^{1.5}} \exp\left[2\pi c \left(\nu - \nu_i\right) \tau_0\right]. \tag{5.105}$$

The exponential wing is consistent with experimental observation (see Refs. 5.23 and 5.35). The general far-wing result for a binary mixture can be obtained by solving a convolution integral of the individual line shape functions (j_a and j_b) in the far-wing limit. Thus, given

$$j_a(\nu) = \frac{1}{2\pi} \int_{-\infty}^{\infty} d\tau \; e^{-j2\pi c\nu} C_a(\tau), \tag{5.106a}$$

$$j_b(\nu) = \frac{1}{2\pi} \int_{-\infty}^{\infty} d\tau \; e^{-j2\pi c\nu} C_b(\tau), \tag{5.106b}$$

and based on Eq. 5.79, the net line shape becomes

$$j(v) = \int\limits_{-\infty}^{\infty} j_a(x) \, j_b(v - v_j - x) \, dx. \tag{5.107}$$

Then using contour integration, in the far-wing limit, we obtain

$$j_{FW}(v) = \left(\frac{\tau_{a2}}{2\pi}\right)^{1/2} \frac{1}{\tau_{a1}} \frac{\exp\left(-2\pi c \, |v - v_i| \, \tau_{a2}\right)}{4\pi^2 \, |v - v_i|^{1.5}} \exp\left[2\pi c \, (v - v_i) \, \tau_0\right]$$

$$+ \left(\frac{\tau_{b2}}{2\pi}\right)^{1/2} \frac{1}{\tau_{b1}} \frac{\exp\left(-2\pi c \, |v - v_i| \, \tau_{b2}\right)}{4\pi^2 \, |v - v_i|^{1.5}} \exp\left[2\pi c \, (v - v_i) \, \tau_0\right]. \tag{5.108}$$

This approach can be expanded to include gas mixtures with more than two different species of molecules. This is important for applications concerning propagation in planetary atmospheres. In particular, the atmosphere of the earth contains nitrogen and oxygen as primary broadeners of an absorbing gas.

The formula for the autocorrelation function given by Eq. 5.94 agrees with theoretical and experimental results with regard to near-line-center and far-wing phenomena. Because the function is continuous in time, a complete line shape function is specified. The closed-form expression for the line shape has been obtained for a pure gas:

$$j(v) = \frac{\tau_1}{\pi} e^{\tau_2/\tau_1} \frac{e^{2\pi c v_- \tau_o} Z_- K_1 (Z_-)}{1 + (2\pi c v_- \tau_1)^2} + \frac{e^{2\pi c v_+ \tau_o} Z_+ K_1 (Z_+)}{1 + (2\pi c v_+ \tau_1)^2}, \tag{5.109}$$

where

$$v_{\pm} = v \pm v_0, \qquad Z_{\pm} = \left[\tau_1^{-2} + v_{\pm}^2/(2\pi c)^2\right]^{1/2} \left(\tau_2^2 + \tau_0^2\right)^{1/2} \tag{5.110}$$

and $K_1(Z_{\pm})$ is the modified Bessel function of the second kind of first order. This line shape is consistent with the near-line-center results obtained earlier and in addition provides insight into the nature of the far wing as previously shown. Most importantly, a complete line shape allows proper normalization according to Eq. 3.31b. The following result is obtained:

$$\int\limits_{-\infty}^{\infty} dv \, g(v, v_0) = \left(1 + \frac{\gamma_1 \gamma_2}{\gamma_0 v_0}\right) \coth\left[hc v_0/(k_B T)\right]. \tag{5.111}$$

For practical values of the parameters this line profile function is normalized to one.

A line shape formula for homogeneous collision-broadened lines has been developed that is compatible with the Phillips Laboratory HITRAN database. The line shape has validity from line center to the far wing. Local line absorption and far-wing continuum absorption can now be modeled in greater detail. The present formalism, however, lacks line overlap or coupling effects. More advanced models are being developed to address these issues in line shape theory (Refs. 5.26–5.31).

5.6.3.2 Inhomogeneous Line Shapes

Doppler Line Shape   The random kinetic motion of molecules is driven by the thermal energy and causes a Doppler shift of the narrow homogeneously broadened molecule. Molecules with different velocities will be shifted by different amounts, so that a new line shape results in the form of an inhomogeneous Doppler profile.

Derivation of this effect begins with Doppler's equation,

$$v = \frac{(c - v)v_0}{c}, \quad \text{or} \quad v = \frac{c(v_0 - v)}{v_0}, \tag{5.112}$$

where v is the velocity of the molecule of mass m and v_0 the radiating frequency of the molecule. Recall the Boltzmann factor for a system in thermal equilibrium,

$$f(E) = e^{-E/k_B T}. \tag{5.113}$$

Using the classical formula for kinetic energy, $E = \frac{1}{2}mv^2$, and the previous equations it follows that

$$f(v) = \exp\left(-\left(\frac{c(v - v_0)}{v_0}\right)^2 \frac{m}{2k_B T}\right). \tag{5.114}$$

This represents the probability distribution of shifted frequencies due to velocity components of the atoms parallel to the incident photon field. Since Doppler lines are very narrow, it is valid to enforce normalization on the spectral density function, accounting for absorption as well as emission, thus

$$\int_0^\infty [j_D(v - v_0) + j_D(v + v_0)] \, dv = 1. \tag{5.115}$$

The Doppler spectral density function is commonly expressed as

$$j_D(v - v_0) = \frac{(\ln 2)^{1/2}}{\gamma_D/\sqrt{\pi}} \exp\left(-\frac{(v - v_0)^2 (\ln 2)}{\gamma_D^2}\right), \tag{5.116}$$

where the Doppler half-width at half-intensity is

$$\gamma_D = \left(\frac{2k_B T \ln |2|}{mc^2}\right)^{1/2} v_0 = 3.578 \times 10^{-7} \sqrt{\frac{T}{m}} \, v_0, \tag{5.117}$$

where T is the temperature in kelvins, m is the molecular mass in amu, and v_0 is the line-center frequency in cm^{-1}. Because Doppler lines are narrow, a good approximation is

$$g_D(v - v_0) \approx j_D(v - v_0). \tag{5.118}$$
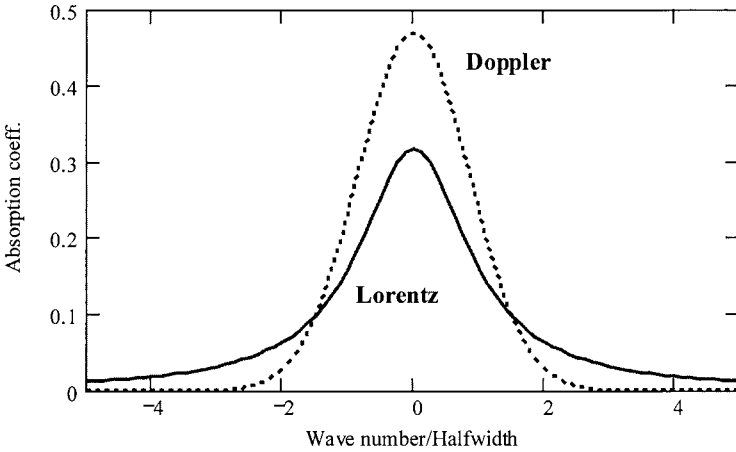
Fig. 5.7 A comparison between the Doppler and Lorentz line shapes for equal line strength and half-width.

Example 5.3 Find the Doppler half-width of H_2O at $T = 295$ K and $\nu_0 = 3600$ cm^{-1}.

The molecular mass of H_2O is 18 amu, therefore the Doppler half-width is $\gamma_D = 0.021$ cm^{-1}. The collision-broadened half-width for H_2O at $T = 295$ K and a total pressure of 1 atm is typically 0.07 cm^{-1}. Thus, neither the Doppler nor the collision-broadened line shape dominates. This situation is examined in the next section.

The Gaussian form is considerably different from the Lorentz function. The wings in the Doppler line shape fall off much more rapidly. This heightens the function at line center. A comparison of the two shapes for equal strength and width is given in Fig. 5.7.

Voigt Line Shape   The Doppler line shape assumes the shifted homogeneous line shapes are delta functions, which is usually a good approximation at very low pressures. The natural line shape is always present in any experiment and, in problems of atmospheric importance, collision broadening is present. Thus the pure Doppler profile is never observed. A real line shape contains the effects of motion on the homogeneous line shape absorbers. This is the Voigt line shape.

Figure 5.8 illustrates the shifted homogeneous line shape weighted by a Gaussian (Doppler) distribution. This process can be thought of as a convolution of a homogeneous shape, $g_H(\nu)$, through a Doppler profile. Thus,

$$g_v(\nu, \nu_0) = \int_0^\infty g_H(\nu, \nu') \left[j_D(\nu' - \nu_0) + j_D(\nu' + \nu_0) \right] d\nu'. \qquad (5.119)$$

The resulting line shape is called the Voigt line shape, $g_v(\nu)$. From the definition of the above equation, the normalization condition can be seen to be satisfied:

$$\int_0^\infty g_v(\nu, \nu_0) \, d\nu = 1. \qquad (5.120)$$
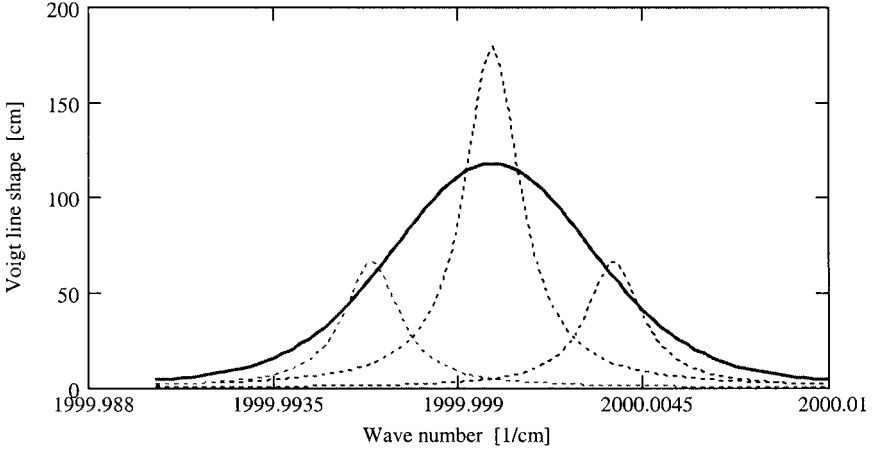
Fig. 5.8 Voigt line shape illustration. The dotted curves are the Doppler-shifted homogeneous line shape components of the Voigt line shape.

The homogeneous line shape most often used is the Lorentz profile (but it may not always apply). Substituting in the Lorentz and Doppler line shapes and ignoring the emission term,

$$g_v(v, v_0) = \frac{\gamma_H}{\pi^{3/2}\gamma_D} (\ln 2)^{1/2} H(v, T) \int_0^\infty \frac{\exp\left\{-\left[(v_0 - v')^2 (\ln 2)/\gamma_D^2\right]\right\}}{[(v - v_0) - (v' - v_0)]^2 + \gamma_H^2} dv'. \tag{5.121}$$

Making the following variable and parameter substitutions,

$$y = \frac{v' - v_0}{\gamma_D} (\ln 2)^{1/2}, \quad \xi(v) = \frac{v - v_0}{\gamma_D} (\ln 2)^{1/2},$$

and

$$a = \frac{\gamma_H}{\gamma_D} (\ln 2)^{1/2},$$

then Eq. 5.121 becomes

$$g_v(v, v_0) = \frac{\gamma_H}{\pi^{3/2}\gamma_D^2} (\ln 2)^{(\ln 2)} H(v, T) \int_{-\infty}^\infty \frac{\exp\left(-y^2\right)}{[\xi(v) - y]^2 + a^2} dy. \tag{5.122}$$

In the low-pressure limit the line profile is Doppler, and in the high-pressure limit the line profile is collision broadened. The collision-broadened line shape dominates when $\gamma_c/\gamma_D > 4$. The half-width of the Voigt shape connects these distinct pressure regions as well. This fact can be seen in Fig. 5.5. No closed-form representation exists for the Voigt profile, and numerical techniques are commonly used (see Ref. 5.36). However, at line center a closed form solution can be obtained, using a complementary error function, to be

$$g_v(\nu_0) = \left(\frac{\ln 2}{\pi}\right)^{\frac{1}{2}} \frac{1}{\gamma_D} e^{a^2} \text{erfc}\,(a). \tag{5.123}$$

5.6.4 Refractivity

Recall from Chapter 2 (Eq. 2.52a) that the index of refraction is the Hilbert transform of the index of absorption. Substituting the expression for the index of absorption in terms of the absorption coefficient into that expression, the following is obtained:

$$n(\nu, T) = 1 + \frac{1}{2\pi^2} \sum_i S_i P \int_0^\infty \frac{g(\nu_i, \nu')}{\nu'^2 - \nu^2}\, d\nu'. \tag{5.124}$$

The index of refraction (real part) comes from local line absorption phenomena based on the Hilbert transform. In the transparent region of a medium where weak absorption features contribute very little to the index of refraction, the refractive index is determined by distant line-center contributions of strong absorption bands. Thus the following approximation can be made:

$$g(\nu, \nu_i) \approx \delta(\nu - \nu_i) + \delta(\nu + \nu_i).$$

Substituting this expression into Eq. 5.124, we obtain a Sellmeier formula (recall Eq. 4.18), as given by

$$n^2(\nu, T) = 1 + \frac{\langle \nu_{Rot}\rangle^2 \Delta\epsilon_{Rot}(T)}{\langle \nu_{Rot}\rangle^2 - \nu^2} + \sum_i \frac{\langle \nu_{Vib}\rangle_i^2 \Delta\epsilon_{vib,i}(T)}{\langle \nu_{Vib}\rangle_i^2 - \nu^2} + \sum_k \frac{\langle \nu_{El}\rangle_k^2 \Delta\epsilon_{El,k}(T)}{\langle \nu_{El}\rangle_k^2 - \nu^2}, \tag{5.125}$$

where $\langle \nu \rangle$ is the average band position for rotational, vibrational, and electronic bands. The sum on i represents the different vibrational bands of a gas. The sum on k represents the different electronic bands of a gas. The oscillator strength is

$$\Delta\epsilon(T) = \frac{8\pi}{3hc\epsilon_0} \rho_a \frac{\langle |\mu_{dp}|^2\rangle}{\langle \nu \rangle} \tanh\left(\frac{hc\langle \nu \rangle}{2k_B T}\right) \tag{5.126}$$

for pure rotational bands and vibrational bands below 500 cm^{-1}, and

$$\Delta\epsilon(T) = \frac{8\pi}{3hc\epsilon_0} \rho_a \frac{\langle |\mu_{dp}|^2\rangle}{\langle \nu \rangle} \tag{5.127}$$

for vibrational and electronic bands (where the approximation $\tanh[hc\langle \nu \rangle/(2k_B T)] \approx 1$ is used for line-center frequencies above 500 cm^{-1}). The sum over all rotational lines within the band negates the contribution from the rotational partition function. Thus the only significant temperature dependence comes from the density of the gas. Equation 5.125 is identical to the classical formula of Eq. 4.18, except more details are represented by the model parameters, in particular the temperature dependence for far-infrared absorption bands.

When weak local line or anomalous dispersion is important, the complete near-line-center profile must be used. A closed-form expression based on Eq. 5.124 cannot be obtained in general. However, closed-form solutions in various limits within the collision broadened regime are tractable. The results are summarized below for frequencies below 400 cm^{-1}, where $\tanh[hc\nu/(2k_BT)] \approx hc\nu/(2k_BT)$ and above 500 cm^{-1}, where $\tanh[hc\nu/(2k_BT)] \approx 1$ and T is in the range of typical atmospheric temperatures.

$\nu < 400\ cm^{-1}$

$$n^2(\nu) = 1 + [2\pi hc/(k_BT)] \sum_i S_i \nu_i \{[(\gamma_i/\nu_i)\, j_{NLC}(\nu) - f(\nu)]$$
$$+ [(\gamma_i/\nu_i)\, j_{NLC}(-\nu) - f(-\nu)]\} \tag{5.128}$$

$\nu > 500\ cm^{-1}$

$$n^2(\nu) = 1 - 4\pi \sum_i S_i [f(\nu) + f(-\nu)], \tag{5.129}$$

where the dispersion shape function is defined to be

$$f(\nu) = \frac{1}{\pi} \frac{\nu - \nu_i}{(\nu - \nu_i)^2 + \gamma_i^2}. \tag{5.130}$$

The above formulas do not include line-mixing contributions (see Ref. 5.37). However, line mixing should be a minor correction.

5.7 Quantum Electronics

As was demonstrated in Chapter 4, the classical oscillator model for vibrational transitions had the same mathematical form whether the medium was in the gas phase or the solid phase. This will basically remain true for the quantum oscillator model as well. This point will be demonstrated in Chapter 8. However, electronic transitions in the solid phase require a new model. The classical oscillator does not represent experimental data at and above the bandgap. This is because the spectral shape is driven, not by the surroundings of the oscillator, but by the density-of-states function for electronic transitions.

Because the application of the models developed in this section emphasizes optoelectronic devices using semiconductor materials, the traditional title is used.

5.7.1 Electronic Band-to-Band Transitions

The electronic band structure of solids and electronic density-of-states was introduced in Chapter 3. We now consider transitions caused by photon absorption between these bands to obtain the complex permittivity and absorption coefficient above the bandgap.

The model derivation begins with Fermi's golden rule for a harmonic perturbation (Eq. 5.40),

$$\Gamma_{i \to f} = \frac{2\pi}{\hbar} \left| \langle f | \hat{H}_{int} | i \rangle \right|^2 \delta(E_f - E_i - \hbar\omega).$$

In this case, E_f is the conduction band energy and E_i the valance band energy of an electron. Thus for a direct bandgap semiconductor of bandgap energy E_g, the electronic energy levels can be expressed as

$$E_f = \frac{\hbar^2 k^2}{2m_c} + E_g \quad \text{and} \quad E_i = -\frac{\hbar^2 k^2}{2m_v}. \tag{5.131}$$

m_c is the effective electron mass in the conduction band and m_v is the effective vacant electron (hole) mass in the valance band. The energy difference between the final and initial electronic states is

$$E_f - E_i = \frac{\hbar^2 k'^2}{2} \left(\frac{1}{m_c} + \frac{1}{m_v} \right) + E_g = \frac{\hbar^2 k'^2}{2\mu_e} + E_g, \tag{5.132}$$

where μ_e is the reduced mass.

The matrix element for a dipole moment operator coupled to a classical electromagnetic field is

$$\langle f | \hat{H}_{int} | i \rangle = \left(q \int d^3 r u_f^*(\mathbf{r}) e^{-j\mathbf{k}_f' \cdot \mathbf{r}} \mathbf{r} u_i(\mathbf{r}) e^{j\mathbf{k}_i' \cdot \mathbf{r}} \right) \cdot \left(\frac{1}{2} \mathbf{E} e^{j\mathbf{k}_{opt}' \cdot \mathbf{R}} + \frac{1}{2} \mathbf{E} e^{-j\mathbf{k}_{opt}' \cdot \mathbf{R}} \right), \tag{5.133}$$

where Eq. 3.153 is used for the electronic wave function. As discussed in Chapter 3 for vibrational modes, the optical wave vector is essentially zero, compared with the wave vector representing lattice dimensions. Thus, we assert that $k_{opt}' \approx 0$. Furthermore, the oscillating factors in the wave function are very rapid and reduce the transition probability, unless the condition $k_i' = k_f'$ is met. (If no phonons are involved in the electronic transition then it is called a direct bandgap transition.) That is, the maximum of the valance band and the minimum of the conduction band align on the k'-axis. Otherwise an indirect bandgap exists (no alignment of the bands), which then involves the creation of a phonon, as well as the conduction electron. Optoelectronic semiconductor materials, such as GaAs and InP, have direct bandgaps. Employing these approximations, Fermi's golden rule for the electronic transition rate now becomes

$$\Gamma_{i \to f} = \frac{2\pi}{\hbar} q^2 |\mathbf{E}|^2 \left| \int d^3 n u^*(\mathbf{r}) \mathbf{r} u(\mathbf{r}) \right|^2 \delta \left(\frac{\hbar^2 k'^2}{2\mu_e} + E_g - \hbar\omega \right). \tag{5.134}$$

The total number of valence to conduction band transitions per second can be computed by multiplying the transition rate by the electronic density-of-states and integrating over all k', as given by

$$\dot{N}_{el} = -\int \Gamma_{i\to f}(k')\rho(k')\,dk'. \tag{5.135}$$

The rate of change is negative because the number of valance band electrons is decreasing. Furthermore, to perform this calculation requires that the dipole moment operator in the transition rate be explicitly described in terms of k' or momentum ($p = \hbar k'$). It can be shown that the interaction Hamiltonian can be rewritten using the magnetic vector potential, a (see Problem 5.17) as

$$q\mathbf{r} \cdot \mathbf{e} = -q\frac{\mathbf{p}}{m} \cdot \mathbf{a} \tag{5.136}$$

where in the Coulomb gauge

$$\mathbf{e} = -\frac{\partial \mathbf{a}}{\partial t}. \tag{5.137}$$

Using the above result and Eq. 3.154 for the electronic density-of-states, Eq. 5.135 becomes

$$\dot{N}_{el} = -\frac{2V}{\pi\hbar}q^2|\mathbf{A}|^2 \int |V_{if}(k')|^2\delta\left(\frac{(\hbar k')^2}{2\mu_e} + E_g - \hbar\omega\right)k'^2\,dk' \tag{5.138}$$

where the reduced matrix element is

$$|V_{if}(k')|^2 = \left|\int d^3r\,u_f(k')\frac{\hat{\mathbf{p}}}{m}u_i(k')\right|^2. \tag{5.139}$$

Let us make the following variable substitution:

$$z = \frac{(\hbar k')^2}{2\mu_e} + E_g - \hbar\omega.$$

It follows that

$$k'(z) = \sqrt{\frac{2\mu_e}{\hbar^2}\left(z - E_g + \hbar\omega\right)} \quad \text{and} \quad dk' = \frac{\mu_e}{\hbar^2}\sqrt{\frac{\hbar^2}{2\mu_e}}(z - E_g + \hbar\omega)^{-\frac{1}{2}}dz.$$

Making these substitutions into Eq. 5.138 and evaluating the integral, we obtain the following result for the number of electronic transitions per unit time:

$$\dot{N}_{el} = -\frac{V}{\pi}q^2|\mathbf{A}|^2|V_{if}\left[k'(0)\right]|^2\frac{(2\mu_e)^{3/2}}{\hbar^4}(\hbar\omega - E_g)^{1/2}. \tag{5.140}$$

The absorption coefficient above the bandgap can be obtained by applying Eq. 5.59 to the above result, thus

$$\beta_{abs}(\omega) = \frac{2q^2(2\mu_e)^{3/2}}{cn(\omega)\epsilon_0\pi\hbar^3}|V_{if}\left[k'(0)\right]|^2\frac{(\hbar\omega - E_g)^{1/2}}{\omega}, \tag{5.141}$$
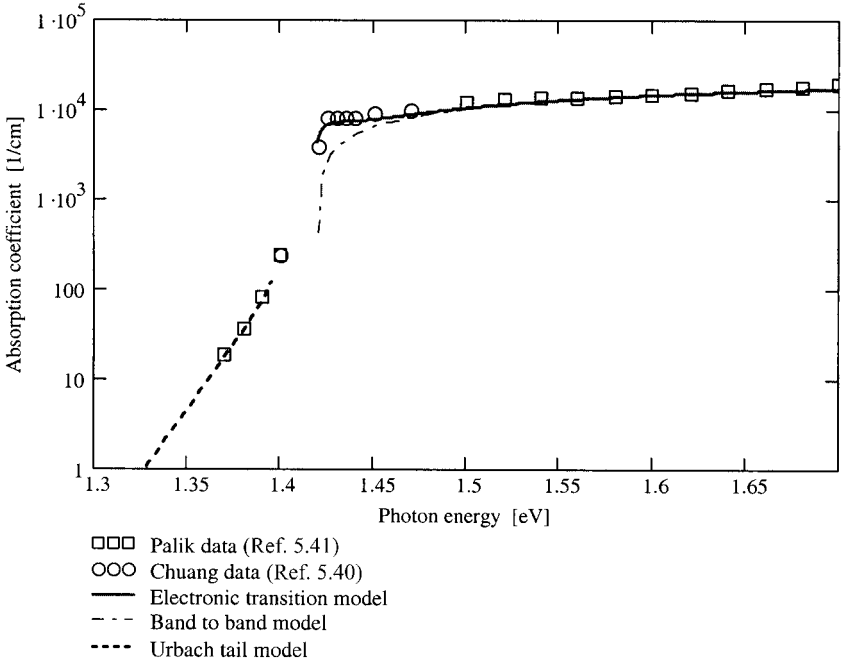
Fig. 5.9 The room-temperature absorption coefficient near the bandgap of intrinsic GaAs.

where we have used the relation $|E|^2 = \omega^2 |A|^2$. Using Eq. 2.29, the corresponding imaginary part of the complex permittivity (electric susceptibility) is obtained:

$$\epsilon_r''(\omega) = \chi''(\omega) = \frac{2q^2(2\mu_e)^{3/2}}{\epsilon_0 \pi \hbar} |V_{if}(k'(0))|^2 \frac{(\hbar\omega - E_g)^{1/2}}{\hbar^2 \omega^2} H\left(1 - \frac{\hbar\omega}{E_g}\right), \qquad (5.142)$$

where $H(\ )$ is a Heaviside step function in the frequency domain. The absorption profile is assumed to be homogeneous. The Hilbert transform of the above (see Appendix 3) produces the real part of the complex susceptibility,

$$\chi'(\omega) = \frac{2q^2}{\epsilon_0 \pi \hbar}\left(\frac{2\mu_e}{E_g}\right)^{3/2}\left|V_{if}\left[k'(0)\right]\right|^2\left(\frac{E_g}{\hbar\omega}\right)^2$$
$$\times\left[2 - \left(1 + \frac{\hbar\omega}{E_g}\right)^{1/2} - \left(1 - \frac{\hbar\omega}{E_g}\right)^{1/2} H\left(1 - \frac{\hbar\omega}{E_g}\right)\right] \qquad (5.143)$$

Other electronic band-to-band transitions exist in real materials, and the above model will refer to as E_0 transitions. An example of this model compared with real complex index data on GaAs is presented in Fig. 5.9.
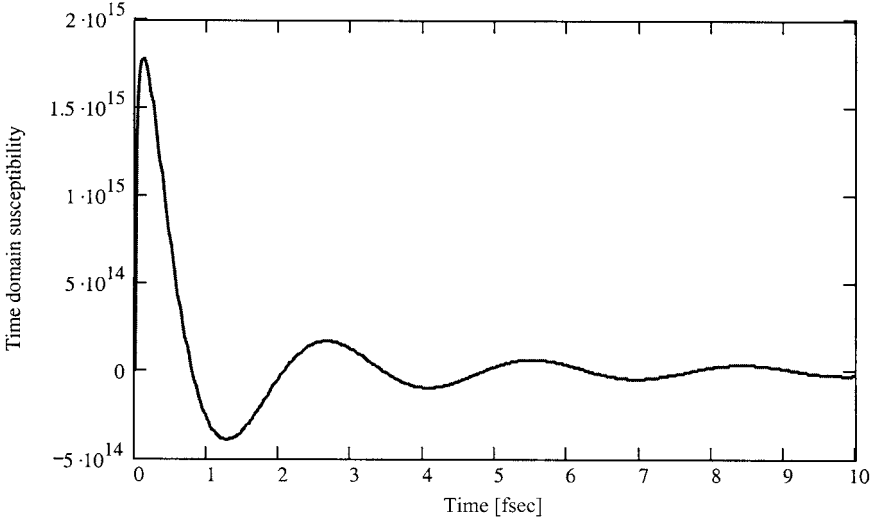
Fig. 5.10 The time-domain electric susceptibility for the E_0 transition of GaAs at room temperature.

The inverse Fourier transform of the complex susceptibility (Eqs. 5.141 and 5.143) leads to the time-domain susceptibility for the E_0 region, as given by

$$\chi_{e0}(t) = \frac{2}{\pi} \frac{A_0}{E^{1.5}} \omega_0 \left\{ \sqrt{\pi \omega_0 t} \cos\left(\omega_0 t + \frac{\pi}{4}\right) - \pi \omega_0 t \right. $$

$$\left. + \pi \left[\left(\omega_0 t + \frac{1}{2}\right) C\left(\sqrt{\frac{2\omega_0 t}{\pi}}\right) + \left(\omega_0 t - \frac{1}{2}\right) S\left(\sqrt{\frac{2\omega_0 t}{\pi}}\right) \right] \right\} h(t), \quad (5.144)$$

where

$$A_0 = \frac{2q^2}{\epsilon_0 \pi \hbar} (2\mu_e)^{3/2} |V_{if} \left[k'(0)\right]|^2,$$

$\omega_0 = E_g/\hbar$, and $C(x)$ and $S(x)$ are the Fresnel cosine and sine integral functions, respectively. The details of this derivation are presented in Appendix 3. A plot of the resulting time-domain electric susceptibility for the E_0 transitions in GaAs is given in Fig. 5.10. Because of the large bandwidth of this transition, the oscillations in the susceptibility decay very rapidly, on the order of femtoseconds.

5.7.2 Exciton Band Absorption

Excitons are electron–hole pairs that are bonded together to form a hydrogen-like structure. These are very weak, broad (at room temperature) structures that are important in certain optoelectronic devices. In this case, excitons act independently and are distinct,

thus a modified form of the classical oscillator model is applied. The lowest frequency exciton is located at the bandgap and the complex permittivity is given by

$$\chi_{ex0}(\omega) = \frac{A_{x0}}{E_g - E_{x0} - \hbar\omega - j\Gamma_{x0}} + \frac{A_{x0}}{E_g - E_{x0} + \hbar\omega - j\Gamma_{x0}}. \qquad (5.145)$$

This function also satisfies the Kramers–Krönig relation. The model is applied to GaAs absorption in Fig. 5.9 (A_{x0} = 2.35 meV, Γ_{x0} = 3.5 meV, and E_{x0} = 4.7 meV). Although better agreement with measurement is obtained just above the bandgap, the model is incorrect below the bandgap. This point will be discussed further in Chapter 8.

5.7.3 Band Edge Absorption and Urbach's Rule

In 1953, Franz Urbach observed that the absorption coefficient of silver chloride increased exponentially for increasing frequency near its bandgap energy. Urbach was able to characterize the frequency dependence with a simple exponential curve. Further improvements include temperature dependence, and now the formula is given by

$$\beta_{abs}(E, T) = \beta_{U0} \exp\left[\sigma_s(E - E_g)/(k_B T)\right], \qquad (5.146)$$

where β_{abs} is the absorption coefficient (typically in cm^{-1}), β_{U0} is a scaling coefficient in units cm^{-1}, E_g is the bandgap energy at absolute zero temperature, typically given in units of eV, k_B is Boltzmann's constant, and T is temperature in kelvins. The exponent factor σ_s was later discovered to be temperature dependent for some materials, and is given by the following equation (see Ref. 5.43):

$$\sigma_s(T) = \sigma_o \frac{2k_B T}{E_p} \tanh \frac{E_p}{2k_B T}, \qquad (5.147)$$

where E_p is an effective acoustic phonon energy of the material. The absorption coefficient, β_{abs}, can then be used to calculate the transmittance. Figure 5.9 illustrates the comparison of the Urbach model with experimental data as a function of frequency. The representation is clearly quite good.

The following is a heuristic derivation of Urbach's rule (see Ref. 5.44). No formal derivation currently exists that fully explains the general applicability of this formula.

Because phonons are bosons, at thermal equilibrium the average number of phonons in the jth mode (ω_j) is given by Eq. 5.15. The standard deviation of the phonon occupation number N_j is

$$\sigma_{Nj} = \left(\langle N_j^2 \rangle - \langle N_j \rangle^2\right)^{1/2} = \langle N_j \rangle \left(1 + 1/\langle N_j \rangle\right)^{1/2}. \qquad (5.148)$$

Thus phonons have comparatively large occupancy fluctuations. This will cause smearing of the bandgap and the generation of exciton red-wing absorption near bandgap frequencies. We assume that the effective local bandgap at a temperature T is the bandgap at 0 K, $E_g(0)$, minus a constant times the average phonon occupation number for each direction:

$$E_g(T) = E_g(0) - \sum_{i=x,y,z} A\langle N_i \rangle. \tag{5.149}$$

Because the speed of light effectively freezes, in time, the fluctuating phonons propagating in any local region of a solid, it is not necessary to compute the average number and we can write

$$E_{g,local}(T) = E_g(0) - A(N_x + N_y + N_z). \tag{5.150}$$

Now the probability that a particular cell of the propagating medium contains a particular phonon occupation number N_x, N_y, N_z is

$$p_n(T) = \frac{e^{-(N_x+N_y+N_z)\hbar\omega_p/k_BT}}{(1 - e^{-\hbar\omega_p/k_BT})^3} = p_{nx}\,p_{ny}\,p_{nz}, \tag{5.151a}$$

where $\omega_p \,(= E_p/\hbar)$ is the phonon frequency. At NTP and uv photon frequencies, the phonon shifts must be large to be important. For such phonons, $\hbar\omega_p/(k_BT)$ is large and it follows that

$$1 - e^{-\hbar\omega_p/(k_BT)} \approx 1.$$

Therefore, Eq. 5.151a reduces to

$$p_n(T) = e^{-(N_x+N_y+N_z)\hbar\omega_p/k_BT}. \tag{5.151b}$$

Using Eq. 5.149 and solving for the phonon occupation number, the following is obtained:

$$N_x + N_y + N_z = \left[E_g(0) - \hbar\omega\right]/A, \tag{5.152}$$

where $E_{g,local} = \hbar\omega$, because this local region couples to the photon field by phonon-shifting the bandgap. The absorption coefficient must be proportional to p_n as a function of the various local bandgaps. Thus, substitution of Eq. 5.152 into Eq. 5.151b suggests the following form of the absorption coefficient:

$$\beta_{abs}(\nu, T) = \beta_{U0}\, e^{-\sigma(E_g(0) - \hbar\omega)/k_BT} \tag{5.153}$$

where the constant σ is defined as

$$\sigma = \frac{\hbar\omega_p}{A}.$$

This result closely matches Urbach's rule, as given by Eq. 5.145.

Problems

5.1 Compute the vibrational partition function for a single harmonic oscillator, given by

$$Q_{Vib} = \sum_v g_v e^{-E_v/(k_B T)}, \quad \text{where} \quad g_v = 1.$$

Compute the ratio of the number of molecules in the vibrational ground state ($v = 0$) to the first excited state ($v = 1$) for $v_e = 1595$ cm^{-1} at room temperature, that is

$$\frac{N_v = 1}{N_v = 0} = ?$$

5.2 Is the rotational partition function as given by Eq. 5.6 valid for OH? Check this by performing a discrete sum (Eq. 5.3) and comparing the result with the closed-form expression.

5.3 Find an expression for the band-limited irradiance of a planar blackbody, that is, find

$$\int_{v_1}^{v_2} dv M_{BB}(v) = ?$$

Find the result for $v_1 = 0$ and $v_2 = \infty$.

5.4 Compute the power spectral density function $j_c(\Delta\omega)$ given

$$C(t) = e^{-\gamma t}, \quad \gamma = \gamma_r - j\gamma_i,$$

where γ is in general complex, $\Delta\omega = \omega - \omega_0$, and

$$j_c(\Delta\omega) = \frac{1}{\pi} \text{Re}\left[\int_0^\infty dt\, e^{-j\Delta\omega t} C(t)\right].$$

5.5 What are the units of S_{lu} given β_{abs}[cm^{-1}] and v[cm^{-1}].

5.6 Use the definition of line strength and the collision line shape $j_c(\Delta\omega)$,

$$j_c(\Delta\omega) = \frac{1}{\pi} \frac{\gamma_c}{(\Delta\omega)^2 + \gamma_c^2}$$

where $\gamma_c = \gamma_0 p_a T^{-1/2}$, to find the temperature and pressure dependence of the absorption coefficient at line center ($\Delta\omega = 0$) for a medium containing only the absorbing gas. Do the same for the far wing ($\Delta\omega \gg \gamma_c$).

5.7 Obtain a closed-form expression for the Voigt line shape at line center.

5.8 Given that, for a diatomic molecule, the magnitude of the dipole moment matrix element squared is proportional to $J + 1$, (a) determine the shape of the pure rotational band for CO by computing the line-center absorption coefficient relative to the line $J = 0$ as a function of J-number ($J = 1$ to 30) at room temperature ($T = 295$ K), and (b) the same for $T = 600$ K. (Assume all half-widths are equal.)

5.9 Find the far-wing absorption coefficient for a binary gas mixture, explicitly showing pressure and temperature dependence. (a) Use the Lorentz line shape. (b) Use the Birnbaum–Cohen line shape.

5.10 Based on Eqs. 5.125 and 5.126, find the temperature and pressure dependence of the index of refraction of a gas with all vibrational bands above 500 cm^{-1}. What is the temperature dependence of the refractive index as ν goes to zero?

5.11 Differential absorption lidar (DIAL) can be used to measure the number density of an absorbing species. To do this accurately requires that the absorption feature be temperature independent. Determine an expression, involving the lower energy level of the transition, that minimizes the temperature dependence of the line-center absorption coefficient of a gas in the collision-broadened regime. (Use the quantum oscillator model.)

5.12 Based on the mode density within a cavity (from Chapter 1, Eq. 1.15f) and the Bose–Einstein distribution, obtain the blackbody formulas, as given by Eqs. 5.16a and b. The relationship between the energy density of the field, u, and the power per unit area (Poynting's vector) must be found to obtain Eq. 5.16b.

5.13 The direction of the dipole moment, $\hat{\mathbf{d}}$, and the direction of the electric field, $\hat{\boldsymbol{\varepsilon}}_\sigma$ ($\sigma = 1, 2$), in many situations are random relative to one another. For this reason, the magnitude of the dot product summed over all possible polarizations can be averaged over all relative dipole orientations. For a TEM wave, the two polarization directions and the direction of propagation form a complete basis set, which spans 3-D coordinate space. Thus, the dipole direction can be expressed in terms of the field coordinates, as given by

$$\hat{\mathbf{d}} = (\hat{\mathbf{d}} \cdot \hat{\boldsymbol{\varepsilon}}_1)\hat{\boldsymbol{\varepsilon}}_1 + (\hat{\mathbf{d}} \cdot \hat{\boldsymbol{\varepsilon}}_2)\hat{\boldsymbol{\varepsilon}}_2 + (\hat{\mathbf{d}} \cdot \hat{\mathbf{k}}')\hat{\mathbf{k}}'.$$

For real basis vectors, we have

$$\sum_\sigma (\hat{\mathbf{d}} \cdot \boldsymbol{\varepsilon}_\sigma)^2 = (\hat{\mathbf{d}} \cdot \boldsymbol{\varepsilon}_1)^2 + (\hat{\mathbf{d}} \cdot \boldsymbol{\varepsilon}_2)^2 = 1 - \cos^2 \theta_d,$$

where θ_d is the angle between the dipole moment and the direction of propagation and $|\hat{\mathbf{d}}|^2 = 1$. Now integrate the above result over all angles θ_d and ϕ_d to obtain the orientational average.

5.14 Derive the far wing form of the Birnbaum line shape for a binary mixture, as given by Eq. 5.108.

5.15 Verify Eq. 5.116 for the Doppler line shape.

5.16 Verify Eq. 5.125, based on Eqs. 5.124 and 5.84.

5.17 Show that the first-order interaction Hamiltonian between the photon field and a molecule

$$\hat{H}_{int} = -\frac{q}{m}\,\hat{\mathbf{p}} \cdot \hat{\mathbf{a}}$$

can be expressed as

$$H_{ap} = \hat{\boldsymbol{\mu}}_{\boldsymbol{dp}} \cdot \hat{\mathbf{E}} \ .$$

Hint: Since the oscillator is driven by the field, both the oscillator and field change at the same rate in time and can be represented by the general form

$$f(t) = f_0 \mathrm{e}^{j\omega t}.$$

5.18 Verify Eq. 5.148 for the standard deviation of a boson occupation number.

5.19 Show that Birnbaum–Cohen autocorrelation function satisfies detailed balance (Eq. 5.85b).

Bibliography

General

5.1 M. Weissbluth, *Photon-Atom Interactions*, Academic Press (1989).

5.2 H. Haken, *Light: Waves, Photons, Atoms*, Vol. I, North Holland (1986).

5.3 E. Goldin, *Waves and Photons: An Introduction to Quantum Optics*, Wiley (1982).

Section 5.2

5.4 N. Davidson, *Statistical Mechanics*, McGraw-Hill (1962).

5.5 R.W. Boyd, *Radiometry and the Detection of Optical Radiation*, Wiley (1983).

Section 5.3

5.6 G. Baym, *Lectures on Quantum Mechanics*, W.A. Benjamin (1973).

5.7 D. Marcuse, *Engineering Quantum Electrodynamics*, Harcourt, Brace and World, (1970); the most recent version is, D. Marcuse, *Principles of Quantum Electronics*, Academic Press (1980).

Section 5.4

5.8 P.W. Milonni and J.H. Eberly, *Lasers*, Wiley (1988).

Section 5.5

5.9 A. Einstein, "Zur Quantentheorie der Strahlang," *Physik, Z.* **18**, 121 (1917).

Section 5.6

5.10 R.G. Breene, Jr., *Theories of Spectral Line Shape*, Wiley (1981).

5.11 C.J. Tsao and B. Curnutte, "Line-Widths of Pressure-broadened Spectral Lines," *J. Quant. Spectrosc. Radiat. Transfer* **2**, 41 (1962).

5.12 R.W. Davies, R.H. Tipping, and S.A. Clough, "Dipole Auto correlation Function for Molecular Pressure Broadening: A Quantum Theory which Satisfies the Fluctuation-Dissipation Theorem; *Phys. Rev.* **26**, 3378 (1982).

5.13 R.G. Gordon, "Correlation Functions for Molecular Motion," *Adv. Mag. Res.* **3**, 1 (1968).

5.14 G. Herzberg, *Infrared and Raman Spectra of Polyatomic Molecules*, Van Nostrand Reinhold (1945).

5.15 G. Herzberg, *Spectra of Diatomic Molecules*, 2nd Ed., Van Nostrand Reinhold (1950).

5.16 G. Herzberg, *Electronic Spectra and Electronic Structure of Polyatomic Molecules*, Van Nostrand Reinhold (1966).

5.17 E.J. McCartney, *Absorption and Emission by Atmospheric Gases*, Wiley (1983).

5.18 J.H. Van Vleck and V.F. Weisskopf, "On the Shape of Collision-Broadened Lines," *Rev. Mod. Phys.* **17**, 227–236 (1945).

5.19 P.W. Anderson, "Pressure Broadening in the Microwave and Infra-red Regions," *Phys. Rev.* **76**, 647 (1949).

5.20 D.L. Huber and J.H. Van Vleck, "The Role of Boltzmann Factors in Line Shape," *Rev. Mod. Phys.* **38**, 187–204 (1966).

5.21 J.H. Van Vleck and D.L. Huber, "Absorption, Emission and Linebreadths: A Semihistorical Perspective," *Rev. Mod. Phys.* **49,** 939–959 (1977).

5.22 G. Birnbaum and E.R. Cohen, "Theory of Line Shape in Pressure-Induced Absorption," *Can. J. Phys.* **54**, 593–602 (1976).

5.23 G. Birnbaum, "The Shape of Collision Broadened Lines from Resonance to the Far Wing," *J. Quant. Spectrosc. Radiat. Transfer* **21**, 597 (1979).

5.24 C. Boulet and D. Robert, "Short Time Behavior of the Dipole Autocorrelation Function and Molecular Gases Absorption Spectrum," *J. Chem. Phys.* **77**, 4288–4299 (l982).

5.25 L.S. Rothman (ed.), *SPIE Proceedings: Modeling of the Atmosphere* **928** (1988).

5.26 Q. Ma and R.H. Tipping, "Water Vapor continuum in the millimeter Spectral Region," *J. Chem. Phys.* **93**, 6127–6139 (1990), and "The Atmospheric Water Continuum in the Infrared: Extension of the Statistical Theory of Rosenkranz," *J. Chem. Phys.* **93**, 7066–7075 (1990).

5.27 P.W. Rosenkranz, "Pressure Broadening of Rotational Bands. I. A Statistical Theory," *J. Chem. Phys.* **83**, 6139 (1985), and "Pressure Broadening of Rotational Bands. II. Water Vapor from 300 to 1100 cm^{-1}," *J. Chem. Phys.* **87**, 163 (1987).

5.28 P.W. Rosenkranz, "Shape of the 5 mm oxygen band in the atmosphere, "*IEEE Trans. Antennas Propagat.* **23**, no. 4, 498–506 (1975).

5.29 P.W. Rosenkranz, "Interference coefficients for overlapping oxygen lines in air," *J. Quant. Spectros. Radiat. Transfer* **39**, 287–297 (1988).

5.30 L.L. Strow, "Line Mixing in Infrared Atmospheric Spectra," *SPIE Proceedings, Modeling of the Atmosphere* **928**, 194–212 (1988).

5.31 J.M. Hartman and C. Boulet, "Line Mixing and Finite Duration of Collision Effects in Pure CO_2 Infrared Spectra: Fitting and Scaling Analysis," *J. Chem. Phys.* **94**, 6406–6419 (1991).

5.32 See 5.12.

5.33 C.H. Wang, *Spectroscopy of Condensed Media: Dynamics of Molecular Interactions*, Academic Press (1985).

5.34 P.L. Roney, "Theory of Spectral Line Shape. I. Formulation and Line Coupling," *J. Chem. Phys.* **101**, 1037–1049 (1994), and "Theory of Spectral Line Shape. II. Collision Time Theory and Line Wing," *J. Chem. Phys.* **101**, 1050–1060 (1994).

5.35 M.E. Thomas, "Infrared- and Millimeter-Wavelength Continuum Absorption in the Atmospheric Windows: Measurements and Models," *Infrared Phys.* **30**, 161–174 (1990).

5.36 C. Young, "Calculation of the Absorption Coefficient for Lines with Combined Doppler and Lorentz Broadening," *J. Quant. Spectros. Radiat. Transfer* **5**, 549 (1965), and J.F. Keilkopf, "New Approximation to the Voigt Function with Applications to Spectral Line Profile Analysis," *J. Opt. Soc. Am.* **63**, 987 (1973).

5.37 K. Tomiyama, S.A. Clough and F.K. Kneizys, "Unified Real Part of the Susceptibility for Collisional Broadening," Report No. AFGL-TR-86-0181, Air Force Geophysics Laboratory, Hanscom AFB, MA, 15 August (1986).

5.38 K. Scholz, "Zur quantum mechanischen Berechnung von Intensitäten ultraroter Banden," *Z. Phys.* **78**, 751 (1932).

Section 5.7

5.39 A. Yariv, *Quantum Electronics*, 2nd Ed., Wiley (1975).

5.40 S.L. Chuang, *Physics of Optoelectronic Devices*, Wiley-Interscience (1995).

5.41 E.D. Palik (ed.), *Handbook of Optical Constants of Solids*, Academic Press (1985).

5.42 P. Bhattacharya, *Semiconductor Optoelectronic Devices*, Prentice-Hall (1994).

5.43 F. Urbach, "The Long-wavelength Edge of Photographic Sensitivity and of the Electronic Absorption of Solids," *Phys. Rev.* **92**,1325 (1953).

5.44 T. Skettrup, "Urbach's Rule Derived from Thermal Fluctuations in the Band Gap Energy," *Phys. Rev. B* **18**, 2622 (1978).

6

Experimental Techniques

This chapter presents basic experimental techniques and various apparatus for measuring the complex index of refraction and related quantities. Generally, measurements of transmittance, reflectance, and emittance are made using spectrometers or lasers. Other important techniques, which measure directly the real refractive index, n, the absorption coefficient, β_{abs}, and the scattering coefficient, β_{sca}, such as interferometry, ellipsometers, calorimetry, and scatterometers, are also introduced. Ultimately, experimental procedures must be taught in the laboratory. Thus, devoting only one chapter to experimental technique and five to theory is not indicative of the importance of this fundamental topic.

By discussing the measurement of basic optical parameters, it is intended that the concepts developed in the first five chapters will be reinforced. All of the theoretical models developed in the previous chapters contain measurable parameters. Basic theory often helps guide the design of a good experiment. Once data is available, it can be used to check the assumptions of the theory. This interplay between experiment and theory is an essential part of definitive work.

The chapter has two main parts; the first covers measurements of the real and imaginary parts of the complex index of refraction and the second covers measurements of scattering.

6.1 Refractive Index and Absorption Coefficient Measurements

As established in Chapter 2, the characterization of bulk absorption mechanisms on optical propagation is accomplished by the complex index of refraction. Considerable

effort was expended in Chapters 3, 4, and 5 to obtain models of the complex index. Thus, at this point, we wish to find ways to experimentally measure the complex index of refraction for various media.

The broad-band spectral response of a medium is commonly measured by a spectrometer. There are two main types of spectrometers, dispersive and interferometric. Generally, spectrometers make broad-band transmission, emission, and reflection measurements, and therefore indirectly measure, $\bar{n}$. Interferometric measurements, are the exception. Lasers, which feature narrow-band, high-intensity, highly directional light are often used to complement and calibrate broad-band spectrometer measurements. The highest accuracy measurements of the absorption coefficient are obtainable by laser techniques, which can directly measure the components of the complex index.

6.1.1 Transmission and Reflection Measurements

Transmission and reflection measurements are the most common methods for determining optical properties of media. The strength of this approach is that broad spectral coverage can be easily obtained with adequate accuracy (1% to 0.1%) for low-power transmission windows and thin films. High-power optics and optical fibers are very sensitive to small absorption coefficient values, and therefore other approaches are needed. Also, other more precise techniques are used to determine the real part of the complex index of refraction. Such alternate approaches will be described later.

Based on Chapter 2, it is known that transmittance measurements are sensitive to both the real and imaginary parts of the complex index of refraction. Recall the specular transmittance formula for near-normal illumination by an unpolarized source, ignoring scattering and interference, as based on Eq. 2.96 and Fig. 2.4,

$$\tau[\bar{n}(\nu,T), \theta_i] = \frac{\{1 - R[n(\nu,T), \theta_i]\}^2 \, e^{-\beta_{\text{abs}}(\nu,T)d(\theta_i)}}{1 - R^2[n(\nu,T), \theta_i] \, e^{-2\beta_{\text{abs}}(\nu,T)d(\theta_i)}}, \tag{6.1}$$

where the internal path length is

$$d(\theta_i) = d/\cos\left[\sin^{-1}\left(\frac{n_1}{n_2}\sin\theta_i\right)\right]$$

and d is the thickness of the medium. Furthermore, recall from Chapter 2 the definition of the complex index and the relation between the absorption coefficient and the imaginary part of the complex index,

$$\bar{n}(\nu,T) = n(\nu,T) - jk_a(\nu,T) \quad \text{and} \quad \beta_{abs}(\nu,T) = 4\pi\nu k_a(\nu,T). \tag{6.2}$$

At normal incidence, the magnitude of the single-surface power reflection coefficient reduces to

$$R[\bar{n}(\nu,T), \theta_i = 0] = \frac{|\bar{n}(\nu,T) - 1|^2}{|\bar{n}(\nu,T) + 1|^2} = \frac{[n(\nu,T) - 1]^2 + k_a^2(\nu,T)}{[n(\nu,T) + 1]^2 + k_a^2(\nu,T)}. \tag{6.3}$$

These formulas are the basis for analysis of most transmittance and reflectance measurements.

For a gaseous medium, R is negligibly small and the transmittance depends only on the absorption coefficient (which is now a function of pressure also) and path length. Thus, in this case, a transmittance measurement is a straightforward way to obtain the absorption coefficient of a gas without knowing the refractive index.

This is not the case for solids and liquids, and a second measurement must also be made to completely determine the complex index, $\bar{n}$. This is usually the reflectance (or some other measure of the real part of the complex index of refraction). Then, by using the total power law, the complex index can be obtained.

This approach and a variety of other experimental techniques are discussed in the following after a brief introduction to spectrometers is completed.

6.1.1.1 Spectrometers and Broad-Band Measurements

Today, spectrometers are of two types, dispersive and interferometric. Dispersive spectrometers spatially separate the frequencies of an incident light beam. Prisms (refractive elements) and gratings (diffractive elements) are used as the dispersive elements. Prisms were first used by Isaac Newton (1672) to study the colors in sunlight. Basically, prisms separate the frequencies because the refractive index increases monotonically with increasing frequency, and by modern standards, are low-resolving instruments. Later, they were replaced by diffraction gratings, which offer higher degrees of dispersion and therefore higher resolution. The first high-quality gratings were made by Professor Henry Rowland of Johns Hopkins University in the 1880s. The governing equation for diffraction gratings was developed by Joseph Fraunhofer. It is called the grating equation and is given by

$$m\lambda = a(\sin\alpha \pm \sin\beta), \tag{6.4}$$

where m is an integer representing the diffracted order, λ is the wavelength of the light incident on the grating, a is the grating constant (distance between successive groves), α is the angle of incident rays relative to the grating normal, and β is the angle of diffraction relative to the grating normal.

The resolving power, R, of a diffraction grating is the ratio of the frequency to the minimum resolvable frequency difference between two closely spaced lines. It is given by

$$R = \frac{mw}{a}, \tag{6.5}$$

where w is the width of the grating. Substituting Eq. 6.4 for m, the resolving power becomes

$$R = w\frac{\sin\alpha \pm \sin\beta}{\lambda}. \tag{6.6}$$

Figure 6.1 is a diagram of a typical grating spectrometer for use in the infrared and visible. Other configurations are used for various applications. For example, tunable laser resonators often incorporate gratings in the Littrow configuration ($\alpha = \beta$). Also, concave gratings are commonly used in single-element ultraviolet spectrometers.

Rotation of the grating generates the frequency axis of the spectrum. A typical measurement sequence begins with a background or reference measurement. This provides a
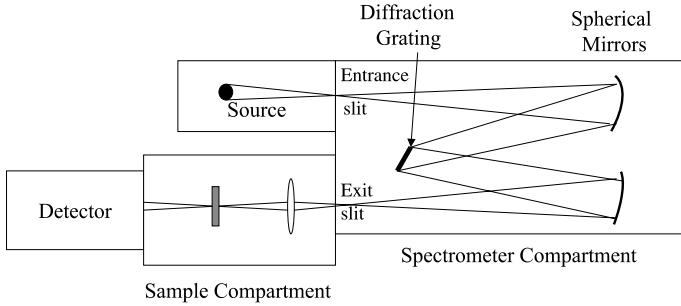
Fig. 6.1 Cernzy–Turner grating spectrometer system for visible and infrared measurements.

calibration of the system at that moment. Then the sample is inserted into the beam and another scan is made. The ratio of these two transmission (or reflection) measurements is the transmittance, τ (or reflectance, ρ). Unfortunately, the background measurement is never perfect, for a variety of reasons. The source can change temperature from the time of the reference run to the sample run, vibrations in the building can cause slight misalignment of the optics, and so on. It is best to keep the time between the reference and sample runs to a minimum. However, no matter what approach is taken, τ will contain errors. A good way to study some of these errors is take two consecutive backgrounds, determine their ratio, and see how close to unity the system can come. This ratio is called a baseline. As a rule of thumb, the experimental parameters should be chosen so that the system noise level is on the order of, or less than, the baseline drift. Baselines can be corrected when other information is available, such as laser measurements or calibrating to a region with no loss. Unfortunately, no compensation can be found for noise.

One partial solution to this background problem is a dual-beam spectrometer. Two sample compartments are used, one for sample and one for reference using the same split source. Thus sample and reference spectra are collected *simultaneously*. Of course, a background-ratioed spectrum must still be taken to calibrate the system and the useful signal is reduced. Dual-beam grating spectrometers have the best baseline stability and greatest absolute accuracy of any spectrometer today.

Three fundamental problems limit grating spectrometer performance:

1. The grating position must be calibrated to obtain an accurate frequency axis.
2. The slits must be made narrower for higher resolution, thus the system throughput is greatly reduced.
3. The time between the measurement of the first frequency and last frequency can be very large, and the sample or system may have changed. (This last item can be overcome if a linear detector array is used to simultaneously measure the spectrum at the output slit.)

Today, most infrared spectroscopy is conducted with Fourier transform spectrometers. They are based on the Michelson interferometer, which is illustrated in Fig. 6.2.
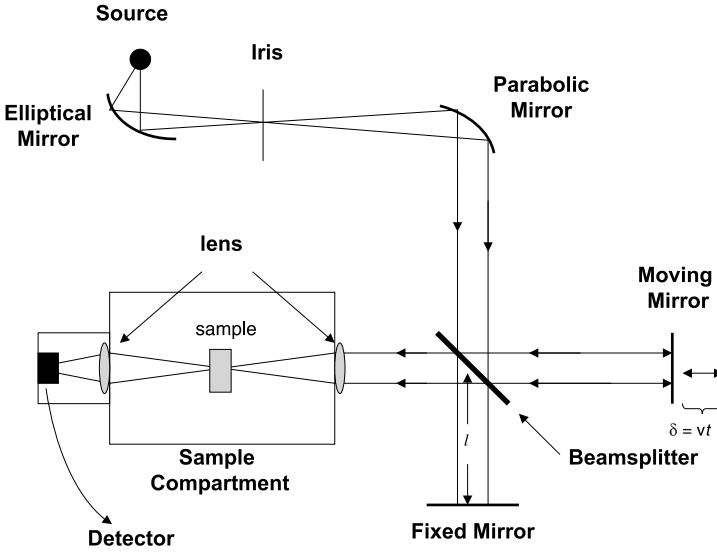
Fig. 6.2 The Fourier transform spectrometer.

To see how the Fourier transform spectrometer (FTS) works, consider a single-frequency source (i.e., a laser). Let the electric field incident upon the beamsplitter be represented by

$$\mathbf{e}_{BS}(t) = \mathbf{e}_0 \cos(\omega t). \tag{6.7}$$

The beam is divided into two equal beams, which travel a path length $2l$ and $2(l + \delta)$ to a mirror, which returns the beams to the beamsplitter. The distance δ is determined by the moving mirror, which moves with constant velocity, v. Thus, δ becomes

$$\delta = vt. \tag{6.8}$$

By superposition at the beamsplitter the field transmitted to the sample compartment becomes

$$\mathbf{e}_{sc}(t) = \frac{1}{2}\mathbf{e}_0 \cos(\omega t + 2k'l) + \frac{1}{2}\mathbf{e}_0 \cos[\omega t + 2k'(l + \delta)] \tag{6.9}$$

where $k' = 2\pi v$. Using standard trigonometric identities, the above equation reduces to

$$\mathbf{e}_{sc}(t) = \mathbf{e}_0 \cos(k'\delta) \cos(\omega t + 2k'l + k'\delta). \tag{6.10}$$

This is the form of an amplitude-modulated high-frequency carrier. Optical detectors cannot respond to the carrier frequency, thus the intensity, I_{sc}, as seen by a detector is determined by a modulation envelope,

$$I_{sc} \propto |\mathbf{e}_{sc}|^2 = |\mathbf{e}_0|^2 \cos^2(k'\delta) = I_{0sc} \cos^2(k'\delta). \tag{6.11}$$

Again using standard trigonometric identities, the above formula becomes

$$I_{sc} = \frac{1}{2}I_{0sc}\left[1 + \cos(2k'vt)\right] \tag{6.12}$$

where Eq. 6.8 was used to represent δ. The moving mirror modulates the single-frequency source, and an oscillating output intensity results. An observer who knows the location of the moving mirror as a function of time can determine the frequency spectrum of the source, based on the modulated beam spectral content by the above formula. This basically explains how a Michelson interferometer can be used to obtain a spectrum for a narrow-band source.

In the case of a broad-band spectrum, consider an incremental portion of that spectrum, then Eq. 6.12 can be applied in the following way:

$$I_{sc}(k',\delta)dk' = \frac{1}{2}I_{0sc}(k')\left[1 + \cos(2k'\delta)\right]dk'. \tag{6.13}$$

The total intensity at the detector as a function of time or the mirror displacement, δ, is obtained by integration of the above equation over the wave vector,

$$i_{sc}(t) = i_{sc}(\delta) = \frac{1}{2}\int_0^\infty I_{0sc}(k')\left[1 + \cos\left(2k'\delta\right)\right]dk'. \tag{6.14}$$

This is a sum of two integrals, as given by

$$i_{sc}(\delta) = \frac{1}{2}\int_0^\infty I_{0sc}(k')\,dk' + \frac{1}{2}\int_0^\infty I_{0sc}(k')\cos(2k'\delta)\,dk'. \tag{6.15}$$

$I_{0sc}(k')$ is the spectral intensity that we wish to determine, based on the measurement of $i_{sc}(t)$. The first term in the above expression for $i_{sc}(\delta)$ is one-half the area under the spectral intensity, or the total intensity of the light in the sample compartment. It can also be expressed as

$$i_{sc}(0) = \int_0^\infty I_{0sc}(k')\,dk'. \tag{6.16}$$

Therefore, the time-domain signal, or interferogram, as it is commonly called, is

$$i_{sc}(\delta) - \frac{1}{2}i_{sc}(0) = \frac{1}{2}\int_0^\infty I_{0sc}(k')\cos(2k'\delta)\,dk'. \tag{6.17}$$

This is an inverse Fourier transform relationship between the spectral intensity and the time-domain interferogram. Thus the spectral intensity can be obtained directly by the following:

$$I_{0sc}(k') = \frac{2}{\pi}\int_0^\infty \left[i_{sc}(\delta) - \frac{1}{2}i_{sc}(0)\right]\cos(2k'\delta)\,d\delta. \tag{6.18}$$

This relationship between the measured signal and the spectral intensity gives this spectrometer its name. The FTS offers a number of advantages over dispersive spectrometers.

1. Higher throughput is realized because slits are not used. However, high resolution requires a highly collimated beam and thus a spatial filter (i.e., iris), which also limits the throughput of the FTS, but not as much as the slits on a grating spectrometer. Thus higher resolution is possible with the FTS. Also, spectra can be obtained more quickly and thus more accurately (less system drift). However, the FTS is a single-beam instrument.
2. Usually, a stabilized He-Ne laser is used to calibrate the location of the moving mirror. This can be done very precisely, and accurate line positions are obtained with great ease as a result.
3. An entire spectrum is measured in one scan, which can be done fairly quickly. By co-adding scans, the noise can be reduced by $\sqrt{m}$ (m is the number of scans).

For these reasons, the FTS is the main tool today in infrared spectroscopy. At visible wavelengths, the stability of the moving mirror becomes an issue, and most commercial spectrometers stop there. For UV and VUV, the grating spectrometer is used, exclusively.

The resolution of an FTS is determined by the distance traveled by the moving mirror. That is, the frequency difference between two cosine waves is found by examining the cosine waves over an adequately long distance. The result is

$$\Delta \nu = \frac{1}{2\delta_{max}}, \tag{6.19}$$

where δ_{max} is the maximum distance traveled by the moving mirror.

No matter what type of spectrometer is used, it is desirable that the resolution be adequate to measure spectra with no distortion to the spectral shape. This is not always the case, and the system instrument function must then be considered. In the frequency domain, the measured spectrum is the convolution of the ideal spectrum with the system instrument function. This is stated mathematically as

$$I_{\text{measured}}(\nu) = I_{\text{ideal}}(\nu) * F_{\text{instr}}(\nu) \tag{6.20}$$

The instrument function for a grating spectrometer is the diffraction pattern of the slits. The instrument function for an FTS is determined by the chosen time-domain window function. To avoid ringing in the spectrum, the interferogram must go to zero smoothly at the end of the scan. A window function accomplishes this task. The distortion of an unresolved spectrum can be significant. This point is illustrated in Fig. 6.3, for Doppler lines with half-widths of 0.007 cm^{-1} measured with a resolution of 0.032 cm^{-1}.

6.1.1.2 Spectrometer Accessories

Many accessories exist for handing special samples or extending the capability of the sample compartment. We will consider transmissometers (single pass, multipath [i.e., White cells], and differential), reflectometers, photoacoustic cells, and total internal reflection or circle cells.

Transmissometers   A transmissometer measures the transmittance, τ, by ratioing a transmission measurement with the sample present against a transmission measurement
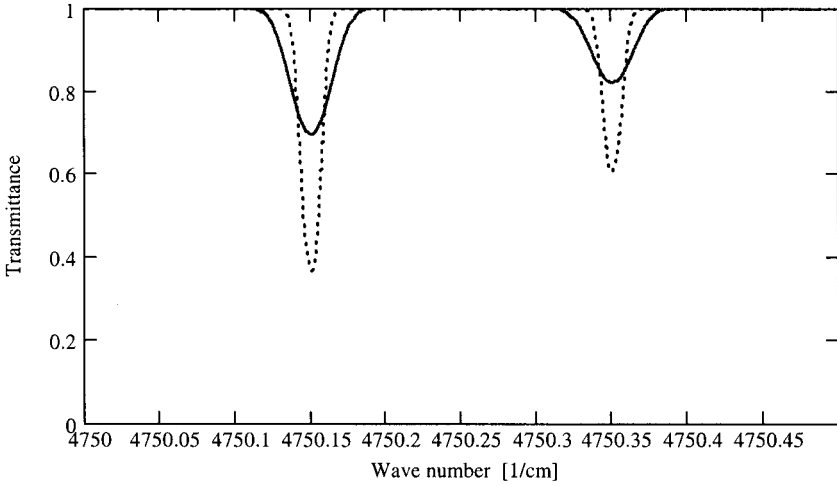
Fig. 6.3 An ideal (unconvolved) spectrum of Doppler-broadened lines with half-widths of 0.007 cm^{-1} (dot) and corresponding convolved FTS spectrum (solid) using a Hamming window with a resolution of 0.032 cm^{-1}.

with no sample present. A cell is used for gases or liquids and, of course, a solid needs no container. A single-pass transmissometer propagates a beam once though a sample, as illustrated in Fig. 6.4. A background run is performed with no sample present for the case of solids and with an empty cell in the case of gases and liquids or a nonabsorbing medium that matches the refractive index of the sample (this is important if the probe beam is focused within the sample).

In the case of gases, R is very close to zero, which simplifies Eq. 6.1. But gas absorption can be weak, often requiring long path lengths for accurate measurements. Multipath cells, such as a White cell, are commonly used to obtain a long optical path within an enclosure of reasonable size. The absorption cell assures reasonable uniformity of the sample pressure and temperature. The White cell is composed of three matched spherical mirrors, a field mirror, and two focusing mirrors, separated by the radius of curvature, as shown in Fig. 6.5.
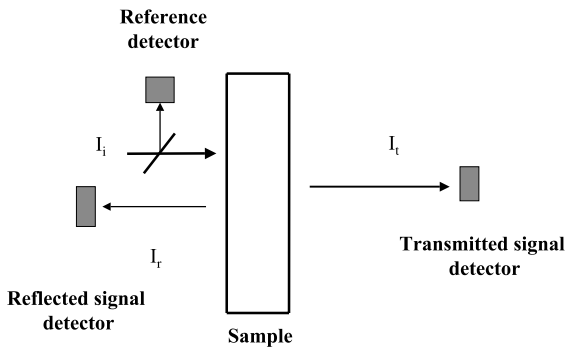
Fig. 6.4 A single-beam transmission/reflection measurement with a monochromatic source.
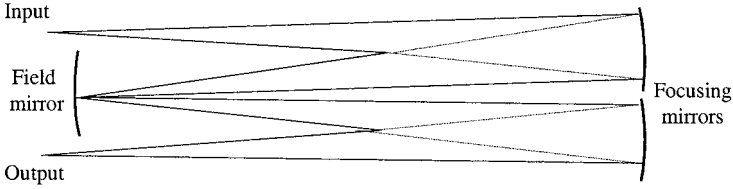
Fig. 6.5 White-type optics for long-path transmission set for four traversals. By tilting the focusing mirrors, the number of traversals can be varied beginning at 4 to some upper number, which can be a few hundred, depending on the size of the field mirror.

EXPERIMENTAL CONSIDERATIONS FOR WHITE-TYPE ABSORPTION CELLS   White-type absorption cells represent an important option for experimental apparatus presently used for the measurement of weak gas-phase absorption coefficients. Also, photoacoustic cells, another sensitive experimental tool based on the photoacoustic effect (see below), require calibration, which is usually accomplished by White cell measurements. White cells have a high surface-to-volume ratio, which makes them less sensitive to outgassing of adsorbed contaminates on the cell walls. Because of their significance, a detailed discussion of the nature of White cell experiments follows.

White cells measure the transmittance through a lossy medium. The transmittance is the ratio of the transmitted flux, $\Phi_t(n)$, attenuated by a lossy medium of path length nL_0, to the transmitted background flux, $\Phi_B(n)$, where the White cell contains a lossless medium. It is often wise to match the pressure of the cell in the sample and background runs to avoid cell motion effects. Furthermore, a reference detector (as shown in Fig. 6.3) is commonly used to monitor and correct for instability of the input flux. Thus, the measured transmittance is

$$\tau = \frac{\Phi_t(n)/\Phi_{Rt}}{\Phi_B(n)/\Phi_{RB}}, \tag{6.21}$$

where

τ	transmittance,
Φ_{Rt}	reference detector signal level during sample measurement,
Φ_{RB}	reference detector signal level during background measurement,
L_0	base path length of cell, and
n	number of traversals.

Φ_{Rt} and Φ_{RB} scale with $\Phi_t(n)$ and $\Phi_B(n)$, respectively to account for different power levels of the source at the different times of the respective measurements. The transmitted sample flux, $\Phi_t(n)$, can be further expressed as

$$\Phi_t(n) = \Phi_{0t}\rho^r(x,y,p_{H_2O})K_t(t)e^{-\beta_{abs}nL_0}, \tag{6.22}$$

where

$\rho(x,y,p_{H_2O})$	mirror reflectance as a function of location (x,y) on the mirror and of surface water vapor partial pressure,

Φ_{0t} flux level at input to White cell during sample measurement,
$K_t(t)$ time-dependent intensity fluctuations caused by windows,
                amplifiers, detectors, mirror drift, and so on, and
r number of reflections inside cell ($r = n-1$).

To eliminate the time-dependent fluctuations, a time average over a number of measurements is taken. Two experimental techniques have been used to accomplish this averaging process.

Since the mirror reflectivity is a function of the position on the mirror surface and cell vibrations can cause mirror drift, which misaligns the cell and changes the position of the spots on the field mirror, intensity variations in the output beam can result. One approach employs path-differencing averages over the mirror surface by changing the path length while keeping the sample fixed and averaging over window, detector, and other noise by taking many measurements at each path length. Another approach maintains the cell alignment throughout an experiment by using optical lasers to account for the drift of the cell mirrors. By greatly reducing the mirror drift problem, no average over the mirror surface is required.

The time-averaged sample flux is expressed as

$$\langle \Phi_t(n) \rangle_t = \Phi_{0t} \rho^r(x, y, p_{H_2O}) \langle K_t(t) \rangle_t e^{-\beta_{ext} n L_0}. \tag{6.23}$$

The background flux signal is similarly written ($\beta_{abs} = 0$):

$$\langle \Phi_B(n) \rangle_t = \Phi_{0B} \rho^r(x, y, p_{H_2O} = 0) \langle K_B(t) \rangle_t. \tag{6.24}$$

Using Eq. 6.21, the time-averaged transmittance becomes

$$\langle \tau \rangle_t = \frac{\langle \Phi_t(n) \rangle_t}{\langle \Phi_B(n) \rangle_t} \frac{\Phi_{RB}}{\Phi_{Rt}}.$$

Substituting Eqs. 6.23 and 6.24 into the above equation, we have

$$\langle \tau \rangle_t = \frac{R^r(x, y, p_{H_2O})}{R^r(x, y, p_{H_2O} = 0)} \frac{\langle K_t(t) \rangle_t}{\langle K_B(t) \rangle_t} e^{-\beta_{abs} n L_0}, \tag{6.25}$$

where the ratio

$$\frac{\Phi_{0t}}{\Phi_{0B}} \frac{\Phi_{RB}}{\Phi_{Rt}} = 1.$$

Sufficient time averaging requires that

$$\langle K_t(t) \rangle_t = \langle K_B(t) \rangle_t.$$

Therefore, the desired measurement of transmittance is

$$\langle \tau \rangle_t = \frac{\rho^r(x, y, p_{H_2O})}{\rho^r(x, y, p_{H_2O} = 0)} e^{-\beta_{abs} n L_0}. \tag{6.26}$$

To obtain the true absorption coefficient, β_{abs}, the mirror reflectivity must be the same in vacuum (or dry gaseous mixture) as it is with water vapor present at any pressure. This point has proven to be a major obstacle in obtaining the true absorption coefficient in humid samples. Water vapor is adsorbed by the mirrors, forming a very thin film ($\sim 1 \, \mu$m). The thickness of the film will depend on mirror temperature and partial pressure of water vapor in the cell. The effect on mirror reflectivity by water vapor will also be frequency dependent (i.e., ρ decreases as ν increases). Interference effects become more important as the wavelength approaches the film thickness. Absorption and refractive index effects exhibit an irregular frequency dependence, since they are related to resonance phenomena. Burch et al. (Ref. 6.8) reported that water vapor adsorption did not cause major difficulties at room temperature with 10 Torr water vapor and 36 reflections. However, Burch has reported that the 4 ìm region has major water vapor adsorption problems.

In the case for solid and liquid transmittance measurements the single surface reflectance must be considered. A general solution for the extinction coefficient, β_{ext}, based on Eq. 6.1, in terms of the transmittance and the single-surface power reflection coefficient R, is

$$\beta_{ext} = \frac{\ln(2R^2\tau) - \ln\left[\sqrt{(1-R)^4 + 4R^2\tau^2} - (1-R)^2\right]}{d/\cos\theta}. \tag{6.27}$$

When R is constant over a spectral region, a different analysis procedure can be used. Assuming R^2 is small and $\exp(-\beta_{ext}d)$ is close to one, then the transmittance can be expanded to be

$$\tau = \frac{1-R}{1+R}\,e^{-\beta_{ext}d} - \frac{R^2(1 - e^{-2\beta_{ext}d})\,e^{-\beta_{ext}d}}{(1+R)^2} + \cdots. \tag{6.28}$$

Because R is basically a constant in frequency over the experimental range, this formula can be used to directly reduce the transmittance to the extinction coefficient. The last term shown in the expansion is small, typically less than 1% unless the absorption is strong.

Differential Transmissometers   In many cases, unwanted loss by the windows on a gas absorption cell or on the surface of a solid cannot be removed with a vacuum or sampleless background measurement. For example, water vapor, or oil from machines, can condense on windows, causing an erroneous signal not compensated in an empty cell background. In the case of liquids, the reflection between a cell and the sample is not the same for an empty cell. Also, a transmission measurement of a solid includes reflectance and surface absorption, which must be removed to obtain bulk extinctance.

A popular technique to solve these issues is called differential transmittance. It involves two samples of different path lengths, L_1 and L_2. To see how it works, consider the near-normal transmittance of two samples,

$$\tau_1 = \frac{(1-R)^2 e^{-\beta_{ext}L_1}}{1 - R^2 e^{-2\beta_{ext}L_1}} \approx (1-R)^2 e^{-\beta_{ext}L_1}$$

and

$$\tau_2 = \frac{(1-R)^2 e^{-\beta_{ext} L_2}}{1 - R^2 e^{-2\beta_{ext} L_2}} \approx (1-R)^2 e^{-\beta_{ext} L_2}.$$

Assuming $L_1 > L_2$ and $R^2 \ll 1$, then the following approximation can be made on the ratio of the two transmittances:

$$\frac{\tau_1}{\tau_2} = \frac{e^{-\beta_{ext} L_1}}{e^{-\beta_{ext} L_2}} = e^{-\beta_{ext}(L_1 - L_2)}. \tag{6.29}$$

Therefore, the bulk extinction coefficient becomes

$$\beta_{ext} = \frac{-1}{L_1 - L_2} \ln\left(\frac{\tau_1}{\tau_2}\right). \tag{6.30}$$

We have assumed the surfaces or boundaries of the two samples are matched so that surface effects will cancel. In practice, surface roughness or degree of polish and surface contaminants can vary between samples. This will represent an error, usually small, to any experiment.

In any measure of transmittance, τ, the accuracy is at best ± 0.001. The problem is in accounting for changes in the optical path of the spectrometer from a thick sample to a thin sample if the sample is tilted or the beam is focused within the sample.

Transmissometer Technique for Unixial Materials   The characterization of the complex index for uniaxial crystals is more complicated, because two complex indices are required and crystallographic orientation must be considered. However, based on Eqs. 4.81 and 4.82, a simple procedure can be formulated. First, near-normal transmittance and reflectance measurements on a sample with the c-axis normal to the surface are made to obtain the ordinary ray complex index of refraction. In fact, this information is usually available for most uniaxial materials. Next, transmittance and reflectance measurements using unpolarized light on a sample with the a- or b-axis normal to the surface is collected. Knowing the o-ray transmittance and applying Eq. 4.81, the e-ray transmittance is obtained. Then Eq. 4.82 is used to obtain the e-ray absorption coefficient, knowing the e-ray single-surface power reflection coefficient.

TRANSMITTANCE MEASUREMENT LIMITATIONS   After the transmittance has been recorded, it is a straightforward matter to calculate the absorption coefficient using Eq. 6.1 and the previous techniques. However, it is instructive to examine the influence that a small uncertainty in internal transmittance has on the calculated value of $\beta_{ext}(\nu)$. This can be done by looking at the differential of $\beta_{ext}(\nu)$ for constant path, L,

$$d\beta_{ext}(\nu) = -\frac{1}{L} \ln\left(1 + \frac{d\tau}{\tau}\right). \tag{6.31}$$

Expanding the natural logarithm for $d\tau/\tau$ small, we have

$$d\beta_{ext}(\nu) = -\frac{1}{L}\left[\frac{d\tau}{\tau} - \frac{1}{2}\left(\frac{d\tau}{\tau}\right)^2 + \cdots\right]. \qquad (6.32)$$

If only terms of order $d\tau$ are retained, the result can be expressed as a normalized extinction coefficient error,

$$\frac{d\beta_{ext}(\nu)}{\beta_{ext}(\nu)} = (\ln\tau)^{-1}\frac{d\tau}{\tau} + o((d\tau)^2). \qquad (6.33)$$

This expression gives the relative change in the extinction coefficient for a small change in the transmittance, that is, it predicts the error that can be expected when the uncertainty in the value of τ is known. Figure 6.6 shows a plot of the percent error in $\beta_{ext}(\nu)$ for a given percent change in internal transmittance versus the extinction coefficient path length product. From these results, it is clear that reasonable accuracy in the extinction coefficient (1%) can only be achieved if there is substantial absorption.

A reasonable objective in designing a good transmittance experiment would be to require that the uncertainty in absorption coefficient equal the uncertainty in the transmittance measurement; looking at Eq. 6.33, this implies that $\ln(\tau) = -1$ or $\tau = 0.368$. This simply says that the optimum path length should be chosen such that

$$L = 1.0/\beta_{ext}(\nu), \qquad (6.34)$$

where the value of $\beta_{ext}(\nu)$ is typical of a particular spectral range of interest.

Reflectometers   Measurements of reflectance are usually made on a solid material in regions of very high absorption ($n \approx k_a$), where transmittance measurements are almost
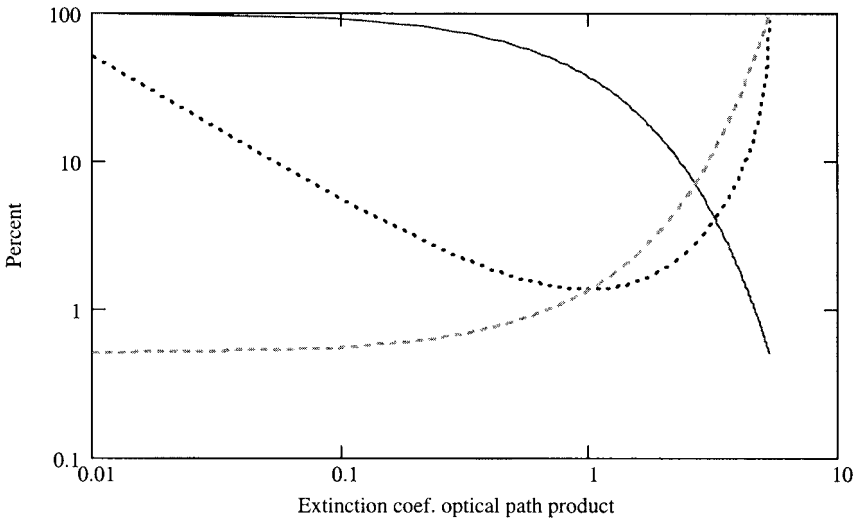
Fig. 6.6 Normalized percentage error in extinction coefficient (solid), the transmittance (dot) and the normalized percent error in the transmittance ($\Delta\tau/\tau$, for $\Delta\tau = 0.005$, dashed) plotted versus the extinction coefficient path length product.

impossible, because extremely thin (i.e., microns) samples are required. Other experimental techniques for determining the refractive index, n, are far superior in the regions of transparency (i.e., ellipsometry, interferometry, and refractometry).

The magnitude of the single-surface reflectance, R, for normal incidence is given by Eq. 6.3. Note that the real and imaginary parts of $\bar{n}$ influence the reflectance. Thus a complete description of a material's optical properties can be obtained in the regions of fundamental lattice vibrations and electronic transitions.

To obtain an absolute measure of the reflectance requires knowledge of the incident flux. This is often obtained by using a $\sim$100% reflecting mirror in place of the sample. (In the ultraviolet it is best to change the geometry of the experiment and directly measure the incident flux.) Thus, based on the definition of reflectance presented in Chapter 2, we have

$$\rho = \frac{\Phi_r(\text{sample})}{\Phi_i(\text{mirror})}.$$

An example of a specular reflectometer attachment for spectrometer sample compartments is illustrated in Fig. 6.7. Some offer angle variation measurements from 5° from normal to 80° from normal. Experimental data on a polycrystalline solid is illustrated in Fig. 6.8. (Diffuse reflectometers will be covered in Section 6.2.1.)

Experimental reflectance spectra can be analyzed in terms of the classical oscillator model in a straightforward manner. In general, a measurement of $|R|$ is not sufficient to determine $\epsilon_r(\omega)$ because phase information is missing. Recall that the classical oscillator model satisfies the Kramers–Krönig relationship and therefore provides the correct relationship between $\epsilon_r'(\omega)$ and $\epsilon_r''(\omega)$. Thus, it also allows for the construction of a physically meaningful representation of $\epsilon_r(\omega)$, using only the magnitude of R as input.
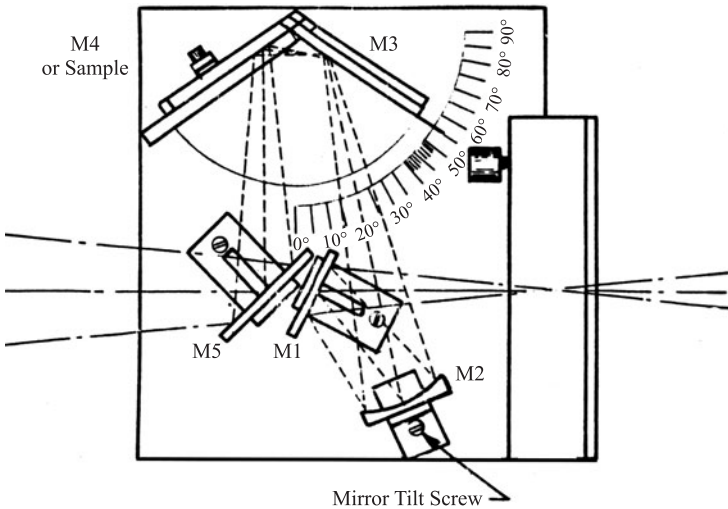
Fig. 6.7 Reflectometer attachment, adjustable for a range of incidence angles, for a broad-band spectrometer.

This point has been extremely useful in optical material modeling efforts. In a crystal with two or more atoms per unit cell, $\epsilon_r(\omega)$ may be phenomenologically represented by the classical oscillator model, as developed in Chapter 4,

$$\epsilon_r(v) = \epsilon_\infty + \sum_i \frac{v_{TOi}^2 \Delta\epsilon_i}{v_{TOi}^2 - v^2 + jv\Gamma_i},$$

where the v_{TOj} represent the long-wavelength transverse optic mode frequencies. In polar crystals the corresponding frequencies of the optically active longitudinal optic modes, v_{LOj}, are not equal to the v_{TO}s.

Equation 2.97 can be combined with the above equations for $\epsilon_r(v)$ and $R(v)$ to give formal expressions for the frequency dependence of either, $\epsilon_r(v)$, or $R(v)$. Such expressions can then be used in conjunction with experimental observations to infer the three parameters for each mode. This is not a trivial problem, since the number of independent parameters can be quite large for a multimode material. In fact, this approach will not work in the electronic region because the mode density is to great and individual modes are indistinguishable. The classical oscillator representation is commonly used to represent the complex permittivity of vibrational modes. The v_{LO}s can then be determined by using the analytic relations developed by Chang et al. (Ref. 10).

It is of considerable interest to be able to directly obtain the v_{LO}s and v_{TO}s without having to determine simultaneously all the classical oscillator parameters. A number of suggestions have been made as to how to do this. Chang et al. (Ref. 10) have suggested that in the case of crystals with multimode damped oscillators, the v_{TO}s may be identified with the maxima in $|\epsilon(v)|$, and while the v_{LO}s with the minima in $|\epsilon_r(v)|$. Barker (Ref. 11) has suggested identification of the v_{TO}s with maxima in ϵ_r'', and the v_{LO}s with maxima in $\text{Im}\,[-1/\epsilon_r]$. Unfortunately, these are not easily measurable quantities. The following develops a technique in derivative reflectance spectroscopy.

Consider the reflectance spectrum in the wavelength domain, λ. The λ_{TO}s and λ_{LO}s correspond to those points where $dR/d\lambda$ is an extremum, that is, where $d^2R/d\lambda^2 = 0$. In particular, the λ_{TO}s correspond to points where $d^2R/d\lambda^2 = 0$ and $dR/d\lambda < 0$, whereas the λ_{LO}s correspond to points where $d^2R/d\lambda^2 = 0$ but $dR/d\lambda > 0$. A simple heuristic argument shows that this method will work to the same extent that Chang's method is valid (Ref. 13).

To illustrate the utility of the proposed method, consider the particular case of Al_2O_3. Barker (Ref. 11) has made a detailed best fit of reflectivity data to theory, and in this way determined the set of parameters reproduced in Table 6.1. Also shown are the corresponding longitudinal-mode frequencies given by Barker (although he does not say

Table 6.1 Parameters for Classical Oscillator Model of Al_2O_3 as Given by Barker (Ref. 6.12)

Mode #	v_{jTO} [cm^{-1}]	λ_{jTO} [μm]	$\Delta\epsilon_j$	Γ_j/v_{jTO}	v_{jLO} [cm^{-1}]
1	$385 \pm 1\%$	26.0	$0.30 \pm 15\%$	$0.015 \pm 25\%$	$388 \pm 1\%$
2	$442 \pm 1\%$	22.6	$2.7 \pm 4\%$	$0.010 \pm 15\%$	$480 \pm 1\%$
3	$569 \pm 1\%$	17.6	$3.0 \pm 15\%$	$0.020 \pm 15\%$	$625 \pm 1\%$
4	$635 \pm 1\%$	16.7	$0.30 \pm 20\%$	$0.020 \pm 20\%$	$900 \pm 1\%$

$$\epsilon_\infty = 3.2$$
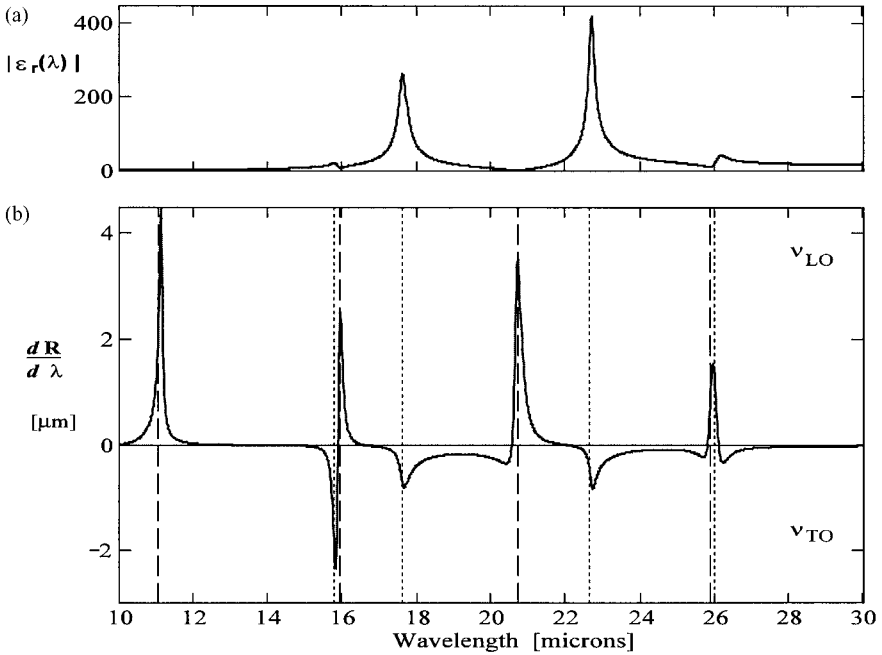
Fig. 6.8 Plot of (a) $|\epsilon_r|$, and (b) $dR/d\lambda$ versus wavelength for room-temperature sapphire (o-ray). The dashed lines locate the ν_{LO}s. The dotted lines locate the ν_{TO}s.

how they were determined). Using these parameters as inputs we numerically computed, $|\epsilon_r(\lambda)|$, and $dR/d\lambda$ ($\lambda[\mu m] = 10^4 \, (\nu \, [cm^{-1}])^{-1}$) and these results are plotted in Fig. 6.8. The results of the longitudinal and transverse mode wave numbers determined by the present method are given in Table 6.2 and compared with the input values given by Barker. The agreement is remarkably good.

The great utility of the present scheme to locate both the ν_{LO}s and ν_{TO}s is that it is based on use of the reflectance alone. Such measurements are relatively easy to make. An example derivative spectrum is shown in Fig. 6.9a, with the corresponding experimental reflectance spectrum and model representation for polycrystalline Y_2O_3 shown in part (b). Good starting values for the oscillator positions are obtained. The final

Table 6.2 Comparison of Modeled Optical Mode Frequencies Against the Results of Derivative Reflectivity Technique

ν_{TO} [cm^{-1}]		ν_{LO} [cm^{-1}]	
Model Input	Present Method	Barker (Ref. 6.21) Result	Present Method
385	382	388	387
442	441	480	483
569	567	625	628
635	635	900	905
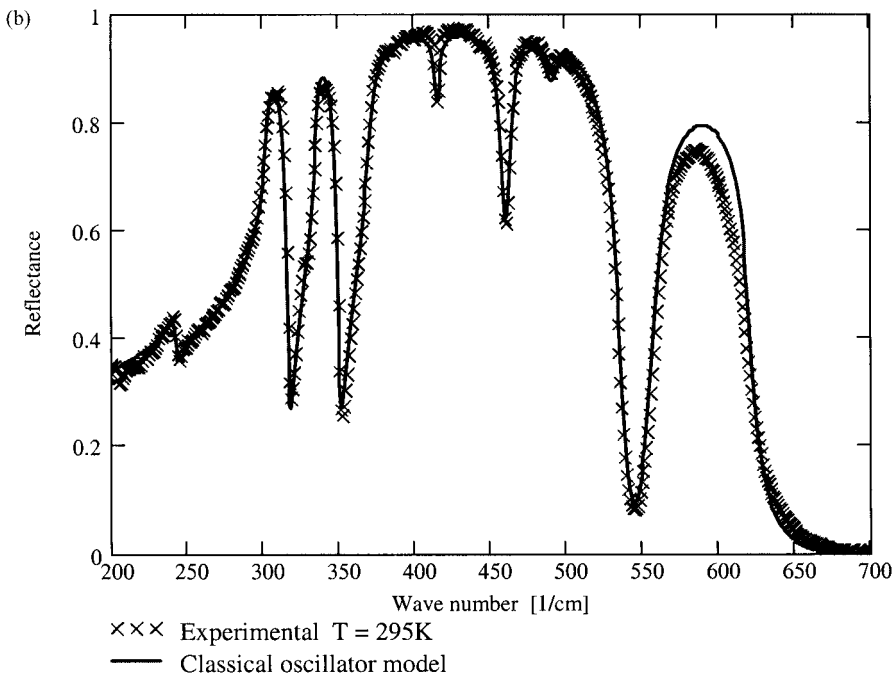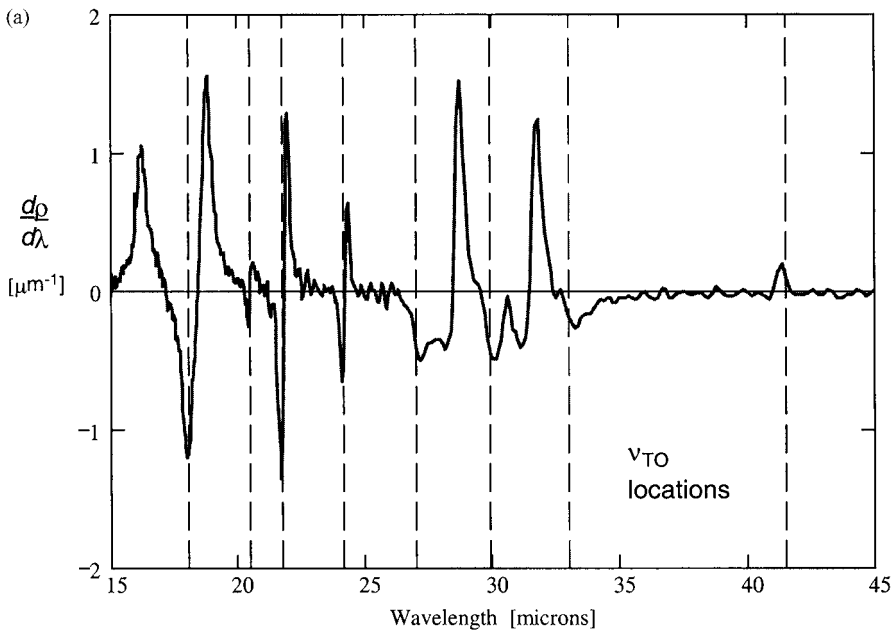
Fig. 6.9 (a) Experimental derivative reflection spectrum of Y_2O_3. (b) Corresponding reflection spectrum experimental and model fit.

values are changed in order to obtain the best fit. In this case, some of the modes overlap and distort the measurement of the true oscillator frequency.

Starting values for the other oscillator parameters can be obtained from the reflectance spectrum and the corresponding derivative spectrum. The Lyddane–Sachs–Teller relation (Eq. 4.46) can be used to estimate the oscillator strengths. Also, the level of reflectance between the TO and LO is indicative of the oscillator dampening factor (see Problem 6.6).

The ultimate goal of optical propagation experiments is to determine the complex index of refraction. However, measurements of τ and ρ are indirect measurements of $\bar{n}$, and this limits our ability to accurately determine $\bar{n}$. This is especially true for measurements of weak absorption. Other such experimental approaches are discussed in the following.

Photoacoustic Cells   When light is absorbed, energy is deposited in the medium in the form of heat. A pressure or acoustic signal is generated, which is directly proportional to the absorption coefficient. Thus, a direct measure of the absorption coefficient is made, as opposed to transmittance measurements. This is important when the absorption is weak and transmittance measurements are inaccurate. This is also useful when scatter is present as well as absorption. Photoacoustic cells are made that can be placed inside the sample compartment of a spectrometer. The incident signal must be modulated, since the acoustic signal is transient. This is ideal for a Fourier transform spectrometer, which always has a modulated light signal. In this way the interferogram is directly measured by a sensitive microphone.

Photoacoustic measurements require calibration. This is typically accomplished by using a sample with a known absorption coefficient.

Photoacoustic signals can be obtained from strongly absorbing (opaque) solids (or liquids) in a gas cell. The solid samples can be powders or unpolished bulk samples. For these particular applications, photoacoustic cells offer unique capabilities.

However, because the broad-band light source is weak in intensity, the measurable signal is also weak, unless the absorption is strong, and this approach generally offers only a minor improvement over transmittance measurements. A laser source greatly enhances the sensitivity this approach, and this is discussed in a later section.

Circle Cells   When the absorption coefficient is very large, transmittance measurements are almost impossible because the sample must be so thin. For small-volume liquids in particular, the sample can partially evaporate away before the end of a measurement. A circle cell can be used to solve this problem; it has path lengths on the order of several microns for a sample with adequate volume.

The circle cell has a rod in the center of the cell, which guides the light probing the liquid sample. The light rays are guided to reflect at critical angles so that total internal reflection occurs. However, at the points of reflection in the crystal, an evanescent field exists in the liquid. Thus the probe light rays are attenuated only by the evanescent field, which provides a very short path length within the liquid of several microns. A diagram of a circle cell is illustrated in Fig. 6.10. The name "circle cell" comes from Cylindrical Internal Reflection.

6.1.1.3 Laser Measurements

Spectrometers with broad-band sources provide spectral information on the optical properties of a medium. However, the weak power of the source per frequency interval
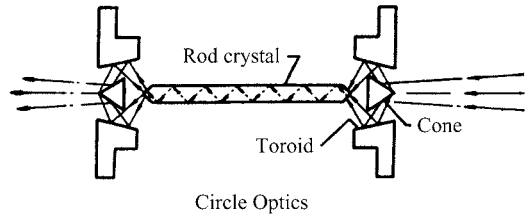
Fig. 6.10 Diagram of circle cell optics.

limits the signal-to-noise ratio and the accuracy of a measurement. Also, the limited res-olution of spectrometers may not be adequate to obtain accurate transmittances. This is especially true for the rapidly varying spectra of gaseous media. The laser offers extremely high resolution with high flux. However, the spectrometer measurement is always needed to see the full spectral structure of a medium. The laser transmittance (reflectance) measurement can calibrate that spectrum at specific frequencies and give insight on the effects of the limited resolution and signal-to-noise ratio of the spec-trometer. Furthermore, the laser is, in many cases, polarized in a particular direction. This property is very useful in anisotropic media, as well. Thus, narrow-band, high-power laser measurements of transmission and reflection complement broad-band coverage with low spectral power spectrometer measurements. Ideally, tunable lasers (the spectroscopist's dream) are used for such measurements.

The high spectral power a laser provides allows dual-beam experiments to be easily realized. A beamsplitter is used to direct a small part of the beam to a reference detec-tor and most of the intensity to the sample. The path lengths must be matched to properly account for beam motion. The detectors, if two separate detectors are used, also should be matched as close as possible.

6.1.2 Laser Techniques

One of the main motivations for using lasers to study optical properties is because of requirements of laser optics. The much higher power levels require lower absorption and scattering coefficients in window materials. Thus, more sensitive techniques are needed than spectrometer measurements can provide. Using a laser as a source instead of a blackbody or lamp is an improvement, but other experimental techniques are needed to truly improve sensitivity to small extinction effects.

Because of the high spatial and temporal coherence with high power of the laser, exper-imental techniques that directly measure the real and imaginary part of the complex index of refraction are possible. Laser measurements of the absorption coefficient are accom-plished by calorimetry and photoacoustics. These techniques offer the highest available accuracy for measurements of the absorption coefficient, as indicated in Table 6.3. Measurement of the index of refraction is accomplished by laser interferometry.

6.1.2.1 Laser Photoacoustics

This is similar to photoacoustics with a broad-band source and a spectrometer, only now a laser source is used. Because the measured signal is proportional to the power

Table 6.3 Sensitivity for Determining the Absorption Coefficient by Various Experimental Methods Using Spectrometers and Lasers

Method	Sensitivity [cm^{-1}]
Differential spectrophotometry	$5\times10^{-3} - 2\times10^{-3}$
Emittance spectroscopy	$1\times10^{-3} - 1\times10^{-5}$
Laser calorimetry	$1\times10^{-4} - 5\times10^{-6}$
Laser photoacoustics	$1\times10^{-6} - 1\times10^{-10}$

absorbed in the medium, a high-power laser can produce a strong signal in weakly absorbing media even over a short path. Thus significant improvement over broad-band source spectrometers is obtained. The most sensitive measurements of the absorption coefficient are made with this approach, and it is commonly applied to weakly absorbing gases.

A chopped laser source is used, which produces a transient pressure signal, as shown in Fig. 6.11, in a closed cell called a spectraphone. The strength of the signal rises exponentially when the laser is on, and decays when the laser is off. A sensitive pressure transducer or microphone is used to detect the signal. For a cylindrical cell of radius r_c and a Gaussian TEM$_{00}$ laser beam, the measured pressure signal P_s is proportional to

$$P_s \propto \frac{\beta_{abs}\Phi_{laser}TR_{GC}\xi_1^2}{16\pi C_V r_c^2 m}, \tag{6.35}$$

where Φ_{laser} is the incident laser flux, T is the period of the chopped laser beam, R_{GC} is the gas constant, ξ_1 is the first root of a zero-order Bessel function, C_V is the specific heat at constant volume, and m is the gram molecular weight of the gas. The above formula is valid for $T/(4\tau) \ll 1$, where τ is the relaxation time of the pressure signal response. From this equation the absorption coefficient can be obtained.

Limitations of this approach include window and wall noise. Window noise is caused by low-level absorption by the window to the cell. High-quality windows are required, but no material is free of bulk absorption and surface contamination absorption, is always a problem. Wall noise is caused by laser light interacting with the walls of the cell. To keep this to a minimum a tightly focused well-aligned beam is desired. The cell temperature must also kept as stable as possible. Also, because of the large surface-to-volume ratio of the cell chamber, strongly absorbing impurities from wall outgassing can be a major problem.
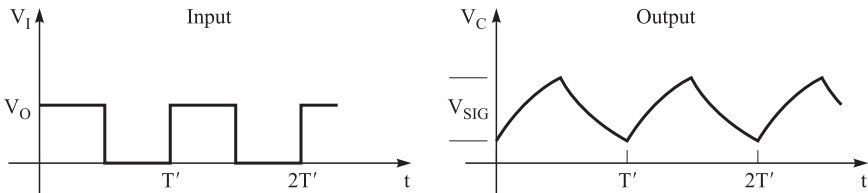
Fig. 6.11 Waveforms for the incident chopped laser and corresponding pressure signal response in a spectraphone.

6.1.2.2 Laser Calorimetry

This approach is similar to photoacoustics, except that a sensitive thermometer is used to measure the temperature change of a weakly absorbing sample illuminated by a laser rather than a pressure sensor measuring an acoustic signal. Laser calorimetry is commonly applied to solids intended for high-power laser windows. The thermometer is a thermocouple in contact with the edge of the sample. The center of the sample is illuminated by a TEM_{00} laser beam. Typically the sample is in vacuum. The absorption coefficient is obtained from measuring the rate of change of the sample temperature with the laser on and off, as given by the following equation (Ref. 6.15):

$$\beta_{abs}(T_1) \approx m \frac{C_p}{LP_\tau} \frac{2n}{n^2+1} \left[\left(\frac{dT_{rise}}{dt} \right)_{T_1} + \left| \frac{dT_{decay}}{dt} \right|_{T_1} \right], \qquad (6.36)$$

where m is the sample mass, C_p is the specific heat at constant pressure, L is the sample thickness, P_τ is the transmitted power, and n is the index of refraction at the laser frequency. The assumption made to obtain this equation is $\beta_{abs}L \ll 1$. The measured signal voltage is similar to that obtained in laser photoacoustic measurements (see Fig. 6.11).

Laser calorimetry measurements are sensitive to both surface and bulk absorption. In fact, surface absorption, due, for example, to residuals from polishing, can dominate low-level loss of a window. This technique has proven useful in studies of surface preparation. This is done by making measurements on identically prepared samples of different thicknesses.

Window materials with scattering introduce errors to calorimetry measurements. First, the thermocouple can be directly illuminated by laser radiation and produce heating not caused by sample absorption. Second, the optical path in the sample has been altered (increased) by an unknown amount and the absorption coefficient cannot be accurately determined. This is especially true in high-index materials where a relatively small critical angle exists and a significant amount of scattered light is reflected back into the material.

6.1.2.3 Laser Interferometry

Laser interferometry is used to measure the real part of the index of refraction. A typical setup, using a Michelson interferometer similar to the one discussed in Section 6.1.1.1, is shown in Fig. 6.12. In this case, a gas cell is placed in one of the arms of the interferometer. Absolute measurements of the refractive index can be obtained on gases by beginning the experiment at vacuum. As gas is injected into the cell, the optical path, nL, of the arm changes and fringes can be counted on the detector. Very sensitive detection schemes are used that are capable of measuring changes much less than the wavelength of light being used. Since L is constant throughout the experiment, the index of refraction is directly measured as a function of gas pressure. A measurement with the cell in vacuum is needed to calibrated the experiment. Sensitivity down to ± 0.0000005 in the index of refraction can be easily obtained.

This procedure can also be used to obtain the thermo-optic coefficient (dn/dT) of a solid. In this case, the gas cell is replaced with a temperature-controlled cell capable of
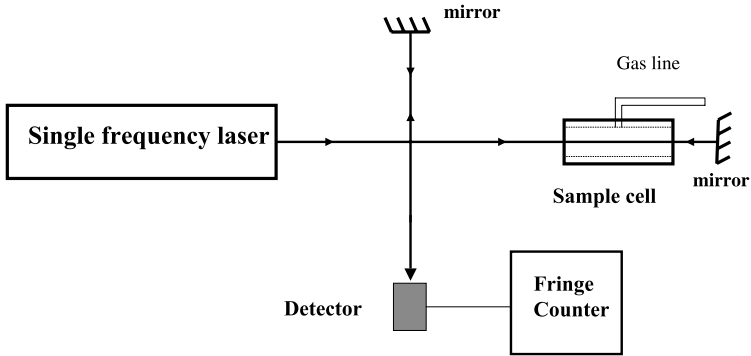
Fig. 6.12 A Michelson interferometer for measurements of the refractive index.

holding a window sample. As the index of refraction of the window changes, the optical path changes, and this causes the fringe to change on the detector. The expansion coefficient of the material must also be known, since this is part of the temperature-dependent optical path ($dnL/dT = (dn/dT)L + n(dL/dT)$). Absolute measurements of the index cannot be made because the sample cannot be introduced slowly enough to keep track of the fringe count.

6.1.3 Ellipsometry

Ellipsometers are part of a more general subclass of polarization sensitive reflectometers called reflection polarimeters. The experiment consists of a collimated polarized monochromatic source illuminating a material, and the detection of the state of polarization of the reflected light. A typical configuration is shown in Fig. 6.13. Ellipsometer measurements are typically made on thin films covering a substrate (determining the
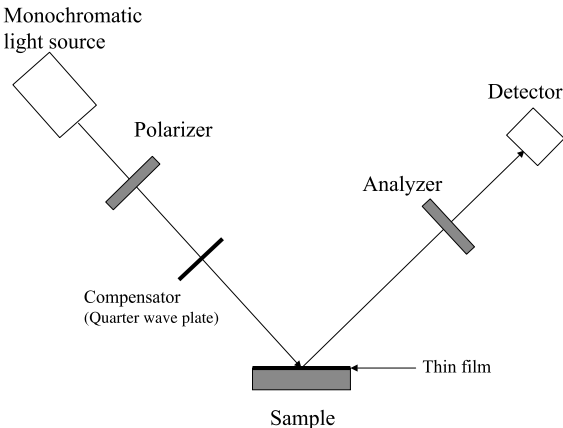
Fig. 6.13 Experimental layout of an ellipsometer.

thickness and n of the film) or on a bulk sample (determining n and k_a). Measurements are made with monochromatic sources, such as lasers, or filtered broad-band sources.

The fundamental equation of ellipsometry can be obtained in a straightforward manner. Consider the ratio of the field reflection coefficients for p- and s-polarizations (e.g., as given by Eqs. 4.68 and 4.70) incident upon a bulk sample. The field reflection coefficients are complex in general. Thus, the ratio is also complex, and is given by

$$\frac{r_p}{r_s} = r = \tan \psi \, e^{-j\Delta}. \tag{6.37}$$

An ellipsometer measures the parameters ψ and Δ. The procedure of the measurement involves rotating the polarizer and analyzer until the reflected intensity from the sample is zero. The polarizer is in the incident beam and the analyzer is in the reflected beam, as indicated in Fig. 6.13.

The details of the data analysis are to involved to discuss here, and it is intended that the references at the end of the chapter be consulted.

6.1.4 Refractometry

Refractometers require that the sample to be measured be in the shape of a prism with apex angle, α. The deviation angle, D, as defined in Fig. 6.14, is measured as a function of the incidence angle, θ_1, under the condition that it is a minimum. For this reason this approach is called the minimum deviation technique. Based on the knowledge of these two angles, the index of refraction of the sample can be determined. This is a popular technique, used for many common optical materials. The index of refraction is only determined in regions of transparency.

The relationship between the deviation angle and the incidence angle, and the index of refraction can be obtain in a straightforward manner. Based on Snell's law (Eq. 4.72) and geometric principles, the following relationships are obtained:

$$\begin{aligned} \sin \theta_1 &= n \, \sin \theta_2, \\ \sin \theta_4 &= n \, \sin \theta_3, \\ \theta_2 + \theta_3 &= \alpha, \text{ and} \\ \theta_1 + \theta_4 &= \alpha + D. \end{aligned} \tag{6.38}$$
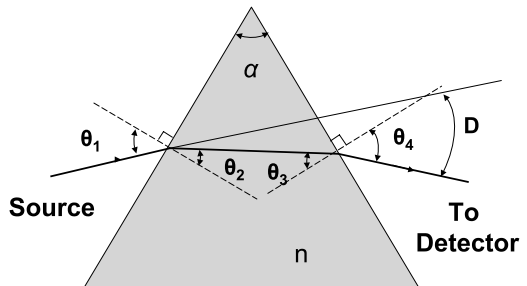
Fig. 6.14 Geometry of a refractometer experiment.

Solving for the minimum deviation angle for variation in θ_1 requires that

$$\frac{dD}{d\theta_1} = 0.$$

Based on the last equation in 6.38, the above requirement can be rewritten in terms of θ_1 and θ_2:

$$\frac{d\theta_1}{d\theta_4} = -1. \tag{6.39}$$

With a little algebra, the following result is obtained:

$$\frac{\cos \theta_1}{\cos \theta_2} = \frac{\cos \theta_4}{\cos \theta_3}. \tag{6.40}$$

The equation is satisfied when $\theta_1 = \theta_4$ and $\theta_2 = \theta_3$. This means the deviation angle is a minimum when the optical arrangement is symmetric. Using this result and Snell's law, the following relationship for the index of refraction is obtained:

$$n = \frac{\sin \theta_1}{\sin \theta_2} = \frac{\sin \left(\frac{1}{2}(D + \alpha)\right)}{\sin \left(\frac{1}{2}\alpha\right)}. \tag{6.41}$$

When the experiment is repeated for different frequencies, the dispersion of a material can also be determined. Highly accurate (± 0.00001) measurements of the refractive index have been made with this technique.

6.1.5 Broad-Band Interferometry

Samples that are flat and parallel exhibit interference in the transmitted beam (recall Eq. 2.100). For a lossless spectral region in a medium ($K = 1$ and R is real), Eq. 2.100 becomes the common Airy formula

$$\tau(\nu) = \frac{[1 - R(\nu)]^2}{1 - 2R(\nu) \cos [4\pi \nu n(\nu)L \cos \theta_a] + R(\nu)^2}. \tag{6.42}$$

The transmittance for near-normal incidence is illustrated in Fig. 6.15 for a diamond etalon. A cyclic modulation pattern is generated with the spectral distance between adjacent peaks termed the free spectral range, $FSR(\nu, T)$. Based on Eq. 6.42, the transmission peaks are located at

$$4\pi \nu n(\nu)L = 2\pi m, \tag{6.43}$$

where m is the order or mode number. For regions of zero dispersion the free spectral range becomes

$$FSR(\nu, T) = \frac{1}{2n(\nu, T)L(T)}. \tag{6.44a}$$

One-hundred percent transmittance is usually not achieved because the sample is not perfectly flat and some spectral averaging is occurring. In Fig. 6.15, the solid curve is
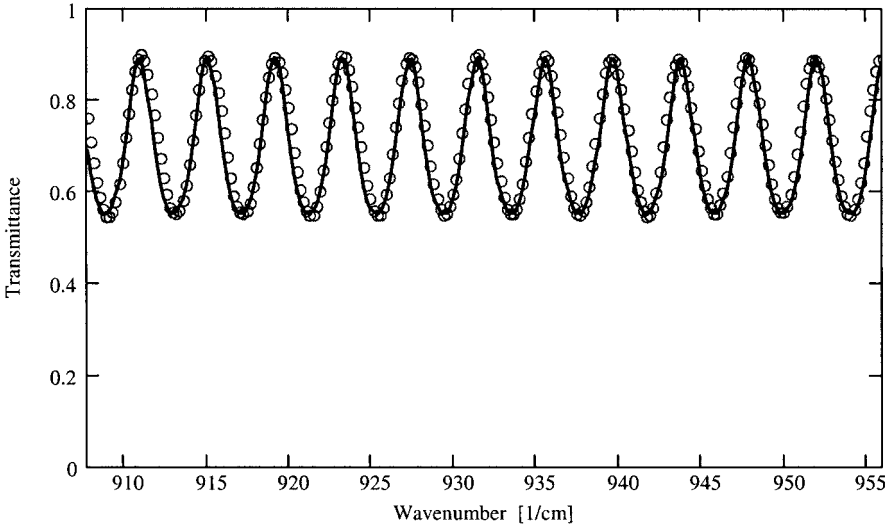
Fig. 6.15 Transmittance of a CVD diamond etalon 512 μm thick at room temperature.

a fit to measured data. It is a linear combination of Eqs. 6.42 and 2.96. Broad-band transmittance measurements with high-resolution spectrometers offer a convenient means of accurately measuring the index of refraction as a function of frequency and temperature. Unfortunately, unless a very large signal-to-noise ratio is achieved, significant modulation must be observed, and samples with large refractive index ($n > 2$) work best.

Nonetheless, a measurement of $FSR(\nu)$ and the sample thickness allows the index of refraction to be determined. As the index of refraction changes with frequency, so does the FSR, and spectral dispersion can be obtained as well. A general solution of Eq. 6.43 including dispersion, leads to the following differential equation:

$$\nu \frac{dn(\nu)}{d\nu} + n(\nu) = \frac{1}{2L\,FSR(\nu)}. \tag{6.44b}$$

This is a first-order differential equation with the following general solution for the index of refraction:

$$n(\nu) = \frac{1}{\nu}\left(\nu_0 n(\nu_0) - \int_{\nu}^{\nu_0} \frac{d\nu'}{2L\,FSR(\nu')}\right) \quad \text{for } \nu < \nu_0, \tag{6.45a}$$

and

$$n(\nu) = \frac{1}{\nu}\left(\nu_0 n(\nu_0) + \int_{\nu_0}^{\nu} \frac{d\nu'}{2L\,FSR(\nu')}\right) \quad \text{for } \nu > \nu_0, \tag{6.45b}$$

where ν_0 is the spectral point of minimum dispersion, thus Eq. 6.44a can be applied and the index of refraction can be determined. The integral between transmission peaks is $1/(2L)$, because the *FSR* between peaks is a constant. Thus, the determination of the index of refraction is reduced to a simple counting of peaks according to

$$n(\nu_m) = \frac{1}{\nu_m}\left(\nu_0 n(\nu_0) - \frac{m}{2L}\right) \quad \text{for} \quad \nu < \nu_0, \tag{6.46a}$$

and

$$n(\nu_m) = \frac{1}{\nu_m}\left(\nu_0 n(\nu_0) + \frac{m}{2L}\right) \quad \text{for} \quad \nu > \nu_0, \tag{6.46b}$$

where $m = 0,1,2,\ldots$, and ν_m locates the transmission peaks. This technique is attractive because it does not require highly accurate peak locations, which is difficult to obtain in a low-finesse spectrum. For high accuracy in the index of refraction, precise knowledge of the sample thickness must be available. This often requires thick samples, which in turn requires higher spectral resolution from the spectrometer.

Temperature measurements of the index of refraction can also be accomplished with this approach. The temperature change in *FSR* of a window of thickness L, together with the thermal expansion coefficient (α_{ex}, see Chapter 8), can be used to determine the change in refractive index with temperature:

$$\begin{aligned}\frac{dFSR(T)}{dT} = \frac{d}{dT}\left(\frac{1}{2n(T)L(T)}\right) &= -FSR \cdot \left(\frac{1}{n}\frac{dn}{dT} + \frac{1}{L}\frac{dL}{dT}\right) \\ &= -FSR \cdot \left(\frac{1}{n}\frac{dn}{dT} + \alpha_{ex}\right).\end{aligned} \tag{6.47}$$

ALTERNATIVE APPROACHES   At a fixed temperature, the measured free spectral range can be fit (e.g., least squares) to a polynomial in ν. Assuming a polynomial form for $n(\nu)$ as well, the coefficients can obtained from knowledge of *FSR*. The procedure is outlined in mathematical form below:

$$FSR(\nu) = A_0 + A_1\nu + A_2\nu^2 + \cdots = \frac{1}{2n(\nu)L} = \frac{1}{2(n_0 + B_1\nu + B_2\nu^2 + \cdots)L}.$$

Assuming that $n_0 \gg B_1\nu, B_2\nu^2$, we obtain leads to the following solution for n_0 and the B coefficients,

$$n_0 = \frac{1}{2A_0 L}, \quad B_1 = -A_1 2n_0^2 L, \quad \text{and} \quad B_2 = \frac{B_1^2}{n_0} - A_2 2n_0^2 L.$$

For high accuracy, precise knowledge of the sample thickness must be available. This requires thick samples, which in turn requires higher spectral resolution from the spectrometer.

Perhaps a better approach is to use a Sellmeier model for $n(\nu)$ and explicitly determine the dispersion in Eq. 6.44b. Then a nonlinear least-squares fit to that equation can be performed. The results will be in the form of Sellmeier model parameters.

6.1.6 Emissometry

When the temperature of the sample is near, or exceeds, the temperature of a source used for transmission measurements, then radiation from the sample is noise to the detector, and this degrades any transmission measurement. It is more straightforward, in this case, to use the sample as the source and measure the emitted light directly. This technique is called emissometry, and still requires a reference for system calibration, which can be as simple as a standard blackbody radiator at a known temperature.

Based on the formula for absorptance and Kirchhoff's law (Eqs. 2.98 and 2.106), the emittance from a flat polished surface is related to the single-surface power reflection coefficient and the bulk absorption coefficient in the following manner for a sample of thickness L:

$$\epsilon(\theta,\nu) = \frac{\{1 - R\left[\theta, \overline{n}(\nu)\right]\}\left(1 - e^{-\beta_a(\nu)L/\cos\theta_a}\right)}{1 - R\left[\theta, \overline{n}(\nu)\right]e^{-\beta_a(\nu)L/\cos\theta_a}}.$$

The emitting object must be in thermal equilibrium. θ_a is the refracted angle, which is related to θ by Snell's law, and the angle θ specifies the observer's angle. For a sample that also contains bulk and surface scatter, care must be exercised in the interpretation of the data. The optical path within the material is altered, and a rough surface changes the emitted radiation pattern as discussed in Chapter 2.

In the limit of strong absorption ($\tau = 0$), the emittance is determined by the first surface reflection, such that

$$\epsilon(\nu, \theta_i) = 1 - R\left[\overline{n}(\nu), \theta_i\right]. \tag{6.48}$$

Because there is no transmission, the reflectance equals the single-surface power reflection coefficient. There are two distinct spectral regions for this case. One is for $n - 1 \approx k_a$, which occurs in the one-phonon region. This region exhibits highly varying emittance, characteristic of a reflectance spectrum in the one-phonon region. The other is for $n - 1 \gg k_a > 0.01$, which occurs in the two-phonon region. This is the spectral region of highest emissivity for a bulk material. In fact, the emittance can be very close to one.

In the limit of weak absorption ($\beta_a L < 0.1$) the emittance is determined by the absorption coefficient and the sample thickness, L,

$$\epsilon(\theta,\nu) = \beta_a(\nu)\frac{L}{\cos\theta_a}. \tag{6.49}$$

In this way, a measure of the emittance can be a direct measure of the bulk absorption coefficient and thus potentially more accurate than high-temperature transmittance measurements, as suggested by Table 6.3. A diagram of a typical emissometer is shown in Fig. 6.16.

When a sample has bulk scatter and the infrared emittance is less than 0.5, then the method of sample heating must be carefully considered. A regular furnace will have
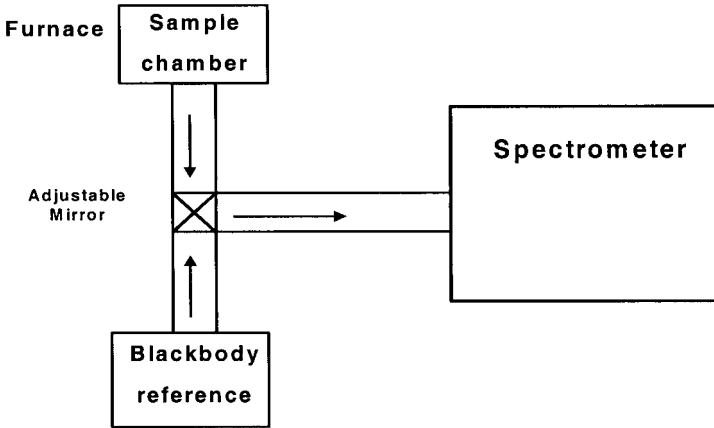
Fig. 6.16 Diagram of a typical emissometer.

broad-band infrared emission that will be scattered into the field of view of the detector to some level. This is a noise source to the emittance measurement. A technique to avoid this problem is to laser-heat the sample. The laser should operate in the two-phonon region of a material where the absorption is high and the reflectance low. Depending on the power of the laser and the size of the sample, very high temperatures can be obtained. An example of a measurement using this approach is illustrated in Fig. 6.17. Note the clean measurement of the multiphonon edge. Furthermore, by measuring the emission in the two-phonon region, a measurement of the sample temperature can be made. Since the two-phonon region is close to a blackbody ($\epsilon \approx 1$) and features very little temperature dependence in the emittance, pyrometric techniques can be used to remotely determine temperature. This is useful for two reasons. First, a measurement of the sample temperature is made at the same location as the low level emittance measurement. Also, a thermometer in contact with the material can introduce radiation noise and act as a means of thermal conduction, cooling the sample. Thus, a contact measurement of surface temperature is not always desirable. Consult the reference at the end of the chapter for more detailed discussion of this approach.

6.2 Scatter Measurements

Scatter measurements are important for understanding and characterizing the propagation loss and imaging properties of a medium, stray light effects from surfaces, and polarization characteristics of reflected light. Two classes of scatter measurements are typically made, by scatter-angle-dependent scatterometers and scatter-angle- independent integrating spheres.

6.2.1 Scatterometers

Scatterometers, which measure angular-dependent scatter, can be classified as two distinct types: those that measure over a sphere (BSDF) and those that measure over
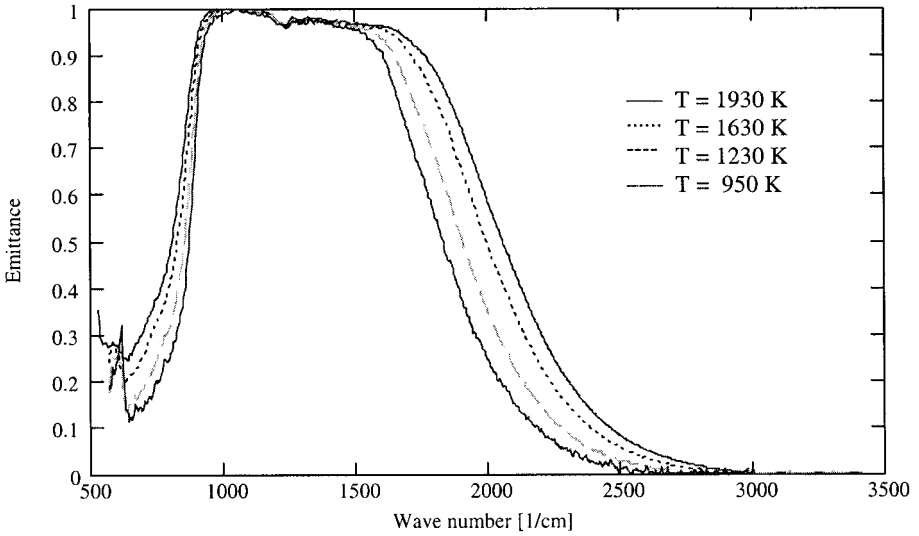
Fig. 6.17 High-temperature near-normal emittance spectra of single crystal sapphire (*o*-ray) 1 mm thick from 950 to 1930 K. The sample was heated in vacuum by a CO_2 laser.

a hemisphere (BRDF). When a medium is opaque, then only hemispheric measurements are needed. When a material is transparent, then the full sphere enclosing the sample must be measured. A description of a general scatterometer, ignoring polarization and assuming no ϕ_s dependence, is given in the following.

A direct measurement of the incremental scattered flux, $\Delta\Phi_{sca}(\theta_s,\theta_i)$, per incremental steradian, $\Delta\Omega_s$, is proportional to the phase function, $P(\theta_s,\theta_i)$, as given below:

$$\frac{\Delta\Phi_{sca}(\theta_s,\theta_i)}{\Phi_i \Delta\Omega_s} = \alpha_{sca}(\theta_s,\theta_i) = \alpha_{sca}(\theta_i)P(\theta_s,\theta_i), \tag{6.50}$$

where Φ_i is the incident flux from a directional source (i.e., a laser) and $\alpha_{sca}(\theta_s,\theta_i)$ is the bidirectional scatter distribution function (BSDF) and $\alpha_{sca}(\theta_i)$ is the total integrated scatter (TIS), as defined in Chapter 2. Similar quantities are defined for BRDF measurements. In practice, the measured fluxes are detector voltages (usually a large-area detector is used). Since there is no dependence on ϕ_s, only measurements on the θ_s-direction within the plane of incidence are required. The incremental angular step size of θ_s for the experiment should be less than $\frac{1}{2}/\Delta\Omega_s$. These concepts are illustrated in Fig. 6.18.

The scatterance is constrained by the total power law to be

$$\alpha_{sca} = 1 - \tau_s - \rho_s \tag{6.51}$$

for a medium with no absorption (e.g., $\alpha_{abs} = 0$). That is, the specular transmittance and reflectance must not be included in the data analysis. It is important to maintain the conservation of power flow in a valid measurement.
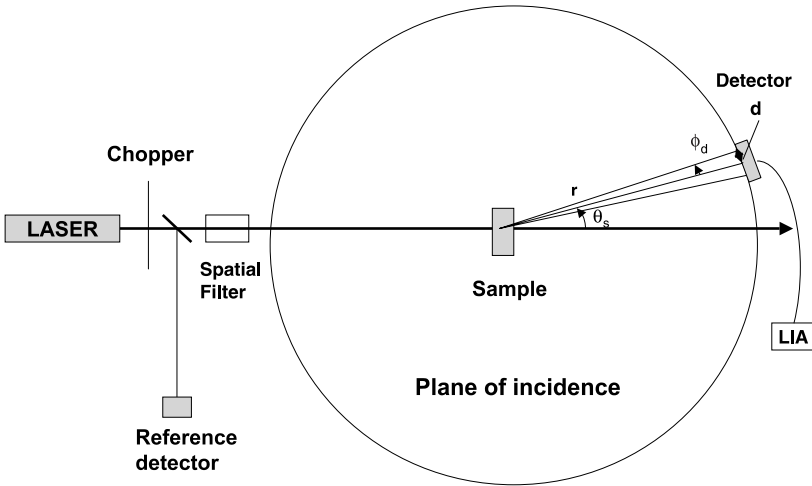
Fig. 6.18 The geometry of a bidirectional scattering measurement.

Integration of both Eq. 6.50 with respect to $d\Omega_s$ leads to the TIS,

$$\frac{\Phi_{sca}}{\Phi_i} = \alpha_{sca}, \tag{6.52}$$

where the phase function is normalized according to Eq. 2.89. This result can be checked against a direct measurement of the TIS as obtained by a integrating sphere (see next section). Agreement also validates the assumption of no ϕ_s dependence.

The incremental solid angle, $\Delta\Omega_s$, can be determined from the experimental geometry. It is given by the following formula:

$$\Delta\Omega_s = 2\pi(1 - \cos\phi_d). \tag{6.53}$$

Based on Fig. 6.18 and for $r \gg d$ (the detector radius),

$$\Delta\Omega_s = 2\pi \left(1 - \frac{r}{r\left[1 + \left(\frac{d}{r}\right)^2\right]^{\frac{1}{2}}} \right) \approx \frac{\pi d^2}{r^2}. \tag{6.54}$$

The detector area, A_d, is πd^2 and the incremental solid angle viewed by the detector is

$$\Delta\Omega_s \rightarrow \frac{A_D}{r^2} \tag{6.55}$$

Using this result in Eq. 6.50 completes the information needed to experimentally determine the BRDF or BSDF of a sample. To complete any directional scatter experiment, a measurement must be taken with no sample present to characterize the

background scattering level. This determines the noise level of the detector and the beam quality of the laser.

It is often interest to compare a BSDF measurement of one material with that of another. To do this meaningfully, the different Fresnel reflection coefficients for each material must be taken into account. This can be done for an absorption-free material by scaling the incident flux by $(1 - R)/(1 + R)$ for forward scatter and by $2R/(1 + R)$ for backward scatter. Therefore, a scaled scatterance function, $\alpha'_{sca}(\theta_s, \theta_i)$, is defined as

$$\alpha'_{sca}(\theta_s, \theta_i) = \begin{cases} \alpha_{sca}\left(\frac{\pi}{2} > \theta_s > -\frac{\pi}{2}, \theta_i\right) & \frac{1+R}{1-R}, \\ \alpha_{sca}\left(-\frac{\pi}{2} > \theta_s > \frac{\pi}{2}, \theta_i\right) & \frac{1+R}{2R}. \end{cases}$$

Ideally, such a comparative scatter measurement would be done in an index-matched fluid, so that surface reflectance would be eliminated. But this is not easy to implement, and the above definition becomes useful.

The results of BRDF measurements in the plane of incidence with an angular resolution of 2° at 0.6328 μm on a white paper label are shown in Fig. 6.19a as a function of the reflection angle referenced to the surface normal. Two angles of incidence are used, one normal to the sample ($\theta_i = 0$) and at 48°. The near specular reflectance is broadened in the 48° case relative to the normal incidence case because the illuminated footprint on the sample broadens as the sample is rotated. The dropouts in the experimental curves occur when the detector blocks the incident beam. The results are fit to the following formula:
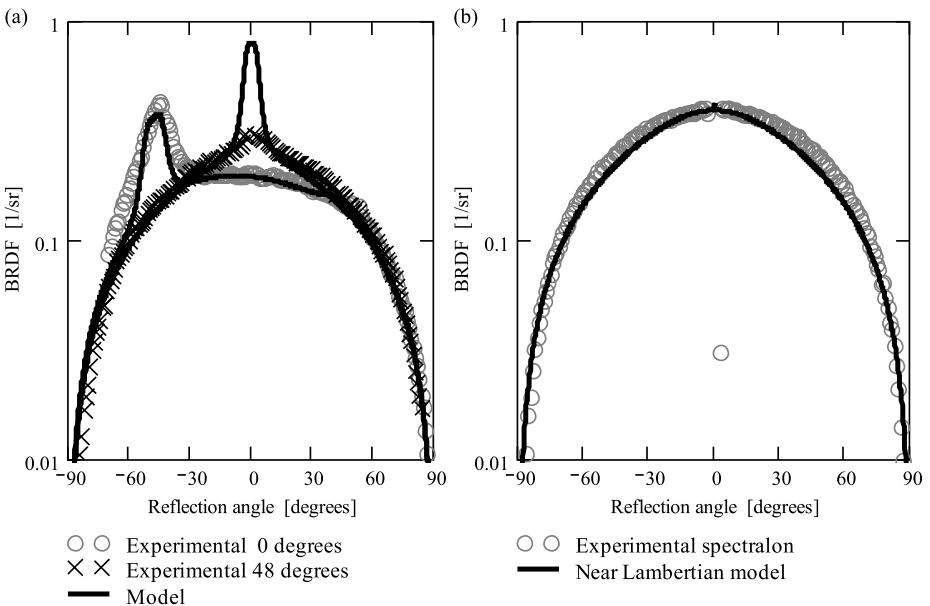
Fig. 6.19 (a) Measured and modeled BRDF for a piece of label paper illuminated at 0.6328 μm. (b) BRDF of Spectralon at a wavelength of 0.6328 μm.

$$BRDF(\theta_r, \theta_i) = 0.012 P_{diff}(\theta_r, \theta_i, 4, 0.07) + 0.13 P_{diff}(\theta_r, \theta_i, 2, 0.8)$$
$$+ 0.007 P_{diff}(\theta_r, -\theta_i, 3, 0.3) + 0.5 P_{Lam}(\theta_r).$$

The first two terms represent near specular and diffuse components, which are also a function of the angle of incidence. The third term represents weak diffuse light retrore-flected back to the source. The last term represents the Lambertian scattering component of the BRDF (see Example 2.1). The Lambertian component is independ-ent of the angle of incidence and the dominant diffuse term. The functional form used to represent the BRDF is based on Eq. 2.91. The phase function that is used in the above formula is given by

$$P_{diff}(\theta_r, \theta_i, n, a) = \frac{n\left(1.15 - \frac{3.3}{n^2} + \alpha^{1.1}\frac{10-n}{n}\right)|\cos(\theta_r)|}{\pi 6.2\alpha\left(1 - \frac{n-2}{10} + 0.9(\alpha - 0.5)^2\right)^{-1}} \frac{\left|\frac{\alpha}{\cos\theta_i}\right|^{n-1}}{|\theta_r + \theta_i|^n + \left|\frac{\alpha}{\cos\theta_i}\right|^n}.$$

It is only approximately normalized, but works for a variety of painted or unpolished surfaces. The integration over all angles of the BRDF is the TIR and the result for normal incidence is 0.64, suggesting the label was an off-white color. Figure 6.19b plots the BRDF of Spectralon^{TM}, a commercially available near-Lambertian surface. The model fit is expressed below,

$$BRDF(\theta_r, \theta_i) = 0.27 P_{diff}(\theta_r, \theta_i, 2, 0.8) + 0.73 P_{Lam}(\theta_r),$$

and shows how close to Lambertian the sample actually comes.

By examining the nature of the BRDF, the optical quality of reflecting surfaces can be determined. Such information is commonly needed in optical design where stray light is a concern or high-quality images are required. Also the emissive properties of surface can be obtained.

6.2.2 Integrating Spheres

An integrating sphere is a nearly closed spherical chamber that typically has a diffuse reflectance coating of high reflectivity on the interior and ports for a large-field-of-view detector, light beam entrance, and light beam exit. This three-port configuration is illus-trated in Fig. 6.20. Also, four-port configurations can be used for scattering measurements. The TIR of the coating should be close to one. All scattered light is col-lected, and thus this is a measurement of the total integrated scatter.

The common sequence of measurement for a three-port sphere is as follows. First the sphere must be calibrated. Essentially, this means the surface reflectance of the sphere, ρ_{sphere}, must be measured. To do this, the exit port is closed and all the incident light is scattered within the sphere. The ratio of the detected flux to the incident flux is given by

$$\frac{\Phi_d}{\Phi_i} = \frac{\frac{A_d}{A_s}\rho_{sphere}}{1 - \rho_{sphere}\left(1 - \frac{A_e}{A_s} - \frac{A_d}{A_s}\right)}, \tag{6.56}$$
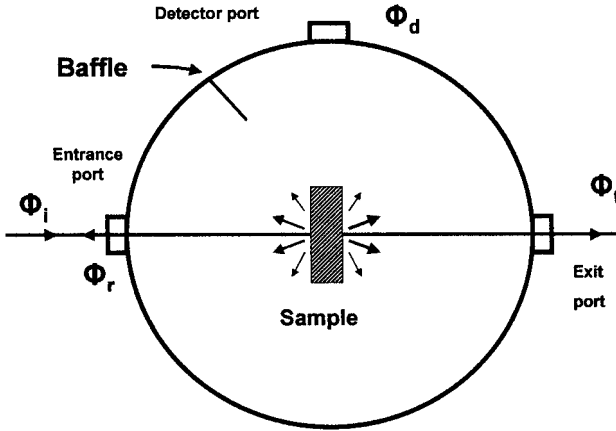
Fig. 6.20 Typical configuration of a three-port integrating sphere.

where A_s is the internal surface area of the sphere, A_d is the area of the detector port, and A_e is the area of the entrance and exit ports (assuming they are equal). This equation can be solved to obtain the reflectance of the sphere.

In the next step, the exit port is opened and a sample is placed inside the sphere. The incident beam is aligned so that the reflected and transmitted beams exit the integrating sphere. In this way, only scattered light can reach the detector. Now, the ratio of the detected flux to the incident flux is given by

$$\frac{\Phi_d}{\Phi_i} = \frac{\frac{A_d}{A_s}\alpha_{sca}}{1 - \rho_{sphere}\left(1 - 2\frac{A_e}{A_s} - \frac{A_d}{A_s}\right)}. \tag{6.57}$$

This equation can be solved to obtain the TIS of the sample.

Measurements of the integrated forward- and back-scatterance are also made with integrating spheres. This is accomplished by placing the sample in the entrance port for integrated forward-scatterance and in the exit port for integrated back-scatterance. From these measurements the forward- to back-scatter ratio can be obtained.

Problems

6.1 List the strengths and weaknesses of spectrometer and laser transmissometers. Do the two experimental approaches complement one another?

6.2 List experimental techniques that directly measure the absorption coefficient. When are such approaches superior to transmittance measurements?

6.3 Find the mathematical expression for the interferogram of a FTS for the spectrum illustrated in Fig. P6.3.

6.4 (a) Given Eq. 6.1 and knowing R and τ, solve for $\beta_{abs}(\nu)$, that is, obtain Eq. 6.27. (b) Can this approach be used when scatter is present?
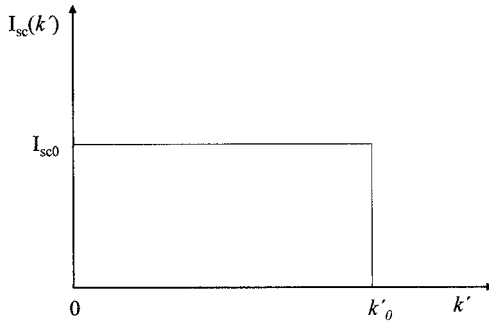
Fig. P6.3

6.5 It is computationally convenient to express $\tau, \rho,$ and α to first order as

$$\tau \approx (1 - R)^2 \, e^{-\beta_{abs} L},$$

$$\rho \approx R + R(1 - 2R)e^{-2\beta_{abs} L},$$

and

$$\alpha \approx \beta_{abs} L.$$

However, these expressions do not satisfy the total power law! Make a consistent set of approximations to $\tau, \rho,$ and α that will satisfy the total power law.

6.6 Show that the single-surface reflection coefficient, R, for normal incidence, reduces to the first-order form

$$R(\omega_{TO} < \omega \leq \omega_{LO}, \theta_i = 0) = 1 - a(\omega)\Gamma,$$

where $(\omega_{TO}^2 - \omega^2)^2 \gg (\omega\Gamma)^2$ and $a(\omega)$ depends on the classical oscillator parameters for a single-mode oscillator.

6.7 Derive Eq. 6.41, which determines the index of refraction of a prism from the minimum deviation technique.

6.8 Show that the free spectral range, $FSR(\nu)$, for normal incidence and zero dispersion is

$$FSR(\nu) = \frac{1}{2n(\nu) \, L},$$

based on the Airy formula. Also, obtain Eq. 6.44b, which includes dispersion.

6.9 Verify the solution for $n(\nu)$ given in Eq. 6.45.

6.10 Compute the TIS for the white label BRDF formula given in Section 6.2.1. (*Note:* The result is 0.62.)

6.11 Derive Eq. 6.57.

Bibliography

On Spectrometers

6.1 R.J. Bell, *Introductory Fourier Transform Spectroscopy*, Academic Press (1972).
6.2 *Diffraction Grating Handbook*, Bausch and Lomb (1977).
6.3 R.A. Sawyer, *Experimental Spectroscopy*, Dover (1963).
6.4 G.J. Zissis, "Radiometry," Chapter 4 in Vol. 1, *Sources of Radiation*, G.J. Zissis (ed.) in *The Infrared and Electro-Optical Systems Handbook*, J.S. Accetta and D.L. Shumaker (exec. eds.) SPIE/ERIM (1993).

On White Cells

6.5 J.U. White, "Long Optical Paths of Large Aperture," *J. Opt. Soc. Amer.* **32**, 285 (1942).
6.6 D. Horn and J.C. Pimentel, "2.5 km Low-temperature Multiple-reflection Cell," Measurements, *Appl. Opt.* **10**, 1892 (1971).
6.7 W.R. Watkins, "Path Differencing: An Improvement to Multipass Absorption Cell Measurements," *Appl. Opt.* **15**, 16 (1976).
6.8 D.E. Burch, D.A. Gryunak, and R.R. Patty, "Absorption of Infrared Radiation by CO_2 and H_2O Experimental Techniques," *J. Opt. Soc. Amer.* **57**, 885 (1967).

On Transmissometers

6.9 P.S. Wayland, M.E. Thomas, R.I. Joseph, and M.J. Linevsky, "Multiphonon Extra-ordinary Ray Absorption Coefficient for Sapphire," *Infrared Phys. Technol.* **41**, 307–312 (2000).

On Reflectance Spectroscopy

6.10 I.F. Chang, S.S Mitre, J.N. Plendl and L.C Mansor, "Long-wavelength Longitudinal Phonons of Multi-mode Crystals," *Phys. Status Solidi* **28**, 663 (1968).
6.11 A.S. Barker, Jr., in *Far Infrared Properties of Solids*, S.S. Mitra and S.Nudelman (eds.), Plenum (1970).
6.12 A.S. Barker, Jr., "Infrared Lattice Vibrations and Dielectric Dispersion in Corundum," *Phys. Rev.* **132**, 1474 (1963).
6.13 R.I. Joseph and M.E. Thomas, "Differential Reflection Spectroscopy: A Direct Determination of Long Wavelength Optical Mode Frequencies in Polar Crystals," *Phys. Stat. Sol. (B)* **141**, K163–K166 (1987).
6.14 G. Kortüm, *Reflectance Spectroscopy*, Springer-Verlag, New York (1969).

On Laser Measurements

6.15 L.H. Skolnik, "A Review of Techniques for Measuring Small Optical Losses in Infrared Transmitting Materials" in *Optical Properties of Highly Transparent Solids*, S.S. Mitra and B. Bendow (eds.) pp. 405-433 (1975).

On Ellipsometry

6.16 R.M.A. Azzam and N.M. Bashara, *Ellipsometry and Polarized Light*, North-Holland, Amsterdam (1977).
6.17 J.A. Woollam and P.G. Synder, "Fundamental and Applications of Variable Angle Spectroscopic Ellipsometry," Mater. Sci. Eng. **B5**, 279–283 (1990).
6.18 H.G. Tompkins, *A User's Guide to Ellipsometry*, Academic Press (1993).

On Refractometry

6.19   M. Born and E. Wolf, *Principles of Optics*, 6th Ed., Pergamon Press (1987).

On Interferometers

6.20   D.F. Edwards and E. Ochoa, "Infrared Refractive Index of Silicon," *Appl. Opt*. **19**, 4130–4131 (1980).

6.21   D. Yang and M.E. Thomas, "Measurement of the Infrared Refractive Index of Sapphire as a Function of Temperature," *Proceedings of SPIE Windows and Dome Technologies and Materials VII* 4375, April 16–17, 2001.

On Emissometers

6.22   R.M. Sova, M.J. Linevsky, and M.E. Thomas, "High Temperature Optical Properties of Oxide Dome Materials," *Proceedings of SPIE–Window and Dome Technologies and Materials III* **1760**, 27–40, July, 1992.
(Also see reference 6.14.)

On Scattering Measurements

6.23   J.C. Stover, *Optical Scattering Measurements and Analysis*, McGraw-Hill (1990).
6.24   D.J. Lovell, *Integrating Sphere Performance*, Labsphere manual (1980).

General

6.25   E.D. Palik (ed.), *Handbook of Optical Constants of Solids*, Academic Press (1985).

PART II

PRACTICAL MODELS FOR VARIOUS MEDIA

This page intentionally left blank

7

Optical Propagation in Gases and the Atmosphere of the Earth

Propagation within the atmosphere is an important consideration concerning the performance of many electro-optical systems. An electro-optical system can be described as containing three basic components: source, detector, and propagation medium. Because of the quality of source and detection systems today, often the limiting factor in overall system performance is the propagation medium. Thus a thorough discussion of the atmosphere and various mechanisms of attenuation is required. Absorption, scattering, and turbulence are the dominant mechanisms of signal loss and distortion. This chapter covers gaseous absorption and scattering in the atmosphere of the earth. Turbulence is not covered, and the reader is referred to other texts (see Chapter 1, Refs. 1.10 and 1.11).

7.1 The Atmosphere of the Earth

The atmosphere surrounds and protects the earth in the form of a gaseous blanket that acts as the transition between the solid surface of the earth and the near-vacuum of the outer solar atmosphere. It acts as a shield against harmful particle radiation, meteors, and high-energy photons. The dynamics of the atmosphere drive the weather on the surface. It provides for life itself as part of the earth's biosphere. Thus optical propagation in this medium has many important characteristics and consequences. These include meteorological optics, infrared and visible astronomy, remote sensing, and electro-optical systems performance in general. Therefore, it is appropriate to begin this chapter with an introduction to the nature of the atmosphere.

7.1.1 Atmospheric Structure

The atmosphere is composed of gases and suspended particles or aerosols at various temperatures and concentrations as a function of altitude and azimuth. The variations in altitude show a marked structure. Six main horizontal layers form the stratified structure of the atmosphere, as shown in Fig. 7.1. The lowest is the troposphere, which extends from ground level to approximately 11 km (36,000 ft or 7 mi.). The temperature in this layer generally decreases with increasing altitude at the rate of 6.5 K/km. However, variations can exist on this rate, which creates interesting refractive effects. The pressure varies from one atmosphere at sea level to a few tenths of an atmosphere at the top of this layer. Most of the important atmospheric attenuators exists in the troposphere (i.e., H_2O, CO_2, clouds, fog, aerosols in general). Water vapor is most important at lower altitudes, for example, due to evaporation over the ocean as part of the marine boundary layer. Also, this is the region of highest pressure or density and therefore has the highest molecular scatter. Aerosols in the troposphere are composed of dust particles, smoke, sea spray, and others with surface-based origins. The next layer is the stratosphere, which extends up to 50 km (30 mi.). In this layer, ozone, which protects life on the surface from ultraviolet radiation, is found. Ozone starts to significantly absorb at and below 0.3 μm, thus extending protection from these high-energy photons relative to molecular oxygen (which begins to strongly absorb below 0.185 μm). Particles in this layer can remain for a long time. Above the stratosphere is the mesosphere. This layer begins at 50 km and extends to 90 km. Most models concerning optical propagation in the atmosphere end with this layer. Above the mesosphere is the ionosphere, which is important for radiowave propagation. However, the plasma resonances that give it reflective properties at radio frequencies are too slow for optical frequencies, and this layer is optically transparent. Also molecules in the ionosphere undergo photochemical dissociation. Thus, the chemical composition significantly changes at this altitude. The ionosphere extends up to nearly 300 km. Above the ionosphere are the thermosphere and the exosphere, and they are influenced by high-energy solar radiation and the joining of the atmosphere of the earth to the solar atmosphere. The outermost altitude is approximately 500 km or 300 miles.

7.1.2 Gas Composition

Table 7.1 lists uniformly mixed, dry atmospheric gases (up to 100 km altitude) and their abundances. These molecules do not vary significantly in relative concentration with time and with altitude, as illustrated in Fig. 7.2. Nitrogen and Oxygen are by far the most abundant. Oxygen has relatively narrow absorption bands at 60 Ghz (2 cm^{-1}) because of a magnetic dipole moment, at 760 nm (13,158 cm^{-1}) and has strong absorption in the ultraviolet (the Schumann–Runge bands). Otherwise, neither gas has dipole-allowed infrared spectra. Only weak collision-induced-absorption bands (CIA) in N_2 and O_2 can be observed for very long tropospheric propagation paths. However, these molecules are very important for Rayleigh scattering (see Section 7.3) and refractive index (see Section 7.2.4) calculations. The inert gases contribute very little to optical propagation phenomena.

The other molecules like CH_4, N_2O, and CO have pronounced infrared spectral features (see Section 7.2) in the atmosphere, even though they have very minor concentrations.
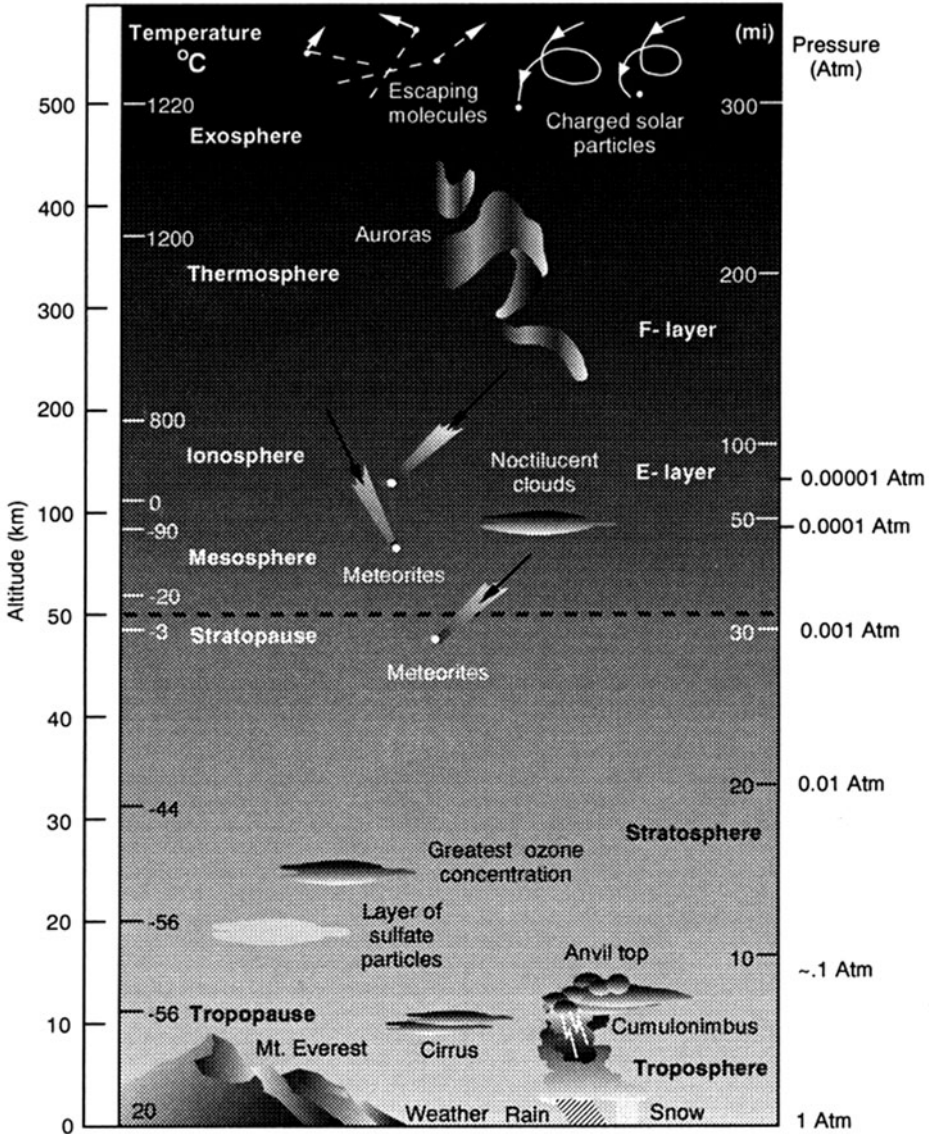
Fig. 7.1   Atmospheric structure as a function of altitude.

Their importance is localized to these spectral features, however. Some seasonal varia-tion is observed in these gases as well, due to fuel burning and other effects.

Some of the most important molecules impacting propagation have variable con-centration. This list is shown in Table 7.2 and includes H_2O, CO_2, and O_3. Water vapor exists primarily in the troposphere and is highly variable from day to day, from season to season, with altitude, and for different geographical locations. Carbon dioxide varies seasonally with a maximum during the early spring and a minimum during the late summer to early fall, and is uniformly mixed with altitude up to 80 km. These points

Table 7.1 Gases Present in Standard Amounts in a Dry Atmosphere
(*CRC Handbook of Chemistry and Physics,* Ref. 7.6)

Constituent	Volume Ratio [%]	Parts per Million
Nitrogen, N_2	78.084 ± 0.004	—
Oxygen, O_2	20.946 ± 0.002	—
Argon, Ar	0.934 ± 0.001	—
Neon, Ne	0.001818	18.18 ± 0.04
Helium, He	5.24×10^{-4}	5.24 ± 0.004
Krypton, Kr	1.14×10^{-4}	1.14 ± 0.01
Xenon, Xe	—	0.087 ± 0.001
Hydrogen, H_2	—	0.5
Methane, CH_4	—	1.75
Nitrous oxide, N_2O[a]	—	0.5 ± 0.1

[a]Has varying concentration in polluted air.

are illustrated in Figs. 7.2 and 7.3. The variable nature of these important atmospheric gases makes the prediction of atmospheric propagation at infrared frequencies a challenge. Furthermore, the concentration of water vapor also influences particle scattering.

At this point, it is useful to review the many different units used to quantify the amount of H_2O in the air. This text will consistently use pressure or number density to indicate the water vapor concentration. Unfortunately, uniform representation is seldom the case in the literature, and unit conversion often needs to be known.

1. Water vapor partial pressure, p_{H_2O}, are commonly given in kilopascal (kPa), millibars (mb), Torr (mm Hg), and atmospheres (atm), where 101.3 kPa $= 760$ Torr $= 1013$ mb $= 1$ atm.
2. Relative humidity, *rh*, is the ratio of p_{H_2O} to the saturation vapor pressure, $E_s(T)$,

$$rh = \left(\frac{p_{H_2O}}{E_s(T)} \right) \times 100\%. \tag{7.1}$$
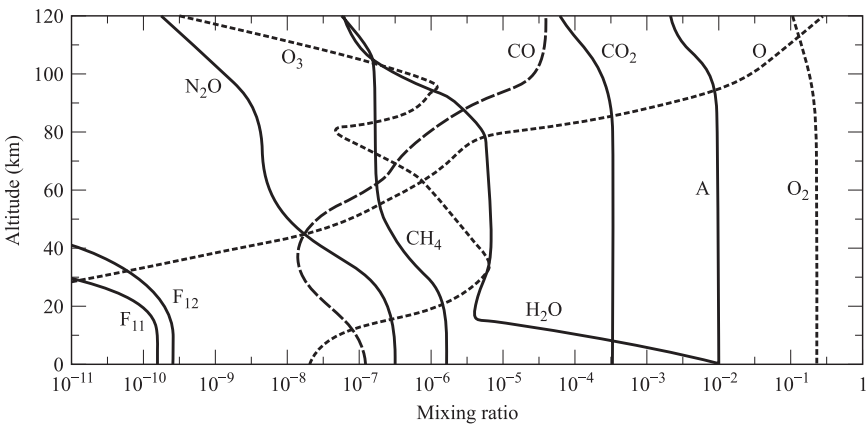
Fig. 7.2 Vertical profiles of mixing ratio relative to nitrogen of selected species at equinox (Allen et al., Refs 7.1, 7.2; Goody and Yung, Ref. 7.3, with permission).

Table 7.2 Atmospheric Gases Present in Variable Amounts (*CRC Handbook of Chemistry and Physics,* Ref. 7.6)

Constituent	Volume Ratio [%]	Parts per Million
Ozone, O_3	—	0–0.3 (tropospheric[a])
	—	1–7 (20–30 km)
Water vapor, H_2O	0–2	—
Carbon dioxide, CO_2	0.035	351 ± 4
Carbon monoxide, CO^a	—	0.19
Nitric acid vapor, HNO_3	—	$(0–10) \times 10^{-3}$
Ammonia, NH_3	—	Trace
Hydrogen sulfide, H_2S	—	$(2–20) \times 10^{-3}$
Sulfur dioxide, SO_2^a	—	$(2–20) \times 10^{-3}$
Nitrogen dioxide, NO_2	—	Trace
Nitric oxide, NO	—	Trace
CFC-11	—	3×10^{-4}

[a]Has varying concentration in polluted air.

$E_s(T)$ is computed by the following formula with an accuracy of 0.1% (Leibe, Ref. 7.5):

$$E_s(T) = 2.4096 \left(\frac{300}{T}\right)^5 10^{\left(\frac{10 - 2950.2}{T}\right)} \quad [\text{kPa}], \tag{7.2}$$

where T is temperature in kelvins. Table 7.3 lists values of $E_s(T)$ based on the above formula.

3. Absolute humidity, a, is defined as

$$a = \frac{2170 p_{H_2O}}{T} \quad [\text{g/m}^3], \tag{7.3}$$
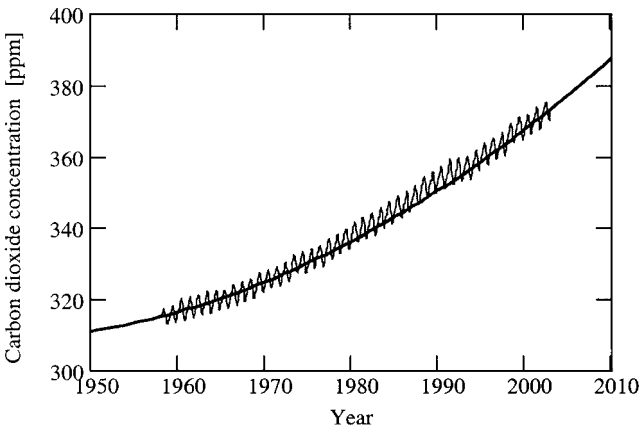
Fig. 7.3 Molecular concentration of CO_2 at Mauna Loa Observatory, Hawaii as a function of year. Both long-term trend (smooth curve given by CO_2 concentration $= 311 + 0.395$ (Year-1950) $+ 0.0148$ (Year$-1950)^2$) and seasonal changes (oscillatory curve) are shown (Bacastow et al., Ref. 7.4).

Table 7.3 Saturation Vapor Pressure of H_2O (*CRC Handbook of Chemistry and Physics,* Ref. 7.6)[a]

T [K]	E_s [kPa]	T [K]	E_s [kPa]
250	0.0760	300	3.535
260	0.1958	305	4.75
270	0.4701	310	7.228
280	0.991	320	10.540
290	1.919	330	17.202
295	2.64		

[a]The following polynomial fit represents E_s with a standard deviation of ± 0.024 kPa: $\ln(E_s) = 17.323 - 3.7496 \times 10^3 T^{-1} - 2.3061 \times 10^5 T^{-2}$.

where p_{H_2O} is in kPa and T in K. This formula can be obtained from the ideal gas law, $P_i = \rho_i k_B T$.

7.1.3 Particle Composition

Particles vary not only in chemical composition and concentration but also in size (from about 0.01 to 10 μm) and shape (spheres, ellipsoids, rods, etc.). Therefore, the description of atmospheric particles is far more difficult than the description of atmospheric molecules. The range of sizes varies for different types of particles, as Table 7.4 indicates. A particle with one size is called monodisperse. A particle with a distribution of sizes is called polydisperse. Size distribution functions specify the concentration of a particle size as a function of particle radius. Height distribution functions specify the concentration as a function of altitude. The first 2 km is a mixed region, and particle characteristics depend greatly on the nature of the surface. In the mid-tropospheric region, the height distribution is exponential much like molecular pressure. At stratospheric altitudes, particle concentrations are driven by volcanic activity. Generally, simple shapes are assumed for model calculations (e.g., spheres, rods); however, shape distribution functions are needed also. Two basic classes of particles determine the majority of scattering attenuation in the atmosphere: aerosols and hydrometers.

Aerosols have radii less than 1 μm. Because these particles are very small, they are suspended in the atmosphere. Scattering by aerosols greatly increases broad-band optical attenuation over molecular scattering, and is called haze. Particles have the highest concentration levels near the surface of the earth and therefore, the highest levels of haze are also near the surface of the earth. This point is readily verified by observing the color of the sky as a function of zenith angle. Overhead, the sky is a distinctive blue, because of molecular Rayleigh scattering, but toward the horizon, the color becomes whiter. This is because the path length increases in the particle-rich lower atmosphere. Examples of aerosols are smog, smoke, fine soil particles, cosmic dust, clouds, and fog. Particles that contain moisture add another dimension to the description as the humidity must also be known. A dry particle acts as a condensation nucleus and grows in size. The particle becomes more spherical and scatter loss is enhanced.

The second class of particles is called hydrometers, which are water-dominated particles in the liquid or solid state. Examples include the many types of clouds, mist, fog, rain, freezing rain, hail, snow, and ocean spray. These particles are typically larger than 1 μm, and stay suspended for shorter periods of time than aerosols because they are more massive.

Table 7.4 Radius Range for Various Types of Particles

Type	Radius [μm]	Concentration [cm^{-3}]
Air molecules	10^{-4}	10^{19}
Aiken nucleus	10^{-3}–10^{-2}	10^{4}–10^{2}
Aerosol	10^{-2}–1	10^{3}–10
Fog	1–10	100–10
Cloud	1–10	300–10
Raindrops	10^{2}–10^{4}	10^{-2}–10^{-5}

The detailed discussion of particle distribution functions and particle scattering is delayed until Chapter 10, since the optical properties of solids (see Chapter 8) and water (see Chapter 9) must be covered first.

7.1.4 Pressure Variation with Altitude

As the altitude increases, the total atmospheric pressure decreases almost exponentially, as illustrated in Fig. 7.4. To see this, consider a column of gas. The incremental pressure, dp, from an incremental altitude, dz, caused by its weight in a gravitational field is

$$dp = -\rho_m(z)g\,dz, \qquad (7.4)$$

where ρ_m is the mass density and g is the gravitational acceleration. However, ρ_m must vary with altitude, z. Now let us use the ideal gas law, to obtain

$$\rho_m(z) = m\rho(z) = \frac{mp(z)}{k_B T(z)}, \qquad (7.5)$$

where $\rho_m(z)$ is the average mass density, $\rho(z)$ is the number density, and m is the average mass per molecule for a dry atmosphere (28.964 amu for $z < 100$ km, for a humid
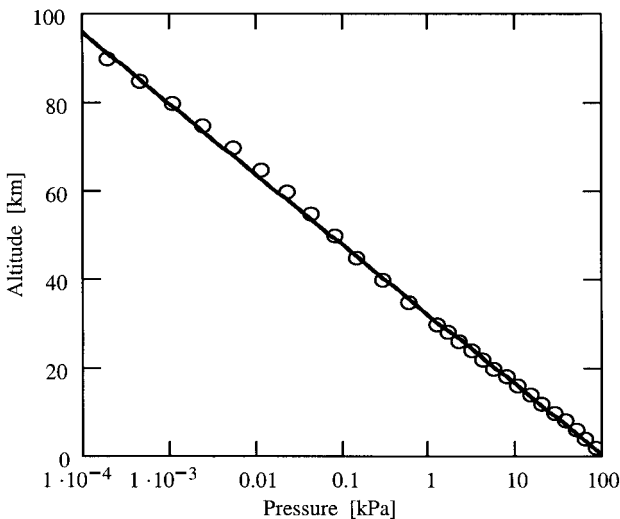
Fig. 7.4 The 1976 U.S. Standard Atmospheric Pressure as a function of altitude (○). The solid curve, as given by $p(z) = 1013\exp(-0.145z)$, is a fit to the data (see Eq. 7.8b).

atmosphere $m \to m(z)$). Thus, substituting this result into Eq. 7.4, we obtain the following first-order differential equation:

$$\frac{dp}{p(z)} = -\frac{m(z)\,g}{k_B T(z)}\,dz. \tag{7.6}$$

The general solution (for m constant) is obtained in a straightforward manner to be

$$p(z) = p(0)\exp\left(-\frac{mg}{k_B}\int_0^z \frac{dz'}{T(z')}\right). \tag{7.7}$$

Now, let us assume $T(z) = T_0 + az$, which is the case for the Standard Troposphere (1976 U.S. Standard Atmosphere), where $a = -6.5$ K/km and $T_0 = 288$ K. The solution of the above differential equation leads to the following result for the vertical pressure profile:

$$p(z) = p(0)\left(\frac{T(z)}{T_0}\right)^{\frac{-mg}{ak_B}} \tag{7.8a}$$

The numerical value of the exponent in this equation for the U.S. Standard Troposphere ($z < 10$ km) is 5.255.

The temperature dependence above the troposphere is not linear. In the stratosphere the vertical temperature profile is almost constant. The atmospheric temperature profile as a function of altitude for the 1976 U.S. Standard Atmosphere is plotted in Fig. 7.5 up to an altitude of 100 km. Based on this figure, the variation from ground to 100 km is modest, staying within $\pm20\%$ of the mean value of 235 K. In the isothermal limit (i.e., $T(z) = T_0$), the solution of Eq. 7.7 simplifies to
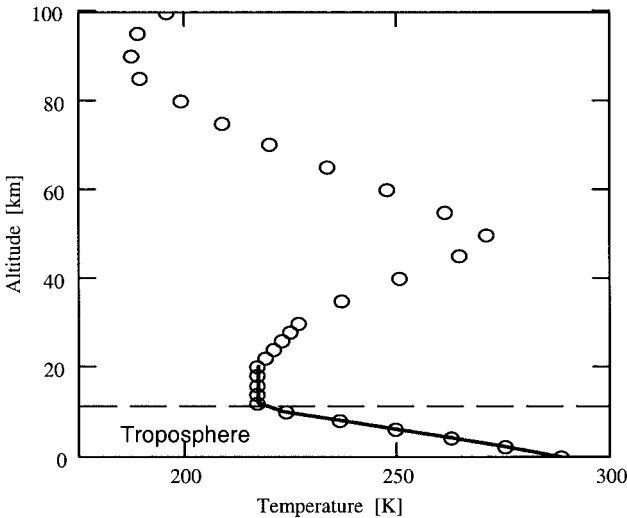
Fig. 7.5 The 1976 U.S. Standard Atmospheric Temperature profile as a function of altitude.

$$p(z) = p(0) \exp\left(\frac{-mgz}{k_B T_0}\right) = p(0) \exp\left(-\frac{34.16z}{T_0}\right), \tag{7.8b}$$

where z is expressed in kilometers, and T_0 in kelvins. Since the temperature variation is small for limited ranges of altitude, this is a good approximation (especially for the stratosphere). Using an average temperature for the first 100 km of 235 K and using $p(0) = 1013$ mb, Eq. 7.8b was used in Fig. 7.4 to obtain the solid curve.

These formulas can be used to form a piecewise continuous representation of the total pressure and uniformly mixed gas partial pressure variation of the real atmosphere with altitude, given the temperature profile.

7.2 Molecular Absorption and Refraction

This section begins with a discussion of molecular absorption in the window regions of the atmosphere. Reviews of experimental data, empirical models, and theoretical models are presented. Molecular absorption dominates the optical properties of the atmosphere in the infrared and ultraviolet. The section then closes with a discussion of atmospheric refraction.

7.2.1 Absorption by Atmospheric Gases

Absorption by molecules defines the atmospheric windows and is an important mechanism of tropospheric attenuation at all millimeter and infrared wavelengths, especially in the marine or relatively humid environments. Therefore, the understanding and accurate modeling of absorption by atmospheric molecules are important to atmospheric remote sensing, open-air communication, infrared imaging systems, long-path laser propagation, electro-optical systems, radar, and atmospheric meteorology. The greenhouse effect of the atmosphere of the earth is caused by absorption of blackbody radiation in the 10 µm region from the surface. The absorbed energy heats the atmosphere, causing an increase in global temperature. Figure 7.6a shows low-resolution infrared transmittance of the atmosphere and demonstrates the importance of water vapor over other atmospheric constituents (Shaw, Ref. 7.7). The H_2O absorption bands, along with those of CO_2, define the atmospheric window regions in the infrared. At millimeter and microwave wavelengths, the rotational band of O_2 at 60 GHz and local rotational lines of H_2O determine the window regions. Figure 7.6c shows the water vapor absorption coefficient for the millimetre–microwave region.

The main rotational and vibrational bands have been extensively characterized by many investigators (Benedict and Calfee, Ref. 7.8; Gates et al., Ref. 7.9; Camy-Peyret and Flaud, Ref. 7.10). This work has resulted in a compendium of absorption-line parameters representing 31 different gases, maintained by the Phillips Laboratory at Hanscom Air Force Base (formerly the Geophysics Directorate and the Air Force Geophysics Laboratory), which represents a significant contribution to absorption calculations. Details of this database are discussed in Section 7.2.2. The database contains parameters for weak absorptions lines in the window regions. However, this information is, in general, not as accurate as that of the main bands, and work continues to improve the spectral line parameters.
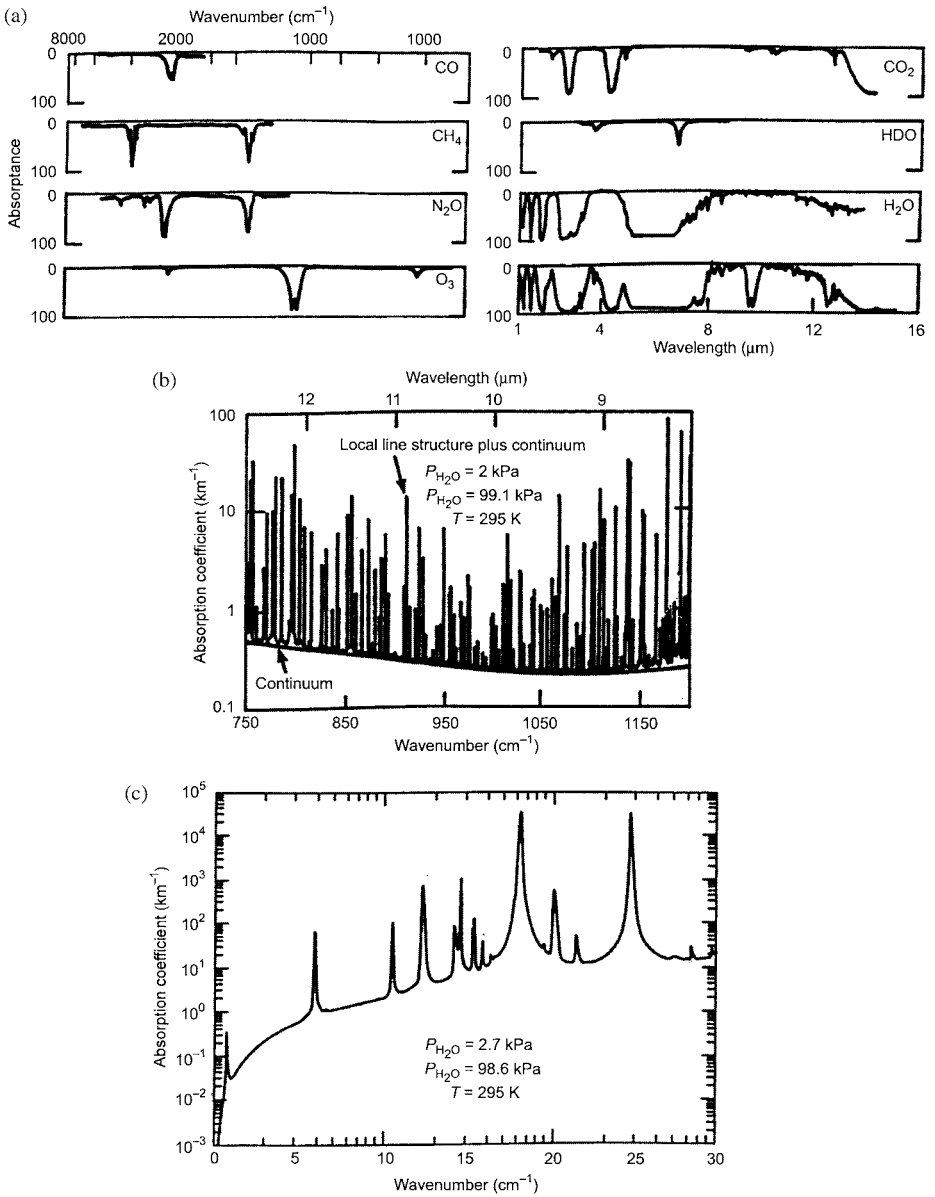
Fig. 7.6 (a) Low-resolution solar spectrum compared with laboratory spectra of atmospheric gases (Shaw, Ref. 7.7, with permission). Synthetic water vapor local line structure plus continuum for a homogeneous path in (b) 10 μm region and (c) microwave–millimeter wave region.

The comparatively weak absorption that does occur in the window regions can be described as arising from two distinct sources, local line and continuum absorption, as illustrated in the high-resolution computed spectrum of Fig. 7.6b for the 10 μm window region. Weak absorption bands of CO_2 and HDO, along with other H_2O absorption lines in the window regions, compose the local line contribution. The continuum contributes an additional, gradually varying, frequency-dependent background to total absorption. A general empirical form for the continuum absorption coefficient is often used to represent eperimental data:

$$\beta_{cont}(v, T, p_{f1}, \ldots p_{fi}, p_a) = \frac{p_a}{R_{GC}T} \sum_{i=1}^{i_{max}} \left[C_{Fi}(v,T)p_{fi} + C_s(v,T)p_a \right], \quad (7.9)$$

where C_s is the self-broadening coefficient of the absorbing gas, C_{Fi} is the foreign broadening coefficient due to the ith type foreign gas, p_a and p_{fi} are the absorber and foreign gas partial pressures, respectively, and R_{GC} is the ideal-gas constant (McClatchey et al., Ref. 7.11). The above formula is consistent in form with a far-wing expansion of the collision-broadened absorption coefficient given in Chapter 5 (recall Problem 5.9). This point will be used later to obtain simple mathematical formulas for continuum absorption. The equation can be rewritten for the case of two broadening gases ($i_{max} = 2$), to obtain

$$\beta_{cont}(v,T) = \frac{C_{F1}(v,T)}{R_{GC}T} p_a[p_{f1} + F(v,T)p_{f2} + B(v,T)p_a], \quad (7.10)$$

where $F = C_{F2}/C_{F1}$ and $B = C_s/C_{F1}$ are the dimensionless foreign and self-broadening coefficients. Near line center, B has a typical value of 5 for water vapor relative to nitrogen (see Table 5.1). In the real atmosphere, the effects of oxygen broadening must also be included. The dimensionless broadening coefficient F accounts for oxygen relative to nitrogen. However, many laboratory experiments ignore the effects of oxygen and use only nitrogen as the broadening gas along with the absorbing gas.

7.2.1.1 Water Vapor Absorption

The strong dipole moment and light hydrogen atoms composing water vapor result in strong, broad rotational absorption bands (high B) and high vibrational frequencies. Also, water vapor is an asymmetric top, thus all the bands are active and feature dense irregular spectra (as illustrated in Fig. 3.9 for the pure rotational band). Thus, water vapor absorption is important in every infrared window region of the atmosphere.

Fundamental Bands   To determine atmospheric window locations and index of refraction contributions, knowledge of band strength and position of the strongest absorption bands is important. Table 7.5 lists band origins and integrated intensities, $S'_n(T)$, defined by

$$S'_n(T) = \frac{1}{\rho_a} \int_{B \text{ and } D} dv\, \beta_{abs}(v,T) \quad [\text{cm}],$$

for several important water vapor absorption bands throughout the infrared. The integrated intensity is the sum of all the line strengths within a band, divided by the absorber density.

Table 7.5 Integrated Intensities of the Major Water Vapor Bands[a] (Goody and Yung, Ref. 7.3, with permission).

Band Origin [cm^{-1}]	Isotope	Upper Vibrational State ($\nu_1\nu_2\nu_3$)	$S_n(295$ K$) \times 10^{21}$ [cm]
0.0	H^{16}OH	000	52700.0
0.0	H^{17}OH	000	19.4
0.0	H^{18}OH	000	107.0
1588.28	H^{18}OH	010	21.0
1591.33	H^{17}OH	010	3.82
1594.75	H^{16}OH	010	10400.0
3151.63	H^{16}OH	020	75.4
3657.05	H^{16}OH	100	487.0
3707.47	H^{16}OD	001	1.42
3741.57	H^{18}OH	001	13.9
3748.32	H^{17}OH	001	2.52
3755.93	H^{16}OH	001	6930.0
5234.98	H^{16}OH	110	37.2
5331.27	H^{16}OH	011	804.0
6871.51	H^{16}OH	021	57.4
7201.48	H^{16}OH	200	52.9
7249.93	H^{16}OH	101	747.0
8807.0	H^{16}OH	111	49.8
9000.0	H^{16}OH	012	1.6
10238.72	H^{16}OH	121	2.1
10613	H^{16}OH	201	10.0
11032	H^{16}OH	003	2.4
12151.26	H^{16}OH	211	0.93
13820.92	H^{16}OH	301	1.08
14318.80	H^{16}OH	103	0.2

[a]The lower state is the ground state 000. S_n for isotopes is calculated on the basis of the total number of molecules of all isotopic species. n indicates the vibrational quantum numbers for a particular transition.

All bands listed originate from the ground state. The locations of the bands match the experimentally observed locations in Fig. 7.6a. It is clear that the these strong absorption bands of water vapor define the atmospheric window regions to be 8–12 µm, 3–5 µm, 2–2.5 µm, 1.5–1.77 µm, 1.18–1.31 µm, and 1–1.1 µm. For shorter near-visible wavelengths, water vapor absorption plays a more minor role.

Window Regions   As previously mentioned, molecular absorption in the window regions manifests itself as local line and continuum-type absorption. Narrow-band systems can often minimize local line effects but not continuum absorption. Broad-band systems must account for both.

LOCAL LINE ABSORPTION   Local line structure within the 10 µm and 4 µm water vapor window regions has been experimentally observed using an FTS and a long-path White cell (Benedict et al., Ref. 7.8.; Gates et al., Ref. 7.9). Field measurements of local line structure in the 10 µm region have been reported by Rinsland et al. (Ref. 7.16). The 1–1.1 µm local line structure based on experimental data has been reported by Gallery et al. (Ref. 7.17). The data demonstrate the importance of the rich local line structure in the case of water vapor and the need for experimental data to validate the

HITRAN database. The HITRAN database represents local line structure based on experimental data and/or theoretical calculations. This database is described in more detail in Section 7.2.2. The database contains information on the line position, strength, lower energy level, foreign half-width, half-width temperature dependence, and the self-half-width. For many applications this is adequate information to develop propagation models of the atmosphere. The accuracy of the information varies for the weak lines in window regions. Line position and lower energy level are known very well, line strength is usually within 10%, and half-widths are known to 20%. The self-half-width is important for accurate local line characterization. For broad-band applications, the average dimensionless self-broadening coefficient value of $B = 5$ can be used.

However, laser propagation, such as remote sensing systems using narrow-band lasers, needs a more through characterization of local line structure. The pressure shift parameter, as defined by Eq. 5.99, must be known when the frequency of the laser corresponds closely to the location of an absorption line. For water vapor in particular, this is an important effect. Experimental observations of the pressure shift in the 2 µm window indicate that it is generally to the red. The self-shift is smaller than the half-width in magnitude, and the nitrogen shift is less than one-tenth of the nitrogen half-width magnitude. The pressure shift for water vapor is unusually large, compared with other common atmospheric molecules. It is attributable to the large dipole moment and is an important aspect of accurate local line characterization. Table 7.6 lists NTP values for the self-, oxygen, and nitrogen half-width, and self- and nitrogen shift for a few water vapor absorption lines in the 2 µm window region.

The effects of oxygen broadening must also be considered. Since most experimental data are taken with nitrogen-buffered water vapor samples, the broadening effects of oxygen must be known for realistic atmospheric models. Based on the definition of F, given by Eq. 7.10, the near-line-center dimensionless foreign broadening coefficient is needed for oxygen relative to nitrogen. The $R(20)$ CO_2 laser line at 975.930 cm^{-1} is nearly coincident with a water vapor absorption line at 975.943 cm^{-1} (unshifted location). CO_2 laser White cell transmittance and laser photoacoustic measurements of the absorption coefficient as a function of oxygen partial pressure indicate $F = 0.62 \pm 0.07$ (Peterson et al., Ref. 7.47; Nordstrom et al., Ref. 7.51) for that line. It is assumed that this result can be applied to lines in this region in general. More accurate determination can be made by high-resolution spectrometer measurements. High-resolution *FTS* measurements in the 2 µm region show that the average value of F is 0.55 ± 0.05 (Sova et al., Ref. 7.18). Values of F for individual lines are listed in Table 7.6. F depends on the rotational quantum number. Taking the average value of F to be 0.55, a dimensionless air-broadening coefficient, F_{air}, of 0.91 is obtained. This means the air-broadened half-

Table 7.6 Half-Width and Shift Parameters for H_2O Absorption at $T = 296$ K in the 2 μm Region (Sova et al., Ref. 7.18)

Line Position [cm^{-1}]	Nitrogen-Half-Width [cm^{-1}/atm]	Self-Half-Width [cm^{-1}/atm]	Oxygen-Half-Width [cm^{-1}/atm]	Self-Shift [cm^{-1}/atm]	Nitrogen-Shift [cm^{-1}/atm]
4757.906	0.103	0.477	0.055	−0.194	−0.009
4758.212	0.0607	1.07	0.024	−0.249	−0.007
4796.554	0.002	0.671	0.049	−0.142	−0.011
4948.155	0.0895	0.944	0.051	−0.156	−0.021

width values are 9% less than the nitrogen-broadened values. For many narrow-band applications, this correction cannot be ignored.

CONTINUUM ABSORPTION   In 1942, Elsasser (Ref. 7.19) recognized a continuum in the 8–13 µm window region, which he attributed to the far wings of the strong, nearby rotational and ν_2 vibrational rotational bands of H_2O. Further verification of this nonlocal line absorption feature was provided by Yates and Taylor (Ref. 7.20), who studied infra-red attenuation along horizontal paths at sea level. Solar spectra studies also indicated continuum absorption in the 8–13 µm window (Adel, Anthony, and Roach and Goody, Refs. 7.21–7.23). The nature of the continuum, judged by those measurements, was uncertain. It could be due to far wings (far from the band center) of strong absorption bands or to scattering and absorption by particulates.

In an effort to determine the cause of continuum absorption in the 8–13 µm window, Bignell et al., in 1963, examined solar spectra while monitoring the atmosphere for aerosol concentrations and studying CO_2 far-wing contributions. He concluded that the amount of continuum absorption observed could not be explained by aerosol attenuation or far-wing absorption by CO_2 (Ref. 7.24). An attempt was then made to model the continuum by far wings of the bordering H_2O bands. The important contribution from this initial work was the realization of major water vapor contributions to the continuum. A second paper by Bignell, in 1970, described a careful examination of water vapor absorption in the window regions by use of a multiple-traversal absorption cell and grating spectrometer (Ref. 7.25). Two important characteristics of the 8–13 µm window as noted: (a) a large ratio of water vapor self-to-foreign-gas broadening ability (see Eq. 5.97) and (b) a strong negative temperature dependence. Neither of these findings were anticipated on the basis of the far-wing approaches of Bignell's et al. 1963 paper (Ref. 7.24). Also reported by Bignell was a similar, but much weaker, continuum absorption in the 4 µm region. (The 4 µm region also features a collision-induced absorption band of nitrogen (Crawford et al., Ref. 7.26; Susskind and Searl, Ref. 7.27). The band is of comparable strength to the water vapor continuum in the earth's atmosphere. It is a smooth absorption band showing no structure; thus, it is often referred to as the nitrogen continuum. Also, a far-wing continuum of CO_2 beyond the ν_3 band head is observed between 4.0 and 4.1 µm (Winters et al., Ref. 7.28). These other continua will be discussed later (see Sections 7.2.1.2 and 7.2.1.4).

Since those initial experimental efforts to characterize water vapor continuum absorption, many measurements have been made. They fall into three categories: (a) measurements within the earth's atmosphere or field measurements, (b) laboratory measurements using a long-path cell and a spectrometer with a broad-band source, and (c) laboratory measurements using a long-path cell or a photoacoustic cell with a laser source. Although continuum absorption was first observed through long-path field measurements, its precise characterization requires control and knowledge of the propagation path. The effects of turbulence, particulate scattering, temperature variations, and partial-pressure variations are difficult to determine in a field measurement. Thus, laboratory measurements are needed to characterize the pressure and temperature dependence of each atmospheric constituent. Spectrometer measurements determine the frequency dependence of the window regions, that is, local lines and continuum absorption. Laser measurements are limited to discrete frequencies, but because of the laser's higher power and stability, greater accuracy can be obtained; this is particularly true for photoacoustic techniques. Laboratory transmission measurements require very long path lengths ($\sim$1 km or longer) and thus are difficult to obtain. The photoacoustic

cell, on the other hand, is compact (about 30 cm) but still maintains considerable sensitivity. Of course, field measurements will have the final say in the validation of atmospheric propagation computer codes.

As a result of these experiments, a good characterization of the commonly used window regions exists today. An excellent review of the field is given by the work of Hinderling et al. (Ref. 7.29) and Grant (Ref. 7.30). They emphasize the 8–14 μm window region, which, along with the millimeter-wave window, is the most extensively measured. A review of the latest continuum experimental data and empirical models covering all the window regions is given in the following subsections, followed by a brief review of theoretical models used to explain the experimental data.

Millimeter-Wave Window   The microwave–millimetre-wave atmospheric window is used extensively today. Atmospheric transparency is very good at the low-frequency end of this window, but absorption phenomena become more important as the frequency increases. Figure 7.7 shows continuum absorption from 10 to 1000 GHz (total absorption minus local lines). The solid line represents an empirical formula given by Gaut and Reifenstein (Ref. 7.32), as given by

$$\beta_{cont}(f) = (1.08 \times 10^{-6})\rho_a \left(\frac{300}{T}\right)^{\frac{1}{2}} \left(\frac{P_T}{101}\right) f^2 \quad [\text{km}^{-1}], \qquad (7.11)$$

where ρ_a is the water vapor mass density in g/m³, P_T is the total pressure in kPa, and f is th frequency in GHz. The plotted points indicate experimental data. The frequency-squared continuum dependence is expected, based on Eq. 5.98 in the low-frequency limit. Although the above formula correctly demonstrates the frequency dependence of the continuum, it does not represent the observed temperature and pressure dependence. More recent work by Liebe (Ref. 7.36) uses a continuum formula, fitted to experimental data at 138 GHz, of the form

$$\beta_{cont}(f) = 4.73 \times 10^{-8} f^2 \left(\frac{300}{T}\right)^3 p_a \left[p_f + 31.6\left(\frac{300}{T}\right)^{7.5} p_a\right] \quad [\text{km}^{-1}] \quad (7.12)$$

where f is in GHz, T is in kelvins, and p_a and p_f ($p_f = P_T - p_a$) are in kPa. A strong dependence on the water vapor partial pressure is shown ($B \gg 5$; recall $B = 5$ at line center for water vapor, see Table 5.1 and Eq. 7.10). The continuum absorption coefficient calculated using Eq. 7.12 is smaller than that calculated using Eq. 7.11 because of improved local line modeling.

On the basis of additional work by Liebe and Layton (Ref. 7.37), and Liebe (Ref. 7.38), B grows as the frequency decreases from 833 to 110 GHz, as demonstrated in Table 7.7. This dependence is expected if the far-wing fall-off due to nitrogen collision is more rapid than the far-wing fall-off due to water vapor collisions. Based on the far-wing model of Birnbaum (see Chapter 5), the following empirical formula (valid for $f < 1000$ GHz and β_{cont} in km⁻¹) is obtained (Thomas, Ref. 7.39)

$$\beta_{cont}(f) = (4.73 \times 10^{-8}) f^2 \theta^4 p_a \left(p_f + 40.9 e^{-0.0025f} \theta^{6.5} p_a\right). \qquad (7.13)$$

where $\theta = (300/T)$, T is in kelvins, and pressure is in kPa.

As Eqs. 7.12 and 7.13 both indicate, B is a strong function of temperature. This is not

expected based on simple Lorentz line shape theory. Although Liebe (Refs. 7.36–7.38) chooses to represent his data in power-law form, a comprehensive study at 213 GHz by Llewellyn-Jones shows that the self-broadening coefficient, C_s, fits an Arrhenius plot of the functional form

$$C_s(v,T) \propto e^{b/T}, \qquad (7.14)$$

where $b = 5 \times 10^4$ K and C_s is defined in Eq. 7.9. Figure 7.8 illustrates the experimental results of Llewellyn-Jones out to 213 GHz. Again, a strong negative temperature dependence is observed at this frequency.

In summary, the millimeter-wave water vapor continuum falls off as frequency squared, has an enhanced self-broadening contribution that grows with decreasing frequency, and has a strong negative temperature dependence.

The 8–12 μm Window   This important atmospheric window has been studied by many investigators for three reasons. Room-temperature blackbody radiation peaks within this spectral window (recall Fig. 5.1). Thus, atmospheric heating by ground radi-
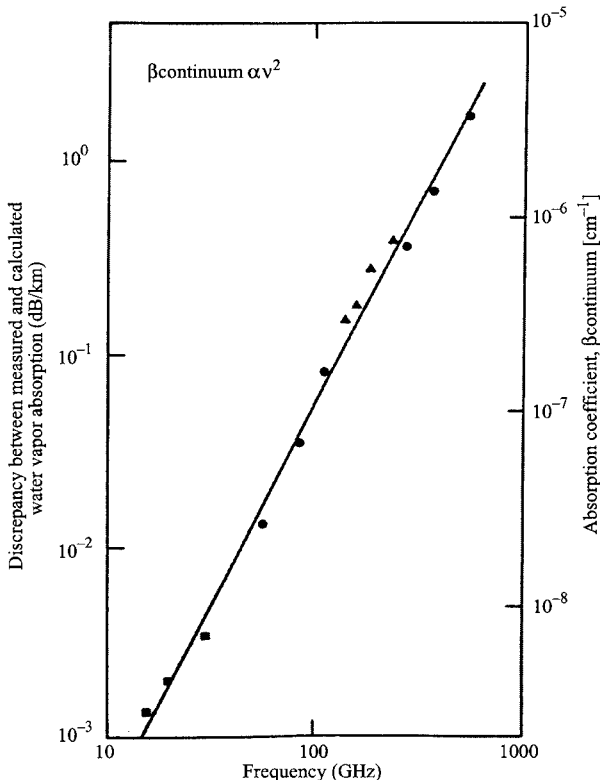
Fig. 7.7 Water vapor continuum absorption coefficient as a function of frequency. The solid line is an empirical fit to the experimental data points as given by Eq. 7.11 (Gaut and Reifenstein, Ref. 7.32). The plotted points are (▲) (Becker and Autler, Ref. 7.33), (●) (Frenkel and Woods, Ref. 7.34) and (■) (Burch, Ref. 7.35) for $T = 300$ K, $P_T = 101$ kPa, and $\rho_a = 10^{-3}$ kg/m^3 (Waters, Ref. 7.31).

Table 7.7 Experimental Frequency Dependence of $B(\nu, 300)$ (Liebe, Ref. 7.38)

f [GHz]	ν [cm^{-1}]	$B(\nu, 300)$
110	3.7	32
138	4.6	31.6
213	7.1	20
833	27.8	7.4

ance depends on the vertical absorptance of the atmosphere. This is a crucial component of climate models. Also, night-vision systems, which use the infrared spectrum to view thermal radiation from targets, often use the 8–12 μm window. The last application, which requires knowledge of the water vapor continuum, is atmospheric remote sensing. The water vapor continuum in this spectral region is strong and cannot be ignored.

Figure 7.9a shows the self-broadening water vapor continuum coefficient, C_s as a function of frequency between 7 and 22 μm at 296 K. The experimental data come from long-path White cell transmittance measurements with spectrometers and CO_2 lasers and photoacoustic measurements with CO_2 lasers. The spectrometer was tuned to microwindow regions where no or minimal local line absorption contributions are made. In Fig. 7.9, the spectrometer data ($\times$), have some local line contamination because they
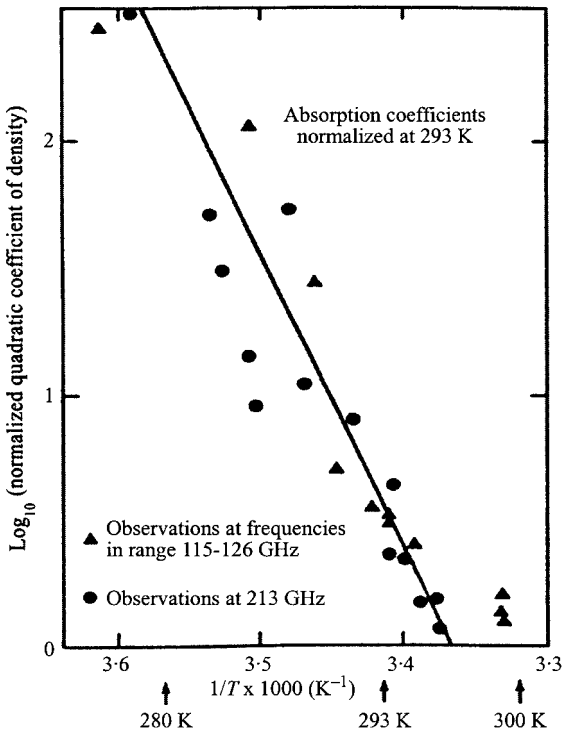
Fig. 7.8 Temperature dependence of millimeter-wave water vapor continuum quadratic term. Solid curve represents empirical fit to data as given by Eq. 7.14 (Llewellyn-Jones, Ref. 7.40).

are strong in this near-band region. The solid curve represents a fit to discrete spectrometer measurements at locations with virtually no contribution from the now weak local lines. The laser frequencies selected (+) have minimal local line contribution. For this reason, the laser data act as an upper bound to the true continuum level. The data scatter is an indication of the success of separation of continuum from local line absorption. Thus, overall, the experimental data directly represent the water vapor continuum. The self-broadening coefficient decreases exponentially as the frequency increases and then increases above 1050 cm⁻¹. The diode laser measurement by Montgomery (Ref. 7.45) and spectrometer measurements by Burch (Ref. 7.53) definitely establish the upward trend toward the ν_2 band. The same functional dependence is exhibited by the nitrogen-broadening coefficient, C_N, as shown in Fig. 7.9b, but the rate of change is more rapid. Thus, $B(= C_S/C_N)$ increases as the frequency increases away from the rotational band and then decreases toward the ν_2 band. Long-path White cell and photoacoustic laser measurements indicate that B can be quite large. Values ranging from 100 to 700 have been measured in the 10 μm region with CO_2 lasers (Peterson et al., Ref. 7.43). Figure 7.10 illustrates a single-frequency spectrometer (900 cm⁻¹) and laser measurement (952.881 cm⁻¹) as a function of the water vapor partial pressure. The total pressure is maintained at 101 kPa (1 atm) with nitrogen as the foreign broadener. Notice the nearly parabolic nature of the absorption coefficient. Based on Eq. 7.10, this indicates strong water vapor–water vapor interaction contributions.

The observed temperature dependence at 944.195 cm⁻¹ (10.6 μm) features a rapid decrease with increasing temperature, as illustrated in Fig. 7.11, just as in the millimeter window region. The temperature dependence has the following functional form over a wide temperature range (Hinderling et al., Ref. 7.29),

$$C_s(\nu,T) = C_s(\nu,T_0)e^{b(1/T - 1/T_0)}, \tag{7.15}$$

where C_s (944.195 cm⁻¹, 296 K) $= 1.83 \times 10^{-22}$ cm⁻²/(atm molecule) and $b = 1680$ K. This result at 10.59 μm is also consistent with other measurements in the 8–12 μm region. This point is made in Fig. 7.11 as well by comparing the same exponential function with temperature dependent data at 1000 cm⁻¹ and 1203 cm⁻¹.

Based on experimental data and Birnbaum's line shape formula in the far-wing limit, a simple formula for the nitrogen-broadened water vapor continuum absorption coefficient from 400 to 1400 cm⁻¹ and for typical atmospheric temperatures is given by

$$\beta_{cont}(\nu,T,p_{H_2O},p_{N_2}) = 7.34 \times 10^{26}(p_{H_2O}/T)(C_N(\nu,T)p_{N_2}$$
$$+ C_s(\nu,T)p_{H_2O}) \quad [\text{km}^{-1}], \tag{7.16}$$

where

$$C_N(\nu,T) = [3.7 \times 10^{-21} \exp(-0.01\nu) + 5.5 \times 10^{-33} \exp(0.016\nu)]$$
$$\times \exp(1680(1/T - 1/T_0))$$

$$C_s(\nu,T) = [2.45 \times 10^{-20} \exp(-0.0051\nu) + 1.9 \times 10^{-29} \exp(0.0125\nu)]$$
$$\times \exp(1680(1/T - 1/T_0)).$$

p is in atmospheres, ν is in wave numbers, and $T_0 = 296$ K. The units of the broaden-
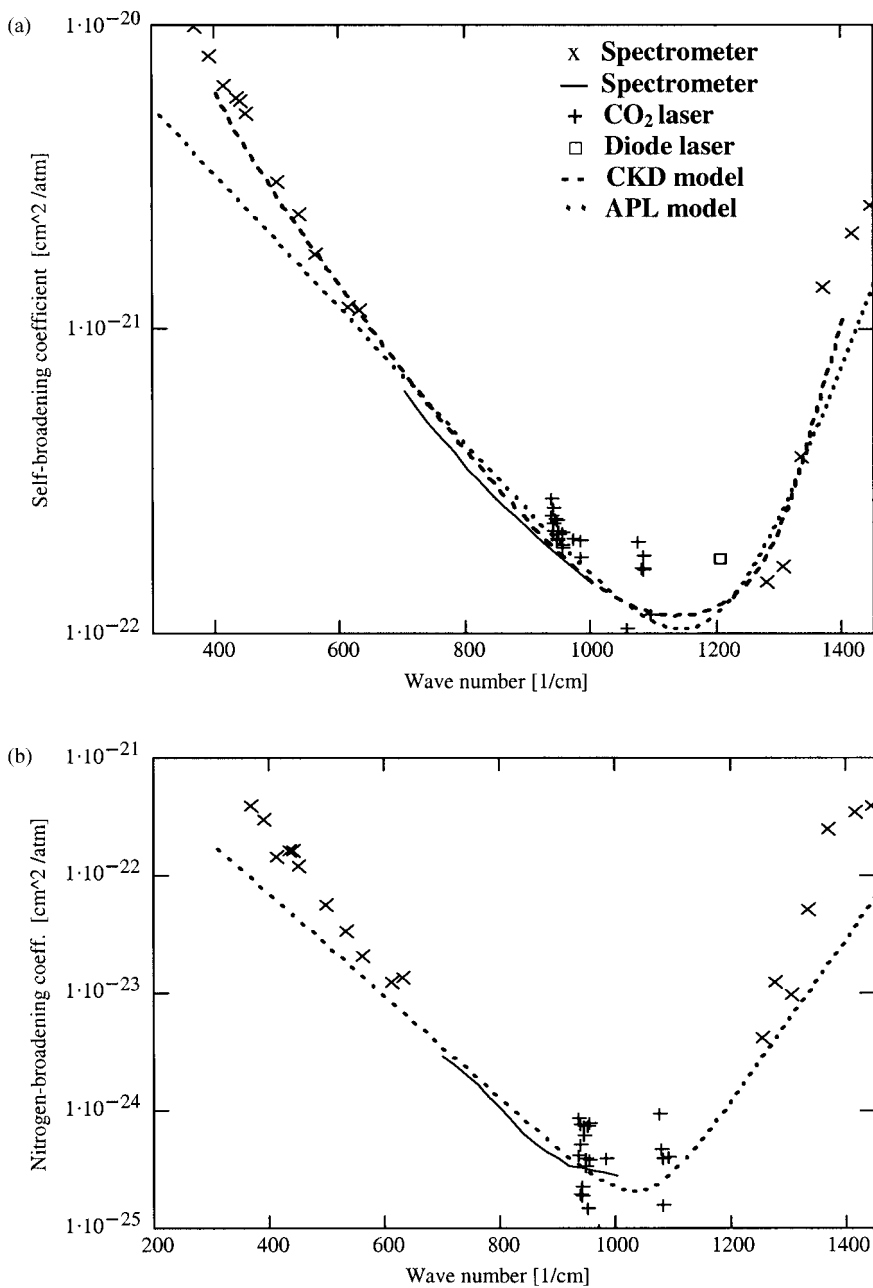
Fig. 7.9 (a) Self-broadening coefficient [cm^2/(atm molecule)] as a function of wave number from 300 to 1400 cm^{-1} at $T = 296$ K. (b) Nitrogen broadening coefficient [cm^2/(atm molecule)] as a function of wave number from 300 to 1400 cm^{-1} at 296 K. The dotted curve is a model fit to the experimental data as given by Eq. 7.16. The dashed curve is the CKD model (Clough et al., Ref. 7.67) scaled to room temperature using Eq. 7.15. [x and solid curve – spectrometer measurements (Burch et al., Ref. 7.53), □ – diode laser measurement (Montgomery, Ref. 7.45), + – CO$_2$ laser measurements (Hinderling et al., Ref. 7.29; Peterson et al., Ref. 7.43; Ryan et al., Ref. 7.44).]

281
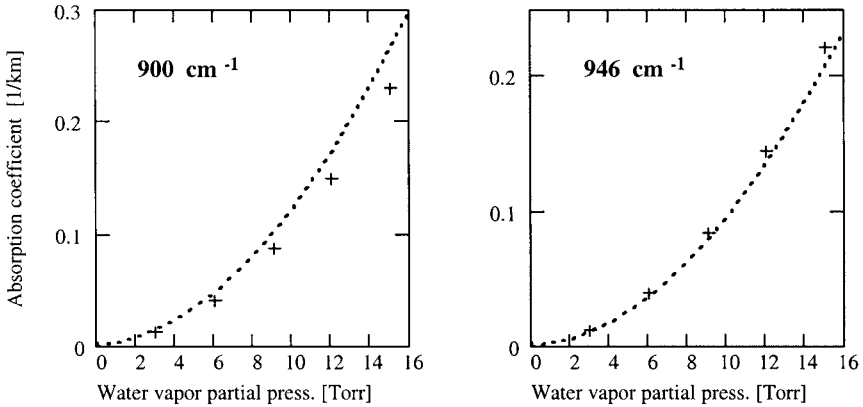
Fig. 7.10 Water vapor partial pressure dependence of the absorption coefficient at 900 cm^{-1} (Burch and Alt, Ref. 7.42) and 945.98 cm^{-1} (Peterson et al., Ref. 7.43).

ing coefficients are cm^2/(atm molecule). The dashed curves in Figs. 7.9–7.11 come from this model. The temperature dependence of the nitrogen broadening coefficient comes from measurements by Hinderling et al. (Ref. 7.29). Good agreement with many different experimental data sets is obtained.

An excellent review of experimental measurements in the 10 μm region by Grant (Ref. 7.30) makes the following additional points:

1. Oxygen does not broaden as effectively as nitrogen and must be included in a realistic model of the earth's atmosphere. A dimensionless broadening coefficient of $F = 0.55 \pm 0.12$ for oxygen relative to nitrogen was determined by Thomas (Ref. 7.50) for continuum absorption based on CO_2 laser measurements. Using Eq. 7.10, this means air has an effective broadening of 0.906 relative to nitrogen (i.e., $C_{air}(\nu, T) = 0.906 C_N(\nu, T)$).
2. Understanding the local line structure is critical in determining the true continuum. Line positions are known reasonably well; however, line strength, shift, and half-width are not known with enough accuracy.

Long-path field measurements by Devir et al. (Ref. 7.52) are in excellent agreement with the laboratory measurements of Burch and Alt (Ref. 7.42), and Peterson et al. (Ref. 7.43) in this window region concerning the water vapor continuum. The measured spectral range of Devir extends the range covered by Burch and Alt and shows the water vapor continuum increasing with increasing frequency. The minimum occurs near 1050 cm^{-1} (9.0 μm). The characterization of 8–12 μm continuum absorption appears to be well in hand on the basis of the agreement between laboratory and field measurements.

The 3–5 μm Window   The 3–5 μm continuum region has a frequency dependence that differs from those of the millimeter and 8–12 μm regions. Figure 7.12 displays a nearly parabolic dependence with a minimum at a wave number of 2600 cm^{-1}. As shown by the spectrometer measurements of Burch and Alt (Ref. 7.42), and Burch (Ref. 7) (Fig. 7.12a), the self-broadening coefficient has a double exponential fall-off from 2000 cm^{-1} up to 2600 cm^{-1}. Long-path CO laser transmittance measurements
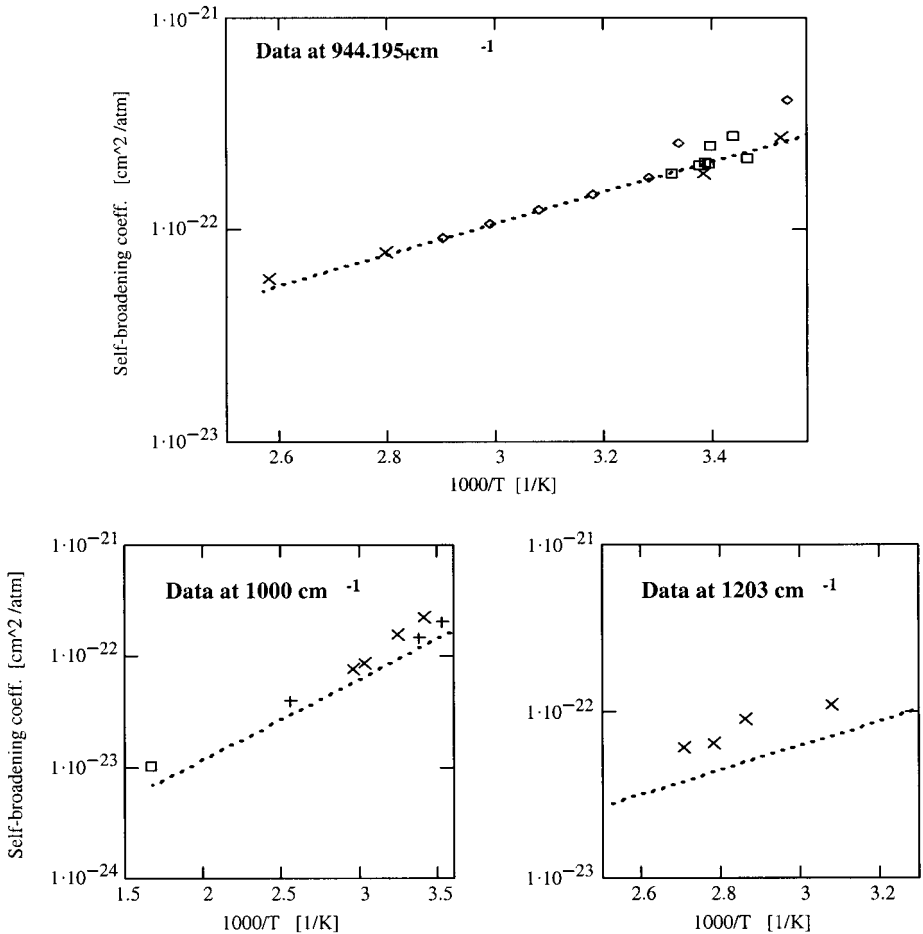
Fig. 7.11 Temperature dependence of self-broadening coefficient in the 10 μm region. (At 944.195 cm^{-1}: x – Burch and Alt, Ref. 7.42; ◇ – Loper et al., Ref. 7.46; □ – Peterson, Ref. 7.47; and + – Aref'ev and Dianov-Klokov, Ref. 7.48. At 1000 cm^{-1}: □ – Thomas, Ref. 7.50; + – Burch and Alt, Ref. 7.42; and x – Varanasi, Ref. 7.49. At 1203 cm^{-1}: x – Montgomery, Ref. 7.44.)

(Thomas, Ref. 7.50) near 2000 cm^{-1} verify the data by Burch (Ref. 7.42). The continuum becomes relatively flat around 2600 cm^{-1}. Figure 7.12a also shows long-path White cell DF laser measurements taken under atmospheric conditions, which indicate continuum absorption levels roughly 50% higher than those indicated by Burch and Alt (Ref. 7.42). As in the case for CO_2 laser measurements, local line absorption distorts the data, and care must be taken in the interpretation. The observed level of continuum absorption in the 4 μm region is roughly an order of magnitude less than that in the 10 μm region. The self-broadening coefficient increases as the wave number approaches 3200 cm^{-1} because the $2\nu_2$ band is located there.

Long-path nitrogen-broadened CO, DF, and HF laser transmittance measurements near room temperature indicate large values for B in this continuum region, ranging from 10 to 20 at 5 μm to approximately 50 to 60 at 4 μm and back down to 10 at 3 μm.
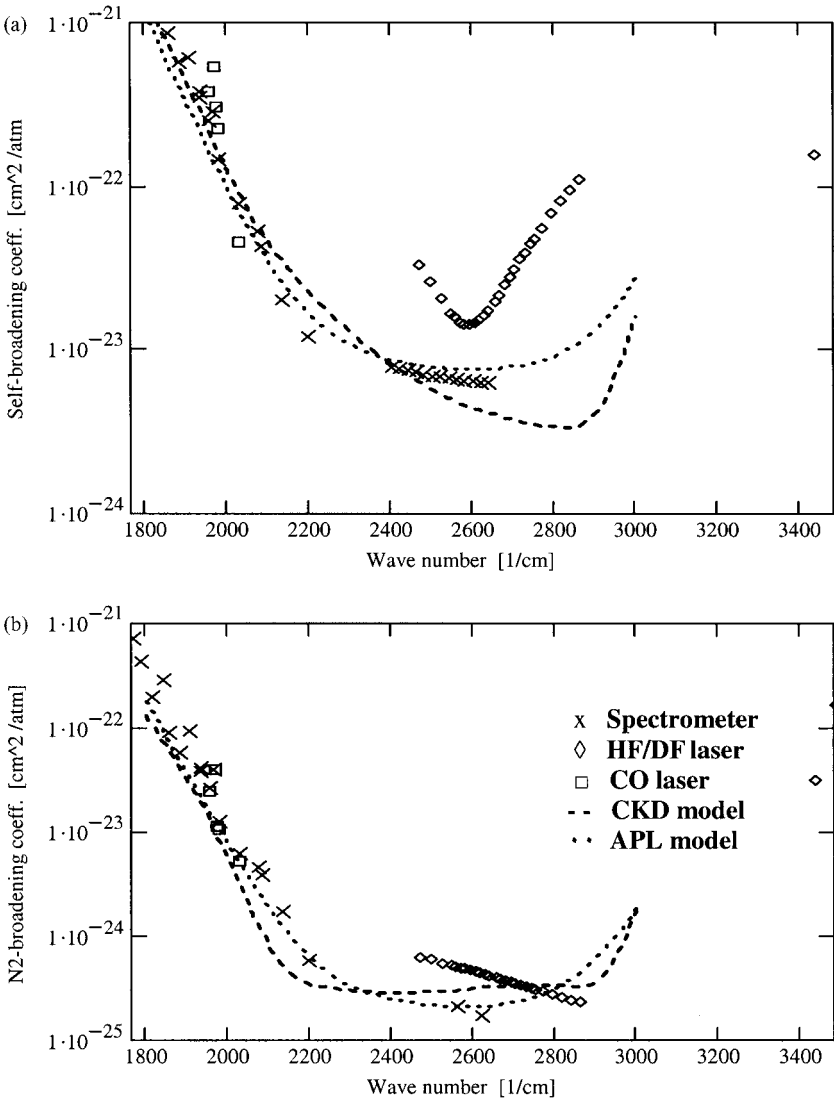
Fig. 7.12. 4 μm water vapor continuum region at $T = 296$ K. (a) $C_s(\nu, 296)$ vs. wave number and (b) $C_N(\nu, 296)$ vs. wave number. The experimental data is indicated by x – Burch and Alt, Ref. 7.42; □ – Thomas, Ref. 7.50; ◇ – White et al., Ref. 7.54 and Watkins et al., Ref. 7.56. The solid curve is from Eq. 7.17. The dashed curve is the CKD model (Clough et al., Ref. 7.67) scaled to room temperature using Eq. 7.15.

This trend is represented in Fig. 7.12b, which shows wave-number-dependent C_N at room temperature. Recall that B is the ratio C_s/C_N.

A strong negative temperature dependence is again observed for the self-broadening coefficient. Figure 7.13 shows the results of laboratory long-path spectrometer measurements by Burch and Alt. The temperature dependence at 2400 cm^{-1} exhibits an exponential fall-off similar to that in the 10 μm and millimeter regions. However, the
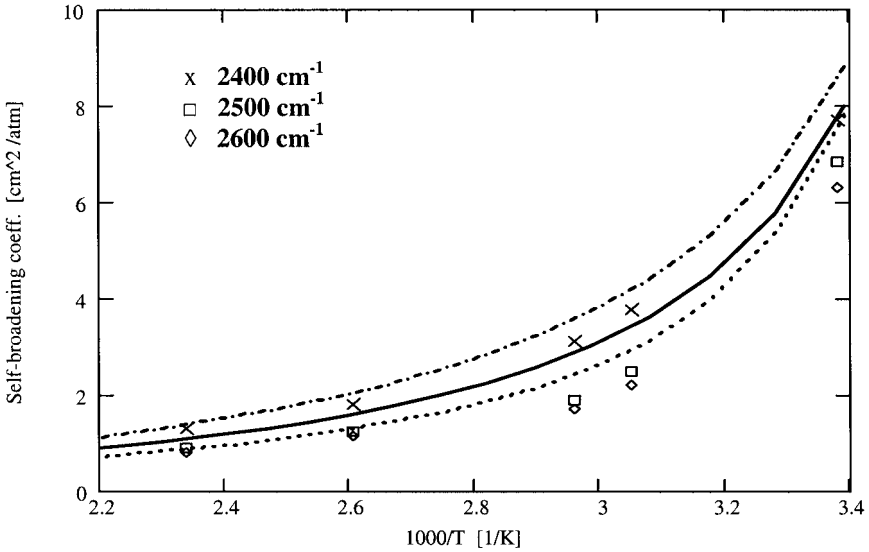
Fig. 7.13 Plots of the water vapor self-broadening coefficients at 2400 (x and dash–dot), 2500 ($\square$ and solid) and 2600 ($\diamond$ and dotted) cm^{-1} versus reciprocal temperature (Burch and Alt, Ref. 7.42). The curves are generated by Eq. 7.17.

curves at 2500 and 2600 cm^{-1} show double exponential trends. The nature of the water vapor continuum in this window region is more complicated than the other windows previously discussed.

More experimental data are needed to generate a meaningful empirical model of the continuum absorption coefficient. However, an attempt at representing the existing data is given by the following empirical formula for nitrogen-broadened water vapor continuum absorption coefficients valid from 1900 to 3000 cm^{-1},

$$\beta_{cont} = 7.34 \times 10^{26} (p_{H_2O}/T) \left[C_s(\nu,T) p_{H_2O} + C_N(\nu,T) p_{N_2} \right] \quad [\text{km}^{-1}] \qquad (7.17)$$

where the broadening coefficients are given by

$$C_s(\nu, T) =$$

$$[1.6 \times 10^{-11} \exp(-0.013\nu) + 7.0 \times 10^{-22} \exp(-0.002\nu)] \exp[1450(1/T - 1/T_0)]$$

$$+[1.0 \times 10^{-41} \exp(0.014\nu) + 1.5 \times 10^{-26} \exp(0.0021\nu)] \exp[6000(1/T - 1/T_0)]$$

and

$$C_N(\nu,T) = (296/T) \left[5.6 \times 10^{-10} \exp(-0.016\nu) + 2.5 \times 10^{-23} \exp(-0.002\nu) \right.$$
$$\left. + 2.0 \times 10^{-45} \exp(0.016\nu) + 5.4 \times 10^{-31} \exp(-0.0045\nu) \right].$$

p is in atmospheres, ν is in wave numbers, and $T_0 = 296$ K. The units of the broadening coefficients are cm^2/(atm molecule). This model is represented in Figs. 7.12 and 7.13.

To appreciate the importance of local line characterization as part of continuum measurements by laser techniques, Fig. 7.14 illustrates the total absorption coefficient (local plus continuum) as a function of wave number. The spectrum is computed based on the HITRAN database and Eq. 7.17. The experimental data points come from White et al. (Ref. 7.54) and Mills (Ref. 7.55).

Again, long-path field measurements by Devir et al. (Ref. 7.52) are in good agreement with Burch and Alt (Ref. 7.42) in this window region concerning the water vapor continuum. The results of Devir et al. (Ref. 7.52) also point out the importance of the water vapor continuum between 4.5 and 5.0 µm. In this region, local line contributions can also be significant, thus masking to some extent water vapor continuum absorption. Another interesting observation, based on the field measurements of Devir et al. (Ref. 7.52), is an absorption feature in the water vapor continuum at 4.8 µm. The water vapor continuum frequency dependence is approximately exponential in this region except for the absorption band, which adds to the exponential background. Liquid water is known to have an association band at 4.8 µm, thus suggesting that the anomalous feature is caused by water vapor. More work is needed on this problem to fully appreciate this observation.

Field measurements between 4.1 and 3.8 µm reveal that other continuum sources exist. The far blue wing beyond the band head of the fundamental ν_3 band of CO_2 (Kyle et al., Ref. 7.57; Delaye and Thomas, Ref. 7.58) and the collision-induced absorption
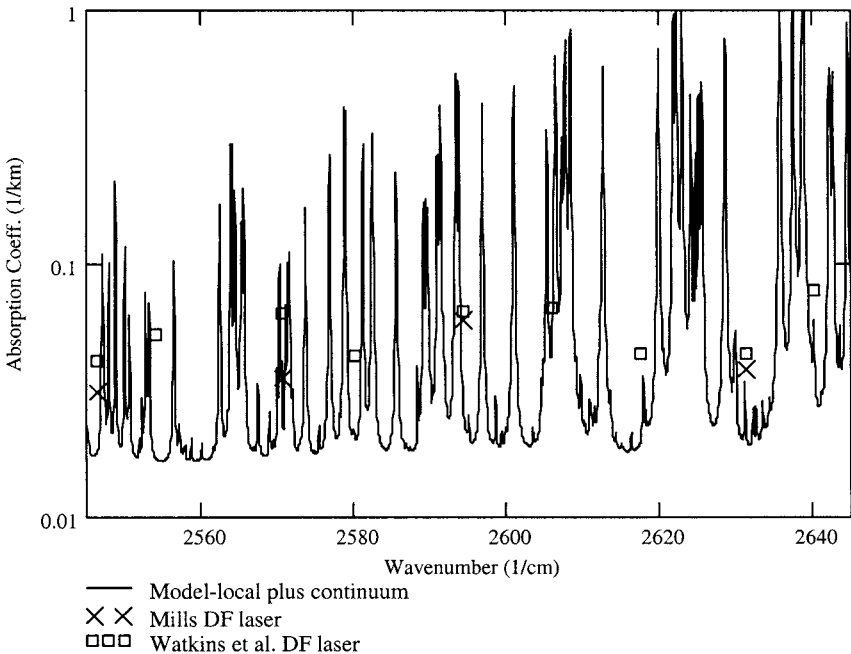
Fig. 7.14 The absorption coefficient ($p_{H_2O} = 14.3$ Torr, $p_{N_2} = 745.7$ Torr, and $T = 296$ K) as a function of wave number. The experimental data points come from DF laser measurements by Watkins et al. (Ref. 7.56) and Mills (Ref. 7.55).
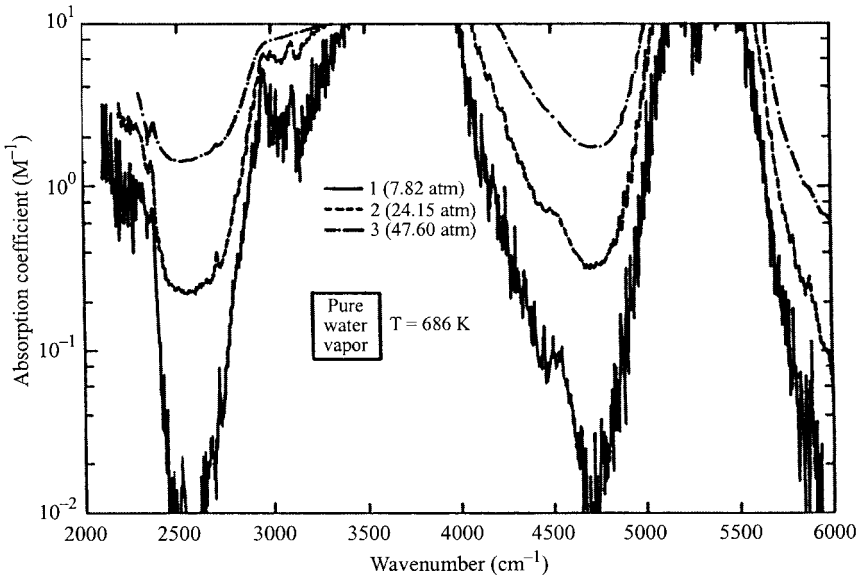
Fig. 7.15 Pure water vapor absorption coefficient at $T \approx 686$ K and three different pressures as indicated.

band of nitrogen (Van Kranendonk, Ref. 7.59, Sheng and Ewing, Ref. 7.60; Reddy and Cho, Ref. 7.61; Shapiro and Gush, Ref. 7.62; Moskalenko et al. Ref. 7.63) also contribute to continuum-type absorption in this window region and will be discussed later (see Sections 7.2.1.2 and 7.2.1.4).

The 2.0–2.5 µm Window   This window region has not received the same attention as the longer wavelength windows; as a result, no experimental continuum absorption has been previously reported. This spectral window is currently being used for eye-safe atmospheric lidar. Knowledge of the water vapor continuum needs to be known for this and any other long path application.

Measurements (Ref. 7.43), however, indirectly suggest that continuum absorption does exist. Transmission measurements on hot ($T = 685$ K) high-pressure (up to 4.8 MPa) water vapor show the continuum absorption in the 2.1 and 4 µm regions (Fig. 7.15). Absorption levels at 4 µm are consistent with the extrapolated values from the curves in Fig. 7.13. The point to be made is that a similar continuum absorption process occurs in the 2.1 µm region, as shown in Fig. 7.15. If we assume that an extrapolation to lower temperature follows the same trend as at 4 µm, then a continuum exists in the 2–2.5 µm window that is very similar to the 3–5 µm window under normal atmospheric conditions.

The 1.7–1.5 µm Window and Beyond   Figure 7.15 shows the beginning of the continuum centered at 1.6 µm. Again, this suggests a water vapor continuum in this window region at a weaker level than at 4 and 2 µm. Based on this observation, it is expected that every window in the infrared has a water vapor continuum at some absorption level. This level should become weaker as the frequency increases.

The 1 μm window water vapor continuum has been measured by a novel interferometric calorimeter technique (Fulghum and Tilleman, Ref. 7.64). A pulsed Nd-glass laser is used to heat a nitrogen-buffered water vapor sample placed in the arm of a He-Ne Mach–Zehnder interferometer. Variations in the index of refraction due to the heating cause measurable fringe shifts proportional to the absorption coefficient. The resulting continuum absorption coefficient measured at 9466 cm^{-1} is 6×10^{-10} cm^{-1} for a water vapor partial pressure of 17.5 Torr buffered by nitrogen to a total pressure of 1 atm at 30°C. Thus, the water vapor continuum is roughly two orders of magnitude weaker near 1 μm than at 4 or 2 μm. Many further measurements to determine the water vapor partial pressure dependence and temperature dependence are needed.

The tragedy of experimental water vapor continuum characterization is that, unlike nitrogen and CO_2 experiments, it presently cannot be done at high pressure. High-pressure water vapor measurements also require high-temperature and thus a theoretical understanding of the continuum absorption temperature dependence is needed in order to extrapolate back to atmospheric temperatures.

Concepts and Models   No universal interpretation of continuum absorption by water vapor presently exists. Clearly, far wings must play a role in continuum absorption because of the observed frequency dependence in every infrared window, and work is continuing to find a line-shape theory valid in the very far wing (Clough et al., Refs. 7.66, 7.67; Zuev and Fomin, Ref. 7.68). The major shortcoming of most line shape theories is the failure to predict the observed strong negative temperature dependence characteristic of all the window regions. [The exception is the recent work of Ma and Tipping (Ref. 5.26) in the millimeter wave and infrared windows.] But this weakness is the very strength of an alternative hypothesis to explain the water vapor continuum: the water dimer (a polymer containing two molecules). The formation of water vapor dimers has a strong negative temperature dependence that closely matches the temperature dependence of the continuum absorption in the 10 μm region based on Eq. 7.15 ($b_{dimmer} = 1800$ K; the model uses $b = 1680$ K). However, this near match does not occur in the microwave window or in the 4 μm window. This approach also requires dimer absorption bands to account for the continuum. However, the hypothesis would require a dimer absorption band in every water vapor window, a condition that has not been experimentally found or theoretically shown [Hinderling et al. and Bohlander et al.]. Furthermore, measurements on supersaturated water vapor indicate that dimer absorption is an order of magnitude too small to account for the water vapor continuum at 10 μm [Hinderling et al.]. In spite of these shortcomings, the dimer hypothesis demonstrates the importance of understanding short-range water vapor–water vapor interactions to explain the continuum absorption temperature dependence.

Because of the lack of closed-form line shape models or fast numerical techniques for line-by-line water vapor continuum absorption calculations, they are commonly characterized by empirical models. One such model, developed at JHU/APL and Ohio State University, uses a far-wing model with a semiempirical line shape and the HITRAN line data (see Section 7.2.2). The model has been applied to the 10 and 4 μm window regions and reproduces the experimental data as a function of frequency, pressure, and temperature. An example is the curve in Fig. 7.17. The water-vapor-broadened far wing falls off less rapidly than the nitrogen-broadened far wing; thus, the self-broadening coefficient grows as the line shape extends from the line center. This is the trend

observed in all the data. The line shape is normalized, and the line-center function is experimentally verified. The far wings of a line shape represent a very small percentage of the total area under an absorption line contour. Nonetheless, it is interesting to note that the magnitude of the continuum absorption can be calculated from the far-wing contributions by this model. Contributions to the 10 μm region are dominated by far wings of the very strong rotational band of water vapor on the long-wavelength side of that window, whereas the 4 μm continuum absorption arises from the bordering strong vibrational bands of almost equal strength. That difference between sources explains the difference between the frequency dependence of the 10 μm continuum region and that of the 4 μm continuum region (see Figs. 7.9 and 7.12). Unfortunately, this model is not valid in the millimeter region and does not fully represent the recent progress in line shape theories, as discussed in Chapter 5. The success of this model, therefore, is by no means a statement of the validity of a far-wing interpretation of continuum absorption, but rather a statement of its feasibility.

The continuum models for the popular Air Force Geophysics Laboratory codes FASCODE and LOWTRAN are based on the efforts of Clough et al. (Refs. 7.66, 7.67), who used far-wing concepts to represent the water vapor continuum throughout the entire infrared region. The experimental data previously described are reasonably represented by these codes (see Figs. 7.9 and 7.12). The strength of this approach and the previously mentioned approach over the APL model is accounting for the fluctuation dissipation theorem in enforcing detailed balance across the entire line shape. This results in a more physically meaningful far wing and a more versatile line shape overall. However, the water vapor line shape still requires an empirical basis. In this case it was found that to achieve agreement with measurement, the mid-wing needed to be super-Lorentzian and the far-wing sub-Lorentzian as illustrated in Fig. 7.16, using the
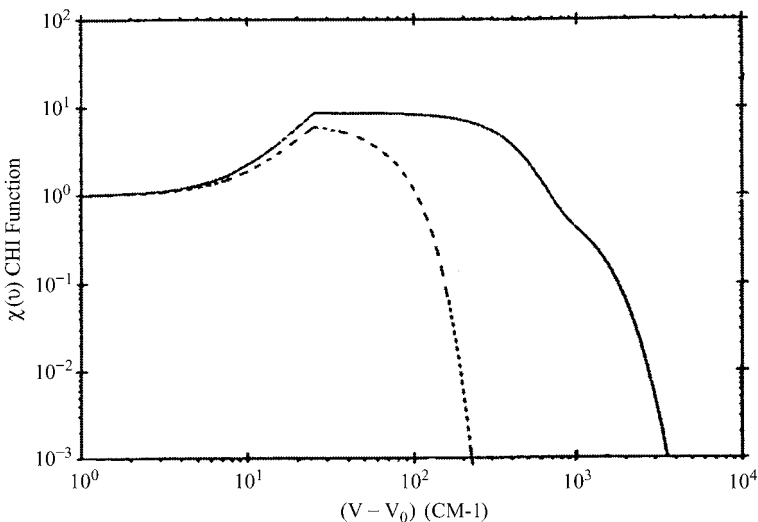
Fig. 7.16 χ-function plot for water vapor line shape at room temperature. The solid curve is for self-broadening and the dashed curve is for nitrogen-broadening (Clough et al., Ref. 7.67, with permission).

so-called χ-function. The χ-function is the ratio of the applied line shape function to the Lorentz line shape, as given by

$$\chi(\nu) = \frac{j_c(\nu)}{j_L(\nu)}.$$

The theoretical work of Ma and Tipping (Ref. 5.26) also produces this line shape for water vapor by appropriately choosing the intermolecular potential functions.

On the basis of these far-wing models, the water vapor continuum is extrapolated to higher frequencies beyond 4 μm in LOWTRAN-7 and FASCODE-2. As the previous section indicates, direct experimental evidence rarely exists beyond 4 μm. Thus, the extrapolated continuum values must be applied with great care. Figure 7.17 illustrates this point by comparing the water vapor continuum models of LOWTRAN-6 and the APL model from 500 to 18,000 cm^{-1}. The figure also shows another continuum-type loss mechanism, molecular Rayleigh scattering, based on the LOWTRAN-7 model. The conditions used in the calculation are for a horizontal path with $p_{H_2O} = 2.0$ kPa, $p_{N_2} = 99.0$ kPa, and $T = 295$ K. The APL model has been extended beyond 4 μm by using the same empirical far-wing parameters of the ν_1 and ν_3 vibrational bands for all vibrational bands to higher frequencies. The fundamental vibrational band far-wing parameters do not vary greatly; thus, this is a reasonable approximation. Fair agreement between the two models exists in the region of the 10 μm window. Good agreement is obtained in the 4 μm region and throughout the infrared. Figure 7.17 illustrates
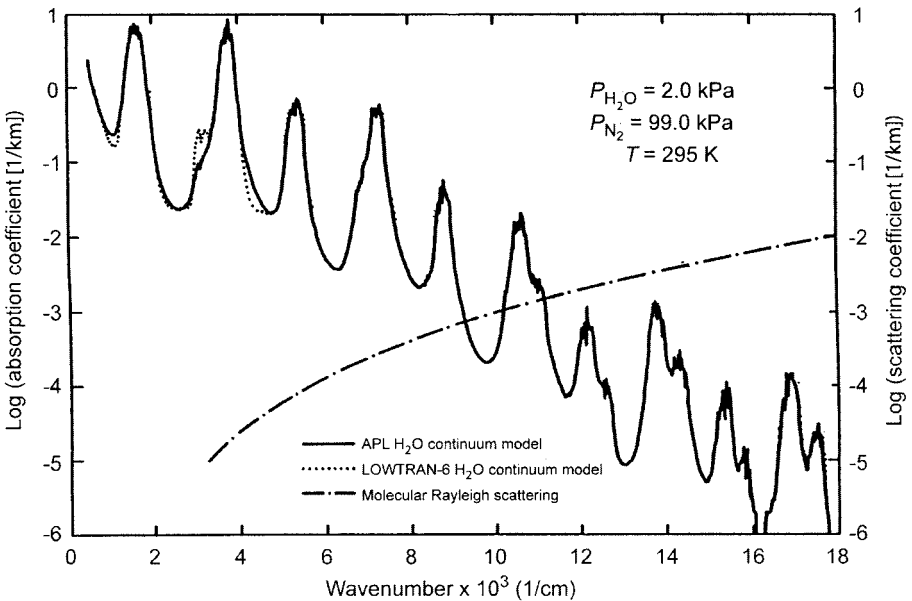
Fig. 7.17 A comparison of water vapor continuum absorption models (Thomas, Ref. 7.50) and molecular Rayleigh scattering (see Section 7.3) in a homogeneous path.

another interesting point. Continuum absorption decreases with increasing frequency, and scattering loss increases with increasing frequency. Thus, for a particular set of atmospheric conditions, an optimal atmospheric window can be selected. Of course, local line effects must be included in a broad-band system, but a narrow-band system can avoid local line attenuation.

Although no definitive interpretation of the water vapor continuum exists, the experimental and theoretical evidence indicates that far-wing absorption contributions by the bordering strong water vapor bands play a dominant role. The evidence is based largely on the frequency dependence of the continuum in all spectral windows reviewed (i.e., the shape of the continuum as a function of frequency and growth of the dimensionless broadening coefficient, B, away from a band as a function of frequency). The shortcoming of the far-wing approach is prediction of the temperature dependence, but the character of a far wing must be driven by close binary interactions much like the creation of a dimer, which nearly exhibits the observed temperature dependence in the 10 μm window region.

7.2.1.2 Carbon Dioxide Absorption

Carbon dioxide (main isotope) is a symmetric (i.e., nonpolar) linear molecule. It has a small rotational constant, B (see Table 5.1), thus dense compact spectra. The dominant fundamental vibrational frequencies of the main isotope are listed in Table 7.8. Only the bending (ν_2) and the asymmetric stretch (ν_3) vibrational modes of the main isotope are infrared active.

Vibrational Bands   The locations of CO_2 and H_2O absorption bands define the boundaries of infrared atmospheric windows. Table 7.8 lists the location and integrated band strength (see Section 7.2.1.1 for definition) of the most important vibrational bands, including isotopic bands.

Because CO_2 does not have a permanent dipole moment, the rotational band is not infrared active. The absorption bands near 667 cm^{-1} are important contributors to the atmospheric greenhouse effect because of the proximity to the peak of the room-temperature blackbody curve. The 4.3 μm (ν_2 band) divides the 3–5 μm window region into two parts. Otherwise, the other CO_2 bands coincide with water vapor absorption bands.

Window Regions   In the window regions of the atmosphere, local line absorption by weak absorption bands of CO_2 is most important. The only continuum-type absorption of concern is the blue wing of the ν_3 fundamental band.

LOCAL LINE ABSORPTION   Weak vibrational bands in the 10 and 5 μm regions have significant local line effects for long-path propagation. In particular, the vibrational transitions used in the CO_2 laser also occur in the atmosphere. Laser radiation is at the line center of the atmospheric CO_2 absorption lines. For this reason, isotopic CO_2 (because of the different masses the vibrational frequencies are slightly shifted) is preferred for optimal atmospheric propagation. Again, it is recommended to consult the HITRAN database for details of the band structure. A typical line shift parameter for nitrogen-broadened CO_2 is approximately −0.008 cm^{-1}/atm at 2 μm.

Table 7.8 Band Locations and Integrated Intensities of Carbon Dioxide[a] (Goody and Yung, Ref. 7.3, with permission)

Band Origin [cm^{-1}]	Isotope	Upper State ($\nu_1 \nu_2^l \nu_3$)	Lower State ($\nu_1 \nu_2^l \nu_3$)	$S_n(295\,\text{K}) \times 10^{20}$ [cm]
618.03	$^{16}\text{O}^{12}\text{C}^{16}\text{O}$	10^00	01^10	14.4
647.06	$^{16}\text{O}^{12}\text{C}^{16}\text{O}$	11^10	10^00	2.22
648.48	$^{16}\text{O}^{13}\text{C}^{16}\text{O}$	01^10	00^00	8.6
662.37	$^{16}\text{O}^{12}\text{C}^{18}\text{O}$	01^10	00^00	3.3
667.38	$^{16}\text{O}^{12}\text{C}^{16}\text{O}$	01^10	00^00	827.0
667.75	$^{16}\text{O}^{12}\text{C}^{16}\text{O}$	02^20	01^10	64.9
668.11	$^{16}\text{O}^{12}\text{C}^{16}\text{O}$	03^30	02^20	3.82
688.68	$^{16}\text{O}^{12}\text{C}^{16}\text{O}$	11^10	10^00	1.49
720.81	$^{16}\text{O}^{12}\text{C}^{16}\text{O}$	10^00	01^10	18.5
2271.76	$^{16}\text{O}^{13}\text{C}^{16}\text{O}$	01^11	01^10	8.18
2283.49	$^{16}\text{O}^{13}\text{C}^{16}\text{O}$	00^01	00^00	97.0
2311.68	$^{16}\text{O}^{12}\text{C}^{16}\text{O}$	03^31	03^30	1.23
2319.74	$^{16}\text{O}^{12}\text{C}^{18}\text{O}$	01^11	01^10	2.58
2324.15	$^{16}\text{O}^{12}\text{C}^{16}\text{O}$	02^21	02^20	30.8
2327.59	$^{16}\text{O}^{12}\text{C}^{16}\text{O}$	10^01	10^00	11.8
2327.43	$^{16}\text{O}^{12}\text{C}^{16}\text{O}$	10^01	10^00	19.3
2332.11	$^{16}\text{O}^{12}\text{C}^{18}\text{O}$	00^01	00^00	33.3
2337.64	$^{16}\text{O}^{12}\text{C}^{16}\text{O}$	01^11	01^10	767.0
2349.15	$^{16}\text{O}^{12}\text{C}^{16}\text{O}$	00^01	00^00	9600.0
3580.33	$^{16}\text{O}^{12}\text{C}^{16}\text{O}$	11^11	01^10	8.04
3612.84	$^{16}\text{O}^{12}\text{C}^{16}\text{O}$	10^01	00^00	104.0
3632.92	$^{16}\text{O}^{13}\text{C}^{16}\text{O}$	10^01	00^00	1.60
3714.78	$^{16}\text{O}^{12}\text{C}^{16}\text{O}$	10^01	00^00	150.0
3723.25	$^{16}\text{O}^{12}\text{C}^{16}\text{O}$	11^11	01^10	11.4
4853.62	$^{16}\text{O}^{12}\text{C}^{16}\text{O}$	20^01	00^00	0.81
4977.83	$^{16}\text{O}^{12}\text{C}^{16}\text{O}$	20^01	00^00	3.50
5099.66	$^{16}\text{O}^{12}\text{C}^{16}\text{O}$	20^01	00^00	1.09
6972.58	$^{16}\text{O}^{12}\text{C}^{16}\text{O}$	00^03	00^00	0.15

[a]S_n for isotopes is scaled according to the fractional isotopic abundance.

CONTINUUM ABSORPTION   Carbon dioxide continuum-type absorption occurs near 4.1 μm. It is the blue wing of the 4.3 μm absorption band, as illustrated in Fig. 7.18 for pure and N_2-broadened CO_2. The figure also shows a line-by-line calculation based on Birnbaum's line shape (Ref. 5.23). The shape of the wing is duplicated, but the magnitude is not because line mixing is not included in the model. However, a simple scaling factor allows good agreement with experimental data (Kyle et al., Ref. 5.23). The wing is exponential in nature as Birnbaum's model (described in Chapter 5, Ref. 5.23) predicts, and covers the spectral region from 2400 to 2500 cm^{-1}.

Based on the data in Fig. 7.18 and the theories discussed in Section 5.4.3, a simple empirical formula for the CO_2 continuum absorption coefficient (far blue wing of the ν_3 band), β_{cont}, valid for typical atmospheric conditions, is given by

$$\beta_{const} = 9.0 \times 10^3 \left(\frac{T_0}{T}\right)^{2.5} p_{CO_2}^2 \exp\left[-5.0 \times 10^{-2}(\nu - 2350)\right]$$

$$+ 1.623 \times 10^3 \left(\frac{T_0}{T}\right)^{2.5} p_{CO_2} P_{N_2} \exp\left[-4.47 \times 10^{-2}(\nu - 2350)\right],$$

(7.18)
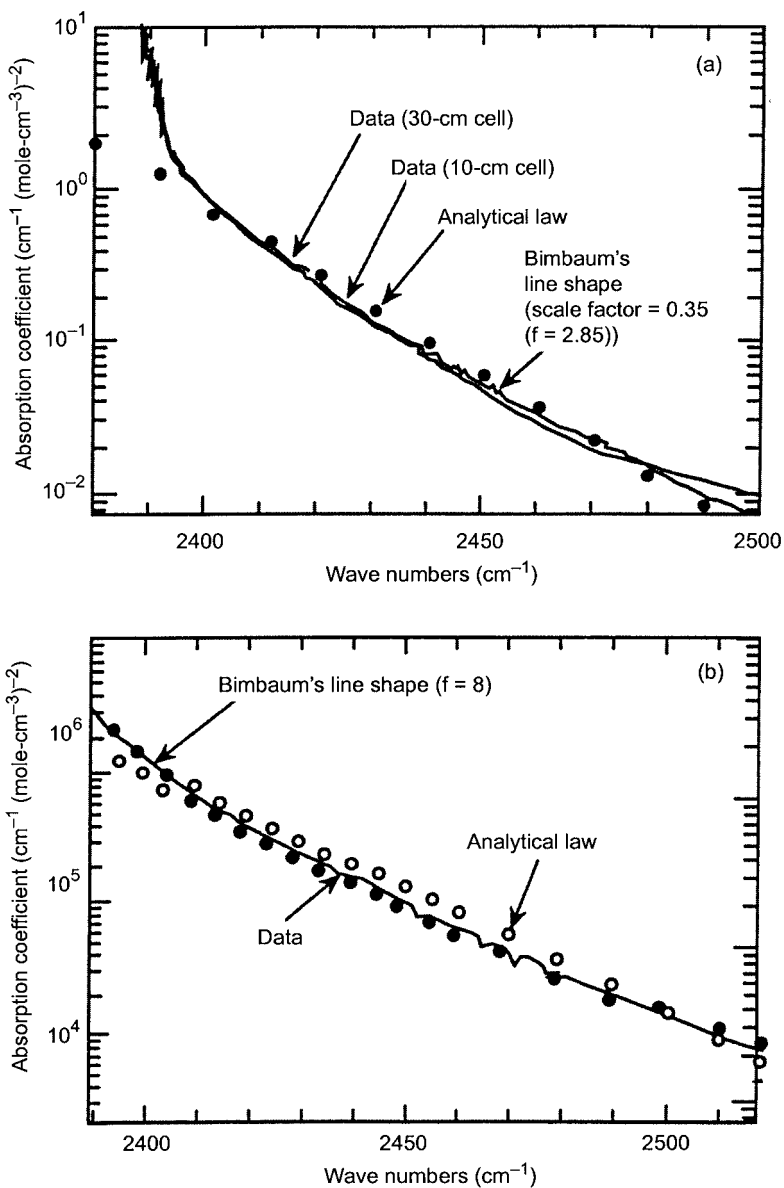
Fig. 7.18 Experimental absorption coefficient divided by the density squared for (a) pure CO_2 at $T = 296$ K and (b) N_2-broadened CO_2 at 296 K. Also shown are calculations based on Eq. 7.18 and a line-by-line calculation based on Birnbaum's line shape (Delaye and Thomas, Ref. 7.58).

293

where p_{CO_2} and p_{N_2} are in atmospheres, β_{cont} is in km^{-1}, and T_0 is equal to 296 K. The first term is the pure CO_2 contribution and the second term is the CO_2–N_2 contribution. The temperature factor exponent of 2.5 comes from the partition function ($1/T$ from Eq. 5.6), the half-width temperature dependence (~.0.5 from Eq. 5.154), and the absorber density ($1/T$). A similar model, empirically derived, has been proposed by Roney et al. (Ref. 7.74) and validated against field measurements over the temperature range 252–303 K.

7.2.1.3 Absorption by Other Gases

Other absorbing gases in the atmosphere of the earth are of low concentration but can be important in limited spectral regions. Only band or local line absorption needs to be considered. An important class of these gases is pollutants.

Methane   Methane is a spherical-top nonpolar molecule with nine fundamental vibrational modes. Degeneracies reduce the number of observable vibrational bands to four, with three bands infrared active (see Table 3.2). Brown gives a recent discussion on methane absorption bands (Brown, Ref. 7.75). Table 7.9 lists the location and integrated intensity of the most important vibrational bands.

Ozone   Ozone is an asymmetric-top polar molecule with three active fundamental vibration bands and an active rotational band. Table 7.10 lists the band locations and the integrated intensities for the most important bands of concern to propagation in the atmosphere. A number of vibrational bands exist in the 10 μm window region and are easily observed when the stratosphere is part of the transmission path. Also, ozone has important electronic transitions that limit the amount of ultraviolet radiation from reaching the surface of the earth (Molina and Molina, Ref. 7.76). These electronic bands are illustrated in Fig. 7.19. Ozone strongly absorbs out to 300 nm, but continues to absorb more weakly out to 350 nm.

Table 7.9 Vibrational Bands of Methane[a] (Goody and Yung, Ref. 7.3, with permission)

Band Origin [cm^{-1}]	Isotope	Upper State ($v_1 v_2 v_3 v_4$)	$S_n(295) \times 10^{20}$ [cm]
1302.77	$^{13}CH_4$	0001	5.7
1310.76	$^{12}CH_4$	0001	504.1
1533.37	$^{12}CH_4$	0100	5.5
2612	$^{12}CH_4$	0002	5.4
2822	$^{13}CH_4$	0101	4.3
2830	$^{12}CH_4$	0101	38.0
3009.53	$^{13}CH_4$	0010	29.3
3018.92	$^{12}CH_4$	0010	1022.0
3062	$^{12}CH_4$	0201	17.4
4223	$^{12}CH_4$	1001	24.0
4340	$^{12}CH_4$	0011	40.8
4540	$^{12}CH_4$	0110	7.2

[a]The lower state is the ground state 000. S_n for isotopes is calculated on the basis of the total number of molecules of all isotopic species.

Table 7.10 Infrared Bands of the Main Isotope of Ozone[a] (Goody and Yung, Ref. 7.3, with permission)

Band Origin [cm^{-1}]	Upper State ($v_1 v_2 v_3$)	Lower State ($v_1 v_2 v_3$)	$S_n(295) \times 10^{20}$ [cm]
0.00	000	000	41.3
700.93	010	000	62.8
1015.81	002	001	17.4
1025.60	011	010	45.0
1042.08	001	000	1394.0
1103.14	100	000	67.1
2057.89	002	000	11.1
2110.79	101	000	113.4
3041.20	003	000	11.0

[a] S_n for isotopes is calculated on the basis of the total number of molecules including all isotopic species.

Nitrous Oxide   Nitrous oxide is a linear polar molecule with a rotational and three vibrational modes (the bending is degenerate). The atomic arrangement within the molecule is N–N–O. This is an asymmetric structure, and a permanent dipole is produced. Thus, the pure rotational band and all three normal vibrational modes are infrared active. Table 7.11 lists band locations and integrated intensities of absorption bands important to atmospheric propagation.

Oxygen   Molecular oxygen is a nonpolar diatomic molecule. Thus, first-order dipole rotational and vibrational bands do not exist. However, because of the high concentration of oxygen in the atmosphere, higher order effects are important. It has a rotational absorption band through magnetic dipole transitions at 60 GHz and a nonresonant band near 10 kHz. The fundamental vibration band at 1557.379 cm^{-1} exists as a collision-induced absorption band and is discussed below (see Section 7.2.1.4). Oxygen has near-infrared electronic bands used in lidar for the remote sensing of temperature.
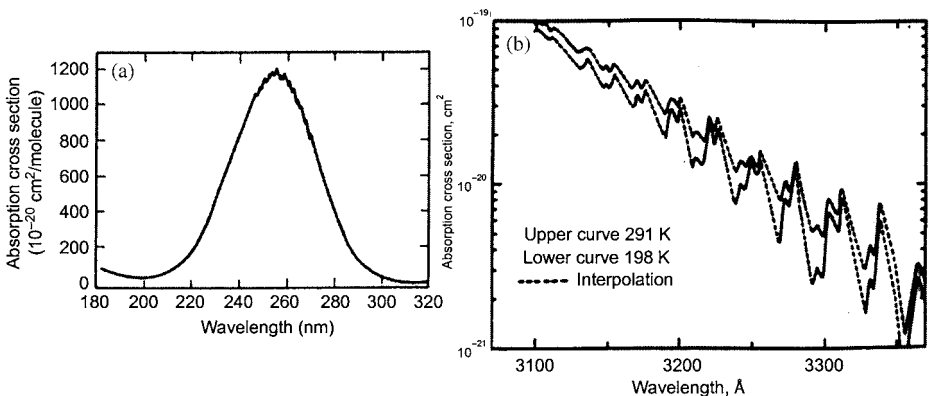
Fig. 7.19 Electronic absorption bands of ozone (a) Hartley and (b) Huggins (Goody and Yung, Ref. 7.3, with permission; Molina and Molina, Ref, 7.76).

Table 7.11 Infrared Bands of Nitrous Oxide[a] (Goody and Yung, Ref. 7.3, with permission)

Band origin [cm^{-1}]	Upper State ($v_1 v_2^l v_3$)	$S_n(295) \times 10^{20}$ [cm]
0.00	00^00	Not listed
588.77	01^10	118
1168.13	02^00	39
1284.91	10^00	996
2223.76	00^01	5710
2462.00	12^00	33
2563.34	20^00	135
3363.97	02^01	11
3480.82	10^01	197

[a]The lower state is the ground state 000. Only the main isotope is considered.

Table 7.12 lists the locations and integrated intensities of the near-infrared bands. Figure 7.20 plots the oxygen absorption cross-section versus wavelength in the ultraviolet region, which determines the end of atmospheric transparency in the troposphere. The air cutoff begins within the Schumann–Runge bands.

Carbon Monoxide   Carbon monoxide is a diatomic polar molecule. The fundamental vibration frequency is at 2143.27 cm^{-1} with an integrated band intensity of 9.81×10^{-18} cm. Figure 3.13 plots experimental low-pressure absorption coefficient of pure CO versus wave number. The formation of the *P*- and *R*-branch structure is clear. Also, a weak isotopic band ($^{13}C^{16}O$) is observed. The line positions of CO are well known, and CO can be used as a frequency standard (Guelachvili and Rao, Ref. 7.77).

Trace Gases   The previous gases significantly contribute to attenuation of radiation in the atmosphere. Trace gases make only minor contributions, and represent pollutants and gases formed naturally in the upper atmosphere. The list includes the freons, NO, SO_2, NO_2, NH_3, HNO_3, OH, HF, HCl, HBr, HI, ClO, OCS, HCN, H_2O_2, C_2H_2, C_2H_6,

Table 7.12 Near-Infrared Band of Molecular Oxygen (Goody and Yung, Ref. 7.3, with permission)

Band Origin [cm^{-1}]	Electronic Transition	Vibrational Transition	Band Intensity [cm]
		Infrared bands	
6327.033	$a \leftarrow X$	$0 \leftarrow 1$	1.13×10^{-28}
7882.425	$a \leftarrow X$	$0 \leftarrow 0$	1.82×10^{-24}
9365.877	$a \leftarrow X$	$1 \leftarrow 0$	8.63×10^{-27}
		Red bands	
11564.516	$b \leftarrow X$	$0 \leftarrow 1$	7.80×10^{-27}
12969.269	$b \leftarrow X$	$1 \leftarrow 1$	9.42×10^{-26}
13120.909	$b \leftarrow X$	$0 \leftarrow 0$	1.95×10^{-22}
14525.661	$b \leftarrow X$	$1 \leftarrow 0$	1.22×10^{-23}
15902.418	$b \leftarrow X$	$2 \leftarrow 0$	3.78×10^{-25}
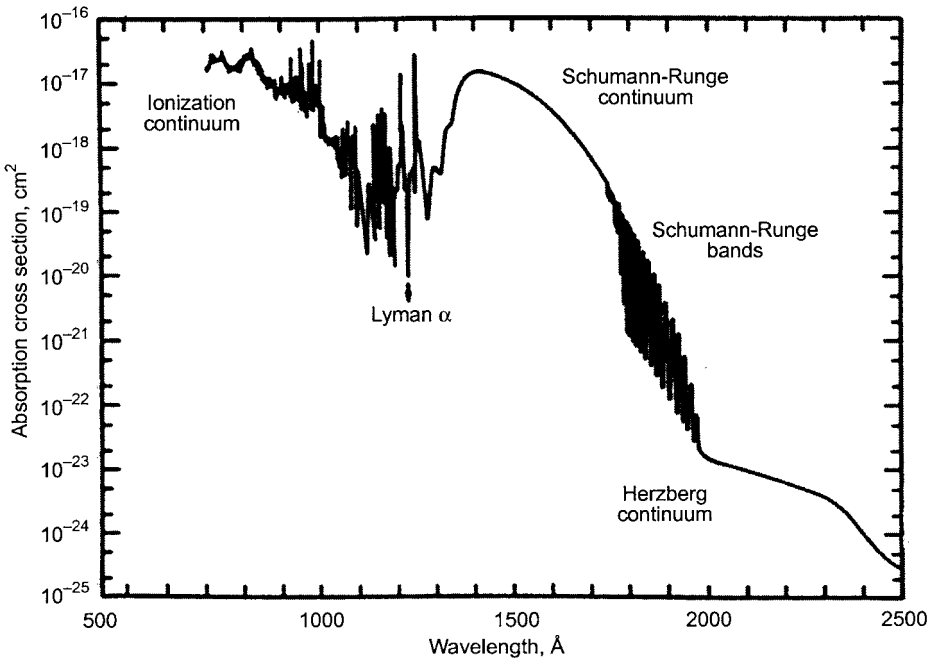
Fig. 7.20 Electronic transitions of molecular oxygen in the ultraviolet (Goody and Yung, Ref. 7.3, with permission).

and so on. Molecular constants for some of these gases can be found in Tables 3.1 and 3.2. Detailed line parameter values of these gases are contained in the HITRAN database, and the reader is expected to use this convenient means of describing the spectroscopic properties of these gases (see Section 7.2.2). Table 7.13 summarizes some basic information on the main isotope of a few trace molecules (Goody and Yung, Ref. 7.3).

7.2.1.4 Oxygen and Nitrogen Continua

The nitrogen continuum, due to collision-induced absorption in the fundamental vibration band, occurs between 4.7 and 3.8 µm; thus, in the earth's atmosphere, it is masked by CO_2 absorption down to 4.1 µm. Figure 7.21a illustrates pure nitrogen spectra at a variety of temperatures. The temperature dependence of the integrated intensity divided by the density squared is also shown in Fig. 7.21b. A minor temperature dependence is observed over the range of atmospheric temperatures, and this dependence is modeled by the theory of Van Kranendonk. Following the work of Sheng and Ewing (Ref. 7.60), we obtain

$$\frac{1}{\rho_a^2} \int \beta(v)\, dv = 1.376 \times 10^{-1} J(T^*) \quad [\mathrm{cm^4 mol^{-2}}] \tag{7.19}$$

Table 7.13 Trace Gas Absorption Bands

Molecule	Classification	Quantum Numbers	Band Locations [cm⁻¹]	Integrated Intensity [cm]
NO_2	Asymmetric top			
		000–000	0.0	2.16×10^{-19}
		010–000	749.65	5.38×10^{-19}
		001–000	1617.85	7.11×10^{-17}
		111–010	2898.19	1.06×10^{-19}
		101–000	2907.07	2.88×10^{-18}
SO_2	Asymmetric top			
		000–000	0.0	2.58×10^{-18}
		010–000	517.75	3.90×10^{-18}
		100–000	1151.71	3.52×10^{-18}
		001–000	1362.03	3.08×10^{-17}
		101–000	2499.87	3.95×10^{-19}
NH_3	Symmetric top			
		0000–0000	0.0	1.77×10^{-17}
		0100–0000a	931.64	1.08×10^{-17}
		0100–0000s	968.12	1.12×10^{-17}
		0001–0000s	1630.00	2.05×10^{-18}
		0001–0000a	1630.34	2.05×10^{-18}
HCl	Linear			
		0–0	0.0	8.07×10^{-18}
		1–0	2885.98	4.52×10^{-18}
		2–0	5667.98	1.07×10^{-19}
HF	Linear			
		0–0	0.0	5.17×10^{-17}
		1–0	3961.44	1.55×10^{-17}
		2–0	7750.79	4.96×10^{-19}
HNO_3	Asymmetric top			
		Rotational	0.0	5.81×10^{-19}
		ν_5	879.11	1.26×10^{-17}
		$2\nu_9$	897.42	9.84×10^{-18}
		ν_2	1709.57	2.01×10^{-17}

where

$$J(T^*) = 12\pi \int_0^\infty x^{-8} \left\{ \exp[-(4/T^*)(x^{-12} - x^{-6})] \right\} x^2 dx, \quad \text{and}$$

$$T^* = \frac{T}{100}.$$

(7.20)

The solid curve in Fig. 7.21b is Eq. 7.20. The coefficient in front of $J(T^*)$ in Eq. 7.19 is obtained by scaling to the experimental data. The band is structureless because the brief duration of the collision determines the lifetime of the induced dipole moment, and this produces broad spectral lines. The broad absorption lines blend together to form the observed continuous absorption spectrum.

In the earth's atmosphere, the effects of oxygen collisions on nitrogen continuum absorption must also be considered. A dimensionless broadening coefficient, B, of 1.28
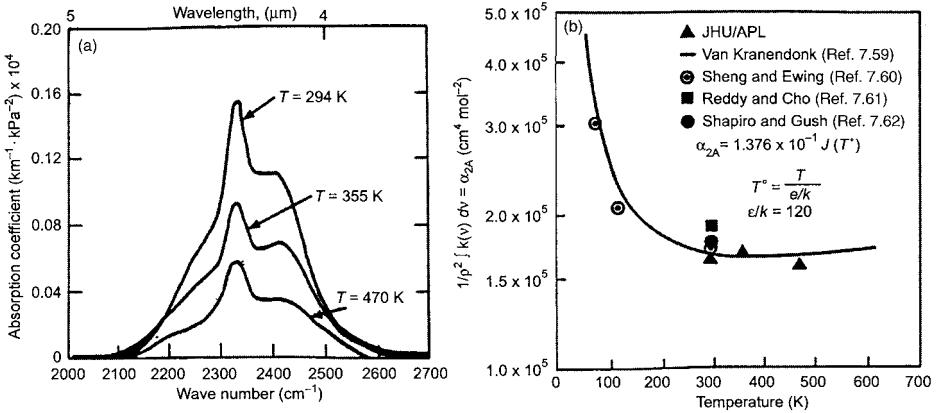
Fig. 7.21 Collision-induced absorption in the fundamental vibration band of N_2. (a) Band shape at various temperatures and (b) integrated intensity versus temperature (Thomas, Ref. 7.50).

was measured by Moskalenko et al. (Ref. 7.63) relative to oxygen (B is 0.78 when relative to nitrogen). Another gas that may be important to nitrogen continuum models is water vapor. Because of the strong dipole moment of water vapor over the quadrupole moment of nitrogen, collisions between water vapor and nitrogen could be very effective in inducing a dipole moment in nitrogen. Thus, the much smaller concentration of water vapor over nitrogen could be neutralized by a large broadening coefficient. The value of B relative to water vapor has not yet been determined. Field measurements suggest this may be important and capable of explaining observed discrepancies between atmospheric measurements and laboratory measurements on pure nitrogen (Thomas, Ref. 7.50). A recent analysis of the nitrogen continuum is given by Roney et al. (Ref. 7.74).

The collision-induced pure rotation band of nitrogen also exists and is important for millimeter-wave propagation modeling in the atmosphere. A simple formula for calculating the absorption coefficient [km^{-1}] is given by

$$\beta_{contN_2}(f) = \frac{\pi a_p}{75}(p_N f)^2 \left(\frac{300}{T}\right)^{4.5} (1 - 1.2f^{1.5}10^{-5})$$

where $a_p = 1.4 \times 10^{-10}$, p_N, the nitrogen partial pressure, is in kPa and f is frequency in GHz.

The oxygen collision-induced absorption vibration band or continuum is centered at 1556 cm^{-1} and is masked by the strong ν_2 vibration band of water vapor in the troposphere. It is very similar in nature to the nitrogen collision-induced absorption band. The oxygen continuum is important for very long path attenuation in the stratosphere. Figure 7.22 illustrates this collision-induced absorption band as a function of frequency (Van Kranendonk, Ref. 7.59).
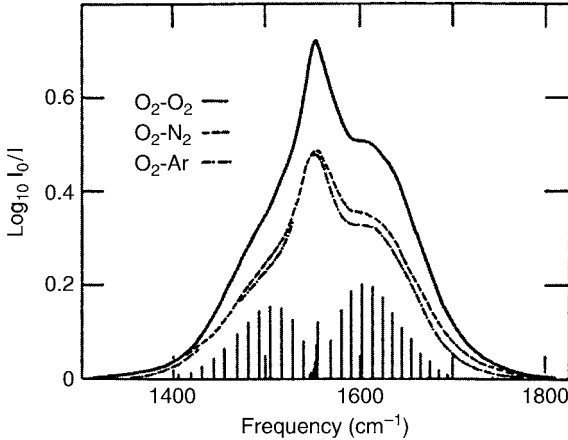
Fig. 7.22 The fundamental absorption band of oxygen for a path length of 40 meters. The densities are: pure oxygen 9.59 Amagats; oxygen–nitrogen mixture, $\rho_{O_2} = 1.09$ Amagats, $\rho_{N_2} = 56$ Amagats; oxygen–argon mixture, $\rho_{O_2} = 1.12$ Amagats, $\rho_{Ar} = 57.9$ Amagats (Shapiro and Gush, Ref. 7.62, with permission). (Note: 1 Amagat is the STP ratio of pressure in atm to temperature in K.)

7.2.2 HITRAN Database

High-resolution calculations require a detailed database of spectral line parameters in order to compute the formulas given in Chapter 5. With projected computer capabilities of the future, computationally intensive atmospheric transmission codes will become more standard. Thus the endeavor to improve and maintain such a database is vital to satisfy the demands of current modeling requirements. The Phillips Laboratory Geophysics Directorate (formally Air Force Geophysics Laboratory [AFGL]) was the United States center for the HITRAN database from the late 1960s (see Ref. 7.78) until recently. The database is now at the Atomic and Molecular Physics Division, Harvard-Smithsonian Center for Astrophysics. The latest version of the database became available in 2000. A comprehensive description of the HITRAN database (describing the 1992 database) is available in the *Journal of Quantitative Spectroscopy and Radiative Transfer* (Rothman et al., Ref. 7.79; also a review, Ref. 7.80).

The HITRAN2000 database is a line-by-line compilation of 1,080,000 spectral lines characterized by eight different parameters (line position, strength, half-width, lower energy level, etc.) representing 38 different molecules of atmospheric importance. The database covers the spectral region from 0 to 23,000 cm^{-1}. Table 7.14 lists the various molecules with the relative isotopic abundance. Table 7.15 shows the parameter format used to organize the data. Each molecule is identified by the number in Table 7.14 along with an indication of the relative isotopic abundance (given by 1 for most abundant, 2 second most abundant, etc.). Line position, ν_i, is given in wave numbers (cm^{-1}). Line strength, S', is given in cm^{-1}/(molec cm^{-2}) (or cm) at $T = 296$ K and $p_a = 1$ atm. To find, S of Eq. 5.84, from the HITRAN definition of line strength, S', use

$$S\ [\text{cm}^{-2}] = N_A p_a S'/R_{GC}T = 7.3388 \times 10^{21} \left(\frac{p_a}{T}\right)(S'[\text{cm}]) \qquad (7.21)$$

Table 7.14 Molecular Species on HITRAN Database with Isotopic Abundance

Molecule (#)	Isotope	Relative Natural Abundance	Molecule (#)	Isotope	Relative Natural Abundance
$H_2O(1)$	161	0.9973	HBr(16)	19	0.5068
	181	0.0020		11	0.4930
	171	0.0004	HI(17)	17	0.99985
	162	0.0003	ClO(18)	56	0.7559
$CO_2(2)$	626	0.9842		76	0.2417
	636	0.0111	OCS(19)	622	0.937
	628	0.0040		624	0.0416
	627	0.0008		632	0.0105
	638	0.00044		828	0.000004
	637	0.000009		822	0.0019
	728	0.000002	$H_2CO(20)$	126	0.9862
$O_3(3)$	666	0.9928		136	0.0111
	668	0.0040		128	0.0020
	686	0.0020	HOCl(21)	165	0.7558
$N_2O(4)$	446	0.9904		167	0.2417
	456	0.0036	$N_2(22)$	44	0.9928
	546	0.0036	HCN(23)	124	0.9852
	448	0.0020	$CH_3Cl(24)$	215	0.7490
	447	0.0004		217	0.2395
CO(5)	26	0.9904	$H_2O_2(25)$	1661	0.9949
	36	0.011	$C_2H_2(26)$	1221	0.9776
	28	0.0020	$C_2H_6(27)$	1221	0.9770
	27	0.0004	$PH_3(28)$	1111	0.99955
$CH_4(6)$	211	0.9952	$COF_2(29)$	269	0.98654
	311	0.0111	$SF_6(30)$	29	0.95018
	212	0.00059	$H_2S(31)$	121	0.94988
$O_2(7)$	66	0.9952	HCOOH(32)	12661	0.983898
	68	0.0040	$HO_2(33)$	16	0.995107
	67	0.0008	O(34)	6	0.997628
NO(8)	46	0.9940	$ClONO_2(35)$	5646	0.74957
$SO_2(9)$	626	0.9454	$NO^+(36)$	46	
	646	0.0420	HOBr(37)	169	0.5056
$NO_2(10)$	646	0.9916		161	0.4919
$NH_3(11)$	4111	0.9960	$C_2H_4(38)$	221	0.9773
	5111	0.0036		231	0.02196
$HNO_3(12)$	146	0.9891			
OH(13)	61	0.9975			
	81	0.0020			
	62	0.00015			
HF(14)	19	0.99985			
HCl(15)	15	0.7576			
	17	0.2423			

Table 7.15 Example of Direct Image of Parameters on 1986 HITRAN Database

iso Mo	Frequency ν_0	Intensity S'	$|R|^2$	γ_{air}	γ_s	E^M	n	δ or γ	v'	v''	Q'	Q''	IER	IREF
31	800.276500	4.316E-25	3.777E-07	.0599	.0000	1162.00600	.76	0.00000	2	1	24 18 6	25 17 9	382	0
281	800.287000	2.270E-23	4.717E-05	.0750	.0000	1483.94700	.50	0.00000	2	1	17 7	18 7	381	0
101	800.301900	4.680E-23	2.421E-07	.0630	.0000	105.93600	.50	0.00000	2	1	8 4 4	− 9 3 7	− 84	0
31	800.304700	1.286E-24	1.131E.05	.0618	.0000	1637.93510	.76	0.00000	2	1	59 9 51	58 8 50	382	0
31	800.322500	1.243E-23	1.274E-07	.0610	.0000	720.65800	.76	0.00000	2	1	16 15 1	16 14 2	382	0
101	800.322700	1.840E-22	2.195E-07	.0630	.0000	277.86000	.50	0.00000	2	1	26 2 24	−25 1 25	− 84	0
23	800.326900	5.380E-26	2.668E-05	.0793	.1103	1327.41920	.75	0.00000	8	3		R 13	186	0
271	800.332030	1.100E-22	3.212E-02	.1000	.0000	2354.24000	.50	0.00000	19	14		4 8	382	0
101	800.361600	1.910E-22	2.278E-07	.0630	.0000	277.80700	.50	0.00000	2	1	26 2 24	+25 1 25	+ 84	0
31	800.379600	7.380E-24	7.554E-07	.0602	.0000	707.21200	.76	0.00000	2	1	15 15 1	15 14 2	382	0
101	800.416400	5.300E-23	1.025E-05	.0630	.0000	851.01800	.50	0.00000	2	1	45 2 44	+44 1 43	+ 84	0
271	800.416750	1.330E-22	2.035E-02	.1000	.0000	2221.36110	.50	0.00000	19	14		3 8	382	0
31	800.434100	4.273E-25	2.225E-05	.0618	.0000	1982.04700	.76	0.00000	3	2	50 10 40	49 9 41	382	0
22	800.444000	7.390E-26	1.396E-04	.0653	.0846	1844.81880	.75	0.00000	8	3		R 38	186	0
101	800.447000	5.180E-23	1.002E-05	.0630	.0000	851.04100	.50	0.00000	2	1	45 2 44	−44 1 43	− 84	0
21	800.451200	3.210E-26	1.731E-05	.0661	.0872	2481.56150	.75	0.00000	14	6		P 37	186	0

FORMAT (I2, I1, F12, 1P2E10.3, 0P2F5.4, F10.4, F4.2, F8.5, 2I3, 2A9, 3I1, 3I2)

       = 100 characters per transition

This format corresponds as follows:

Mo - I2   Molecule number
iso - I1   Isotope number (1 – most abundant, 2 – second, etc.)
ν - F12.6   Frequency in cm^{-1}
S' - E10.3   Intensity in cm^{-1}/(Molec $\cdot$ cm^{-2}) @ 296 K

R - E10.3   Transition probability in Debyes^2 (presently lacking internal partition sum)
γ - F5.4   Air-broadened half-width (HWHM) in cm^{-1}/atm @ 296 K
γ_s - F5.4   Self-broadened half-width (HWHM) in cm^{-1}/atm @ 296 K
E'' - F10.4   Lower state energy in cm^{-1}
n - F4.2   Coefficient of temperature dependence of air-broadened half-width
y - F8.5   Shift of transition due to pressure (presently empty; some coupling coefficients inserted)
ν' - I3   Upper state global quanta index
ν'' - I3   Lower state global quanta index
Q' - A9   Upper state local quanta
Q'' - A9   Lower state local quanta
IER - 3I1   Accuracy indices for frequency, intensity, and half-width
IREF - 3I2   Indices for look up of references for frequency, intensity, and half-width

IER code for frequency when used:

IER	estimated error in wave number
0	$\geq 1.$ or undefined
1	≥ 0.1 and <1.0
2	≥ 0.01 and <0.1
3	≥ 0.001 and <0.01
4	≥ 0.0001 and <0.001
5	≥ 0.00001 and <0.0001
6	<0.00001

IER code for intensity and half-width:

IER	estimated error in wave number
0	Undefined
1	Default or constant
2	Average or estimate
3	$\geq 20\%$
4	$\geq 10\%$ and $\leq 20\%$
5	$\geq 5\%$ and $\leq 10\%$
6	$\geq 2\%$ and $\leq 5\%$
7	$\geq 1\%$ and $\leq 2\%$
8	$<1\%$

where T is in kelvins and p_a is in atm. The transition probability, $R(= 3 \times 10^{36} \sum |\mu_{dp}|I_{ab}/g_l)$, where I_{ab} is the isotopic abundance, is listed next in debyes squared.

Air-broadened (collision) half-widths, $\gamma_{c0air}(= \gamma_{cair}(T_0))$, are given in cm^{-1}/atm for $T = 296$ K. Self-broadened half-widths, γ_{c0a}, are given in the same units where available. (Otherwise Table 5.1 must be used.) The lower state energy, $E^n(= E_l)$, is given in cm^{-1}. The temperature dependence of the collision half-width follows a power law of the form

$$\gamma_c = \gamma_{c0}(T_0/T)^n, \tag{7.22}$$

where, based on Eq. 5.97,

$$\gamma_{c0} = \gamma_{c0air}\, p_{air} + \gamma_{c0a}\, p_a,$$

and $p_{air} + p_a = 1$ atm. Based on the kinetic theory of gases, n is 0.5. However, experimental data and more complete theories have shown that $n = 0.5$ is not always obeyed. For this reason, the database also lists n, the coefficient of temperature dependence of the air-broadened half-width.

Collisions with the absorbing molecule also produce shifts of line position. This is called pressure shift, $\gamma_{c,i}$ (see Eq. 5.138), and is generally a weak effect. A location for this parameter is included on the database. Coupling coefficients, y_i, are given, accounting for line mixing (see Section 5.6.3.1, and Eq. 5.101) for a few gases (e.g., O_2) in this position as well.

The quantum numbers of the upper and lower levels are listed next. The last two entries cover data accuracy and references.

The HITRAN database is available from Dr. L.S. Rothman, Atomic and Molecular Physics Division, Harvard-Smithsonian Center for Astrophysics or ONTAR Corp., 9 Village Way, North Andover, MA 01845-2000 (www.ontar.com).

Other databases exist as well, and one is worth mentioning briefly. The GEISA database is maintained by a French group and is very similar to the HITRAN database. It includes molecules of importance to other planetary atmospheres and therefore may be a useful source for molecules not included in HITRAN.

7.2.3 Band Models

Realistic models of the atmosphere that include aerodynamics, surface effects, and clouds, as well as propagation, cannot handle detailed line-by-line absorption calculations. Also, broad-band systems do not require high-resolution models for meaningful calculations. For these reasons, simplified models of vibration and rotation absorption bands are often used.

7.2.3.1 Introduction

The most practical approach to computing atmospheric broad-band absorption (transmittance) is to use an approximate, mathematically workable model of the band structure. This assumes that line positions and strengths are distributed in a way that can be represented by a simple mathematical formula. Band models compute transmittance averaged over a spectral band as defined by

$$\overline{\tau}(v) = \frac{1}{\Delta v} \int_{v - \frac{\Delta v}{2}}^{v + \frac{\Delta v}{2}} \tau(v) \, dv. \tag{7.23}$$

The most commonly used band models are listed below (from LaRocca, Ref. 7.82a, p. 5.11):

1. The Elsasser, or regular model, assumes spectral lines of equal strength, equal spacing, and identical half-widths. The transmission function is averaged over an interval equal to the spacing between the line centers.
2. The statistical, or random model, originally developed for water vapor, assumes that the positions and strengths of the lines are given by a probability function. The statistical model was worked out by Mayer [Ref. 7.82b] and (independently) by Goody [Ref. 7.82c].
3. The random-Elsasser model is a generalization of the Elsasser and the statistical models. It assumes a random superposition of any number of Elsasser bands of different strengths, spacings, and half-widths.
4. The most accurate, presently available model, is the quasi-random model, provided the averaging interval can be made sufficiently small. It requires the greatest amount of computation of all the models.

Assuming that the shape of a single spectral line for a homogeneous path containing a single absorbing gas is represented by the Lorentz formula, the absorptance for an arbitrary path is given by

$$(1 - \overline{\tau}) \, \Delta v = \overline{\alpha_{abs}} \Delta v = \int_{\Delta v} \left[1 - \exp\left(-\frac{1}{\pi} \int_{path} \frac{S' \gamma \rho_a}{(v - v_0)^2 + \gamma^2} dz \right) \right] dv. \tag{7.24}$$

This limits the model to the collision broadened regime, which is valid for lower altitudes. Assuming γ is independent of position; Eq. 7.24 then further reduces to

$$\overline{\alpha_{abs}} \Delta v = \int_{\Delta v} \left[1 - \exp\left(-\frac{S'}{\pi} \int_{path} \frac{\gamma w}{(v - v_0)^2 + \gamma^2} \right) \right] dv, \tag{7.25}$$

where $w = \int_{path} \rho_a dz \, (= \rho_a z$ for a homogeneous path), and is defined as the absorber amount in cm^{-2}.[1]

A plot of single-line absorptance versus frequency is shown in Fig. 7.23 for different path lengths, or for different values of w. For a short optical path of length z_1, the absorption is small, even at the line center. For a long path of length z_3, the center of the line is completely absorbed and any further increase in path length would only change the absorption in the wings of the line. Absorption by paths of length equal to or greater than z_2 is considered strong-line absorption.

If, in Eq. 7.25, one assumes that the interval Δv is such that substantially the entire line is included, then the limits of integration can be taken from $-\infty$ to ∞ without introducing significant error. When these limits are used, Eq. 7.25 can be solved exactly for
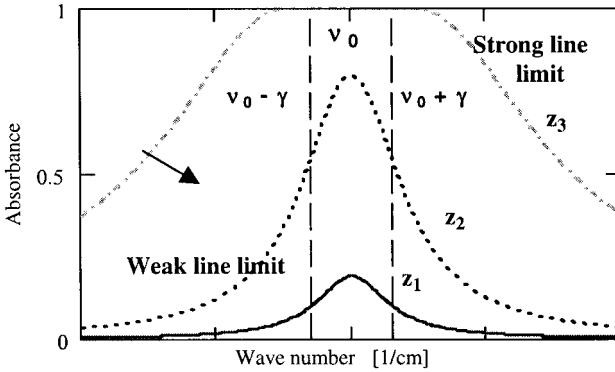
Fig. 7.23 Absorbance versus frequency for a single line and for different path lengths or absorber amounts.

the total absorptance. Ladenburg and Reiche (Ref. 7.83) have evaluated the integral to obtain

$$\overline{\alpha_{abs}}\Delta\nu = 2\pi\gamma\psi e^{-\psi}\left[I_0(\psi) + I_1(\psi)\right], \tag{7.26}$$

where $\psi = S'w/(2\pi\gamma)$ and I_0 and I_1 are modified Bessel functions. For weak-line absorption ($\psi \ll 1$), Eq. 7.26 reduces to

$$\overline{\alpha_{abs}}\Delta\nu = 2\pi\gamma\psi = S'w. \tag{7.27}$$

and absorptance is linear with the absorber amount, w. Under conditions of strong-line absorption, ψ is large and Eq. 7.26 reduces to

$$\overline{\alpha_{abs}}\Delta\nu = 2\sqrt{S'\gamma w}, \tag{7.28}$$

known as the square-root approximation. The above formulations for a single spectral line are also valid for absorption when many spectral lines are present but do not overlap.

7.2.3.2 LOWTRAN Method

This method is empirical, yielding a form for the transmittance given by (wave number resolution = 20 cm^{-1})

$$\overline{\tau}(\lambda) = f[G_\nu, w, P^n] = f[G(\lambda), w^*], \tag{7.29}$$

where
$G_\nu =$ spectral coefficients, independent of temperature and pressure, derived from the HITRAN database with a resolution of 20 cm^{-1} and data points every 5 cm^{-1}
$w =$ absorber amount for path from z_0 to $z = \int_{z_0}^z \rho_a(z')\,dz'$,
$P =$ net atmospheric pressure, and
$w^* =$ equivalent absorber amount $= w[P/P_0(T_0/T)^{1/2}]^n$,

where $P_0 = 1$ atm and $T_0 = 273$ K. This is a single-parameter band model that depends only on $w^*(P,T)$, a density–path-length variable times pressure divided by the square root of temperature raised to an empirical exponent n, and does not fully represent the correct temperature dependence. For this reason, LOWTRAN calculations should be checked against more complete models (such as FASCODE, introduced in Section 7.4.4.2) before a series of similar calculations are made. The pressure and temperature factor in w^* represents contributions from absorption line half-widths. The spectral coefficients, G_v, are spectrally averaged according to the formula

$$G_v(T_0) = \langle S'(T_0, v) \rangle_{\Delta v}.$$

G_v is determined from the HITRAN database degraded to 20 cm^{-1} resolution and at a fixed temperature ($T = 273$ K). Such an approach ignores the temperature dependence of the Boltzmann factor and partition function. This is particularly important at the band edges, where the rotational line J number is high.

The functional form of τ is determined empirically for three classes of atmospheric gases: water vapor, ozone, and uniformly mixed gases (CO_2, CH_4, N_2O, etc.). Figure 7.24 illustrates these different curves (McClatchey et al., Ref. 7.84; Fenn et al., Ref. 7.85). The details of the band structure are represented empirically by τ, which greatly simplifies the previously described band model approach. Setting n in Eq. 7.29 to zero or unity, we will obtain the weak-line or the strong-line approximation, respectively. The mean values of n are determined to be 0.9 for H_2O, 0.75 for the uniformly mixed gases, and 0.4 for ozone. The fact that such simple curves can be generated by a diverse database is the strength of the LOWTRAN method. Figures 7.25 to 7.27 present the G_v functions for ozone, water vapor, and the uniformly mixed gases, respectively, from 0 to 5000 cm^{-1}. The equivalent absorber amount is

$$w^* = \int_0^\infty \rho_a(z') \left(\frac{P}{P_0} \sqrt{\frac{T_0}{T}} \right)^n dz'. \tag{7.30}$$
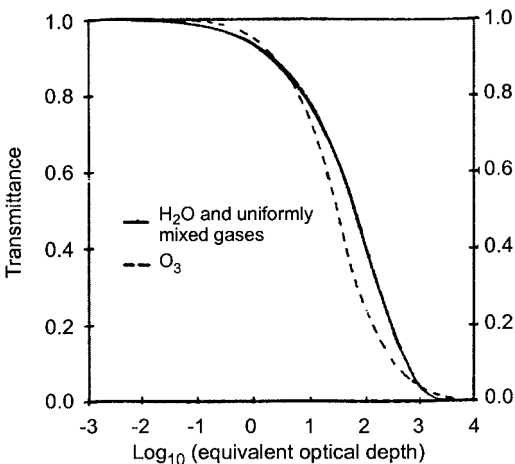
Fig. 7.24 LOWTRAN empirical transmittance functions versus $\log_{10}$ of the equivalent opticaldepth ($G_v w^*$) (Fenn et al., Ref. 7.85).
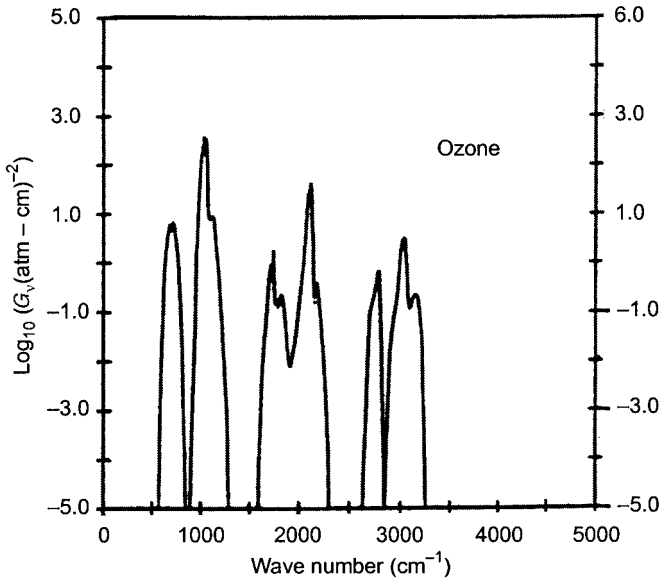
Fig. 7.25 Absorption coefficient G_ν for ozone from 350 to 5000 cm^{-1} (Fenn et al., Ref. 7.85).
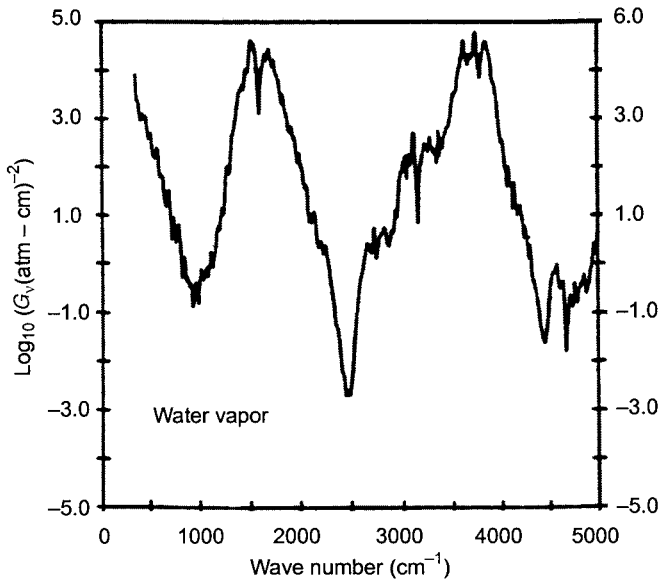
Fig. 7.26 Absorption coefficient G_ν for water vapor from 350 to 5000 cm^{-1} (Fenn et al., Ref. 7.85).
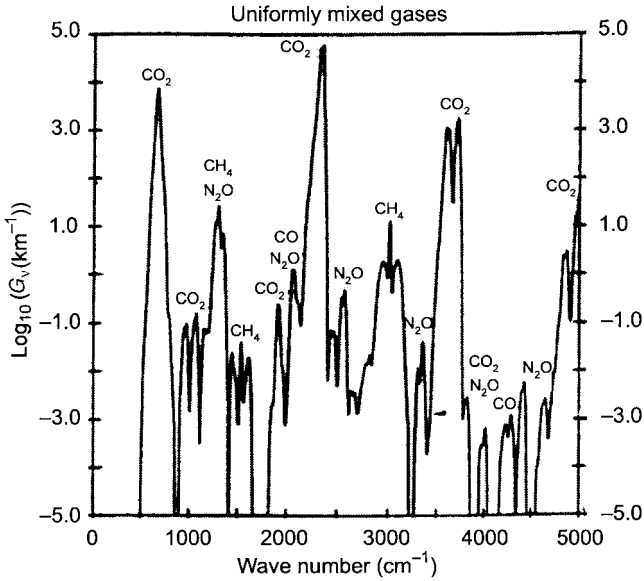
Fig. 7.27 Absorption coefficient G_ν for the uniformly mixed gases from 350 to 5000 cm^{-1} (Fenn et al., Ref. 7.85).

The absorber density must be known as a function of altitude. Standard curves are used for specific latitudes and time of year (McClatchey et al., Ref. 7.84). An example for water vapor is given in Fig. 7.28.

7.2.3.3 MODTRAN Method

The single-parameter LOWTRAN approach is upgraded by a two-parameter MODTRAN (Refs. 7.3, 7.4) model, which features 2 cm^{-1} resolution. MODTRAN is also supported by Phillips Laboratory. The main goal of MODTRAN is to improve temperature dependent calculations. Significant improvements are listed below:

1. A 2 cm^{-1} resolution (FWHM) band model is used, so that spectral parameters are calculated every wave number.
2. A more realistic temperature-dependent model is implemented. This is accomplished by using the partition function in Eq. 5.118 for line strength temperature dependence, which is now included in the spectral parameter.
3. The molecules represented include water vapor, carbon dioxide, ozone, nitrous oxide, carbon monoxide, methane, oxygen, nitric oxide, sulfur dioxide, ammonia, and nitric acid.
4. High-altitude transmittance/radiance calculations are allowed, up to 60 km, where local thermal equilibrium (LTE) is satisfied. This is made possible by including the Voigt line shape (see Chapter 5) in the band model formalism. The Voigt line shape also represents the pressure dependence of the band more accurately.
5. The Curtis–Godson approximation is used, which replaces an inhomogeneous path with a homogeneous one by using average values for the various band model parameters.
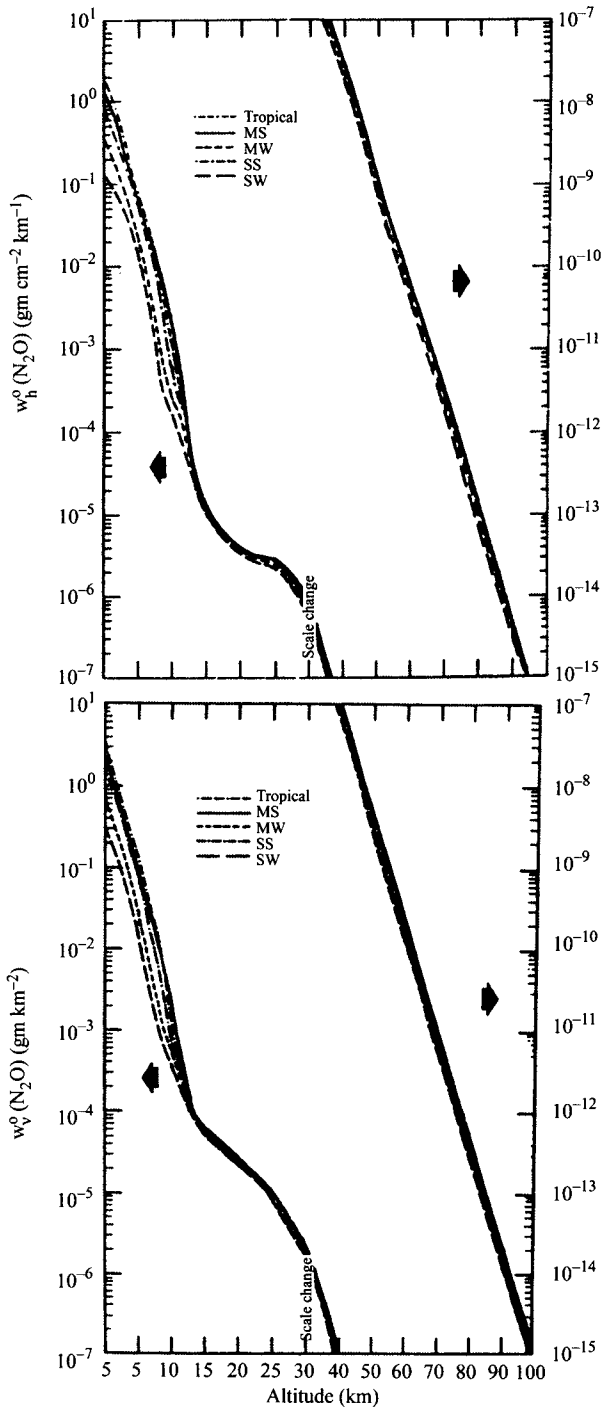
Fig. 7.28 Values obtained for model atmospheres tabulated for the so-called standard seasonal conditions (LaRoccha, Ref. 7.82a).

Examples of the MODTRAN band model improvements are given in Section 7.4.

7.2.4 Refractive Effects of the Atmosphere

Precise spatial measurements within the atmosphere by remote electromagnetic techniques require equally precise knowledge of the effects of atmospheric refraction. Astronomical observations near the horizon must account for refraction. Ground-to-ground line-of-sight communication links must account for the variable refractive nature of the atmosphere. This is because the ray path is not rectilinear. Thus, atmospheric refractivity must be understood as a function of observer's position, range, frequency, and atmospheric pressure and temperature. At infrared through ultraviolet frequencies, refractivity primarily depends on the vertical temperature profile, and an explicit relationship between refractivity and temperature is obtainable for a dry atmosphere. At microwave frequencies, the vertical water vapor profile also contributes significantly to refraction. In this section, a model for the atmospheric index of refraction is constructed and a geometrical optics solution of the eikonal equation for the optical ray path is developed for the earth coordinate system in the lower atmosphere. For example, this is needed to precisely locate low-altitude lidar measurements. Also, a more general model is presented for astronomical observations.

The real part of the atmospheric index of refraction is a function of pressure, temperature, and frequency. Many interesting low-altitude refractive effects exist because of tropospheric variations in density and water vapor partial pressure as a function of position. Atmospheric refraction situations are broken down into three main categories; astronomical, terrestrial and geodesic. Astronomical refraction addresses ray-bending effects of objects outside the atmosphere of the earth relative to an observer within the atmosphere. Terrestrial refraction considers the case when both object and observer are within the atmosphere of the earth. Geodesic refraction is a special case of terrestrial refraction where the object and observer are at low altitudes, as is commonly the case for surveying.

This section begins with a discussion of atmospheric index of refraction models at optical frequencies and then examines different propagation effects caused by refractive index variations.

7.2.4.1 Index of Refraction of Atmospheric Gases

Because of their abundance, nitrogen and oxygen make significant contributions to the refractivity of the earth's atmosphere. These molecules have no infrared bands of importance to the refractive index, thus only electronic bands need to be considered for a model valid from near DC to the ultraviolet. Based on the work of Edlen (Ref. 7.89), a simple Sellmeier-type model for the dry atmospheric refractivity, N_{Dry}, can be obtained (Fenn et al., Ref. 7.90):

$$N_{Dry} = (n-1) \times 10^6 = \left(237.2 + \frac{527.3 v_1^2}{v_1^2 - v^2} + \frac{11.69 v_2^2}{v_2^2 - v^2} \right) P_{Dry}/T \quad (7.31a)$$

with the corresponding Cauchy model given by

$$N_{Dry} = (776.2 + 4.36 \times 10^{-8}\nu^2)\frac{P_{Dry}}{T}, \tag{7.31b}$$

where ν is the wave number in cm^{-1}, $\nu_1 = 114000.0$ cm^{-1}, $\nu_2 = 62400.0$ cm^{-1}, P_{Dry} is the total dry air pressure in kilopascals (kPa), and T is the temperature in kelvins. This model is valid up to altitudes where the mixing ratio between O_2 and N_2 is fixed and over the spectral region from 0.2 to 2000 μm. Equation 7.31b compares well with other models (Lorah and Rubin, Ref. 7.91; and Barrell and Sears, Ref. 7.92). Based on Eq. 7.7 for total pressure and given the temperature profile, the altitude dependence can also be included in the dry air refractivity,

$$N_{Dry}[\nu, T(z)] = (776.2 + 4.36 \times 10^{-8}\nu^2)\frac{P(z_0)}{T(z)} \exp\left(-\frac{mg}{k_B} \int_{z_0}^{z} \frac{dz'}{T(z')}\right), \tag{7.31c}$$

where z_0 is the initial altitude, m is the average molecular mass of the atmosphere, g is gravitational acceleration, and k_B is Boltzmann's constant. For altitudes up to 100 km, mg/k_B equals 34.16 K/km.

Moist air requires an additional term that accounts for water vapor. Based on the work of Hill and Lawrence (Ref. 7.93) a Sellmeier-type term is obtained that represents the electronic transition contributions of pure water vapor:

$$N_{H_2O} = \frac{651.7\nu_3^2}{\nu_3^2 - \nu^2} P_{H_2O}/T, \tag{7.32a}$$

and the corresponding Cauchy model is

$$N_{H_2O} = (651.7 + 5.23 \times 10^{-8}\nu^2) P_{H_2O}/T \tag{7.32b}$$

where $\nu_3 = 111575.0$ cm^{-1} and P_{H_2O} is in units of kPa. The net refractivity for a humid atmosphere in the visible and near-infrared is the sum of N_{Dry} plus N_{H_2O}.

The model becomes more complicated at infrared wavelengths because the strong infrared vibration–rotation bands of water vapor must be considered. The importance of water vapor is demonstrated by the refractivity at radar frequencies, which is the sum of all oscillator strengths, as given by (Refs. 7.93, 7.94)

$$N_{Rf} = (777.4 P_{Dry}/T + 717 P_{H_2O}/T) + 3.744 \times 10^6 P_{H_2O}/T^2. \tag{7.33}$$

The RF refractivity can vary from 250 to 500 over the range of sea-level atmospheric temperatures and water vapor partial pressures (Ref. 7.95). Most of this variability is caused by water vapor. In particular, the last term in Eq. 7.33 represents the rotational band of water vapor. A model can be constructed, based on Eqs. 5.125 and 5.126, and Table 7.5, allowing reasonable prediction of refractivity at infrared wavelengths. Temperature- and pressure-dependence of the band strength is determined by the gas number density. The exception is the rotational band, where because of the low-frequency band center, the tanh function in Eq. 5.126 contributes another factor of $1/T$ to the band strength. Table 7.16 lists parameters for a refractivity Sellmeier model that includes the effect of water vapor. This Sellmeier model reproduces available experimental data at visible and microwave frequencies (Gray, Ref. 7.97; Crain, Ref. 7.98)

Table 7.16 Oscillator Parameters for Atmospheric
Refractivity

Mode Number	ν_i [cm^{-1}]	$\Delta\epsilon_i^a$
1	∞	$4.744 \times 10^{-4}\ P_{Dry}/T$
2	114000.0	$1.046 \times 10^{-3}\ P_{Dry}/T$
3	62400.0	$2.338 \times 10^{-5}\ P_{Dry}/T$
4	111575.0	$1.303 \times 10^{-3}\ P_{H_2O}/T$
5	3740.0	$1.480 \times 10^{-5}\ P_{H_2O}/T$
6	1595.0	$1.158 \times 10^{-4}\ P_{H_2O}/T$
7	125.0	$7.488\ P_{H_2O}/T^2$

$^a P_{Dry}$, P_{H_2O} are in kilopascals, T is in kelvins.

and allows reasonable predictions ($\pm$ 0.5 N units) at infrared frequencies for a humid atmosphere. More accurate line-by-line models are possible, but will be more numerically complicated. A small discrepancy also exists between $N_{Dry}(\nu = 0)$, predicted from Table 7.16, and N_{Rf} from Eq. 7.33, which can be explained by the neglected contributions of the 60 GHz O$_2$ band and other minor contributions from CO$_2$, N$_2$O, and CH$_4$ infrared absorption bands. A plot of atmospheric refractivity based on this Sellmeier model is given in Fig. 7.29. This figure clearly points out the differences in refractivity in the different spectral window regions of the atmosphere. At microwave frequencies, refractivity is very sensitive to water vapor density and is larger in magnitude than for the other spectral regions. The visible and infrared are regions of minimal refractivity. Refractivity at infrared and higher frequencies depends mostly on temperature and very weakly on water vapor density. The ultraviolet refractivity is large and features strong dispersion.
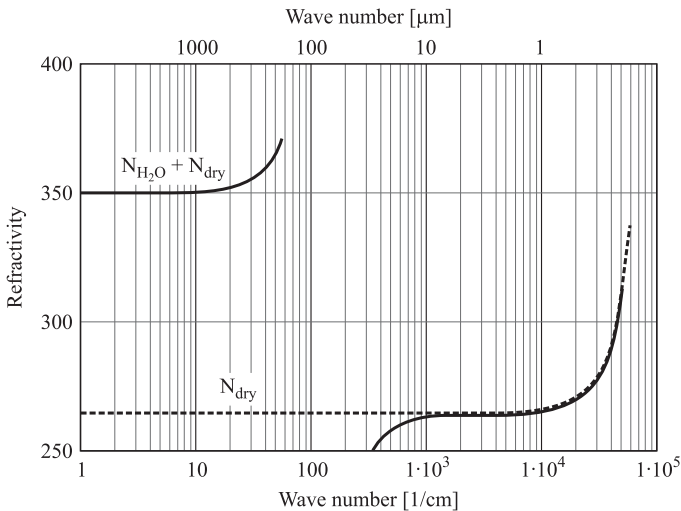
Fig. 7.29 Atmospheric refractivity for $T = 288$ K, $P_{Dry} = 99$ kPa, and $P_{H_2O} = 2$ kPa (dotted curve) and $T = 288$ K, $P_{Dry} = 101$ kPa, and $P_{H_2O} = 0$ kPa (solid curve), as a function of frequency in units of wave number.

7.2.4.2 Earth–Atmosphere Ray Path Geometry

Given that the index of refraction depends on density and the density of the atmosphere depends on altitude (see Section 7.1), then light propagating in the atmosphere will be bent (typically toward lower altitudes or regions of higher density). The density of the atmosphere does not vary greatly in the horizontal direction and only vertical structure need be considered in most cases. To describe the ray path analytically, a suitable coordinate system must be used, such as illustrated in Fig. 7.30. The surface of the earth and the structure of the atmosphere can be conveniently represented by a spherical coordinate system, as given by

$$x = r \sin\theta \cos\phi$$
$$y = r \sin\theta \sin\phi$$
$$z = r \cos\theta$$

In the above coordinate system for a spherically symmetric atmosphere, the angle $\theta(r)$, satisfying the eikonal equation, is expressible as (Born and Wolf, Ref. 1.8, p. 123)

$$\theta(r) = \int_{r_0}^{r} \frac{dr'}{r' \sqrt{\frac{n^2(r')r'^2}{const^2} - 1}}, \tag{7.34}$$

where *const* is a constant and r_0 is the initial altitude of the optical path. The constant *const* is unspecified, which prevents immediate application of this formula. It will be determined later by comparing it with the limiting form of another solution via the eikonal equation. The above model is very general and allows rapidly varying vertical structures and long path lengths to be handled in a straightforward manner. It will be useful for astronomical refraction.
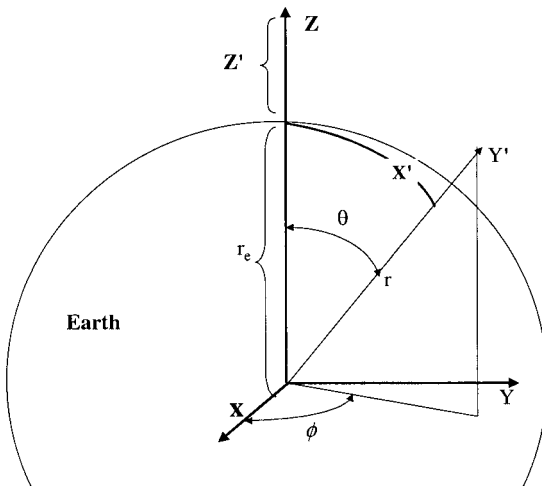
Fig. 7.30 Earth–atmosphere coordinate system.

The above geometry puts the origin of the coordinate system at the center of the earth, and this is not a practical location. It is more natural to locate the origin on the surface at the location of the observer. Thus, translating along the r-direction by the radius of the earth, r_e, one obtains

$$r = r_e + z' = r_e \left(1 + \frac{z'}{r_e} \right) = r_e \eta. \tag{7.35}$$

This leads to the definition of a prime coordinate or earth coordinate system for small angles θ and ϕ as illustrated in Fig. 7.30 and stated as

$$x' = r\theta = \eta r_e \theta$$
$$y' = r\theta\phi = \eta r_e \theta\phi \tag{7.36}$$
$$z' = r - r_e = (\eta - 1)r_e.$$

x' and y' represent arc-lengths along the surface of the earth. The small-angle approximation is valid for surface ranges up to 600 miles (i.e., θ does not exceed $10°$). Although this is a logical coordinate system for describing beam propagation in the atmosphere, it has the unfortunate property that the metric in the x'- and y'-directions changes with altitude. This is described by the metric tensor, g, for this coordinate system,

$$g = \begin{pmatrix} \eta^2 & 0 & 0 \\ 0 & \eta^2 & 0 \\ 0 & 0 & 1 \end{pmatrix}. \tag{7.37}$$

This coordinate system is orthogonal because the metric tensor is diagonal. The metric tensor is useful because it allows the definition of differential operators in a curvilinear coordinate system (see Stratton, Ref. 4.1).

Let us now examine geometrical optics to find the ray path within this coordinate system, given a refractive index profile. Of particular interest is transforming the vector eikonal equation as given by Eq. 2.117 to the earth coordinate system. For nearly horizontal propagation, it is known that Maxwell's equations are modifiable by replacing $n(r')$ by $\eta(z')n(r')$ and treating the coordinate system as rectangular (see Freehafer et al., Ref. 7.106). This approach is also consistent with evaluating the gradient, given the metric tensor of Eq. 7.37, for nearly horizontal propagation. Thus the eikonal equation becomes

$$\Delta \psi(r') = \eta(z')n(r')\hat{s} = m(r')\hat{s}. \tag{7.38}$$

$m(r')$ is the commonly used modified refractive index. Effectively, this refractive index profile correction accounts for the curvature of a spherical earth. It is worth noting that $\eta(z')$ can be modified to include deviations from a spherical surface (mountains, etc.). Since n is close to one, then

$$m(r') = n(r') + \frac{z'}{r_e}. \tag{7.39}$$

For $r_e = 6378.4$ km, then $1/r_e = 1.568 \times 10^{-4}$ km^{-1}.

Geometrical optics equations in two dimensions ($x'z'$-plane) describing the ray path in the earth coordinate system assuming a vertically varying atmosphere (i.e., $m(r') = m(z')$), are given by the following form of the eikonal equation (see Eq. 2.119 and Born and Wolf, Ref. 1.8)

$$\frac{d}{ds}\left(m(z'(s))\frac{dx'(s)}{ds} \right) = 0,$$

$$\frac{d}{ds}\left(m(z'(s))\frac{dz'(s)}{ds} \right) = \frac{dm(z')}{dz'}.$$

(7.40a)

Given the vertical atmospheric refractivity, these equations can be used to describe the optical ray path. Note that the gradient of the refractivity determines the ray path. The following boundary conditions are applied at $x' = 0$ for a ray initially launched at z'_0 with slope $\tan\delta$,

$$\text{at} \quad z' = z'_0, \quad \frac{dx'}{ds} = \cos\delta \quad \text{and} \quad \frac{dz'}{dx'} = \tan\delta, \tag{7.40b}$$

where $(dx')^2 + (dz')^2 = (ds)^2$ is satisfied. To be consistent with the approximations leading to Eq. 7.38, δ must be kept small. The differential, ds, is the incremental path length. It can be expressed in terms of the vertical incremental path by solving the first equation in Eq. 7.40a with the boundary conditions of Eq. 7.40b and requiring the above equation to be satisfied. This process leads to the following useful relationship:

$$ds = \frac{dz'}{\sqrt{1 - \frac{m^2(z'_0)}{m^2(z')}\cos^2\delta}}. \tag{7.41a}$$

Integration along s yields the path length in a refractive atmosphere, thus

$$s(z') = \int_{z'_0}^{z'} \frac{dz''}{\sqrt{1 - \frac{m^2(z'_0)}{m^2(z'')}\cos^2\delta}}, \tag{7.41b}$$

where $s(z'_0) = 0$.

Again applying the above boundary conditions, to the second equation in Eq. 7.40a, reduces the two equations to a single differential equation, as given by

$$\frac{d^2z'(x')}{dx'^2} = \frac{m(z')}{m^2(z'_0)}\sec^2\delta\,\frac{dm(z')}{dz'} = \frac{\sec^2\delta}{2m^2(z'_0)}\frac{dm^2(z')}{d'z}. \tag{7.42}$$

By inverting the above differential equation to solve for $x'(z')$, an integral equation can be obtained for $\delta \geq 0$,

$$x'(z',\delta) = r_e\theta(z') = \int_{z'_0}^{z'} \frac{dz''}{\sqrt{\frac{m^2(z'')}{m^2(z'_0)}\sec^2\delta - 1}}. \tag{7.43a}$$

The quantity in the square root must be positive for a real path, thus $m(z') \sec \delta$ must be greater than $m(z'_0)$ for all $z' \geq z'_0$. This is the case for a standard atmosphere and other conditions (see Section 7.2.4.5), but will not be satisfied for trapping $(m(z') = m(z'_0)$ for all z', $\delta = 0)$ or ducting (see Section 7.2.4.6). For $z' < z'_0$ and $\delta < 0$, the solution for $x'(z')$ is

$$x'(z',\delta) = \int_{z'}^{z'_0} \frac{dz''}{\sqrt{\frac{m^2(z'')}{m^2(z'_0)} \sec^2 \delta - 1}}. \tag{7.43b}$$

When $z' = 0$ the ray grazes the surface of the earth or terminates there. This locates the optical horizon. These integral equations are the basis for terrestrial refraction for any m-profile that satisfies $m(z') \sec \delta > m(z'_0)$. Note that Eq. 7.43a is of a somewhat similar form to Eq. 7.34.

Although Eqs. 7.43a and b are useful for most cases, they require numerical solution. Possible exact solutions of Eq. 7.42 for $z'(x')$ also should be examined. Equation 7.42 can be simplified by assuming $m(z')$ can be represented by a polynomial. Let us examine Eq. 7.42 when the modified index is expressible in the general quadratic form,

$$m(z) = 1 + A + Bz + Cz^2. \tag{7.44}$$

The coefficients, A, B, and C are functions of temperature, total atmospheric pressure (dry), water vapor partial pressure, and frequency. Using the above form for $m(z')$, Eq. 7.42 simplifies to

$$\frac{d^2 z'(x')}{dx'^2} = \frac{1 + A + B'_z + Cz'^2}{(1 + A + Bz'_0 + Cz'^2_0)^2}(B + 2Cz') \sec^2 \delta \tag{7.45a}$$

with the initial boundary conditions that

$$z'(x' = 0) = z'_0 \quad \text{and} \quad \frac{dz'}{dx'}(x' = 0) = \tan \delta. \tag{7.45b}$$

Also, it is of interest at infrared, visible, and ultraviolet frequencies to establish the relationship between the ray path and the vertical temperature profile. This can be done in a straightforward manner by assuming that $m(z') \approx 1$ (e.g., $A + Bz' + Cz'^2 \ll 1$ or $z' < 20$ km). For low-altitude propagation modeling, this is an excellent approximation. Also using Eqs. 7.31c and 7.39, the gradient of the modified index can be determined. Based on Eq. 7.42, the resulting differential equation then becomes

$$\frac{d^2 z'}{dx'^2} = \frac{dm(z')}{dz'} \sec^2 \delta = \frac{\sec^2 \delta}{r_e} - \frac{(7.762 \times 10^{-4} + 4.36 \times 10^{-14} v^2) P(0)}{T^2(z') \cos^2 \delta}$$

$$\times \left(\frac{dT(z')}{dz'} + \frac{mg}{k_B}\right) \exp\left(-\frac{mg}{k_B} \int_0^{z'} \frac{dz''}{T(z'')}\right). \tag{7.46}$$

The approximations are consistent with applications supporting low-altitude refraction and this differential equation is the basis for refractivity models used for geodesic

refraction. Also, Eq. 7.44 leads to $z'(x')$ rather than $x'(z')$, which is the function of practical interest.

The above approaches are fundamentally different from past ray-trace methods. One common approach is to apply Snell's law to a vertically stratified medium with layers of constant refractivity. A better approach is based on the eikonal equation applied to a vertically stratified atmosphere with layers of constant refractive gradient. The layer thickness must be thin enough so that the refractivity is accurately modeled. The ray path is then determined by integrating along the layers. These past models are numerically intensive because many layers are needed, which is not an issue for past applications. However, Raman and DIAL lidar require considerable signal processing to achieve the final results, especially when high spatial resolution is required and efficient ray-path models are needed. The approaches given above provide this efficiency by using at least a quadratic representation of the refractivity and can be plotted in a flat or spherical earth geometry. As the next section will show, ray tracing is not always necessary at low altitude, since a closed-form solution to the eikonal equation is obtainable if the vertical refractive profile is quadratic in altitude.

7.2.4.3 Terrestrial and Geodesic Refraction

An interesting solution to Eq. 7.46 is terrestrial refraction within the troposphere. In this region the temperature decreases linearly ($T(z') = T_0 + az'$) with altitude as discussed in Section 7.1. Thus Eq. 7.7 is used to represent the pressure as a function of altitude. A Taylor series expansion of Eq. 7.7 generates an expression for the pressure with reasonable accuracy in polynomial form. To third order in the expansion, it is

$$\frac{P(z)}{P(0)} = 1 - \frac{mg}{k_B T_0} z + \frac{1}{2}\left(\frac{mg}{k_B T_0}\right)\left(\frac{a}{T_0} + \frac{mg}{k_B T_0}\right) z^2$$
$$- \frac{1}{6}\left(\frac{mg}{k_B T_0}\right)\left(\frac{a}{T_0} + \frac{mg}{k_B T_0}\right)\left(\frac{2a}{T_0} + \frac{mg}{k_B T_0}\right) z^3 + \cdots .$$

$$(7.47)$$

For a standard atmosphere ($P(0) = 101.3$ kPa, $T_0 = 288$K, and $a = -6.5$ K/km), the above equation becomes

$$P(z) = 101.3 - 12.0z + 0.577z^2 - 0.0141z^3, \tag{7.48}$$

where z is in km. This formula agrees closely with values for the U.S. 1976 Standard Atmosphere in the troposphere. Using this result and knowing the temperature dependence with altitude, a cubic polynomial for visible and infrared refractivity as a function of altitude can be obtained from Eq. 7.31,

$$N(z,\nu) = (272.6 + 1.53 \times 10^{-8}\nu^2)(1 - 0.096z + 3.5 \times 10^{-3}z^2$$
$$- 5.94 \times 10^{-5}z^3).$$

$$(7.49)$$

Based on Eq. 7.39, the modified refractivity is

$$M(z,\nu) = N(z,\nu) + 156.8z. \tag{7.50}$$

Based on Eqs. 7.46 and 7.47, an explicit differential equation can be obtained, where a quadratic representation of the modified index is used. The result is

$$\frac{d^2 z'(x')}{dx'^2} = (B + 2Cz')\sec^2\delta, \tag{7.51a}$$

where the coefficients B and C are frequency dependent as,

$$B(v) = \left[156.8 - \eta(v)\frac{P(0)}{T_0}\left(\frac{34.16}{T_0} + \frac{a}{T_0}\right)\right] \times 10^{-6} \quad [\mathrm{km}^{-1}], \tag{7.51b}$$

$$C(v) = \eta(v)\frac{P(0)}{T_0^2}17.08(3a + 34.16) \times 10^{-6} \quad [\mathrm{km}^{-2}], \tag{7.51c}$$

and based on Eq. 7.31b, the dispersion factor is defined to be

$$\eta(v) = 776.2 + 4.36 \times 10^{-8}v^2, \tag{7.51d}$$

where v has units of wave numbers. The solution of Eq. 7.51a, using the boundary conditions of Eq. 7.45b, for the ray path is obtained in a straightforward manner to be

$$z'(x',\delta) = \left(z_{0'} + \frac{B}{2C}\right)\cosh\left(\sec\delta\sqrt{2C}x'\right) + \frac{\sin(\delta)}{\sqrt{2C}}\sinh\left(\sec\delta\sqrt{2C}x'\right) - \frac{B}{2C}. \tag{7.52}$$

This result describes the path an optical ray takes as it propagates through the lower atmosphere ($z' < 20$ km). The coefficient B represents the reciprocal radius of curvature of the ray to the zeroth order or in regions of constant refractivity gradient. It is this term that is used in many ray-tracing procedures. The quantity $1/(Br_e)$ is called the refraction coefficient and can be used to correct the geometric horizon to the optical horizon (see Eq. 7.55). For a typical standard atmosphere ($dN/dz' = -40$), the value of $1/Br_e$ is approximately 1.33 or 4/3. (This procedure is often referred to as the 4/3 earth correction).

The function $z'(x')$ is in terms of a rectangular coordinate system. To plot results in a curved earth or spherical coordinate system, the following transformation is used to obtain z'_e,

$$\theta(x',z') = \sin^{-1}\left(\frac{x'}{r_e + z'}\right),$$

$$z'_e = (r_e + z')\cos\left[\theta(x',z')\right] - r_e.$$

In the case of the 1976 U.S. Standard Atmosphere model, Eqs. 7.47 and 7.48 can be applied and results are plotted in Fig. 7.31a for a curved earth.

For near-horizon observations within the lower troposphere (i.e., when $\sqrt{2}C'_x \ll 1$ and $\delta \approx 0$), Eq. 7.52 reduces to a quadratic form, as given by

$$z'(x') = z'_0 + \delta x' + \frac{B + 2Cz'_0}{2}x'^2. \tag{7.53}$$

(a)

(b)
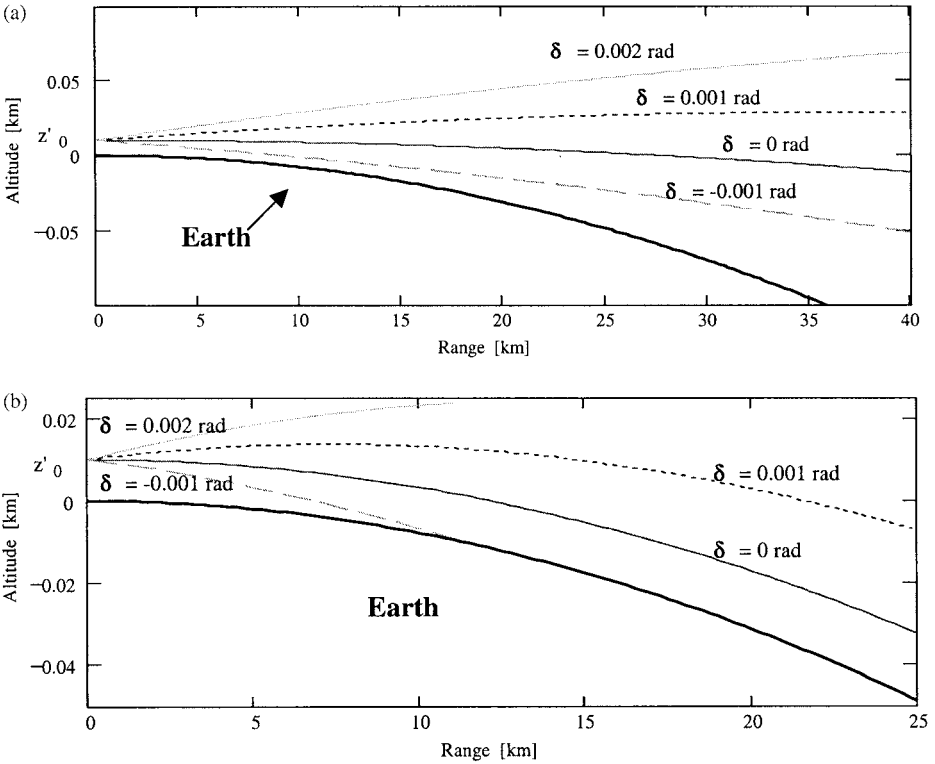
Fig. 7.31 (a) 1976 U.S. Standard Atmosphere $(a = -6.5\text{K/km}, dN/dz' = -26 \text{ km}^{-1})$ and (b) temperature inversion $(a = 90 \text{ K/km}, dN/dz' = -136 \text{ km}^{-1} \lambda = 0.5 \text{ μm and } z_0' = 0.01 \text{ km})$.

This formula can be used to compute the location of the optical horizon, x_{oh}', when $B + 2Cz_0' > 0$. This occurs when $z'(x') = 0$ for the smallest downward-looking angle, δ_{oh}. Solving Eq. 7.53, for an observer located at $x' = 0$ and altitude $z' = z_0'$, we obtain

$$x_{oh}' = \sqrt{\frac{2}{B + 2Cz_0'}}\sqrt{z_0'} = 10^3 \sqrt{\frac{2z_0'}{\left(\frac{dM(z')}{dz'}\right)_{z'=z_0'}}} \qquad (7.54a)$$

where the units are km. The optical horizon angle, δ_{oh}, is

$$\delta_{oh} = -\sqrt{(4Cz_0' + 2B)z_0'} = -10^{-3}\sqrt{2\left(\frac{dM(z')}{dz'}\right)_{z'=z_0'} z_0'}. \qquad (7.54b)$$

For low altitudes, $z_0' \ll 1$ km, $B \gg 2Cz_0'$, and the 1976 U.S. Standard Atmosphere (i.e., $B = 130 \times 10^{-6} \text{ km}^{-1}$), a simple formula for x_{oh}' is obtained:

$$x_{oh}' = 124\sqrt{z_0'} \quad \text{[km]}.$$

This result closely compares to other published formulas for the optical horizon (McCartney, Ref. 7.99). Thus, an observer at altitude, z_0' can see beyond the geometrical horizon ($x_{gh}' = (2r_e)^{1/2}z_0'^{1/2} = 113z_0'^{1/2}$ km). How far beyond the geometrical horizon depends on the refractivity gradient, B (for a constant m-gradient profile). In terms of the refraction coefficient, the optical horizon is

$$x_{oh}' = x_{gh}'\sqrt{\frac{1}{Br_e}}. \qquad (7.55)$$

The formula for calculating the optical horizon, x_{oh}', (in nautical miles) given the observer altitude (in units of feet), in a standard atmosphere is given by

$$x_{oh}' = 1.14z_0'^{1/2} \quad [\text{nmi}].$$

The accuracy of Eq. 7.43 depends on deviations of atmospheric density from standard which are almost always present. Temperature inversions are a good example of a common deviation from standard and are illustrated in Fig. 7.31b. This point is discussed further in future sections after the discussion of astronomical refraction.

7.2.4.4 Astronomical Refraction

The prior formulas for terrestrial refraction cannot be applied to long ray paths that propagate completely through the atmosphere and for near-vertical viewing angles. Therefore, for the development of astronomical refraction models, we return to Eq. 7.34, which does not use the approximations that lead to Eq. 7.42 and the modified index.

The boundary condition of Eq. 7.45b can be applied to determine the unknown constant, $const$, in Eq. 7.34. In spherical coordinates, Eq. 7.45b becomes

$$\frac{dx'}{dz'} = \cot\delta = r_e\frac{d\theta(r)}{dr} \quad \text{at} \quad z' = z_0'.$$

The solution of Eq. 7.34, imposing the above conditions, leads to

$$const = n(z_0')(r_e + z_0')\cos\delta.$$

Thus, for an observer at altitude z_0' viewing an astronomical object at an altitude z' above a spherically stratified earth, the refracted path zenith angle for $\delta \geq 0$ is

$$\theta(z',\delta) = \int_{z_0'}^{z'} \frac{d''z}{(r_e + z'')\sqrt{\frac{[n(z'')(r_e+z'')]^2}{[n(z_0')(r_e+z_0')]^2}\sec^2\delta - 1}}. \qquad (7.56a)$$

The above equation has been applied by astronomers and navigators for many years to correct for atmospheric refraction. An approximate solution has been obtained by Garfinkel (Ref. 7.102) for a standard atmosphere. For general index of refraction

vertical profiles, numerical techniques to obtain the refracted path are necessary. A simple variable substitution leads to the following equivalent form for Eq. 7.56a:

$$\theta(Z(z',\delta),\delta) = \int_{Z(z',\delta)}^{\cos\delta} \frac{1}{\sqrt{1 - Z'(z'',\delta)^2}} \frac{dZ'}{\frac{dn[Z'(z'',\delta)]}{dz''} \frac{C(\delta)}{Z'(z'',\delta)} + 1}, \qquad (7.56b)$$

where the following substitutions have been made:

$$C(\delta) = \frac{n(z_0')(r_e + z_0')}{\sec\delta}, \quad Z(z',\delta) = \frac{n(z_0')(r_e + z_0')}{n(z')(r_e + z')}\cos\delta, \quad \text{and}$$

$$Z'(z'',\delta) = \frac{n(z_0')(r_e + z_0')}{n(z'')(r_e + z'')}\cos\delta.$$

The above integral can be solved exactly when the index of refraction is constant. This is essentially true above the atmosphere of the earth ($n \propto 1$). Within the atmosphere a numerical approach is needed. A reasonably efficient numerical approach is to apply Gauss–Chebyshev quadrature to the above integral. The implementation of a 200-term Gauss–Chebyshev quadrature from z_0' to $(z_1' =)$ 100 km and the exact solution for constant index from 100 km to z' leads to the following approximate form:

$$\theta(z',\delta) = \sum_{i=1}^{200} \frac{\pi f(Z_i'(z_1',\delta),\delta)}{200} + \sin^{-1}\left(\frac{r_e + z_0'}{r_e + z_1'} n(z_0')\cos\delta\right)$$

$$- \sin^{-1}\left(\frac{r_e + z_1'}{r_e + z'}\cos\delta\right), \qquad (7.56c)$$

where the first argument of $f()$ is defined as

$$Z_i'(z_1',\delta) = \frac{\cos\delta + Z(z_1',\delta)}{2} + \frac{\cos\delta - Z(z_1',\delta)}{2}\cos\left(\frac{2i-1}{400}\pi\right)$$

and the function is

$$f(Z_i',\delta) = \frac{\sqrt{[Z_i' - Z(z_1',\delta)](\cos\delta - Z_i')}}{\sqrt{1 - Z_i'^2}} \frac{1}{\left(\frac{dn[z''(Z')]}{dz''}\right)_{Z_i'} \frac{C(\delta)}{Z_i'} + 1}.$$

Of particular interest is the computation of the deviation angle, δ_{dev}, as a function of the inclination angle (or elevation angle $= \pi/2 - \delta_{dev}$), as defined in Fig. 7.32. The unrefracted ray path can be determined exactly from Eq. 7.56 for n constant. The result is

$$\theta_{unrefr}(z',\delta) = \sin^{-1}(\cos\delta) - \sin^{-1}\left(\frac{r_e + z_0'}{r_e + z'}\cos\delta\right).$$
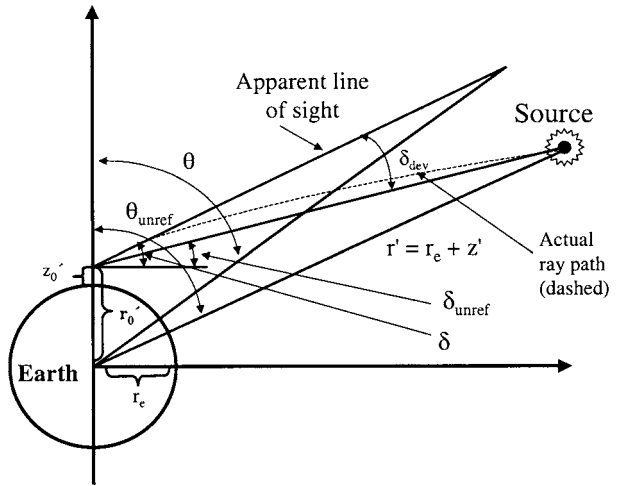
Fig. 7.32 Illustration of the angle of deviation.

The difference between the unrefracted and refracted inclination angles is the deviation angle, $\delta_{dev}(z'_0, \delta)$. It is given in terms of the refracted and unrefracted zenith angles by

$$\delta_{dev}(z'_0, \delta) = \theta_{unrefr}(z', \delta) - \theta(z', \delta) + \frac{r_e + z'_0}{r_e + z'}(\sin\theta_{unrefr} - \sin\theta). \qquad (7.57)$$

This result is checked by computing the angular deviation of an astronomical object observed through the 1976 U.S. Standard Atmosphere. Table 7.17 lists the results based on prior data and this approach. The temperature profile as given by Fig. 7.5 is that of the Standard Atmosphere and is used in conjunction with Eq. 7.31c to provide a model of the vertical refractivity. Using this profile, Eq. 7.57 reproduces the results of Table 7.17.

It is interesting to note that the angular extent of the sun is 32 arc-min and the maximum deviation or refraction correction angle for a standard atmosphere is 34.5 arc-min, thus even though the setting sun is below the geometrical horizon it can still be observed. Note also from Table 7.17 that the refraction correction angle varies across the angular extent of the sun near the horizon and thus the sun appears more flattened at the bottom than at the top. This point is illustrated in Fig. 7.33, which shows a photograph of the setting sun and the corresponding computed shape based on the above model. The photo was taken during the summer at an elevation on approximately 130 m. The temperature at the observer was 31°C. Typical variations in atmospheric index of refraction cause an uncertainty in refraction correction angles listed in Table 7.17 with an RMS deviation of 0.16 arc-sec (Schaefer and Liller, Ref. 7.103). Also, the Standard Atmosphere refractivity profile seldom occurs in the lower troposphere and significant differences from the standard deviation angle do occur. Commonly observed mirage effects testify to variability of atmospheric conditions.

Also, dispersion of the refractive index causes the refraction correction angle to vary slightly for different frequencies (colors). Thus, the setting sun disappears one color at a time, red first, blue last. This refractive condition explains the observance of the "green spot" (Aden and Meinel, Ref. 7.100) at sunset when the horizon is exceptionally clear in a standard atmosphere. The popular but rarely observed "green flash" requires
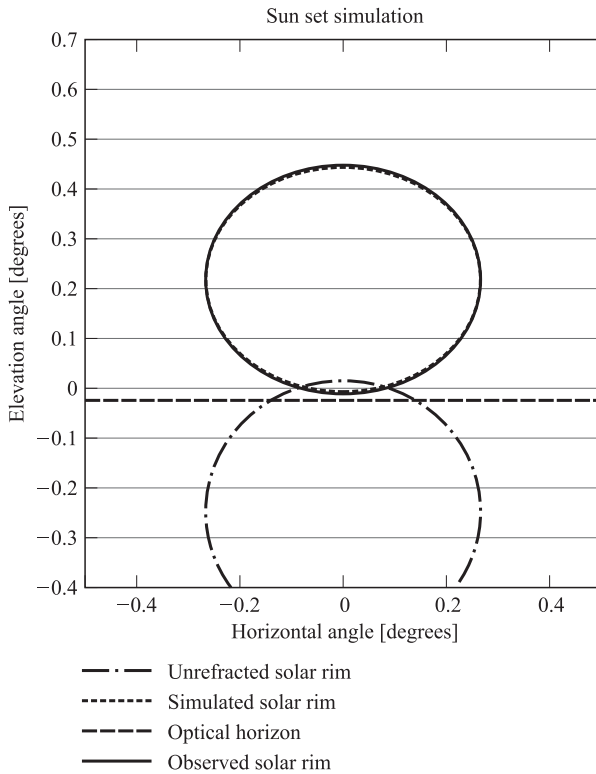
Fig. 7.33 The flattening of the setting sun just above the the horizon, an example of astronomical refraction.

Table 7.17 Sea-level Refraction Correction Angles for Elevation Angles of Astronomical Lines of Sight Through a Standard Atmosphere

Observed Altitude [deg min]	Refraction Correction [min]	Observed Altitude [deg]	Refraction Correction [min]
0 00	34.5	11	4.9
15	31.4	12	4.5
30	28.7	13	4.1
45	26.4	14	3.8
1 00	24.3	15	3.6
15	22.5	16	3.3
30	20.9	17	3.1
45	19.5	18	2.9
2 00	18.3	19	2.8
15	17.2	20	2.6
30	16.1	25	2.1
45	15.2	30	1.7
3 00	14.4	35	1.4
4 30	10.7	50	0.8
5	9.9	55	0.7
6	8.5	60	0.6
7	7.4	65	0.5
8	6.6	70	0.4
9	5.9	80	0.2
10	5.3	90	0.0

ducting phenomena (Ref. 7.100) and this situation is presented in the last section.) Dispersion effects can also be computed using Eqs. 7.55 and 7.56 by including the frequency dependence of the index of refraction. For example, Greenler's book contains a photo of Venus near the horizon (Ref. 7.101). The color separation of the image is distinct and estimated to be 0.006° degrees from red to green. This value is consistent with the computed angle, based on the above model, for the 1976 U.S. Standard Atmosphere.

7.2.4.5 Subrefractive, Superrefractive, and Trapping Effects

As mentioned previously, the standard refractive profile of the atmosphere hardly ever exists, and corrections to this special case must be made if high accuracy is required. Either the atmospheric index of refraction increases less rapidly (or even decreases) with altitude than standard, which produces subrefractive conditions, or the atmospheric index increases more rapidly with altitude, which produces superrefractive conditions. Such conditions produce non normal images or mirages. Subrefractive effects are termed inferior mirages and superrefractive effects are also called superior mirages (Ref. 7.101). Because these are nonstandard processes, detailed knowledge of the temperature and pressure as a function of position are required to calculate such effects along an optical path. Subrefractive effects typically occur over a hot surface such as a road in the summer time. An apparent reflective surface is observed because the rays are bent upward, toward the cooler, denser air. Superrefractive effects typically occur over cold surfaces, such as snow or ice. A good example is the fata morgana, which can produce amplified images of rough snow and make them appear as pillars or walls

Table 7.18 Refractivity Gradients for Different Refractive Conditions

Refractivity Gradient [km^{-1}]	Modified Refractivity Gradient [km^{-1}]	Category
$dN/dz > 0$	$dM/dz > 157$	Subrefractive
$0 > dN/dz > -79$	$157 > dM/dz > 78$	Standard
$-79 > dN/dz$	$78 > dM/dz$	Superrefractive
$dN/dz = -157$	$dM/dz = 0$	Trapping

on the horizon (Ref. 7.101). Figure 7.31b illustrates the ray path for superrefractive condition. Trapping is a special case of superrefraction and exists when the refractivity gradient matches $-1/r_e$. The modified index is zero and the ray path matches the curvature of the earth. Based on Eq. 7.54a, the optical horizon goes to infinity when trapping occurs. This situation frequently occurs in the arctic region, when the earth appears abnormally flat (Ref. 7.16). It is called the Hillingar effect. Figure 7.34 plots the ray path as a function of range for $dM/dz' = 0$.
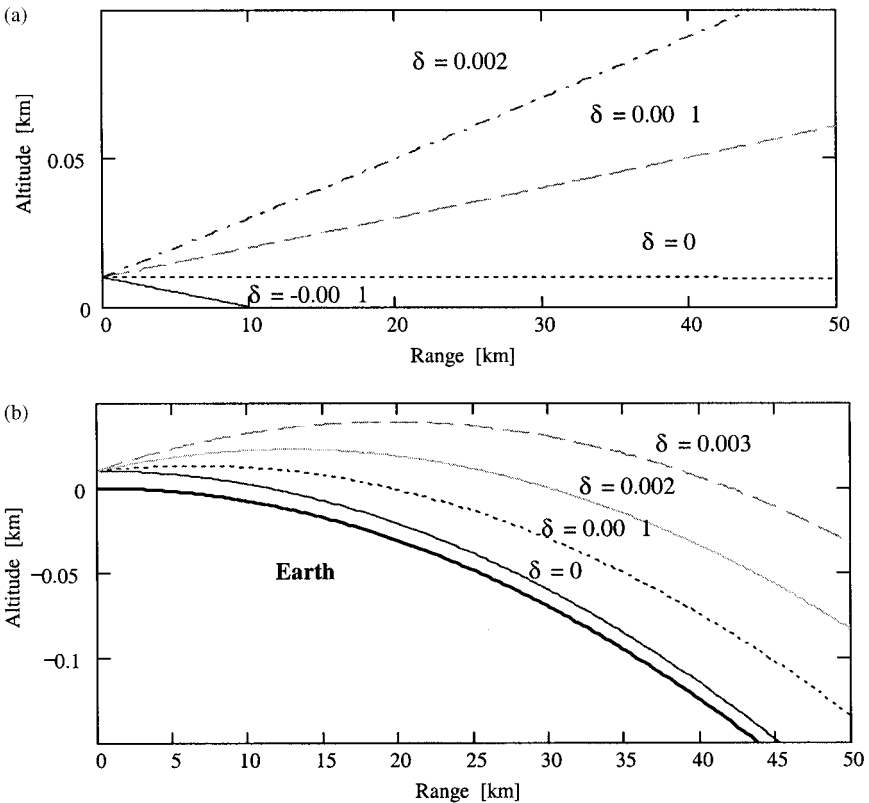
Fig. 7.34 The atmospheric ray path for green light in a trapping environment: (a) flat earth geometry and (b) spherical earth geometry.
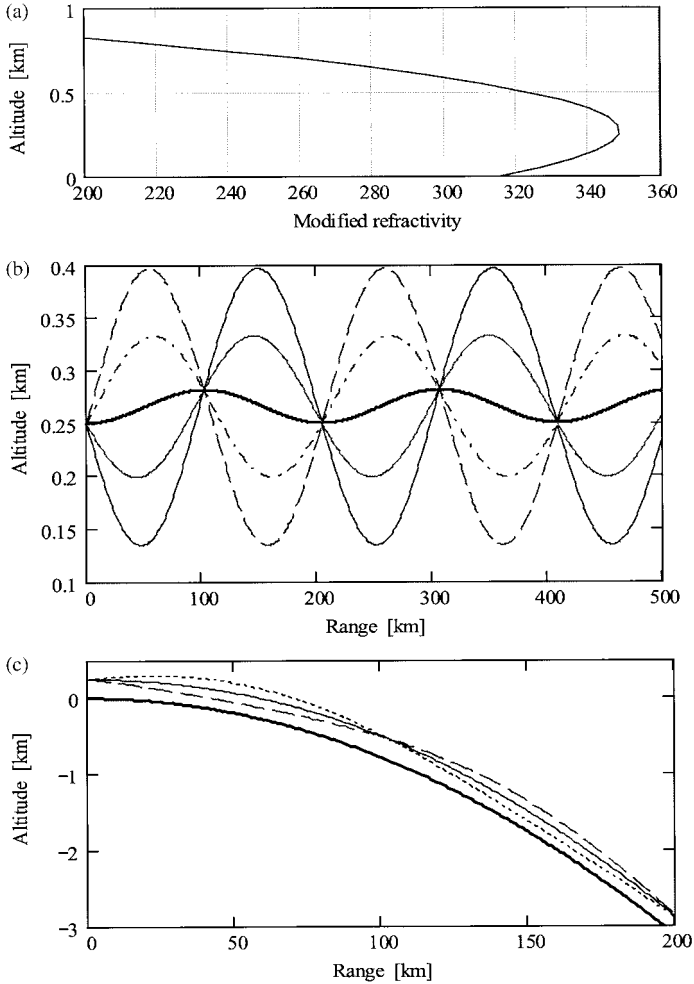
Fig. 7.35 Ray path in a ducting atmosphere for an observer at 0.25 km and frequency of 20,000 wave numbers. (a) Modified refractivity profile as a function of altitude. (b) The ray path in a flat earth geometry for viewing angles of $\delta = -0.004$ (solid black), -0.002 (solid gray), 0 (solid heavy black), 0.002 (dash–dot), and 0.004 (dash) radians. (c) The ray path in a spherical earth geometry for $\delta = -0.004$, 0, and 0.004 radians (bottom curve = surface of the earth). All distances are in km.

The different refractive conditions of the atmosphere are commonly categorized according to ranges of vertical refractivity or vertical modified refractivity gradient. They are listed in Table 7.18 lists them below. This categorization is useful but not complete, since higher order derivatives are not considered. Higher order derivatives are needed to describe ducting phenomena.

7.2.4.6 Ducting Effects

A duct is an atmospheric dielectric waveguide that limits electromagnetic ray propagation to one-dimensional (horizontal) spreading, maintaining intensity for long distances.

This condition requires a layered atmosphere with a high-index layer surrounded by low-index layers (this can occur during a temperature inversion). Good visual examples are the rarely observed "green flash," the Novaya Zemlya effect, and the more common serrated edge of the setting sun (Refs. 7.12–7.16).

To understand how ducting may occur, consider Eq. 7.52. When C is negative, the hyperbolic functions become oscillatory. Thus the rays do not diverge, as they normally do, but remain within a fixed altitude range. For example, given $B = 2.2 \times 10^{-4}$ and $C = -3.15 \times 10^{-4}$, an atmospheric waveguide is formed, as illustrated in Fig. 7.35a. This represents a high-density layer above a low-density layer. The resulting ray path is computed based on Eq. 7.52 for flat-earth and curved-earth geometries. The results are plotted in Fig. 7.35. A duct height, z'_{duct}, can be defined, based on Eq. 7.43. A ray cannot propagate above the altitude where $m(z'_{duct}) \approx m(z'_0)$, since δ is kept small. A more useful definition that allow for multiple angles is $m(z'_{duct}) = m(0)$. Thus, in a ducting environment, the maximum altitude (Eq. 7.43) that can be evaluated is z'_{duct}. This point is illustrated in Fig. 7.35a. The duct height is approximately 0.7 km. The ray trace in Fig. 7.35b shows no rays above this height for the range of angles chosen.

7.3 Molecular Scattering

Scattering phenomena dominate in the visible and near-UV, whereas absorption phenomena dominate in the vacuum-UV and -IR. Generally, molecular scatter by atmospheric gases is weak but can dominate over other loss mechanisms in the ultraviolet. Particle scatter is always present, to some degree, in every spectral window.

7.3.1 Molecular Rayleigh Scatter

Based on Sections 7.2.4 and 4.4.1, the scatter coefficient for molecular Rayleigh scatter in a dry atmosphere can be obtained to be (in cm^{-1})

$$\beta_{sca}(v) = \frac{32\pi^3}{3N_A}\eta^2(v)\frac{P_{Dry}}{R_{GC}T}v^4, \qquad (7.58)$$

where R_{GC} is the ideal gas constant, N_A is Avogadro's number ($N_A k_B = R_{GC}$), P_{Dry} is in atm, T is in K and $\eta(v) = (n(v) - 1)R_{GC}T/P_{Dry}(= 6.452 + 3.62 \times 10^{-10}v^2)$. By defining the function $\eta(v)$, the pressure and temperature dependence of the molecular Rayleigh scatter coefficient is explicitly indicated. This result assumes an isotropic polarizability of atmospheric molecules. This is seldom the case, and a depolarization factor δ must be included in the following empirical manner:

$$\beta_{sca}(v) = \frac{32\pi^3}{3N_A}\eta^2(v)\frac{P_{Dry}}{R_{GC}T}v^4\left(\frac{6 + 3\delta}{6 - 7\delta}\right), \qquad (7.59)$$

where $\delta = 0.035$ for air. Figure 7.36 plots the Rayleigh scatter coefficient for sea-level conditions from 1000 cm^{-1} to the air cutoff. Notice the strong attenuation in the UV, thus molecular scatter provides some protection against the UV rays from the sun.
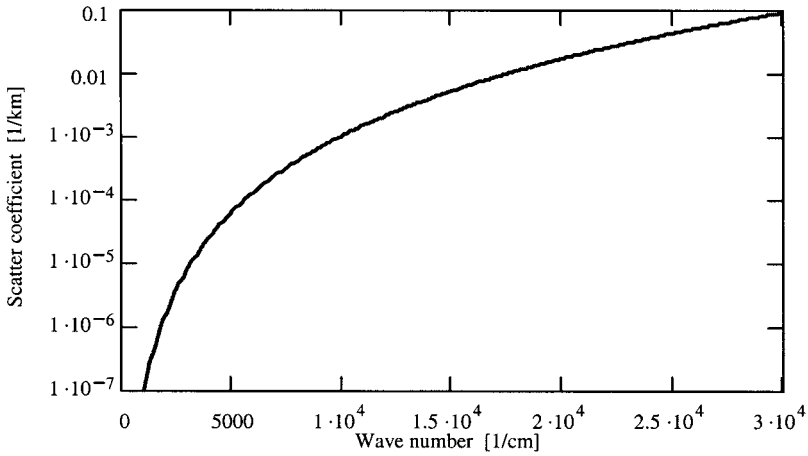
Fig. 7.36 Molecular Rayleigh scatter coefficient for $P_{Dry} = 1$ atm and $T = 288$ K, based on Eq. 7.59.

7.3.2 Blue Sky Background

The blue sky is an example of molecular Rayleigh scatter. To fully appreciate this fact, we must consider the radiant source (the sun), propagation medium (the atmosphere), and detector (the human eye). In Chapter 5, it was suggested that the photosphere of the sun is in thermal equilibrium and radiates like a 5900 K blackbody. Although this is true in the infrared, it is not an accurate representation in the visible and ultraviolet. The real sun features a non-thermal-equilibrium radiation peak in the blue spectral region above the thermal-equilibrium level and is below the thermal-equilibrium level in the ultraviolet, as illustrated in Fig. 7.37a. Using this solar irradiance model and the spectral response function of the eye plotted in Fig. 7.37b with the source-free radiation transfer equation, we obtain yields the observed sky radiance. Thus, using Eqs. 7.59, 4.88, and 2.85, we have the sky radiance as a function of wavelength, zenith angle and altitude:

$$L_{sky}(\lambda,\theta,z) = \int\limits_{z_0}^{z} \beta_{sca}(\lambda, z')\, P_s(\theta)\, M_{solar}(\lambda)\, e^{(\tau_{OD}(\lambda,z'\beta) - \tau_{OD}(\lambda,z,\theta))}\, \frac{d'z}{\cos(\theta)}. \qquad (7.60)$$

For an observer at different altitudes viewing the clear sky at a 45° angle with the sun directly overhead, the sky radiance can be obtained. Figure 7.37b illustrates the results. Note that the observed radiance peaks at 0.49 μm, the color of the blue sky. There is also some minor ozone absorption, which weakly reduces the green and yellow portions of the spectrum and enhances the purity of the blue sky color. The blue sky color is also observed at altitudes of 10 km (typical airplane altitude); however, above 20 km, the darkness of space begins to dominate. More complete models for background radiance are presented in Chapter 11.
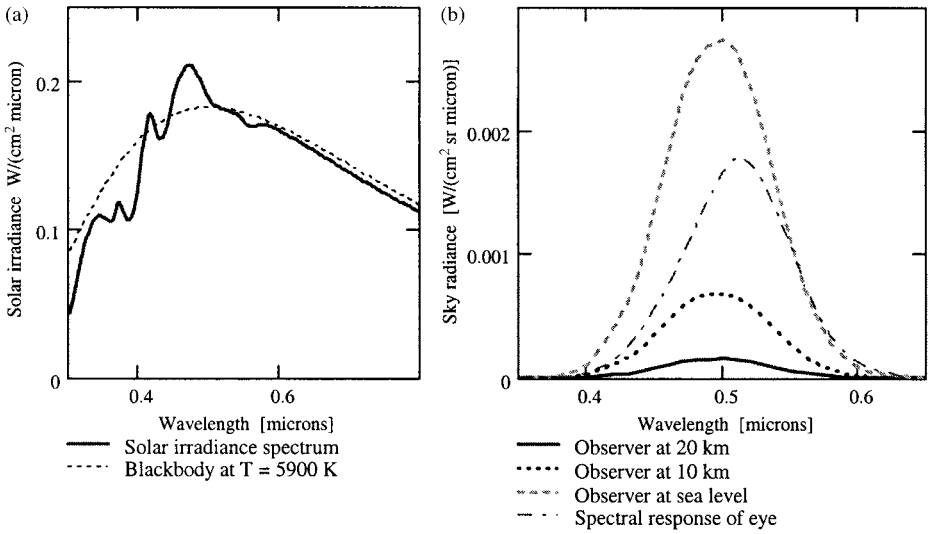
Fig. 7.37 (a) Solar irradiance model compared with a blackbody at 5900 K. (b) Observed sky radiance for a 45° viewing angle and the sun at 0° zenith.

7.4 Applications and Computer Codes

7.4.1 Remote Sensing of Gases

The history of optical remote sensing begins with early astronomy. Knowledge of the sun, moon, and planets was based on remote sensing using visible wavelengths. When spectroscopic techniques were developed, the useful spectrum extended beyond the visible and into the infrared and ultraviolet. Information on temperature, molecular species, and concentration became available. Today, optical remote sensing represents the ability to measure the nature of a medium at a distance in a noninvasive manner. This section is only an introduction to this topic, and coveris a few established techniques (Ref. 7.138 for overview).

7.4.1.1 Boltzmann Thermometer for Gases

This technique is based on the quantum oscillator formula for the absorption coefficient and a medium in rotational and vibrational thermal equilibrium. Consider two absorption lines closely spaced (e.g., within the tuning range of your laser or high-resolution spectrometer) of the same molecular species that originate from transitions between two different vibration–rotation energy levels. A measurement of the line-center transmittance of equal path length is made for each absorption line. The corresponding line-center absorption coefficient ratio of line 1 at ν_{01} to line 2 at ν_{02} is

$$\frac{\ln \tau(\nu_{01})}{\ln \tau(\nu_{02})} = \frac{\beta_{abs1}(\nu_{01})}{\beta_{abs2}(\nu_{02})} = \frac{S_1 g(\nu_{01})}{S_2 g(\nu_{02})}. \tag{7.61}$$

The quantum oscillator formula for the line strength (recall Eq. 5.84) is

$$S(T) = \rho_a \frac{8\pi^3 \nu_0}{3hn} \frac{e^{-E_l/k_B T}}{Q(T)} \tanh\left(\frac{hc\nu_0}{2k_B T}\right) \sum |\mu_{dp}|^2$$

$$= \rho_a S_0'(T_0) \frac{e^{-E_l/k_B T}}{Q(T)} \frac{Q(T_0)}{e^{-E_l/k_B T_0}} \frac{\tanh\left(\frac{hc\nu_0}{2k_B T}\right)}{\tanh\left(\frac{hc\nu_0}{2k_B T_0}\right)}$$

(7.62)

where S_0' is the line strength related to the HITRAN listing (with reference temperature $T_0 = 296$ K). Furthermore, at line center, the line profile function can be simplified to the power spectral density function (i.e., $g(\nu_0) = j(\nu_0)$) and the absorption coefficient ratio becomes

$$\frac{S_{01}'}{S_{02}'} \exp\left((E_{l1} - E_{l2})\frac{T - T_0}{k_B T_0 T}\right) \frac{\left(\frac{\tanh[hc\nu_{01}/(2k_B T)]}{\tanh[hc\nu_{01}/2(k_B T_0)]}\right)}{\left(\frac{\tanh[hc\nu_{02}/(2k_B T)]}{\tanh[hc\nu_{02}/(2k_B T_0)]}\right)} \frac{j(\nu_{02})}{j(\nu_{02})}.$$

(7.63)

Assuming a vibration–rotation band is being used and $\nu_{01} \approx \nu_{02}$, then Eq. 7.61 becomes

$$\frac{\beta_{abs}(\nu_{01}, T)}{\beta_{abs}(\nu_{02}, T)} = \frac{S_{01}'}{S_{02}'} \exp\left((E_{l1} - E_{l2})\frac{T - T_0}{k_B T_0 T}\right) \frac{j(\nu_{01}, T)}{j(\nu_{02}, T)}.$$

(7.64)

Solving the above equation for T, one obtains

$$T = \frac{T_0}{1 - \frac{k_B T_0}{E_{l1} - E_{l2}} \ln\left(\frac{\ln[\tau(\nu_{01})]}{\ln[\tau(\nu_{02})]} \frac{S_{02}'}{S_{01}'} \frac{j(\nu_{02})}{j(\nu_{01})}\right)}.$$

(7.65)

When the line shape is Doppler dominated, the line center result then becomes

$$j_D(\nu_0) = \frac{(\ln 2)^{1/2}}{\gamma_D \sqrt{\pi}},$$

(7.66a)

where the Doppler half-width is given by Eq. 5.173. Since the line-center frequencies are similar, the Doppler half-widths are essentially equal, and it follows that

$$\frac{j_D(\nu_{02})}{j_D(\nu_{01})} = 1.$$

When the line shape is collision broadened, the line-center result is

$$j_c(\nu_0) = \frac{1}{\pi \gamma_c}.$$

(7.66b)

The collision-broadened half-width, γ_c, is a function of the rotational quantum number and does vary from line to line. The degree of variation is not strong but can be important

for lines with considerably different rotational quantum number. The ratio of collision-broadened power spectral density functions is given by

$$\frac{j_c(\nu_{01})}{j_c(\nu_{02})} = \frac{\gamma_{c1}}{\gamma_{c2}}.$$

This approach is independent of the absorber concentration and path length (see Gearhart and Thomas, Ref. 7.109).

7.4.1.2 Lidar Equation

Lidar stands for *light detection and ranging* and is similar in many ways to radar. Lasers are commonly used as sources for lidar systems, and for this reason lidars are also called "ladars" or laser radars. Lidars are configured in a variety of different ways for a variety of different applications covering hard target ranging, atmospheric remote sensing of aerosols, temperature, water vapor, pollutants, wind velocity, and so on.

To understand how lidar works, let us begin with the lidar equation. The received power from a target is proportional to the transmitter power times the transmittance to the target at a distance R, times the back reflectance (or back scatter) within the receiver acceptance solid angle, times the transmittance back to the receiver. An efficiency factor, ξ, is also included to account for loss due to imperfections in the optics. In the form of an equation for the received power (flux), Φ_r [W], this becomes

$$\Phi_r(R) = \Phi_t \tau(R) \Delta\Omega \rho(0,\pi) \tau(R) \xi + \Phi_{background} + \Phi_{detector}, \tag{7.67}$$

where Φ_t is the transmitter power, $\Delta\Omega = A_0/R^2$ is the acceptance solid angle [sr] for a telescope with collector area A_0, R is the range, τ is the transmittance, $\rho(0,0)$ is the BRDF for the case of back-reflectance [sr^{-1}] into the receiver acceptance angle (i.e., $\theta_i = 0$ and $\theta_r = 0$), $\Phi_{background}$ is the background flux, and $\Phi_{detector}$ is the noise-equivalent power for the detector system. Equation 7.67 assumes that the target completely intercepts the illuminating beam. The BRDF is used for hard targets, and the BSDF is used for distributed targets. In the latter case, for a monostatic system, the BSDF is written in terms of the volume back-scatter coefficient. Based on the definition of the BSDF, and in the single-scatter limit, the BSDF can be expressed in terms of the angle-dependent-scatter coefficient,

$$\alpha_{sca}(0,\pi) = \left(\frac{d\beta_{sca}(\theta_s)\Delta R}{2\pi \, \sin\theta_s \, d\theta_s}\right)_{\theta_s=\pi}. \tag{7.68}$$

ΔR is called the range cell and represents the range resolution. The minimum range cell is related to length of the laser pulse. In general, it is related to the laser pulse duration and speed of the receiver. The volume back-scatter coefficient is defined to be

$$\beta_{Vol} = \left(\frac{d\beta_{sca}(\theta_s)}{\sin\theta_s \, d\theta_s}\right)_{\theta_s=\pi}. \tag{7.69}$$

Thus in a similar fashion to Eq. 7.67, the lidar equation applied to media with distributed scatters then becomes

$$\Phi_r(R) = \Phi_t \, \Delta R \beta_{Vol} A_0 \tau^2(R) \xi / (2\pi R^2) + \Phi_{background} + \Phi_{detector} \qquad (7.70)$$

This equation is relevant when molecular, and aerosol (see Chapter 10), back-scatter are used to obtain a return signal. Such a lidar can be used to map aerosol and/or molecular density as a function of position. To distinguish between aerosol returns and molecular returns, a multiple-frequency lidar is needed.

Another application of the above equation is to determine the concentration or temperature as a function of position of a molecular species that absorbs in the atmosphere. One common approach is called differential absorption lidar, or DIAL. A DIAL lidar measures the average transmittance, $\langle \tau \rangle$, over a range cell, ΔR, and from this the average line-center absorption coefficient at that location in space can be determined. Two frequencies from the transmitter are used. One is tuned to the line center of an absorption line and the other tuned to a nearby spectral location with no absorption. In this manner, all the parameters in the lidar equation are matched, except the transmittance function. The ratio of the on line return to the off-line return as a function of range becomes

$$\frac{\Phi_{on}(R)}{\Phi_{off}(R)} = \exp\left(-2\int_0^R \left[\beta_{ext}(\nu_{on}, R') - \beta_{ext}(\nu_{off}, R')\right] dR'\right). \qquad (7.71)$$

The transmittance function assumes a narrow-band source (or receiver) so that the absorption feature is fully resolved. The extinction coefficient is the sum of the absorption coefficient and the scatter coefficient in the single-scatter limit. Since the off-line extinction coefficient is due to only scatter loss and the scatter loss is the same for both on- and off-line frequencies, the difference produces the on-line absorption coefficient.

In the lower troposphere, collision broadening dominates the line shape. The formula for the line-center absorption coefficient ($\nu = \nu_0$) for this case, based on Eqs. 7.62 and 7.66b (in km^{-1}), is

$$\beta_{abs}(\nu_0, T, p_a, p_f) = 7.33882 \times 10^{26} \, \frac{p_a}{T} \, S_0 \frac{e^{-E_l/k_B T}}{e^{-E_l/k_B T_0}} \, \frac{Q(T_0)}{Q(T)} \, \frac{1}{\pi \gamma_c(T, p_a, p_f)} \qquad (7.72)$$

where for a binary mixture the half-width is

$$\gamma_c(T, p_a, p_f) = (\gamma_{ca0} p_a + \gamma_{cf0} p_f)\left(\frac{T_0}{T}\right)^n, \qquad (7.73)$$

S_0, γ_{ca0}, γ_{cf0}, E_l, and n come from the HITRAN database. The partial pressures, p_a and p_f, are in atm, and $T_0 = 296$ K. Even though the spectral line parameters listed in the HITRAN database are incomplete and often not of sufficient accuracy to support DIAL measurements, they are sufficiently accurate for line selection, since the line-center frequency, lower energy level, and line strength are all that are needed. The partition function ratio is typically given by

$$\frac{Q(T_0)}{Q(T)} = \left(\frac{T_0}{T}\right)^m, \qquad (7.74)$$

where m is 1 for O_2 and CO_2, and 1.5 for H_2O (recall Chapter 5). Substituting for the half-width and partition function into Eq. 7.72, we obtain

$$\beta_{abs}(\nu_0, T, p_a, p_f) = 7.33882 \times 10^{26} \frac{p_a}{T_0} S_0 \frac{e^{-E_l/k_B T}}{e^{-E_l/k_B T_0}} \left(\frac{T_0}{T}\right)^{1+m-n} \frac{1}{\pi(\gamma_{ca0} p_a + \gamma_{cf0} p_f)}.$$

(7.75)

The absorption coefficient can be broken up into two factors; one depends on absorber pressure and the other depends on temperatures. To determine the absorber concentration, it is desired to find a line with little temperature dependence. To determine the temperature requires a gas with a known concentration, such as a uniformly mixed gas. In either case, we wish to invert Eq. 7.75 to obtain the absorption coefficient. The result is

$$\beta_{abs}(p_a, T) = \frac{1}{2} \frac{d}{dR} \ln\left(\frac{\Phi_{off}(R)}{\Phi_{on}(R)}\right).$$

(7.76)

TEMPERATURE SENSITIVITY OF SPECTRAL LINES   To find the sensitivity of the absorption coefficient to temperature, the derivative of the absorption coefficient with respect to temperature is needed. It is given by

$$\frac{d\beta_{abs}(\nu_0, T, p_a, p_f)}{dT} = \frac{7.33882 \times 10^{26} p_a S_0}{T_0 \pi(\gamma_{ca0} p_a + \gamma_{cf0} p_f)} \frac{e^{-E_l/k_B T}}{e^{-E_l/k_B T_0}} \left(\frac{T_0}{T}\right)^{1+m-n} \left[\frac{E_l}{k_B T^2} - \frac{1+m-n}{T}\right].$$

The above equation is plotted in Fig. 7.38 as a function of E_l (in cm^{-1}) for various temperatures for the case of CO_2 ($n = 0.75, m = 1$). Below a certain lower energy level value (determined by $E_l = (1 + m - n)T/1.4398$ cm^{-1} and desired for temperature-insensitive lines), the derivative is negative, and above that value it is positive. Based on this plot, temperature-sensitive lines must have the largest possible value of E_l.

Evaluating the derivative and changing from differential to incremental values, the DIAL signal is obtained to be

$$\beta_{abs}(R) = \frac{1}{2\Delta R} \left(\frac{\Phi_{off}(R + \Delta R)}{\Phi_{off}(R)} - \frac{\Phi_{on}(R + \Delta R)}{\Phi_{on}(R)}\right).$$

(7.77)

ΔR is the range cell, as defined earlier. From this equation, the absorber pressure or local temperature can be determined at $R + \Delta R/2$.

Three-Wavelength DIAL   Greater sensitivity to temperature in the DIAL technique can be obtained if the Boltzmann factor ($\exp[-E_1/(k_B T)]$) in Eq. 7.75 can be isolated from the partition function, density, and half-width power-law temperature dependence. Unfortunately, these factors compete against one another for the net temperature dependence of the absorption coefficient. The Boltzmann factor will dominate if the lower energy level is large enough. To enhance the temperature dependence of the DIAL technique, a ratio of absorption coefficients for two different absorption lines is
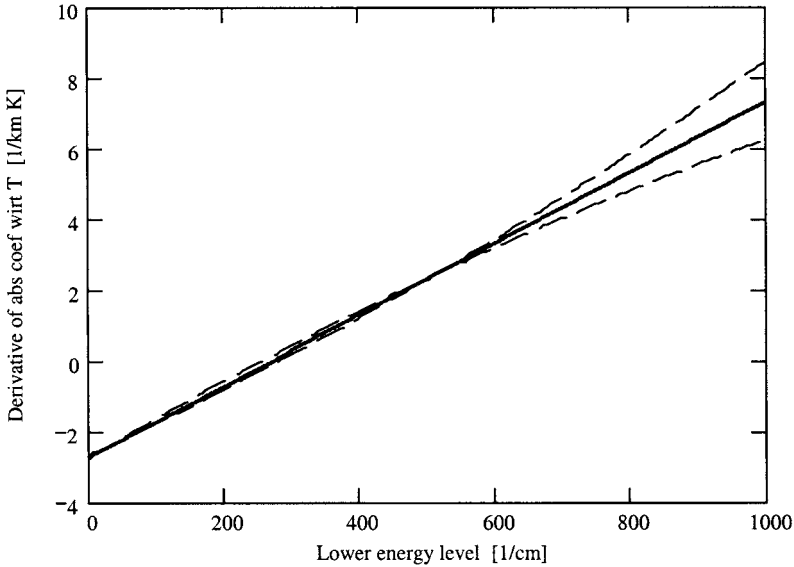
Fig 7.38 Derivative of the line-center absorption coefficient for CO_2 with respect to temperature (times 100) as a function of the lower transition energy for different temperatures. (Dashed curves represent ± 15 K about 295 K solid curve.)

desired. Since the partition function, density, and half-width have the same temperature dependence from line to line, these factors cancel upon ratioing.

To implement this technique in DIAL, the line-center absorption coefficient of two candidate lines must be measured. This requires three laser frequencies (or wavelengths), two matching the line-center frequencies of absorption lines, and the third is off-line for a reference. Based on Eq. 7.75, the ratio of the absorption coefficient for two different lines ($\nu_{01} \approx \nu_{02}$) is

$$\frac{\beta_{abs}(\nu_{01}, T)}{\beta_{abs}(\nu_{02}, T)} = \frac{S_{01}}{S_{02}} \exp\left((E_{l1} - E_{l2})\frac{T - T_0}{k_B T_0 T}\right) \frac{\gamma_{ca02} p_a + \gamma_{cf02} p_f}{\gamma_{ca01} p_a + \gamma_{cf01} p_f}. \qquad (7.78)$$

Solving for T, one obtains a result similar to Eq. 7.65, as given by

$$T = \frac{T_0}{1 - \frac{k_B T_0}{E_{l1} - E_{l2}} \ln(ax)} \qquad (7.79)$$

where

$$x = \frac{\beta_{abs1}}{\beta_{abs2}} \quad \text{and} \quad a = \frac{S_{01}(\gamma_{ca02} p_a + \gamma_{cf02} p_f)}{S_{02}(\gamma_{ca01} p_a + \gamma_{cf01} p_f)}.$$

The subscript "1" pertains to the line at ν_{01} and "2" pertains to the line at ν_{02}. The resulting temperature uncertainty, ΔT, for $\Delta x = 0.02$ is plotted in Fig. 7.39 as a function of x for the short-range (weak) pair of O_2 absorption lines. For typical spring mid-latitude temperatures ($\sim 288K$), $x \approx 5.5$ and $\Delta T \approx 0.2$ K. This represents an improvement by
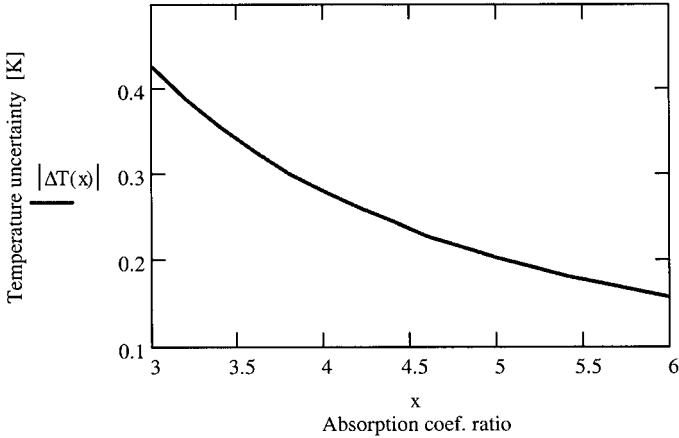
Fig. 7.39 Three-wavelength DIAL temperature uncertainty as a function of the absorption coefficient ratio for the short range O_2 line pair.

a factor of 5 over the two-wavelength DIAL technique. Similar results can be obtained for other gases. The key in this approach is to have the lower energy levels in the lines selected as far apart as possible.

7.4.2 Synthetic Spectra

Another useful application of the quantum oscillator model of the absorption coefficient is the computation of synthetic spectra. This is easily accomplished using the HITRAN database. Assuming no coupling (or line mixing) between absorption lines exists, the net absorption coefficient (in km^{-1}) as a function of frequency is

$$\beta_{abs}(\nu_0, T, p_a, p_f) =$$
$$\sum_i 7.33882 \times 10^{26} \frac{p_a}{T} S_0'i \frac{e^{-E_{li}/(k_B T)}}{e^{-E_{li}/(k_B T_0)}} \frac{Q(T_0)}{Q(T)} g_V(\nu, T, \nu_i, \gamma_{ci}, \gamma_D, p_a, p_f), \qquad (7.80)$$

where, for a binary mixture, the collision half-width is

$$\gamma_c(T, p_a, p_f) = (\gamma_{ca0} p_a + \gamma_{cf0} p_f)\left(\frac{T_0}{T}\right)^n, \qquad (7.81)$$

γ_{ca0i} is the self-broadened half-width, γ_{cf0i} is the foreign broadened half-width, n_i is the temperature exponent for the collision half-width, S_{0i} is the NTP line strength, and E_{li} is the lower energy level of the ith line. These parameters all come from the HITRAN database. The index i represents all lines within the spectral interval of interest. The partial pressures, p_a and p_f, are in atm, and $T_0 = 296$ K. An example of a synthetic spectrum, based on the HITRAN database, is shown in Fig. 3.9.

7.4.3 Human Breath Spectra

Of the infrared active gases, humans exhale carbon dioxide (4% is typical) and water vapor. Carbon dioxide is greatly concentrated over atmospheric levels because of processed oxygen in the lungs. Spectroscopic analysis of breath can be used for biomedical diagnostics.

7.4.4 Computer Codes

Many of the models previously discussed are contained in atmospheric transmission codes, which provide a powerful tool for quantifying atmospheric effects. The most commonly used codes are maintained by Phillips Laboratory at Hanscom Air Force Base, Massachusetts. They are LOWTRAN, MODTRAN, and FASCODE, and are briefly described below. These codes allow for complex atmospheric transmittance and radiance (see Chapter 11) calculations based on absorption and scattering phenomena for a variety of path geometries and atmospheres. LOWTRAN is a low-resolution (20 cm^{-1}) code, MODTRAN is a moderate resolution (2 cm^{-1}) code, and FASCODE is a high-resolution code (specified by user). FASCODE uses the HITRAN database directly, and LOWTRAN and MODTRAN use the HITRAN database indirectly to determine band model spectral parameters. The widespread availability and use of these codes make extensive figures and tables on atmospheric transmittance and radiance calculations of limited value.

7.4.4.1 LOWTRAN and MODTRAN

LOWTRAN is the name of a series of computer codes beginning with LOWTRAN2 (first available in 1972) and ending with the most recent version LOWTRAN7 (first available in 1989) (see Refs. 7.113–7.119). LOWTRAN calculates the transmittance and/or radiance for a specified path through the atmosphere based on the LOWTRAN band model previously discussed, molecular continuum absorption, molecular scattering, rain models, fog models, and aerosol absorption and scattering models. Radiance calculations include atmospheric self-emission, solar and/or lunar radiance single-scattered into the path, direct solar irradiance through a slant path to space, and multiple-scattered solar and/or self-emission of atmospheric radiance into the path. The model covers the spectral range from 0 to 50,000 cm^{-1} at a resolution of 20 cm^{-1}. The band model spectral parameters are tabulated every 5 cm^{-1}.

The atmosphere is represented as 32 layers from 0 to 100 km altitude. Layer thickness varies from 1 km thicknesses up to an altitude of 25 km, 5 km for altitudes from 25 to 50 km (the top of the stratosphere), and the last two layers are 20 and 30 km thick, respectively. Detailed structure just above the land or sea is not represented by this model, and thus model predictions can be inaccurate if nonstandard conditions exist (see Section 7.1). Attenuation and refractive effects are calculated for each layer and summed along the path. The physical characteristics of each layer are determined by inputs and predetermined standard models (see Table 7.19 for possible inputs into LOWTRAN 6) of various regions, path geometries, and seasons. The option for a user-defined atmosphere based on meteorological data also exists. The atmosphere is assumed to be in thermal equilibrium, thus the code should not be used above 100 km (thus the model is valid below the ionosphere).
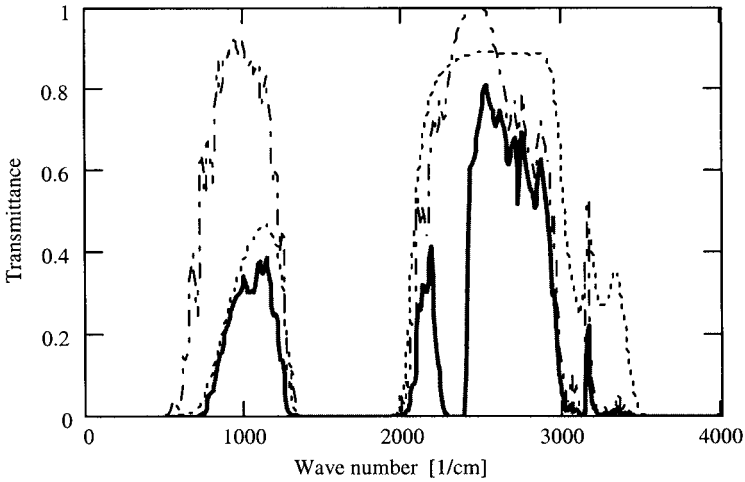
Fig. 7.40 LOWTRAN calculation of the 10 and 4 μm window regions for the mid-latitude summer model and horizontal sea-level path of 5 km. The solid curve represents the total transmittance, the dot–dash curve the water vapor local line contributions, and the dotted curve the water vapor continuum.

Figures 7.40 through 7.42 illustrate typical LOWTRAN outputs for various types of atmospheres, spectral regions, mechanisms of attenuation, path emission, and path geometries. Figure 7.40 illustrates the transmittance in the infrared, showing the windows from 800 to 1200 cm^{-1} and from 2000 to 3000 cm^{-1}. Note that the far-infrared, window is dominated by the water vapor continuum and the other window is dominated by local line absorption. Figure 7.41 displays the transmittance in the near infrared region. It demonstrates the importance of aerosol scattering in a low-altitude marine environment. Figure 7.42 shows the transmittance as a function of wave number in the near-infrared and visible. Note the absence of absorption band loss in the visible and the importance of molecular scatter loss.

LOWTRAN has been successfully validated against field measurements (Devir et al., Refs. 7.120, 7.121) and is widely used for many broad-band system performance studies. However, the single-parameter band model used in LOWTRAN has limited validity concerning temperature dependence. Calculations above and below room temperature should be checked against more physically complete codes such as FASCODE. In particular, LOWTRAN works best at low altitudes with moderate temperatures. High-altitude calculations (>40 km) will have the least accurate results. Because of the limited resolution of LOWTRAN, it should not be applied to laser propagation modeling when local line absorption in important.

MODTRAN is identical to LOWTRAN, except it contains the MODTRAN band model, as previously described in Section 7.2.3.3. Thus, MODTRAN offers moderate resolution (2 cm^{-1}) calculations with improved temperature and pressure dependence over LOWTRAN for non-NTP conditions. Figure 7.43 compares a MODTRAN transmittance spectrum with a LOWTRAN transmittance spectrum and clearly demonstrates the improved representation when resolution is an issue. Furthermore, high-altitude (<60 km)
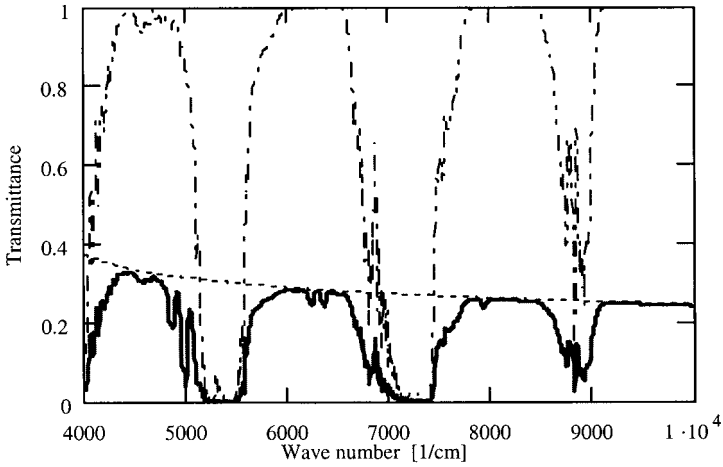
Fig. 7.41 LOWTRAN calculation for the subartic winter model with the navy maritime aerosol model at sea level and a 10 km horizontal path. The solid curve is the total transmittance, the dot–dash curve represents water vapor absorption band contributions, and the dotted curve represents aerosol contributions.

calculations by MODTRAN are more valid than LOWTRAN calculations. In this case, LOWTRAN 7 does not accurately model the radiance at low temperature, producing significant error.

These codes are available from the Geophysics Directorate, Phillips Laboratory, PL/GPOB Hanscom AFB, MA 01731-3010. A PC version with a user-friendly interface is commercially available from ONTAR Corporation (978-681-4585, www.ontar.com).
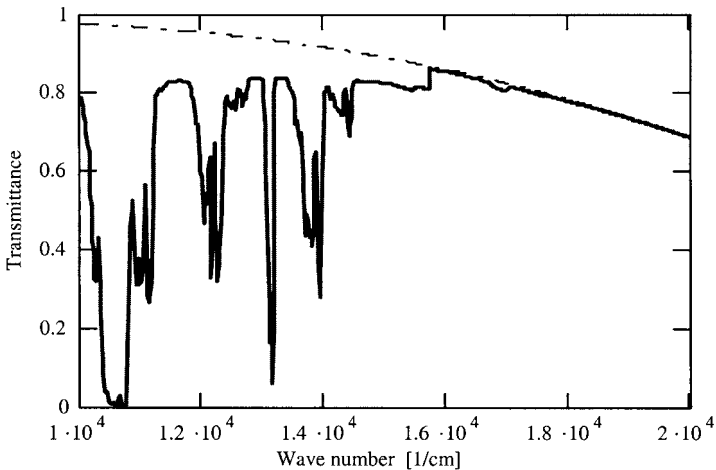
Fig. 7.42 LOWTRAN calculation of the near-IR and visible regions for the tropical model and a horizontal path at 1 km altitude with a path length of 25 km. The solid curve represents the total transmittance and the dash–dot curve represents molecular scattering.

Table 7.19 LOWTRAN 6 Inputs

Input	Options
Model Atmosphere	Mid-latitude summer model
	Mid-latitude winter
	Tropical
	Subartic summer
	Subartic winter
	Meteorological data input
	1962 Standard Atmosphere
Type of atmospheric path	Slant path to space
	Horizontal path
	Slant path
Mode of execution	Transmittance
	Radiance
	Radiance w/ scattering
	Trans. solar irradiance
Temperature and pressure altitude profile	Mid-latitude summer, etc.
Water vapor altitude profile	Mid-latitude summer, etc.
Ozone altitude profile	Mid-latitude summer, etc.
Radiosonde data are to be input	Yes/no
Suppress profile output	Yes/no
Temp. at boundary	Surface temp.
($0.0 - T$ @ 1st level)	
Surface albedo	$0 - 1$
(0.0 – blackbody)	
Extinction type and default range	Rural – VIS = 23 km
	Rural – VIS = 5 km
	Navy maritime
	Maritime – VIS = 23 km
	Urban – VIS = 5 km
	Tropospheric – VIS = 50 km
	User-defined – VIS = 23 km
	Fog advection – VIS = 0.2 km
	Fog radiation – VIS = 0.5 km
	No aerosol attenuation
Seasonal aerosol profile	Determined by model
	Spring–summer
	Fall–winter
Aerosol profile and extinction type	Background stratospheric
	Moderate/Aged volcanic
	High/fresh volcanic
	High/aged volcanic
	Moderate/fresh volcanic
Air mass character	0
Inclusion of cirrus attenuation	Yes/no
Use of army (VSA) for aerosols	Yes/no
Surface range (0.0 – Default)	—
Current wind speed (m/sec)	—
24 hr average wind speed (m/sec)	—
Rain rate	—
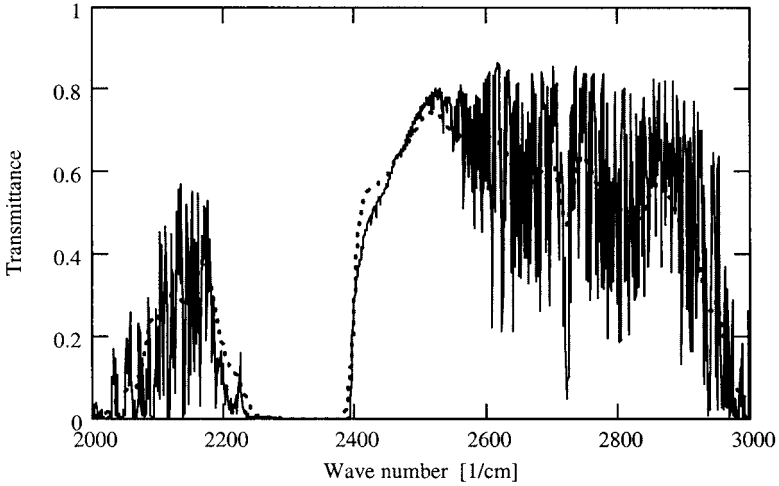
Fig. 7.43 Comparison between a MODTRAN calculation (solid curve) and LOWTRAN calculation (dotted curve) for the same atmospheric conditions and path geometry.

7.4.4.2 FASCODE

FASCODE is a high-resolution line-by-line atmospheric transmission computer code, which uses the HITRAN database (see Section 7.2.2). FASCODE employs a fast algorithm for computing the line shape, which is the basis of the code's name. The Voigt line shape is used for general validity in atmospheric spectra calculations. The code contains the same broad-band models as used in LOWTRAN and MODTRAN for continuum absorption and scattering. It has also been developed by Phillips Laboratory.
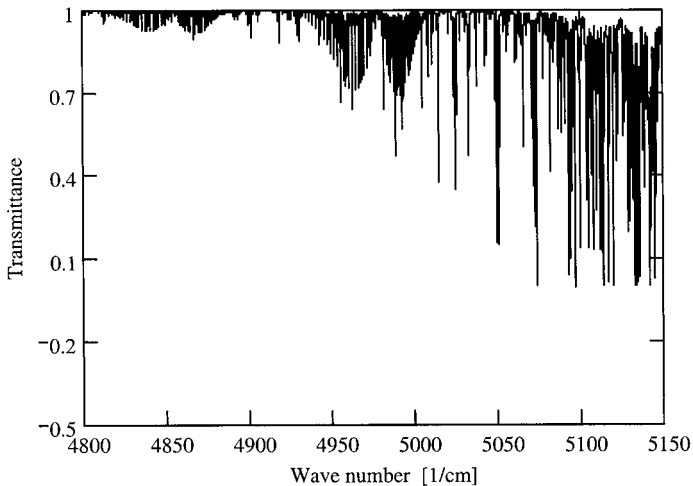
Fig. 7.44 FASCODE calculation for a 100 meter horizontal path in a U.S. Standard Atmosphere in the 2 μm region, showing CO_2 bands centered at 2.01 and 2.06 μm. The other absorption lines are primarily water vapor.

A PC-version is also commercially available from ONTAR corporation. An example output of a high-resolution transmittance spectrum in the 2 μm region is shown in Fig. 7.44. FASCODE is required for laser propagation modeling and other cases requiring high resolution.

This code is available from the Geophysics Directorate, Phillips Laboratory, PL/GPOB Hanscom AFB, MA 01731-3010. A PC version with a user friendly interface is commercially available from ONTAR Corporation (978-681-4585, www.ontar.com).

Problems

7.1 (a) Given that the absorption coefficient, β_{abs}, equals 0.2 km^{-1} at a single laser frequency, calculate the absorptance for a homogeneous 10 km path. (b) The above value of the absorption coefficient is typical of the 10 μm region in the troposphere. How would absorption change in the stratosphere?

7.2 The absorption coefficient in the atmospheric window regions can be expressed by the formula

$$\beta_{abs}(v,T) = \frac{p_a\left[C_s(v,T)p_a + C_F(v,T)p_f\right]}{(R_{GC}T)}.$$

When the partial pressure dependence of β_{abs} is nearly linear or quadratic with respect to p_a, what is the dominant mechanism of absorption for each case? (Recall absorption by water vapor.)

7.3 (a) Explain the nature of the N_2 and O_2 continua. (b) Explain the nature of the water vapor and carbon dioxide continua.

7.4 At what optical wavelengths are atmospheric scattering effects typically dominant and at what wavelengths are atmospheric absorption effects typically dominant?

7.5 In an atmospheric window region, the absorption coefficient of CO_2 is 0.05 km^{-1} at sea level. Compute the vertical transmittance through the atmosphere of the earth. Compute the corresponding slant path transmittance for a path 30° from the vertical. (Assume an isothermal model for the atmosphere.)

7.6 Construct a model of the index of refraction (real part) for a humid atmosphere valid over all optical frequencies based on Eqs. 7.31b, 7.32, and 7.33, and Table 7.5, which contains integrated intensities divided by absorber density, ρ_a:

$$\frac{S_{\text{int}}}{\rho_a} = \int\limits_{Band} \frac{dv\beta_{abs}(v)}{\rho_a} \quad [\text{cm}],$$

and band-center locations of infrared water vapor absorption bands. The Cauchy approximation is adequate for the electronic band contributions, but the Sellmeier model is needed for infrared bands. Can you explain the $1/T^2$ factor in the pure water vapor term for RF refractivity? Are CO_2 vibrational bands important in a model for the atmospheric index of refraction? (Compare your results with Table 7.16.)

7.7 Derive the formulas for the optical horizon distance (Eq. 7.54a) and angle (Eq. 7.54b), beginning with Eq. 7.53. How does the optical horizon vary for the different types of refracting atmospheres as listed in Table 7.18?

7.8 Show that Eq. 7.43a leads to Eq. 7.52 when Eq. 7.44 is used for the modified index of refraction.

7.9 Although lidar is commonly accomplished with lasers, they are not necessary; lidar systems can be realized with incoherent broad-band sources. This changes the analysis to one similar to band model theory. (a) Examine the behavior of Eq. 7.25 when $\alpha_{abs}(\Delta\nu = 1 \text{ cm}^{-1})$ is between 0 and 0.5 ($\psi < 1$ but not necessarily $\ll 1$) as a function γ, w, and S'.

Hint: From Abramowitz and Stegun (eds.) *Handbook of Mathematical Functions*, Dover (1965).

$$I_n(z) = \left(\frac{1}{2}z\right)^n \sum_{k=0}^{\infty} \frac{\left(\frac{1}{4}z^2\right)^k}{k!\,\Gamma(n+k+1)}.$$

(b) Plot your approximate result against the exact solution given by Eq. 7.26 as a function of w for $\gamma = 0.1 \text{ cm}^{-1}$ and $S' = 1 \text{ cm}^{-2}$.

7.10 A UV lidar system for measuring molecular Rayleigh returns is to be designed. The laser is an unpolarized, tripled Nd:YAG operating at 355 nm with a pulse energy of 50 mJ and pulse width, τ_p, of 15 ns. The receiver contains a 12-inch diameter telescope and a photomultiplier tube detector with a noise equivalent power (NEP) of 10^{-15} watts and a bandwidth of 500 MHz. The dominant atmospheric loss mechanism in the near uv is molecular scatter. Assume the system efficiency is 30% and an isothermal atmosphere with a surface temperature 235 K. (a) Use the lidar equation to compute the maximum vertical range for a single shot with a spatial resolution of $\tau_p c/2$ and a minimum signal-to-noise ratio of 10. (b) How would the lidar equation be modified to handle a near-vertical slant path range and near-horizon (horizontal) paths, including atmospheric refraction?

7.11 Differential absorption lidar (DIAL) can be used to measure the number density of an absorbing gaseous species. To do this accurately requires that the absorption feature be temperature independent. Determine an expression, involving the lower energy level of the transition, that minimizes the temperature dependence of the line-center absorption coefficient of a gas in the collision-broadened regime. (Use the quantum oscillator model of Chapter 5.)

7.12 Derive Eq. 7.65. Obtain the line-center line shape ratio within this equation for the Voigt line shape.

7.13 Find the volume back-scatter coefficient for molecular Rayleigh scatter. With this result, obtain the ratio of received power to transmitted power for a molecular back-scatter lidar. What information can be obtained from such a system?

7.14 Derive Eq. 7.79.

7.15 Compute a synthetic spectrum of the absorption coefficient of air-broadened water vapor using the spectral parameters listed in Table P7.15. The temperature

Table P7.15

ν_0 [cm^{-1}]	S_0 [cm]	E_l [cm^{-1}]	γ_{ca0} [cm^{-1}]	γ_{cf0} [cm^{-1}]	n
6677.3296	1.78×10^{-23}	1201.9	0.301	0.068	0.68
6670.4590	7.93×10^{-24}	206.3	0.460	0.098	0.59

is 295 K, the water vapor partial pressure is 10 Torr and the total pressure is one atmosphere. The units of the various spectral parameters are typical of the HITRAN database.

7.16 A CO_2 laser is composed of 80% N_2, 19% He, and 1% CO_2 at a total pressure of 20 Torr at room temperature. The index of refraction at 10 μm of N_2 is 1.00029, He is 1.00003, and CO_2 is 1.00042 at NTP (1 atm and T = 298 K). (a) Find the index of refraction for this laser mixture. (b) The laser mode positions of the resonant cavity containing this gain medium will be shifted as the pressure of the gain medium changes. Find

$$\left(\frac{dn}{dp} \right)_T = ?,$$

where p is the total pressure of the gain medium and T is the temperature. (c) Considering that CO_2 lasers have been constructed with 100 Hz bandwidth and stability, is pressure variation of the index of refraction a significant concern for flowing gas lasers?

Note

1 The basic unit for the absorber amount is g cm^{-2}, or alternatively, molecules cm^{-2}. These units refer to the amount of absorber in a transmission path confined within an imaginary cylindrical volume, one square centimeter in cross-section. Other units are used in the case of water vapor where one considers the resulting depth of water if the vapor in the cylinder were all condensed. The units are "precipitable centimeters," pr cm. In the case of the atmospheric compressible gases, the amount of absorber is treated as if it were compressed within the cylinder until sea-level atmospheric pressure is reached. The length of the resulting gas volume would then be designated "atmospheric centimeters," atm cm.

Bibliography

Section 7.1

7.1 M. Allen, Y.L. Yung, and J.W. Waters, "Vertical Transport and Photochemistry in the Terrestrial Mesosphere and Lower Thermosphere 50–120 km)," *J. Geophys. Res.* **86**, 3617 (1981).

7.2 M. Allen, J.I. Limine, and Y.L. Yung, "The Vertical Distribution of Ozone in the Mesosphere and Lower Thermosphere," *J. Geophys. Res.* **89**, 4841 (1984).

7.3 R.M. Goody and Y.L. Yung, *Atmospheric Radiation Theoretical Basis*, 2nd Ed., Oxford University Press (1989).

7.4 R.B. Bacastow, C.D. Keeling, and T.P. Whorf, "Seasonal Amplitude Increase in the Atmospheric CO_2 Concentration at Mauna Loa, Hawaii, 1959–1982," J. Geophys. Res. **90**, 10529 (1985); *CRC Handbook of Chemistry and Physics*, 72nd Ed., D.R. Lide (ed.), pp. 14–20, CRC Press (1991).

7.5 H.J. Liebe, "A Contribution to Modeling Atmospheric Millimeter-wave Properties," *Frequenz* **41**, 31–36 (1987).

7.6 *CRC Handbook of Chemistry and Physics*, 84th Ed., D.R. Lide (ed.), CRC Press (2003).

Section 7.2.1

7.7 J. H. Shaw, "Solar Radiation," *Ohio J. Sci.* **53**, 258 (1953).

7.8 W.S. Benedict and R.F. Calfee, "Line Parameters for the 1.9 and 7.3 Micron Water Vapor Bands," ESSA Professional Paper 2, U.S. Government Printing Office, Washington, D.C. (Jun. 1987).

7.9 D.M. Gates, R.F. Calfee, D.W. Hansen, and W.S. Benedict, "Line Parameters and Computed Spectra for Water Vapor Bands at 2.7 μm," National Bureau of Standards Monograph 71, U.S. Government Printing Office, Washington, D.C. (1964).

7.10 C. Camy-Peyret and J.M. Flaud, "Line Positions and Intensities in the Band of H_2O," *Mol. Phys.* **32**, 523 (1976).

7.11 R.A. McClatchey, W.S. Benedict, S.A. Clough, D.E. Burch, R.F. Calfee, K. Fox, L.S. Rothman, and J.S. Garing, "AFCRL Atmospheric Absorption Line Parameters Compilation," AFCRL-TR-73-0096, Air Force Cambridge Research Laboratories, Bedford, Mass. (Jan. 1973).

7.12 See Section 7.2.2, reference 7.78.

7.13 See Section 7.1, reference 7.3.

7.14 M.E. Thomas, "Tropospheric Water Vapor Absorption in the Infrared Window Regions," Dissertation, The Ohio State University (Aug. 1979).

7.15 R.K. Long and E.K. Damon, "An Atlas of Pure Water Vapor Spectra from 500 to 5000 cm^{-1} Vol. I and II," Ohio State University/ElectroScience Laboratory, Report No. 713774-3 (Sept. 1984).

7.16 C.P. Rinsland, A. Goldman, M.A.H. Smith, and V. Malathy Devi, "Measurements of Lorentz Air-Broadening Coefficients and Relative Intensities in the $H_2^{16}O$ Pure Rotational and ν_2 Bands from Long Horizontal Path Atmospheric Spectra," *Appl. Opt.* **30**, 1427–1438 (1991).

7.17 W.O. Gallery, J.L. Manning, D.R. Longtin, and L.S. Rothman, "Revised Water Vapor Line Parameters in the 1.0 to 1.1 micrometer Region," *Propagation Engineering: Third in a Series, SPIE* **1312** (1990).

7.18 R.M. Sova, M.E. Thomas, D. Tobin, D. Byrum, and L.L. Strow, "Characterization of Candidate DIAL Lidar Water Vapor and Carbon Dioxide Absorption Lines in the Two Micron Region," *SPIE Proceedings – Optical Instrumentation for Regional and Global Atmospheric Studies* **2365** (Nov. 1994).

7.19 W.M. Elsasser, *Heat Transfer by Infrared Radiation in the Atmosphere*, Harvard University Press (1942).

7.20 H.W. Yates and J.H. Taylor, "Infrared Transmission of the Atmosphere," NRL Report 5453 (1960).

7.21 A. Adel, *Astrophys. J.* **89**, 1 (1939).

7.22 R. Anthony, "Atmospheric Absorption of Solar Infrared Radiation," *Phys. Rev.* **85**, 674 (1952).

7.23 W.T. Roach and R.W. Goody, "Absorption and Emission in the Atmospheric Window from 770 to 1250 cm^{-1}," *Q. J. R. Meteorol. Soc.* **84**, 319 (1958).

7.24 K. Bignell, F. Saiedy, and P.A. Sheppard, "On the Atmospheric Infrared Continuum," *J. Opt. Soc. Am.* **53**, 466 (1963).

7.25 K. Bignell, "The Water-vapour Infrared Continuum," *Q. J. R. Meteorol. Soc.* **96**, 390 (1970).

7.26 M.F. Crawford, H.L. Welsh, and J.L. Locke, "Infra-red Absorption of Oxygen and Nitrogen Induced by Intermolecular Forces," *Phys. Rev.* **75**, 1607 (1949).

7.27 J. Susskind and J.E. Searl, "Atmospheric Absorption near 2400 cm1," *J. Quant. Spectrosc. Radiat. Transfer* **18**, 581 (1977).

7.28 B. H. Winters, S. Silverman, and W.S. Benedict, "Line Shape in the Wing Beyond the Band Head of the 4.3μ Band of CO_2," *J. Quant. Spec. Rad. Trans.* **4**, 527 (1964).

7.29 J. Hinderling, M.W. Sigrist, and F.K. Kneubuhl, "Laser Photoacoustic Spectroscopy of Water-Vapor Continuum and Line-Absorption in the 8- to 14-μm Atmospheric Window," *Infrared Phys.* **27**, 63 (1987).

7.30 W.B. Grant, "A Critical Review of Measurements of Water Vapor Absorption in the 840 to 1100 cm^{-1} Spectral Region," *Appl. Opt.* **29**, 451–462 (1990).

7.31 J.W. Waters, *Methods of Experimental Physics, Volume 12 Part B, Astrophysics Radio Telescopes*, M.L. Meeks (ed.), Academic Press (1976).

7.32 N.E. Gaut and E.C. Reifenstein III, Environmental Research and Technical Report, No. 13, Lexington, Mass. (1971).

7.33 G.E. Becker and S.H. Autler, "Water Vapor Absorption of Electromagnetic Radiation in the Centimeter Wavelength Range," *Phys. Rev.* **70**, 300 (1946).

7.34 L. Frenkel and D. Woods, "The Microwave Absorption by H_2O Vapor and Its Mixtures with Other Gases Between 100 and 300 GHz," *Proc. IEEE* **54**, 498 (1966).

7.35 D.E. Burch, "Absorption of Infrared Radiant Energy by CO_2 and H_2O. III. Absorption by H_2O Between 0.5 and 36 cm^{-1} (278μ–2 cm)," *J. Opt. Soc. Am.* **58**, 1383 (1968).

7.36 H.J. Liebe, "A Contribution to Modeling Atmospheric Millimeter-Wave Properties," *Frequenz* **41**, 31 (1987).

7.37 H.J. Liebe and D.H. Layton, "Experimental and Analytical Aspects of Atmospheric EHF Refractivity," in *Proc. URSI Commission F 1983 Symposium*, Louvain, Belgium (Jun. 1983).

7.38 H.J. Liebe, "An Updated Model for Millimeter Wave Propagation in Moist Air," *Radio Sci.* **20**, 1069 (1985).

7.39 M.E. Thomas, "Atmospheric Absorption Model from 0.01 to 10 Wave Numbers," *SPIE Proceedings*, **1312** (April 1990).

7.40 D.T. Llewellyn-Jones, "Laboratory Measurements of Absorption by Water Vapour in the Frequency Range 100 to 1000 GHz," in *Atmospheric Water Vapor*, A. Deepak, T.D. Wilkerson, and L.H. Ruhnke (eds.), Academic Press, New York, p. 255 (1980).

7.41 D.A. Gryvnak and D.E. Burch, "Infrared Absorption by CO_2 and H_2O," Aeronutronic Publication U-6417, Air Force Geophysics Laboratories, Contract F19628-76-C-0302 (May 1978).

7.42 D.E. Burch and R.L. Alt, "Continuum Absorption by H_2O in the 700?1200 cm^{-1} and 2400–2800 cm^{-1} Windows," AFGL-TR84-0128, Ford Aerospace and Communications Corporation, Aeronutronic Division (May 1984).

7.43 J.C. Peterson, M.E. Thomas, R.J. Nordstrom, E.K. Damon, and R.K. Long, "Water Vapor Nitrogen Absorption at CO_2 Laser Frequencies," *Appl. Opt.* **18**, 834 (1979).

7.44 J.S. Ryan, M.U. Hubert, and R.A. Crane, "Water Vapor Absorption at Isotopic CO_2 Laser Wavelengths," *Appl. Opt.* **22**, 711 (1983).

7.45 G.P. Montgomery, Jr., "Temperature Dependence of Infrared Absorption by the Water Vapor Continuum near 1200 cm1," *Appl. Opt.* **17**, 2299 (1979).

7.46 G.L. Loper, M.A. O'Neill, and J.A. Gelbwachs, "Water-Vapor Continuum CO_2 Laser Absorption Spectra Between 27°C and 10°C," *Appl. Opt.* **22**, 3701 (1983).

7.47 J.C. Peterson, "A Study of Water Vapor Absorption at CO_2 Laser Frequencies Using a Differential Spectrophone and White Cell," Dissertation, The Ohio State University (Jun 1978).

7.48 V.N. Aref'ev and V.I. Dianov-Klokov, "Attenuation of 10.6-μm Radiation by Water Vapor and the Role of $(H_2O)2$ Dimers," *Opt. Spectrosc.* **42**, 488 (1977).

7.49 P.S. Varanasi, S. Chou, and S.S. Penner, "Absorption Coefficients for Water Vapor in the 600–1000 cm-1 Region," *J. Quant. Spectrosc. Radiat. Transfer* **8**, 1537 (1968); P. Varanasi and S. Chadamani, "Self- and N_2-Broadened Spectra of Water Vapor Between 7.5 and 14.5 μm," *J. Quant. Spectrosc. Radiat. Transfer* **38**, 407 (1987); and P. Varanasi, "Infrared Absorption by Water Vapor in the Atmosphere," *SPIE Proceedings Modeling of the Atmosphere*, **928** 213 (1988).

7.50 M.E. Thomas, "Infrared and Millimeter-Wavelength Absorption in the Atmospheric Windows by Water Vapor and Nitrogen: Measurements and Models," *Infrared Physics*, **30**, 161 (1990); and M.E. Thomas, "Empirical Water Vapor Continuum Models for Infrared Propagation," *Proceedings of SPIE–Atmospheric Propagation and Remote Sensing IV* **2471** (1995).

7.51 R.J. Nordstrom, M.E. Thomas, J.C. Peterson, E.K. Damon, and R.K. Long, "Effects of Oxygen Addition on Pressure-Broadened Water Vapor Absorption in the 10-μm Region," *Appl. Opt.* **17**, 2724 (1978).

7.52 A.D. Devir, A. Ben-Shalom, E. Trakhovsky, E. Raz, M. Engel, S.G. Lipson, and U.P. Oppenheim, "Experimental Validation of Atmospheric Transmittance Codes," *Proc.*

SPIE, Optical, Infrared, and Millimeter-Wave Propagation Engineering **926,**
W.B. Miller and N.S. Kopeika (eds.), 54 (1988).

7.53 D.E. Burch, "Continuum absorption by H_2O," AFGL-TR-81-0300 (1981) and
"Absorption by H_2O in Narrow Windows Between 3000–4200 cm^{-1}," AFGL-TR-85-
0036 (1985).

7.54 K.O. White, W.R. Watkins, C.W. Bruce, R.E. Meredith, and F.G. Smith, "Water Vapor
Continuum Absorption in the 3.5 to 4.0 μm region," *Appl. Opt.* **17,** 2711 (1978); and
W.R. Watkins, K.O. White, L.R. Bower, and B.Z. Sojka," Pressure Dependence of the
Water Vapor Continuum Absorption in the 3.5 to 4.0 Micrometer Region," U.S. Army
Electronics Research and Development Command, Report No. ASL-TR-0017 (Sept
1978).

7.55 F.S. Mills, "Absorption of Deuterium Fluoride Laser Radiation by the Atmosphere,"
Dissertation, The Ohio State University (Aug 1975).

7.56 W.R. Watkins, R.L. Spellicy, K.O. White, B.Z. Sojka, and L.R. Bower, "Water Vapor
Absorption Coefficients at HF Laser Wavelength (2.64 & 2.93 μm)," *Appl. Opt.* **18,**
1582 (1979).

7.57 T.G. Kyle, D.G. Murcray, F.H. Murcray, and W.J. Williams, "Absorption of Solar
Radiation by Atmospheric Carbon Dioxide," *J. Opt. Soc. Am.* **55,** 1421 (1965).

7.58 C.T. Delaye and M.E. Thomas, "Atmospheric Continuum Absorption Models," *SPIE
Proceedings, Propagation Engineering: Fourth in a Series* **1487,** 291–298 (1991).

7.59 J. Van Kranendonk "Induced Infrared Absorption in Gases: Calculation of the Binary
Absorption Coefficients of Symmetrical Diatomic Molecules," *Physica* **24,** 347 (1958).

7.60 D.T. Sheng and G.E. Ewing, "Collision-Induced Infrared Absorption of Gaseous
Nitrogen at Low Temperatures," *J. Chem. Phys.* **55,** 5425 (1971).

7.61 S.P. Reddy and C.W. Cho, "Induced Infrared Absorption of Nitrogen and
Nitrogen-Foreign Gas Mixtures," *Can. J. Phys.* **43,** 2331 (1965).

7.62 M.M. Shapiro and H.P. Gush, "The Collision-Induced Fundamental and First Overtone
Bands of Oxygen and Nitrogen," *Can. J. Phys.* **44,** 949 (1966).

7.63 N.I. Moskalenko, Yu.A. Ilin, S.N. Parzhin, and L.V. Rodionov, "Pressure-Induced IR
Radiation Absorption in Atmospheres," *Izv. Atmos. Ocean Phys.* **15,** 632 (1979).

7.64 S.F. Fulghum and M. M. Tilleman, "Interferometric Calorimeter for the Measurement
of Water-Vapor Absorption," *J. Opt. Soc. Am. B* **8,** 2401 (1991).

7.65 See references 5.22–5.27 in Chapter 5.

7.66 S.A. Clough, F.X. Kneizys, R. Davies, R. Gamache, and R.H. Tipping, "Theoretical
Line Shape for H_2O vapor; Application to the Continuum," in *Atmospheric Water
Vapor*, A. Deepak, T.D. Wilkerson, and L.H. Ruhnke (Eds.), Academic Press, p. 25
(1980).

7.67 S.A. Clough, F.X. Kneizys and R. Davies, "Line Shape and Water Vapor Continuum,"
Atmospheric Research **23,** 229–241 (1989).

7.68 V.E. Zuev and V.V. Fomin, "Consideration of Continuum Absorption in the Problems
of Sounding from Outer Space," Presented at *Symposium on Remote Sensing of the
Atmosphere from Space*, Innsbruck, Austria (Jun. 1978).

7.69 E. Hudis, Y. Ben-Aryeh, Y.P. Oppenheim, " Third Order Linear Absorption by Pairs of
Molecules," *Phys. Rev.* **A43,** 3631–3639 (1991).

7.70 S.S. Penner, "Effect of Dimerization on the Transmission of Water Vapor in the Near-
infrared," *J. Quant. Spectrosc. Radiat. Transfer* **13,** 383 (1973).

7.71 R.A. Bohlander, R.J. Emery, D.T. Llewellyn-Jones, G.G. Gimmestad, H.A. Gebbie,
O.A. Simpson, J.J. Gallagher, and S. Perkowitz, "Excess Absorption by Water Vapor
and Comparison with Theoretical Dimer Absorption," in *Atmospheric Water Vapor*, A.
Deepak, T D. Wilkerson, and L.H. Ruhnke (eds.), Academic Press, p. 241 (1980).

7.72 M.E. Thomas and R.J. Nordstrom, "The N_2-Broadened Water Vapor Absorption Line
Shape and Infrared Continuum Absorption I. Theoretical Development," *J. Quant.
Spectrosc. Radiat. Transfer* **28,** 81(1982); M.E. Thomas and R.J. Nordstrom, "The
N2-Broadened Water Vapor Absorption Line Shape and Infrared Continuum
Absorption II. Implementation of the Line Shape," *J. Quant. Spectrosc. Radiat.
Transfer* **28,** 103 (1982); M.E. Thomas and R.J. Nordstrom, "Line Shape Model for
Describing Infrared Absorption by Water Vapor," *Appl. Opt.* **24,** 3526 (1985).

7.73 C.B. Farmer, "Extinction Coefficients and Computed Spectra for the Rotational Band of Water Vapor Between 0.7 and 1000 cm^{-1}," EMI Electronics Ltd., Contract No. KHG5828CB19(d)3 (Apr. 1967).

7.74 P.L. Roney, F. Reid, and J.-M. Theriault, "Transmission Window Near 2400 cm^{-1}: an Experimental and Modeling Study," *Appl. Opt.* **30**, 1995–2004 (1991).

7.75 L.R. Brown, "Methane Line Parameters from 3700 to 4136 cm^{-1}," *Appl. Opt.* **27**, 3275–3279 (1988).

7.76 L.T. Molina and M.J. Molina, "Absolute Absorption Cross Sections of Ozone in the 185- to 350-nm Wavelength Range," *J. Geophys. Res.* **91**, pp. 14501–14508 (1986).

7.77 G. Guelachvili and K.N. Rao, *Handbook of Infrared Standards: With Spectral Maps and Transition Assignments Between 3 and 2600* μm, Academic Press (1986).

Section 7.2.2

7.78 R.A. McClatchey et al., "AFCRL Atmospheric Absorption Line Parameter Compilation," AFCRL Technical Report 0096 (1973); L.S. Rothman and R.A. McClatchey, "Updating of the AFCRL Atmospheric Absorption Line Parameters Compilation," *Appl. Opt.* **15**, 2616 (1976); L.S. Rothman et al., " AFGL Trace Compilation," *Appl. Opt.* **17**, 507 (1978); L.S. Rothman, "Update of the AFGL Atmospheric Absorption Line Parameters Compilation," *Appl. Opt.* **17**, 3517–3518 (1978); L.S. Rothman, "AFGL Atmospheric Absorption Line Parameters Compilation: 1980 Version," *Appl. Opt.* **20**, 791–795 (1981); L.S. Rothman et al., " AFGL Trace Compilation: 1980 Version," *Appl. Opt.* **20**, 1323–1228 (1981); L.S. Rothman et al., "AFGL Atmospheric Absorption Line Parameters Compilation: 1982 Version," *Appl. Opt.* **22**, 2247–2256 (1983); L.S. Rothman et al., " AFGL Trace Compilation: 1982 Version," *Appl. Opt.* **22**, 1616–1627 (1983). L.S. Rothman et al., "The HITRAN database: 1986 Edition," *Appl. Opt.* **26**, 4058–4097, (1987).

7.79 L.S. Rothman, et al., "The HITRAN Molecular Spectroscopic Database and HAWKS (HITRAN Atmopheric Workstation): 1996 Edition," *J. Quant. Spectrosc. Radiat. Transfer* **60**, 665–710 (1998); and L.S. Rothman, et al. "The HITRAN Molecular Database: Editions of 1991 and 1992," *J. Quant. Spectrosc. Radiat. Transfer* **48**, 469–507 (1992).

7.80 L.S. Rothman, "The Spectroscopic Database for High Resolution Atmospheric Modeling," *Modeling of the Atmosphere*, *SPIE* **928**, L.S. Rothman (ed.), pp. 79–93 (1988).

7.81 N. Husson et al., "The GEISA Spectroscopic Line Parameter Data Bank in 1984," *Ann. Geophys.* **4 A2**, 185-190 (1986); N Husson, B. Bonnet, N.A. Scott, and A. Chedin, "Management and Study of Spectroscopic Information: The Geisa Program," *J. Quant. Spectrosc. Radiat. Transfer* **48**, 509–518 (1992). N. Jacquinet-Husson et al., "The 1997 spectroscopic GEISA Databank," *J. Quant. Spectrosc. Radiat. Transfer* **62**, 205-254 (1999).

Section 7.2.3

7.82a A.J. LaRocca, "Atmospheric Absorption," Chapter 5 in *The Infrared Handbook*, W.L. Wolfe and G.J. Zissis (eds.), ERIM (1978).

7.82b H. Mayer, "Methods of Opacity Calculations, V. Effects of Lines on Opacity, Methods for Treating Line Contributions," Report No. AECD-1870, Los Alamos Scientific Laboratory, Los Alamos, CA (1947).

7.82c R.M. Goody, "A Statistical Model for Water-Vapour Absorption," *Q. J. R. Meteorol. Soc.* **58**, 165–169 (1952), Royal Meterological Society, Berkshire, England.

7.83 R. Ladenburg and F. Reiche, "Über Selektive Absorption," in *Annalen dev Physik*, Johann Ambrosius Barth Verlag, Vol. 42 of p. 181 (1913).

7.84 R.A. McClatchey et al., "Optical Properties of the Atmosphere," AFCRL-72-0497, 3rd Ed., Air Force Cambridge Research Laboratories, Bedford, MA (Aug. 1972).

7.85 R.W. Fenn, et al., "Optical and Infrared Properties of the Atmosphere," Chapter 18 in the *Handbook of Geophysics and Space Environment*, A. S. Jeursa (Ed.), Air Force Geophysics Laboratory (1985).

7.86 D.C. Robertson, L.S. Bernstein, R. Haimes, J. Wunderlich, and L. Vega, "5-cm^{-1} Band Model Option to LOWTRAN5," *Appl. Opt.* **20**, 3218–3226 (1981).

7.87 A. Berk, L.S. Bernstein, and D.C. Robertson, "MODTRAN: A Moderate Resolution Model for LOWTRAN7," Report No. GL-TR-89-0122, Geophysics Laboratory Air Force Systems Command, Hanscom AFB, MA (April 1989).

Section 7.2.4

7.88 F. Kasten, "A New Table and Approximation Formula for the Relative Optical Air Mass," *Arch. Meteorol. Geophys. Bioklim.* **14**, 206–223 (1966).

7.89 B. Edlen, "The Refractive Index of Air," *Metrologia* **2**, 71–80 (1966).

7.90 R.W. Fenn et al., see Ref. 7.85.

7.91 L.D. Lorah and E. Rubin, "Aerodynamic Influences on Infrared System Design," Chapter 24th, *The Infrared Handbook*, 2nd Ed., W.L. Wolfe and C.J. Zissis (eds.), ERIM (1985).

7.92 H. Barrell and J.E. Sears, "The Refraction and Dispersion of Air for the Visible Spectrum," *Phil. Trans. Roy. Soc. London* A **238**, 1–64 (1939).

7.93 R.J. Hill and R.S. Lawrence, "Refractive Index of Water Vapor in Infrared Windows," *Infrared Phys.* **26**, 371–376 (1986).

7.94 H.J. Leibe, "An Updated Model for Millimeter Wave Propagation in Moist Air," *Radio Sci.* **20**, 1069–1089 (1985).

7.95 B.R. Bean and E.J. Dutton, *Radio Meteorology*, Dover (1968).

7.96 H.W. Ko, J.W. Sari, and J.P. Skura, "Anomalous Microwave Propagation Through Atmospheric Ducts," *Johns Hopkins APL Tech. Dig.* **4**, No. 1, 12–26 (1983).

7.97 D.E. Gray (ed.), *American Institute of Physics Handbook*, 3rd Ed., McGraw-Hill, pp. 6–110 (1972).

7.98 C.M. Crain, "The Dielectric Constant of Several Gases at a Wavelength of 3.2 Centimeters," *Phys. Rev.* **74**, 691–693 (1948).

7.99 E.J. McCartney, *Optics of the Atmosphere: Scattering by Molecules and Particles*, Wiley (1976).

7.100 A. Aden and M. Meinel, "At Sunset," *Opt. News*, **14**, No. 11, 6 (1988).

7.101 R. Greenler, *Rainbows, Halos, and Glories*, Cambridge University Press (1980).

7.102 B. Garfinkel, "Astronomical Refraction in a Polytropic Atmosphere," *Astron. J.* **72**, 235–254 (1967).

7.103 B.E. Schaefer and W. Liller, "Refraction Near the Horizon," *Publ. Astron. Soc. Pacific* **102**, 796–805 (1990).

7.104 D.J.K. O'Connell S.J., "The Green Flash and Other Low Sun Phenomena," North Holland, Vatican Observatory (1958).

7.105 W.H. Lehn, "The Novaya Zemlya Effect: An Artic Mirage," *J. Opt. Soc. Am.* **69**, 776–781 (1979).

7.106 J.E. Freehafer, W.T. Fishback, W.H. Furry, and D.E. Kerr, "Theory of Propagation in a Horizontally Stratified Atmosphere," Chapter 2 in *Propagation of Short Radio Waves*, D.E. Kerr (ed.), Dover (1965).

7.107 W.M. Smart, *Spherical Astronomy*, 6th Ed., Cambridge University Press (1977).

Section 7.3

7.108 P.M. Teillet, "Rayleigh Optical Depth Comparisons from Various Sources," *Appl. Opt.* **29**, 1897–1900 (1990).

Section 7.4.1

7.109 S.A. Gearhart and M.E. Thomas, "Evaluation of a Temperature Remote Sensing Technique," *Appl. Opt.* **27**, 3630–3637 (1988).

7.110 J.E. Kalshoven, Jr., C.L. Korb, G.K. Schwemmer, and M. Dombrowski, "Laser

Remote Sensing of Atmospheric Temperature by Observing Resonant Absorption of Oxygen," *Appl. Opt.* **20,** 1967–1971, (1981).

7.111 T.M. Taczak and D.K. Killinger, "DIAL Measurements of CO_2 Using a Tunable Narrow-Linewidth 2.066 μm Ho,Tm:YLF Laser," presented at *OSA 7th Topical Meeting, Optical Remote Sensing of the Atmosphere*, Salt Lake City, Utah, Feb. 5–9, 1995.

7.112 J.B. Mason, "Lidar Measurement of Temperature: a New Approach," *Appl. Opt.* **14**, 76–78 (1975).

Section 7.4.4

7.113 J.E.A. Selby and R.A. McClatchey, "Atmospheric Transmittance from 0.25–28.5 μm: Computer Code LOWTRAN 2," Air Force Cambridge Research Laboratory, Report AFCRL-72-0745 (Dec. 1972).

7.114 *Ibid*., "Computer Code LOWTRAN 3," AFCRL-75-0255 (Feb 1975).

7.115 *Ibid*., "Computer Code LOWTRAN 3B," AFCRL-TR-76-0258 (Nov 1976).

7.116 J.E.A. Selby, F.X. Kneizys, J.H. Chetwynd, and R.A. McClatchey, "Atmospheric Transmittance/Radiance: Computer Code LOWTRAN 4," AFGL-TR-78-0053 (Feb 1978).

7.117 F.X. Kneizys, E.P. Shettle, W.O. Gallery, J.H. Chetwynd, L.W. Abreu, J.E.A. Selby, R.W. Fenn, and R.A. McClatchey, "Atmospheric Transmittance /Radiance: Computer Code LOWTRAN 5," AFGL-TR-80-0067 (Feb 1980).

7.118 F.X. Kneizys, E.P. Shettle, W.O. Gallery, J.H. Chetwynd, L.W. Abreu, J.E.A. Selby, S.A. Clough, and R.W. Fenn, "Atmospheric Transmittance /Radiance: Computer Code LOWTRAN 6," AFGL-TR-83-0187 (Feb. 1985).

7.119 F.X. Kneizys, E.P. Shettle, L.W. Abreu, G.P. Anderson, J.H. Chetwynd, W.O. Gallery, J.E.A. Selby, and S.A. Clough, "Atmospheric Transmittance /Radiance: The LOW-TRAN 7 Model," (in preparation).

7.120 A.D. Devir, A. Ben-Shalom, S.G. Lipson, U.P. Oppenheim, and E. Ribak, "Atmospheric Transmittance Measurements: Comparison with LOWTRAN 6, Report RAA/99-85, Technion-Israel Institute of Technology, Haifa 32000, Israel (1985).

7.121 A.D. Devir, A. Ben-Shalom, E. Trakhovsky, E. Raz, M. Engel, S.G. Lipson, and U.P. Oppenheim, "Experimental Validation of Atmospheric Transmittance Codes," *Proc. SPIE, Optical, Infrared, and Millimeter-Wave Propagation Engineering* **926**, W.B. Miller and N.S. Kopeika (eds.), 54 (1988).

7.122 C.F. Bohren and D.R. Huffman, *Absorption and Scattering of Light by Small Particles*, Wiley-Interscience (1983).

7.123 E.P. Shettle and R.W. Fenn, "Models for the Aerosols of the Lower Atmosphere and the Effects of Humidity Variations on Their Optical Properties," Air Force Geophysics Laboratory Report AFGL-TR-79-0214, Environmental Research Papers, N0676 (Sept 1979).

7.124 S.A. Clough, F.X. Kneizys, L.S. Rothman and W.O. Gallery, "Atmospheric Spectral Transmittance and Radiance: FASCOD1B," *Proceedings of SPIE on Atmospheric Transmission* **277**, 152–166 (1981).

7.125 W.L. Ridgeway, R.A. Moose, and A.C. Cogley, "Atmospheric Transmittance/ Radiance Computer Code FASCOD2," Final Report AFGL-TR-82-0392 (Oct 1982).

Additional Bibliography

7.126 E.J. McCartney, *Optics of the Atmosphere: Scattering by Molecules and Particles*, Wiley (1976).

7.127 E.J. McCartney, *Absorption and Emission by Atmospheric Gases: The Physical Processes*, Wiley (1983).

7.128 A. Deepak, T.D. Wilkerson, and L.H. Ruhnke (eds.), *Atmospheric Water Vapor*, Academic Press (1980).

7.129 A.J. LaRocca, "Atmospheric Absorption," Chapter 5, *The Infrared Handbook*, 2nd Ed., W. L. Wolfe and G. J. Zissis (eds.), ERIM (1985).

7.130 V.E. Zuev, *Laser Beams in the Atmosphere*, Plenum Press (1982).

7.131 V.E. Zuev, *Propagation of Visible and Infrared Radiation in the Atmosphere*, Wiley (1974).

7.132 R.M. Goody and Y.L. Yung, *Atmospheric Radiation Theoretical Basis*, 2nd Ed., Oxford University Press (1989).

7.133 W.B. Grant (ed.), *Ozone Measuring Instruments for the Stratophere*, Optical Society of America (1989).

7.134 J.-M. Flaud, C. Camy-Peyret, C.P. Rinsland, M.A.H. Smith, and V. Malathy Devi, *Atlas of Ozone Spectral Parameters from the Microwave to Medium Infrared*, Academic Press (1990).

7.135 R.D. Bojkov and P. Fabian (eds.), *Ozone in the Atmosphere*, A. Deepak (1989).

7.136 T.G. Kyle, *Atmospheric Transmission, Emission and Scattering*, Pergamon Press (1991).

7.137 M.E. Thomas and D.D. Duncan, "Atmospheric Transmission," Chapter 1 in *Atmospheric Propagation of Radiation*, F.G. Smith (ed.), Vol. 2 of *The Infrared & Electro-Optical Systems Handbook*, J.S. Accetta and D. Shoemaker (exec. eds), SPIE/ERIM, pp. 1–156 (1993).

7.138 R.M. Measures, *Laser Remote Sensing Fundamentals and Applications,* Wiley-Interscience (1984).

7.139 D.K. Killinger, J.H. Churnside and L.S. Rothman, "Atmospheric Optics," Chapter 44 in *OSA Handbook of Optics*, Vol. I, M.B. Bass (ed. in chief), E.W. Van Stryland, D.R. Williams, and W.L. Wolfe (assoc. eds.) McGraw-Hill (1995).

This page intentionally left blank

8

Optical Propagation
in Solids

This chapter emphasizes the linear optical properties of solids as a function of frequency and temperature. Such information is basic to understanding the performance of optical fibers, lenses, dielectric and metallic mirrors, window materials, thin films, and solid-state photonic devices in general. Optical properties are comprehensively covered in terms of mathematical models of the complex index of refraction based on those discussed in Chapters 4 and 5. Parameters for these models are listed in Appendix 4. A general review of solid-state properties precedes this development because the choice of an optical material requires consideration of thermal, mechanical, chemical, and physical properties as well.

8.1 Solid-State Optics

This section introduces the classification of optical materials and surveys other material properties that must be considered as part of total optical system design involving solid-state optics.

8.1.1 Classification of Materials

Solid-state materials can be classified in several ways. The following are relevant to optical materials.

Three general classes of solids are **insulators**, **semiconductors,** and **metals**. Insulators and semiconductors are used in a variety of ways, such as lenses, windows materials, fibers, and thin films. Semiconductors are used in electrooptic devices and optical detectors.

Metals are used as reflectors and high-pass filters in the ultraviolet. This type of classification is a function of the material's electronic bandgap. Materials with a large room-temperature bandgap ($E_g > 3 \, \text{eV}$) are insulators. Materials with bandgaps between 0 and 3 eV are semiconductors. Metals have no observable bandgap because the conduction and valence bands overlap. Optical properties change drastically from below the bandgap, where the medium is transparent, to above the bandgap, where the medium is highly reflective and opaque. Thus, knowledge of its location is important. Appendix 4 lists the bandgaps of a wide variety of optical materials.

To characterize a medium within the region of transparency requires an understanding of the mechanisms of low-level absorption and scattering. These mechanisms are classified as **intrinsic** or **extrinsic**. Intrinsic properties are the fundamental properties of a perfect material, caused by lattice vibrations, electronic transitions, and so on, of the atoms composing the material. These processes cannot be altered without changing materials. Extrinsic properties are caused by impurities, defects, degree of polish, grain boundaries, and other flaws introduced by the limitations of the manufacturing process. These effects can always be improved by better processing techniques. Extrinsic effects represent the real material properties rather than the ideal or intrinsic properties. The optical properties in transparent regions are often dominated by extrinsic effects. If an undesirable extrinsic spectral feature is found in a material, then a more optimal manufacturing process can be found to reduce the feature to an acceptable level. If, however, the feature is intrinsic, then a new material must be found. A good example is the SiO_2 class of optical fiber in use today. The first fiber had limited transmission range because of extrinsic absorption and scattering. It took many years of development to improve the manufacturing process to produce the nearly intrinsically limited fibers of today. Thus, it is important to distinguish between these two types of material properties.

Another type of important classification is based on the material structure. Optical materials can be **crystalline**, **polycrystalline,** or **amorphous (noncrystalline)**. Single-crystal materials are the most structured and are highly regular from the microscopic to the macroscopic. Good examples are salts, minerals, some ceramics, most semiconductors, and metals. Recall from Chapter 3 that crystalline structures are further divided into **cubic**, **uniaxial**, and **biaxial** subclassifications. Many of the physical properties of crystalline materials vary with direction and are tensor in nature. Polycrystalline materials are formed from hot-pressed crystalline powders, chemical vapor deposition (CVD) and other methods. These materials are easier to make in large sizes and various shapes than crystals. Good examples are optical ceramics (e.g., spinel, yttria and AlON) and CVD materials such as ZnS, ZnSe, and diamond. Because of the random orientation of the powder grains, physical properties of polycrystalline materials are isotropic. Amorphous materials lack long-range order and are typically mechanically weaker, and have more scatter and higher thermal conductivity than the crystalline counter part. However, they are easily manufactured and represent most of the solid-state optical elements in use today. Examples are glasses and plastics. Glasses of high optical quality (low scatter and absorption in the near-IR and visible) are commonly available. The physical properties of amorphous materials are isotropic to first order.

8.1.2 Thermal, Mechanical, and Chemical Properties

It is not enough to know only the optical properties of a material when designing a system. The thermal, mechanical, and chemical properties must also be known to

ensure satisfactory performance. For example, an optical window in a vacuum system must have the strength to withstand atmospheric pressure to avoid catastrophic failure. Also, material properties are interrelated. For example, materials with high strength require light atoms. As we know from Chapter 3, light atoms mean high lattice vibration frequencies and thus limited infrared transparency. For this reason, materials that transmit in the 8–12 μm region are usually not as hard and strong as materials that transmit in the 3–5 μm region. The following introduces various relevant physical and chemical properties.

8.1.2.1 Thermal Properties

Thermal properties of importance to optical design are the melting temperature, phase transition temperatures, ability to store heat (heat capacity or specific heat), thermal expansion, and heat conduction. Specific values of these quantities are found in Table 8.1. A good example is the design of a high-power window for a laser. It is desired that the window does not break and does not distort the transmitted beam. This requires a material with low specific heat, high thermal conductivity, and low thermal expansion. These thermal properties are discussed below.

Heat Capacity   Heat capacity is the change in thermal energy (heat) of a material per unit mass corresponding to a $1°$ change in temperature. Most of the thermal energy is

Table 8.1 Thermal Properties of Selected Optical Materials

Material	Melting Temperature [K]	Specific Heat	T [K]	Thermal Conductivity [W/(mK)]	T [K]	CTE × 10⁶ [K⁻¹]	T [K]
Al_2O_3	2300	0.18	298				
(*o*-ray)				35.1	299	5.6	293
(*e*-ray)				33.0	296	5.0	293
BaF_2	1550			11.7	286	18.4	273–573
BeO	2800	0.26	320	370	300	6.3	293
BP	2270	0.17	298	350	300	3.0	300
C(diamond)	3770	0.12	298	2200	293	1.38	17–300
CaF_2	1630	0.204	273	10	273	24	293–333
GaAs	1240	0.76	273	52	300	5.7	291–560
Ge	1210	0.074	273–373	59	293	6.1	298
KBr	1000	0.104	273	4.8	319	39	273
$MgAl_2O_4$	2320	0.026	441	13.8	308	5.9	313
MgF_2	1528	0.24	298	21	300		
(*o*-ray)						14	310
(*e*-ray)						8.9	310
NaCl	1070	0.20	273	6.5	298	40	273
Si	1690	0.18	298	163	313	3.1	373–473
SiO_2	1740	0.17	273				
(*o*-ray)				10.7	323	8.0	273–353
(*e*-ray)				6.2	323	13.4	273–353
Fused silica	1983	0.18	295	1.4	295	0.5	295
ZnS	2100	0.12	273	27	300	6.7	300
ZnSe	1790	0.081	295	13	300	7.1	300

stored in the acoustic modes, until very high temperatures are reached that can excite the optical modes. Based on the theory of Debye, the heat capacity as a function of temperature is

$$C_V = 9Nk_B \left(\frac{T}{\theta_D}\right)^3 \int_0^{x_D} \frac{x^4 e^x dx}{(e^x - 1)^2},$$ (8.1)

where $x = \hbar\omega/k_B T$, $x_p = \hbar\omega_p/k_B T = \theta_p/T$, θ_D is the Debye temperature, ω_D is the Debye frequency (the maximum fundamental frequency of the lattice), and N is the number of atoms per mole. The heat capacity is illustrated in Fig. 8.1 for a variety of materials as a function of temperature. As the temperature increases above the Debye temperature, the heat capacity approaches a constant value, as given by the law of Dulong and Petit:

$$C_V = 3Nk_B.$$ (8.2)

Specific heat is the heat capacity of a material relative to the heat capacity of water ($C_V = 4.184$ J/(gK) at $14°$C). Specific heat is therefore dimensionless, and values for various materials are listed in Table 8.1.

Coefficient of Thermal Expansion (CTE)   The thermal expansion of a material is related to the degree of anharmonicity and the depth of the potential well binding the molecules together. To see this, consider the mean value of the separation between the atoms, as given by

$$\langle r \rangle = \frac{\int_0^\infty dr\, r e^{-V(r)/k_B T}}{\int_0^\infty dr\, e^{-V(r)/k_B T}}.$$ (8.3)
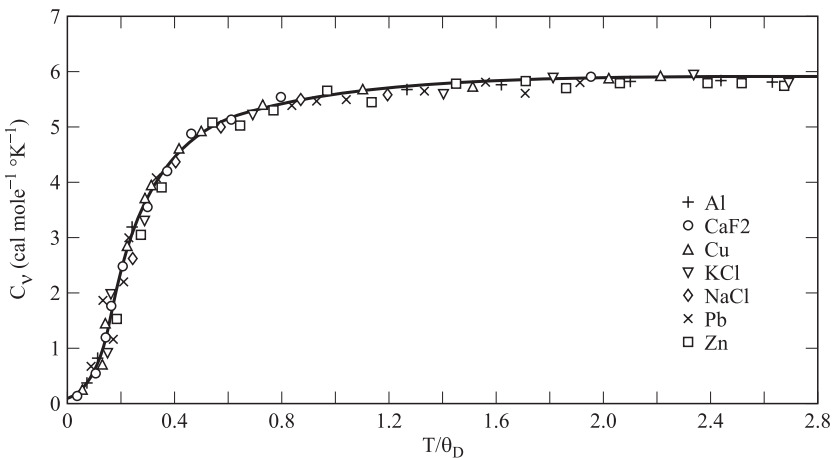
Fig. 8.1 Heat capacity as a function of a normalized temperature for a number of materials (Burns, Ref. 8.2, with permission).

Using the Morse potential and the expansion as given by Eq. 3.102, the following result is obtained to terms in the potential of order $(r - r_e)^4$:

$$\langle r \rangle = r_e + \frac{3 k_B T}{4 D_0 a^2}, \tag{8.4}$$

where r_e locates the minimum potential energy. Expansion is caused by odd-powered anharmonic terms in the intermolecular potential. Thus, materials with highly symmetric potentials and low anharmonicity have low thermal expansion. Good examples are diamond and oxides. Also, materials with deep potential wells have low thermal expansion, such as the ceramic oxides.

The linear thermal expansion coefficient, α_{ex}, is the fractional change in length, $\langle r \rangle$, per incremental temperature change:

$$\alpha_{ex} = \frac{1}{\langle r \rangle} \frac{d \langle r \rangle}{dT} \approx \frac{1}{r_e} \frac{d \langle r \rangle}{dT}. \tag{8.5}$$

Cubic anharmonic terms lead to a temperature-independent thermal expansion coefficient, depending on the depth of the well and the degree of anharmonicity. Higher odd-order anharmonic terms will provide temperature-dependent terms in the thermal expansion coefficient. Values of the coefficient of thermal expansion for optical materials are listed in Table 8.1 for a specific temperature or over a temperature range.

Thermal Conductivity Intrinsic thermal conductivity, κ_p, of an insulator depends on phonon–phonon scattering, which impedes the flow of phonons carrying the thermal energy. Materials with highly harmonic potentials have very high thermal conductivity, because such potentials do not scatter phonons. A real material always has some degree of anharmonicity, and a wide variety of thermal conductivities are expected, as demonstrated in Table 8.1. A simple formula for κ_p is given by

$$\kappa_p = \langle d \rangle v \frac{C_v}{3}, \tag{8.6}$$

where $\langle d \rangle$ is the phonon mean free path and v is the speed of sound in the medium. As the temperature increases, the phonon cross-section increases, depending on the degree of anharmonicity of the material, and $\langle d \rangle$ decreases. The temperature dependence of the thermal conductivity depends on $C_v(T)$ at low temperature and $\langle d \rangle$ at high temperature. The thermal conductivity as a function of temperature for a variety of materials is illustrated in Fig. 8.2.

Extrinsic thermal conductivity depends on the degree of order of the material. That is, a high number of defects and impurities create many strong scattering centers in the material impeding the flow of heat. Thus the thermal conductivity of a glass is always lower than that of the single crystal form of the same molecule.

8.1.2.2 Mechanical Properties

The relevant mechanical properties are the hardness to maintain polish and material strength to avoid structural failures.
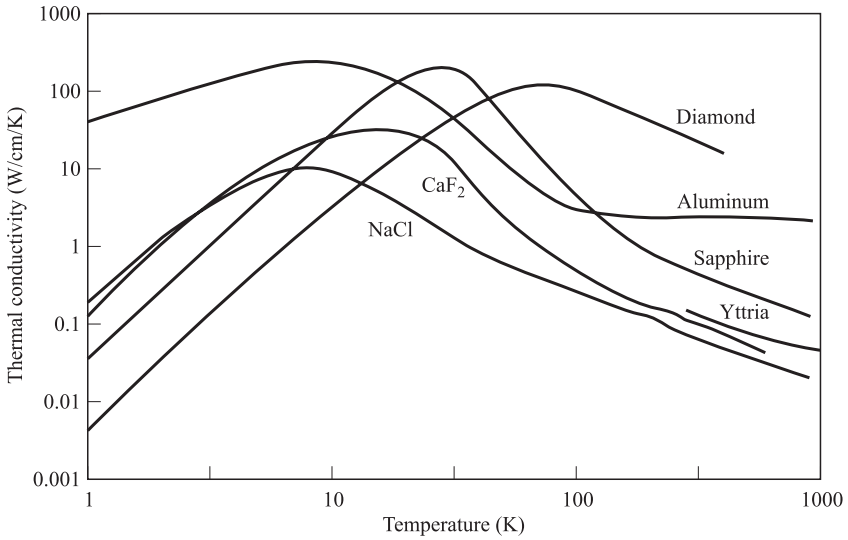
Fig. 8.2 Thermal conductivity as a function of temperature for a variety of optical materials.

Hardness   The hardest known material, at this time, is diamond. However, this is not a common optical element, and many other softer materials are often used. A simple scale for specifying hardness is the Moh scale, which is based on the ability of one material to scratch another. Specific materials are listed below in order of their ranking:

1. Diamond
2. Sapphire (corundum)
3. Topaz
4. Quartz
5. Orthoclase
6. Apatite
7. Fluorite
8. Calcite
9. Gypsum
10. Talc

Strength   Of particular interest is the elastic limit (flexure apparent elastic limit), F_a, of a material. This indicates the strength of a material so that it will not break under a load. A good example is a vacuum window. Table 8.2 lists apparent elastic limits for various materials.

Simple formulas (Ref. 8.1) can be used to design window thickness (d) to diameter (dia) ratios for clamped and unclamped circular windows for vacuum chambers or pressure vessels. Clamped and unclamped windows are illustrated in Fig. 8.3. Including a safety factor of four, circular windows can be specified according to the formula

Table 8.2 Apparent Elastic Limit (Mechanical Strength) for Various Windows

Material	Apparent Elastic Limit, F_a	
	[psia][a]	[kPa]
Al_2O_3	70000	482000
BaF_2	3900	26700
BK7 glass	5600	38590
Diamond (crystalline)	400000	2760000
(CVD)	58000	400000
CaF_2	5300	36500
CaF_2 (polycrystalline)	8000	55100
CsI	810	5580
KRS-5	3800	26200
LiF	1580	10900
KCl	330	2270
KCl (polycrystalline)	1600	11000
KBr	160	1100
MgF_2	7200	49000
$MgAl_2O_4$ (polycryst. spinel)	26000	179000
NaCl	350	2400
NaCl (polycrystalline)	1400	9650
Polyethylene	3100	21400

[a] 14.7 psia = 101.3 kPa = 1 atm.

$$\frac{d}{\text{dia}} \geq \text{const}\left(\frac{P}{F_a}\right)^{1/2}, \tag{8.7}$$

where P is the pressure difference across the window and const equals 0.866 for clamped windows and 1.06 for unclamped windows. Again, including a safety factor of four, rectangular windows can be specified according to the formula

$$\frac{d}{\text{dia}} \geq \text{const } b\left(\frac{P}{F_a(1 + c^2)}\right)^{1/2}, \tag{8.8}$$

where P is the pressure difference across the window, const equals 1.23 for clamped windows and 1.5 for unclamped windows, b is the length of the window, and c is the length-to-width ratio.

Clamped of fixed edge   Unclamped of freely supported edge
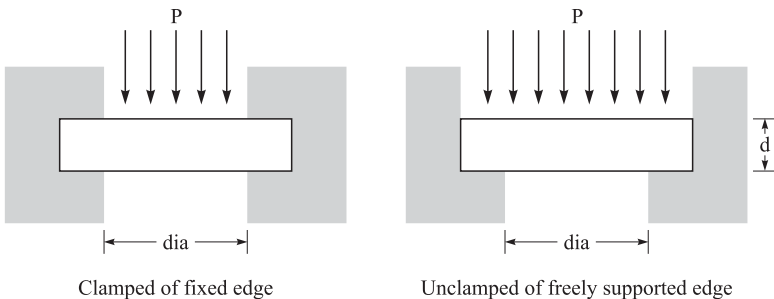
Fig. 8.3 Illustration of clamped and unclamped windows.

Example 8.1 Design a circular clamped window, 2 inches in diameter, made of Al_2O_3, for an InSb focal plane array that requires a vacuum dewar. What is the necessary thickness?

Using $F_a = 70,000$ psia and $P = 14.7$ psia in Eq. 8.7, the required thickness is 0.025 inches. This is a very thin window, indicating the high strength of sapphire.

8.1.2.3 Chemical Properties

The most important chemical property is water solubility. Humidity of the earth's atmosphere can damage window materials, this being particularly true for the alkali halides. If the surface is attacked by chemicals in the environment about the window, then the optical properties can be greatly affected. The water solubility of a number of optical materials is listed in Table 8.3. To help interpret the numbers, BaF_2 is virtually unaffected by a humid atmosphere but will spot if subjected to liquid water. Thus, materials less soluble than BaF_2 are stable in a humid atmosphere. KBr will easily spot and cannot be breathed upon. Materials more soluble than KBr must be protected from water vapor or used in very dry environments.

Good references for these effects are *The Infrared Handbook* (Ref. 8.4) and the *CRC Handbook of Laser Science and Technology* (Ref. 8.3), which are listed at the end of this chapter.

Table 8.3 Solubility of Selected Crystals in Water

Crystal	Temp. [°C]	Solubility [g/100 g of Water]	Crystal	Temp. [°C]	Solubility [g/100 g of Water]
Al_2O_3	20	insoluble	CdF_2	20	4.4
AgBr	20	12×10^{-6}	KDP	25	33.0
CdS	18	1.3×10^{-4}	KCl	20	34.7
AgCl	20	1.5×10^{-4}	NaCl	20	36.0
MgO	−20	6.2×10^{-4}	ADP	20	36.8
ZnS (hexagonal)	18	6.9×10^{-4}	KBr	20	65.2
$CaCO_3$	25	1.4×10^{-3}	CsI	25	85.5
CaF_2	20	1.51×10^{-3}	$NaNO_3$	20	88.0
MgF_2	18	8.6×10^{-3}	NaBr	20	91.0
SrF_2	20	1.17×10^{-2}	KF^a	18	92.3
KRS-5	20	< TlBr	CsBr	25	124.0
TlBr	20	4.76×10^{-2}	KI	20	144.0
PbF_2	20	6.4×10^{-2}	CsT	61	160.0
BaF_2	25	0.12	LiI^a	−20	164.0
LiF	18	0.27	NaI^a	20	185.0
KRS-6	20	< TlCl	CsCl	20	186.0
TlCl	20	0.32	CaI_2^a	20	209.0
$PbCl_2$	−20	0.99	CsF	18	368.0
NaF	20	4.2			

[a]Stable solid in contact with saturated solution is a hydrated form rather than an anhydrous salt.

8.2 Absorption and Refraction

The intrinsic optical properties of any material are determined by three basic physical processes: free carriers, lattice vibrations, and electronic transitions. However, the dominant physical process depends on the material. All materials have contributions to the complex index of refraction from electronic transitions. Metals and semiconductors are additionally influenced by free-carrier effects. The strength of these effects depends on the carrier concentration, and is very important in metals. Insulators and semiconductors also require the characterization of the lattice vibrations (or phonons) to fully understand the optical properties.

In the range of transparency, more subtle aspects of material composition and structure become important, such as impurities and defects. Intrinsic Rayleigh scattering is a very weak effect, but is important in long-path optical fibers and UV-transparent materials. Extrinsic scattering, caused by defects or grains in polycrystalline solids, is typically much larger than Rayleigh scattering. Impurity and defect absorption features can be of great concern, depending on the spectral region.

8.2.1 Crystalline Insulators

The temperature, T, and frequency, ν (in wave numbers), dependence of the real part of the index of refraction, $n(\nu, T)$ (index of refraction), are determined by the dominant physical processes previously mentioned. Figure 8.4a illustrates this point for the case of an insulating polar crystal. The value of $n(\nu, T)$ is essentially the sum of the strengths of all oscillators with fundamental oscillation frequencies above ν. Minor contributions near the infrared edge of transparency come from multiphonon contributions. Thus, the temperature dependence of those oscillations must be known to fully characterize $n(\nu, T)$ at any frequency. Figure 8.4a also indicates regions of validity for the popular Sellmeier and Cauchy models.

The temperature and frequency dependence of the imaginary part of the index of refraction, $k_e(\nu, T)$ (index of extinction), are more involved and require consideration of not only the dominant physical processes but also higher order processes, impurities, and defects, as illustrated in Fig. 8.4b. The spectral regions of the fundamental oscillations are opaque. Transparency of a nonconducting thin film (thickness on the order of 1 μm or less) ranges from below the minimum active transverse optical vibrational mode, to above the maximum longitudinal optical vibrational mode, and ends at the material's bandgap. Transparency of a bulk insulator (thickness 0.1–1 cm) is determined by three different absorption edges. Far-infrared transparency ends in the region of two-phonon difference bands and the one-phonon red wing (the low-frequency side of the absorption band). Infrared transparency of a bulk solid begins in the region of three-phonon sum bands (essentially the third harmonic of the one-phonon bands). Visible/ultraviolet transparency ends at the Urbach tail, which can be phenomenologically interpreted as thermal fluctuations in the bandgap energy. For most window applications involving low power levels, the absorption coefficient needs to be known down to 10^{-3} cm^{-1}. Transparency for optical fibers (thickness 1 km or greater) and high-power laser windows requires low-level absorption below 10^{-3} cm^{-1}. For such low absorption, higher order intrinsic processes, extrinsic impurities, and material defects become important.
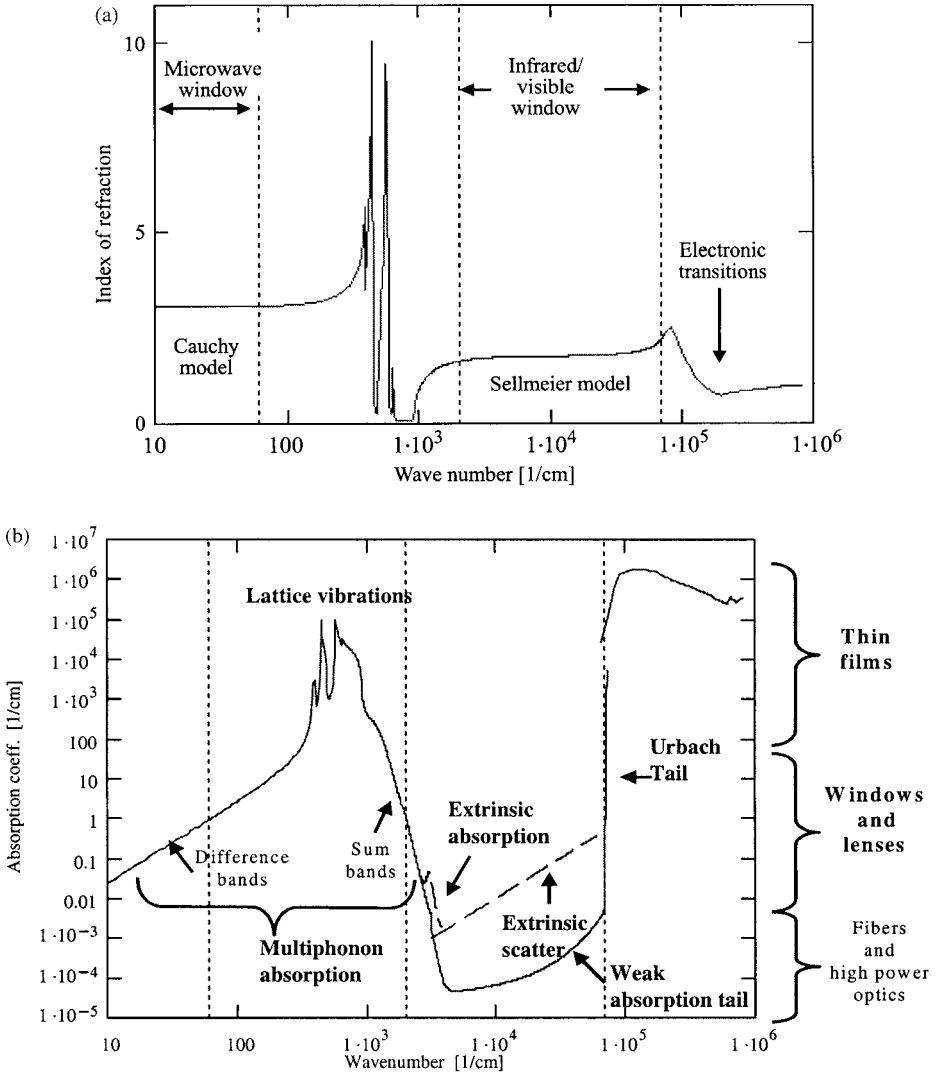
Fig. 8.4 Optical properties of a typical polar crystalline insulator at room temperature: (a) index of refraction and (b) absorption coefficient.

The temperature dependence of intrinsic Rayleigh scattering will not be considered because it is usually too small to be of concern. Extrinsic scatter in polycrystalline materials has been observed to be constant with temperature for low-expansion materials. Impurity and defect absorption, which may be significant, are highly material and manufacturing-process dependent and cannot be properly treated within the limits of this chapter. A brief discussion will be presented in a later section.

8.2.1.1 One-Phonon and Electronic Band Transitions

The optical properties of an insulating material can be completely specified by the complex index of refraction, $\bar{n}(v,T)$, or the complex relative permittivity, $\epsilon_r(v,T)$, where v is the wave number (reciprocal wavelength). In the following, only intrinsic absorption phenomena will be considered. Materials are opaque in the spectral region of first-order processes. Thus, reflection measurements must be used to obtain the optical properties. As discussed in Chapter 6, the magnitude of the spectral reflectance is a routine measurement. In opaque regions, the reflectance becomes the single-surface reflection. Based on the models of Chapter 4, the magnitude of the single-surface reflectance, R, of a medium (at normal incidence) is given by

$$R = \frac{(n-1)^2 + k_a^2}{(n+1)^2 + k_a^2}.$$
(8.9)

Generally, a measurement of R is not sufficient to determine ϵ_r (e.g., both n and k_a). Hence, it is necessary to describe the relationship between n and k_a. The "classical oscillator model" can be used to represent ϵ_r in terms of the lattice vibrations (recall from Chapter 4),

$$\epsilon_r(v,T) = \epsilon_\infty(T) + \sum_i \frac{\Delta\epsilon_i(T)v_i^2(T)}{v_i^2(T) - v^2 + j\Gamma_i(v,T)v},$$
(8.10)

where $\Delta\epsilon_i$, Γ_i, and v_i are the ith mode strength, line width, and long-wavelength transverse optical frequency, v_{TO}, respectively. The sum on i is over all transverse optical modes. This model is well known to adequately describe n in the infrared and radar frequency regions. Using Eq. 8.10, the static dielectric constant, $\epsilon_s(T) = \epsilon_r'(0,T)$, becomes

$$\epsilon_s(T) = \epsilon_\infty(T) + \sum_i \Delta\epsilon_i(T).$$
(8.11)

The implied frequency dependence of Γ_i represents a cutoff beyond the one-phonon region blue wing caused by anharmonicities of the potential. This is not unexpected, since the classical oscillator model required modification in the far wing for gas phase absorption as well. No exact theory exists, thus the cutoff function is empirically chosen to be

$$\Gamma_i(v,T) = \Gamma_i(T) \begin{cases} 1 & v \le v_{cutoff}, \\ \exp\left(-\alpha\left[\left(\frac{v}{v_{cutoff}}\right)^2 - 1\right]\right) & v \ge v_{cutoff}, \end{cases}$$
(8.12)

where α and v_{cutoff} are arbitrary parameters. Good results are obtained by choosing $\alpha = 4$ and v_{cutoff} as the highest infrared-allowed longitudinal-optical-mode frequency. Although those values for $\alpha = 4$ and v_{cutoff} are not unique, they are adequate for the present purpose. Now, the fundamental phonon bands can be joined with higher order phonon bands without the distortion of the one-phonon blue wing, as illustrated in Fig. 8.5.
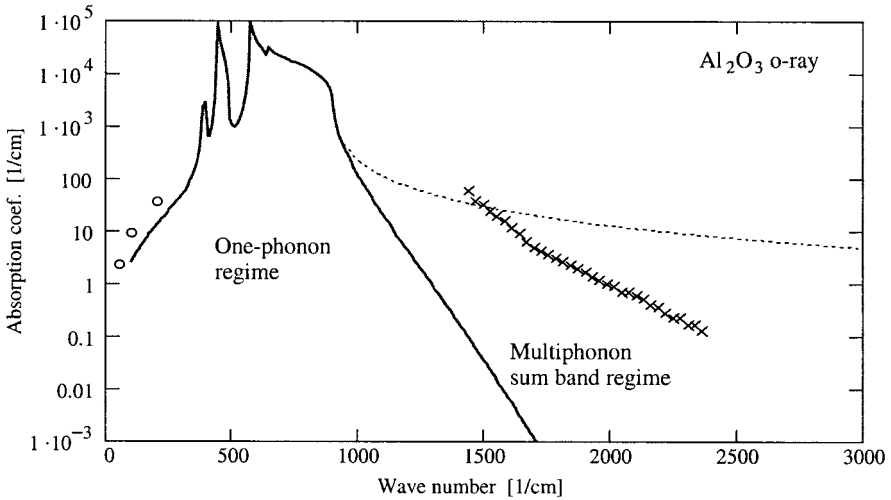
Fig. 8.5 Absorption coefficient as a function of frequency for pure sapphire at $T = 295$ K, showing the one-phonon model with the cutoff (solid curve) and the one-phonon model without the cutoff (dashed curve). Experimental data points (o and x) show experimental multiphonon absorption.

The figure also shows experimental data from transparent regions that clearly indicate the need for the blue-wing cutoff. The next section will present models of multiphonon sum and difference bands that will complete the complex index of refraction model in regions of transparency.

Another commonly used "pole-fit" model features four parameters per transition, as given by the expression (Lyddane et al., Ref. 8.9)

$$\epsilon_r(\nu, T) = \epsilon_\infty(T) \prod_i \frac{\nu_{iLO}^2(T) - \nu^2 + j\nu\Gamma_{iLO}(\nu, T)}{\nu_i^2(T) - \nu^2 + j\nu\Gamma_i(\nu, T)}, \tag{8.13}$$

where the additional subscript LO indicates longitudinal-optical-mode parameters. A product instead of a sum is now used. Equation 8.13 in the static limit reduces to the Lyddane–Sachs–Teller relation

$$\frac{\epsilon_s}{\epsilon_\infty} = \prod_i \frac{\nu_{iLO}^2}{\nu_i^2}. \tag{8.14}$$

This is a statement similar to Eq. 8.11, except now in the form of a product.

As an introduction to the temperature dependence of the complex index of refraction, $\bar{n}(\nu, T) = n(\nu, T) - jk_a(\nu, T)$, consider the Lorentz–Lorenz formula,

$$\frac{n^2 - 1}{n^2 + 2} = \frac{1}{3\epsilon_0} \rho(T) \alpha_e(\rho, T), \tag{8.15}$$

where ρ is the number density of oscillators per unit volume ($= N/V$, where N is the number of oscillators and V is volume) and α_e is the polarizability. The derivative of n with respect to T becomes

$$2n\epsilon_0 \frac{dn}{dT} = (n^2 + 2)(n^2 - 1)\left\{\frac{1}{3\rho}\left(\frac{d\rho}{dT}\right) + \frac{1}{3\alpha_e}\left[\left(\frac{\partial\alpha_e}{\partial\rho}\right)_T \frac{d\rho}{dT} + \left(\frac{\partial\alpha_e}{\partial T}\right)_\rho\right]\right\}. \quad (8.16)$$

Furthermore, the derivative of volume, $V(T)(= (L_0 + L\alpha_{ex}T)^3)$ with respect to temperature can be written to first order in terms of the linear coefficient of expansion, α_{ex}, as

$$\frac{dV}{dT} = 3V\alpha_{ex}. \quad (8.17)$$

Now, Eq. 8.16 can be rewritten in a more meaningful form:

$$2n\epsilon_0 \frac{dn}{dT} = -(n^2 + 2)(n^2 - 1)\alpha_{ex}\left[1 - \frac{V}{\alpha_e}\left(\frac{\partial\alpha_e}{\partial V}\right)_T\right] + \frac{(n^2 + 2)(n^2 - 1)}{3\alpha_e}\left(\frac{\partial\alpha_e}{\partial T}\right)_V. \quad (8.18)$$

The first term depends on changes in volume with respect to temperature. Thermal expansion is the dominant contributor. Lithium (Ref. 8.6) is able to show a direct proportionality between the expansion coefficient and dn/dT for the alkali halides. The second term represents the temperature changes in the polarizability. The polarizability is determined by two fundamental processes in an insulating material, electronic transitions and vibrational transitions. The electronic transitions contribute to the index of refraction from the ultraviolet/visible region to DC. The vibrational transitions also contribute to the index of refraction from the far-infrared to DC. They are more temperature sensitive than the electronic transitions, thus dn/dT in the far-infrared below the optical phonons is usually positive and greater than dn/dT in the visible/IR.

A more detailed discussion of the temperature dependence of the lattice vibrations is given in the following. As Eq. 8.10 suggests, the reflectance is a function not only of frequency but also of temperature. Experiments reported by Jasperse et al. (Ref. 8.10) have demonstrated that the optical parameters $\Delta\epsilon_i$ and ν_i have a linear temperature dependence, while calculations by Maradudin and co-workers have successfully utilized a quadratic temperature dependence for Γ_i at high temperatures. A theoretical calculation by Wallis and Maradudin (Ref. 8.12) has shown that the temperature dependence of ν_i and Γ_i comes from cubic anharmonic terms in the lattice potential energy. The origin of the temperature dependence of the mode strengths, $\Delta\epsilon_i$, is not well established but can be understood by considering the static dielectric constant. Szigeti (Ref. 8.14) has shown that not only do anharmonic terms in the lattice potential energy contribute to the temperature dependence of $\epsilon_s(T)$, but also that a contribution arises from terms in the dipole moments that are of higher order in the displacement coordinates. These latter higher order terms have their origin in the deformation of the electronic shells.

The temperature dependence of the transverse-mode frequencies, ν_i, and the mode strengths, $\Delta\epsilon_i$, can be represented by quadratic equations of the form

$$\nu_i(T) = \nu_i(T_0) + a1_i \cdot (T - T_0) + a2_i \cdot (T - T_0)^2 \quad (8.19a)$$

and

$$\Delta\epsilon_i(T) = \Delta\epsilon_i(T_0) + b1_i \cdot (T - T_0) + b2_i \cdot (T - T_0)^2, \qquad (8.19b)$$

where T_0 is a reference temperature (typically room temperature) and $a1_i, a2_i, b1_i$ and $b2_i$ are mode- and material-specific constant coefficients that are empirically determined. The dependence of the line width on temperature can be described by a quadratic equation in T:

$$\frac{\Gamma_i}{\nu_i}(T) = \frac{\Gamma_i}{\nu_i}(T_0) + c1_i \cdot (T - T_0) + c2_i \cdot (T - T_0)^2, \qquad (8.19c)$$

where T_0 is again a reference temperature and $c1_i$ and $c2_i$ are also mode- and material-specific constant coefficients. The high-frequency permittivity, ϵ_∞, is temperature dependent and is represented by

$$\epsilon_\infty(T) = \epsilon_\infty(T_0) + e_\infty \cdot (T - T_0). \qquad (8.19d)$$

Note that $e_\infty = d\epsilon_\infty/dT = 2n_\infty (dn_\infty/dT)$; thus, in most cases, e_∞ can be determined from visible dn/dT measurements in a spectral region of low dispersion.

Table 8.4 lists the model parameters of Y_2O_3, based on the previously discussed temperature–dependent formulas. The parameters are determined from reflectance spectra, as shown in Fig. 6.9. A comparison is made between the experimental data and the one-phonon-model representation. The fit to the experimental data as a function of temperature is good, justifying the model, as demonstrated in Fig. 8.6 for sapphire. This model of the complex index of refraction is important for spectral-emissivity calculations and index of refraction calculations from microwave to ultraviolet over a wide range of temperatures. Classical oscillator parameters are given for a wide variety of optical materials in Appendix 4 using the format of Table 8.4.

Table 8.4 Optical Constants of Y_2O_3 Classical Oscillator Parameters[a]

Mode	$\nu_{TOi}(T_0)$ [cm^{-1}]	$a1_i$ [cm^{-1} K^{-1}]	$\Delta\epsilon_i(T_0)$	$b1_i$	$\Gamma_i/\nu_{TOi}(T_0)$ [K^{-1}]	$c1_j$ [K^{-1}]	$c2_i$ [K^{-2}]
1	120.0	0.01	0.2	—	0.035	—	—
2	172.0	0.01	0.1	—	0.025	—	—
3	182.0	0.01	0.15	—	0.025	—	—
4	241.0	0.0072	0.200	8.10×10^{-5}	0.025	1.46×10^{-5}	—
5	303.0	0.0144	2.600	6.24×10^{-4}	0.0135	3.35×10^{-5}	—
6	335.0	0.0109	1.749	-3.55×10^{-4}	0.0115	2.38×10^{-5}	—
7	371.0	0.0109	2.651	6.38×10^{-5}	0.021	2.51×10^{-5}	—
8	415.0	0.0109	0.040	3.55×10^{-5}	0.011	3.24×10^{-5}	—
9	461.0	0.0144	0.050	3.55×10^{-5}	0.015	1.80×10^{-5}	—
10	490.0	0.0180	0.005	3.55×10^{-6}	0.018	2.12×10^{-5}	—
11	555.0	0.0210	0.095	9.36×10^{-5}	0.025	1.21×10^{-5}	—
12[b]	72100.0	—	2.579	1.40×10^{-4}	—	—	—

[a]$T_0 = 295$ K and $\epsilon_\infty(T) = 1.00$.
[b]Electronic transition.
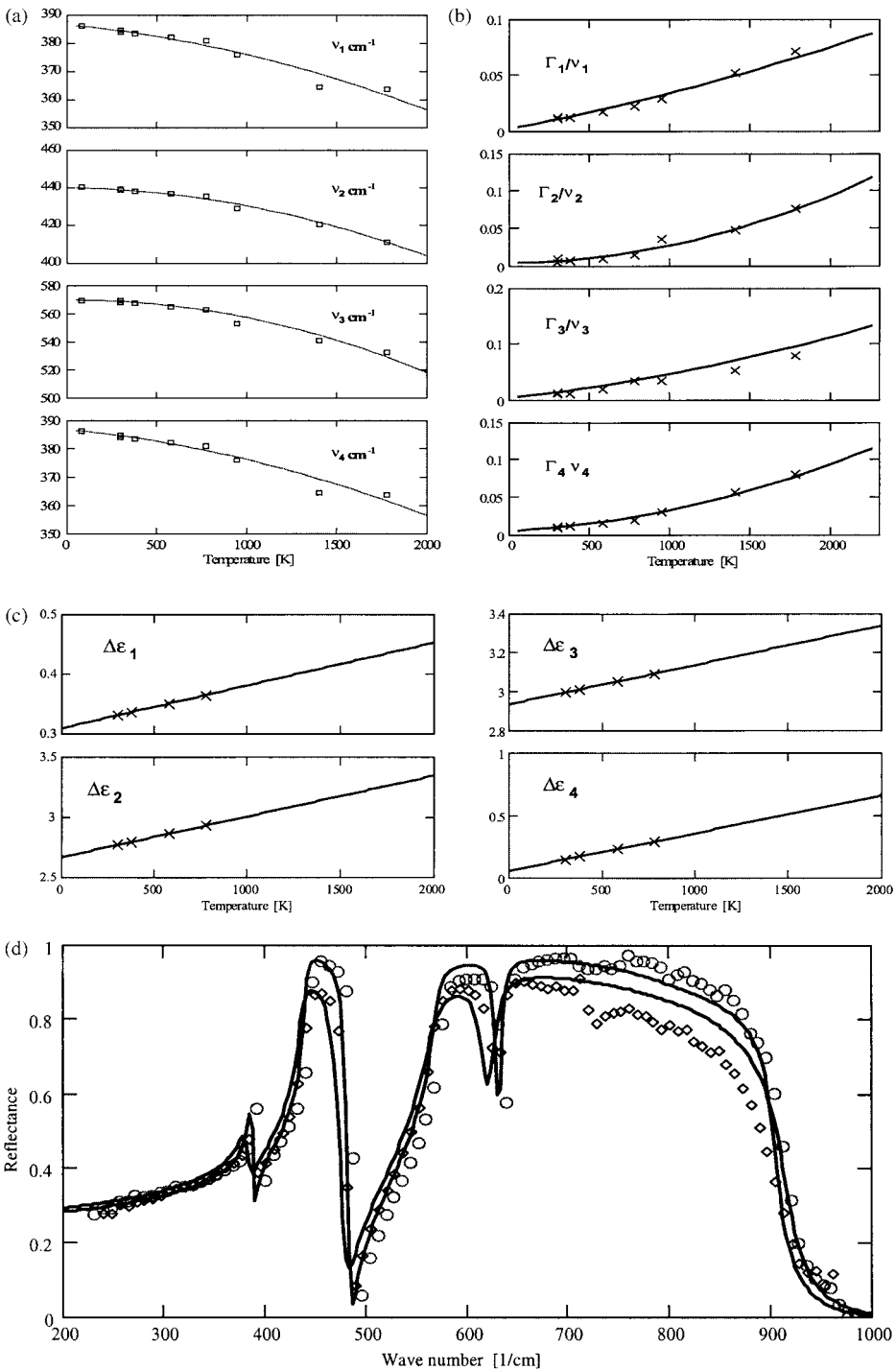
Fig. 8.6 (a), (b), and (c) Temperature dependence of line position, ν_i, line strength, $\Delta\epsilon_i$, and damping factor divided by the line position, Γ_i/ν_i, respectively, for sapphire o-ray. (d) Reflection spectra of sapphire o-ray at two temperatures ($\circ\, T = 295$ K and $\diamond\, T = 773$ K) compared with model (solid line).

In the region of transparency (i.e., $n \gg k_a$ and $(v_i^2 - v^2) \gg \Gamma_i(v)$) a simple expression for the real part of the temperature–dependent index of refraction is obtained, based on Eqs. 8.10 and 4.42:

$$n^2(v,T) = 1 + \sum_i \frac{v_i^2(T)\Delta\epsilon_i(T)}{v_i^2(T) - v^2}. \tag{8.20}$$

Recall that this convenient equation for $n(v,T)$ is known as Sellmeier's formula. The sum is over all transitions, thus $\epsilon_\infty = 1$. Further approximations on Eq. 8.20 for $n(v)$, below the lowest v_i, leads to the Cauchy formula, as given by

$$n(v) = A + Bv^2 + Cv^4. \tag{8.21}$$

Differentiating Eq. 8.20 with respect to temperature leads to the thermo-optic coefficient, similar in form to Eq. 8.16. The oscillator strength is related to the ith oscillator polarizability, as defined in Section 2.3.2 (e.g., $\epsilon_0 \Delta \epsilon_i = \rho \Delta \alpha_i$). With this substitution, the following expression is obtained (assuming $\Delta\alpha_i$ is independent of ρ):

$$\frac{\partial n(v,T)}{\partial T} = \frac{1}{2n\epsilon_0} \sum_i \rho\alpha_i \left(\frac{1}{\Delta\alpha_i} \frac{\partial \Delta\alpha_i}{\partial T} - 3\alpha_{ex} + \frac{2v^2/v_i}{v_i^2 - v^2} \frac{\partial v_i}{\partial T} \right), \tag{8.22a}$$

where $\partial\rho/\partial T = -3\rho\alpha_{ex}$, α_{ex} is the linear coefficient of expansion, and

$$\alpha_i = \frac{\Delta\alpha_i v_i^2}{v_i^2 - v^2}. \tag{8.22b}$$

For materials with large electronic polarizability and small volume expansion (e.g., the oxides), the values of dn/dT in the visible and IR are small and positive. This is in contrast to experimental results for the alkali halides and the fluorides, which have negative dn/dT because of significant volume expansion and smaller polarizabilities. Based on Eqs. 8.19a–c, dn/dT is linear in temperature to first order. Also, as the frequency approaches an absorption band, the magnitude of dn/dT increases. In the microwave region, the static dielectric constant (see Eq. 8.11) includes strong contributions from the lattice vibrations. Thus, the value of the net polarizability can greatly increase, and $d\epsilon_s/dT$ is usually positive. Figure 8.7 illustrates the experimental frequency and temperature dependence of $n(\rho)$ and $\epsilon_s(T)$ for the ordinary ray of sapphire. The solid curve in Fig. 8.7b shows the temperature range of validity of the linear approximations used in obtaining Eqs. 8.19b and 8.19d (see Appendix 4).

Dispersion of n (typically stated as $dn/d\lambda$, $\lambda = 1/v$) can also be easily computed based on Eq. 8.20. The resulting formula is

$$\frac{\partial n(\lambda,T)}{\partial \lambda} = -\frac{\lambda}{n} \sum_i \frac{\lambda_i^2 \Delta\epsilon_i}{(\lambda^2 - \lambda_i^2)^2}. \tag{8.23}$$

The magnitude of dispersion depends on the location and strength of the oscillators. The wavelength locating the minimum dispersion point of a material is important for long-path, high-bandwidth optical fibers.

(a)

(b)
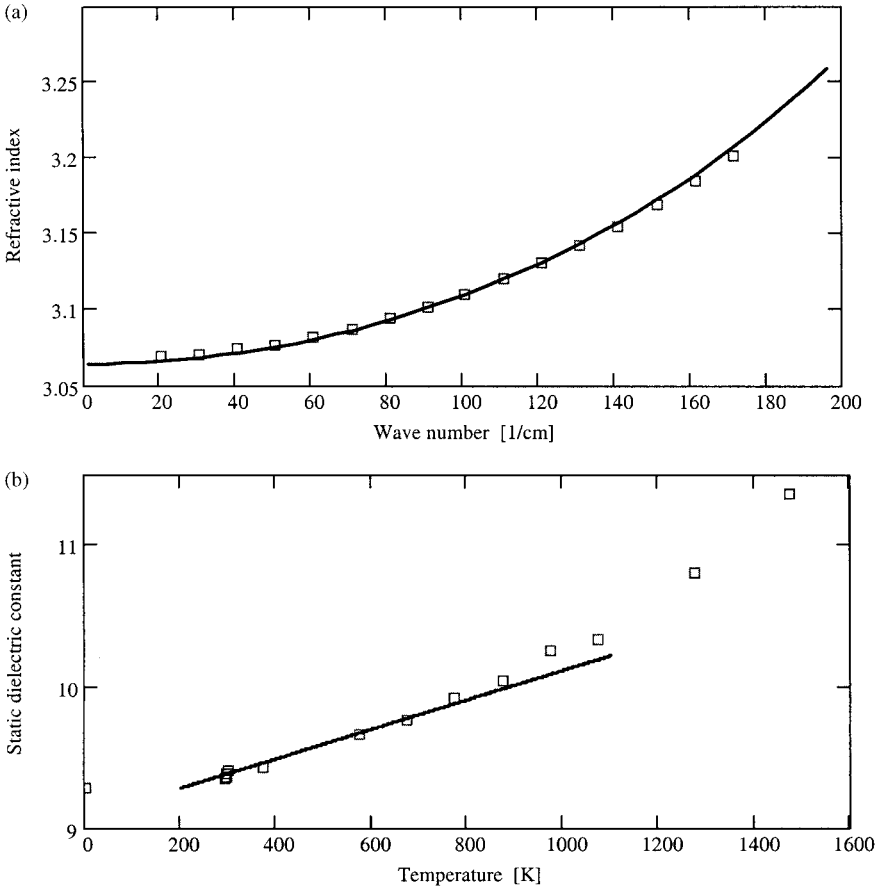
Fig. 8.7 (a) The frequency dependence of the room-temperature index of refraction and (b) the temperature dependence of the static dielectric constant for the ordinary-ray of Al_2O_3. The solid curve represents one-phonon model plus multiphonon model.

Unfortunately, electronic transitions, which drive optoelectronic device perform-ance, cannot be modeled in such a straightforward manner as vibrational transitions. This is because most electronic transitions are coupled together to form broad homo-geneous absorption bands. Thus, the shape of the density-of-states function determines the spectral response, which is seldom in the functional form of the classical oscillator model. In the following, the models developed by Adachi (see Ref. 8.19) are used to represent the complex permittivity as a function of frequency and temperature.

Figure 8.8 illustrates the energy band structure for GaAs. The various electronic inter-band transitions, from valence to conduction band, peak at various critical point (CP) locations. The transitions are designated as E_0, $E_0 + \Delta_0$, E_1, $E_1 + \Delta_1$, and E_2(Δ indi-cates energy level shifts caused by spin–orbit coupling). Most of the various transitions are indicated in Fig. 8.8. The figure shows that GaAs is a direct bandgap semiconduc-tor. Thus the complex susceptibility model developed in Chapter 5 can be applied.
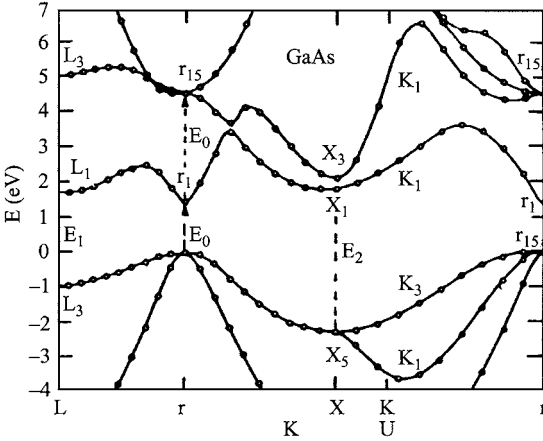
Fig. 8.8 Energy band structure of room temperature GaAs (Burns, Ref. 8.2, with permission).

The E_0 and $E_0 + \Delta_0$ transitions of GaAs are located at the center of the Brillouin zone (Γ point where $k'_{opt} \approx 0$). The E_0 transition is the first intrinsic electronic absorption band and is located at the bandgap energy. The shape of this band is determined by the density-of-states for parabolic energy distributions in phase space. The next electronic absorption band is the $E_0 + \Delta_0$. Based on Eqs. 5.142 and 5.143, the complex electric susceptibility function for these two homogeneous transitions is given by

$$\chi_0''(\omega) = \frac{A}{(\hbar\omega)^2} \left((\hbar\omega - E_0)^{0.5} H(\chi_0 - 1) + \frac{1}{2}(\hbar\omega - E_0 - \Delta_0)^{0.5} H(\chi_{s0} - 1) \right), \quad (8.24a)$$

which represents the imaginary part and

$$\chi_0'(\omega) = \frac{A_0}{E_0^{1.5}} \left[f(X_0) + \frac{1}{2} \left(\frac{E_0}{E_0 + \Delta_0} \right)^{1.5} f(X_{s0}) \right], \quad (8.24b)$$

which represents the real part, where A_0 is an amplitude parameter, E_0 and $E_0 + \Delta_0$ are the bandgap energies (see Appendix 4, Table A4.6),

$$f(X) = \frac{1}{X^2} [2 - (1 + X)^{0.5} - (1 - X)^{0.5} H(1 - X)],$$

$$X_0 = \frac{\hbar\omega}{E_0}, \quad \text{and} \quad X_{s0} = \frac{\hbar\omega}{E_0 + \Delta_0}.$$

$H(z)$ is a Heaviside step function such that $H(z \geq 0) = 1$ and $H(z < 0) = 0$. The inverse Fourier transform of the first half of Eq. 8.24 leads to the time-domain susceptibility for the E_0 region, given by Eq. 5.144. A plot of the resulting time-domain susceptibility for the E_0 transition in GaAs is given in Fig. 5.10.

The E_1 and $E_1 + \Delta_1$ transitions are located at the L-point in the Brillouin zone. Again, the shape of these bands is driven by the density-of-states function in this region of the energy band structure, as illustrated in Fig. 8.8. The corresponding complex permittivity for these transitions is given by (Adachi, Ref. 8.19)

$$\chi_1''(\omega) = \frac{1}{X_1^2} \left\{ B_{01}^* - \mathrm{Im} \left[B_1 \ln(\hbar\omega - E_1 + j\Gamma) \right] \right\}$$
$$+ \frac{1}{X_{1s}^2} \left\{ B_{02}^* - \mathrm{Im} \left[B_2 \ln(\hbar\omega - E_1 - \Delta_1 + j\Gamma) \right] \right\}, \tag{8.25a}$$

which represents the imaginary part and

$$\chi_1'(\omega) = \mathrm{Re} \left[-\frac{B_1}{X_{1d}^2} \ln(1 - X_{1d}^2) - \frac{B_2}{X_{1sd}^2} \ln(1 - X_{1sd}^2) \right], \tag{8.25b}$$

which represents the real part, where E_1 and $E_1 + \Delta_1$ are the bandgap energies, Γ is a damping parameter common to both transitions, $B_{01}^* = \pi B_1$ and $B_{02}^* = \pi B_2$ at room temperature,

$$X_{1d} = \frac{\hbar\omega + j\Gamma}{E_1}, \quad \text{and} \quad X_{1sd} = \frac{\hbar\omega + j\Gamma}{E_1 + \Delta_1}.$$

The corresponding time-domain response can be obtained in analytical form if the damping parameter is set to zero. This is a reasonable approximation because $\Gamma \ll E_1$ (see Appendix 4). Then the complex permittivity for a single E_1-type band simplifies to

$$\chi_1'(\omega) = -\frac{B}{X^2} \ln(1 - X^2) - j\frac{\pi B}{X^2} H(X - 1), \tag{8.26}$$

where $X = \hbar\omega/E$. The inverse Fourier transform of Eq. 8.26 leads to the time-domain electric susceptibility for E_1-type transitions, as given by

$$\chi_{e1}(t) = 2B\frac{E}{\hbar} \left[\sin\left(\frac{E}{\hbar}t\right) - \frac{E}{\hbar}t\, Ci\left(\frac{E}{\hbar}t\right) \right] h(t), \tag{8.27}$$

where $Ci(x)$ is the cosine integral function. The details of the derivation are presented in Appendix 3.

The E_2 transitions are the strongest and are inhomogeneous in nature, because they occur in several closely spaced homogeneous regions of the energy band structure. However, Adachi (Ref. 8.19) employed only two modes (located at E_2 and E_0'), which are characterized by the classical oscillator model of the form

$$\chi_2''(\omega) = \frac{C_2 X_2 \gamma_2}{(1 - X_2^2)^2 + X_2^2 \gamma_2^2} + \frac{C_0 X_0' \gamma_0}{(1 - X_0'^2)^2 + X_0'^2 \gamma_0^2}, \tag{8.28a}$$

representing the imaginary part and

$$\chi_2'(\omega) = \frac{C_2(1 - X_2^2)}{(1 - X_2^2)^2 + X_2^2\gamma_2^2} + \frac{C_0(1 - X_0'^2)}{(1 - X_0'^2)^2 + X_0'^2\gamma_0^2}, \qquad (8.28b)$$

representing the real part, where the C and $\gamma\,(= \Gamma/E_2)$ parameters are listed in Appendix 4,

$$X_2 = \frac{\hbar\omega}{E_2} \quad \text{and} \quad X_0' = \frac{\hbar\omega}{E_0'}.$$

Electroreflectance measurements have shown a multitude of modes in this region (Adachi, Ref. 8.19). Assuming all the modes in this band are properly represented, then the correct time-domain susceptibility for E_2 type transitions can be obtained from the application of Eq. 4.49.

Excitons near the bandgap must also be included in a complete model. A model for the complex frequency-domain susceptibility for the E_0 exciton is given by Eq. 5.145. The next significant exciton is associated with the E_1 band. The complex permittivity in this case is given by

$$\chi_{1ex}(\omega) = \frac{B_{1x}}{E_1 - E_{x1} - \hbar\omega - j\Gamma} + \frac{B_{2x}}{E_1 + \Delta_1 - E_{x1} - \hbar\omega - j\Gamma}. \qquad (8.29)$$

The inverse Fourier transform of Eq. 4.145 leads to the time-domain susceptibility for the E_0 exciton, as given by

$$\chi_{0ex}(t) = 2\frac{A_{0x}}{\hbar}e^{-\frac{\Gamma_{0x}}{\hbar}t}\sin\left(\frac{E_0 - E_{x0}}{\hbar}t\right)h(t). \qquad (8.30)$$

A similar formula is obtained for the E_1 excitons.

Table A4.6 lists the parameter values for all the electronic transition models for GaAs. The parameters are temperature dependent and follow a simple linear dependence of the form

$$F(T) = F(T_0) + aT.$$

The corresponding temperature coefficients are also listed in Table A4.6. The linear fits to the model parameter values listed by Adachi (Ref. 8.19) cover the temperature range from 22 to 754 K. Good agreement is obtained. Optical materials with infrared bandgaps (e.g., semiconductors) have very temperature-sensitive optical constants, thus the inclusion of temperature dependence is critical for real device modeling.

The net electronic relative permittivity is the sum of all of the band susceptibilities previously discussed plus higher frequency contributions represented by $\epsilon_{1\infty}$ (see Table A4.6). The real and imaginary parts of the permittivity are given by

$$\epsilon_{re}'(\omega) = \chi_0'(\omega) + \chi_1'(\omega) + \chi_2'(\omega) + \chi_{0ex}'(\omega) + \chi_{1ex}'(\omega) + \epsilon_{1\infty}, \qquad (8.31a)$$

and

$$\epsilon_{re}''(\omega) = \chi_0''(\omega) + \chi_1''(\omega) + \chi_2''(\omega) + \chi_{0ex}''(\omega) + \chi_{1ex}''(\omega), \qquad (8.31b)$$

respectively. The net time-domain susceptibility is also the sum of the individual time-domain susceptibilities, as given by

$$\chi(t) = \chi_0(t) + \chi_1(t) + \chi_2(t) + \chi_{0ex}(t) + \chi_{1ex}(t). \qquad (8.31c)$$

The electronic time-domain susceptibility for GaAs is plotted in Fig. 8.9. Electronic transitions are very rapid, in the femtosecond regime.

To obtain the complex index of refraction from the complex permittivity the following formulas are used,

$$n_e(\nu) = \left[\frac{1}{2} \left(\sqrt{\epsilon_{re}'^2(\nu) + \epsilon_{re}''^2(\nu)} + \epsilon_{re}'(\nu) \right) \right]^{0.5} \qquad (8.32a)$$

and

$$\beta_{abs}(\nu) = \frac{2\pi}{n_e(\nu)} \nu \epsilon_{re}''(\nu), \qquad (8.32b)$$

where ν is frequency in wave numbers. The Adachi model is compared with frequency-domain experimental data for the room-temperature complex index of refraction (Palik, HOC I, Ref. 8.1) in Fig. 8.9. Good agreement is obtained between the experimental data and the model for the index of refraction and the absorption coefficient.

The net first-order permittivity for bound-charge phenomena is the sum of the electronic and vibrational permittivities, as given by

$$\epsilon_r(\omega) = \chi_{rv}(\omega) + \epsilon_{re}(\omega). \qquad (8.33)$$

Classical oscillator model parameters for GaAs can be found in Table A4.5. In this manner, a comprehensive complex index of refraction model accounting for first-order transitions is obtained that allows wide frequency and temperature representation.

8.2.1.2 Higher Order Phonon Processes

The classical oscillator model represents the fundamental lattice vibrations or one-phonon transitions in a material and the Adachi models represent the electronic transitions. But the absorption coefficient obtained from the model is valid only in the vicinity of the one-phonon frequencies. The absorption coefficient needs to be known in the regions of transparency as well, requiring a description of multiphonon absorption bands in which more than one-phonon excitation occurs upon the absorption of a single photon. The millimeter-wave region is dominated by the one-phonon red wing and multiphonon difference bands. The IR region is dominated by multiphonon sum bands.

Recall from Chapter 3 that net absorption coefficient is generally expressed as

$$\beta_{abs}(\nu, T) = \sum_l S_{lu}(T \; ; \; \nu_{lu}) g(\nu, T \; ; \; \nu_{lu}), \qquad (8.34)$$
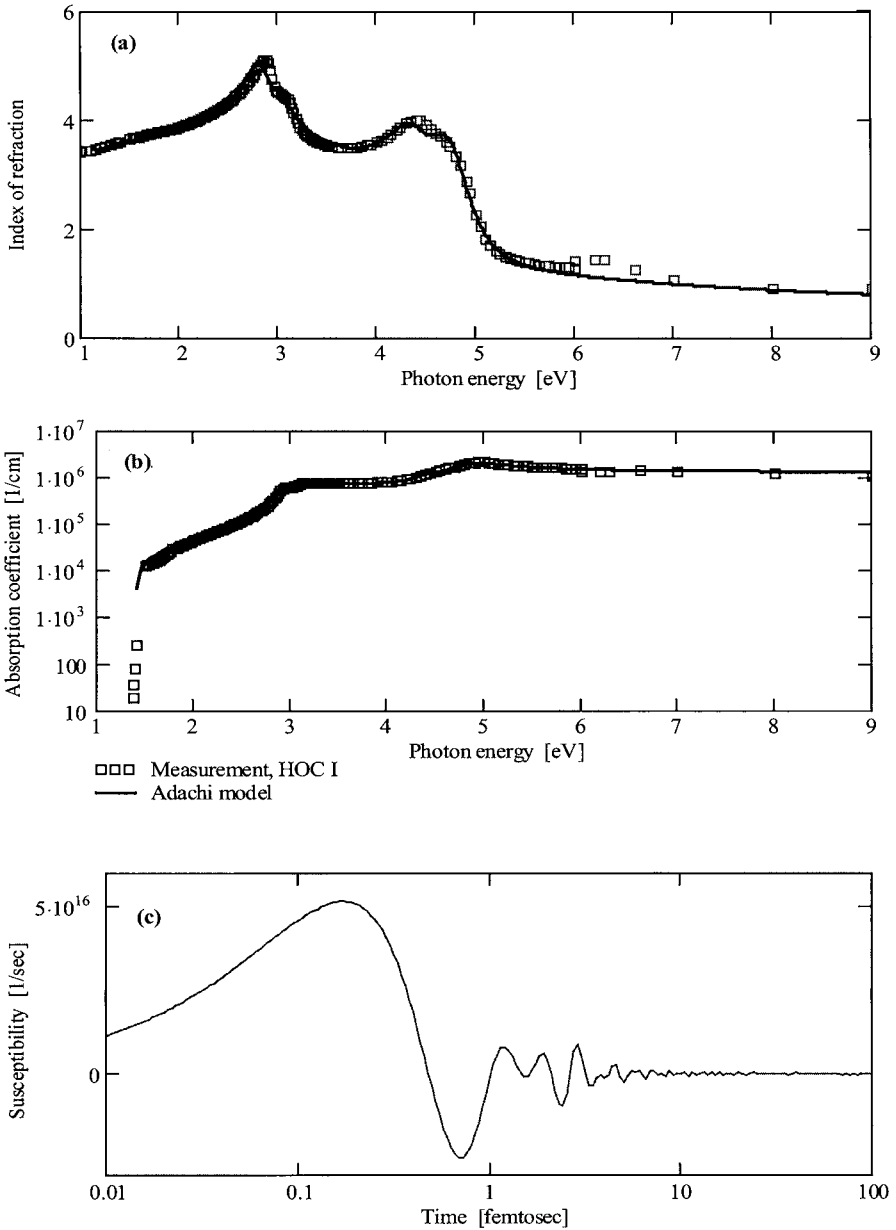
Fig. 8.9 The infrared to ultraviolet complex index of refraction of GaAs at room temperature as a function of wave number where (a) is the real part and (b) is the absorption coefficient. The boxes are experimental data points from Palik HOC I and the solid curves represent the Adachi model using the parameters from Table A4.6. (c) The corresponding time domain susceptibility of GaAs.

where ν_{lu} is the center frequency of the transition from level l to level u, $S_{lu}(T)$ is the transition strength, $g(\nu,T)$ is the spectral distribution function, and the sum is over all initial states. Based on the quantum oscillator model of Chapter 5, the strength and shape functions are expressed as

$$S_{lu} = \frac{8\pi^3 \nu_{lu}}{3hn}\rho_a \frac{e^{-E_l/k_BT}}{Q(T)}\tanh\left(\frac{hc\nu_{lu}}{2k_BT}\right)|\mu_{dp}|^2 \tag{8.35}$$

and

$$g(\nu,T) = \frac{\nu}{\nu_{lu}}\frac{\tanh\left(\frac{hc\nu}{2k_BT}\right)}{\tanh\left(\frac{hc\nu_{lu}}{2k_BT}\right)}[j(\nu)+j(-\nu)], \tag{8.36}$$

respectively, where h is Planck's constant, ρ_a is the density of dipoles per unit volume, E_l is the lower energy of the transition, $Q(T)$ is the partition function, k_B is Boltzmann's constant, $|\mu_{dp}|^2$ is the dipole matrix element, and $j(\nu)$ is the Fourier transform of the dipole autocorrelation function or power spectral density. On the basis of this theory, the low-frequency (i.e., <50 cm^{-1}) absorption coefficient falls off as ν^2 multiplied by the line shape function. A simple ν^2 fall-off will dominate in two cases. The first is the far red wing of an absorption band and the second is for broad line shape functions featuring very little frequency dependence throughout a band. These conditions are met for many materials of interest in the far infrared, because the absorption is dominated by intrinsic processes. Thus, a simple formula such as

$$\beta_{abs}(\nu,T) = A(T)\nu^2 \tag{8.37}$$

can be used to represent experimental data of these materials.

Based on the classical oscillator model of Eq. 8.10, the one-phonon red wing (e.g., in the limit as $\nu \rightarrow 0$) absorption coefficient becomes

$$\beta_{1p}(\nu \rightarrow 0,T) = A_{1p}(T)\nu^2 = \left(\frac{2\pi}{n(\nu=0,T)}\sum_i\frac{\Delta\epsilon_i(T)\Gamma_i(\nu,T)}{\nu_i^2(T)}\right)\nu^2. \tag{8.38}$$

Even though Eq. 8.38 comes from a phenomenological model, this extrapolation to the red wing works for many materials (see Table 8.5). In addition to the one-phonon contributions, difference bands of two and three phonons must also be included. Detailed models are extremely difficult to obtain, and thus only empirical formulas are currently used.

It is straightforward to show (see Problem 8.10) that in the high-temperature limit ($hc\nu \ll k_BT$) the n-phonon difference-band temperature dependence varies as

$$\beta_{np}(\nu,T) = A_{np}\left(\frac{T}{T_0}\right)^{n-1}\nu^2. \tag{8.39}$$

Thus, experimental data in this high-temperature limit can be represented by the formula

$$\beta_{abs}(\nu,T) = \sum_n \beta_{np}(\nu,T), \tag{8.40}$$

Table 8.5 The Far-infrared Absorption Coefficient Parameters for $T_0 = 295$ K

Material		$A(T_0)$ [cm²]	$A_{1p}(T_0)$ [cm²]	A_{2p} [cm²]	A_{3p} [cm²]
MgO		—	6.1×10^{-4}		
SiO₂	o-ray	1.07×10^{-4}	8.9×10^{-5}		
	e-ray	8.2×10^{-5}	1.39×10^{-4}		
Al₂O₃	o-ray	9.15×10^{-4}	2.2×10^{-4}	4.7×10^{-4}	2.2×10^{-4}
	e-ray	1.28×10^{-3}	8.6×10^{-4}		
Y₂O₃		2.1×10^{-3}	8.4×10^{-4}		
MgAl₂O₄		2.2×10^{-3}	1.6×10^{-3}		
ALON		1.1×10^{-3}	—		
ZnS		5.8×10^{-4}	9.8×10^{-4}		
NaCl		1.2×10^{-2}	3.0×10^{-3}	9.0×10^{-3}	

and using Eqs. 8.38 and 8.39 the absorption coefficient becomes

$$\beta_{abs}(\nu,T) \underset{\nu \to 0}{=} \left[\frac{2\pi}{n(0,T)} \sum_i \frac{\Delta\epsilon_i(T)\Gamma_i(\nu,T)}{\nu_i^2(T)} + A_{2p}\frac{T}{T_0} + A_{3p}\left(\frac{T}{T_0}\right)^2 \right]\nu^2 \qquad (8.41)$$

$$= A(T)\nu^2.$$

Based on Eq. 8.41, the far-infrared absorption coefficient increases with increasing temperature and the frequency squared. This frequency dependence is demonstrated for the ordinary ray of sapphire and quartz in Fig. 8.10a. Temperature-dependent data is needed to determine the contributions from two-phonon and three-phonon difference bands. Figure 8.10b compares experimental data for sapphire to the model based on the parameters given in Table 8.5 and Eq. 8.41. A good fit is obtained from above 200 K to 1000 K for a variety of wave numbers. The fact that the absorption coefficient does not go to zero as the temperature goes to zero is a clear indication of the existence of the one-phonon red wing. The one-phonon red wing is frequently ignored in interpreting far-infrared absorption data, and this is not correct. Extrapolation to lower frequencies more typical of millimeter-wave frequencies works reasonably well at room temperature. However, the temperature dependence may change because three-phonon contributions will be greater at frequencies below two-phonon absorption than this simple model represents. This fact is demonstrated in Fig. 8.10; the model underpredicts the experimental absorption coefficients at 50 cm⁻¹ at elevated temperatures, Whereas the higher frequency curves show good agreement at high temperature.

The absorption coefficient also increases with increasing temperature at the infrared edge of transparency above the Debye temperature. This region is dominated by multiphonon sum bands. Fortunately, in this case, there are theoretical models that accurately characterize the absorption loss, and one such model only requires a few material-dependent parameters.

There are several models that have been developed to describe multiphonon absorption. Criteria of simplicity, minimum number of parameters, and an exact solution to the Schrödinger equation for an anharmonic potential that allows general applicability have led to models based on the Morse interatomic potential, which (recall from Chapter 3) is given by

$$V(r) = -D_0 + D_0 \{1 - \exp[-a(r - r_e)]\}^2.$$
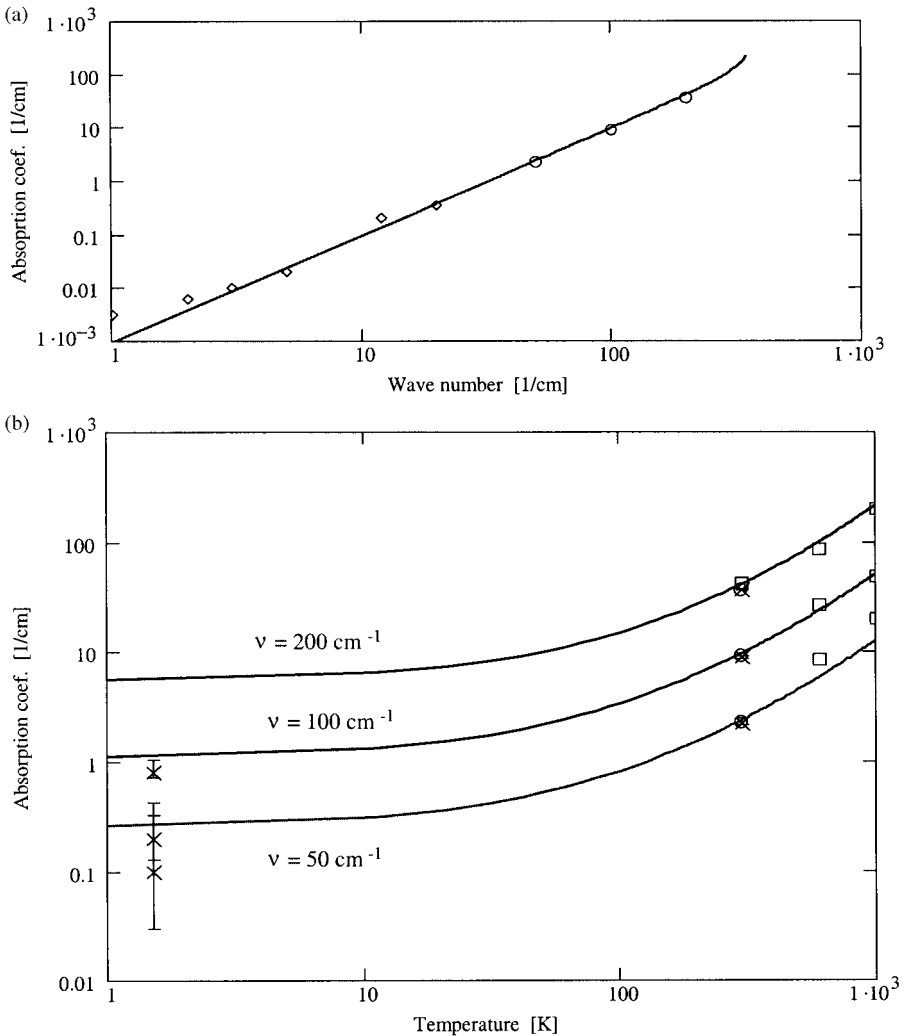
Fig. 8.10 Comparison of experimental data with the JHU/APL model for the far-infrared absorption coefficient as a function of (a) frequency and (b) temperature, for the ordinary ray of Al_2O_3.

D_0 is the dissociation energy, r_e is the location of the equilibrium position, $a = \omega_0 \left(\mu'/2D_0\right)^{1/2}$, ω_0 is the fundamental lattice-vibration frequency, and μ' is the reduced mass. The potential is plotted in Fig. 8.11. Both classical and quantum-mechanical models exist. The Morse potential includes anharmonic effects to all orders. These characteristics make this model much simpler than others. The strong anharmonic nature of the true potential for most materials means that the harmonic-oscillator perturbational approaches have questionable validity and require major correction factors.
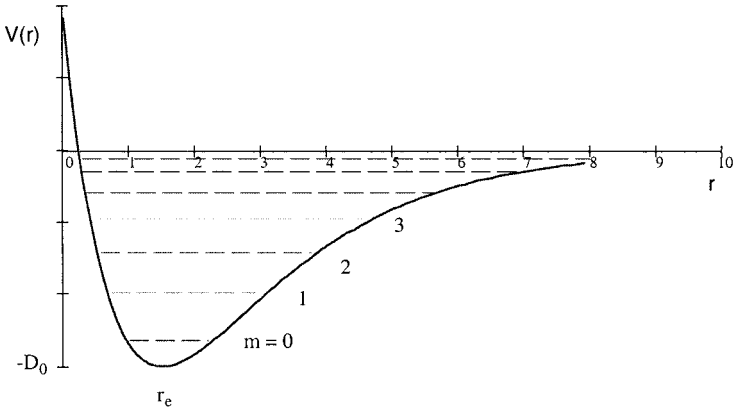
Fig. 8.11 Energy diagram of vibration energy level structure for the Morse potential as a function of intermolcular separation [Å].

A brief discussion of the quantum-mechanical Morse-potential multiphonon model is presented here. Assumptions used in the model, besides use of the Morse potential, are as follows:

1. A single generalized dissociation energy is sufficient.
2. No impurities and defects are considered, that is, only intrinsic properties are of interest.
3. Phonon density-of-state functions quickly approach the Gaussian form dictated by the central-limit theorem as the order of the harmonic increases.

The solution of the stationary-state Schrödinger wave equation using the Morse potential produces the following energy eigenvalues (recall from Chapter 3)

$$E_m = \hbar\omega_0 \left[\left(m + \frac{1}{2} \right) - \frac{1}{j'} \left(m + \frac{1}{2} \right)^2 \right],$$

where m is an integer, $m = 0, 1, 2, 3, \ldots$, $m_{max} \leq \frac{1}{2}(j' - 1)$, $\hbar = h/(2\pi)$, and $j' = 4D_0/(\hbar\omega_0)$.

Based on Eqs. 8.34-8.36 the absorption coefficient β_{abs} for a single oscillator as a function of temperature T and wave number ν is

$$\beta_{abs}(\nu, T) = \frac{8\pi^3 \rho \nu}{3hQ(T)n} \tanh\left(\frac{hc\nu}{2k_B T} \right) \sum_{n=1}^{m_{max}} \sum_{m=0}^{m_{max}-n} e^{-E_m/k_B T} |\mu_{dp,nm}|^2 j(\nu, \nu_{nm}), \quad (8.42)$$

where

$$\nu_{nm} = \frac{E_{n+m} - E_m}{hc} = \nu_0 \left[n - \frac{1}{j}(n^2 + 2nm + n) \right] = N\nu_0. \quad (8.43)$$

n represents the number of vibrational quanta or the number of phonons in the transition and can not exceed m_{max}. Thus transitions originate from an initial state m. The transition matrix element for the Morse potential is given by Eq. 5.87. For dominantly ionic bond materials, dissociation energy is large, thus $m \ll j'$ (i.e., below the material melting temperature) is generally true. Applying this approximation, then the dipole transition matrix element as given by Eq. 5.87 reduces to

$$|\mathbf{\mu}_{dp,nm}|^2 \approx \frac{q^2 h}{8\pi^2 c v_0 \mu'} \frac{(m+n)!}{m! n^2 j'^{(n-1)}}. \tag{8.44}$$

Substituting the above result into Eq. 8.42, we obtain the single oscillator absorption coefficient

$$\beta_{abs}(v,T) = K \frac{v \tanh\left(\frac{hcv}{2k_B T}\right)}{v_0 Q'(T)} \sum_{n=1}^{m_{max}} \frac{j'^{-(n-1)}}{n^2} \sum_{m=0}^{m_{max}-n} \frac{(m+n)!}{m!} e^{-\gamma M} j(v - v_{nm}), \tag{8.45}$$

where the following parameter substitutions have been made

$$Q'(T) = \sum_{m=0}^{m_{max}} \exp(-\gamma M), \gamma = \frac{hcv_0}{k_B T}, K = \frac{\pi \rho q^2}{3c\mu' n} \quad \text{and} \quad M = m\left(1 - \frac{1}{j'}\right) - \frac{m^2}{j'}.$$

Note   In the classical or continuum limit, where $j' \to \infty$ (that is $hcv \ll 4D_0$), and T large ($\gamma \ll 1$), the absorption coefficient at integer multiples of the fundamental oscillator frequency reduces to

$$\beta_{abs}(nv_0, T) \approx Kn! \left(\frac{k_B T}{4D_0}\right)^{n-1} j(0), \tag{8.46}$$

which agrees with the classical result (Ref. 8.24). Therefore, for high temperature the multiphonon sum band absorption coefficient follows the same power law as for multiphonon difference bands.

The model at this point represents a single oscillator without considering band structure created by many closely spaced oscillators in a lattice. As discussed in Chapter 3, the bringing together of many oscillators broadens the energy level structure into a continuum of states. The spectral shape of these vibrational bands is specified by the vibrational density-of-states function. The net absorption coefficient, $\beta_{abs,net}$, for a solid is the integration of the individual oscillator absorption coefficient, β_{abs}, over all appropriately weighted oscillators as given by the n-phonon vibrational density-of-states,

$$\beta_{abs,net}(v,T) = \sum_{n=1}^{m_{max}} \int_0^\infty dv_0 S_n(v_0,T) g(v, N v_0) \rho_n(N v_0). \tag{8.47}$$

Following the development of Boyer et al. (Ref. 8.29), the transition line shape function is considerably narrower than the vibrational density-of-states distribution and can

be approximated by a Dirac-delta function sum (e.g., $j(v, Nv_0) = \delta(v - Nv_0) + \delta(v + Nv_0)$). Evaluating the integral leads to the following fundamental result:

$\beta_{abs,net}(v, T) =$

$$K \tanh\left(\frac{hcv}{2k_BT}\right) \sum_{n=1}^{m_{max}} \frac{\rho_n(v) + \rho_n(-v)}{n^2 Q'(T)} \sum_{m=0}^{m_{max}-n} \frac{(m+n)!}{m!} \frac{\exp\left(-\frac{hcvM}{k_BTN}\right)}{j'^{(n-1)}}, \quad (8.48)$$

where

$$Q'(T) = \sum_{m=0}^{m_{max}} \exp\left(-\frac{hcvM}{k_BTN}\right), \quad j'(v) = \frac{2D_0n}{hcv}\left[1 + \sqrt{1 - \frac{hcv(n+1)}{nD_0}}\right],$$

$\rho_n(v)$, the n-phonon density-of-states, is given by

$$\rho_n(v) = \int_0^\infty dv' \rho_{n-1}(v')\rho_1(v - v'). \quad (8.49)$$

The n-phonon density-of-states function is determined by an n-fold convolution of the one-phonon density-of-states. In terms of the individual n-phonon absorption coefficients in standard form, the net absorption coefficient is

$$\beta_{abs,net}(v, T) = \sum_{n=1}^{m_{max}} \beta_{abs,n}(v, T) = \sum_{n=1}^{m_{max}} S_n(v, T)[\rho_n(v) + \rho_n(-v)], \quad (8.50)$$

where the n-phonon band strength is

$$S_n(v, T) = K \tanh\left(\frac{hcv}{2k_BT}\right) \frac{1}{n^2 Q'(T)} \sum_{m=0}^{m_{max}-n} \frac{(m+n)!}{m!} \frac{\exp\left(-\frac{hcvM}{k_BTN}\right)}{j'^{n-1}}.$$

The n-phonon density-of-states function, $\rho_n(v)$, is the probability of finding n-phonons in the lattice whose energies add up to hcv. It is required that this function be normalized according to

$$\int_0^\infty \rho_1(v) \, dv = 1. \quad (8.51)$$

Using Eq. 8.49, it can be shown that all $\rho_n(v)$ values normalize to unity. As n increases, if the vibrational modes are reasonably close together, $\rho_n(v)$ rapidly becomes Gaussian. This is a manifestation of the central-limit theorem. (For sapphire, even $\rho_2(v)$ can be somewhat approximated by a Gaussian profile.) Based on the results of Boyer et al. (Ref. 8.29), Sparks and Sham (Ref. 8.30), and the asymptotic expansion of the central-limit theorem, $\rho_n(v)$ can be approximately represented by the form

$$\rho_n(v) = \frac{1}{\sigma'_n\sqrt{2\pi}}\left[1 - \frac{\alpha_3}{\sqrt{n}}(3x - x^3)\right]\exp\left(-\frac{x^2}{2}\right); \quad n \geq 3, \quad (8.52)$$

where

$$x = \frac{v - n\alpha_1 v_{\max}}{\sigma'_n}. \tag{8.53}$$

The standard deviation of the distribution is

$$\sigma'_n = \alpha_2 v_{\max} \sqrt{n}. \tag{8.54}$$

The coefficients α_1, α_2, and α_3 are determined from the moments of the density-of-states distribution, as defined by

$$\alpha_1 = \frac{\langle v \rangle}{v_{max}}, \quad \alpha_2 = \frac{\left(\langle v^2 \rangle - \langle v \rangle^2 \right)^{1/2}}{v_{max}}, \tag{8.55a}$$

and

$$\alpha_3 = \frac{\langle v^3 \rangle - 3\langle v^2 \rangle \langle v \rangle + 2\langle v \rangle^3}{6 \left(\langle v^2 \rangle - \langle v \rangle^2 \right)^{3/2}}, \tag{8.55b}$$

based on the standard formula for the spectral moments

$$\langle v^r \rangle = \int_0^\infty dv \rho_1(v) v^r, \quad r = 1, 2, 3. \tag{8.56}$$

Here v_{max} is the maximum fundamental lattice-vibration frequency. It is taken to be the maximum longitudinal-optical-mode frequency of the crystal. v_{max} is experimentally determined for each material from far-infrared reflectance spectra. A derivative reflection-spectroscopy technique, as described in Chapter 6, can be used to determine the values in a straightforward manner. This approach works for dominantly ionic bond materials such as the alkali halides, oxides, and fluorides.

The shape of the distribution is determined by three parameters: α_1, the distribution mean normalized by v_{max}; α_2, the distribution standard deviation normalized by v_{max}; and α_3, the distribution skewness divided by 6. The parameters α_1, α_2, and α_3 are directly determined from $\rho_1(v)$. In the case of sapphire, an approximate density-of-states function is given by Billard et al. (Ref. 8.32), as illustrated in Fig. 8.12. The results are $\alpha_1 = 0.537$, $\alpha_2 = 0.213$, and $\alpha_3 = 0.052$. However, in practice, the α_2 parameter requires modification, because the true phonon distribution function, $\rho_n(v)$, goes to zero at nv_{max}. Thus, the value for α_2 is too large and can artificially produce steps in the net absorption coefficient caused by the assumption of a Gaussian phonon distribution function. Based on sapphire absorption data, a simple but effective empirical correction is used. By letting $\alpha_2 = 0.153$ and multiplying the strength by N (i.e., $S_n \rightarrow NS_n$) yields an increased slope in the net β_{abs} caused by the narrower $\rho_n(v)$. In this way, a smooth and realistic representation of the absorption coefficient is obtained. Because material transparency typically begins with the three-phonon band, a simple rule for the edge of transparency of ionic materials can be obtained from the density-of-states parameters according to
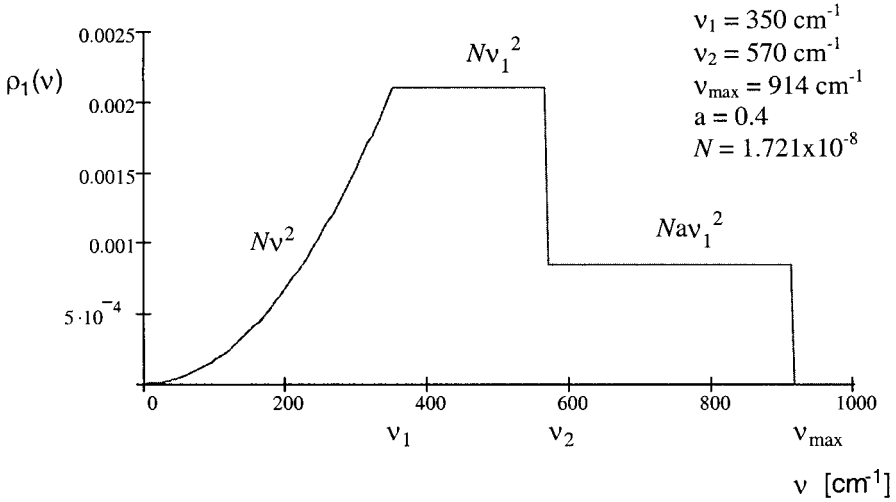
Fig. 8.12 Approximate one-phonon density-of-states function for sapphire. (N is a normalization factor.)

$$\nu_{trans} \approx 3\alpha_1 \nu_{\max}. \tag{8.57}$$

The statistical parameters for the density-of-states function varies somewhat for different classes of materials. The crystalline and polycrystalline oxides and fluorides use the same values as sapphire (see Appendix 4). The alkali-halides require a slightly different set of numbers; $\alpha_1 = 0.530, \alpha_2 = 0.145$, and $\alpha_3 = 0.052$. Unlike other oxides, quartz and fused silica feature well separated one-phonon frequencies, and in this case the statistical parameters are $\alpha_1 = 0.510, \alpha_2 = 0.140,$ and $\alpha_3 = 0.052$.

Figure 8.13 illustrates the structure of $\beta_{abs,net}(\nu, T)$ in terms of $\beta_{abs,n}(\nu, T)$, the absorption coefficient of a single n-phonon process. The individual $\beta_{abs,n}$ values are nearly Gaussian in shape, yet the sum produces a nearly exponential curve for $\beta_{abs,net}$, as commonly observed in experiment. Based on this observation, the following empirical formula has been used by Deutsch to represent experimental data on a variety of optical materials:

$$\beta_{abs}(\nu) = A \exp(-a\nu), \tag{8.58}$$

where A and a are material-dependent parameters. This model does not represent the temperature dependence, since more complete models, such as previously developed in this Section, are needed to adequately accomplish this.

Now the temperature dependence of the multiphonon sum-band edge can be understood in a straightforward way. From very low to roughly room temperature, the absorption coefficient is nearly constant, because the vast majority of oscillators are in the ground state ($m = 0$). Thus, the Boltzmann factors are temperature insensitive. At high temperature, when the upper levels achieve enough population according to a Boltzmann distribution, then photon absorption for $m > 0$ becomes important. Also, the dipole
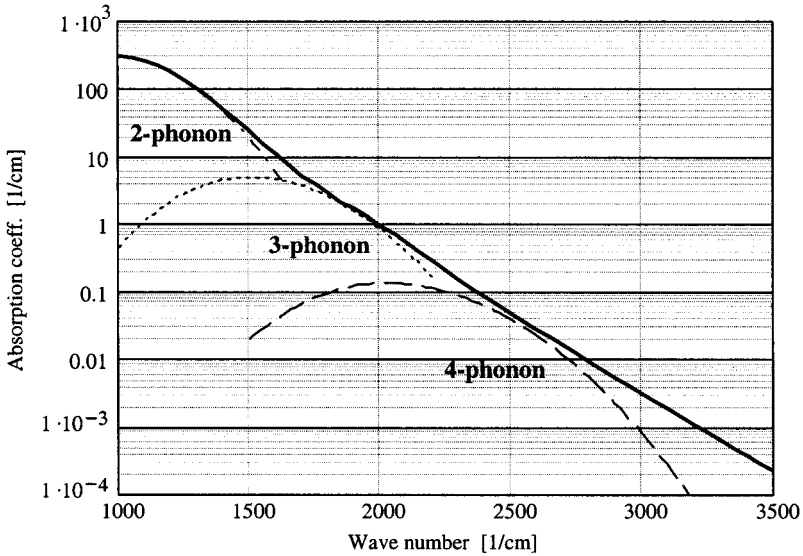
Fig. 8.13 *n*-Phonon absorption bands for room-temperature sapphire (*o*-ray) absorption coefficient at room temperature.

matrix element increases with increasing *m*. Thus, the absorption coefficient increases with increasing temperature because the Boltzmann distribution increases the population of the upper vibrational states and absorption from higher vibrational states ($m > 0$) increases in strength as *m* increases. Figure 8.14 illustrates this point by comparing model predictions against experimental data for Al_2O_3, and NaCl. Figure 8.15 illustrates the comparison of the experimental and model frequency dependence. Good agreement is obtained. This multiphonon sum-band model has been successfully applied to a variety of window materials, and Appendix 4 lists model parameters for many such optical materials. Three parameters, besides the phonon density-of-states statistical parameters, are needed to specify a material; K the scaling constant representing the dipole density, D_0 the dissociation energy, and ν_{max} the maximum longitudinal-optical-mode frequency. All of these parameters can be determined from room-temperature measurements. Thus the model provides a means of predicting $\beta_{abs}(\nu, T)$ as a function of temperature for a material with known $\beta_{abs}(\nu, T_0)$ at a fixed temperature T_0.

Although the above figures suggest excellent agreement for a wide variety of materials, this multiphonon sum model has limitations. The first is illustrated in Fig. 8.16 for quartz. In this case, the density-of-states function has structure in the two- and three-phonon regions and is not approximated by the Gaussian approximation with sufficient accuracy until at least the four-phonon absorption band. A reflection spectrum of quartz *o*-ray is shown in Fig. 8.16a. It shows a wide separation between two strong one-phonon bands. Therefore the *n*-phonon density-of-states function requires more convolutions or higher order phonon absorption to obtain a near Gaussian form.

Another limitation of the multiphonon sum band model is that it works only for materials which are dominantly composed of ionic bonds. Many materials of optical
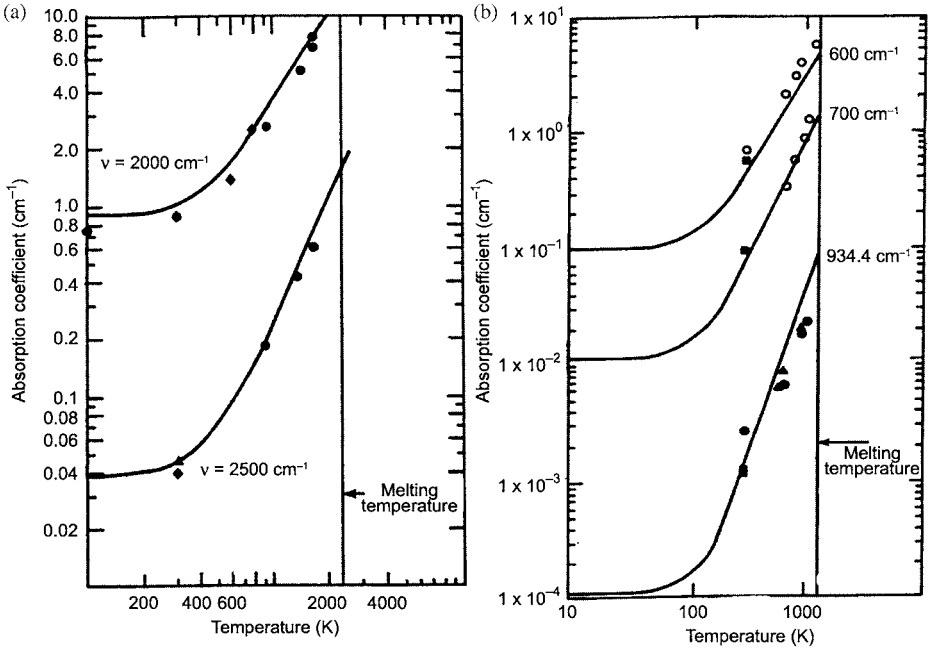
Fig. 8.14 (a) Temperature dependence of multiphonon absorption at fixed wave numbers for Al_2O_3 (▲ Deutsch, Ref. 8.35; • Billard et al., Ref. 8.32; and ♦ Thomas et al., Ref. 8.34). (b) Temperature dependence of the multiphonon absorption coefficient at fixed wave numbers for NaCl (■ Boyer et al., Ref. 8.29; • Namjoshi and Mitra, Ref. 8.13; Deutsch, Ref. 8.35; ○ Barker, Ref. 8.36 and ▲ Harrington and Hass, Ref. 8.37).
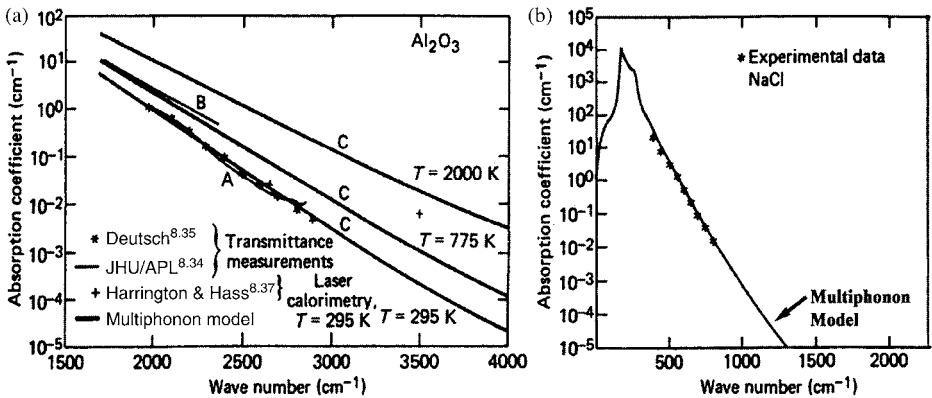
Fig. 8.15 (a) Frequency dependence of the multiphonon absorption coefficient at three fixed temperatures for sapphire ordinary-ray (Ref. 8.34). Curves A and B are experimental for $T = 295$ and 775 K, respectively. The curves marked C are generated by the multiphonon model. (b) Frequency dependence of the one-phonon and multiphonon absorption coefficient at room temperature for NaCl.
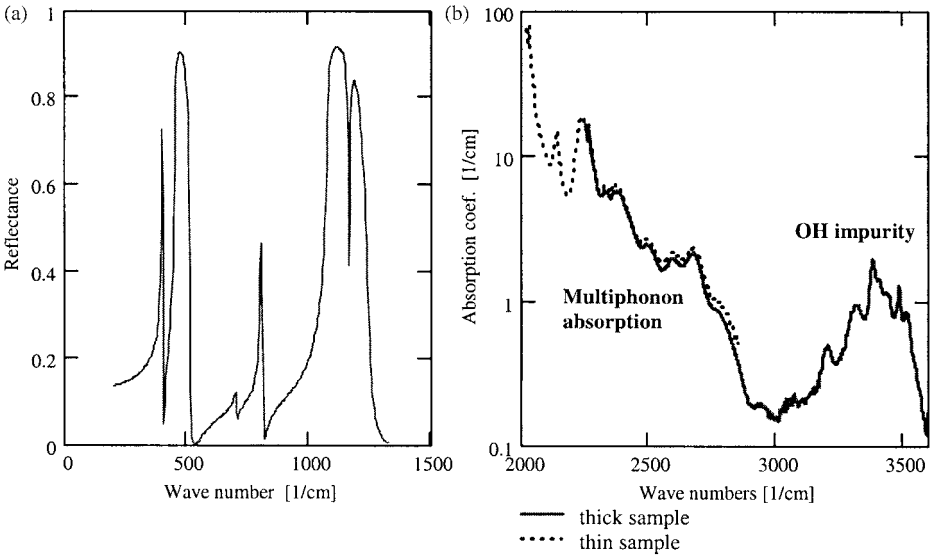
Fig. 8.16 Room-temperature (a) far-infrared reflection spectrum and (b) midwave absorption coefficient for quartz *o*-ray.

importance are composed of mixed ionic and covalent bonds or are purely covalent. In this case, the covalent-bond vibrational modes are typically too weak to show up in a reflection spectrum and thus the density-of-states function cannot be fully determined, because, as previously mentioned, ν_{max} cannot be correctly found from a reflection spectrum only. This is the case for mixed-bond materials such as ZnS, ZnSe, and GaAs, and purely covalent-bond materials such as diamond, silicon, and germanium.

Some insight into how this problem may be overcome can be obtained from the infrared absorption spectrum of diamond, as illustrated in Fig. 8.17. Diamond is purely covalent, with no fundamental infrared active vibrational modes. Intrinsic diamond is completely transparent below the bandgap except for second, third, and higher order multiphonon absorption bands. The two-phonon cutoff ($2\nu_{max}$) is twice the fundamental Raman frequency at 1332 cm^{-1}. Also, to obtain a fit to the experimental data, the phonon density-of-states function required considerable modification relative to the other ionic materials studied. For the optical density-of-states, $\rho_{O2}(\omega)$, the Gaussian statistical parameters were significantly modified to $\alpha_1 = 0.814, \alpha_2 = 0.12$, and $\alpha_3 = 0.05$. However, the two-phonon red wing is poorly modeled by this density-of-states function as indicated in Fig. 8.17. Diamond absorptance near 10 μm is of particular interest because many infrared sensors operate at this atmospheric window. Evidence indicates that the absorption in this region is caused by two-phonon acoustic–acoustic interactions. Normally, pure acoustic multiphonon absorption would not be measurable because it is obscured by strong one-phonon optical mode absorption. Diamond has very high acoustic frequencies owing to its strong bonds, and the lack of fundamental absorption unmasks the pure acoustic contribution. This contribution is modeled by applying a Debye acoustic single-phonon density-of-states distribution, $\rho_{a1}(\omega)$, as
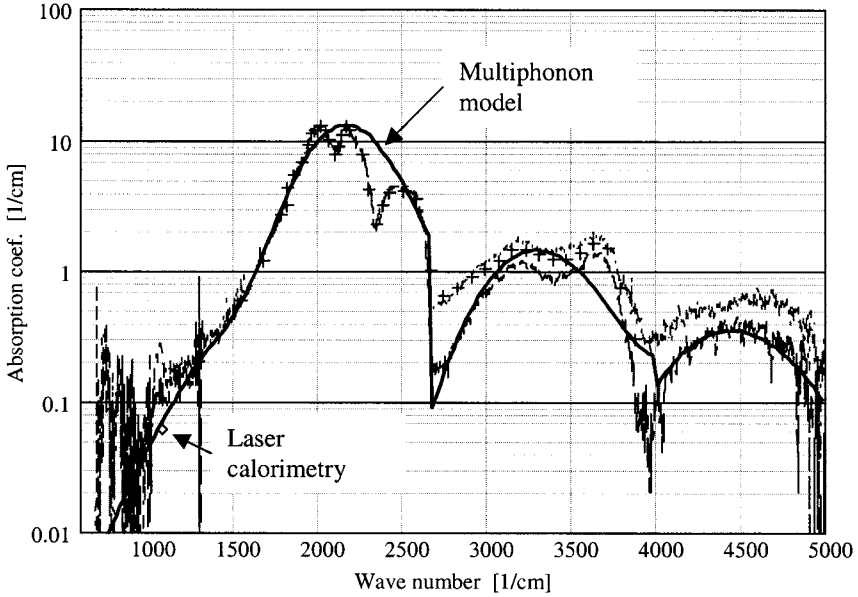
Fig. 8.17 Comparison of experimental and theoretical multiphonon absorption for Type IIa diamond at $T = 295$ K. (Solid line – multiphonon model, dashed line – experimental data: $\diamond$ – laser calorimetry measurements, and + – experimental data from HOC II, Palik, Ref. 8.58.)

given by Eq. 3.140. Higher order (nth) acoustic phonon distributions are computed by convolving this distribution with the $(n-1)$-phonon distribution as specified by Eq. 8.49. For the case of the two-phonon acoustic distribution function, $\rho_{a2}(\omega)$, the result is

$$\rho_{a2}(\omega) =$$

$$\begin{cases} \frac{9}{\omega_{\max}^6} \left\{ \frac{\omega^2}{3} \left[\omega_{\max}^3 - (\omega - \omega_{\max})^3 \right] - \frac{\omega}{2} \left[\omega_{\max}^4 - (\omega - \omega_{\max})^4 \right] \right. \\ \qquad \left. + \frac{1}{5} \left[\omega_{\max} - (\omega - \omega_{\max})^5 \right] \right\} & \omega_{\max} \leq \omega \leq 2\omega_{\max,} \\ \frac{0.3\omega^5}{\omega_{\max}^6} & 0 \leq \omega \leq \omega_{\max}. \end{cases}$$

$$(8.59)$$

The maximum acoustic frequency of diamond, $\omega_{a,max} = 1183$ cm^{-1}, is used for the acoustic density-of-states cutoff frequency. The Gaussian function is used for the optical phonon density-of-states. Combining these two functions and requiring the normalization condition of Eq. 8.51, the resulting net two-phonon density-of-states function is

$$\rho_2(\omega) = 0.91\rho_{o2}(\omega) + \frac{1}{9}\rho_{a2}(\omega). \qquad (8.60)$$

The density-of-states function for $n \geq 3$ is only composed of the optical contributions and is a Gaussian function.

The multiphonon band strength for diamond requires the full solution of the transition matrix element as given by Eq. 5.87. This is because the dissociation energy is small and the maximum lattice vibration frequency is large, making the approximation used for ionic materials invalid. This improves the model representation of the $n \geq 3$ multiphonon absorption bands and the temperature dependence in general. Figure 8.17 illustrates the agreement between experimental data on natural type IIa diamond and this multiphonon model at room temperature.

The two-phonon acoustic contribution, although weak, is important because it lies in the 8–12 μm atmospheric window frequently used by infrared sensors. Note that our selected value of 1183 cm^{-1} is consistent with the highest observed acoustic frequency for diamond, which is 1185–1191 cm^{-1} (longitudinal acoustic frequency at the X critical point). Diamond uniquely offers the opportunity to study the two-phonon red wing. Weak higher order multiphonon absorption bands are important for high-power diamond laser windows. The agreement between theory and experiment validates the existence of the four-phonon band in diamond.

The multiphonon sum band model can also be applied to refractive index modeling at frequencies near the two- and three-phonon bands. Although room-temperature multiphonon contributions to the real index are typically very small compared with one-phonon contributions, they are important for two cases in the infrared: 1) when the optical propagation path through a material requires knowledge of the refractive index beyond two decimal places and 2) when a material is heated to high temperatures. In the first case, the cumulative effect of the multiphonon contributions to the index over a large optical distance can be significant. In the second case, the magnitude of the higher order multiphonon modes increase significantly with increasing temperature, since the temperature dependence of the nth mode is approximately T^{n-1}.

An expression for multiphonon contributions to the real part of the index of refraction is derived using the Kramers–Krönig (Hilbert transform) relationship and the previously described multiphonon absorption model in a straightforward manner. Based on Eqs. 8.50 and 3.34, the multiphonon refractive index, $n_{mp}(v,T)$, can be expressed as

$$n_{mp}(v,T) - 1 = \frac{1}{2\pi^2} \sum_{n=1}^{m_{max}} P \int_0^\infty \frac{S_n(v',T)\left[\rho_n(v') + \rho_n(-v')\right]}{v'^2 - v^2} \, dv'. \qquad (8.61)$$

Although $\rho_n(v)$ can vary significantly for different values of n (i.e., different multiphonon modes), the frequency dependence of $S_n(v,T)$ for a given n is most important in the vicinity of the peak of the density-of-states function and is relatively constant in frequency over that region. By neglecting the frequency dependence of S_n, and evaluating it at the peak of the n-phonon density-of-states function, an approximate expression for the real index can be obtained and is given by

$$n_{mp}(v,T) - 1 \approx \frac{1}{2\pi^2} \sum_{n=1}^{m_{max}} S_n(\overline{v}_n,T)\delta_n(v), \qquad (8.62)$$

where

$$\delta_n(v) = P \int\limits_{-\infty}^{\infty} \frac{\rho_n(v')}{v'^2 - v^2}\, dv' \tag{8.63}$$

and $\bar{v}_n = n\alpha_1 v_{\max}$. The dispersion profile, $\delta_n(v)$, is the Hilbert transform of the density-of-states function. The skewness factor in the phonon density-of-states function, given by Eq. 8.52, is a minor correction, important for the absorption model but, not necessarily for a refraction model. Therefore, the phonon density-of-states function is simplified to a Gaussian function,

$$\rho_n(v) \approx \frac{1}{\sigma_n'\sqrt{2\pi}} e^{\frac{-x^2}{2}} \tag{8.64}$$

where

$$x = \frac{v - \bar{v}_n}{\sigma_n'} \quad \text{and} \quad \sigma_n' = \alpha_2 v_{\max}\sqrt{n}.$$

Substituting the above density-of-states function into Eq. 8.63, we obtain result

$$\delta_n(y) = \frac{1}{2\sigma_n'^2\sqrt{\pi}} P \int\limits_{-\infty}^{\infty} dt \frac{e^{-(t - w_n)^2}}{t^2 - y^2}, \tag{8.65}$$

where the following variable changes have been made:

$$w_n = \frac{\bar{v}_n}{\sqrt{2}\sigma_n'}, \quad y = \frac{v}{\sqrt{2}\sigma_n'}, \quad \text{and} \quad t = \frac{v'}{\sqrt{2}\sigma_n'}.$$

To solve Eq. 8.65, it is helpful to rewrite the Gaussian function in integral form, as given by

$$e^{-(t - w_n)^2} = \frac{2}{\sqrt{\pi}} \int\limits_{0}^{\infty} ds\, e^{-s^2} \cos\left[2s(t - w_n)\right]$$

and also apply the trigonometric identity for angle differences,

$$\cos\left[2s(t - w_n)\right] = \cos(2st)\cos(2sw_n) + \sin(2st)\sin(2sw_n).$$

After some straightforward algebra, the multiphonon dispersion profile now simplifies to

$$\delta_n(y) = \frac{-1}{\sigma_n'^2 y} \int\limits_{0}^{\infty} ds\, e^{-s^2} \cos(2sw_n)\sin(2sy). \tag{8.66}$$

This result can be reduced to a tractable form by applying the trigonometric identity

$$2\cos(2sw_n)\sin(2sy) = \sin[2s(y - w_n)] + \sin[2s(y + w_n)].$$

The multiphonon dispersion profile finally becomes

$$\delta_n(y) =$$

$$\frac{-1}{2y\sigma_n'^2}\left[\int_0^\infty ds\, e^{-s^2}\sin[2s(y + w_n)] + \text{sgn}(y - w_n)\int_0^\infty ds\, e^{-s^2}\sin(2s|y - w_n|)\right]. \quad (8.67)$$

The integrals in the dispersion profile are in the form of Dawson integrals, as given by

$$D(a) = \int_0^\infty ds\, e^{-s^2}\sin(2sa). \quad (8.68)$$

Polynomial representations and asymptotic solutions exist for the Dawson integral and are presented in Appendix 2. In terms of the Dawson integral, and substituting back to wave numbers, the multiphonon dispersion profile becomes

$$\delta_n(\nu) = \frac{-1}{\sqrt{2}\sigma_n'\nu}\left[D\left(\frac{\nu + \overline{\nu}_n}{\sqrt{2}\sigma_n'}\right) + \text{sgn}(\nu - \overline{\nu}_n)D\left(\frac{|\nu - \overline{\nu}_n|}{\sqrt{2}\sigma_n'}\right)\right]. \quad (8.69)$$

Substituting this result into Eq. 8.62, we obtain the solution for the multiphonon refractive index, $n_{mp}(\nu,T)$,

$$n_{mp}(\nu,T) - 1 \approx \frac{-\sqrt{2}}{4\pi^2\nu}\sum_{n=1}^{m_{max}}\frac{S_n(\overline{\nu}_n,T)}{\sigma_n'}\left[D\left(\frac{\nu + \overline{\nu}_n}{\sqrt{2}\sigma_n'}\right) + \text{sgn}(\nu - \overline{\nu}_n)D\left(\frac{|\nu - \overline{\nu}_n|}{\sqrt{2}\sigma_n'}\right)\right].$$

$$(8.70)$$

The initial assumptions of a spectrally constant $S_n(\nu,T)$ and simple Gaussian density of vibrational states must be tested. This is accomplished by applying Eqs. 2.54b (for $g(\omega) \approx \delta(\omega)$), 3.30, 3.36a, and 3.36b. It is required that

$$S_n(\overline{\nu}_n, T) = \int_0^\infty d\nu \beta_{abs,n}(\nu,T), \quad \delta(0) = \frac{1}{\overline{\nu}_n^2} \quad \text{and} \quad \int_0^\infty d\nu\, \delta(\nu) = 0.$$

The first condition is met with reasonable accuracy. However, the dispersion formula does not satisfactorily satisfy the last two requirements for the case sapphire because of approximations made at the beginning of the derivation. Deviations on the order of 10% exist. The two- and three-phonon density-of-states are not Gaussian, and this has resulted in a slightly incorrect dispersion profile. An empirical correction is made that
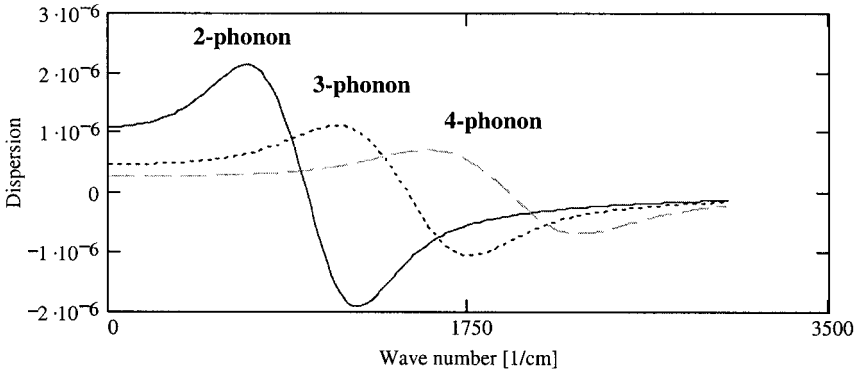
Fig. 8.18 Multiphonon anomalous dispersion curves, $\delta_n(\nu)$ versus wave number calculated for the second-, third-, and fourth-order phonon modes.

significantly improves the agreement with the above requirements by multiplying the dispersion profile, $\delta_n(\nu)$, by the following function:

$$0.09 \tanh\left[(\nu - \overline{\nu}_n)0.01\right] + 1.$$

Now agreement with the above conditions is within a few percent.

The corrected multiphonon index of refraction is a summation of nth order phonon modes. The anomalous dispersion curves for the multiphonon model, as given by Eq. 8.69 times the correction factor, have been calculated for the ordinary ray of sapphire, and are shown in Fig. 8.18. The dispersion profile for each n-phonon process from $n = 2$ to 4 is illustrated. As expected, the profile broadens as n increases. The net multiphonon refractive index can be computed based on Eq. 8.70, and is illustrated in Fig. 8.19 for
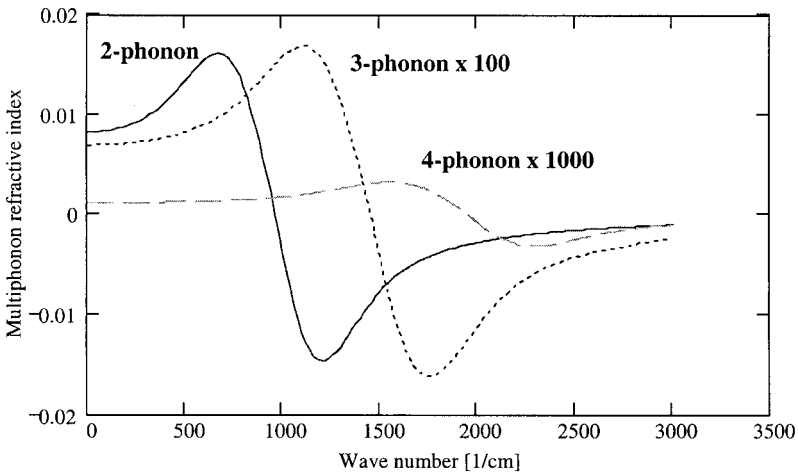
Fig. 8.19 Multiphonon contributions ($n = 2$- through 4-phonon modes) to the index of refraction for sapphire (o-ray) at 295 K.

room-temperature sapphire (ordinary ray). The curve includes the contributions for $n = 2$ through 4. Only two- and three-phonon anomalous dispersions are significant because the n-phonon band strength, $S_n(\bar{v}_n, T)$, decreases rapidly for increasing n. However, since the strength increases as $T^{(n-1)}$, at very high temperatures 3- and 4-phonon contribution can become important. Thus, a complete model of the complex index of refraction as a function of temperature and frequency must include one-phonon, multiphonon, and electronic contributions.

Table 8.6 compares the real index values calculated with the Sellmeier model to the values calculated with the one-phonon/electronic model and the sum of the one-phonon and multiphonon models (see Appendix 4 for parameter values). From these results, it can be seen that the multiphonon contributions to the real index of refraction at 295 K are small but important for many design applications. (They generally affect the magnitude of the real index in the third decimal place at room temperature.) The Sellmeier model is only valid at the temperature of the data set it represents (normally room temperature). The phonon model (one and multiphonon), plus a Sellmeier model for electronic transitions, accurately represents the temperature and frequency dependence, and therefore provides a more complete representation. Table 8.6 demonstrates that the model closely matches the precision of the room-temperature Sellmeier model (± 0.00002).

Normally, absorption and refraction processes are additive in the permittivity and not in the complex index. However, because the multiphonon contributions to the complex index of refraction are comparatively small relative to first-order phonon processes, they can be directly added to the first-order complex index with good accuracy.

The intrinsic multiphonon complex index of refraction is important in determining transmittance in materials used for windows and fibers. Two- through four-phonon

Table 8.6 Comparison of Calculated Values of the Real Index of Refraction for Sapphire (o-Ray) at 295.0 K in the Spectral Region of Transparency. Values Calculated with the One-phonon/ Electronic and Multiphonon Models are Compared with Values Calculated with the Sellmeier Model (i.e., $\Delta n = n - n_{Sellmeier}$)

Frequency v [cm^{-1}]	Sellmeier Model $n_{Sellmeier}$	One-Phonon/Electronic Model		One-Phonon/Electronic and Multiphonon Model	
		n	Δn	n	Δn
1800.0	1.58807	1.5921	+0.0041	1.58814	+0.00007
1900.0	1.60774	1.6112	+0.0034	1.60778	+0.00004
2000.0	1.62402	1.6271	+0.0029	1.62403	+0.00001
2100.0	1.63768	1.6403	+0.0026	1.63768	0.00000
2200.0	1.64927	1.6516	+0.0022	1.64926	−0.00001
2300.0	1.65919	1.6612	+0.0020	1.65917	−0.00002
2400.0	1.66776	1.6696	+0.0018	1.66773	−0.00003
2500.0	1.67522	1.6768	+0.0016	1.67518	−0.00004
2600.0	1.68176	1.6832	+0.0014	1.68171	−0.00005
2700.0	1.68753	1.6888	+0.0013	1.68747	−0.00006
2800.0	1.69264	1.6938	+0.0012	1.69258	−0.00006
2900.0	1.69719	1.6983	+0.0011	1.69714	−0.00005
3000.0	1.70127	1.7023	+0.0010	1.70122	−0.00005

bands are important for window material characterization. Two- through six-phonon bands are important for optical fibers.

8.2.1.3 Transparency Near the Bandgap and Urbach's Rule

Just as in the case for infrared transparency, higher order processes are needed to represent the absorption edge below the bandgap. As discussed in Chapter 5, Urbach's rule represents the absorption coefficient below the bandgap of a material. The temperature- and frequency-dependent formula is given by Eqs. 5.146 and 5.147. Figure 8.20 illustrates the comparison of the Urbach model with experimental data on fluorides as function of frequency for a variety of temperatures. The representation is clearly quite good over a wide range of temperatures. Urbach tail model parameters are listed in Appendix 4 (Table A4.4) for a limited number of materials when experimental data is available. This model has been found to work for a wide variety of insulators and semiconductors.

8.2.1.4 Extrinsic Effects

Extrinsic optical effects are those caused by the manufacturing process. They can be categorized as structural, and as defects and impurities.

Good examples of materials with structural extrinsic properties are polycrystalline and amorphous (glass) materials. Polycrystalline materials are formed by hot-pressing a powder composed of high-purity single crystals to full density. Glasses are considered supercooled liquids. They have no long-range order and are made by fusing molten materials together and then rapidly cooling to prevent crystallization. Polycrystalline materials and glasses are easier to make in large sizes and in various shapes, than the single crystal counterpart. Therefore, they are less expensive than single crystals. High-quality optical polycrystalline and amorphous materials are commercially available. Glasses are commonly used in visible optical systems (e.g., cameras, projectors etc.).

Defects and impurities in all types of material structure affect the optical properties. Since defects and impurities are usually in very small concentrations, they only affect the absorption coefficient in local spectral regions and have virtually no effect on the refractive index. A good example of impurity absorption is hydrogen in oxides such as sapphire, quartz, spinel, etc. The hydrogen bonds to oxygen and gives rise to an extrinsic vibration band near 3 μm, which is characteristic of OH (see Table 3.2). The spectral location varies with the host material. An example of this is presented in Fig. 8.21 for yttria (Y_2O_3). (Another example for fused silica is shown in Fig. 8.23.) Because the impurity level varies from sample to sample, the strength of the impurity absorption feature varies as well. Thus each sample must be measured to determine the absorption level.

8.2.2 Amorphous Insulators: Glasses

Most commercially available optical window materials for near-infrared and visible applications are glasses. Glasses are easily shaped and finished so that component cost can be much less than crystal-based optical elements. A wide variety of optical properties are available, giving designers great flexibility in meeting the requirements for a particular application.
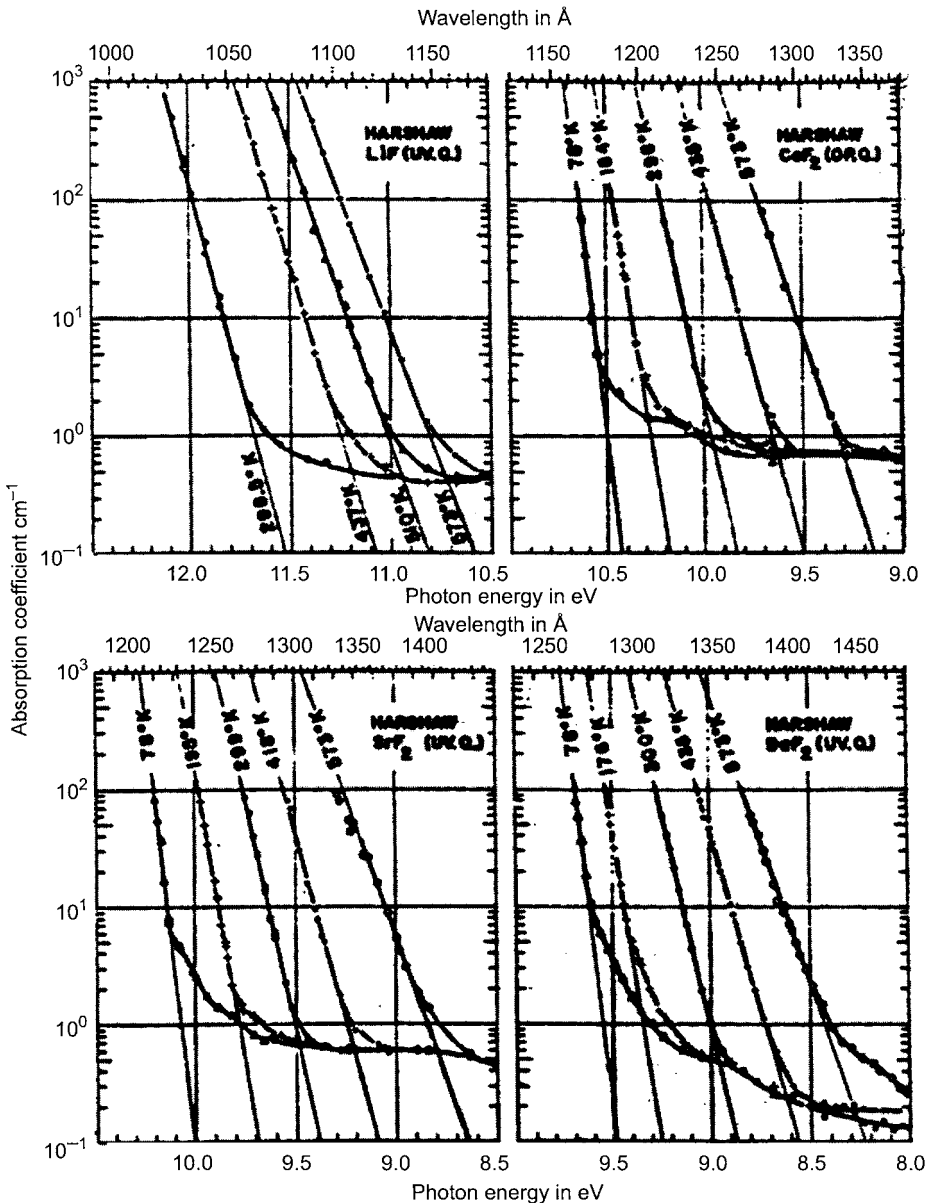
Fig. 8.20 The absorption coefficient near the bandgap of LiF, CaF$_2$, SrF$_2$, and BaF$_2$ for a variety of temperatures. The straight-line fits are the Urbach tail model and the points are experimental data (Tomiki and Miyata, Ref. 8.43, with permission).
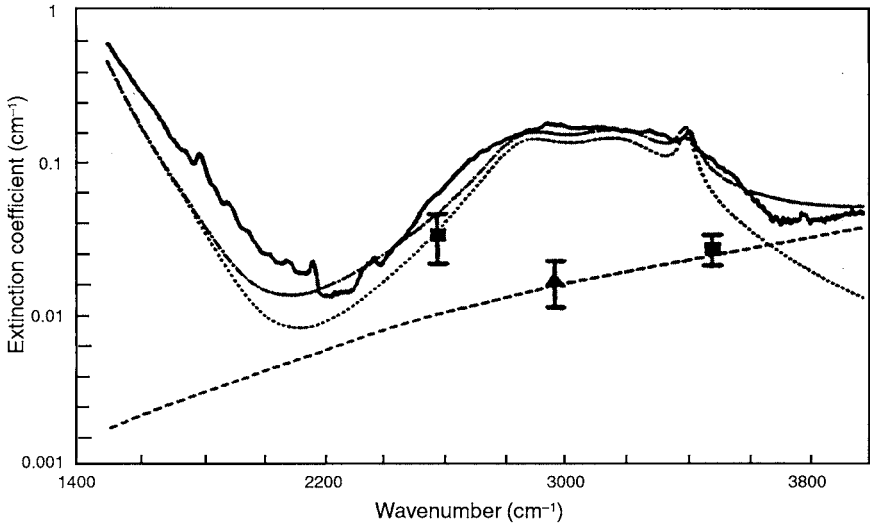
Fig. 8.21 Hydroxyl (OH⁻) impurity absorption in yttria for $T = 295$ K. The solid squares represent the absorption coefficient based on laser calorimetry data and the solid triangle represents the scatter coefficient from a laser scatterometer measurement. The solid curve is experimental data. The dashed curve is the scatter coefficient. The dash–dot curve is a model for the extinction coefficient and the dotted curve is a model for the absorption coefficient.

A glass is an amorphous solid because it lacks long-range order. But it is a special kind of amorphous material, because it is also a nonequilibrium state of matter that happens to be very stable. Glasses can be classified as high-viscosity liquids. For example, glass windows in old buildings are slightly thicker at the bottom than at the top! Another characteristic feature of a glass is that it has a transition temperature above which it abruptly changes thermodynamic properties (e.g., heat capacity, thermal expansion) from crystal-like to liquid-like quantities. This temperature is called the glass transition temperature, which is much less than the melting temperature. This represents the upper temperature limit for any application involving glass optics.

Most common glasses are composed of oxides, in particular, silicates (SiO_2), borates (B_2O_3), and phosphates (P_2O_3). Usually a variety of other oxides in minor concentration compose most glasses as well. Perhaps the most important oxide glass is fused silica. It is the main material composing most glasses, optical fibers, and desert sand. The infrared reflectance spectrum for fused silica is plotted in Fig. 8.22. Because of the lack of long-range order, the vibrational modes have considerably broadened over that of crystalline quartz (see Fig. 8.16). This tends to shift the infrared edge of transparency to higher frequencies. Figure 8.23 plots the experimental absorption coefficient and compares the multiphonon model (see Appendix 4 for the model parameters) to these results. The model is extrapolated to the near-infrared where optical fiber communication systems operate. Experimental points from a GeO_2-doped silica fiber are also shown for comparison.

The popular glass BK7 is primarily composed of borates and silicates and is classified as a borosilicate crown glass. Figure 8.24a shows infrared reflectance and transmittance spectra of BK7 glass. The spectra are similar to fused silica, indicating
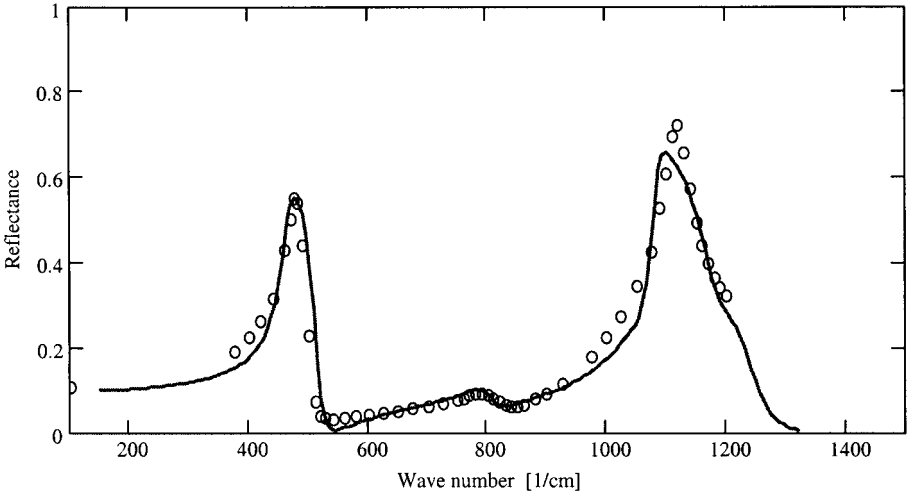
Fig. 8.22 Infrared reflectance spectrum of fused silica at $T = 295$ K ($\circ$ – experimental points, solid curve – classical oscillator model fit).
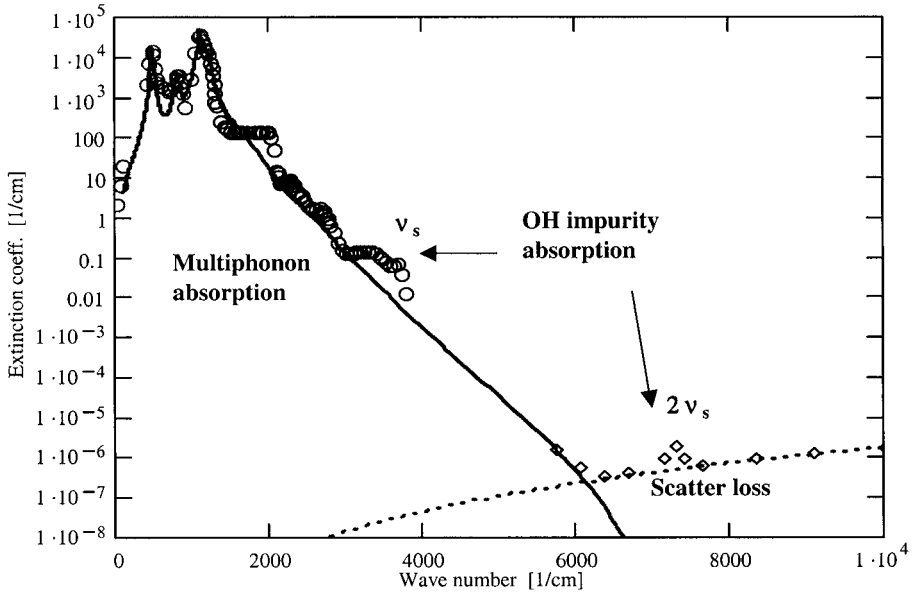
Fig. 8.23 Comparison of the experimental ($\circ$ and $\diamond$) and theoretical multiphonon absorption coefficient (solid curve) as a function of frequency for fused silica at room temperature. The dashed curve represents Rayleigh scattering loss.
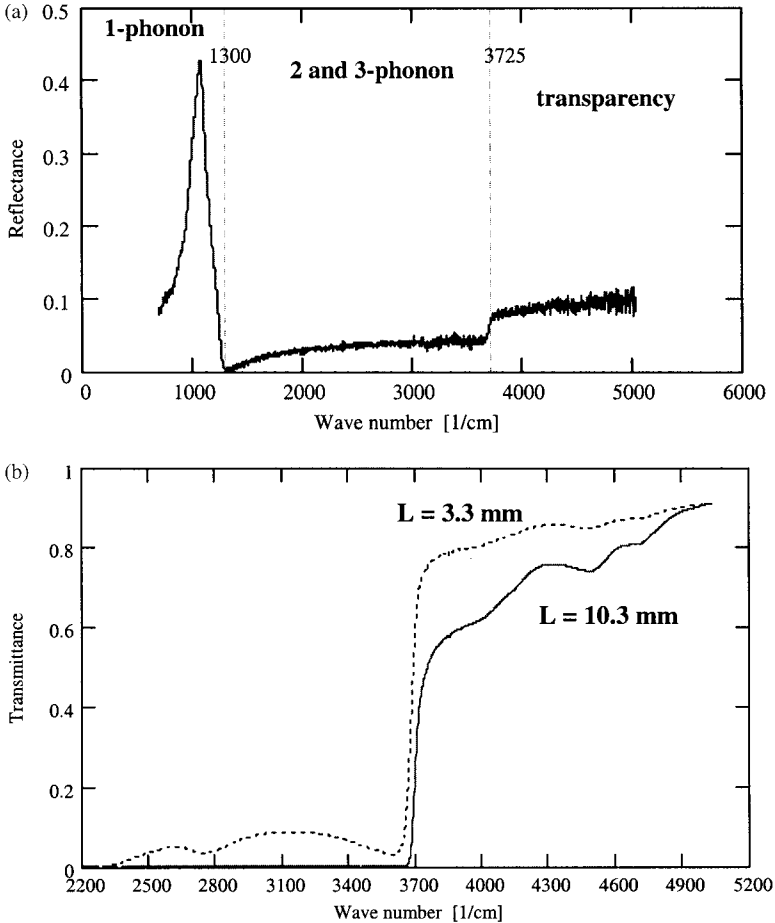
Fig. 8.24 The room-temperature infrared (a) reflectance and (b) transmittance for BK7 glass for two different thicknesses.

that BK7 is dominantly silica based (50% to 70%). OH impurity absorption in BK7 limits useful transparency to 2.5 μm. Most glasses are transparent into the near-infrared. Unfortunately, optical property characterization typically does not exist for wavelengths longer than 1 μm. The short-wavelength ultraviolet edge of transparency of BK7 glass is shifted to 300 nm from roughly 160 nm for high-purity fused silica.

Another useful characterization of a glass is a measure of dispersion in the visible. This is commonly accomplished with the Abbe number, ν_d. It is defined as

$$\nu_d = \frac{n_d - 1}{n_F - n_C}, \tag{8.71}$$

where n_d, n_F, and n_C are the indices of refraction at 587.6, 486.1, and 656.3 nm, respectively. The Abbe number for BK7 is 64.17. The adjustment of the composition of the

glass alters the dispersion. The great variety of dispersion that is available is a great aid to lens designers.

The index of refraction of many glasses is commonly represented by the empirical Schott glass formula, as given by

$$n^2(\lambda) = A_0 - A_1\lambda^2 + A_2\lambda^{-2} + A_3\lambda^{-4} + A_4\lambda^{-6} + A_5\lambda^{-8}.$$

This formula is applied from 0.365 to 1.014 μm with a precision of ±0.000005. The Schott glass formula can be obtained from an expansion of the Sellmeier formula. In fact, an equivalent Sellmeier model will work equally well, but uses fewer parameters and offers greater spectral coverage. This is important, since optical glasses transmit beyond 1 μm. Based on Fig. 8.23, pure fused silica transmits out to 4 μm. Given today's interest in optics at 1.55 μm, it is necessary to extend the characterization of the index of refraction of glasses throughout the near infrared. Sellmeier models for a limited set of glasses are given in Appendix 4.

The magnitude and dispersion of the refractive index of a glass can be adjusted by changing the glass composition. Oxides with heavier cations increase the index of refraction and shift the electronic transitions to lower frequencies, thus increasing dispersion. Oxides with lighter cations lower the refractive index and shift electronic transitions to higher frequencies, thus decreasing dispersion. For example, in an optical fiber, the inner core is composed of pure SiO_2 doped with GeO_2 to increase the refractive index of silica, and the outer cladding is SiO_2 doped with B_2O_3 to decrease the refractive index of silica. A modified Sellmeier equation can be used to compute the refractive index of a multicomponent glass. For a glass composed of silica and germania of the form $xGeO_2:(1-x)SiO_2$ where $0 \leq x \leq 1$, the Sellmeier formula becomes

$$n^2(x,\lambda) = 1 + \sum_i \frac{\left[\Delta\epsilon_{silica,i} + x(\Delta\epsilon_{germania,i} - \Delta\epsilon_{silica,i})\right]\lambda^2}{\lambda^2 - \left[\lambda_{silica,i} + x(\lambda_{germania,i} - \lambda_{silica,i})\right]},$$

where the Sellmeier parameters for germania and silica can be found in Appendix 4. This model assumes that the changes in oscillator strength and location are linear in x, which may not always be the case.

Other types of glasses also exist, such as fluorides and calcogenides. They offer transparency farther into the infrared than oxide glasses, but are not as durable as oxide glasses and therefore are seldom used unless the application demands mid-infrared (fluorides) and longwave infrared (calcogenides) transparency. For example, fluoride glasses are attacked by water.

8.2.3 Semiconductors

A class of optical materials with established optoelectronic importance that continues to grow is semiconductors. Many applications involving semiconductors are currently being considered requiring high speed, compactness, and high reliability. This includes photonic and optoelectronic devices in the form of sources (light emitting diodes and lasers), detectors (PIN, quantum well, and APD photodiodes), modulators and switching devices. The main materials of interest are Si, GaAs, InP, $Al_xGa_{1-x}As$, InGaAs, InGaP, PbSnTe, and $In_{1-x}Ga_xAs_yP_{1-y}$.

Many semiconductor devices operate at frequencies near the bandgap energy, which must have a direct bandgap for transmitting devices. For the materials of interest this covers the near-infrared. For example, the room-temperature bandgap of GaAs is 1.52 eV (0.815 µm); however, the ternary semiconductor bandgap can be tuned by adjusting the element concentrations. Thus, devices can be made for the important communication wavelengths of 1.3 and 1.5 µm. Furthermore, tunable mid-infrared (3 to 6 µm) laser sources are made from PbSnTe. Also, pure intrinsic semiconductor materials, such as Ge, Si, and GaAs, are commonly used as infrared windows and lenses. Device structures can be as common as the *pn*-junction or as novel as multiple quantum wells. Current semiconductor lasers with low thresholds are made of heterojunction structures, were the junction is composed of two different materials with different bandgaps. Multiple quantum well devices offer greater design flexibility for achieving desired properties. Fundamental to device design and operation is the complex index of refraction in both the time and frequency domain as a function of frequency and temperature.

Because of the low-energy bandgap of semiconductors, free-carrier effects are important, especially at elevated temperatures. Thus, semiconductor optical properties require the characterization of free carriers, phonon bands, and electronic transitions. Complete frequency-domain characterization above the bandgap of most of these semiconductor materials has been accomplished by Adachi (Ref. 8.19) in the form of the standard permittivity models, as presented in Section 8.2.1.1. In the following, intrinsic semiconductor materials are briefly examined, and then extrinsic materials commonly used in optoelectronic devices are discussed.

8.2.3.1 Intrinsic Properties

Intrinsic properties are those of the ideal pure material. For many materials, intrinsic properties can be obtained. Free-carrier effects are covered first, followed by phonon effects and then electronic processes at the bandgap.

Free Carrier   Low-energy bandgap semiconductors ($E_g \leq 0.65$ eV) possess strong free-carrier absorption near room temperature at microwave frequencies. As these materials are moderately heated, absorption by free carriers becomes significant for the infrared. This is because of thermally generated negative carriers in the conduction band and positive carriers in the valence band. The negative carriers are electrons and the positive carriers are called holes. The intrinsic carrier concentration as a function of temperature closely follows a Boltzmann factor dependence as given by

$$\rho_{carrier}(T) = \rho_{0carrier} \left(\frac{T}{T_0} \right)^{\frac{3}{2}} \exp\left[-\frac{E_g}{2k_B} \left(\frac{1}{T} - \frac{1}{T_0} \right) \right],$$

where T_0 is a reference temperature. Based on Eq. 4.63b and the above result, the plasma frequency for each carrier type as a function of temperature becomes,

$$\omega_p(T) = \sqrt{\frac{\rho_p(T)}{m\epsilon_0}} e = \omega_{p0} \left(\frac{T}{T_0} \right)^{\frac{3}{4}} \exp\left[-\frac{E_g}{4k_B} \left(\frac{1}{T} - \frac{1}{T_0} \right) \right].$$

According to Eq. 4.55, the carrier mobility is related to the carrier damping parameter. Using an empirical relationship for the temperature-dependent mobility, the following temperature-dependent model for the carrier damping parameter is obtained:

$$\Gamma_c(T) = \Gamma_c(0)\left(\frac{T}{T_0}\right)^{2.6}.$$

Figure 8.25 plots the computed transmittance for germanium ($E_g = 0.664$ eV) and silicon ($E_g = 1.11$ eV) using the temperature-dependent free-carrier model (Eq. 4.63 with the above temperature-dependent parameters for each carrier type). The infrared free-carrier absorption coefficient decreases with increasing frequency as ν^{-2}, as predicted by the free-carrier model presented in Chapter 4. This is the case for silicon and germanium. However, the conductivity relaxation time is frequency dependent, which is not represented in the Drude model. The nature of the frequency response depends on the charge-carrier scattering mechanism. There are two types of scatters that impede carrier motion, phonons and impurity ions. Also, recall that there are two types of phonons, acoustic and optical. The experimental absorption coefficient fall-off for acoustic phonons is $\nu^{-1.5}$, for optical phonons is $\nu^{-2.5}$, and for ion impurities is $\nu^{-3.5}$. In most materials a combination of effects occurs. For example, phonon scattering dominates in n-doped silicon and germanium and the net fall-off is ν^{-2}. For n-doped GaAs
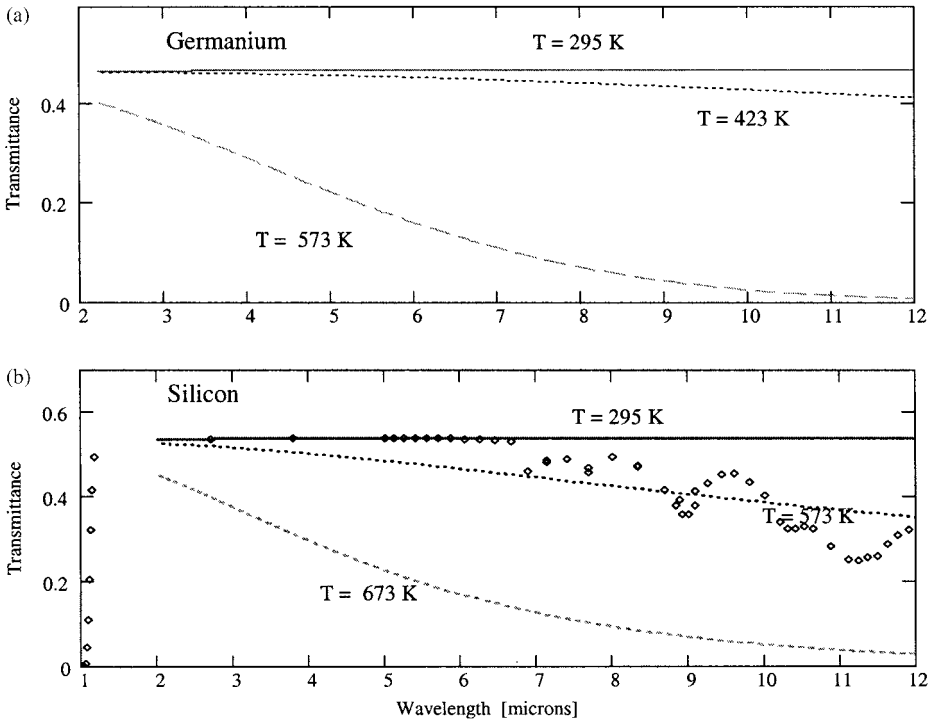
Fig. 8.25 The transmittance of intrinsic germanium (30 Ω cm) and silicon ($2 \times 10^5 \Omega$ cm) at different temperatures (model parameters are listed in Appendix 4).

a more rapid fall-off is observed, where $\beta_{abs} \propto \nu^{-3}$. Thus ion impurity scattering must be playing a role.

Phonons   Purely covalent semiconductors, such as Si and Ge, have no infrared active phonon absorption bands to first order. This is the same situation for diamond, which possesses a large bandgap and was discussed with the other insulating materials. The optical properties are very similar, but because of the more massive atoms of Si and Ge, the vibrational frequencies are lower (see Fig. 8.26). Thus the multiphonon absorption bands occur at lower frequencies. Table 8.7 lists the Raman frequencies for the purely covalent type IV semiconductors along with diamond. Recall that the integer multiple of the Raman frequency in diamond marks the location of the phonon bands. The same is true for Si and Ge. Materials with ionic bonds have infrared active phonon bands. A good example is GaAs. Figure 8.26 plots the absorption coefficient of GaAs as a function of photon energy. Also plotted in this figure is the multiphonon absorption coefficient of Si; notice the lack of one-phonon structure and the comparatively weaker two-phonon structure than that of GaAs. Also purely covalent bonded materials that do not have a symmetrical structure can have infrared active vibrational modes. A good example in this case is SiC.

The frequency-domain classical oscillator model accurately represents the permittivity of semiconductor phonon bands, just as it did for insulators. Also, recall that the classical oscillator blue wing requires modification to match experimental absorption coefficient data (see Eq. 8.12). Another aspect of characterization that is important for high-speed, high-bandwidth applications of semiconductor materials is the time-domain response. If the classical oscillator model is used to represent the complex index of refraction, then a closed-form time-domain result can be obtained, as was demonstrated in Section 4.2.4. The result for room-temperature GaAs is presented in
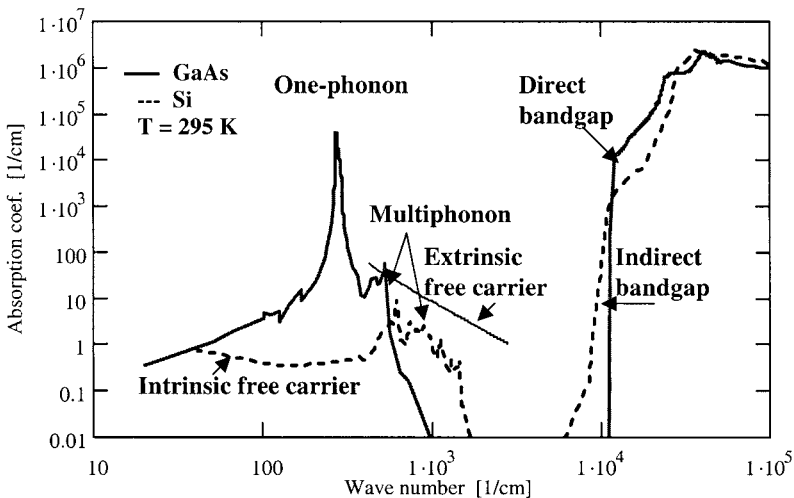
Fig. 8.26 The room-temperature absorption coefficient of doped and intrinsic GaAs and Si as a function of photon energy.

Table 8.7 The Raman Active Vibrational Frequencies of
Type IV Materials

Material	Raman Frequency [cm^{-1}]
Diamond	1332.4
Silicon	519.5
Germanium	300.6

Fig. 4.7. However, because of the blue-wing modification, the time-domain representation given is incomplete for very short-time behavior (probably on the order of picoseconds). Each of the classical oscillator parameters, ω_i, $\Delta\epsilon_i$, and Γ_i is temperature dependent. The optical properties of semiconductors are very temperature sensitive, and it is important to include this dependence in a realistic model.

Electronic Transitions   High-speed (100 GHz and greater) optoelectronic and photonic devices are currently in the research phase of development. There is great need for modeling performance of such devices, which will ultimately lead to computational design and evaluation tools of the future. A full solution to the time-domain Maxwell's equations is required. This is necessary because of the high speed and bandwidths involved, the component size, and the inhomogeneous nature of the media. The standard frequency-domain approaches are not always practical because Maxwell's equations are solved assuming monochromatic, steady-state behavior. The transient response of materials is now important as well as frequency-dependent complex index of refraction of device materials, and the time domain is a more natural setting for such problems. One promising numerical approach for solving Maxwell's equations uses a finite-difference–time-domain (FD-TD) technique. This requires knowledge of the time-domain characterization of the intrinsic and extrinsic optical properties of the materials used in a device. For realistic modeling, temperature dependence must be known as well. Such information currently does not exist to a satisfactory level.

Applying the Adachi models of Section 8.2 yields a comprehensive representation of the intrinsic complex index of refraction for direct bandgap materials. The model can be applied to indirect bandgap semiconductors as well. Recalling Section 5.7.1, an electron and phonon transition are required, thus $k_f' = k_i' + k_{phonon}'$. Based on Eq. 5.133, the net transition probability is much smaller than direct bandgap transitions (see Fig. 8.26, which compares the absorption coefficient of Si and GaAs). The imaginary part of the susceptibility near the bandgap in this case is represented by (Adachi, Ref. 8.19)

$$\chi_{indirect}(\omega) = \frac{G}{(\hbar\omega)^2} \left(\hbar\omega - E_g^{id} \pm \hbar\omega_{phonon}\right)^2 H \left(1 - \frac{E_g^{id} \pm \hbar\omega_{phonon}}{\hbar\omega}\right),$$

where E_g^{id} is the indirect bandgap energy, ω_{phonon} is the phonon frequency, and G is a scaling parameter. Because of the weakness of the indirect band transition, the real part is insignificant and can be ignored. Model parameters for a variety of semiconductor materials are listed in Appendix 4 (Tables A4.6–A4.9).

8.2.3.2 Extrinsic Properties

Semiconductor materials are commonly doped to alter some electrical property in a controlled manner. This is also the case for optical properties. Figure 8.26 shows the important effect of p- and n-doping has on free-carrier absorption levels in GaAs. Such an effect can be used to provide RF shielding to an optical window. The equilibrium or intrinsic carrier density is related to electron and hole concentrations by

$$\rho_i^2 = \rho_n \rho_p.$$

For an intrinsic semiconductor the electron and hole carrier density are equal. An n-doped semiconductor requires an impurity that has a valence greater than the host thus donating an electron. A p-doped semiconductor requires an impurity that has a valence less than the host, thus removing or accepting an electron. Therefore, impurity concentrations are denoted as either ρ_{donor} or $\rho_{acceptor}$. The number density for electrons in an n-doped semiconductor is given by

$$\rho_n(T) = \frac{1}{2} \left(\rho_{donor} + \sqrt{\rho_{donor}^2 + 4\rho_i(T)} \right).$$

The corresponding number of holes in the doped material is obtained by applying the above formula for the intrinsic carrier density, thus

$$\rho_p^{doped}(T) = \frac{\rho_i(T)^2}{\rho_n^{doped}(T)}.$$

A similar set of equations are used for a p-doped semiconductors where n is replaced p, and p is replaced by n. Figure 8.26 plots the absorption coefficient for n-doped GaAs.

Extrinsic semiconductor structures are often used in making optoelectronic devices. Such devices usually operate near the bandgap, of the material. This is where dispersion is high and absorption is beginning to become significant. An exciton band also exists near the bandgap, as illustrated in Fig. 8.26. The location of the exciton band affects the complex index of refraction and thus optical propagation. The exciton band is also influenced by external electric fields, and this allows optical and electronic coupling. A particular class of optoelectronic devices based on this effect are called SEED (Self-Electro-optic Effect Devices). Precise knowledge of such optical properties is required for careful design of any optoelectronic device.

8.2.4 Metals

High concentrations of free electrons exist in metals at any temperature, because the conduction and valance bands overlap. Thus, microwave and infrared properties of metals are dominated by free-carrier effects, as described in Section 4.2.5. Free-carrier model parameters are listed in Appendix 4 (Table A4.5) for a variety of metals. Figure 8.27 compares the complex index model based on Eq. 4.63 with experimental data for gold. Good agreement is shown throughout the far-infrared and infrared. This result is true for all metals. However, from the near infrared to ultraviolet, interband electronic transitions become important, and significant deviations from the free-carrier model exist. This is demonstrated in Fig. 8.28, which plots the experimental and modeled
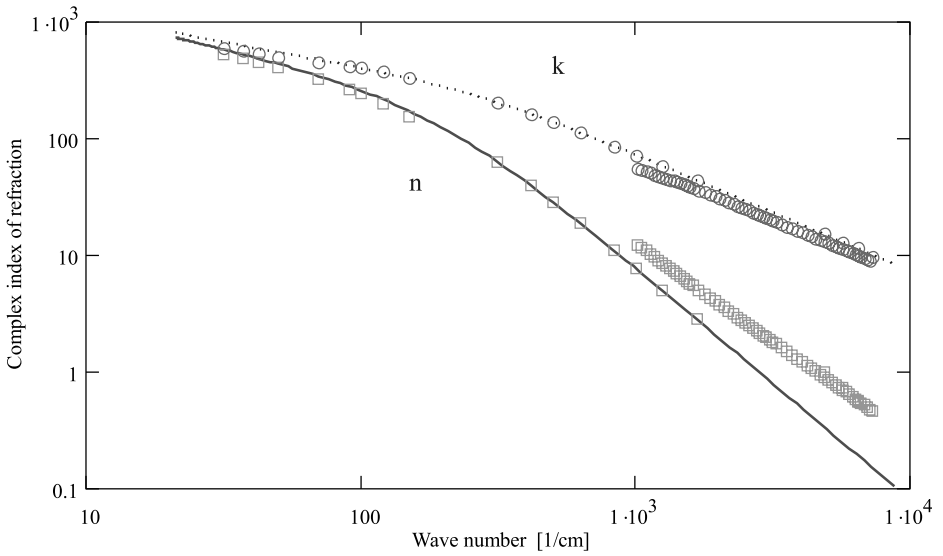
Fig. 8.27 Free-carrier contributions to the infrared properties of gold in terms of the real and imaginary parts of the complex index. The figure compares experimental values (*n*, □ and *k*, ○) to a free-carrier model using parameters from Appendix 4 (*n*, solid and *k*, dotted).
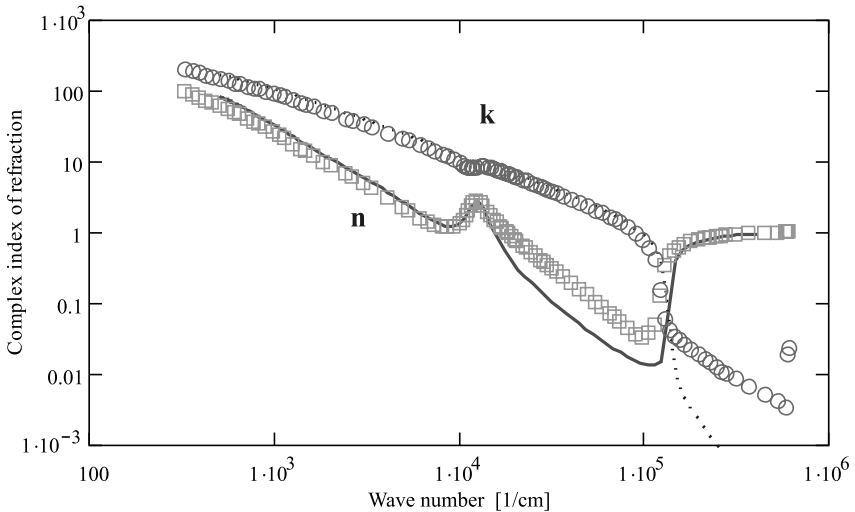
Fig. 8.28 The room temperature complex index of refraction of aluminum from the infrared to ultraviolet. The figure compares experimental values (*n*, □ and *k*, ○) to a free-carrier model using parameters from Appendix 4 (*n*, solid and *k*, dotted).
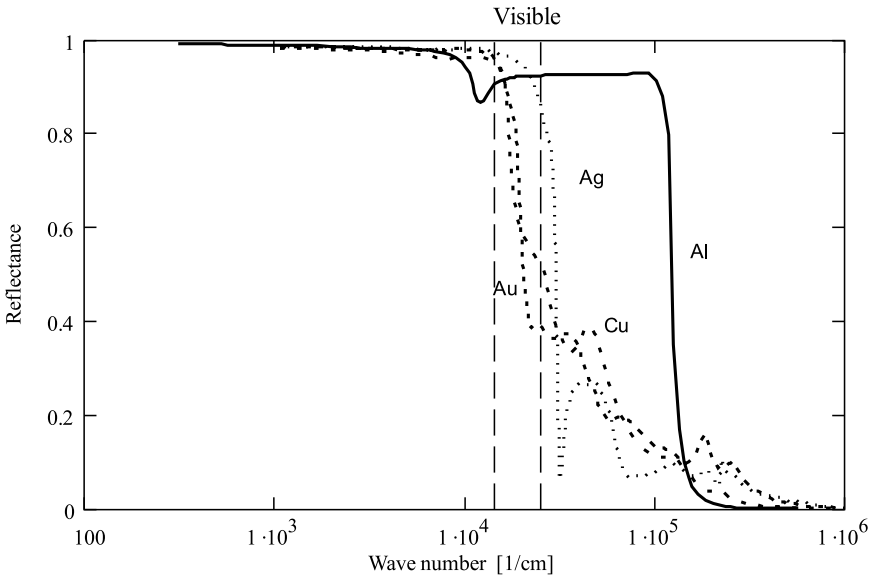
Fig. 8.29 Metal mirror near-normal reflectance for ultraviolet, visible, and infrared frequencies.

n and k values of aluminum as a function of wave number from the far infrared to the ultraviolet. The classical oscillator model is used to represent the interband transitions for aluminum (see Appendix 4 for parameter values). This improves the agreement in the infrared, but discrepancies in the visible do exist.

The strong absorption exhibited by metals makes them excellent optical reflectors. Figure 8.29 plots the near normal reflectance of a variety of metals from the infrared to the ultraviolet. Although the far-infrared reflectance of metals is uniformly good, they deviate considerably as the ultraviolet is approached. At ultraviolet frequencies, most metallic reflectors are poor and must be used at oblique angles to be efficient. Only aluminum is useful in the ultraviolet, but it rapidly loses reflectance in the vacuum ultraviolet.

8.3 Scattering

For perfect crystals, with no variation of the index of refraction and a perfect surface, scattering is manifested by specular reflection only. This is rarely, if ever, the case because of materials defects, isotopic variations, surface roughness, and so on. Intrinsic scatter in crystals is difficult to compute, but will be of Rayleigh form. Formulas for intrinsic scatter in glasses do exist. Extrinsic scatter must, in general, be empirically characterized.

8.3.1 Intrinsic

Intrinsic scatter for single-crystal solids will be Rayleigh in character and at a fairly low level for most optical materials.

8.3.2 Extrinsic

Extrinsic scatter is composed of two types, bulk and surface. Surface scatter depends on the quality of the polish. Bulk scatter depends on the internal structure of a material.

Extrinsic bulk scatter occurs in processed materials such as polycrystalline solids. A combination of scatter mechanisms exist in this case. Rayleigh, Rayleigh–Gans, and geometrical blocking all make contributions. The emphasis will vary, depending on the frequency of interest. A simple empirical scatter model is commonly used. The scatter coefficient is given by

$$\beta_{sca}(v) = A + Bv^b + Cv^4. \tag{8.72}$$

Only the single-scatter phenomenon is considered in this model. Recall that this requires that $\beta_{sca}L \ll 1$. Scatter is usually temperature independent, depending on the structural stability of the materials as a function of temperature. Figure 8.30 displays the scatter coefficient as a function of frequency and the phase function for a polycrystalline window material. The frequency dependence is fairly linear ($b \approx 1$), indicating a wide distribution of scatter sizes. The phase function has the unusual feature of a peak at $1°$. This suggests that a particular scatter size is most common. From the phase function, the modulation transfer function (MTF) can be obtained.

Although highly polished materials are required for many applications, it is perhaps equally worthwhile to consider a rough surface for an optical black. A Lambertian surface is desired, which also absorbs light and allows multiple reflections. Although black paints contain absorbing material, it is assumed that $k \ll n$. Thus the surface reflectance is dominated by the real part of the complex index of refraction only. In the BRDF measurements made, two distinct phenomena are observed. A percentage of the BRDF is completely diffuse (or Lambertian) and independent of the angle of incidence, and the remaining portion of the BRDF follows an angle-averaged, power reflection coefficient Fresnel equation and depends on the angle of incidence.

From the development in Chapter 2, the formula for a Lambertian BRDF is

$$\rho_{Lam}(\theta_r) = \frac{\rho_{Lam}}{\pi} \cos \theta_r. \tag{8.73}$$

ρ_{Lam} is the Lambertian hemispherical reflectance, as defined by

$$\rho_{Lam} = \int_{hemisphere} \rho_{Lam}(\theta_r) \sin(\theta_r) \, d\theta_r d\phi_r. \tag{8.74}$$

The diffuse (Fresnel coefficient dependent) portion of the BRDF typically takes the mathematical form of a power-law function of the form $(\sin \theta_r + \sin \theta_i)^{-m}$. To obtain a normalizable representation, a Lorentz-type phase function is used. Based on this intuition, a Fresnel-based BRDF model suitable for many rough surfaces, is given by

$$\rho_{Fres}(\theta_i, \theta_r) = R_{ave}(\theta_i, \alpha, n) \frac{\rho_{TIR} - \rho_{Lam}}{\rho_{TIR}} N \frac{(\alpha \cos \theta_i)^{m-1} \cos \theta_r}{(\sin \theta_r + \sin \theta_i)^m + (\alpha \cos \theta_i)^m}, \tag{8.75}$$

where α is the half-width at half maximum, N is a normalization factor that satisfies Eq. 2.90, and R_{ave} is the total integrated reflectance (see Eq. 2.91) or the angle-averaged
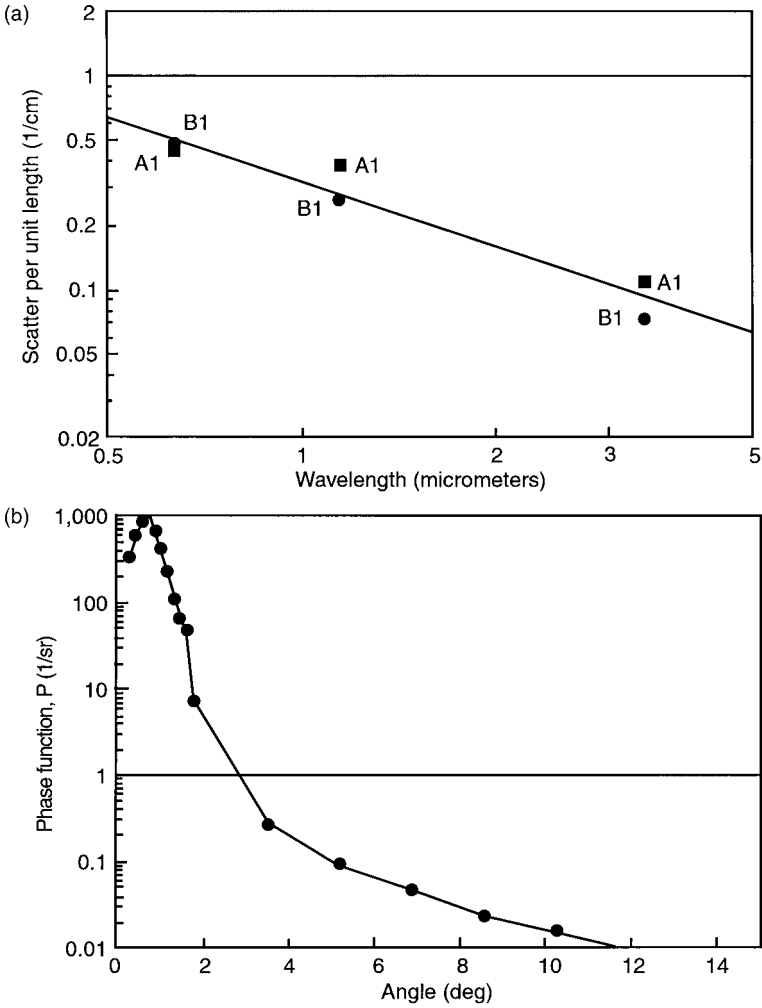
Fig. 8.30 (a) The scatter coefficient as a function of wavelength and (b) the phase function as a function of scatter angle for room-temperature polycrystalline AlON ($Al_{23}O_{27}N_5$).

Fresnel reflection coefficient, as given by the following empirical form:

$$R_{ave}(\theta_i,\alpha,n) = \frac{\int_{0}^{\frac{\pi}{2}} [\Phi(\theta - \theta_i + \alpha) - \Phi(\theta - \theta_i - \alpha)]\, R(\theta,n)d\theta}{\int_{0}^{\frac{\pi}{2}} [\Phi(\theta - \theta_i + \alpha) - \Phi(\theta - \theta_i - \alpha)]\, d\theta}, \qquad (8.76)$$

where $\Phi(\theta)$ is the Heaviside step function and $R(\theta_i,n)$ is the Fresnel power reflection coefficient for unpolarized light and $k \ll n$, as given by

$$R(\theta_i,n) = \frac{1}{2}\left[\left(\frac{n^2\cos\theta_i - \sqrt{n^2 - \sin^2\theta_i}}{n^2\cos\theta_i + \sqrt{n^2 - \sin^2\theta_i}}\right)^2 + \left(\frac{\cos\theta_i - \sqrt{n^2 - \sin^2\theta_i}}{\cos\theta_i + \sqrt{n^2 - \sin^2\theta_i}}\right)^2\right]. \quad (8.77)$$

To check the reasonableness of the model for R_{ave}, examine α, as α approaches $\pi/2$. Then R_{ave} becomes independent of θ_i (the same is true for the phase function). Therefore, the Fresnel BRDF model approaches the Lambertian case in the limit of $\alpha \to \pi/2$. Equation 8.76 satisfies this test. A more rigorous approach for obtaining R_{ave} can be constructed by processing the phase function in Eq. 8.75. Information on the surface roughness is contained in the phase function. However, this requires a deconvolution between the phase function and the Fresnel reflection coefficients, which makes the analysis more complicated.

The hemispherical reflectance factor is the integration of Eq. 8.75 over the back hemisphere, resulting in the following

$$\rho_{Fres}(\theta_i) = \rho_{TIR}(\theta_i) = R_{ave}(\theta_i,n,\alpha). \quad (8.78)$$

For this to be true, over the range of typical values of $\alpha(<\pi/2)$ and m, the phase function must be normalized according to

$$N \int_{hemisphere} \frac{(\alpha\cos\theta_i)^{m-1}\cos\theta_r}{(\sin\theta_r + \sin\theta_i)^m + (\alpha\cos\theta_i)^m} \sin(\theta_r + \theta_i)\, d\theta_r\, d\phi_r = 1 \quad (8.79)$$

Fig. 8.31 plots the experimental and modeled BRDF for flat polyurethane ($\theta_i = 12.8°$) and epoxy ($\theta_i = 17°$) paints illuminated by a He-Ne laser operating at 0.633 and 3.39 μm wavelengths as a function of the reflection angle. The angular resolution is 2°. The model sums the Lambertian and diffuse (Fresnel coefficient dependent) reflectance pieces together. Model parameters for the polyurethane paint are $\rho_{Lam} = 0.006$, $\rho_{TIR} = 0.019$, $m = 3$, $n = 1.32$, and $\alpha = 0.06$ radians. Model parameters for the epoxy paint are $\rho_{Lam} = 0.012$, $\rho_{TIR} = 0.045$, $m = 2$, $n = 1.5$, and $\alpha = 0.55$ radians.

8.4 Computer Codes and Examples

The models previously presented provide more than physical insight into the optical properties of materials. Because of the sound physical basis for these theories, meaningful interpolations and extrapolations can be made as a function of frequency and temperature. This is very useful for obtaining accurate and comprehensive information on material properties when experimental data is lacking. Unfortunately, this quite often is the case. Furthermore, models provide a precise and convenient means of communicating optical properties data and represent an improvement over conventional figures and tables. The formulas are easily programmed on a computer, providing quick and easy access to the complex index of refraction for many optical materials, such as those listed in Appendix 4. These results can then be used to calculate transmittance, reflectance, absorptance, scatterance, and emittance of fibers, windows and thin films, scatterance of aerosols, dispersion, and thermal-optic effects for optical design applications. Such a
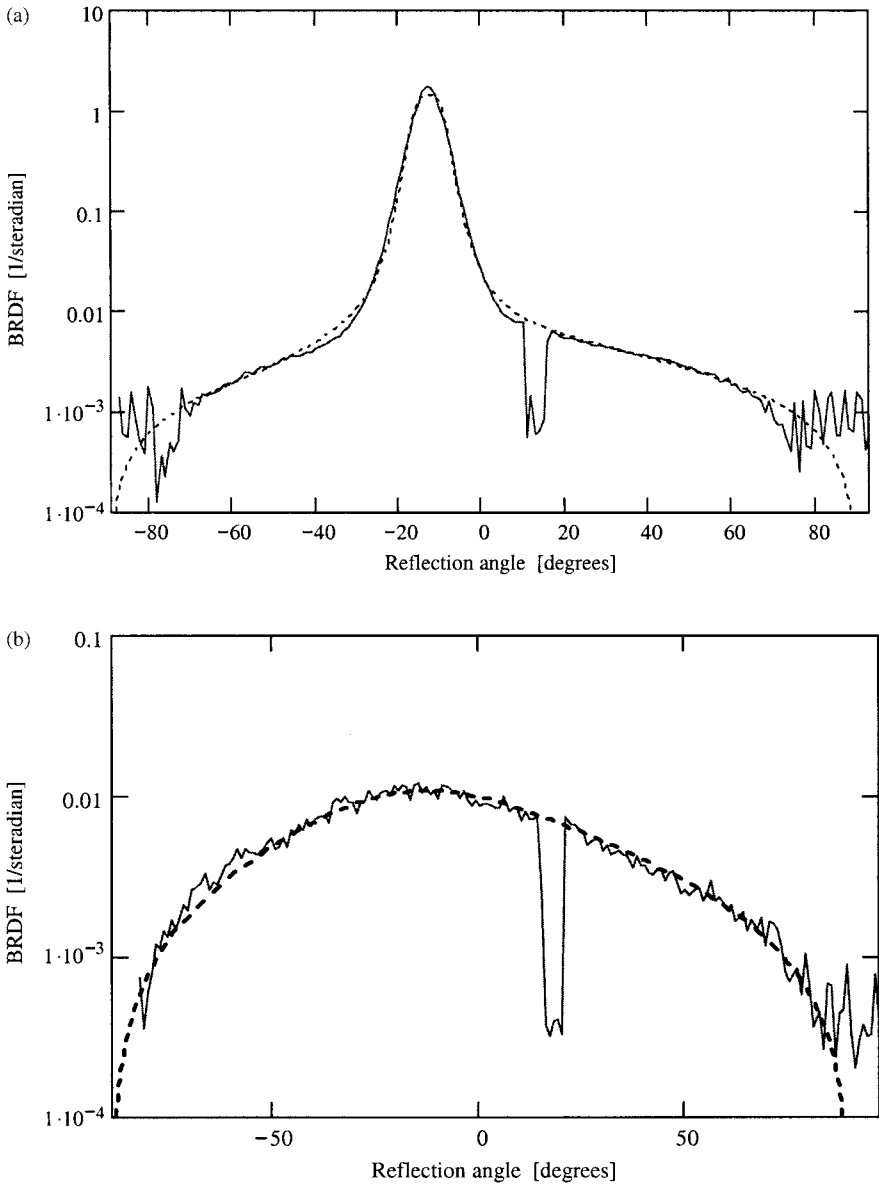
Fig. 8.31 Experimental (solid) and modeled (dashed) BRDF of (a) polyurethane paint ($\theta_i = 12.8°$) illuminated by a He-Ne laser operating at 0.633 μm wavelength and (b) epoxy paint ($\theta_i = 17°$) illuminated by a He-Ne laser operating at 3.39 μm wavelength as a function of the reflection angle. (The dropouts near 10° and 20° occur because the illuminating beam is blocked by the detector.)

computer code and database can potentially enhance system design and performance modeling. Considering that the atmospheric codes MODTRAN and FASCODE have been developing for over 30 years and are widely recognized for their utility, it is surprising that no similar past effort exists for a solid–state optics code.

8.4.1 OPTIMATR

Early efforts at JHU/APL (1988–89) to characterize the infrared properties of primarily crystalline insulators resulted in a FORTRAN-based computer code, called PHONONB. This code contained one-phonon, multiphonon sum band absorption, and Sellmeier models for approximately 30 materials (primarily oxides, fluorides, and alkali halides). The code calculated the complex index of refraction in terms of n and β_{abs} as a function of frequency (in wave numbers) and temperature.

Based on the interest in and utility of PHONONB, this work continued, and a more comprehensive version was developed in 1993, called OPTIMATR™. This code also contains the one-phonon, multiphonon sum band absorption, Sellmeier (for room temperature) models, and in addition, Urbach tail, free-carrier, and scatter models for over 70 optical materials (crystals, glasses, semiconductors, and metals), as listed in Appendix 4. The code calculates n, β_{abs}, and β_{sca}, as a function of frequency in cm^{-1} (or wavelength in μm) for fixed temperatures as chosen by the user. Urbach tail modeling extends the spectral range of characterization up to a material's bandgap. Free-carrier modeling allows metals and semiconductors to be included. Scatter models in OPTIMATR typically characterize extrinsic properties in spectral regions of transparency. Thus OPTIMATR represents microwave, infrared, visible, and ultraviolet optical materials. An example output for sapphire is listed in Table 8.8.

The code contains a data file, which stores the parameters for the various optical property models. The parameters represent the intrinsic properties as completely as possible. This is important because it depicts the ideal optical properties. Extrinsic properties are also included, but not completely because these properties vary from material to material. This is important for polycrystalline and amorphous materials. In some cases the extrinsic properties, such as impurity absorption, must be specified by the manufacturer to be meaningful.

Such an optical property database is essential for optical lens design (including the effects of spectral and temperature dispersion), thin-film design, system performance analysis, aerosol scatter calculations, and many other optical system design problems. Currently, optical property data is quite dispersed among reference books and journal articles, and generally available for limited spectral region and typically, room temperature. Having the physically based models to interpolate and extrapolate the experimental data as a function of frequency and temperature greatly and reliably extends the optical property data base available in the literature. OPTIMATR™ is commercially available from Echoscan, Inc. (www.echoscaninc.com).

8.4.2 Reflectance and Emittance Calculations of Bulk Materials and Coatings

The following examples are presented to demonstrate the utility of the optical property models presented in this chapter to common applications in optics.

Table 8.8 OPTIMATR^{TM} Output for o-Ray of Sapphire at $T = 295$ K

Material Name: Al$_2$O$_3$ o-ray
Minimum Wave number = 100.0 cm^{-1}
Maximum Wave number = 2500.0 cm^{-1}
Temperature (K) = 295.0 (Sellmeier Model used)

Wave numbers [cm^{-1}]	Index of Refraction	Absorption Coefficient [cm^{-1}]	Scatter Coefficient [cm^{-1}]
100.0	3.100237	.000E+00	—
200.0	3.259553	.000E+00	—
300.0	3.671500	.000E+00	—
400.0	4.666635	.000E+00	—
500.0	2.643119	.889E+01	—
600.0	.266841	.362E+02	—
700.0	.049241	.986E+02	—
800.0	.054489	.193E+03	—
900.0	.160193	.278E+03	—
1000.0	.899295	.304E+03	—
1100.0	1.153252	.258E+03	—
1200.0	1.296547	.177E+03	—
1300.0	1.389662	.102E+03	—
1400.0	1.455000	.508E+02	—
1500.0	1.503199	.232E+02	—
1600.0	1.540053	.105E+02	—
1700.0	1.569015	.521E+01	—
1800.0	1.592273	.292E+01	—
1900.0	1.607737	.170E+01	—
2000.0	1.624024	.953E+00	—
2100.0	1.637684	.516E+00	—
2200.0	1.649270	.271E+00	—
2300.0	1.659192	.145E+00	—
2400.0	1.667763	.807E−01	—
2500.0	1.675223	.467E−01	—

Example 8.2   Specular reflectance as a function of the refractive index

When the index of refraction is real ($\beta_{abs} = 0$) the material is transparent; based on Eq. 2.97, the specular reflectance becomes

$$\rho_s(n,\theta_i) = \frac{R_s(n,\theta_i)}{1 + R_s(n,\theta_i)} + \frac{R_p(n,\theta_i)}{1 + R_p(n,\theta_i)}. \tag{8.80}$$

Figure 8.32 is a plot of $\rho_s(n,0)$ for normal incidence for a lossless medium. Low-index materials, such as the fluorides, have high transparency with no antireflective coating. High-index materials such as GaAs ($n = 3.3$), Ge ($n = 4.0$), Si ($n = 3.4$), on the other hand, lose nearly 50% of the light by reflection with no other loss mechanism present. Oxides have a range of indices from 1.6 to 1.9 and typically
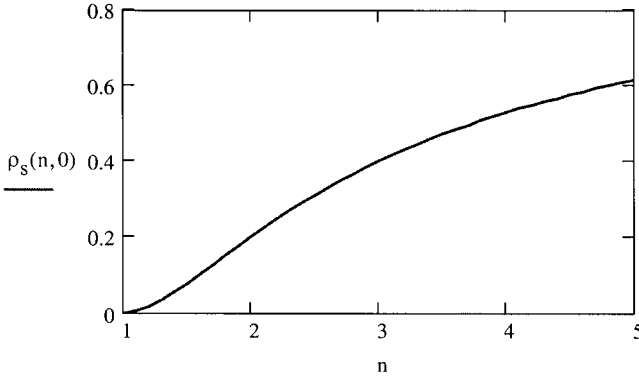
Fig. 8.32 The reflectance for normal incidence as a function of the refractive index for a flat window in air ($\beta_{abs} = 0$).

have reflectance losses around 10%. These materials often require antireflection coatings to reduce transmission loss. A simple antireflection coating is a thin film of another optical material with an index of refraction equal to the square root of the bulk material. A good example of this is MgF_2 ($n = 1.38$, $n^2 = 1.90$) coatings on high-index oxides. The index of refraction at microwave frequencies is much larger than the corresponding infrared/visible values and therefore the reflectance is much higher. For this reason, microwave windows are often made as etalons to avoid reflectance loss in limited spectral regions.

Example 8.3 Thin-film mirrors

Optical properties of thin films are based on the properties of the bulk material. However, thin films are often not full density and bulk properties must be appropriately scaled.

Thin-film devices are band filters and mirrors. A common application is the design of highly reflective multilayer ($2N$ layers) laser resonator mirrors. The single-surface reflection coefficient formula for a $2N$-layer coating composed of two different materials (with indices n_2 and n_3) on a substrate with index n_1 is

$$R(N) = \left(\frac{1 - \left(\frac{n_1}{n_4}\right) \left(\frac{n_3}{n_2}\right)^{2N}}{1 + \left(\frac{n_1}{n_4}\right) \left(\frac{n_3}{n_2}\right)^{2N}} \right)^2. \tag{8.81}$$

For example, for $n_4 = n_{air} = 1.0028$, $n_2 = 1.38$, $n_3 = 2.35$, and $n_4 = 1.543$, the reflection coefficient for $N = 7$ is 0.999. This is impossible to achieve with a metallic mirror in the visible.

Example 8.4   Emittance

Direct measurements of near-room-temperature emissivity of a surface are difficult to perform because of high-level room-temperature background noise. Cryogenic enclosures are required. This is an expensive and cumbersome approach. For this reason, measurements of reflectance and transmittance are made to infer the emissivity. When a surface is opaque only the reflectance is needed. Since a bright external source can be used (in this case a laser) the background radiance is not a problem.

Recalling the discussion in Chapter 2, the directional emissivity is obtained by integrating over all internal sources, Ω'_e. Using the principle of reciprocity, this is equivalent to integrating the external reflectance over Ω_r. Thus, the following relationship is obtained:

$$\epsilon(\Omega_e, \omega) = \epsilon(\Omega_i, \omega) = 1 - \int_{hemisphere} \rho(\Omega_r, \Omega_i, \omega) \, d\Omega_r = 1 - \rho_{hem}(\Omega_e, \omega). \tag{8.82}$$

This is a useful result. Furthermore, Eq. 8.82 remains true for a finite semitransparent medium, when emitted light is observed at angles where no transmitted light from an external source exists.

The spectral hemispherical emittance is also desired for many applications in electro-optics. It is the integral of Eq. 8.82 times $\cos\theta$ over a hemisphere as given by

$$\epsilon(\omega) = \frac{1}{\pi} \int_0^{2\pi} \int_0^{\frac{\pi}{2}} \epsilon(\omega, \theta, \phi) \cos\theta \sin\theta \, d\theta d\phi. \tag{8.83}$$

The total hemispherical emittance is also desired for thermal calculations. It is defined as

$$\epsilon = \frac{1}{\sigma T^4} \int_0^\infty \epsilon(\omega) M_{bb}(\omega) \, d\omega, \tag{8.84}$$

where σ is the Stefan-Boltzmann constant, 5.6697×10^{-8} W/(m^2 K^4), T is temperature, and M_{bb} is the blackbody irradiance.

The two-phonon region of insulators features high emissivity and can be used to determine the surface temperature by single-band or two-color pyrometer technique. Figure 8.33 illustrates the normal emittance of the o-ray of sapphire at a temperature of 750 K. Knowing the emittance in the two-phonon region, which is stable with temperature, and applying the blackbody formula allows the measurement of temperature from a ratio of measured emission at two different frequencies. Further discussion on pyrometry is given in Section 8.4.5.

8.4.3 Athermal Materials

It is often of interest to design an optical system that is insensitive to temperature variations. The optical path is the index of refraction times the path length (nL). The thermal change in the optical path becomes
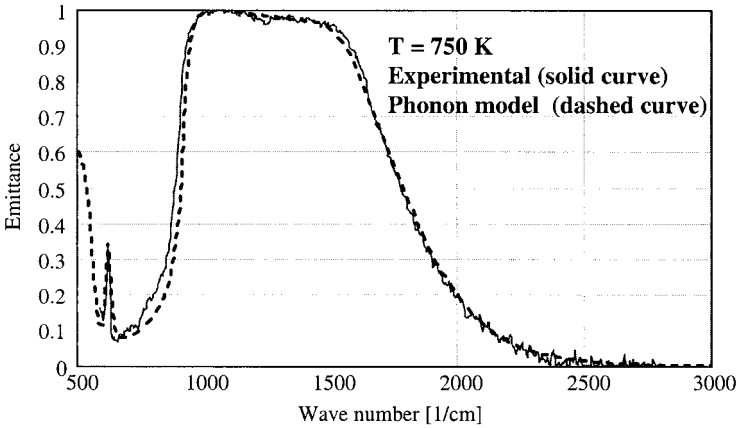
Fig. 8.33 Normal emittance of *o*-ray of sapphire at $T = 750$ K.

$$\frac{dnL}{dT} = nL \left(\frac{1}{L} \frac{dL}{dT} + \frac{1}{n} \frac{dn}{dT} \right). \tag{8.85}$$

The first term in the above expression is the thermal expansion and is almost always positive for window materials. Thus, to make the material athermal, it is desired to have a material with a negative thermo-optic coefficient (dn/dT). Consultation of Appendix 4 indicates that fluorides and alkali halides are candidate athermal materials. Applications include lens system design and solid-state laser gain media. For laser design, the important formula is resonator output frequency, given by

$$\nu_m(T) = \frac{\pi m}{2n(T)L(T)}.$$

8.4.4   Optical Fibers

Optical fibers offer tremendous improvement in data transmission bandwidth over conducting wires and coaxial cables, because carrier frequencies can be in the near infrared and visible (10^{13} to 10^{15} Hz). Furthermore, because of low-loss glasses, long propagation distances in dielectric waveguides are now possible. Full utilization of this technology is not yet realized because of limited-bandwidth modulators and detectors.

Geometrical optics solutions will be presented for various fiber geometries. Geometrical optics offers a simple interpretation for understanding optical waveguides and is thus a good place to begin. Physical optics solutions are more complete and general, but more difficult to obtain.

8.4.4.1 Geometrical Optics Solutions

A typical optical fiber has a central core and an outer cladding as illustrated in Fig. 8.34. Common values for silica fiber core radius and outer cladding radius are in the range
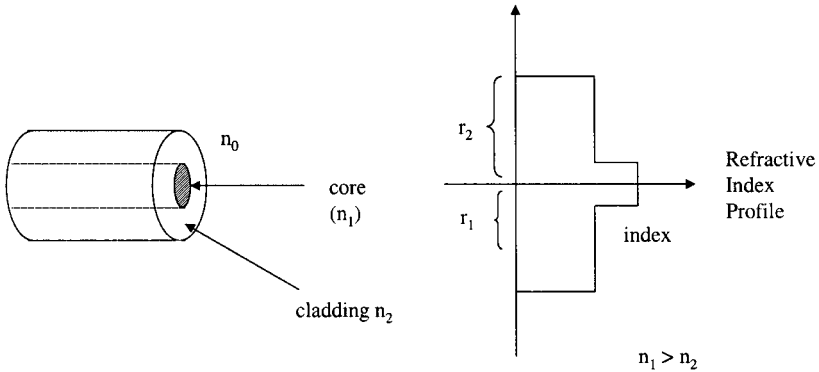
Fig. 8.34 Optical fiber construction.

$r_1 \approx 3\text{--}10$ μm and $r_2 \approx 125$ μm, respectively. Recall Snell's law from Chapter 4 (Eq. 4.72) and the angle convention defined in Fig. 2.5, to obtain

$$\frac{\cos \alpha_1}{\cos \alpha_2} = \frac{n_2}{n_1}, \tag{8.86}$$

where $\alpha_{1,2}$ are the complementary angles to ψ. Total internal reflection occurs at the complementary critical angle α_c, given by

$$\alpha_c = \cos^{-1}\left(\frac{n_1}{n_2}\right). \tag{8.87}$$

Thus, $\alpha_2 = 0°$ and no transmission of light into medium 2 occurs. Light is contained within the guide. (A more complete solution shows that total internal reflection is not 100% with some very minor loss because of evanescent fields in the cladding.)

Coupling of Light into a Fiber   Consider a bundle of rays incident on the end of a fiber, as illustrated in Fig. 8.35. Due to refraction at the core interface, it follows that

$$\frac{\sin \alpha'}{\sin \alpha_1} = n_1 \quad \text{(from Snell's law)}.$$

Thus, rays within the cone α'_c will propagate with minimal attenuation because they are within the internal critical angle, where $n_0 \sin \alpha'_c = n_1 \sin \alpha_c$ must be satisfied. Now it is convenient to define the relative refractive index difference, Δ, as
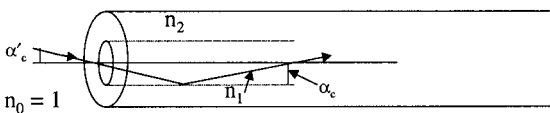
Fig. 8.35 Coupling of light rays into a fiber.

$$\Delta \equiv \frac{n_1^2 - n_2^2}{2n_1^2} \approx \frac{n_1 - n_2}{n_1} \quad \text{for} \quad n_1 - n_2 \ll n_1. \tag{8.88}$$

Therefore, the internal critical angle as a function of the relative refractive index becomes

$$\alpha_c = \cos^{-1}\left(\frac{n_2}{n_1}\right) = \cos^{-1}\left(\frac{n_1}{n_1} - \frac{n_1 - n_2}{n_1}\right) = \cos^{-1}(1 - \Delta).$$

For Δ small, the following approximation can be made using a binomial expansion

$$\cos^2\alpha_c = (1 - \Delta)^2 \approx 1 - 2\Delta, \quad \text{thus} \quad 2\Delta \approx 1 - \cos^2\alpha_c = \sin^2\alpha_c.$$

Using the above formula, we obtain

$$\alpha_c \approx \sin^{-1}(\sqrt{2\Delta}) \approx \sqrt{2\Delta} \quad \text{for} \quad \Delta \ll 1. \tag{8.89}$$

Now, the numerical aperture, *NA*, becomes

$$NA = \sin\alpha_c' = n_1 \sin\alpha_c \approx n_1\sqrt{2\Delta}. \tag{8.90}$$

Example 8.5   For $n_1 = 1.5$ and $\Delta = 0.01$. Then,

$$NA = 1.5(0.02)^{\frac{1}{2}} = 0.21 \quad \text{and}$$
$$\alpha_c' = 12.25°.$$

Modes in a Fiber   Figure 8.36 illustrates two different ray optic modes in a fiber. For the case that $\alpha_c > \alpha_1 > \alpha_2$, the modes will propagate. Thus, many modes can exist in a fiber. However, each mode will travel a different distance and thus arrive at the detector at different times at the end of the fiber, creating pulse spreading. Thus, it is often the case that single-mode operation is desired. The following condition can be used to ensure single-mode operation; let
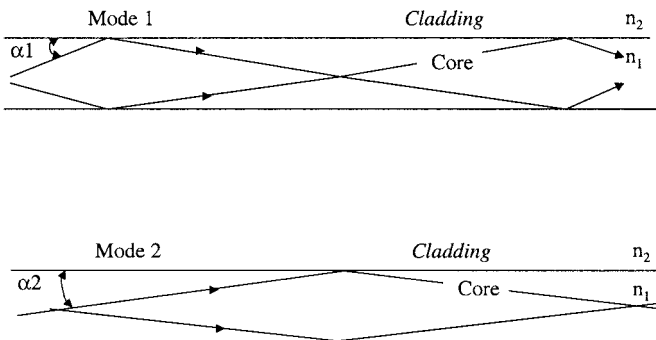
Fig. 8.36 Ray modes propagating in a fiber.

$$V = n_1 k_0' a (2\Delta)^{\frac{1}{2}} = k_0' a (NA).$$ (8.91)

where $k_0' = 2\pi/\lambda$ and a is the core radius. For $V > 2.4$, multimode operation exists and for $V < 2.4$, single-mode operation occurs.

Example 8.6   Find the required fiber radius for single-mode operation using the Example 8.4 result for *NA*. Thus, $NA = 0.21$ and

$$V = k_0' a (0.21)$$

$$V = 2\pi \tfrac{a}{\lambda}(0.21) < 2.4$$

$$\therefore \tfrac{a}{\lambda} < 1.82.$$

At near-visible wavelengths (e.g., $\lambda \approx 1$ μm, requires $a \approx 2$ μm), very fine radius fibers result.

8.4.4.2 Dispersion and Propagation Time

To understand the dispersion characteristics of a fiber, consider the group velocity, as given by

$$v_g = \left(\frac{\partial k'}{\partial \omega} \right)^{-1}.$$

Using the fact that $k' = k_0' n_1$, we obtain

$$v_g = \frac{c}{n_1 \left(1 + \frac{\omega}{n_1} \frac{\partial n_1}{\partial \omega} \right)} = \frac{c}{n_1 \left(1 - \frac{\lambda}{n_1} \frac{\partial n_1}{\partial \lambda} \right)}.$$ (8.92)

Define the refractive propagation time, τ_n, to be

$$\tau_n = L/v_g,$$ (8.93)

where L is the length of fiber. Substituting Eq. 8.92 into Eq. 8.93, we obtain

$$\tau_n = \frac{L}{c} \left(n_1 - \lambda \frac{\partial n_1}{\partial \lambda} \right).$$ (8.94)

The refractive propagation time has two parts; the first term accounts for zero dispersion and the second term accounts for dispersion. The second term is the change in propagation time due to dispersion and is expressed as

$$\Delta \tau_n = -L \frac{\lambda}{c} \frac{\partial n_1}{\partial \lambda}.$$ (8.95)

Consider an expansion of $n_1(\lambda)$ about a point λ_0 of the following form:

$$n_1(\lambda) = n_1(\lambda_0) + \frac{\Delta n_1}{\Delta \lambda} \Delta \lambda \approx n_1(\lambda_0) + \frac{\partial n_1}{\partial \lambda} \Delta \lambda.$$

Substituting the above result into Eq. 8.95, we obtain

$$\Delta \tau_n = -L \frac{\lambda}{c} \frac{\partial^2 n_1}{\partial \lambda^2} \Delta \lambda. \tag{8.96}$$

This important result shows that minimum change occurs at the wavelength of minimum dispersion.

Another dispersion term is caused by the different mode propagation paths, as illustrated in Fig. 8.36. The axial velocity is

$$v_a = v_g \cos \alpha$$

and the transverse velocity is

$$v_t = v_g \sin \alpha.$$

Obviously, the axial velocity determines the arrival time, thus it is desirable to have $\alpha \approx 0$ and $v_a \approx v_g - \alpha v_g \approx v_g (1 + \alpha)^{-1}$. Therefore, the modal propagation time becomes

$$\tau_m + \Delta \tau_m = \frac{L}{v_a} \approx \frac{L}{v_g}(1 + \alpha). \tag{8.97}$$

Again two terms are formed, the change in modal propagation time is

$$\Delta \tau_m \approx \frac{L}{v_g} \alpha. \tag{8.98}$$

Single-mode operation avoids this problem characteristic of multimode waveguides. (The index of refraction is also weakly nonlinear [$n = n_o + N_2 I$] and this is called waveguide dispersion. This is very important because for single-mode operation the waveguide dispersion and refractive index dispersion can cancel and dispersion-free propagation exists. This is the topic of solitons.)

8.4.4.3 Spectral Transmission Properties

Internal transmittance is given by

$$\tau_\infty = e^{-\beta L}.$$

(Internal transmission loss is often expressed in dB km^{-1} = 4.34 [β km^{-1}]. See Table A1.4.) It is of interest to determine the spectral location of the minimum intrinsic extinction coefficient. This occurs at the intersection of multiphonon absorption coefficient and Rayleigh scatter coefficient. This point is illustrated in Fig. 8.37 for a variety of fiber materials.

8.4.5 Pyrometry

Pyrometry is the noninvasive radiometric determination of a target temperature. Remote measurements are possible, requiring no contact with the target. This can be accomplished
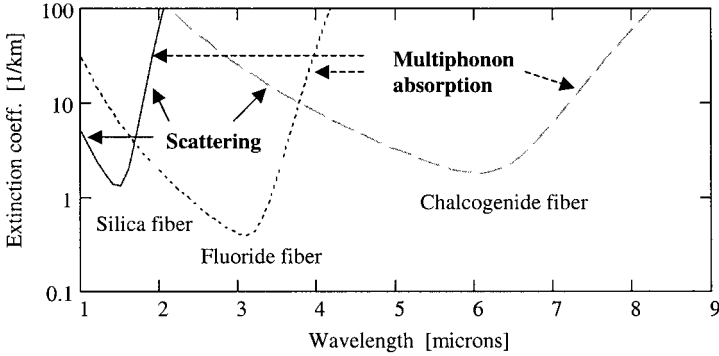
Fig. 8.37 Optical fiber loss curves for a variety of optical materials.

with a single-element optical detector, a spectrometer, or an imaging camera. The two-phonon region in solids presents an ideal spectral region for the remote measurement of surface temperature. The band-averaged emittance is near one (see Fig. 8.33, the two-phonon region is between 1000 and 1500 cm^{-1}) and independent of temperature. (See Terry et al., Ref. 8.57 for an example.)

To calibrate the sensor a variable temperature cavity blackbody is viewed that matches the optical path of the experiment and the electronic recording equipment. The average number of counts is determined as a function of temperature. The measured counts are then converted to radiance. The theoretical blackbody spectral radiance, $L_{bb}(v,T)$, in W/(cm^2 sr cm), is used in the calibration procedure to determine the band-averaged computed radiance, according to

$$L_{computed}(T) = \int_{band} L_{bb}(v,T) SRF(v) \, dv \; \left[\text{W/} \left(\text{cm}^2 \text{ sr} \right) \right], \qquad (8.99)$$

where $SRF(v)$ is the system transfer function, T is temperature in kelvins, and v is wave number in cm^{-1}. This requires mathematical representation of the system transfer function of all the components in the optical path.

The ability to compute the measured blackbody radiance allows direct conversion of counts to radiance. This is accomplished by a least-squares linear fit of measured camera counts to the computed radiance, as specified by

$$L_{measured}(T) = \frac{Counts(T) - \alpha}{\beta}, \qquad (8.100)$$

where α is the camera background and β is a scaling factor to obtain radiance in W/(cm^2 sr). The agreement between the measured and computed radiance as a function of temperature is typically very good.

The last step is to invert Eq. 8.100 to obtain the temperature. This is accomplished by equating the measured radiance (Eq. 8.100) to the computed radiance (Eq. 8.99).

In general, the inversion of this complicated equation to obtain temperature is not tractable. However, the following function accurately fits the computed radiance as given by Eq. 8.99:

$$L_{fit}(T) = \exp\left(a + \frac{b}{T} + \frac{c}{T^2}\right).$$

(8.101)

This functional form allows a tractable solution for temperature, knowing the band-limited blackbody radiance of the target.

The practical application of imaging pryometry usually requires the remote measurement of temperature of a nonblackbody surface. Thus, the spectral and spatial aspects of the target radiance must be known. Corrections for the nonblackbody character must be incorporated into Eq. 8.100. The correction factor is determined by computing the band-averaged emittance, as defined by

$$\epsilon(T) = \frac{\int\limits_{band} L_{bb}(v,T)\,\epsilon(v,T)\,SRF(v)\,dv}{\int\limits_{band} L_{bb}(v,T)\,SRF(v)\,dv},$$

(8.102)

where $\epsilon(v,T)$ is the spectral emittance. In Eq. 8.100, it is assumed that the target is a blackbody (i.e., $L_{measured}(T) = \langle L_{bb}\rangle_{band}(T)$). For a nonblackbody or graybody target, $L_{measured}(T) = \epsilon(T)\langle L_{bb}\rangle_{band}(T)$ in Eq. 8.100 must be replaced by $L_{measured}(T)/\epsilon(T)$. Obviously, it is desirable that ϵ be independent of temperature.

Problems

8.1 A 15 cm diameter KCl window is needed for a vacuum chamber. The window will be clamped to prevent the window from falling when the chamber is brought up to air pressure. How thick must the window be made?

8.2 Sapphire has a complex index of $n = 1.75$ and $\beta_{abs} = 0.94$ cm^{-1} at 2000 cm^{-1} frequency and 295 K. Find the spectral emissivity, ϵ_λ, for a slab with thickness $L = 0.6$ cm for viewing the surface in the normal direction.

8.3 Recall, in the long-wavelength limit ($k' \to 0$) the optical mode frequencies, ω_{TO}, are given by

$$\omega_{TO} \approx \left(\frac{2\beta_s}{\mu'}\right)^{\frac{1}{2}},$$

where β_s is the spring constant and μ' the reduced mass.

(a) For polar diatomic molecules, plot the beginning of infrared transparency against the reduced mass. Assume that v_{TO} is directly proportional to v_{max}. Use Appendix 4 as a reference for v_{max} and then use Eq. 8.57 to find v_{trans}. Obtain an expression for $v_{trans}(\mu')$. How does it compare with the above formula? Explain the observed trend for the alkali halides.

(b) Plot the bandgap energies, which mark the end of visible transparency for the alkali halides, as a function of the reduced mass. What is the relationship you

obtain in this case, and what can be said about the range of transparency (from the IR to the UV) for these materials?

8.4 Using the Sellmeier formula for n, compute the dispersion formula, $dn/d\lambda$. What characteristics are required for materials with low dispersion?

8.5 Infrared transparency in solids is determined by multiphonon sum band absorption. Explain the nature of this absorption mechanism and how it is related to one-phonon bands.

8.6 A window material 1 cm thick with scatter but no absorption loss and an index of refraction of 1.5 is observed to transmit 50% of the incident light to a detector with a $\pm 7°$ acceptance angle about the specular direction. Assuming that the total integrated scatter (TIS) is 0.5, what is the specular contribution to the transmittance?

8.7 Using the classical pole-fit model for $\epsilon_r(v,T)$, as given by

$$\epsilon_r(v,T) = \epsilon_\infty(T) + \sum_i \frac{\Delta\epsilon_i(T)v_i^2(T)}{v_i^2(T) - v^2 + j\Gamma_i(v,T)v},$$

show, for $v \ll v_i$ and $v \to 0$, that the following equations are true:

$$n(v,T) = \sqrt{\epsilon_r(0,T)} + \left(\sum_i \frac{\Delta\epsilon_i(T)}{2v_i^2(T)\sqrt{\epsilon_r(0,T)}} \right) v^2$$

and

$$\beta_{abs}(v,T) = 4\pi v k_a(v,T) = \left(\frac{2\pi}{\sqrt{\epsilon_r(0,T)}} \sum_i \frac{\Delta\epsilon_i(T)\Gamma_i(v,T)}{v_i^2(T)} \right) v^2.$$

8.8 Find the magnitude of the single-surface power reflection coefficient at an interface between two lossy media, for normal incidence (Fig. P8.8).
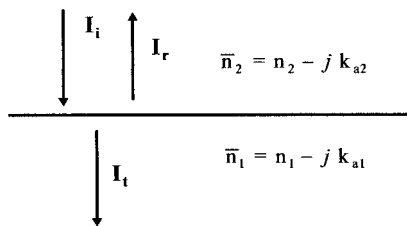
Fig. P8.8

8.9 Show that the n-phonon density-of-states function satisfies the following normalization condition:

$$\int_0^\infty dv\rho_n(v) = 1, \quad \text{given} \quad \int_0^\infty dv\rho_1(v) = 1.$$

8.10 Based on Eq. 8.45, show that the multiphonon sum band model for the nth phonon band absorption coefficient, (a) is independent of temperature for $T \to 0$

$$\lim_{T \to 0} \beta_{abs,n}(\nu, T) = K(n-1)!\left(\frac{1}{j'}\right)^{(n-1)} g(\nu - n\nu_0).$$

and (b) reduces to the classical limit for $h \to 0$ ($j' \to \infty$ and $T \to$ large),

$$\lim_{h \to 0} \beta_{abs,n}(\nu, T) = Kn!\left(\frac{k_B T}{4D_0}\right)^{n-1} g(\nu - n\nu_0).$$

8.11 Verify Eq. 8.39 for the far-infrared difference band temperature dependence using the fact that

$$\beta_{np} \propto N_p^n \tanh\left(\frac{hc\nu}{2k_B T}\right)\nu$$

where N_p is the phonon occupation number (remember phonons are bosons).

Athermal Optical Materials

8.12 Based on Table 8.1 and Table A4.5 (Appendix), find materials such that

$$\frac{d(nL)}{dT} \approx 0,$$

where n is the index of refraction (real part) and L is the path length.

Dispersion

8.13 Find materials with visible transparency and good IR transparency with minimum dispersion from the visible to the IR. This combination of properties is desirable for visible alignment of IR system optics.

Dielectric Mirror

8.14 Design a high-reflectance dielectric mirror on a glass substrate with an index of refraction of 1.6. Use two different coating materials, one with a low refractive index and the other with a high refractive index. Determine the coating materials and the number of layers to achieve a reflectance of 0.99.

Lasers

8.15 A ruby laser of length $L (= 10$ cm) and output wavelength of 0.694 μm, uses a Fabry–Perot resonator with the mirrors at each end of the rod. The mode locations are given by

$$\nu_m(T) = \frac{cm}{2n(T)L(T)}[Hz]$$

where n is the index of refraction, c is the speed of light, and m is an integer index.

(a) Find the thermal change in the mode position,

$$\frac{d\nu_m}{dT} = ?,$$

given

$$\frac{dn}{dT} = 12 \times 10^{-6}\,[K^{-1}], \quad \frac{1}{L}\frac{dL}{dT} = 7 \times 10^{-6}\,[K^{-1}],$$

and the background permittivity of the host medium (Al_2O_3) is

$$\epsilon_r = 1 + \sum_i \frac{A_i\lambda^2}{\lambda^2 - \lambda_i^2},$$

where $A_1 = 1.4313493$, $A_2 = 0.65054713$, $A_3 = 5.3414021$, $\lambda_1 = 0.0726631$ μm, $\lambda_2 = 0.1193242$ μm, and $\lambda_3 = 18.028251$ μm.

(b) For a required coherence time of 1 μsec in a flashlamp pumped ruby laser, is this thermal effect significant? (*Note*: A flashlamp produces a significant amount of nonuniform heating as well as optical pumping energy. Thus thermal stability and uniformity are not easily obtained. This is especially true for pulsed laser operation where the flashlamp is pulsed also.)

8.16 Semiconductor lasers are frequency tunable by changing the junction temperature. For a GaAs laser operating at a wavelength 0.8 μm with a thickness of $L = 100$ μm and room-temperature index of refraction of 3.32, find the frequency tuning rate, as given by

$$\frac{d\nu_m}{dT} = ?,$$

where

$$\frac{dn}{dT} = 250 \times 10^{-6}[K^{-1}], \quad \frac{1}{L}\frac{dL}{dT} = 5 \times 10^{-6}\,[K^{-1}].$$

Optical Fibers

8.17 Using the Sellmeier model given in Appendix 4 for fused silica, find the wavelength of minimum dispersion. How is the minimum dispersion point affected by germania doping? Obtain a formula that describes the effect. Why is the minimum dispersion wavelength significant for femtosecond pulse transmission in an optical fiber?

Pyrometry

8.18 Obtain an explicit expression for temperature from Eqs. 8.100 and 8.101. Also, correct for the graybody character of the surface.

Bibliography

Section 8.1

8.1   E.D. Palik (ed.), *Handbook of Optical Constants of Solids*, Academic Press (1985).

8.2   G. Burns, *Solid State Physics*, Academic Press (1985).

8.3   M.J. Weber (ed.), *Handbook of Laser Science and Technology, Vol. III: Optical Materials, Part 1: Properties*, CRC Press (1987).

8.4   W.L. Wolfe, "Optical Materials," in *The Infrared Handbook*, 2nd Ed., W.L. Wolfe and G.J. Zissis (eds.), ERIM (1985).

Section 8.2.1

8.5   A.J. Bosman and E.E. Havinga, "Temperature Dependence of Dielectric Constants of Cubic Ionic Compounds," *Phys. Rev.* **129**, 1593 (1963).

8.6   H.H. Li, "Refractive Index of Alkali Halides," *J. Phys. Chem. Ref. Data*, **5**, 329 (1976).

8.7   M.E. Thomas and R.I. Joseph, "A Comprehensive Model for the Intrinsic Transmission Properties of Optical Windows," in *Proc. of SPIE Infrared Optical Materials* **929**, 87 (1988).

8.8   F. Gervais and B. Piriou, "Temperature Dependence of Transverse- and Longitudinal-Optic Modes in TiO_2 (rutile)," *Phys. Rev.* B **10**, 1642 (1974).

8.9   R.H. Lyddane, R.G. Sachs, and E. Teller, "On the Polar Vibrations of Alkali Halides," *Phys. Rev.* **59**, 673 (1941).

8.10 J.R. Jasperse, A. Kahan, J.N. Plendly, and S.S. Mitra, "Temperature Dependence of Infrared Dispersion in Ionic Crystals LiF and MgO," *Phys. Rev.* **146**, 526–542 (1966).

8.11 A.A. Maradudin, J.P. Ipatoua, and R.F. Wallis, "Temperature Dependence of the Width of the Fundamental Lattice-Vibration Absorption Peak in Ionic Crystals II. Approximate Numerical Results," *Phys. Rev.* **155**, 882 (1967).

8.12 R.F. Wallis and A.A. Maradudin, "Lattice Anharmonicity and Optical Absorption in Polar Crystals: III. Quantum Mechanical Treatment in the Linear Approximation," *Phys. Rev.* **125**, 1277 (1962).

8.13 K.V. Namjoshi and S.S. Mitra, "Infrared Absorption by Alkali Halides in the Transport Regime and Its Temperature Dependence," *Solid State Commun*. **15**, 317–320 (1974).

8.14 B. Szigeti, "Higher-Order Terms in the Dielectric Constant of Ionic Crystals," *Proc. Roy. Soc.* A **252**, 217 (1959).

8.15 W.W. Ho, "High-Temperature Dielectric Properties of Polycrystalline Ceramics," *MRS Symposium M*, April 6, 1988.

8.16 E.V. Loewenstein, D.R. Smith, and R.L. Morgan, "Optical Constants of Far-Infrared Materials 2: Crystalline Solids," *Appl. Opt.* **12**, 398 (1973).

8.17 S. Roberts and D.D. Coon, "Far-Infrared Properties of Quartz and Sapphire," *J. Opt. Soc. Am.*, **52**, 1023 (1962).

8.18 Kerem Optronics, Manufacturer's data sheet.

8.19 S. Adachi, "Excitonic effects in the Optical Spectrum Of GaAs," *Phys. Rev. B* **41**, 1003–1013 (1990).

8.20 M.E. Thomas, J. Miragliotta and R.I. Joseph, "Time Domain Susceptibility of Intrinsic GaAs," *J. Appl. Phys.* **91**, 9723–9730 (2002).

8.21 J.H. Van Vleck and D.L. Huber, "Absorption Emission and Linebreadths: A Semihistorical Perspective," *Rev. Mod. Phys.* **49**, 939 (1977).

8.22 R. Stolen and K. Dransfedl, "Far-Infrared Lattice Absorption in Alkali Halide Crystals," *Phys. Rev.* **139**, 3A1295 (1965).

8.23 S.S. Mitra, in "Optical Properties of Nonmetalic Solids for Photon Energies Below the Fundamental Bandgap," in *Handbook of Optical Constants*, (E.D. Palik, ed.), Academic Press, p. 213 (1985).

8.24 M. Stead and G. Simonis, "Near Millimeter Wave Characterization of Dual Mode Materials," *Appl. Opt.* **28**, 1874 (1989).

8.25 J.R. Hardy and A.M. Karo, "Theoretical Study of the Long-Wavelength Optical Properties of NaCl, KCl, KBr and KI," *Phys. Rev.* B **26**, 3327 (1982).

8.26   M.E. Thomas, R.I. Joseph, G.J. Simonis, and M. Stead, "Characterization of the Infrared and Far-Infrared Properties of Sapphire and Quartz," in *13th International Conf. on Infrared and Millimeter Waves, SPIE Conf. Digest* **1039** (R.J. Temkin, ed.), p. 339 (1988).

8.27   D.L. Mills and A.A. Maradudin, "Theory of Infrared Absorption by Crystals in the High Frequency Wing of Their Fundamental Lattice Absorption," *Phys. Rev.* B **8**, 1617 (1973).

8.28   A.A. Maradudin and D.L. Mills, "Temperature Dependence of the Absorption Coefficient of Alkali Halides in the Multiphonon Regime," *Phys. Rev. Lett.* **31**, 718 (1973).

8.29   L.L. Boyer, J.A. Harrington, M. Hass, and H.B. Rosenstock, "Multiphonon Absorption in Ionic Crystals," *Phys. Rev.* B **11**, 1665–1679 (1975).

8.30   H.B. Rosenstock, "Multiphonon Absorption in Alkali Halides: Quantum Treatment of Morse Potential," *Phys. Rev.* B **9**, 1963 (1974).

8.31   M. Sparks and L.J. Sham, "Theory of Multiphonon Absorption in Insulating Crystals," *Phys. Rev.* B **8**, 3037 (1973).

8.32   D. Billard, F. Gervais, and B. Piriou, "Analysis of Multiphonon Absorption in Corundum," *Phys. Status Solidi* B **75**, 117 (1976).

8.33   H. Cramer, *Random Variables and Probability Distributions*, Cambridge University Press (1970).

8.34   M.E. Thomas, R.I. Joseph, and W.J. Tropf, "Infrared Transmission Properties of Sapphire, Spinel, Yttria and ALON as a Function of Temperature and Frequency," *Appl. Opt.* **27**, 239 (1988).

8.35   T.F. Deutsch, "Absorption Coefficient of Infrared Laser Window Materials," *J. Phys. Chem. Solids* **34**, 2091 (1973).

8.36   A.J. Barker, "The Effect of Melting on the Multiphonon Infrared Absorption Spectra of KBr, NaCl, and LiF," *J. Phys.* C **5**, 2276 (1972).

8.37   J.A. Harrington and M. Hass, "Temperature Dependence of Multiphonon Absorption," *Phys. Rev. Lett.* **31**, 710 (1973).

8.38   H.G. Lipson, B. Bendow, N.E. Massa, and S.S. Mitra, "Multiphonon Infrared Absorption in the Transparent Regime of Alkaline-Earth Fluorides," *Phys. Rev.* B **13**, 2614 (1976).

8.39   M.E. Thomas, W.J. Tropf, and A. Szpak, "Optical Properties of Diamond," *Diamond Films and Technology* **5** No 3, 159–180 (1995).

8.40   F. Urbach, "The Long-wavelength Edge of Photographic Sensitivity and of the Electronic Absorption of Solids," *Phys. Rev.* **92**, 1325 (1953).

8.41   T. Skettrup, "Urbach's Rule Derived from Thermal Fluctuations in the Bandgap Energy," *Phys. Rev. B* **18**, 2622 (1978).

8.42   H. Mori and T. Izawa, "A New Loss Mechanism in Ultralow Loss Optical Fiber Materials," *J. Appl. Phys.* **51**, 2270–2271 (1980).

8.43   T. Tomiki and T. Miyata, "Optical Studies of Alkaline Earth Fluorides in the VUV Region," *J. Phys. Soc. Japan* **27**, 658–678 (1969).

8.44   M.E. Thomas, W.J. Tropf and S. Gilbert, "Ultraviolet Absorption Edge Characterization of Sapphire, Spinel and ALON," *Opt. Eng.* **32**, 1340–1343 (1993).

Section 8.2.2

8.45   D.R. Uhlmann and N.J. Kreidl, *Optical Properties of Glass*, The American Ceramic Society (1991).

8.46   P.W. France, M.G. Drexhage, J.M. Parker, M.W. Moore, S.F. Carter, and J.V. Wright, *Fluoride Glass Optical Fibres*, CRC Press (1990).

Section 8.2.3

8.47   J.I. Pankove, *Optical Processes in Semiconductors*, Dover (1971).

8.48   S.L. Chuang, *Physics of Optoelectronic Devices*, Wiley Series in Pure and Applied Optics (1995).

8.49 M. Kohin, S.J. Wein, J.D. Traylor, R.C. Chase, and J.E. Chapman, "Analysis and Design of Transparent Conductive Coatings and Filters," *Opt. Eng*. **32**, 911–925 (1993).

Section 8.2.4

8.50 M.A. Ordal, L.L. Long, R.J. Bell, S.E. Bell, R.R. Bell, R.W. Alexander Jr., and C.A. Ward, "Optical Properties of the Metals Al, Co, Cu, Au, Fe, Pb, Ni, Pd, Pt, Ag, Ti, and W in the Infrared and Far infrared," *Appl. Opt.* **22**, 1099–1119 (1983).

Section 8.3

8.51 J.A. Ogivy, *Theory of Wave Scattering from Random Rough Surfaces*, Institute of Physics Publishing, Bristol (1992).

Section 8.4

8.52 M.E. Thomas, "A Computer Code for Modeling Optical Properties of Window Materials," in Window and Dome Technologies and Materials, *Proc. of SPIE*, **1112**, 260-267 (1989).
8.53 M.E. Thomas and W.J. Tropf, "Models of the Optical Properties of Solids," *Proceedings of SPIE, Window and Dome Technologies and Materials III* **1760**, July (1992).
8.54 P. Yeh, *Optical Waves in Layered Media*, Wiley-Interscience (1988).
8.55 W.J. Tropf and M.E. Thomas,"Measurements and Estimation Techniques for High-Temperature Radiative Properties of Solids," *1995 ASME International Mechanical Engineering Congress & Exposition*, Pamphlet No. 95-WA/HT-31, ASME Technical Publishing (1995).
8.56 T. Katsuyama and H, Matsumura, *Infrared Optical Fibers*, Adam Hilger (1989).
8.57 D.H. Terry, M.E. Thomas, M.J. Linevsky, and D.T. Prendergast, "Imaging Pyrometry of Laser-Heated Sapphire," *Johns Hopkins APL Tech. Dig.* **20-2**, 7–14 (1999).

Other General Reference Books on Optical Properties of Solids

8.58 E.D. Palik (ed.), *Handbook of Optical Constants of Solids II*, Academic Press, (1991).
8.59 E.D. Palik (ed.), *Handbook of Optical Constants of Solids III*, Academic Press, (1998).
8.60 M.J. Weber (ed.), *Handbook of Laser Science and Technology Vol. IV: Optical Materials, Part 2: Properties*, CRC Press (1987).
8.61 M.J. Weber (ed.), *Handbook of Laser Science and Technology Vol. V: Optical Materials, Part 3: Properties*, CRC Press (1987).
8.62 P. Klocek, *Handbook of Infrared Optical Materials*, Marcel Dekker, (1991).
8.63 W J. Tropf, T.J. Harris and M.E. Thomas, "Optical Materials for the Visible and Infrared," Chapter 11 in *Electro-optics Handbook*, R. Waynant and M. Ediger (eds.), McGraw-Hill, pp. 11.1–11.97 (1993).
8.64 W.J. Tropf, M.E. Thomas and T.J. Harris, "Optical Properties of Crystals and Glasses," Chapter 33 in *Optical Society of America Handbook of Optics, Vol. 2, Optical Materials and Devices*, E. VanStryland, D. Williams, and W.L. Wolfe (eds.), McGraw-Hill (1994).
8.65 D.C. Harris, *Materials for Infrared Windows and Domes, Properties and Performance*, SPIE Optical Engineering Press (1999).
8.66 J.H. Simmmons and K.S. Potter, *Optical Materials*, Academic Press (2000).

This page intentionally left blank

9

Optical Propagation in Water

From a basic physics perspective, liquids are the least understood state of matter. Yet this medium plays an important role in the process of life on this planet. The human body is largely composed of liquids, and three-quarters of the surface of the earth is covered by seawater. The main liquid of interest in this chapter, and to the applied scientist and engineer, is water. The importance of understanding the optical properties of water cannot be overemphasized.

9.1 Optical Properties of Pure Water

The chapter appropriately begins with a discussion of the optical properties of pure water, since it is the main ingredient in seawater and in biomedical fluids. Pure water is an insulator with a strong dipole moment and an effective electronic band edge in the ultraviolet near 0.16 μm (62,500 cm^{-1}). Absorption near the band edge shows similar structure to that observed in solids. Water has extensive infrared vibrational bands just as in the gas phase. Dipoles in a liquid can partially rotate in response to the polarization of the incident microscopic field, and Debye relaxation bands occur in the microwave region.

9.1.1 Debye Relaxation

A permittivity model for Debye relaxation was presented in Chapter 4 by Eq. 4.60. This is an important mechanism that describes the optical properties of liquids at far-infrared

and microwave frequencies. Figure 9.1 presents a comparison of experimental optical constant data collected at approximately 298 K and at a pressure of 1 atm to a single oscillator Debye model of the form

$$\epsilon_D(\omega, T) = \epsilon_\infty(T) + \frac{\Delta\epsilon_D(\nu, T)}{1 + j\frac{2\pi c\nu}{\Gamma_D(T)}}, \tag{9.1}$$

using the values $\Delta\epsilon_D = 74.335$, $\epsilon_\infty = 3.97$, and $\Gamma_D/2\pi c = 0.65$ cm^{-1}. Recall that the dampening parameter corresponds to the Debye relaxation time, τ_D, according to

$$\tau_D = 1/\Gamma_D = 8.162 \times 10^{-12} \text{ sec.} \tag{9.2}$$

Good agreement with observation is obtained up to about 10 cm^{-1} (300 GHz). Then two processes cause deviation from the Debye model. One is contributions from higher frequency vibrational modes, which are discussed in the next section. The other is the Debye blue absorption wing overpredicts the true absorption level and requires a cutoff function. Recall that a similar cutoff function is required for the classical oscillator model as given by Eq. 8.12. In this case, the oscillator strength is empirically modified to become

$$\Delta\epsilon_D(\nu) = \Delta\epsilon_D \begin{Bmatrix} 1 & \nu \leq 20\Gamma_D \\ \exp(-0.002(\nu - 20\Gamma_D)) & 20\Gamma_D \leq \nu \end{Bmatrix}. \tag{9.3}$$
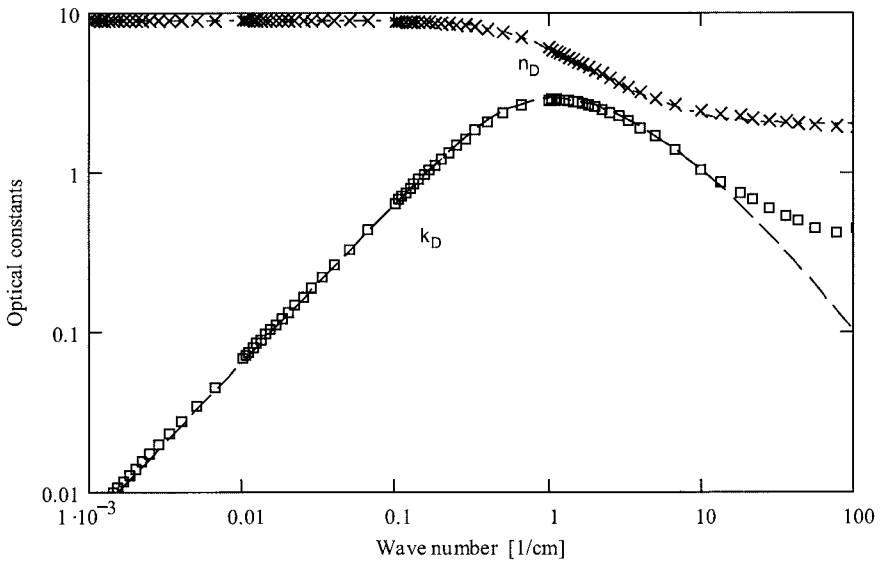
Fig. 9.1 A comparison of experimental optical constant data to the Debye relaxation model presented in the text for pure water at room temperature ($T = 298$ K) and a pressure of one atmosphere. (x – experimental n, Querry et al., Ref. 9.1; □ – experimental k, Querry et al., Ref. 9.1; dash–dot curve – Debye model for n_D; and dashed curve – Debye model for k_D using Eq. 9.1.)

The three parameters in the Debye model are temperature dependent. A least-squares fit to an Arrhenius-type function of temperature, representing the Debye relaxation time data from 0° to 75° C, yields

$$\tau_D(T) = \frac{5.39}{T} e^{1835.5/T} \quad \text{p sec.} \tag{9.4}$$

The temperature dependence of the static dielectric constant, $\epsilon'(0)$, from 0° to 100° C is represented by

$$\epsilon_s(T) = 87.740 - 0.40008(T - 273) + 9.398 \times 10^{-4}(T - 273)^2$$
$$- 1.41 \times 10^{-6}(T - 273)^3. \tag{9.5}$$

Once the temperature dependence of $\epsilon_\infty(T)$ is known, then the temperature dependence of $\Delta\epsilon_D(T)$ can be determined from Eq. 9.1. The pressure dependence of the Debye model parameters is weak and unfortunately not well characterized.

9.1.2 Vibrational Modes

Throughout the infrared, vibrational absorption bands dominate the optical properties of pure water. Figure 9.2 plots experimental index of refraction and absorption coefficient data for pure water in the infrared region based on data from Querry et al. (Ref. 9.1). The vibrational bands of water are identified, along with the corresponding classical oscillator model parameters, in Table 9.1. There are similarities between water vapor vibrational band structure and pure water spectra. First, note the similarity between the water vapor continuum spectra of Fig. 7.17 and Fig. 9.2. Both show an exponentially decreasing background in the absorption coefficient with vibrational band structure on top. Second, for every fundamental vibrational band in water vapor there is a corresponding fundamental band in liquid water. As Table 9.1 indicates, there are also new intermolecular vibrational modes in liquid water. The first is the hindered translation band, ν_T. The second is a hindered rotation band called the libration band, ν_L. The first two bands have no gas-phase counterpart because these motions are not hindered in a gas. They represent hindered movement of normal gas-phase motion in a liquid state with much higher density. The next vibration band is the bending mode, ν_B, which corresponds to the ν_2 band in the gas phase. The association band, ν_A, has no corresponding gas-phase band, but is also found in ice spectra. It is most likely a combination band of $\nu_B + \nu_L$. The next vibrational mode is the strongly absorbing stretching mode, ν_S. The remaining vibrational bands in liquid water are combination or overtone bands of these previously mentioned bands, as designated in Table 9.1. The strength of these bands decreases as the frequency increases such that a transparency window opens in the visible.

The classical oscillator model is again modified to account for the vibrational band blue-wing cutoff just as in the solid-state case (recall Eq. 8.12). The functional form is different, however, and an exponential function is empirically chosen (similar to the gas-phase line shape correction to the Lorentz line shape discussed in Section 5.6.3) as given by
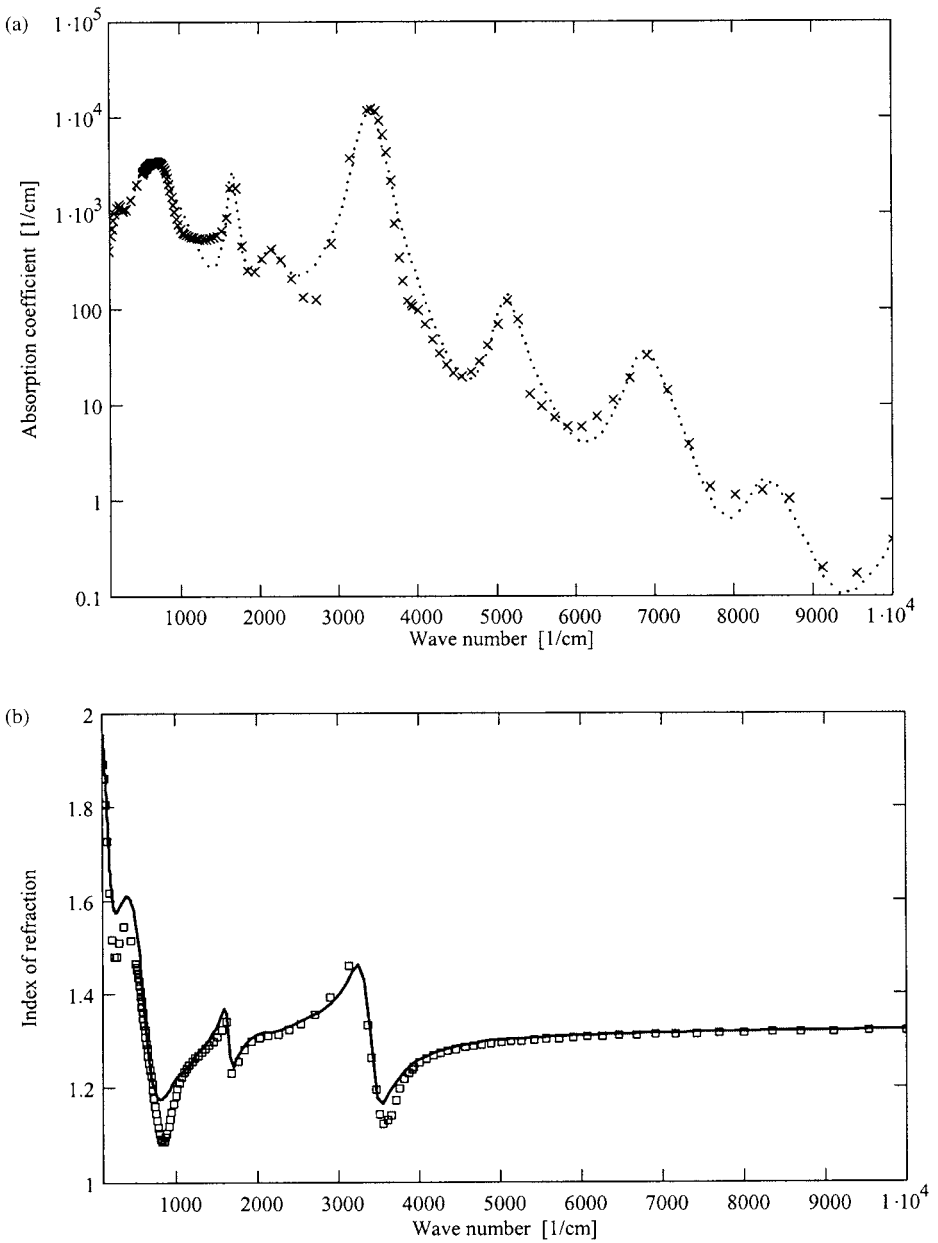
Fig. 9.2 The far-infrared to near-infrared spectrum of the complex index of refraction of pure water at room temperature and one atmosphere pressure: (a) absorption coefficient versus wave number (x – experimental from Querry et al., Ref. 9.1; dashed curve represents the classical oscillator model), and (b) index of refraction versus wave number (□ – experimental from Querry et al., Ref. 9.1; solid curve represents the classical oscillator model).

430

Table 9.1 Vibrational and Electronic Mode Parameters (at $T_0 = 296$ K) of Pure Water for the Classical Oscillator Model at One Atmosphere Pressure

Band Identification	Spectral Location ν_i [cm^{-1}]	Thermal Spectral Shift [cm^{-1}/K]	Strength $\Delta\epsilon_i$	Thermal Slope [1/K]	Full-Width Γ_i [cm^{-1}]
Vibrational					
Hindered translation, ν_T	175	−0.2	1.481	—	200
Libration, ν_L	595	−0.7	0.841	—	408
Bending, ν_B	1642	−0.1	0.02	—	91
Association, ν_A	2127	−0.9	0.0055	—	350
$2\nu_B$	3248	—	0.005	—	115
Stretching, ν_S	3387	0.418	0.052	-3×10^{-4}	230
$\nu_S + \nu_{L_-}$	3985	—	5×10^{-5}	—	200
$\nu_S + \nu_B$	5125	—	3×10^{-4}	—	265
$\nu_S + \nu_A$	5600	—	2×10^{-5}	—	500
$2\nu_S$	6875	—	7×10^{-5}	—	400
$2\nu_S + \nu_B$	8400	—	2.5×10^{-6}	—	500
$3\nu_S$	10250	—	7.5×10^{-7}	—	650
$3\nu_S + \nu_B$	11750	—	4.2×10^{-8}	—	700
$4\nu_S$	13300	—	3.5×10^{-8}	—	1000
$5\nu_S$	15900	—	4.5×10^{-9}	—	1600
$6\nu_S$	18500	—	4.0×10^{-10}	—	2000
Electronic					
	71684.6	—	0.335	-2.65×10^{-4} $-3.2 \times 10^{-6}(T - T_0)$	—
	155038.8	—	0.421		—

$$\Gamma_i(\nu) = \begin{Bmatrix} \Gamma_i & \nu \le \nu_i + \Gamma_i \\ \Gamma_i \exp(-0.0028(\nu - \nu_i - \Gamma_i) & \nu_i + \Gamma_i \le \nu \end{Bmatrix}. \tag{9.6}$$

This modification is crucial in obtaining a good fit to the experimental absorption coefficient as demonstrated in Fig. 9.1. Other attempts in the past to fit the classical oscillator model to experimental data have been successful for the real part of the complex index only. This is a first attempt to obtain a model representation of the full complex index of refraction of water.

The room-temperature index of refraction in the near-infrared and visible region also can be represented by the Sellmeier model. Converting Eq. 8.20 to wavelength, one obtains

$$n^2(\lambda) = 1 + \sum_i \frac{S_i \lambda^2}{\lambda^2 - \lambda_i^2}. \tag{9.7}$$

Based on the above equation, the Sellmeier parameters for the index of refraction of water from 0.16 to 2.0 μm and at a temperature of 20°C are listed in Table 9.2. Two modes represent electronic transitions and one mode represents the combined contribution of the many infrared vibrational bands of water. The same electronic

Table 9.2 Sellmeier Model Parameters for Room-temperature
(NTP) Liquid Water Index of Refraction

Mode	Strength	Location	
		[μm]	[cm^{-1}]
1	0.42295	0.0644866	155070.98
2	0.33452	0.139532	71668.15
3	0.15797	3.42372	2920.80

transitions are also listed in Table 9.1. Figure 9.3a compares the Sellmeier model to experimental data from Querry et al.(Ref. 9.1).

The visible index of refraction has a strong temperature dependence, as demonstrated by the following formula based on experimental data at a wavelength of 0.5893 μm:

$$n_{0.5893}(T) = 1.333 - a(T - T_0) - b(T - T_0)^2, \qquad (9.8)$$

where $T_0 = 19.9$ °C, $a = 9.46036 \times 10^{-5}$ °C^{-1}, and $b = 1.231257 \times 10^{-6}$ °C^{-2}. This result is used to determine the temperature-dependent strength parameters for the electronic transition in Table 9.1. The spectral shift values in Table 9.1 are obtained from Pinkley et al. (Ref. 9.6), and Eisenberg and Kauzmann (Ref. 9.2). The functional forms for temperature-dependent line position and strength are the same as Eqs. 8.19a and 8.19b.

The index of refraction change with pressure is also important for optical systems operating in the deep ocean. The change in visible refractive index with respect to pressure is experimentally determined to be

$$\frac{dn}{dp} = 1.5 \times 10^{-2} \quad \text{atm}^{-1}$$

at $T = 0$°C.

9.1.3 Electronic Band Edge

In the ultraviolet region, two exponential absorption features are clearly indicated, as illustrated in Fig. 9.3b from 45,000 to 60,000 cm^{-1}. In a similar fashion to solids, these can be interpreted as the Urbach edge (given by Eq. 8.59) and the weak absorption tail (given by Eq. 8.68). The corresponding Urbach tail parameters for water are $E_g = 7.439$ eV, $\beta_{U0} = 1.1 \times 10^5$ cm^{-1}, and $\sigma_s = 0.37$. The weak-absorption tail model parameters aree $\beta_{wa0} = 5.5 \times 10^{-12}$ cm^{-1} and $E_0 = 0.27$ eV. These functions provide a good fit to experimental observations until the scatter properties dominate in the visible. This fact should not come as a surprise, since other amorphous materials (e.g., glasses) also exhibit similar behavior.

9.1.4 Scattering

Bulk scattering in a pure liquid is based on intrinsic density and temperature fluctuations. The fluctuating volume is small in size or has a small change in the refractive

(a)

HOC II
Model
Lauscher, T = 20 C
Sellmeier model

(b)
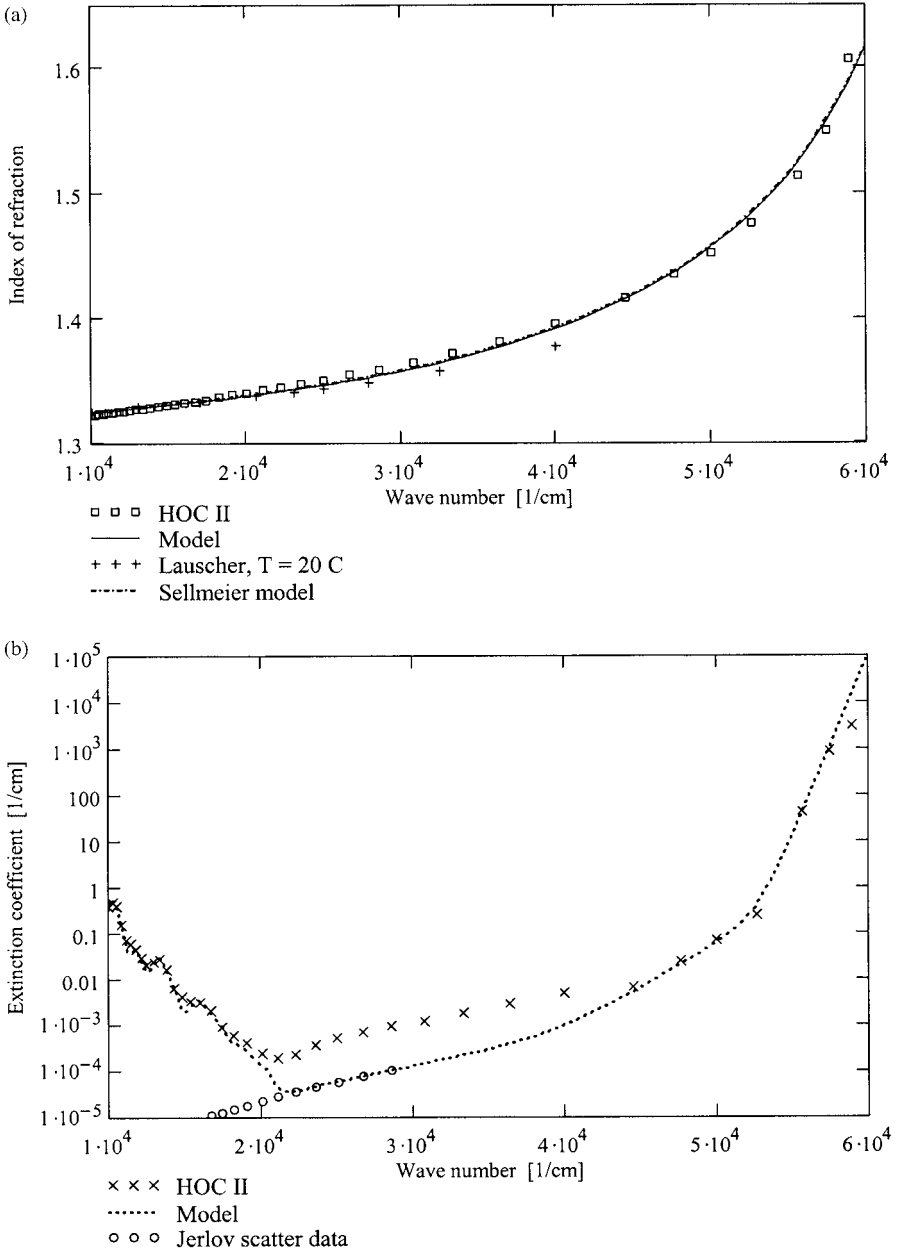
Fig. 9.3 The near-infrared to ultraviolet spectrum of the complex index of refraction of pure water at room temperature and one atmosphere pressure (from Querry et al., Ref. 9.1): (a) index of refraction versus wave number (experimental from □ – Querry et al., Ref. 9.1, and + – Lauscher, Ref. 9.4; solid curve represents the classical oscillator model [Table 9.1]); (b) extinction coefficient versus wave number (x – experimental from Querry et al., Ref. 9.1, ○ – Jerlov scatter model, Ref. 9.10 [Eq. 9.9], and dotted curve represents the classical oscillator, electronic band edge, and scatter models).

index, thus Rayleigh-type scatter is observed. Scatter measurements on room-temperature high-purity water by Morel fit the following:

$$\beta_{sca}(\nu) = 1.3875 \times 10^{-22}\nu^4 \frac{n^2(\nu)}{n^2(20{,}000)}. \tag{9.9}$$

This function and experimental data points are plotted in Fig. 9.3b. The data from Querry et al. are above the Morel data, suggesting that the water purity for the Querry data set is not the same as the Morel data set, or that there is some other absorption or scattering mechanism present in this spectral region. It is most likely that the extinction coefficient of water from 20,000 to 40,000 cm^{-1} is dominated by scatter. The phase function for pure water is slightly different than for isotropic Rayleigh scatter, accounting for anisotropy in the water molecule. It is given by the following formula:

$$P_{seawater}(\theta) = 0.06225\,(1 + 0.835\cos^2\theta). \tag{9.10}$$

9.2 Seawater

This section begins with a brief introduction to optical oceanography. The ocean has two useful spectral windows in which electromagnetic energy can propagate practical distances. One is at extremely low frequencies (ELF, from 1 to 1000 Hz) and the other is the visible region. For high-data-rate communication or remote sensing with reasonable spatial resolution, the optical spectrum must be used. Thus, detailed knowledge of the optical properties of seawater is important in the implementation of these and other technologies.

9.2.1 Introduction to Optical Oceanography

A basic understanding of the physical and chemical properties of seawater is a necessary requirement for the operation of any electro-optical system in the ocean. A brief introduction to ocean structure relevant to optics, chemical and particle composition, and pressure dependence is given in the following sections.

9.2.1.1 Ocean Structure

Of critical importance to optical oceanography are the ocean surface and the illumination depth of the ocean. The ocean surface is an important component of the weather on earth. The high heat capacity of water moderates the air temperature above the ocean. Thus, the ocean surface temperature is an important measure for weather model input. Since water and seawater are nearly blackbody in the longwave IR, simple radiometric techniques can be used to measure surface temperature.

The ocean surface is not smooth, but rough with a wide variety of temporal and spatial scales. Tidal waves have very long periods (12–24 hours), swell waves with periods on the order of minutes are generated by remote storms, wind-generated waves have periods on the order of seconds, and capillary waves have periods on the order of millisecond. Wind and capillary waves are the most important to optical systems.

Based on Fig. 9.3, the minimum extinction coefficient of pure water is 1×10^{-2} m^{-1} located at 21,000 cm^{-1} (0.476 µm). This means that only 2% of blue light from a source at the surface makes it to a depth of 400 m. All other wavelengths are extinguished at this depth. Below 400 m we expect the ocean to become a very dark place. This is why very little biological life exists below this illumination depth and what life does exist is very different from that of the upper ocean.

9.2.1.2 Ocean Chemical Composition

Pure seawater is a solution that contains no organic chemicals, no gas, and no particles. It is dominantly composed of water and the following common solutes: $NaCl$, $MgSO_4$, $CaCl_2$, K_2CO_3, and $Ca(HCO_3)_2$. Pure seawater contains many other minor constituents. The solutes separate into hydrated ions that give seawater electrical conduction properties. The most abundant positive and negative ions composing seawater are listed in Table 9.3, along with the relative concentration to other solutes.

The salinity of seawater is defined as the ratio of the solute mass to the total mass of the solution. The typical salinity of seawater in the deep ocean is 35 parts per thousand (‰). Salinity is lowered in coastal regions near the mouth of a river where fresh water is added. Salinity is increased in regions of high evaporation, such as in the Mediterranean sea. Salinity varies in the upper portion of the ocean, typically in the mixed region, and then becomes nearly constant with depth.

Organic materials composed of hydrocarbons, carbohydrates, proteins, vitamins, lipids, and humic acids are also dissolved or exist as very fine particles in the ocean. Most dissolved organic material does not absorb in the visible. But some compounds, called yellow matter or yellow substance, strongly absorb the short wavelengths of visible light and rapidly weaken as the wavelength approaches red light. Organic material in the ocean is dominantly composed of dissolved matter.

9.2.1.3 Ocean Particle Composition

Marine particles have a variety of sources. They are terrigenous (from rivers and wind), phytoplankton cells, bacteria, detritus (decomposed cells and small skeletons of zooplankton), volcanic ash, and cosmic (meteorites). The concentration of particles varies

Table 9.3 Ion Composition in Seawater

Ion	Relative Concentration	Parts per Thousand of Seawater	Percentage as Free Ion [%]
Na^+	30.61	10.7	99
Mg^{++}	3.69	1.3	87
Ca^{++}	1.16	0.4	91
K^+	1.1	0.38	99
Cl^-	55.04	19.3	100
SO_4^-	7.68	2.7	50
HCO_3^-	0.41	0.14	67
Br^-	0.19	0.07	100

for different locations, but ranges from 0.01 to 0.13 mg/l (g/cm^3). A large portion of oceanic particles are organic in nature. A representative relative index of refraction (to that of water) for organic particles is 1.05 and for inorganic particles is between 1.15 to 1.2. Although the majority of particles are less than a micron in diameter, particles as large as 1 mm can be found. Large particles have a strong influence on the scattering properties of the ocean. An empirical formula is used to compute the number of particles larger the diameter d,

$$N = N_0 d^{-\gamma},$$

where γ is typically between 1 and 4. Terrigenous particles are very small, typically less than 1 μm. On the other hand, biological particles are typically larger than 1 μm. The character of the particle composition depends on location (e.g., location to rivers and land mass) and water temperature, which affects the organic content of the ocean. The shape of particles in the ocean is extremely varied. This is especially true for the large numbers of unicellular and multicellular phytoplankton that exist in the ocean. For example, one group of phytoplankton, the diatoms, has approximately 10,000 species. There are over nine different groups of phytoplankton.

9.2.1.4 Pressure Variation with Depth

Water is an incompressible fluid, thus the mass density in Eq. 7.4 is independent of depth, and

$$dp = -\rho_m g\, dz. \tag{9.11a}$$

The mass density of seawater is 1035 kg m^{-3}. Solving the above equation yields a simple formula for seawater pressure as a function of depth,

$$p(z) = p(0) - \rho_m g z = 101.3 \times 10^3 - 101.4 \times 10^2 z\,[\text{Pa}] \quad z < 0, \tag{9.11b}$$

where z is has units of meters. The result shows that the water pressure increases linearly with depth by 1 atm every 10 m.

9.2.2 Absorption and Refraction

The optical properties of pure seawater are similar to pure water except at microwave frequencies. The complex index of refraction is only slightly altered in the visible because of the addition of dissolved salts. In general, seawater contains dissolved organic material and suspended particles as well. These additional constituents are variable, which complicates the optical characterization of seawater.

Seawater is a conductor with a conductivity of 4.8 ℧/m, corresponding to a salinity of 35% (parts per thousand). Thus, free-carrier effects significantly contribute to the complex index of refraction. The charge carriers in this case are massive hydrated ions due to the dissolve salts. The conductivity relaxation time is expected to be much longer than that of metals. In fact, based on the discussion in Section 3.5.1, we expect the conductivity relaxation time to be similar to the Debye relaxation time. Using Eq. 4.65 with the above values for seawater conductivity and conductivity relaxation time, the pure seawater complex index of refraction can be computed. The results are displayed in

Fig. 9.4 for the millimeter to far-infrared. The plasma frequency for seawater can be computed based on Eq. 4.63b. The result is 1.37 cm^{-1}, or 41 Ghz. The plasma frequency effectively marks the end of significant contributions to dielectric properties from free-carrier effects. This is especially true for water, since the strong Debye and vibrational absorption bands begin above 0.1 cm^{-1}. Thus, above this frequency, seawater is a dielectric in nature, and below this frequency, seawater is a conductor in nature. Also, until
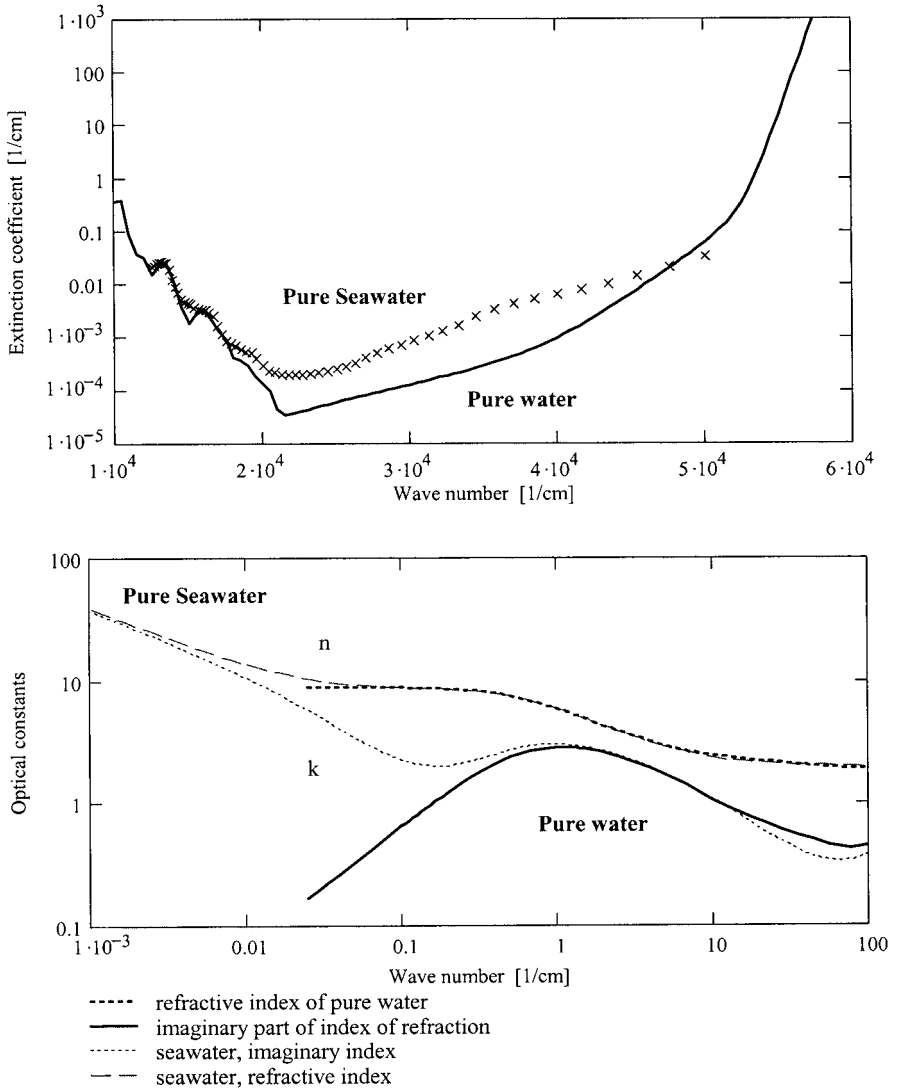
Fig. 9.4 The complex index of refraction of room-temperature pure seawater with a salinity of 35% compared with pure water. (The solid curves are for comparison with pure water absorption as shown in Figs. 9.1. and 9.3 In upper plot, x shows data from Mobley, Ref. 9.9.)

the ultraviolet region is reached, the solutes in seawater have virtually no effect on the pure seawater absorption coefficient. The visible index of refraction, however, is affected by the salinity. Based on the study of Sager (Ref. 9.5) at 0.5893 μm, the index of refraction of seawater at a temperature 293 K as a function of salinity (s in parts per thousand) is

$$(n_{sw}(s) - 1) \times 10^4 = 18.347s + 3330. \tag{9.12}$$

Dissolved organic material affects the absorption coefficient of seawater. A simple model for the absorption coefficient of yellow matter is given by

$$\beta_{abs}(\lambda) = \beta_{abs,ym}(\lambda_0) \exp\left[-0.014(\lambda - \lambda_0)\right], \tag{9.13}$$

where λ is in nm. Values of $\beta_{abs,ym}(440)$ range from near zero to 19 m^{-1}. The lowest values are in the open ocean and highest values are in land-based lakes and rivers.

9.2.3 Scattering

Pure seawater, with no large particulates, scatters approximately 30% more than pure water. (Scattering by large particles in the ocean will be covered in the next chapter.) Therefore, Eq. 9.9 can be multiplied by 1.3 to obtain the scatter coefficient for particle-free seawater. The phase function for pure seawater is the same as for pure water (see Eq. 9.10).

The minimum extinction coefficient of pure water and pure seawater occurs in the blue, where vibrational absorption ends and scatter begins. This is a situation similar to that observed for oxide glasses, which exhibit minimum loss in the near-IR, as discussed in Chapter 8. This is why illumination at depths below 100 m begins to be predominantly blue and back-scattered light in clear ocean water is blue.

9.3 Applications

The optical properties of water are commonly applied to systems involving oceanography and biomedicine. A few examples are given in the following sections.

9.3.1 Ocean Reflectance and Emittance

The magnitude of normal reflectance from water varies considerably for different spectral regions. The reflectance is highest in the microwave and lowest in the long-wave infrared. This point is illustrated in Fig. 9.5, which uses the model for the complex index of refraction for pure water described in the first section. Because water is opaque for most practical thicknesses and has low infrared reflectance, the infrared emittance is near one. Also recall the locations of the gas-phase absorption bands of water (Chapter 7), which will block light in the regions of anomalous dispersion. Thus the regions of high reflectance are blocked from sensors, and water is nearly a blackbody throughout the infrared for all practical purposes. These facts allow the surface temperature of the ocean to be remotely measured with a simple pyrometer (see Problem 9.4).

Although the reflectance of water in the visible is low for normal incidence, at oblique angles the reflectance is nearly one. This is the case for all dielectrics (recall Chapter 4, Section 4.3). Also because the ocean surface is not smooth, some level of oblique
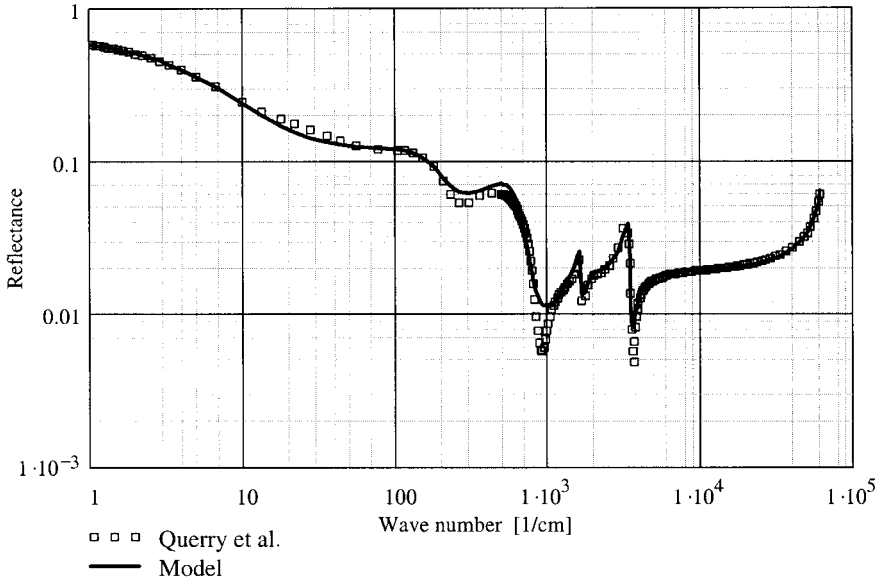
Fig. 9.5 The infrared reflectance of NTP pure water for normal incidence (Querry et al., Ref. 9.1).

reflection of sunlight always occurs no matter what the angle of the sun and observer. This leads to a phenomenon called glint. At sunset, a glint corridor is formed that appears as a yellow stripe on the surface of the ocean (or sea or lake).

The BRDF of the ocean surface depends on wind speed and direction and is highly variable. It is a topic in statistical optics and is beyond the scope of this book. The reader is referred to Ref. 9.12 in the bibliography at the end of this chapter for further information.

9.3.2 Biomedical Media

As mentioned in the introduction to this chapter, the human body is largely composed of water. The optical properties of biological tissue and fluids are dominated by the optical properties of water. Water in the body contains 7% NaCl. Such solutions are called saline solutions. The near-infrared optical window in the human body is created by the infrared fall-off of vibrational band absorption in water with increasing frequency and the decrease of hemoglobin absorption with decreasing frequency from the visible. The window occurs in the region of 0.7–0.8 μm. Hemoglobin spectra are displayed in Fig. 9.6 for a hemoglobin concentration of 1 millimolarity. The normal concentration of hemoglobin in human blood is 2 millimolarity. Figure 9.6 shows that the transmission through the body (a thin part such as a finger tip) changes based on the amount of oxygen in the blood. This fact is used by anesthesiologist to noninvasively monitor the oxygen content of blood (see Harris et al., Ref. 9.13).

The human eye is a visible light sensor that is nearly spherical in shape with approximately by a 2.5 cm diameter. It is composed of an outer surface called the cornea, a lens, and a focal plane array on the back inner surface called the retina. The central region of the eye is primarily composed of water called the vitreous humor. Thus for
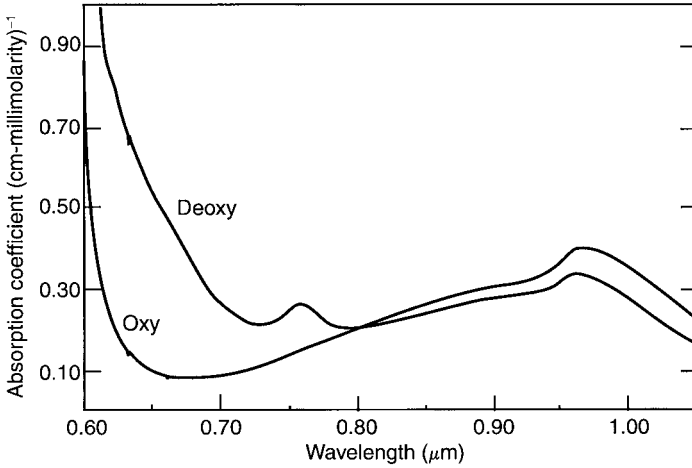
Fig. 9.6 Absorption coefficient of oxygenated and deoxygenated hemoglobin normalized to a concentration of 1 millimolarity (Harris et al., Ref. 9.13).

light to reach the retina it must transmit through water. The cornea blocks the UVC and UVB bands. The cornea and lens block the UVB and UVA bands. Visible light and IRA light (out to 1.3 μm) transmits to the retina. Wavelengths longer than 1.3 μm are absorbed by the water in the vitreous humor and prevented from reaching the retina. The transmittance through 2.5 cm of water is plotted in Fig. 9.7.

Since the retina is the most sensitive component of the eye, the transmission properties of water are an important considertation concerning eye safety. Based on Fig. 9.7,
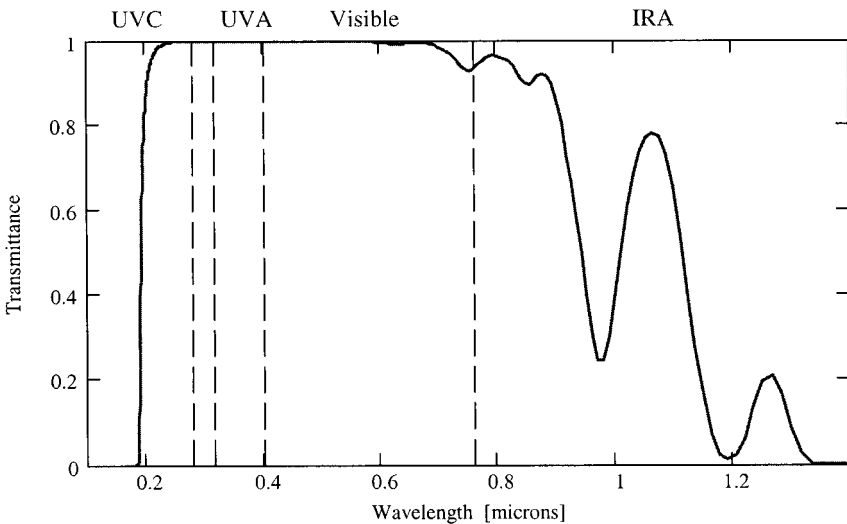
Fig. 9.7 The transmittance through 2.5 cm of liquid water at a temperature of 293 K and pressure of 1 atm.

intense visible and near-infrared light can reach and damage the retina. Wavelengths outside this region will not propagate to the retina, but can damage other components of the eye. For example, long-term exposure to UV light will damage the lens of the eye. Cataract formation is the accumulation of UV damage over many years. Mid-wave and long-wave infrared heat the eye and can cause thermal damage.

There are a variety of applications in biomedical optics today. Many of them depend on knowledge of the optical properties of water.

Problems

9.1 Compute the normal spectral emittance of pure water at 10 μm based on the complex index values in Fig. 9.2.

9.2 Explain the difference in performance between microwave cooking (N3 GHz) and infrared cooking based on Figs. 9.1 and 9.2.

9.3 Compute the complex index of refraction in the microwave region (0.01–1 cm^{-1}) for fresh water with a conductivity of 1×10^{-3} Ω/m.

9.4 Devise a technique to measure the surface temperature of the ocean using infrared pyrometry. Justify your approach using the optical properties models in this chapter. Show that radiation from the surface originates from a region very close to the surface. How does the surface emissivity vary with temperature and viewing angle?

9.5 Explain how ocean color can be used to determine water clarity.

Bibliography

Section 9.1

9.1 M.R. Querry, D.M. Wieliczka, and D.J. Segelstein, "Water," in *Handbook of Optical Constants of Solids II*, E.D. Palik (ed.), Academic Press (1991).

9.2 D. Eisenberg and W. Kauzmann, *The Structure and Properties of Water*, Oxford University Press (1969).

9.3 A. Morel, "Optical Properties of Pure Water and Pure Seawater," in *Optical Aspects of Oceanography*, N.G. Jerlov and E.S. Nielsen (eds.), Academic Press (1974).

9.4 F. Lauscher, Optik der Gerwasser."Sonnenund Himmelstrahlung im Meer und in Gewassern," in: *Handbuch der Geophysik*, pp. 723–763, Springer (1955).

9.5 G. Sager, "Zur Refraktion von Licht im Meerwasser," *Beitr. Meersek.* **33**, 63–72 (1974).

9.6 L.W. Pinkley, P.P. Sethna and D. Williams, "Optical Constants of Water in the Infrared: Influence of Temperature," *J. Opt. Soc. Am.* **67**, 494–499 (1977).

Section 9.2

9.7 K.S. Stowe, *Ocean Science*, Wiley (1979).

9.8 K.S. Shifrin, *Physical Optics of Ocean Water*, American Institute of Physics (1988).

9.9 C.D. Mobley, "The Optical Properties of Water," in *Handbook of Optics*, 2nd Ed., Vol. I, M. Bass (ed.), sponsored by OSA, published by McGraw-Hill (1995). C.D. Mobley, *Light and Water, Radiative Transfer in Natural Waters*, Academic Press (1994).

9.10 N.G. Jerlov, *Marine Optics*, Elsevier Oceanography Series (1976).

9.11 M.E. Thomas, "The Electrical Properties of Seawater (Including Conductivity Relaxation)," JHU/APL STD-R-1071, Contract N00024-83-C-5301, July 1984.

Section 9.3

9.12 R.E. Walker, *Marine Light Field Statistics*, Wiley Interscience (1994).

9.13 A.P. Harris, M.J. Sendak, R.T. Donham, D.D. Duncan, and M.E. Thomas "Absorption Characteristics of Human Fetal Hemoglobin at Wavelengths Used in Pulse Oximetry," *J. Clin. Monitor.* **4**, 175–177 (1988).

9.14 V. Tuchin, *Tissue Optics Light Scattering Methods and Instruments for Medical Diagnosis*, Tutorial Texts in Optical Engineering, Vol. **TT38**, SPIE Press (2000).

9.15 D.D. Duncan, S.L. Jacques, and P.C. Johnson (eds.), *SPIE Proceedings Laser Interaction XII: Photochemical, Photothermal and Photomechanical* **4257**, 21–24 January 2001.

9.16 D.C. Winburn, *Practical Laser Safety*, 2nd Ed., Marcel Dekker (1990).

9.17 D.A. Atchison and G. Smith, *Optics of the Human Eye*, Butterworth-Heinemann (2000).

10

Particle Absorption
and Scatter

Particles are composed of solids and/or liquids, thus the bulk optical properties of these media must be known before propagation modeling within a medium of suspended particles (called aerosols when in air) can begin. We return to our discussion of propagation in the atmosphere and oceans of the earth that began in Chapters 7 and 9, and we now include attenuation by small particles.

10.1 Particle Distributions and Composition

Particles vary in size, shape, concentration, and composition. Size and concentration distributions are described in the following two sections. The composition of the most common particles is presented in the last section. Unfortunately, a representation of shape variation does not exist.

10.1.1 Particle Size Distribution Function

As mentioned in Chapter 4 (Section 4.4.2 on Mie scattering), a collection of real aerosols will have a range of different radii. This is called a polydisperse medium. Various models are used to represent particle size distributions. One commonly used model for particle number density as a function of radius is the modified gamma distribution function, as given by

$$\rho_p(r) = Ar^\alpha \exp(-br^\gamma), \tag{10.1}$$

where $A, b, \alpha,$ and γ are empirically determined parameters. This function represents the number of particles per unit volume and unit radius as a function of radius r. The total particle number density is obtained by integrating $\rho_p(r)$ over all r. The result is

$$\rho_p = \int_0^\infty dr\, \rho_p(r) = \frac{Ab^{-\frac{\alpha+1}{\gamma}}}{\gamma}\Gamma\left(\frac{\alpha+1}{\gamma}\right). \tag{10.2}$$

The particle radius having maximum population, called the modal radius, r_N, is computed to be

$$r_N = \frac{\alpha^{\frac{1}{\gamma}}}{b\gamma}. \tag{10.3}$$

Size distribution parameters for various types of aerosols such as hazes, fogs, clouds, and rain are listed in Table 10.1. Figure 10.1 illustrates this model for type L haze and a cumulus cloud.

A bimodal modified gamma distribution is used for particles in the ocean, of the form

$$\rho(r) = A_1 r^2 \exp\left(-52r^{\gamma_1}\right) + A_2 r^2 \exp\left(-17r^{\gamma_2}\right), \tag{10.4}$$

where $0.145 \leq \gamma_1 \leq 0.195$ and $0.192 \leq \gamma_2 \leq 0.322$. The first term represents small particles less than 0.5 μm in diameter such as small colloids and viruses. The second term represents particles greater than 0.5 μm in diameter such as large colloids, bacteria, and plankton.

10.1.2 Particle Vertical Concentration Profile

The vertical distribution of atmospheric aerosol number density is highly variable and requires real-time measurements. However, a general structure is commonly observed. In

Table 10.1 Modified Gamma Function Parameters for Various Atmospheric Particles (Deirmendjian, Ref. 10.1 and Shettle, Ref. 10.2).

Aerosol Type	ρ_p [cm^{-3}]	A [cm$^{-(3+\alpha)}$]	α	γ	b	r_N [μm]
Haze M	100	5.3333×10^4	1	0.5	8.94433	0.05
Haze L	100	4.9757×10^6	2	0.5	15.1186	0.07
Haze H	100	4.000×10^5	2	1.0	20.0	0.10
Cumulus cloud	250	2.604	3	1.0	0.5	6.0
Stratus cloud	250	210.0	2	1.0	0.6	3.33
Strato-cumulus	250	52.734	2	1.0	0.75	2.67
Alto-stratus	400	6.268	5	1.0	1.111	4.5
Nimbo-stratus	200	7.676	2	1.0	0.425	4.7
Cirrus cloud	0.025	2.21×10^{12}	6	1.0	0.09375	64
Thin cirrus cloud	0.5	0.01187	6	1.0	1.5	4
Heavy fog (advective)	20	2.70×10^2	3	1.0	0.3	10.0
Moderate fog (radiative)	20	6.075×10^2	6	1.0	3.0	2.0
Rain M	10^{-3}	5.333×10^5	1	0.5	8.94433	50
Rain L	10^{-3}	4.976×10^7	2	0.5	15.1186	70
Hail H	10^{-5}	4.000×10^4	2	1.0	20.0	100
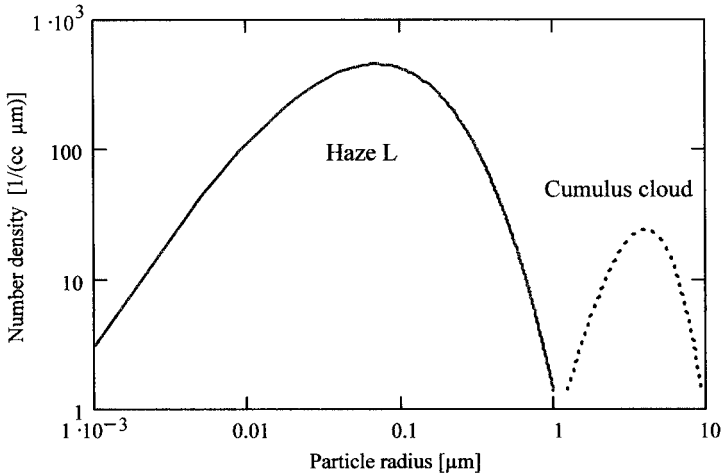
Fig. 10.1 Particle size distribution curves for haze L and cumulus cloud based on the models in Table 10.1.

the boundary layer (usually the first couple of kilometers above the surface of the earth) the concentration decreases exponentially. Such aerosols are referred to as haze, and representative concentration levels are listed in Table 10.1. The aerosol concentration in the mid to upper troposphere is constant at about 300 cm^{-3}. A simple empirical formula for the vertical number density profile is given by (Jaenicke, Ref. 10.5)

$$\rho_p(z) = \rho_p(0) \left[\exp\left(-\frac{z}{|h_p|} \right) + \left(\frac{\rho_{pB}}{\rho_p(0)} \right)^\alpha \right]^\alpha, \tag{10.5}$$

where $\alpha = \pm 1$ ($\alpha = 1$ when $h_p > 0$, $\alpha = -1$ when $h_p < 0$) and $\rho_{pB} \approx 300$ cm^{-3}. Values of h$_p$ range from 0.8 to 1.2 km for continental regions, and −0.29 to 0.44 km for maritime regions; it is around 2 km for desert regions.

Particle concentrations in the ocean are much higher than in the atmosphere. Small particles (diameter < 0.5 μm) are on the order of 10^8 cm^{-3} and large particles (diameter > 0.5 μm) are on the order of 10^4 cm^{-3}.

10.1.3 Particle Composition

The chemical composition of aerosols in the troposphere strongly depends on location, such as urban, rural, maritime, and desert. In other words, it depends on the surface character of the earth for a particular region. In addition, all regions have some level, of water vapor content. Many aerosols are hygroscopic or act as condensation nuclei and therefore will contain water at some level, depending on the relative humidity. Dryer particles exist during the winter and wetter particles exist during the summer. Regions of high humidity (near 100%) lead to the formation of fog (near ground level) and clouds (higher altitude regions), which are particles dominantly composed of water. High-altitude clouds, such as cirrus, exist at subfreezing altitudes and are composed of ice particles (optical property model parameters for ice type Ih are listed in Table A.4.4).

Maritime aerosols are wet, and contain the salts that are in the ocean (see Table 9.3), although this can change as chemical reactions occur. Desert aerosols are typically composed of dry silica (SiO_2). Urban particles are composed of sulfate, nitrate, and ammonium compounds. A greater diversity of particle composition for urban areas exists because of anthropogenic sources. The burning of fossil fuels produces soot or carbon-based particles, for example. Rural and urban areas include organic particles such as pollen. Small organic aerosols such as spores, viruses, and bacteria exist in rural and urban environments as well. Such particles are a concern for public health.

In the stratosphere, particles originate from volcanic-type activity and reside there for a long time (years), since this layer only weakly mixes with the troposphere. At even higher altitudes, particles can have extraterrestrial origins, such as disintegrated meteors.

10.2 Particle Absorption and Scatter

Particle scatter adds complexity, utility, and beauty to atmospheric and ocean propagation phenomena. A great variety of particle compositions, size distributions, concentrations, and shapes exist. Now the optical properties of solids (Chapter 8) and liquids (Chapter 9) composing the particles must be known. Infrared lidars for atmospheric remote sensing would have no measurable return without atmospheric aerosols. Also, imaging and communication systems operating within the atmosphere are adversely affected by scatter.

10.2.1 Extinction Coefficient

Recall that the extinction coefficient for particles is the integral of the particle extinction cross-section times the size distribution function, as given by Eq. 4.102. The particle concentration, the integral of the size distribution function, is variable in time and location. Once the particle composition and corresponding complex index of refraction are known, the cross-section can be determined. Thus the cross-section is a quantity of fundamental importance that dictates frequency and angle dependence of the scattered light.

Intuitively, the scatter cross-section should be related to the geometrical cross-section. Larger particles scatter more light than small particles with the same concentration level. For the case of a sphere, the geometrical cross-section is the area of a circle that is constrained to the surface of the sphere and the center of the circle, as given by

$$C_{Geo}(r) = \pi r^2, \tag{10.6}$$

where r is the radius of the particle. Of course, the actual cross-section depends on the complex index of refraction, and actual cross-sections can be greater than or less than C_{sca}. Nonetheless, real particle cross-sections are typically close in magnitude to the geometrical cross-section. Thus a comparison with Eq. 10.6 is a useful check on the reasonableness of a computed or measured cross-section value. For this reason, the scatter efficiency, Q_{sca}, is often used to represent a normalized cross-section. It is defined as

$$Q_{sca}(r) = \frac{C_{sca}(r)}{\pi r^2}. \tag{10.7}$$

The observed frequency dependence of the scatter cross-section for aerosols is similar to Eq. 8.72. Often only the middle term is needed to represent scatter in the visible and near-infrared.

Figure 10.2 illustrates the strength and wavelength dependence of the extinction coefficient for various types of aerosol and fog extinction, and molecular Rayleigh scatter coefficient. A large dynamic range is observed. Note that molecular scatter dominates over haze scatter loss in the ultraviolet. In the visible both types of scatter are important. In the infrared, aerosol scatter dominates. On the other hand, the scattering properties of fog and clouds are fairly flat with wavelength. This explains the whitish color during the day and the insulating effect clouds have at night. Infrared radiation emanating from the surface of the earth peaks around 10 μm wavelength (see Fig. 5.1), where water and ice strongly absorb, and is blocked by clouds to some extent. Thus, the night-time air temperature does not change much. The same clouds will keep the surface of the earth cooler during the day because of strong back-scatter of sunlight with peak intensity in the visible.

The results in Fig. 10.2 are consistent with the bulk index of refraction of the particles and Mie theory. Cumulus and stratus clouds contain large liquid water particles that are spherical in shape. Variations in aerosol size distribution functions create the distinction in the scatter properties.

The extinction coefficient is the sum of the absorption coefficient and the scatter coefficient. The scatter properties of particles are of great importance to many applications in ocean and atmospheric optics. For this reason, it is also useful to represent scatter with the volume scatter coefficient. This quantity was partially introduced in Chapter 7 (Eq. 7.69) as the derivative of the angle-dependent scatter coefficient with
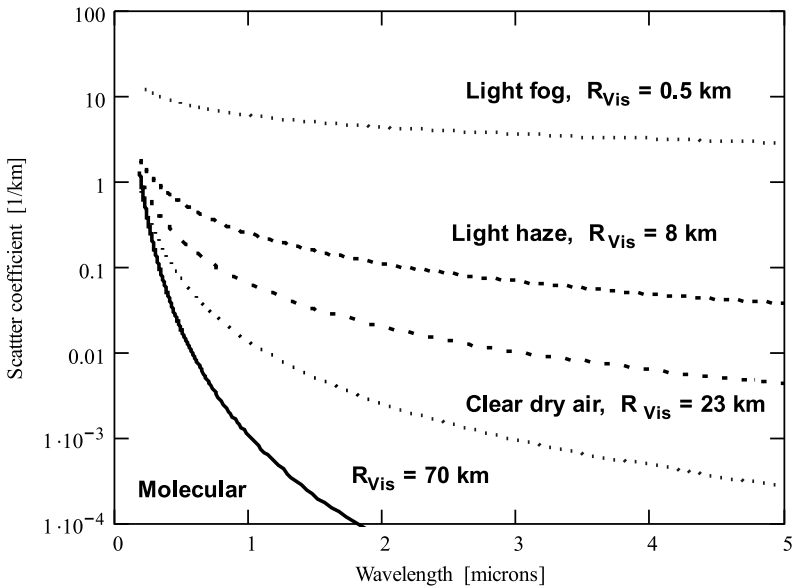
Fig. 10.2 Scatter coefficient as a function of wavelength for a purely molecular atmosphere and various visibility ranges (Wright et al., Ref. 10.3).

respect to the scatter angle. If the phase function is constant over the receiver solid angle, then the product of the scatter coefficient and the phase function is the volume scatter coefficient, as given by

$$\beta_{Vol}(\lambda,\,\theta) = \beta_{sca}(\lambda)P(\theta)\,, \tag{10.8}$$

with units of reciprocal length times reciprocal steradians. Consistent with Eq. 7.69, the volume back-scatter coefficient is the volume scatter coefficient evaluated at 180°. This quantity is needed for the lidar equation (Eq. 7.70).

10.2.2 Visibility Range

A useful and simple measure of the importance of scatter loss is the visibility range, R_v It is defined as

$$R_v = \frac{1}{\beta_{ext}} \ln\left(\frac{C}{\epsilon}\right)\,, \tag{10.9}$$

where C is the inherent contrast of the target being viewed and ϵ is the threshold contrast of the observer. In the visible, no significant particle absorption occurs and it is often justified to replace β_{ext} with β_{sca}. The meteorological range is defined for a high-contrast target ($C = 1$), and for a 2% threshold contrast at a visible wavelength of 0.55 μm, to be

$$R_M = \frac{3.912}{\beta_{sca}}. \tag{10.10}$$

For an aerosol-free lower atmosphere, only molecular scatter loss dominates the scatter coefficient, and therefore $R_M = 391.2$ km. Obviously, this is seldom the case, and aerosol scatter loss is always a limiting factor in atmospheric visibility (see Fig. 10.2).

An extension of Eq. 10.5 for the extinction coefficient that includes wavelength dependence has been empirically determined by Kruse et al. (Ref. 10.7) to be

$$\beta_{ext}(\lambda) = \frac{3.912}{R_v}\left(\frac{0.55}{\lambda}\right)^{0.585R_v^{0.33}}\,, \tag{10.11}$$

where R_v is in km. This is an approximate result that can be applied when no other information on scatter loss is available.

10.2.3 Henyey–Greenstein Phase Function

A commonly used phase function for approximately representing polydisperse aerosols or ocean particles is the Henyey–Greenstein phase function as given by

$$P_{H-G}(\theta) = \frac{1}{4\pi}\frac{1 - g^2}{\left(1 + g^2 - 2g\cos\theta\right)^{3/2}}, \tag{10.12}$$

where g is called the asymmetry parameter, defined for any phase function as

$$g = \langle cos\theta \rangle = 2\pi \int\limits_0^\pi d\theta \, cos(\theta) P(\theta). \tag{10.13}$$

The phase function is normalized according to Eq. 2.90. Because there is no surface involved in particle scatter, the $\cos\theta$ factor involving the dot product of the scattered ray from a point and the unit normal on an enclosing sphere is always one. A plot of the Henyey–Greenstein phase function for different values of g as a function of θ is presented in Fig. 10.3a.

g is a measure of the net angular area in the forward or backward direction of the phase function. For example, if the phase function is isotropic, $g = 0$. For the case of the Henyey–Greenstein phase function, the asymmetry parameter is built into the function. One way to experimentally determine g is to measure the forward-to-back-scatter ratio and then apply the following formula:

$$\text{for} \quad \frac{P_{H-G}(0)}{P_{H-G}(\pi)} = x, \quad \text{then} \quad g = \frac{\sqrt{x} - 1}{\sqrt{x} + 1}. \tag{10.14}$$

Figure 10.3b shows the forward-to-back-scatter ratio as a function of g for the Henyey–Greenstein phase function. As g approaches ± 1, the forward-to-back-scatter ratio becomes very large.

The Henyey–Greenstein phase function is intended to represent the forward-to-back-scatter ratio, but does not accurately represent the shape of the phase function. There is no physical reason to believe that the forward-to-back-scatter ratio dictates the phase function shape. Thus, this phase function must be carefully applied. It is popular because it is computationally simple. This trait is desirable for complex models such as those used in radiation transfer calculations.

10.2.4 Humidity and Cross-Section

When the humidity of the atmosphere is above 70%, a dry-particle cross-section is increased in size by the absorption of water. This is especially true for hygroscopic particles (see Table 8.4). The particle size increases as the humidity increases. The exact process is complicated and beyond the scope of this book. The fact that humidity increases the size of aerosols explains why summertime haze is thicker in appearance than in the wintertime.

10.3 Scatter and Atmospheric Optics

Although the accomplishment of understanding scattering phenomena within the atmosphere of the earth is rewarding, it does not compare to the simple joy of observing the beauty of the atmospheric light show caused by scattering that is often displayed. The following discusses a few commonly observed phenomena in atmospheric optics.

(a)

$g < 0$

$g > 0$

(b)

$$\frac{P_{HG}(0,g)}{P_{HG}(\pi,g)}$$

g
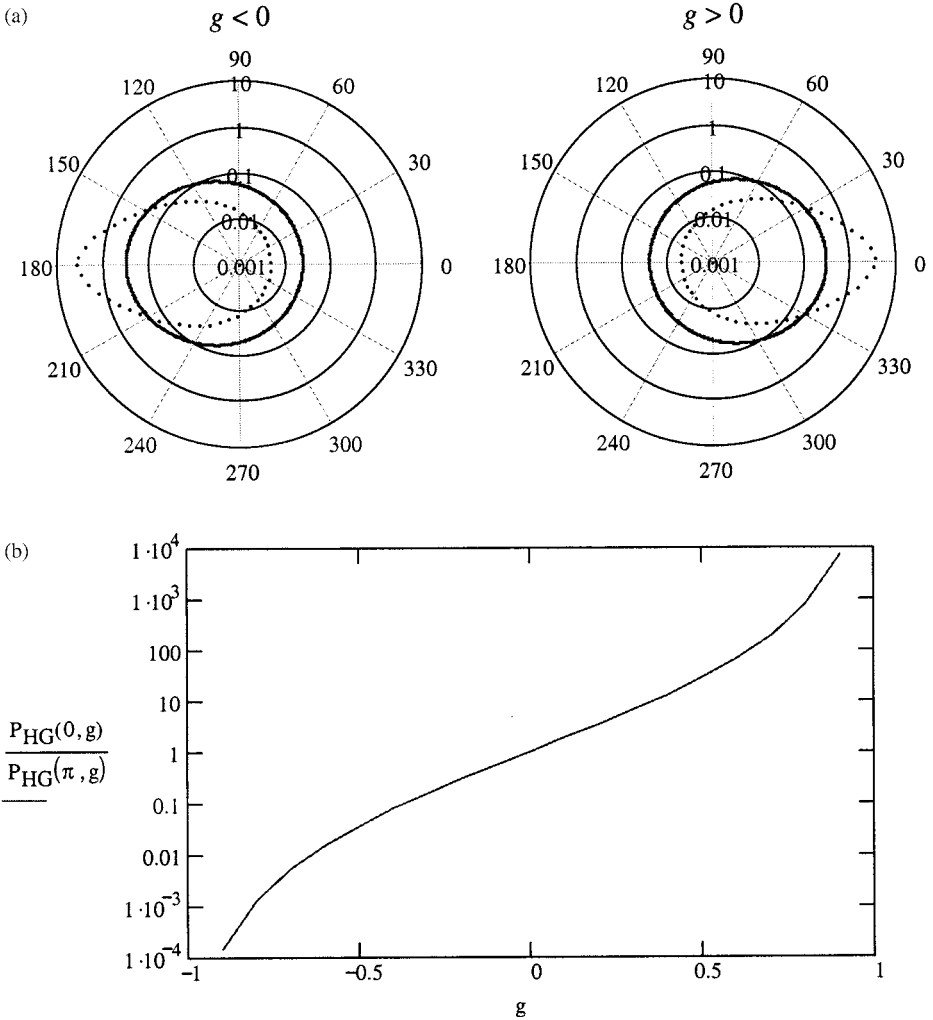
Fig. 10.3 (a) Henyey–Greenstein phase function for different values of g. (b) The forward-to-back-scatter ratio as a function of g.

10.3.1 Raindrops and Rainbows

Rainbows are a back-scatter phenomenon that can be explained by spherical waters droplets and geometrical optics. The large size of the raindrop, when compared with the wavelength of light, allows a geometrical optics interpretation. Figure 10.4 illustrates the location of sunlight, raindrops, and observer necessary for rainbow observation. The white light that enters the spherical raindrop is refracted at the interface of a dispersive medium, which causes the white light to separate into distinct colors. The light then experiences total internal reflection at the back of the raindrop. The primary rainbow undergoes only one refection and the secondary rainbow has two reflections. For this reason, the secondary rainbow displays the color spectrum in reverse order to the primary
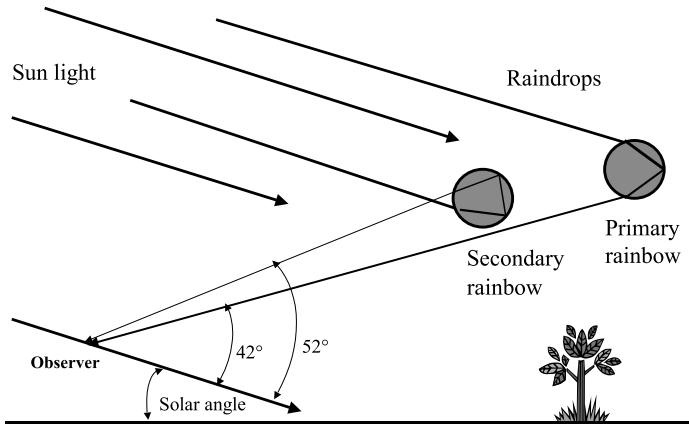
Fig. 10.4 Geometrical illustration of rainbow formation for both the primary and secondary bows.

rainbow, as illustrated in Fig. 10.4. The light then exits the raindrop to be viewed by an observer who faces in the opposite direction to the sun (toward the antisolar point). Only raindrops at certain altitudes, given the angle of incidence of the sunlight, can experience total internal reflection, and thus efficient back-scatter, that is observable. Thus the rainbow has a limited spatial display to a single observer. Also, raindrops below those raindrops that produce an observable rainbow tend to back-scatter the sunlight directly back (small angles of incidence) to the observer. For this reason, a whitish hue often appears within the rainbow. Rainbows can also be formed by dew on the ground, or the mist from a water fountain. It is important that the particle size be large to observe a standard rainbow. If the particle size is small and uniform, as is sometimes the case for fog, then diffraction effects will dominate over geometrical refraction and a white bow will appear.

10.3.2 Ice Crystal Effects

Ice crystals are present all the time in the upper atmosphere and therefore can produce effects observable during any season. Ice crystals have a hexagonal cross-section that are either thin (platelets) or thick (pencil-like rods) as illustrated in Fig. 10.5. The size of suspended ice crystals range from 50 to 300 μm, thus geometric optics can be used to understand the ice crystal light show. The first and fairly common phenomenon to be described is the 22° halo seen around the sun or moon. The hexagonal shape of ice particles can be fit into a 60° prism. Applying Snell's law (Eq. 4.72) along with the index of refraction of ice at visible wavelengths ($n = 1.3$), the resulting deviation angle is 22° (see Problem 10.5). Of course, for this effect to be observed the particles must be uniformly oriented.

10.3.3 Clouds and Cloud Color

Clouds in the atmosphere of the earth are composed of either liquid water particles or ice particles, depending upon the altitude. In order for clouds to form, the air must have
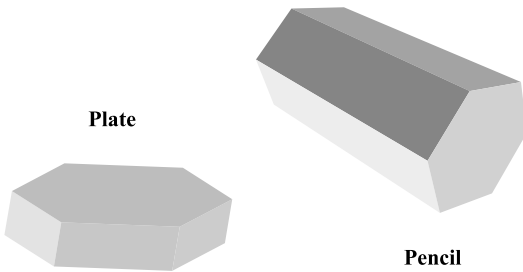
Plate

Pencil

100% humidity and condensation nuclei must be available. Thus the base height of a cloud is at the dew point temperature (that temperature in which the air mass must be cooled to reach saturation). The base height of a cloud is also called the condensation level. Since the air temperature normally decreases with increasing altitude (see Chapter 7), rising humid air will frequently experience these conditions and form clouds.

Cloud formations are classified as stratus, cumulus, and cirrus. Stratus clouds have a horizontally layered structure. Cumulus clouds are puffy in form and often appear as cotton balls in the sky. Stratus and cumulus clouds are composed of spherical water particles and exist within the troposphere. The exception is the large cumulonimbus cloud (also called thunderhead), which can extend into the stratosphere. Cirrus clouds are wispy and feathery in structure and occur at high altitudes. They are composed of ice particles such as illustrated in Fig. 10.4. Notice that these particles are not spherical in shape. Thus polarization-sensitive lidars can be used to distinguish between water and ice clouds. Particle size distribution functions for these cloud types are listed in Table 10.1.

As mentioned previously, most clouds appear white to all observers. This is because of near-uniform scattering at all visible frequencies, due to the large particle size, when compared with the wavelength of visible light, and the fact that the particle absorption is low, thus light penetrates through the cloud. Also, because of multiple scattering, the light intensity is diffuse. This is true for reflected as well as transmitted light. However, there are cases when clouds are not white. If the cloud is so thick, as is the cumulonimbus, that no transmitted light occurs, then the cloud is dark. Also, at the time of sunrise or sunset, the spectral content of sunlight is spatially separated, and distinct colors exist at various altitudes. Thus, transmitted and reflected light from clouds can feature these distinct colors, often yellows and reds.

10.3.4 Fog

Fog is very much like a low-altitude cloud that forms on the ground. There are two main types of fog, radiative and advective. Radiation fog is caused by radiative heat loss in an air mass that cools the air to the dew point. This type of fog is also called ground fog. Radiation fog typically forms at night as the air cools. Advection fog forms when warm moist air moves over a cold surface. This often occurs in coastal regions where air over warm water moves inland over the cooler ground. Particle size distribution functions for these fog types are listed in Table 10.1. Fog significantly affects transmittance in the visible and near-infrared. The mid- and long-wave infrared spectral regions are not as sensitive to fog. These points are illustrated in Fig. 10.6
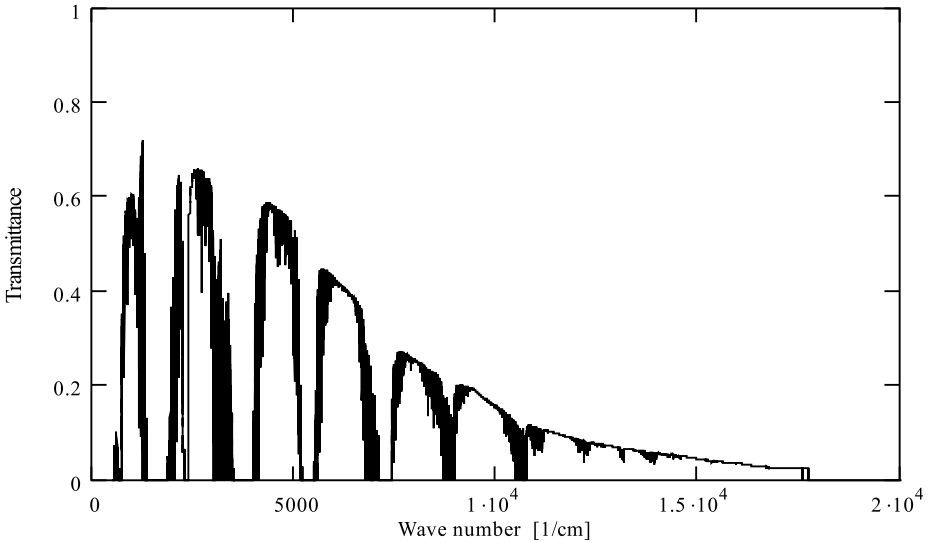
Fig. 10.6 Transmittance through a uniform fog with a visibility of 1 km for a 1 km horizontal path.

10.4 Scatter and Ocean Optics

The effective index of refraction for computing scatter cross-sections of particles in the ocean is reduced by the background index of refraction of water (1.3). This yields smaller cross-sections than would be obtained for a particle suspended in air. However, the ocean is a condensed medium and much higher particle concentrations exist (see Section 10.1.2). The net result is that the extinction coefficient for the ocean is large, compared with that of the atmosphere. For example, the visibility range for pure sea-water (using Eq. 10.10) and β_{ext} ($\gamma = 0.55\,\mu m$) $= 0.066\,m^{-1}$ is 59 m. Of course, if the wavelength is changed to 0.45 μm, then the visibility range increases to 206 m. This is the very best visibility range the ocean can offer, since these values are for pure seawa-ter. A visibility of 200 m for the atmosphere is considered very poor. Now, if we include particle scatter and yellow-matter absorption, the poor visibility often observed in coastal regions can be understood.

Visibility range is often inferred in the ocean by submerging a white disk. The depth at which the disk is no longer visible determines the state of clarity of the water. Such a meas-urement leads to so-called apparent "optical properties" of the ocean. Such information can be used to obtain some idea of the scatter and absorption characteristics of the ocean.

The color of deep ocean water is a combination of back-scattered sunlight and reflected skylight. On cloudless days, the dominant effect is the bulk back-scatter of sunlight. Since the longest paths penetrating the ocean are the deep blue portions of the visible spectrum in the range 0.42–0.47 μm, the strongest back-scattering will occur in this wavelength band. This explains the deep blue color often observed over the ocean. On cloudy days, when the sun is blocked, the ocean has a gray appearance similar to that of the clouds. In this case the bulk back-scatter light is weak and sky reflectance dominates the color.
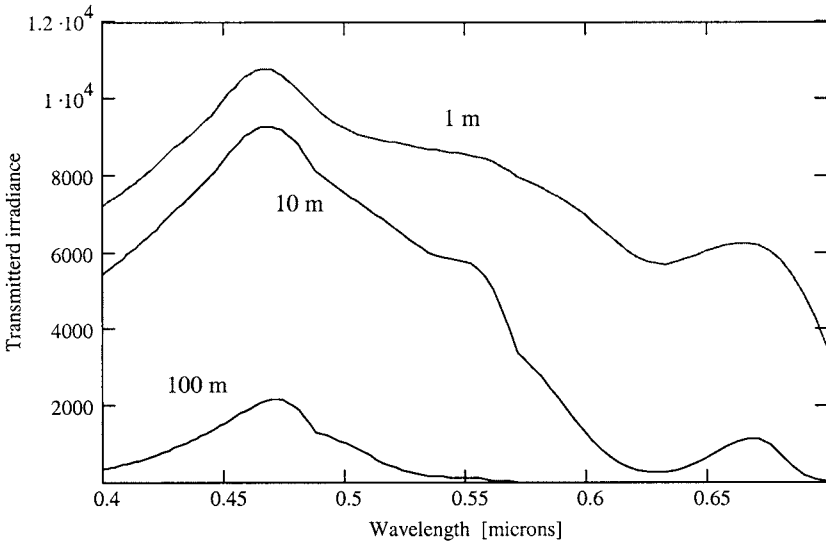
Fig. 10.7 Transmitted solar spectral irradiance (W/(cm^2 μm)) for three different depths in pure seawater.

The spectrum of sunlight that penetrates the ocean becomes more and more attenuated as the depth increases. The rate of attenuation depends on frequency. For the case of pure seawater, the minimum loss occurs in the blue. Thus we expect as an observer goes deeper and deeper into the ocean the light of the sun becomes more and more blue. This point is illustrated in Fig. 10.7, which plots the computed solar spectral irradiance covering the visible spectrum transmitted to depths of 1, 10, and 100 meters. It is clear that the spectrum becomes more blue as the depth increases. It is also important to realize that blue light is the most heavily scattered of the available frequencies from the sun. The red portion of the spectrum is strongly absorbed. Thus at a depth of 100 m, blue light is observed in all directions. Of course, based on the visibility range, as discussed above, the ocean ultimately becomes a very dark place at depths below 200 m. The character of life below that depth changes significantly relative to our experience with life near the surface of the earth.

10.5 Computer Codes and Examples

MODTRAN, a moderate resolution atmospheric transmission code, was initially introduced in Chapter 7. It includes a variety of scatter models for particles describing important propagation effects in the atmosphere. A useful example is the blurring effect that is produced by light propagating through a scattering medium. These topics are covered in the following sections.

10.5.1 MODTRAN

The transmission and radiation effects of low-altitude haze, fog, stratospheric aerosols, and clouds are represented by MODTRAN. In this case, high spectral resolution is not necessary, and the moderate resolution of MODTRAN is fine. In fact, MODTRAN is one of the main codes available for atmospheric propagation calculations.

Atmospheric aerosols significantly affect propagation loss in the visible and near-infrared. They have less of an effect on transmission in the mid- and long-wave infrared than in the visible. This point is demonstrated in Fig. 10.6, which is an example of a MODTRAN 3 computation for fog. This point is further illustrated in Fig. 10.8a, which compares the transmittance from the infrared with the ultraviolet for two different visibility ranges. Visibility is primarily determined by haze. (Other visibility ranges
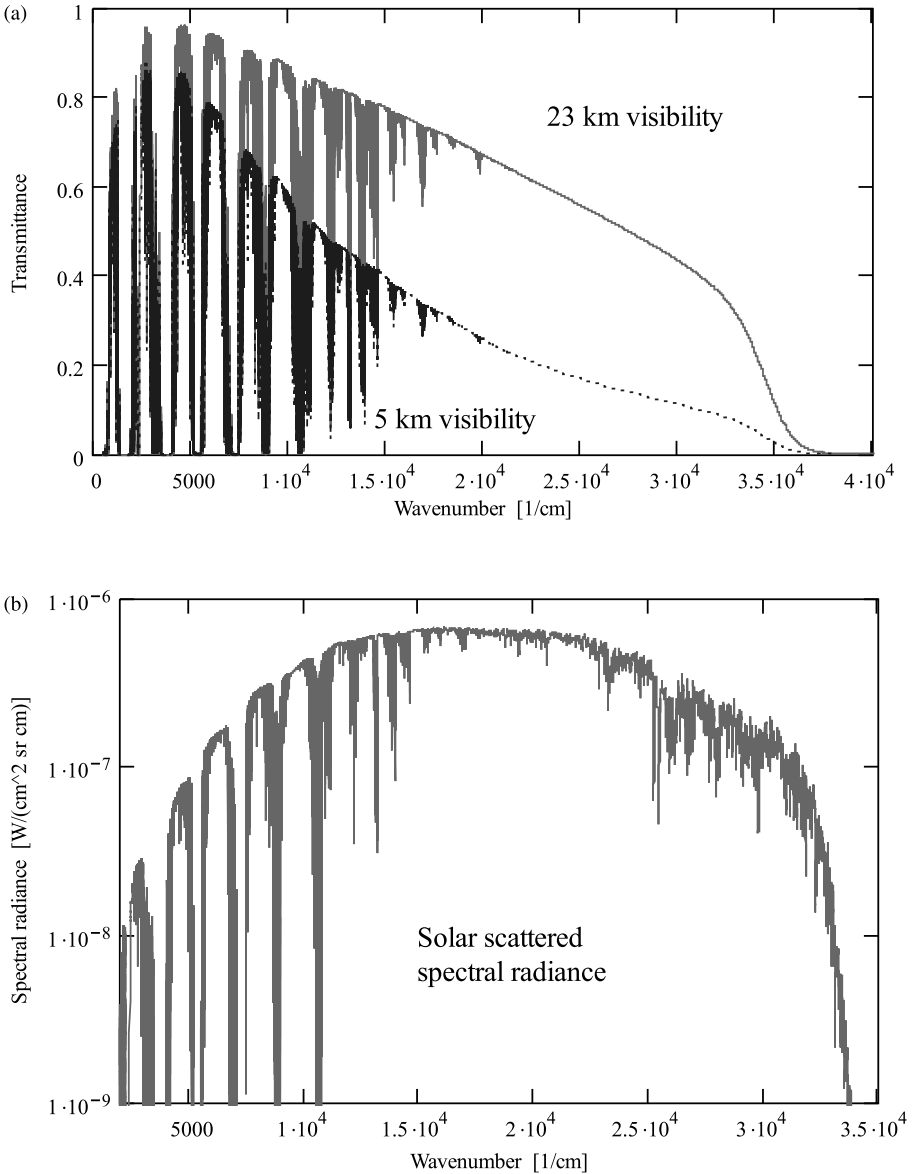
Fig. 10.8 (a) The transmittance from ground to space through the atmosphere during the late spring at noon. (b) The solar scattered radiance for an observer looking up with the same time and atmospheric conditions as the 23 km visibility case in part (a).

are selectable by the user.) The curves are generated using MODTRAN 3. Figure 10.8b plots the scattered solar radiance for an atmosphere with 23 km visibility. The general spectral shape of the scattered radiance is determined by scatter at the low- and middle-frequency regions and by ozone absorption at the high-frequency end.

10.5.2 Imaging within Scattering Media

The performance of an imaging system that operates within the atmosphere or ocean is degraded by scatter, resulting in a blurred image. This phenomenon can be quantitatively represented by the point spread function (*PSF*). The *PSF* is the Fourier transform of the optical transfer function (*OTF*). In the single scatter limit and for small scatter angles, it has been shown that *OTF* becomes (Wells, Ref. 10.12),

$$OTF(\rho z) = e^{-\beta_{sca} z} + (1 - e^{-\beta_{sca} z})\, OTF_{sca}(\rho, z), \qquad (10.15a)$$

where

$$OTF_{sca}(\rho, z) = \frac{e^{-\beta_{sca} z[1 - f(\rho)]} - e^{-\beta_{sca} z}}{1 - e^{-\beta_{sca} z}}, \qquad (10.15b)$$

and

$$f(\rho) = \int_{4\pi} P(\theta)\, d\Omega \int_0^1 J_0(k' \rho u \sin\theta)\, du, \qquad (10.15c)$$

$P(\theta)$ is the phase function, $J_0(\ )$ is a zero-order Bessel function of the first kind, $\rho = \lambda \kappa(fl)$, λ is the mean wavelength, κ is the spatial frequency, and fl is the focal length of the imaging system. The first term in Eq. 10.15a represents *OTF* for unscattered light. The light has been attenuated but not redirected. Thus the image will be less intense with no blur effect. The second term represents *OTF* for scattered light. In this case, the image component obtained is blurred. It is not surprising to see that the phase function is involved in calculating the scatter *OTF*. Examples of *OTF* and *PSF* are illustrated in Fig. 10.9. The low spatial frequencies are unaffected and *OTF* decays to the unscattered light level as the spatial frequency increases.

Problems

10.1 Given the particle distribution function in Eq. 10.1, verify the result for the total particle density in Eq. 10.2.

10.2 Propose a technique using a multifrequency lidar to distinguish between molecular and particle returns.

10.3 Show that the Henyey–Greenstein phase function is normalized according to Eq. 2.90.
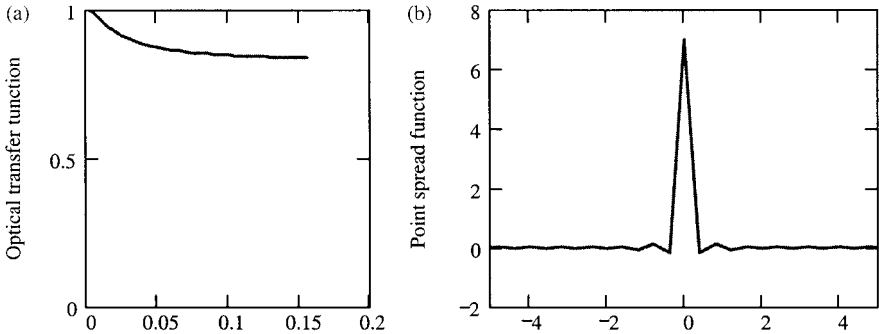
Fig. 10.9 The *OTF* and *PSF* for a 1 km scattering path, with $\tau_\infty = 0.2$, $\lambda = 0.5\mu$m, and $g = 0.8$ in the Henyey–Greenstein phase function.

10.4 Apply Snell's law and geometrical optics to verify the back-scatter angles listed in Fig. 10.4 for the primary and secondary rainbows. Consider green light with a wavelength of 0.5 μm.

10.5 Apply Snell's law and geometrical optics to verify the forward-scatter angle of ice crystals. Consider green light with a wavelength of 0.5 μm.

Bibliography

Section 10.1

10.1 D. Deirmendjian, *Electromagnetic Scattering on Spherical Polydispersions*, American Elsevier Publishing (1969).

10.2 E.P. Shettle, "Models of Aerosols, Clouds and Precipitation for Atmospheric Propagation Studies," *AGARD Conference Proceedings No. 454 on Atmospheric Propagation in the UV, Visible, IR and MM-wave Region and Related Systems Aspects,* pp. 15-1 to 15-13 (1989).

10.3 M.L. Wright, E.K. Proctor, L.S. Gasiorek, and E.M. Liston, "A Preliminary Study of Air-Polution Measurements by Active Remote Sensing Techniques," NASA CR-132724 (1975).

10.4 J.H. Seinfeld and S.N. Pandis, *Atmospheric Chemistry and Physics*, Wiley Interscience (1998).

10.5 R. Jaenicke, "Tropospheric Aerosols," in *Aerosol-Cloud-Climate Interactions*, P.V. Hobbs (ed.), Academic Press, pp. 1–31 (1993).

Section 10.2

10.6 R.M. Measures, *Laser Remote Sensing Fundamentals and Applications*, Wiley-Interscience (1984).

10.7 P.W. Kruse, L.D. McGlauchlin, and R.B. McQuistan, *Elements of Infrared Technology*, Wiley (1963).

10.8 L.C. Heney and J.L. Greenstein, "Diffuse Radiation in the Galaxy," *Astrophys. J*. **93,** 70–83 (1941).

Section 10.3

10.9 R. Greenler, *Rainbows, Halos, and Glories*, Cambridge University Press (1980).

10.10 M.G.J. Minnaert, *Light and Color in the Outdoors*, Springer-Verlag (1992).

Section 10.4

See references in Chapter 9, Section 9.2.

Section 10.5

10.11 N.S. Kopeika, *A System Engineering Approach to Imaging*, SPIE Press (1998).

10.12 W.H. Wells, "Loss of Resolution in Water as a Result of Multiple Small-Angle Scattering," *J. Opt. Soc. Am.* **59**, 686–691 (1969).

11

Propagation Background and Noise

Noise from the detector and source is always considered in a system design study. However, as an optical field propagates, it acquires additional noise and background radiance from the path defined by the source and by the field of view of the detector. This is typically in the form of propagation path emission and background emission, and bulk scattering within the propagation medium and surface scattering at the propagation medium boundaries of hot-object radiation (e.g., the sun) into the sensor field of view. In many cases this severely limits system performance. Also, in a passive system when no source is present, the background radiance is the signal of interest.

11.1 Path and Background Emission

Path emission can be modeled by the radiation transfer equation given by Eq. 2.85a. The source function, $\wp_+(s)$, must now be given an explicit representation. Figure 11.1 illustrates the incremental emittance per incremental length and bandwidth along an optical path in thermal equilibrium. The source function becomes this emittance ratio times the blackbody radiance at that location, as given by

$$\wp_+(s) = \frac{\Delta\epsilon(s)}{\Delta s} L_{bb} T(s) . \tag{11.1}$$

Using this result and for no source at the beginning of the path (i.e., $L(0) = 0$), the radiation transfer equation for the path radiance becomes,
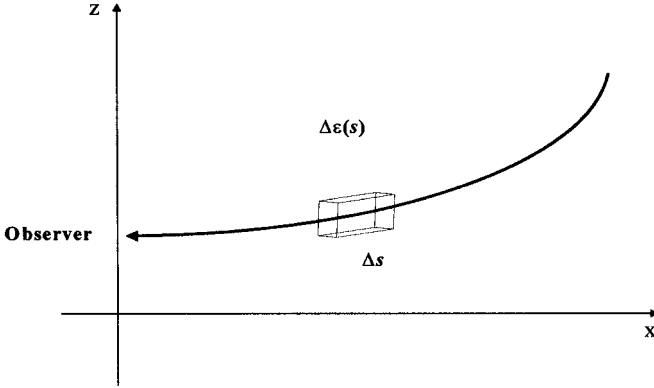
Fig. 11.1 Incremental emittance along an optical path described by s for a medium in thermal equilibrium.

$$L_{path}(s) = \int\limits_0^s \frac{\Delta\epsilon(s')}{\Delta s'} L_{bb} T(s') \, e^{(\tau_{OD}(s') - \tau_{OD}(s))} \, ds'. \tag{11.2}$$

Ignoring boundaries (i.e., reflectance) within a medium, the incremental emittance can be expressed solely in terms of the internal transmittance along an incremental path, thus

$$\Delta\epsilon(s') = 1 - \tau(s') = 1 - e^{-\beta_{abs}(s')\Delta s'}. \tag{11.3}$$

The incremental path length can be made arbitrarily small, so that the following simplification can be made:

$$\Delta\epsilon(s') \approx \beta_{abs}(s')\Delta s'. \tag{11.4}$$

Substituting this result into Eq. 11.3, the path radiance at s then becomes

$$
\begin{aligned}
L_{path}(s) &= \int\limits_0^s \beta_{abs}(s') L_{bb} T(s') \, e^{(\tau_{OD}(s') - \tau_{OD}(s))} ds' \\
&= e^{-\tau_{OD}(s)} \int\limits_0^s L_{bb} T(s') \, e^{\tau_{OD}(s')} d\tau_{OD}(s'),
\end{aligned}
\tag{11.5}
$$

where the following substitution is made.

$$d\tau_{OD}(s') = \beta_{abs}(s') \, ds'.$$

When a solid or liquid boundary is present, multiply Eq. 11.5 by $(1 - \rho)$.
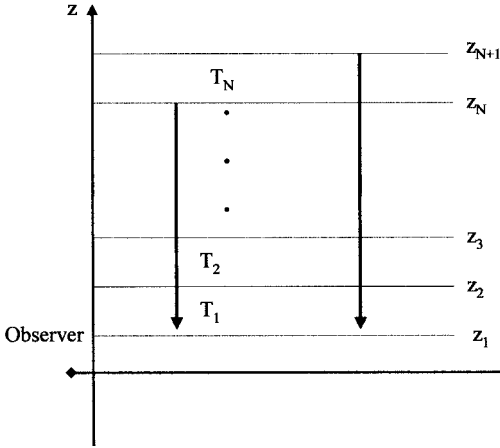
Fig. 11.2 Down-welling radiance in a vertically stratified N-layered medium with each layer at constant temperature T_i.

Consider the simple case when $T(s') = T_0$ is a constant, then the solution to Eq. 11.5 is

$$L_{path}(s) = L_{bb}(T_0)(1 - e^{-\tau_{OD}(s)}) = \epsilon_{path}(s)L_{bb}(T_0), \tag{11.6}$$

as expected. With this insight, a common numerical approach can be developed. Layer a propagation medium into stratified N-regions of constant temperature, as illustrated in Fig. 11.2. Then Eq. 11.5 is broken up into a sum of integrals over the constant temperature regions for a vertically downward path to an observer at z_1. Defining the transmittance from z_i to z_1 to be

$$\tau_{i,1} = e^{-\tau_{OD}(z_i)}, \tag{11.7}$$

substituting $s = z_{N+1} - z$, and using Eq. 11.6, the general solution to Eq. 11.5 becomes

$$L_{path}(z_1) = \sum_{i=1}^{N} L_{bb}(T_i)(\tau_{i,1} - \tau_{i+1,1}). \tag{11.8}$$

For slant-path radiance, take the vertical transmittance to the cse δ power, where δ is the elevation angle. For spectral band considerations, the path radiance must be integrated over the spectral region of interest, thus

$$L_{path}^{band}(s) = \int_{\lambda_1}^{\lambda_2} e^{-\tau_{OD}(s,\lambda)} \int_{0}^{s} L_{bb}(T(s'), \lambda)e^{\tau_{OD}(s',\lambda)} ds' d\lambda. \tag{11.9}$$

Because the transmittance in a window region is relatively flat, a band-averaged value can be used, as defined in Eq. 7.23. Now the only wavelength-dependent quantity is the blackbody radiance. The band-integrated blackbody radiance is defined to be

$$L_{bb}^{band}(T) = \int_{\lambda_1}^{\lambda_2} L_{bb}(T, \lambda) d\lambda. \tag{11.10}$$

The path emission model can be applied to two cases. One is path emission coming from the path taken by the source to the receiver. The other is emission within the field of view of the receiver but outside the field of view of the source. This is a type of background emission coming from within the propagation medium. Background emission from surfaces is another source of noise to the receiver and will be considered next.

To determine the background emission from a surface (the ground, a building, etc.), the directional emittance must be known. As presented in Chapter 2, it is obtained by integrating over all internal sources, Ω_e'. Using the principle of reciprocity, this is equivalent to integrating the external bidirectional reflectance over Ω_r. The BRDF is a commonly used characterization for many surfaces and can be easily measured. Thus, the following relationship for the directional emittance is obtained in terms of the total integrated reflectance (see Eq. 2.106a):

$$\epsilon(\Omega_e, \omega) = \epsilon(\Omega_i, \omega) = 1 - \int_{hemisphere} \rho(\Omega_r, \Omega_i, \omega) \, d\Omega_r = 1 - \rho_{TIR}(\Omega_e, \omega). \tag{11.11}$$

This is the desired result where the viewing solid angle is Ω_e. Recall that Eq. 11.11 remains true for a finite semitransparent medium in thermal equilibrium, when emitted light is observed at angles where no transmitted light from an external source exists.

For a Lambertian surface the total integrated reflectance is constant with viewing angle. Thus, the directional emittance is also constant. This is true for a flat surface, spherical surface, and cylindrical surface. As an example, consider the sun. The solar disk has a constant radiant output. The moon also has a constant reflected radiance for the same reason.

The spectral hemispherical emittance is also often desired as a figure of merit for a surface. It is defined as

$$\epsilon(\omega) = \frac{1}{\pi} \int_0^{2\pi} \int_0^{\frac{\pi}{2}} \epsilon(\omega, \theta, \phi) \, \cos\theta \sin\theta \, d\theta \, d\phi. \tag{11.12}$$

The total hemispherical emittance is also often desired, and given by

$$\epsilon = \frac{\pi}{\sigma_{SB} T^4} \int_0^\infty \epsilon(\omega) L_{bb}(\omega) \, d\omega,$$

where σ_{SB} is the Stefan–Boltzmann constant (5.6697×10^{-8} W/(m^2 K^4)), T is temperature, and L_{bb} is the blackbody radiance.

The source function for emitted radiance from a surface at s_s is given by

$$\wp_+(s) = \epsilon(\Omega_e, s) L_{bb}(T_{surface}) \delta(s_s). \tag{11.13}$$

Based on Eq. 11.11 and substituting Eq. 11.13 into Eq. 2.85, the emitted surface radiance measured by an observer then becomes

$$L_{surface}(\Omega_e) = [1 - \rho_{TIR}(\Omega_e)]L_{bb}(T_{surface})e^{[\tau_{OD}(s_s)-\tau_{OD}(s)]} \qquad (11.14)$$

11.2 Scattering into the Path

Scattering into the path can also be modeled by the radiation transfer equation, given by Eq. 2.85. Two distinct sources must be considered, scattered light from within the propagation medium and reflected light from the boundaries. The source function now becomes the scattered or reflected intensity per unit volume. Based on Eq. 2.88 for bulk scatter, the incremental scattered radiance per incremental path element from an external source (not necessarily in the direct field of view of the receiver), L_{ext}, into the field of view of the observer is expressed as

$$\wp_+(\Omega_i,\Omega_s,s) = \frac{\alpha_{sca}(\Omega_i,\Omega_s(s))\Delta\Omega_i(s)L_{ext}(\Omega_i)}{\Delta s}. \qquad (11.15)$$

The concept is illustrated in Fig. 11.3. Following a procedure similar to that used in the first section and recalling Eq. 2.91, the BSDF can be decomposed into a product of the total integrated scatter and the phase function. Also, in the single scatter approximation, based on Eqs. 2.145 and 2.146, the total integrated scatter is the scatter coefficient times the incremental path length. Thus,

$$\alpha_{sca}(\Omega_i,s) = \beta_{sca}(\Omega_i,s)\Delta s.$$

Substituting these results into Eq. 11.15, the following expression for the scatter source function is obtained:

$$\wp_+(\Omega_i,\Omega_s,s) = \beta_{sca}(\Omega_i,s)P_s(\Omega_i,\Omega_s,s)M_{ext}(\Omega_i), \qquad (11.16)$$
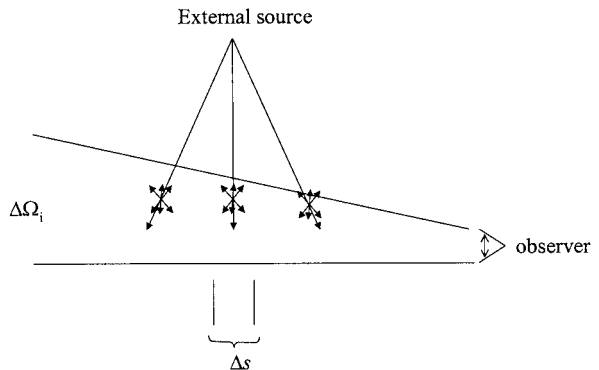
Fig. 11.3 Incremental scatterance created by an external source along an optical path.

where the irradiance, $M_{ext} = \Delta\Omega L_{ext}$. Based on Eq. 2.85 with no source present, the scattered radiance into the field of view of an observer is

$$L_{sca}(\Omega_i, \Omega_s, s) = \int_0^s \beta_{sca}(\Omega_i, s') P_s(\Omega_i, \Omega_s, s') M_{ext}(\Omega_i) e^{[\tau_{OD}(s') - \tau_{OD}(s)]} ds'. \quad (11.17)$$

To obtain the observed irradiance, Eq. 11.17 must be integrated over the solid angle of the detector.

A similar expression for the reflected radiance from an opaque surface at a fixed location, s_r, along the path can be obtained for reflected light by replacing the BSDF by the BRDF in Eq. 11.15. Also, the incremental path element shrinks to a single point on the reflecting surface. Thus, the source function in this case becomes

$$\wp_+(\Omega_s) = \rho(\Omega_i, \Omega_r) M_{ext}(\Omega_i) \delta(s_r). \quad (11.18)$$

Based on the radiation transfer equation (Eq. 2.85) with no source present and using the above source function, the reflected radiance measured by an observer is

$$L_{refl}(\Omega_i, \Omega_r, s) = \rho(\Omega_i, \Omega_r) M_{ext}(\Omega_i) e^{[\tau_{OD}(s_r) - \tau_{OD}(s)]}. \quad (11.19)$$

Example 11.1 Consider a surface illuminated uniformly in all directions with irradiance M_{ext}. Using Eq. 11.18 and integrating both sides with solid angle, the reflected radiance within the solid angle $\Delta\omega_r$, ignoring propagation loss, becomes

$$L_{refl}(\Omega_r) = \frac{M_{ext}}{\pi} \int_{hemisphere} d\Omega_i \rho(\Omega_r, \Omega_i).$$

Recall that the irradiance divided by π is the radiance, and based on reciprocity, the above equation becomes

$$L_{refl}(\Omega_r) = L_{ext} \int_{hemisphere} d\Omega_r \rho(\Omega_i, \Omega_r) = L_{ext} \rho_{TIR}(\Omega_r).$$

Thus, the observed reflected radiance depends only on the single solid angle of the receiver.

11.3 Photon Noise

The background radiance, as presented so far, represents a nearly constant flux level to a detector. Of course, the dynamics of a scene will introduce a temporal behavior, but

this is often a slow variation. The observed temporal variation is in part due to photon fluctuations. This appears as noise on the measured signal in addition to the noise of the detector (see Boyd, Ref. 11.3). The statistics of photon fluctuations differs if the source of photons comes from stimulated emission or spontaneous emission. Since background radiance is normally from spontaneous emission sources, we will consider fluctuations from that source type only. This means applying the Bose–Einstein distribution function introduced in Chapter 5.

Based on Eq. 5.148, the standard deviation (root mean square) of the number of bosons (photons) is

$$\sqrt{\langle \Delta N^2 \rangle} = \sqrt{\langle N \rangle + \langle N^2 \rangle} \tag{11.20}$$

In terms of the fluctuations in radiance or radiance noise, we use Eq. 5.15 and 5.17a to convert the above equation to

$$\sqrt{\Delta L_{BB}^2} = \sqrt{2hc^2\nu^3 L_{BB} + L_{BB}^2}. \tag{11.21}$$

Knowing the geometry of the receiver, the fluctuations in the light field power can be obtained. The large fluctuations predicted by Eq. 11.21 are significantly reduced by including the observation time and the detector bandwidth as well in a real detection system (see Boyd, Ref. 11.3).

11.4 Examples of Path Emission and Scatter

A variety of examples are presented in this section to demonstrate background radiance in optical systems.

11.4.1 Clear Sky Radiance

An interesting application of Eq. 11.8 that includes the slant-path correction is the band-averaged sky radiance as a function of the zenith angle. This is an important consideration for infrared systems operating in the 8–12 μm and 3–5 μm window regions. A reasonably accurate model can be simply generated by using a two-layer model of the atmosphere. This works because an observer near the surface of the earth sees radiance dominated by two different temperatures: the surface temperature in the horizontal direction and an effectively lower temperature radiance in the vertical direction. For $N = 2$, Eqs. 11.8–11.10, the band-integrated sky radiance becomes

$$L_{sky}^{band}(\theta) = L_{bb}^{band}(T_1)(\overline{\tau}_{1,1}^{\sec\theta} - \overline{\tau}_{1,2}^{\sec\theta}) + L_{bb}^{band}(T_2)(\overline{\tau}_{1,2}^{\sec\theta} - \overline{\tau}_{1,3}^{\sec\theta}). \tag{11.22}$$

Using the following relationships for the transmittance

$$\overline{\tau}_{1,1} = 1 \quad \text{and} \quad \overline{\tau}_{1,3} = \overline{\tau}_{1,2}\overline{\tau}_{2,3}, \tag{11.23}$$

Eq. 11.20 reduces to

$$L_{sky}^{band}(\theta) = L_{bb}^{band}(T_1) - \left\{ \left[L_{bb}^{band}(T_1) + L_{bb}^{band}(T_2)\overline{\tau}_{2,3}^{\sec\theta} - L_{bb}^{band}(T_2) \right] \overline{\tau}_{1,2} \right\} \frac{\overline{\tau}_{1,2}^{\sec\theta}}{\overline{\tau}_{1,2}}.$$

(11.24)

Based on the above result, the following semiempirical formula for sky radiance is proposed:

$$L_{sky}^{band}(\theta) = A - B \exp[-C(\sec\theta - 1)],$$

(11.25)

where

$$A = L_{bb}^{band}(T_1), \ B = \left[L_{bb}^{band}(T_1) + L_{bb}^{band}(T_2)\overline{\tau}_{2,3} - L_{bb}^{band}(T_2) \right] \overline{\tau}_{1,2} \quad \text{and}$$

$$C = -\ln(\overline{\tau}_{1,2}).$$

It is assumed that B is independent of θ and

$$\overline{\tau}_{2,3} = \overline{\tau}_{1,2}^{0.6}.$$

Thus, A represents the in-band horizontal radiance and C is an effective optical depth of the first layer. A–B is the in-band vertical radiance. This model has been successfully applied to the 8–12 μm window region sky radiance by Saunders (Ref. 11.4) in the vicinity of Boston, Massachusetts over an entire year. The coefficients change with the expected seasonal variability of surface temperature ($275 \le T_1 \le 295$ K) and water vapor content. The effective temperature of the second layer is $T_2 \approx 260$ K and is relatively constant with season. Figure 11.4 plots the winter sky radiance as a function of the zenith angle based on this model and using the parameters determined by Saunders. Equation 11.25 can be applied to other spectral regions (e.g., 3–5 μm) as well.
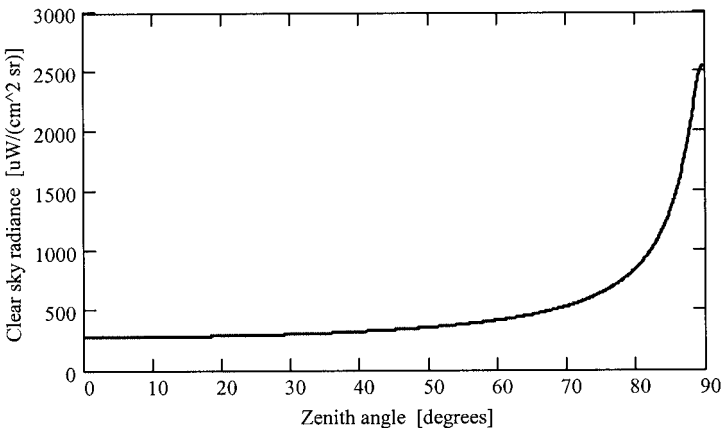
Fig. 11.4 Wintertime clear sky radiance as a function of the zenith angle near Boston, Massachusetts for $A = 2550$ μW cm^{-2} sr^{-1}, $B = 2270$ μW cm^{-2} sr^{-1}, and $C = 0.062$.

In this model, a rectangular coordinate system is used. For realistic predictions near the horizon, the effects of earth curvature also must be considered. This is accomplished by employing Eq. 7.41a for $n = 1$ in the equation for the optical depth,

$$\tau_{OD}(z_i) = \int_{z_{N+1}-z_0}^{z_{N+1}-z_i} \beta_{abs}(z') \frac{dz'}{\sqrt{1 - \frac{(r_e+z_0)^2}{(r_e+z_i)^2}\sin^2\theta}}.$$

The vertical dependence of the absorption coefficient must at least follow the total pressure fall-off as given by

$$\beta_{abs}(z') = \beta_{abs}e^{-0.145z'},$$

where z' is in km. The ratio of the optical depth, including earth curvature, to the optical depth in a rectangular earth as a function of the zenith angle is plotted in Fig. 11.5. The result is a decrease in the optical depth as the horizon is approached. The correction is significant at the largest zenith angles. However, the sky radiance near the horizon is that of a blackbody because the propagation path is optically thick. This means the sky radiance in that direction is not sensitive to the optical depth and the correction for a curved earth is generally not important.

11.4.2 Detector Window Radiance

Detectors often require protection from the outside environment. Also, some detectors are cooled, which requires a vacuum environment and a vacuum window. For these reasons, detectors often have windows in front of them at ambient temperature. The window has two effects on detector performance. The window will irradiate the cold detector region,
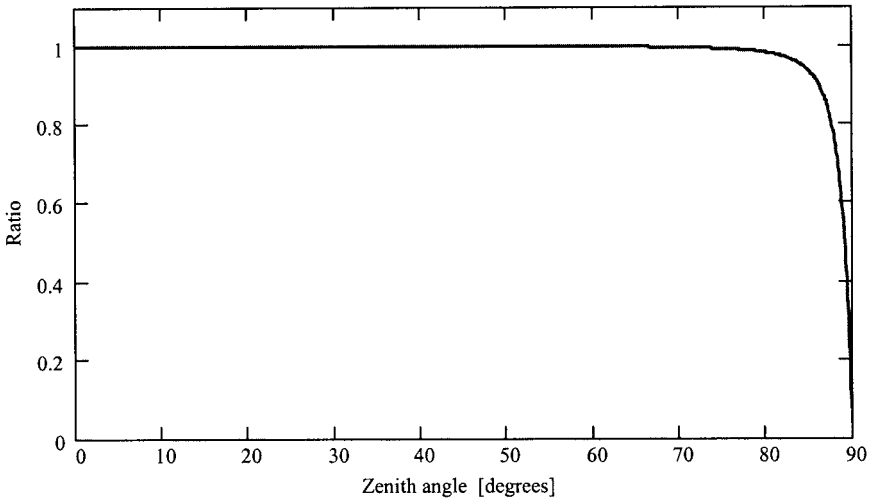
Fig. 11.5 The ratio of the optical depth including earth curvature to the optical depth in a rectangular earth as a function of the zenith angle.

thus warming it, and possibly providing background radiance in the spectral region the detector is operating. The latter effect becomes important when viewing a weak source.

For example, consider a sapphire window in front of an InSb detector. The detector is sensitive out to 5.5 μm. For a window 2 mm thick, with uniform temperature, the window emittance can be approximated by

$$\epsilon = \beta_{abs} d,$$

where d is the window thickness. The room-temperature absorption coefficient of sapphire at 5 μm is 0.95 cm^{-1}, thus the window emittance is 0.19. Furthermore, InSb has peak sensitivity around 5 μm. Clearly, window radiance is a concern in this case, limiting sensor performance. If the window temperature is nonuniform in depth, then Eq. 11.5 or Eq. 11.8 must be applied.

11.4.3 Atmospheric Spectral Radiance

Just as the atmosphere absorbs radiant energy, as discussed in Chapter 7, it must emit energy to maintain thermal equilibrium. A measurement of the down-welling spectral radiance in the mid-wave infrared of the atmosphere is presented in Fig. 11.6. This radiance is a background source to infrared sensors operating in the atmosphere. It can also
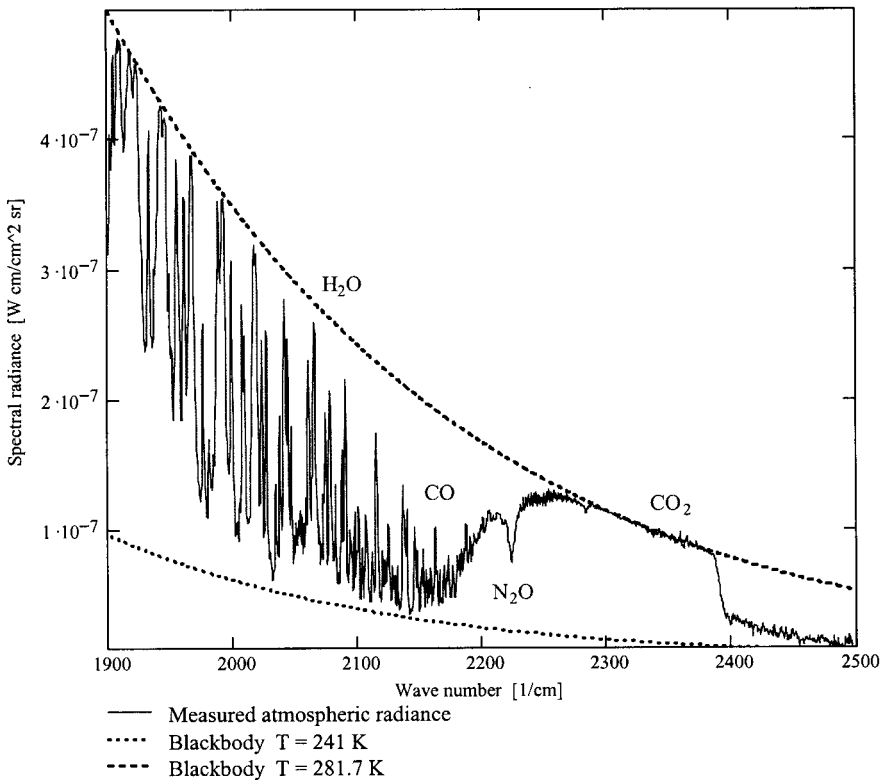
Fig. 11.6 The down-welling spectral radiance of a clear atmosphere at night. The upper blackbody curve is at the local air temperature of the observer.

be used to remotely sense chemical species (see Fig. 11.6) in the atmosphere and obtain vertical temperature and water vapor profiles. This can be accomplished by using down-welling (ground-based spectroradiometer) or up-welling (space-based spectroradiometer) spectral radiance .

As an example, a technique for obtaining a low-spatial-resolution vertical temperature profile from down-welling mid-wave spectral radiance is presented. Consider a highly absorbing, temperature-insensitive spectral point (recall Fig. 7.37), ν_{T0}, within the ν_3 band of $^{12}CO_2$. In this case, the path length for 1% transmittance is only several meters. This is why the blackbody curve in Fig. 11.6 at the local air temperature agrees with measured atmospheric radiance in the vicinity of the CO_2 band. Let the first layer be that thickness, then based on Eq. 3, the observed radiance becomes

$$L_{path}(z_0, \nu_{T0}) = 0.99 L_{bb}(T_0, \nu_{T0}). \tag{11.26}$$

T_0 can also be determined by a thermometer above the sensor, thus this measurement also calibrates the instrument. T_0 can be determined radiometrically if the instrument is calibrated, but changes in the system with time make continuous recalibration desirable. Next, choose a second temperature-insensitive spectral point, ν_{T1}, with a somewhat smaller absorption coefficient, then the transmittance will be to a greater range. Let the height of the second layer be such that $\tau_{2,0} \approx 0.01$. Then the solution of Eq. 11.8 becomes

$$\begin{aligned} L_{path}(z_0, \nu_{T1}) &= L_{bb}(T_0, \nu_{T1}) \left[1 - \tau_{1,0}(\nu_{T1})\right] \\ &+ L_{bb}(T_1, \nu_{T1}) \left[\tau_{1,0}(\nu_{T1}) - 0.01\right]. \end{aligned} \tag{11.27}$$

Solving for the blackbody radiance at ν_{T1}, from the second layer yields

$$L_{bb}(T_1, \nu_{T1}) = \frac{L_{path}(z_0) - L_{bb}(T_0, \nu_{T1}) \left[1 - \tau_{1,0}(\nu_{T1})\right]}{\tau_{1,0}(\nu_{T1}) - 0.01}. \tag{11.28}$$

Using the blackbody formula, the temperature, ν_{T1}, now can be determined. In general, for the Kth layer the blackbody radiance at ν_{TK} is given by

$$L_{bb}(T_K, \nu_{TK}) =$$

$$\frac{L_{path}(z_0, \nu_{TK}) - \sum_{i=0}^{K-1} L_{bb}(T_i, \nu_{TK}) \tau_{i,0}(\nu_{TK}) \left[1 - \tau_{i+1,i}(\nu_{TK})\right]}{\tau_{K0}(\nu_{TK}) - 0.01}, \tag{11.29}$$

where

$$\tau_{K,0} = \prod_{k=1}^{K} \tau_{k,k-1}. \tag{11.30}$$

The temperature is obtained by inverting the blackbody equation. However, only a few of the available spectral points have absorption coefficients that are relatively insensitive to temperature. Thus a low-spatial-resolution temperature profile results. A measured vertical temperature profile using this technique is presented in Fig. 11.7.
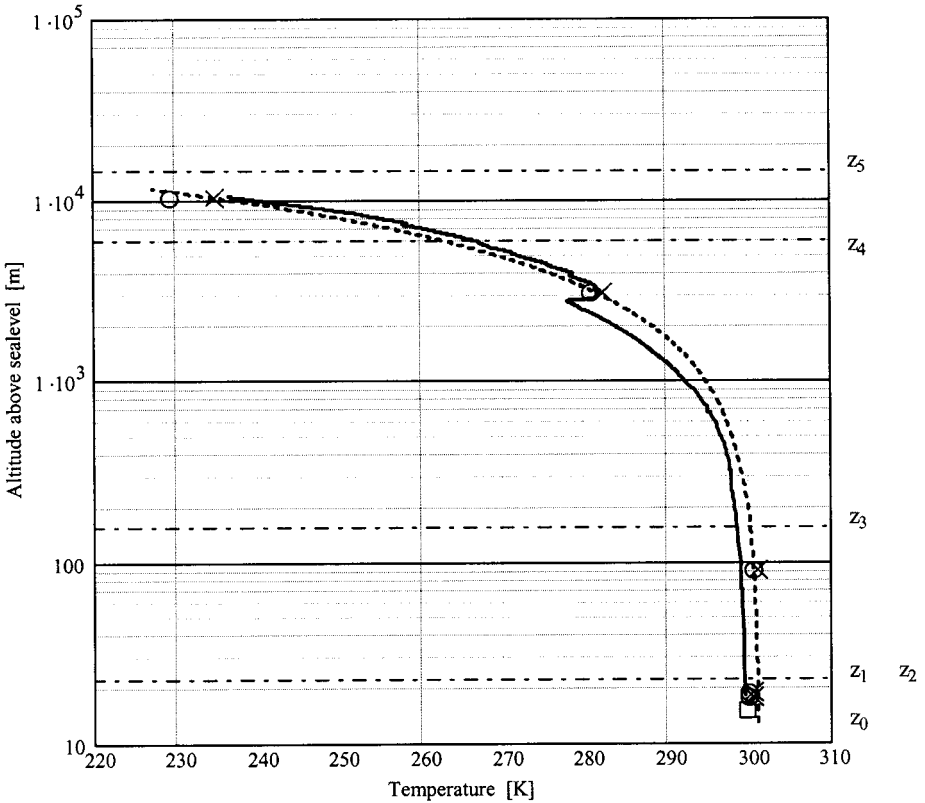
Fig. 11.7 Vertical temperature profile of the troposphere measured with an infrared spectrora-diometer (x and ○) and a balloonsonde (solid curve). The spectroradiometer data points are fit to a linear function (dotted curve).

The measured (path-averaged) points are compared with a curve generated by an ascending balloonsonde. The spectroradiometer measurement takes 2 minutes. The balloonsonde takes 2 hours to ascend to the top of the troposphere. Thus two spectro-radiometer measurements are presented that were collected during the ascent of the balloon. Good agreement between these two different techniques is demonstrated.

To sharpen the spatial resolution of this radiometric technique, temperature-sensitive spectral lines must now be used. Since the standard troposphere has a linear vertical tem-perature profile, the temperature-insensitive results are used to obtain a least-squares fitted vertical temperature profile. Then an iterative procedure can be used to obtain the final profile. In this manner, the vertical temperature profile can be constructed with rea-sonable spatial resolution, depending upon the spectrometer resolution, number of spectral points used, and system noise. The accuracy can be checked by computing the down-welling spectral radiance using standard computer codes employing the HITRAN database (i.e., FASCODE) and comparing with the measured radiance spectrum.

To this point we have assumed a clear atmosphere and have ignored contributions from aerosols and clouds. Clouds, in particular, will terminate the vertical path radiance. However, the presence of clouds can be detected by looking in the microwindows

between water vapor emission lines. For clear sky conditions we expect low spectral radiance in these windows. If a cloud is present, the spectral radiance background will significantly increase in the microwindows.

11.4.4 Solar Reflection and Scatter

The solar irradiance outside the atmosphere of the earth can be closely approximated by multiplying the solar blackbody radiance by the solid angle subtended by the sun,

$$M_{solar}(\nu) = L_{bb}(T_{sun}, \nu) \frac{\pi r_{sun}^2}{R_{sun}^2}, \tag{11.31}$$

where r_{sun} (= 6.9638×10^5 km) is the radius of the sun, R_{sun} (= 1.4968×10^8 km) is the mean distance from the sun to the earth and T_{sun} (= 5800 K) is the temperature of the photosphere. However, this model breaks down for frequencies above 20,000 cm^{-1} (below 0.5 µm) and the sun becomes a non-thermal-equilibrium radiator. An empirical fit to experimental data yields a more accurate model. Equation 11.31 is modified according to the following formula:

$$M_{solar}(\lambda) = [L(T_{sun}, \lambda) f1_{solar}(\lambda) + f2_{solar}(\lambda)] \frac{\pi r_{sun}^2}{R_{sun}^2}, \tag{11.32}$$

where

$$f1_{solar}(\lambda) = 1 - [6(0.45 - \lambda) - 10(0.45 - \lambda)^2] h(0.45 - \lambda)$$

and

$$f2_{solar}(\lambda) = 800 \exp\left[\frac{(\lambda - 0.335)^2}{0.001}\right] + 280 \exp\left[\frac{(\lambda - 0.372)^2}{0.000065}\right]$$

$$+ 665 \exp\left[\frac{(\lambda - 0.413)^2}{0.00016}\right] + 450 \exp\left[\frac{(\lambda - 0.47)^2}{0.00055}\right]$$

$$- 90 \exp\left[\frac{(\lambda - 0.55)^2}{0.0002}\right] - 80 \exp\left[\frac{(\lambda - 0.735)^2}{0.03}\right].$$

A comparison of the extraterrestrial solar irradiance model to experimental data is presented in Fig. 11.8. solar light reaches the earth collimated or unidirectional with a total band-integrated irradiance at the top of the atmosphere of 1.39 kW/m^2. The irradiance at the surface of the earth is affected by atmospheric transmittance and therefore is variable.

Solar scatter reflected from a surface can be computed using Eq. 11.18 and substituting M_{sun} for M_{ext}. For a Lambertian surface and a lossless path to the receiver, the reflected radiance becomes

$$L_{reflsolar}(\theta_r, \nu) = \frac{\rho_{TIR}}{\pi} \cos\theta_r M_{solar}(\nu), \tag{11.33}$$

assuming the receiver spatially resolves the angle dependence. For reflected light from land the above formula is often used. For reflected light from the ocean surface, a non-Lambertian BRDF is used (see Ref. 11.10).
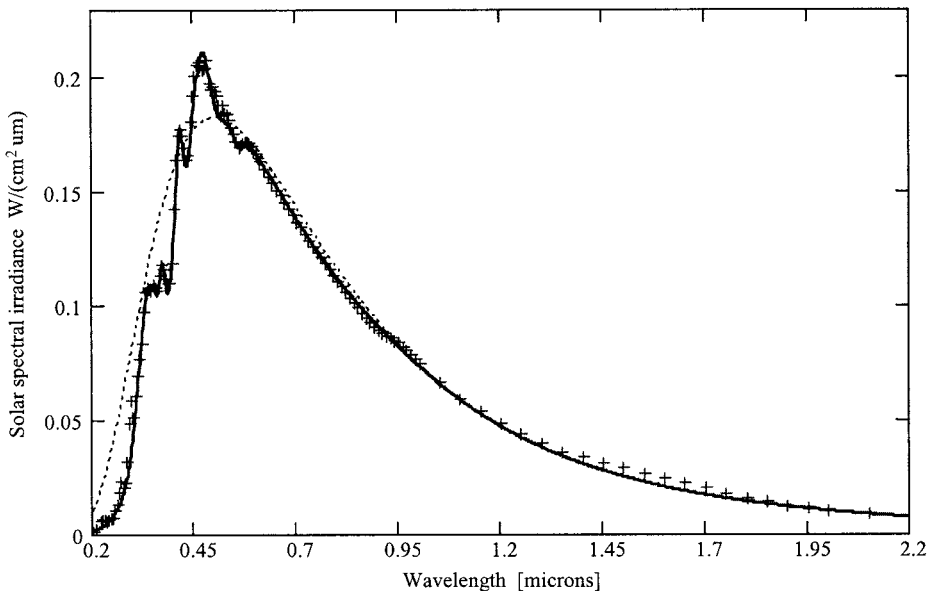
Fig. 11.8 Spectral irradiance of the sun above the atmosphere of the earth. The +s are experimental data points and the curve is Eq. 11.32. The dotted curve is the spectral radiance of a blackbody at $T = 5800$ K.
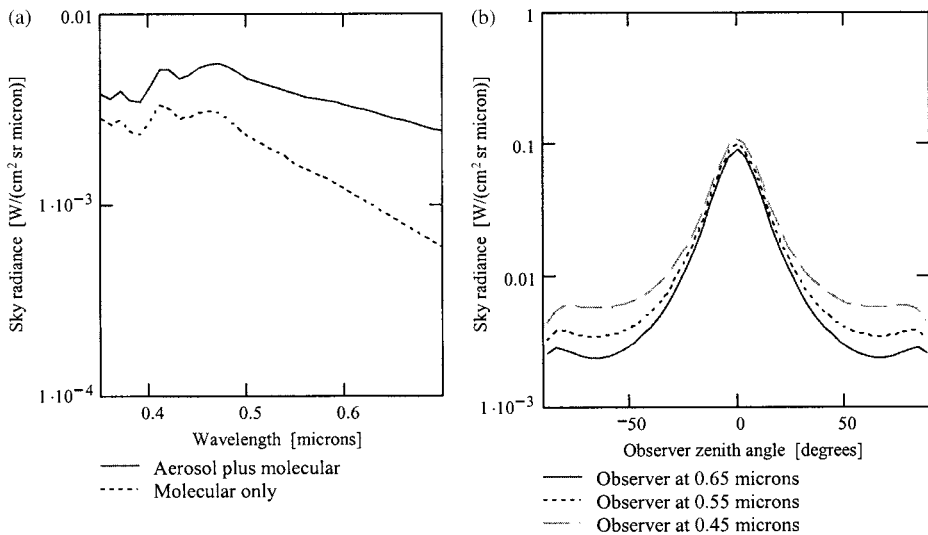
Fig. 11.9 (a) Sky spectral radiance for the solar angle at $0°$ zenith and the observer at $85°$ zenith. (b) Sky spectral radiance at three different wavelengths as a function of observer angle.

472

As sunlight propagates through the atmosphere of the earth, it is scattered and absorbed. The path is inhomogeneous and depends on the solar zenith angle. The observed solar irradiance depends on the viewing angle as well. Equation 11.17 is used to compute the scattered spectral radiance to an observer. A good example of this was presented in Chapter 7 (Section 7.3.2) concerning solar scattered light by molecules. This lead to an explanation of the blue sky background. If aerosols are present in the path, the sky background whitens when viewing near the horizon. This point is illustrated in Fig. 11.9a, which shows a whiter background with aerosols present than with a pure molecular atmosphere. The aerosol model used in the calculations for Fig. 11.9 employs Eq. 10.5 for the vertical concentration profile, where $\rho_p(0) = 400$ particles per cm^3, $h_p = 1.1$ km^{-1}, and $\rho_{pB}(0) = 0$. The Henyey–Greenstein phase function is also used, with $g = 0.8$. This produces a narrow and highly forward-scattered phase function. The aerosol scatter cross-section is 4×10^{-9} cm^2 for all wavelengths. Figure 11.9b shows the scattered spectral radiance for the above conditions as a function of observer angle. In the vicinity of the sun, the scattered radiance shows the shape of the forward phase function. Based on Mie theory the phase function depends on the particle size. Thus a measurement of this sky radiance can yield important information about the particles scattering the light. Also, Fig. 11.9b shows an angle dependence very different from purely molecular scatter, which is almost constant with observer angle. This is another aspect of the different phase functions for the two different sizes of particles.

Problems

11.1 Compute the path radiance for the conditions of Problem 7.5. Use the standard vertical temperature profile of the atmosphere, as given in Fig. 7.5.

11.2 Beginning with Eq. 11.5, derive Eq. 11.8.

11.3 Determine the reflected solar radiance of a Lambertian ocean surface as a function of the solar angle.

11.4 Assuming that the reflectance of the moon is 10%, independent of frequency, and Lambertian, compute the reflected radiance of sunlight by a full moon. What is corresponding irradiance of the full moon to an observer on earth?

11.5 Verify Fig. 7.37 for molecular Rayleigh scatter. Use Eqs. 7.59 and 4.88 to generate the figure.

Bibliography

Section 11.1

11.1 G. Finger and F.K. Kneubühl, "Spectral Thermal Infrared Emission of the Atmosphere," Chapter 4 in *Infrared and Millimeter Waves, Vol. 12, Electromagnetic Wave in Matter, Part II*, K.J. Button (ed.), Academic Press (1984).

Section 11.2

11.2 A. Kokhanovsky, *Optics of Light Scattering Media Problems and Solutions*, Wiley-Praxis Series in Atmospheric Physics and Climatology, Wiley (1999).

Section 11.3

11.3 R.W. Boyd, *Radiometry and the Detection of Optical Radiation*, Wiley (1983).

Section 11.4

11.4 P.M. Saunders, "Radiance of Sea and Sky in the Infrared Window 800–1200 cm^{-1}," *J. Opt. Soc. Am.* **49**, 645–652 (1968).

11.5 W.L. Smith, H.E. Revercomb, H.B. Howell, H.-L. Huang, R.O. Knuteson, E.W. Koenig, D.D. LaPorte, S. Silverman, L.A. Sromovsky, and H.M. Woolf, "GHIS-The GOES High-Resolution Interferometer Sounder," *J. Appl. Meteor.* **29**, 1189–1204, (1990).

11.6 W.F. Feltz, W.L. Smith, R.O. Knuteson, H.E. Revercomb, H.M. Woolf and H.B. Howell, "Meteorological Applications of Temperature and Water Vapor Retrievals from the Ground_Based Atmospheric Emitted Radiance," *J. Appl. Meteor.* **37**, 857–875 (1998).

11.7 W.L. Smith, W.F. Feltz, R.O. Knuteson, H.E. Revercomb, H.M. Woolf and H.B. Howell, "The Retrieval of Planetary Boundary Layer Structure Using Ground-Based Infrared Spectral Radiance Measurements," *J. Atmos. Oceanic Technol.* **16**, 323–333, (1999).

11.8 M.E. Thomas with M.D. Banta, "Passive Remote Sensing of the Atmosphere by a Ground Based Spectroradiometer," *Proceedings of the International Geoscience and Remote Sensing Symposium*, July 24–28, 2000.

11.9 W.L. Wolfe and G.J. Zissis (eds.), Chapter 3 in "Natural Sources" *The Infrared Handbook*, ERIM (1978).

11.10 R.E. Walker, *Marine Light Field Statistics*, Wiley-Interscience (1994).

Appendix 1

Symbols and Units

Table A1.1 lists symbols with the corresponding meaning and units used in this book. An attempt is made to consistently use MKS units, however, convention does not always allow this. Also, the defined symbols are used consistently throughout the text. However, absorption and scattering phenomena in various media were developed separately, and a variety of different symbols are often used for the same quantity. This is very disturbing to a student trying to learn the material for the first time. For this reason, an attempt is made to use the most common symbols with both sets of literature and to otherwise select symbols in the most unambiguous way. When the usage should clearly indicate the meaning, the same symbol is used for two different quantities. Fortunately, this is rarely the case.

Table A1.1 Symbols, Nomenclature, and Units

Symbol	Meaning	Units[a]
a	Absolute humidity	gm^{-3}
$a = C_{sca}/C_{ext}$	Single-scatter albedo	—
a_n and b_n	Complex Mie coefficients	—
b	Time-domain magnetic flux density	Wm^{-2}
B	Frequency-domain magnetic flux density[b]	Wm^{-2}
C_{ext}	Extinction cross-section	m^2
C_{abs}	Absorption cross-section	m^2
C_{sca}	Scatter cross-section	m^2
C_V	Heat capacity	$J\,\mu g^{-1}K^{-1}$
c	Speed of light in vacuum (2.99792458×10^8)	m/s
$C(\tau)$	Autocorrelation function	$sec^{-1}cm$

(continued)

Table A.1 Symbols, Nomenclature, and Units—cont'd

Symbol	Meaning	Units[a]
d	Time-domain electric flux density	Cm^{-2}
D	Frequency domain electric flux density[b]	Cm^{-2}
e	(2.7182818284)	—
e	Elementary charge ($1.60217733(49) \times 10^{-19}$)[c]	C
e	Time-domain electric field intensity	Vm^{-1}
E	Energy	J
E	Frequency-domain electric field intensity[b]	Vm^{-1}
$E_s(T)$	Saturation vapor pressure	kPa
g	Gravitational acceleration (9.80665)	ms^{-2}
$g(\nu)$	Line shape function	cm
h	Planck's constant ($6.6260755(40) \times 10^{-34}$)	J sec
h	Time-domain magnetic field intensity	Am^{-1}
H	Frequency-domain magnetic field intensity[b]	Am^{-1}
I	Radiant intensity	$W sr^{-1}$
I_ν	Spectral radiant intensity	$W sr^{-1} cm$
$[I\ Q\ U\ V]$	Stokes vector	—
j	$\sqrt{-1}$	—
$j(\nu)$	Spectral density function	cm
k_a	Index of absorption	—
k_s	Index of scatter	—
k_e	Index of extinction or attenuation	—
k_B	Boltzmann's constant ($1.380658(12) \times 10^{-23}$)	$J K^{-1}$
$k' = 2\pi/\lambda$	Wave vector magnitude	m^{-1}
L	Radiance (also sterance)	$W cm^{-2} sr^{-1}$
$\mathscr{L}$	Poynting vector (time domain)	$W cm^{-2} sr^{-1}$
M	Irradiance	$W cm^{-2}$
M	Modified refractivity	—
m	Mass	kg
m_e	Mass of an electron ($9.1093897(54) \times 10^{-31}$)	kg
m_p	Mass of a proton ($1.6726231(10) \times 10^{-27}$)	kg
m_n	Mass of a neutron ($1.6749286(10) \times 10^{-27}$)	kg
m	Modified index of refraction	—
$\bar{n} = n - jk$	Complex refractive index	—
N	Number of particles	—
N_A	Avogadro's number ($6.0221367(36) \times 10^{23}$)	Particles mol^{-1}
N	Refractivity	—
n	Index of refraction real part	—
P, p	Pressure	Pa
$P(\theta), P_i(\theta)$	Phase functions	—
$\mathscr{P}$	Source function	$W m^{-2} sr Hz$
q	Electric charge	C
Q_{ext}	Extinction efficiency	—
Q_{abs}	Absorption efficiency	—
Q_{sca}	Scatter efficiency	—
Q_{back}	Back-scatter efficiency	—
$Q(T)$	Partition function	—
R, r	Distance	m
R	Reflection coefficient	
rh	Relative humidity	—
r	Particle radius	m
R_{GC}	Gas constant = 82.0575	atm $cm^3 K^{-3} mol^{-1}$
R_v	Visibility range	km
R_m	Meteorological range	km

Table A.1 Symbols, Nomenclature, and Units—cont'd

Symbol	Meaning	Units[a]
S_1 and S_2	Dimensionless complex field amplitudes	—
S_i	Line strength of ith line	$cm^{-1}\,km^{-1}$
t	Time	sec
T	Temperature	K
T	Transmission coefficient	
V	Volume	m^3
w	Absorber amount	
$x = k'r$	Dimensionless size parameter	—
x, y, z	Cartesian coordinates (z directed upward)	m
z_R	Rayleigh range	m
α_{ex}	Expansion coefficient	K^{-1}
α_{ext}	Extinctance (absorptance plus scatterance)	—
α_{abs}	Absorptance, absorptivity	—
α_{sca}	Scatterance	—
α_e	Electronic polarizability	—
β_{ext}	Extinction coefficient or extinction cross-section per unit volume	km^{-1}
β_{abs}	Absorption coefficient or absorption cross-section per unit volume	km^{-1}
β_{sca}	Scattering coefficient or scatter cross-section per unit volume	km^{-1}
Γ	Full-width at half-maximum	cm^{-1}
γ	Half-width at half-maximum	cm^{-1}
δ	Depolarization factor	—
ϵ	Emittance, emissivity	—
ϵ_0	Permittivity of free space ($8.8541878 \times 10^{-12}$)	Fm^{-1}
ϵ_r	Relative permittivity	—
ζ	Zenith angle	rad or degrees
Θ, φ	Polar, azimuthal angles	rad or degrees
κ	Spatial frequency	m^{-1}
κ_p	Thermal conductivity	$Wm^{-1}\,K^{-1}$
λ	Wavelength	µm
μ	$= \cos\theta$	—
μ'	Reduced mass	kg
μ_0	Permeability of free space ($4\pi \times 10^{-7}$)	Hm^{-1}
μ_r	Relative permeability	—
ν	Wave number ($1/\lambda$)	cm^{-1}
π	Pi (3.1415926535)	—
ρ_i	Number density of species i (N_i/V)	cm^{-3}
ρ_m	Mass density	$g\,cm^{-3}$
$\rho_p(r)$	Particle size distribution function	$cm^{-3}\,µm^{-1}$
ρ	Reflectance, reflectivity	—
σ	Conductivity	$\mho m^{-1}$
σ_b	Back-scatter cross-section	m^2
σ_{SB}	Stefan-Boltzmann constant (5.6697×10^{-8})	$W\,m^{-2}\,K^{-4}$
τ	Transmittance, transmissivity	—
τ_{OD}	Optical distance or depth	—
Φ	Flux	W
χ	Electric susceptibility	—
ω	Angular frequency ($2\pi f$)	$rad\,sec^{-1}$
Ω	Solid angle	sr

[a]— indicates a dimensionless quantity.
[b]Frequency-domain field quantities are defined for a unit bandwidth of one to be consistent with phasor notation.
[c]Digits in parentheses indicate the standard deviation uncertainty in the last digits of the given value.

Table A1.2 Unit Conversions

1 amu $= 1.6605654 \times 10^{-27}$ kg
1 cm^{-1} $= 30$ GHz
1 eV $= 8065.5$ cm^{-1} $= 1.602189 \times 10^{-19}$ J
1 μm $= 1000$ nm $= 10,000$ Å
1 atm $= 760$ Torr $= 1013.25$ mb $= 14.7$ psia $= 101.325$ kPa $= 1.01325 \times 10^5$ N m^{-2}
1 in $= 2.54$ cm
1 dB/km $= 2.3026 \times 10^{-6}$ cm^{-1}
1 cal $= 4.185$ J
1 Debye $= 3.33564 \times 10^{-30}$ C m

Table A1.3 Additional Useful Constants

$hc/k_B = 1.438786 \times 10^{-2}$ m K
Mean radius of earth $= 6.378388 \times 10^3$ km
Mean radius of sun $= 6.9638 \times 10^5$ km
Mean distance from earth to sun $= 1.4968 \times 10^8$ km
Mean angle of the solar photosphere as observed on earth $= 31.988$ arc min
Average molecular weight of the atmosphere (below 90 km) $= 28.964$ amu

Table A1.4 Unit Conversions for the Absorption Coefficient (Given the Row Unit to Convert to the Column Unit Multiply by the Number in the Column)

β_{abs}	cm^{-1}	m^{-1}	km^{-1}	dB km^{-1}
cm^{-1}	1	10^2	10^5	4.3429×10^5
m^{-1}	0.01	1	10^3	4.3429×10^3
km^{-1}	10^{-5}	10^{-3}	1	4.3429
dB km^{-1}	2.3026×10^{-6}	2.3026×10^{-4}	0.23026	1

Table A1.2 lists commonly used unit conversions in optical propagation computations. Table A1.3 lists constants used in various models discussed in the text. Table A1.4 lists conversion factors between various units for the power absorption coefficient. The field absorption coefficient has units of nepers per meter.

Bibliography

A1.1 E.R. Cohen and B.N. Taylor, "The Fundamental Physical Constants," *Phys. Today* **47**, BG9–BG16, (1994); E.R. Cohen and B.N. Taylor, "The 1986 Adjustment of the Fundamental Physical Constants," *Rev. Mod. Phys.* **59**, 1121–1148 (1987).

A1.2 R.M. Goody and Y.L. Yung, *Atmospheric Radiation Theoretical Basis*, 2nd Ed., Oxford University Press (1989).

Appendix 2

Special Functions

Special functions of importance to applied spectroscopy and optical propagation are listed in the following.

The rigid rotor wavefunctions are associated Legendre functions in θ and complex exponential functions in ϕ. The net functions are spherical harmonics and are listed in Table A2.1.

Table A2.1 Spherical Harmonics $Y_{lm}(\theta,\phi)$

$Y_{0,0} = \left(\frac{1}{4\pi}\right)^{1/2}$	(A2.1)
$Y_{1,-1} = \left(\frac{3}{8\pi}\right)^{1/2} \sin\theta \, e^{j\phi}$	(A2.2)
$Y_{1,0} = \left(\frac{3}{4\pi}\right)^{1/2} \cos\theta$	(A2.3)
$Y_{1,1} = -\left(\frac{3}{8\pi}\right)^{1/2} \sin\theta \, e^{-j\phi}$	(A2.4)
$Y_{2,-2} = \left(\frac{15}{32\pi}\right)^{1/2} \sin^2\theta \, e^{2j\phi}$	(A2.5)
$Y_{2,-1} = \left(\frac{15}{8\pi}\right)^{1/2} \sin\theta \cos\theta \, e^{j\phi}$	(A2.6)
$Y_{2,0} = \left(\frac{5}{16\pi}\right)^{1/2} (3\cos^2\theta - 1)$	(A2.7)
$Y_{2,1} = -\left(\frac{15}{8\pi}\right)^{1/2} \sin\theta \cos\theta \, e^{-j\phi}$	(A2.8)
$Y_{2,2} = \left(\frac{15}{32\pi}\right)^{1/2} \sin^2\theta \, e^{-2j\phi}$	(A2.9)

These functions are orthonormal, satisfying the following normalization condition:

$$\int\limits_0^{2\pi} \int\limits_0^{\pi} |Y_{lm}(\theta), \phi)|^2 \sin\theta \, d\theta d\phi = 1. \tag{A2.10}$$

The solution to the quantum-mechanical harmonic oscillator produces Hermite–Gauss functions for the wave function. These functions contain Hermite polynomials, and are listed in Table A2.2.

Table A2.2 Hermite Polynomials, $H_n(\xi)$

$H_0(\xi) = 1$	(A2.11)
$H_1(\xi) = 2\xi$	(A2.12)
$H_2(\xi) = 4\xi^2 - 2$	(A2.13)
$H_3(\xi) = 8\xi^3 - 12\xi$	(A2.14)
$H_4(\xi) = 16\xi^4 - 48\xi^2 + 12$	(A2.15)

The Hermite–Gaussian functions are

$$\phi_n(\xi) = N_n \, e^{-\xi^2/2} H_n(\xi), \tag{A2.16}$$

where the normalization factor is

$$N_n = (2^n n! \sqrt{\pi})^{-1/2}, \tag{A2.17}$$

with the following normalization condition on ϕ_n:

$$\langle \phi_n | \phi_n \rangle = \int\limits_{-\infty}^{\infty} \phi_n^*(\xi)\phi_n(\xi) \, d(\xi) = 1. \tag{A2.18}$$

The function $D(x)$ given by Eq. 8.56 is the Dawson integral. To implement Eq. 8.56 in a computer program, it is necessary to simplify the expression for $D(x)$, when x is large. A series approximation for $D(x)$ can be derived in this case. To obtain the large x approximation for $D(x)$, we note that $D(x)$ satisfies the differential equation

$$\frac{dD(x)}{dx} + 2x D(x) = 1. \tag{A2.19}$$

Assuming a solution of Eq. (A2.19) of the form

$$D(x) = \sum_{k=0}^{\infty} \frac{D_k}{x^{2k+1}} , \quad \text{for large } x, \tag{A2.20}$$

we have, upon substitution of the above equation into Eq. A2.19 and equating like powers of x, the recurrence relation

$$2D_0 = 1,$$
$$2D_k = (2k - 1) D_{k-1,} \quad k \geq 1 \tag{A2.21}$$

for the unknown coefficients D_k. It is directly verifiable that these equations are solved by

$$D_k = \frac{1 \cdot 3 \cdot 5 \cdots (2k - 1)}{2^{k+1}}, \quad k \geq 1 \tag{A2.22}$$

where, based on Eq. A2.22, $D_0 = 1/2$. Combining the results of Eqs. A2.20 and A2.22 gives the form

$$D(x) = \frac{1}{2x} \left[1 + \sum_{n=1}^{\infty} \frac{1 \cdot 3 \cdot 5 \cdots (2n - 1)}{2^n x^{2n}} \right]. \tag{A2.23}$$

The series can be truncated after $n = 5$ for reasonable accuracy and works well for x values greater than 3.

For values of x less than 3, the integral expression for $D(x)$ (Eq. 8.56) can be evaluated using common numerical integration techniques, such as Simpson's rule.
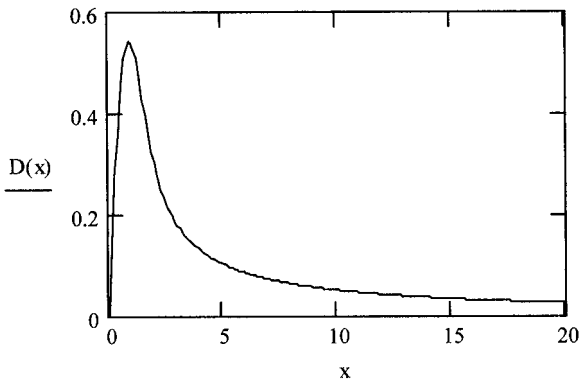
Fig. A2.1 Dawson integral, $D(x)$ versus x generated using a numerical integration of Eq. 7.56 for $x \leq 3$ and Eq. A2.23 for $x > 3$.

Table A2.3 Comparison of Dawson Integral Values

x-Value	$D(x)$, Computed	$D(x)$, Handbook[a]	% Difference
0.02	0.019995	0.0199947	0.001501
0.20	0.194751	0.1947510	0.000000
0.50	0.424436	0.4244364	0.000094
1.00	0.538080	0.5380795	0.000093
1.50	0.428251	0.4282491	0.000444
2.00	0.301350	0.3013404	0.003186
2.94884	0.182033	0.181915	0.064865
3.0151	0.177110	0.177226	0.065453
4.0825	0.126542	0.1265439	0.001501
5.00	0.102134	0.102134	0.000000
10.0	0.050254	0.0502539	0.000199
14.1421	0.035444	0.0354440	0.000000

[a]See *Handbook of Mathematical Functions*, Ref. A2.1, p. 319.

The Dawson integral, based on the above numerical techniques, has been implemented in Fortran and is plotted in Fig. A2.1. For x-values less than 3, $D(x)$ was calculated by integrating with Simpson's rule. For this integration, the interval from 0 to x was divided into 15 equal increments. For x-values greater than 3, Eq. A2.23 was used to calculate $D(x)$. (Note that only the first five terms of the series are needed.) In Table A2.3, the computed values for $D(x)$ are compared to values found in a mathematical handbook (Ref. A2.1). Good agreement is obtained.

Bibliography

A2.1 M. Abramowitz and I.A. Stegun, *Handbook of Mathematical Functions*, NBS (1972).

Appendix 3

Hilbert and Fourier Transforms

Functions that satisfy a Hilbert transform are of great importance to the development of practical models of the permittivity. Table A3.1 lists Hilbert transform pairs, as defined by Eq. 2.48, where $x = \omega'$ and $y = \omega$. The Hilbert transform is a linear operator.

Because of the importance of the classical oscillator model, a proof is presented to demonstrate that it is a causal model. The mathematical statement of the Hilbert transform

Table A3.1 Hilbert Transform Pairs

$\chi''(x)$	$\chi'(y)$
$\chi''(x - a)$	$\chi'(y - a)$
$\dfrac{d\chi''(x)}{dx}$	$\dfrac{d\chi'(y)}{dy}$
$x\chi''(x) + \frac{1}{\pi}\int\limits_{-\infty}^{\infty} dx\,\chi''(x)$	$y\chi'(y)$
$\delta(x - a)$	$\dfrac{1}{\pi(a - y)}$
$\dfrac{x\Gamma}{(a^2 - x^2)^2 + (x\Gamma)^2}$	$\dfrac{a^2 - y^2}{(a^2 - y^2)^2 + (y\Gamma)^2}$
$\dfrac{\gamma}{x^2 + \gamma^2}$	$-\dfrac{y}{y^2 + \gamma^2}$
$\frac{1}{x}H(x - a), \quad a > 0, \quad x \neq a$	$\dfrac{1}{\pi y}\ln\left|\dfrac{a}{y - a}\right|, \quad y \neq a$

(or Kramers–Krönig relation) for the classical oscillator model, as given in Chapter 2, can be compactly restated as

$$\epsilon_r(\omega) = 1 + \frac{j}{\pi} P \int_{-\infty}^{\infty} \frac{[\epsilon_r(\omega') - 1]}{\omega' - \omega} \, d\omega'. \tag{A3.1}$$

Furthermore, recall $\epsilon_r(\omega) = 1 + \chi(\omega)$, and for a single oscillator that

$$\chi(\omega) = \frac{j}{\pi} P \int_{-\infty}^{\infty} \frac{\chi(\omega)}{\omega' - \omega} \, d\omega' \quad \text{and} \quad \chi(\omega) = \frac{\omega_0^2 \Delta\epsilon}{\omega_0^2 - \omega^2 + j\Gamma\omega}. \tag{A3.2}$$

To prove that the classical oscillator model satisfies the Hilbert transform, we factor the susceptibility function into the form

$$\frac{1}{\omega_0^2 - \omega^2 + j\Gamma\omega} = \frac{-1}{(\omega - \omega_+)(\omega - \omega_-)} = -\frac{1}{(\omega_+ - \omega_-)} \left(\frac{1}{\omega - \omega_+} - \frac{1}{\omega - \omega_-} \right)$$

where ω is now complex and

$$\omega_\pm = j\frac{\Gamma}{2} \pm \sqrt{\omega_0^2 - \left(\frac{\Gamma}{2}\right)^2}.$$

Only these poles will be included within the contour, as shown in Fig. A3.1. The residue theorem can be applied to evaluate the integral. The result is

$$\chi(\omega) = -2 \sum_{i=+,-} \operatorname*{Res}_{\omega'=\omega_i} \frac{\chi(\omega')}{\omega' - \omega} - \operatorname*{Res}_{\omega'=\omega} \frac{\chi(\omega')}{\omega' - \omega}.$$

Evaluating the residues, the susceptibility function is obtained and the equality is proven. Thus, the classical oscillator model satisfies the Kramers–Krönig relation or the Hilbert transform. For this reason, the simplistic classical oscillator model is very useful in representing physical systems.

We desire the time-domain function

$$F(t) = \frac{1}{2\pi} \int_{-\infty}^{\infty} d\omega \, e^{j\omega t} \chi(\omega) \tag{A3.3}$$

where $\chi(\omega)$ is the complex frequency-domain susceptibility:

$$\chi(\omega) = \chi'(\omega) - j\chi''(\omega). \tag{A3.4}$$

Recall that $\chi'(\omega)$ and $\chi''(\omega)$ satisfy the symmetry conditions
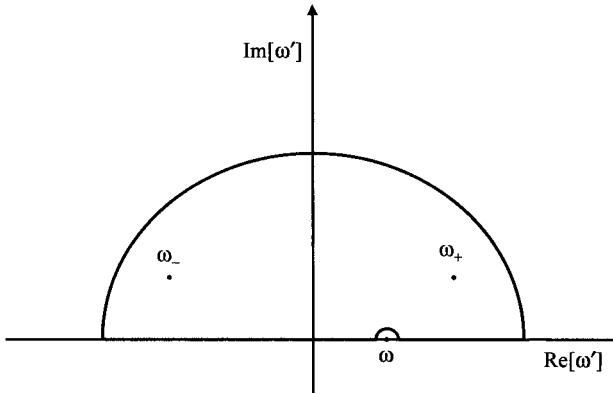
Fig. A3.1 Contour integration path enclosing the poles in the complex ω-plane.

$$\chi'(-\omega) = \chi'(\omega)\,,$$
$$\chi''(-\omega) = -\chi''(\omega) \tag{A3.5}$$

(e.g., $\chi^*(\omega) = \chi(-\omega)$). Substituting Eq. (A3.4) into Eq. (A3.3) and making use of Eq. (A3.5), we obtain

$$F(t) = \frac{1}{\pi} \left[E(t) + O(t) \right], \tag{A3.6}$$

where

$$E(t) = \int\limits_0^\infty d\omega\, \chi'(\omega) \cos \omega t \tag{A3.7a}$$

and

$$O(t) = \int\limits_0^\infty d\omega\, \chi''(\omega) \sin \omega t. \tag{A3.7b}$$

(Note that $E(-t) = E(t)$ and $O(-t) = -O(t)$.)

We now restrict our attention to the case of $t > 0$ and prove that $E(t) = O(t)$. The Kramers–Krönig relation (Hilbert transform) between the real and imaginary parts of the permittivity takes the form

$$\chi'(\omega) = \frac{P}{\pi} \int\limits_{-\infty}^\infty d\omega' \frac{\chi''(\omega)}{\omega' - \omega}$$

$$= \frac{P}{\pi} \int\limits_0^\infty d\omega' \chi''(\omega) \left[\frac{1}{\omega' - \omega} + \frac{1}{\omega' + \omega} \right]. \tag{A3.8}$$

Here P denotes a principal value. We now make use of the well-known result that

$$P\frac{1}{x} = \lim_{\epsilon \to 0} \frac{1}{x + j\epsilon} + \pi j\delta(x). \tag{A3.9}$$

Substituting Eq. (A3.9) into Eq. (A3.8) gives for $\omega > 0$

$$\chi'(\omega) = j\chi''(\omega) + \frac{1}{\pi} \int_0^\infty d\omega' \chi''(\omega') \left(\frac{1}{\omega' - \omega + j\epsilon} + \frac{1}{\omega' + \omega + j\epsilon} \right). \tag{A3.10}$$

We now substitute Eq. (A3.10) into Eq. (A3.7a):

$$E(t) = \int_0^\infty d\omega \cos \omega t \left[j\chi''(\omega) + \frac{1}{\pi} \int_0^\infty d\omega' \chi''(\omega') \left(\frac{1}{\omega' - \omega + j\epsilon} + \frac{1}{\omega' + \omega + j\epsilon} \right) \right]$$

$$= j \int_0^\infty d\omega \chi''(\omega) \cos \omega t + \frac{1}{\pi} \int_0^\infty d\omega' \chi''(\omega') G(t, \omega'), \tag{A3.11}$$

where

$$G(t, \omega') \equiv \int_0^\infty d\omega \cos \omega t \left(\frac{1}{\omega' - \omega + j\epsilon} + \frac{1}{\omega' + \omega + j\epsilon} \right). \tag{A3.12}$$

The evaluation of this integral is straightforward:

$$G(t, \omega') = \int_{-\infty}^\infty dx \cos t(x - \omega') \left(\frac{x - j\epsilon}{x^2 + \epsilon^2} \right)$$

$$= 2j\epsilon \cos(t\omega') \int_0^\infty \frac{dx \cos tx}{x^2 + \epsilon^2} + 2 \sin t\omega' \int_0^\infty \frac{dx\, x \sin tx}{x^2 + \epsilon^2} \tag{A3.13}$$

$$= \left[-\pi j \cos(t\omega') + \sin(t\omega') \right] e^{-\epsilon\tau}.$$

Taking the limit $\epsilon \to 0$, we have, on substituting Eq. (A3.13) into Eq. (A3.11), that

$$E(t) = \int_0^\infty d\omega' \chi''(\omega') \sin \omega' t$$

$$= O(t). \tag{A3.14}$$

Whence, we have, using the time-reversal properties of E and O, that

$$F(t) = \frac{2O(t)}{\pi}, \quad t \geq 0$$

$$= 0, \quad t \leq 0,$$

(A3.15)

where $H(\ )$ is the Heaviside step function.

For Case I we have

$$O(t) = \frac{BE_0}{\hbar} \hat{O}(\tau),$$

(A3.16)

where

$$\hat{O}(\tau) = \int_1^\infty \frac{dx}{x^2} \sin \tau x$$

(A3.17)

and

$$\tau \equiv \frac{E_0}{\hbar} t.$$

(A3.18)

Integration by parts gives

$$\hat{O}(\tau) = \sin \tau + \tau \int_1^\infty \frac{dx}{x} \cos x\tau$$

$$= \sin \tau - \tau \, \text{Ci}(\tau)$$

(A3.19)

where Ci is the cosine integral (see Abramowitz and Stegun, Ref. A3.2):

$$\text{Ci}(z) \equiv -\int_z^\infty du \frac{\cos u}{u}.$$

(A3.20)

For Case II we have

$$O(t) = \frac{BE_0}{\hbar} \hat{O}(\tau)$$

(A3.21)

where τ is given by Eq. (A3.18) and

$$\hat{O}(\tau) = \int_1^\infty \frac{dx}{x^2} \sqrt{x-1} \sin \tau x,$$

(A3.22)

which upon integrating by parts gives

$$\hat{O}(\tau) = \tau P(\tau) + \frac{1}{2} Q(\tau), \tag{A3.23}$$

with

$$P = \int_{1}^{\infty} \frac{dx}{x} \sqrt{x-1} \cos x\tau,$$

$$Q = \int_{1}^{\infty} \frac{dx}{x\sqrt{x-1}} \sin x\tau. \tag{A3.24}$$

$P(\tau)$ can be rewritten as

$$P(\tau) = R(\tau) - S(\tau), \tag{A3.25}$$

where

$$R = \int_{1}^{\infty} \frac{dx}{\sqrt{x-1}} \cos \tau x$$

$$S = \int_{1}^{\infty} \frac{dx}{x\sqrt{x-1}} \cos \tau x. \tag{A3.26}$$

R may be directly obtained from integral tables:

$$R = \sqrt{\frac{\pi}{\tau}} \cos \left(\tau + \frac{\pi}{4} \right). \tag{A3.27}$$

To obtain S, we first compute $dS/d\tau$:

$$\frac{dS}{d\tau} = -\int_{1}^{\infty} \frac{dx}{\sqrt{x-1}} \sin \tau x$$

$$= \sqrt{\frac{\pi}{2\tau}} (\sin \tau + \cos \tau) \tag{A3.28}$$

from tables. Whence,

$$S(\tau) = -\sqrt{\frac{\pi}{2}} \int_{o}^{\tau} d\tau' \left(\frac{\sin \tau' + \cos \tau'}{\sqrt{\tau'}} \right) + S(\tau = 0)$$

$$= \pi \left[1 - \left\{ S \left(\sqrt{\frac{2\tau}{\pi}} \right) + C \left(\sqrt{\frac{2\tau}{\pi}} \right) \right\} \right] \tag{A3.29}$$

where the $S(\ )$ and $C(\ )$ are Fresnel integrals:

$$\begin{pmatrix} C(z) \\ S(z) \end{pmatrix} = \int_0^z dt \begin{pmatrix} \cos\frac{\pi}{2}t^2 \\ \sin\frac{\pi}{2}t^2 \end{pmatrix}, \tag{A3.30}$$

and based on Eq. (A3.26),

$$S(\tau = 0) = \pi.$$

To find Q, we first compute $dQ/d\tau$:

$$\frac{dQ}{d\tau} = \int_1^\infty \frac{dx}{\sqrt{x-1}} \cos x\tau$$

$$= \sqrt{\frac{\pi}{2\tau}}(\cos\tau - \sin\tau) \tag{A3.31}$$

from tables. Whence

$$Q(\tau) = \pi \left[C\left(\sqrt{\frac{2\tau}{\pi}}\right) - S\left(\sqrt{\frac{2\tau}{\pi}}\right) \right]. \tag{A3.32}$$

Combining Eqs. (A3.23), (A3.25), (A3.27), (A3.29), and (A3.32), we have

$$\hat{O}(\tau) = \sqrt{\pi\tau} \cos\left(\tau + \frac{\pi}{4}\right) - \pi\tau$$

$$+ \pi \left[(\tau + \tfrac{1}{2}) C\left(\sqrt{\frac{2\tau}{\pi}}\right) + (\tau - \tfrac{1}{2}) S\left(\sqrt{\frac{2\tau}{\pi}}\right) \right]. \tag{A3.33}$$

Using Eq. (A3.15), the time-domain result for the two cases is obtained directly,

$$F_I(t) = \frac{2}{\pi}\frac{BE_0}{\hbar} \left[\sin\frac{E_0}{\hbar}t - \frac{E_0}{\hbar}t\,\mathrm{Ci}\left(\frac{E_0}{\hbar}t\right) \right] \tag{A3.34a}$$

and

$$F_{II}(t) = \frac{2}{\pi}\frac{BE_0}{\hbar} \left[\sqrt{\pi\frac{E_0}{\hbar}t}\cos\left(\frac{E_0}{\hbar}t + \frac{\pi}{4}\right) - \pi\frac{E_0}{\hbar}t \right]$$

$$+ \pi \left[\left(\frac{E_0}{\hbar}t + \frac{1}{2}\right) C\left(\sqrt{\frac{2E_0 t}{\pi\hbar}}\right) + \left(\frac{E_0}{\hbar}t - \frac{1}{2}\right) S\left(\sqrt{\frac{2E_0 t}{\pi\hbar}}\right) \right]. \tag{A3.34b}$$

Bibliography

A3.1 A.D. Poularikas (ed.-in-chief), *The Transforms and Applications Handbook*, CRC Press and IEEE Press (1996).

A3.2 M. Abramowitz and I.A. Stegun, *Handbook of Mathematical Functions*, National Bureau of Standards (1970).

Appendix 4

Model Parameters for Gases, Liquids, and Solids

This appendix contains several tables of model parameter values for specific gases, solids, and liquids. All the models have been previously developed in the text. Thus the appendix provides the practical information needed to apply the models to real media.

A4.1 Model Parameters for Gases

Table A4.1 lists Sellmeier model (see Eq. 4.18a) parameters for various gases and is valid over the wavelength range from about 3 to 0.3 µm for STP conditions ($T = 273$K and $P = 1$ atm). This is a single-oscillator model of the general form

$$\frac{1}{2}[n^2(\lambda) - 1] = n(\lambda) - 1 = \frac{\lambda^2 A_0}{\lambda^2 - \lambda_0^2}.$$

(A4.1)

Only electronic transitions are represented, thus this model should not be applied in the infrared unless vibrational modes are included.

Since the electronic transitions in gases dominate the index of refraction in the regions of visible transparency, the Cauchy model (see Eq. 4.18b) is often applied to gases. Table A4.2 lists Cauchy model parameters of the form

$$n(\lambda) - 1 = A_0 \left(1 + \frac{B}{\lambda^2} + \frac{C}{\lambda^4}\right)$$

(A4.2)

Table A4.1 Sellmeier Model Parameters for Various Gases at STP (Ref. A4.1)

Gas	A_0	λ_0 [μm]
Ar	277.3×10^{-6}	0.073
Br$_2$	1093.2×10^{-6}	0.152
Cl$_2$	759.5×10^{-6}	0.097
CO	327.3×10^{-6}	0.090
CO$_2$	437.5×10^{-6}	0.080
H$_2$	136.3×10^{-6}	0.085
He	34.7×10^{-6}	0.051
H$_2$O	245.6×10^{-6}	0.092
HCl	435.3×10^{-6}	0.092
HBr	593.5×10^{-6}	0.102
HI	883.1×10^{-6}	0.117
H$_2$S	619.1×10^{-6}	0.107
Kr	418.6×10^{-6}	0.084
N$_2$	294.5×10^{-6}	0.073
Ne	66.6×10^{-6}	0.048
NH$_3$	364.6×10^{-6}	0.105
NO	288.2×10^{-6}	0.086
N$_2$O	496.6×10^{-6}	0.089
O$_2$	265.3×10^{-6}	0.084
SO$_2$	641.5×10^{-6}	0.100
Xe	681.8×10^{-6}	0.100

for various gases with validity from the visible to the near-infrared. Of course, if the molecule has no infrared-active vibrational or rotational modes (e.g., Ar, O$_2$, and N$_2$), then the model is valid from the visible to the microwave.

To scale the model parameters to other pressures and temperatures, Eq. 4.8a is applied. Only the A coefficient needs to be scaled in the following way:

$$A(p, T) = A_0 \frac{p}{T} \frac{273}{1},$$

where T is temperature in kelvins and p is pressure in atmospheres. The index of refraction of gaseous mixtures (such as the atmospheres of planets) can be obtained by applying Eq. 4.11 in the Sellmeier approximation with the parameters in Table A4.1.

Table A4.2 Cauchy Model Parameters for Various Gases at STP (Refs. A4.1, A4.2)

Gas	A_0	B [μm^2]	C [μm^4]
Ar	277.83×10^{-6}	5.6×10^{-3}	
N$_2$	294.0×10^{-6}	5.6×10^{-3}	
He	34.8×10^{-6}	2.3×10^{-3}	
H$_2$	136.1×10^{-6}	7.5×10^{-3}	73×10^{-6}
O$_2$	269.7×10^{-6}	1.38×10^{-3}	467×10^{-6}
Dry Air	287.57×10^{-6}	4.63×10^{-3}	120×10^{-6}
Ethane	736.5×10^{-6}	9.08×10^{-3}	
CH$_4$	426.0×10^{-6}	14.41×10^{-3}	

Table A4.3 Refractive Virial Coefficients for Various Gases at Room Temperature and at a Wavelength of 0.633 μm (Refs. A4.3–A4.5)

Gas	A_R [cm^3 mol^{-1}]	B_R [cm^6 mol^{-2}]
N_2	4.45	0.75
He	0.52	
Ar	4.2	1.49
CO_2	6.65	3.2
SF_6	11.35	36.0

Gases at high density also require the refractive virial coefficients, as defined by Eq. 4.29, for the computation of the infrared/visible refractive index. Values for these coefficients are listed in Table A4.3.

To include gas-phase absorption phenomena, the HITRAN database needs to be applied. This is discussed in Chapter 7 (Sections 7.2.2. and 7.4.2).

A4.2 Model Parameters for Solids

Table A4.4 lists the various optical materials that have been characterized in terms of the models discussed in Chapter 8. Included in the listing are the optical models that are available for a specific material. Based on this information, one can determine whether the spectral region's model calculations are valid. Also included are the space group (2— cubic, 1— uniaxial, — biaxial, and 0 amorphous) and the melting temperature.

Table A4.4 Optical Property Models Available for Various Solids

Name	SP#	T_{melt} [K]	ν_{LOMAX} [cm^{-1}]	E_g [eV]	CO	SM	FC	MP	UT	SC
			Insulators							
			Oxides							
ADP *o-ray*	122	463.0	1500.0	7.0	Y	Y	N	N	N	N
ADP *e*-ray	122	463.0	1500.0	7.0	Y	Y	N	N	N	N
Al_2O_3 *o*-ray	167	2319.0	914.0	9.0	Y	Y	N	Y	Y	N
Al_2O_3 *e*-ray	167	2319.0	871.0	9.0	Y	Y	N	Y	Y	N
AlON poly	227	2323.0	969.0	6.50	Y	Y	N	Y	Y	Y
BeO *o*-ray	186	2725.0	1095.0	10.60	Y	Y	N	N	N	N
BeO *e*-ray	186	2723.0	1083.0	10.60	Y	Y	N	N	N	N
BeO poly	186	2725.0	1100.0	10.60	Y	N	N	Y	N	N
Cr_2O_3 *o*-ray	167	2602.0	—	—	Y	N	N	N	N	N
Cr_2O_3 *e*-ray	167	2602.0	—	—	Y	N	N	N	N	N
GeO_2 *o*-ray	136	1388.0	815.0	5.60	Y	N	N	N	N	N
GeO_2 *e*-ray	136	1388.0	811.0	5.60	Y	N	N	N	N	N
Y_2O_3:HfO_2	225	3074.0	680.0	4.50	Y	Y	N	N	N	N
Ice Type Ih (H_2O)	194	0.0	3134.5	8.1	Y	Y	N	N	N	N
KDP *o*-ray	122	526.0	1500.0	7.0	Y	Y	N	N	N	N

(continued)

Table A4.4 Optical Property Models Available for Various Solids—cont'd

Name	SP#	T_{melt} [K]	ν_{LOMAX} [cm^{-1}]	E_g [eV]	CO	SM	FC	MP	UT	SC
Oxides										
KDP e-ray	122	526.0	1500.0	7.0	Y	Y	N	N	N	N
KNbO$_3$ nx	38	1373.0	842.0	3.30	Y	Y	N	N	N	N
KNbO$_3$ ny	38	1373.0	838.0	3.30	Y	Y	N	N	N	N
KNbO$_3$ nz	38	1373.0	827.0	3.30	Y	Y	N	N	N	N
KTP(KTiOPO$_4$) nx	33	1172	995.0	3.60	Y	Y	N	N	N	N
KTP(KTiOPO$_4$) ny	33	1172	1136.20	3.60	Y	Y	N	N	N	N
KTP(KTiOPO$_4$) nz	33	1172	1119.0	3.60	Y	Y	N	N	N	N
LiNbO$_3$ o-ray	161	1513.0	878.0	4.65	Y	Y	N	N	Y	N
LiNbO$_3$ e-ray	161	1513.0	869.0	4.65	Y	Y	N	N	Y	N
MgAl$_2$O$_4$ poly	227	2408.0	869.0	7.75	Y	Y	N	Y	Y	Y
MgO	225	3073.0	725.0	7.80	Y	Y	N	Y	N	N
Quartz										
SiO$_2$ o-ray	152	845.0	1235.0	8.40	Y	Y	N	N	N	N
SiO$_2$ e-ray	152	845.0	1235.0	8.40	Y	Y	N	N	N	N
TiO$_2$ o-ray	136	2128.0	831.0	3.03	Y	Y	N	N	N	N
TiO$_2$ e-ray	136	2128.0	796.0	3.04	Y	Y	N	N	N	N
Y$_2$O$_3$ poly	206	2711.0	620.0	6.08	Y	Y	N	Y	Y	Y
La$_2$O$_3$:Y$_2$O$_3$ poly	206	2670.0	612.0	6.0	Y	Y	N	Y	N	Y
YAG	230	2193.0	841.0	7.01	Y	Y	N	N	Y	N
Y$_2$O$_3$:ZrO$_2$	225	3110.0	668.0	5.60	Y	Y	N	Y	N	N
Alkali-halides										
AgBr	225	705.0	138.0	2.79	Y	Y	N	N	Y	N
AgCl	225	728.0	193.0	3.44	Y	Y	N	N	Y	N
CsBr	221	908.0	112.0	6.90	Y	Y	N	N	N	N
CsI	221	898.0	90.0	6.30	Y	Y	N	Y	N	N
KBr	225	1007.0	166.0	6.84	Y	Y	N	Y	Y	N
KCl	225	1044.0	213.0	7.83	Y	Y	N	Y	Y	N
KF	225	1131.0	326.0	10.80	Y	Y	N	N	N	N
KI	225	954.0	150.0	5.89	Y	Y	N	Y	Y	N
KRS-5	221	696.0	90.0	2.60	Y	Y	N	N	N	Y
LiF	225	1121.0	673.0	12.75	Y	Y	N	Y	Y	N
NaBr	225	1020.0	209.0	6.77	Y	Y	N	N	Y	N
NaCl	225	1074.0	268.0	8.02	Y	Y	N	Y	Y	N
NaF	225	1296.0	414.0	10.70	Y	Y	N	N	Y	N
NaI	225	933.0	181.0	5.67	Y	Y	N	N	Y	N
TlBr	221	733.0	116.0	3.10	Y	Y	N	N	N	N
TlCl	221	703.0	173.0	3.43	Y	Y	N	N	UY	N
Fluorides										
BaF$_2$	225	1641.0	338.0	10.16	Y	Y	N	Y	Y	N
CaF$_2$	225	1691.0	479.0	11.23	Y	Y	N	Y	Y	N
MgF$_2$ o-ray	136	1536.0	621.0	11.80	Y	Y	N	Y	Y	N
MgF$_2$ e-ray	136	1536.0	625.0	11.80	Y	Y	N	Y	Y	N
PbF$_2$	225	1103.0	337.0	5.0	Y	Y	N	N	N	N
SrF$_2$	225	1750.0	389.0	10.67	Y	Y	N	Y	Y	N
YLF o-ray	88	1098	566.0	7.0	Y	Y	N	N	N	N
YLF e-ray	88	1098	600.0	7.0	Y	Y	N	N	N	N

Table A4.4 Optical Property Models Available for Various Solids—cont'd

Name	SP#	T_{melt} [K]	ν_{LOMAX} [cm^{-1}]	E_g [eV]	CO	SM	FC	MP	UT	SC
			Others							
AlAs	216	2013.0	402.0	2.95	Y	Y	N	N	N	N
AlN o-ray	186	3273.0	895.0	5.88	Y	Y	N	N	N	N
AlN e-ray	186	3273.0	888.0	5.74	Y	Y	N	N	N	N
BN (cubic)	216	3239.0	1338.0	8.0	Y	N	N	N	N	N
BP	216	1398.0	834.0	6.0	Y	Y	N	N	N	N
CaLa$_2$S$_4$	220	—	314.0	2.70	N	N	N	Y	N	N
Diamond (C)	227	4713.0	1332.0	6.50	Y	Y	N	Y	Y	N
GaN o-ray	186	3048.0	746.0	3.70	Y	Y	Y	N	N	N
GaN e-ray	186	3048.0	744.0	3.50	Y	Y	Y	N	N	N
GaP	216	1730.0	403.0	2.27	Y	Y	N	N	N	N
ZnS (cubic)	216	1973.0	347.0	3.54	Y	Y	N	N	N	N
			Glasses							
As$_2$S$_3$ glass	0	583.0	358.0	—	Y	Y	N	N	N	N
As$_2$Se$_3$ glass	0	533.0	255.0	—	Y	Y	N	N	N	N
BK7 glass	0	1250.0	1230.0	7.70	Y	Y	N	N	Y	N
GeO$_2$ glass	0	1388.0	811.0	5.60	Y	Y	N	N	N	N
Silica (glass)	0	1983.0	1263.0	8.40	Y	Y	N	Y	N	Y
			Semiconductors							
CdS o-ray	186	2023.0	306.0	2.58	Y	Y	N	N	Y	N
CdS e-ray	186	2023.0	300.0	2.58	Y	Y	N	N	Y	N
CdSe o-ray	186	1513.0	212.30	1.89	Y	Y	N	N	Y	N
CdSe e-ray	186	1513.0	212.10	1.90	Y	Y	N	N	Y	N
CdTe	216	1315.0	169.0	1.65	Y	Y	N	N	Y	N
GaAs	216	1511.0	292.10	1.50	Y	Y	N	N	N	N
Germanium (Ge)	227	1211.0	300.60	0.664	Y	Y	Y	N	N	N
InAs	216	1215.0	240.0	0.41	Y	Y	N	N	N	N
InP	216	1335.0	345.0	1.43	Y	Y	N	N	Y	N
PbS	225	1386.0	212.0	0.41	Y	Y	N	N	N	N
PbSe	225	1351.0	115.90	0.27	Y	Y	Y	N	N	N
PbTe	225	1197.0	116.0	0.31	Y	Y	Y	N	N	N
Silicon (Si)	227	1687.0	519.50	1.10	Y	Y	N	N	N	N
SiC (cubic)	216	3103.0	969.0	2.40	Y	Y	N	N	N	N
VO$_2$ poly (26C)	14	2240.0	710.0	0.75	Y	N	N	N	N	N
VO$_2$ poly (80C)	136	2240.0	700.0	2.0	Y	N	Y	N	N	N
ZnSe	216	1373.0	251.0	2.70	Y	Y	N	N	N	N
ZnTe	216	1512.0	206.0	2.56	Y	Y	N	N	Y	N
			Metals							
Aluminum (Al)	225	933.5	—	0.0	N	N	Y	N	N	N
Cobalt (Co)	194	1768.0	—	0.0	N	N	Y	N	N	N
Copper (Cu)	225	1357.0	—	0.0	N	N	Y	N	N	N
Gold (Au)	225	1337.0	—	0.0	N	N	Y	N	N	N
Iron (Fe)	229	1811.0	—	0.0	N	N	Y	N	N	N
Lead (Pb)	225	600.0	—	0.0	N	N	Y	N	N	N
Molybdenum (Mo)	229	2896.0	—	0.0	N	N	Y	N	N	N
Nickel (Ni)	225	1728.0	—	0.0	N	N	Y	N	N	N

Table A4.4 Optical Property Models Available for Various Solids—cont'd

Name	SP#	T_{melt} [K]	ν_{LOMAX} [cm^{-1}]	E_g [eV]	CO	SM	FC	MP	UT	SC
Metals										
Palladium (Pd)	225	1827.0	—	0.0	N	N	Y	N	N	N
Platinum (Pt)	225	2041.0	—	0.0	N	N	Y	N	N	N
Silver (Ag)	225	1235.0	—	0.0	N	N	Y	N	N	N
Titanium (Ti)	194	1941.0	—	0.0	N	N	Y	N	N	N
Tungsten (W)	229	3695.0	—	0.0	N	N	Y	N	N	N
Vanadium (V)	229	2183.0	—	0.0	N	N	Y	N	N	N

SP#:	Space group number.
T_{melt}:	Melting temperature [K].
ν_{LOMAX}:	Maximum longitudinal optical vibration frequency [cm^{-1}].
E_g:	Bandgap of material at $T = 295$ K [eV].
CO:	Classical oscillator model available (Y = yes).
SM:	Sellmeier model available (T = 295 K) (Y = yes, N = no).
FC:	Free carrier model available (Y = yes).
MP:	Multiphonon model available (Y = yes).
UT:	Urbach tail model available (Y = yes).
SC:	Scatter model available (Y = yes).

Table A4.5 lists the model parameters for all the materials indicated in Table A4.4. All of the models represented are discussed in Chapter 8. This database is used by the computer code OPTIMATR, which is also described in Chapter 8. The classical oscillator model parameters are listed in the same way and with the same dimensions as Table 8.5. The most accurate representation of the refractive index (the precision is in the fourth or fifth decimal place) is given by the Sellmeier model, limited to room temperature only. The lower and upper spectral bounds of validity for applying the Sellmeier model are also listed.

Table A4.5 Solid-State Complex Index of Refraction Model Parameter

Insulators

Oxides

Material [ADP *o*-ray]   Space group #: 122

Classical oscillator model parameters:

Mode	ν_i	$a1_i$	$\Delta\epsilon_i$	$b1_i$	Γ_i/ν_i	$c1_i$	$c2_i$
1	290.10	.0	43.2	.000E+00	.000	.000	.000
2	105861.40	.0	1.30	−.983E−04	.000	.000	.000

$\epsilon_\infty = 1.000000$ $d\epsilon_\infty/dT = .0000000$
Allowed IR Modes: 12

Sellmeier parameters: Lower & upper wave number: 9434.000–25000.000

Mode	Location	Strength
1	105861.40	1.29899
2	290.06	43.1736

Bandgap [eV]: 7.000000

Table A4.5 Solid-State Complex Index of Refraction Model Parameter—cont'd

Oxides

Material [ADP *e*-ray]   Space group #: 122

Classical oscillator model parameters:

Mode	ν_i	$a1_i$	$\Delta\epsilon_i$	$b1_i$	Γ_i/ν_i	$c1_i$	$c2_i$
1	346.70	.0	12.0	.000E+00	.000	.000	.000
2	107875.20	.0	1.16	.000E+00	.000	.000	.000

$\epsilon_\infty = 1.000000$ $d\epsilon_\infty/dT = .0000000$
Allowed IR Modes: 6

Sellmeier parameters: Lower & upper wave number: 9434.000–25000.000

Mode	Location	Strength
1	107875.20	1.16217
2	346.72	12.0200

Bandgap [eV]: 7.000000

Material [Al$_2$O$_3$ *o*-ray]   Space group #: 167

Classical oscillator model parameters:

Mode	ν_i	$a1_i$	$\Delta\epsilon_i$	$b1_i$	Γ_i/ν_i	$c1_i$	$c2_i$
1	384.0	−.63E−02	.330	.716E−04	.110E−01	.230E−04	.000
2	439.0	−.72E−02	2.77	.336E−03	.400E−02	.222E−04	.000
3	568.10	−.11E−01	2.99	.203E−03	.105E−01	.760E−06	.109E−06
4	633.0	−.14E−01	.145	.303E−03	.110E−01	.185E−04	.000
5	805.90	−.19E−01	.185E−01	.165E−03	.240	.382E−03	.000
6	83805.30	.0	.650	.340E−04	.100E−03	.000	.000
7	137621.40	.0	1.43	.000E+00	.100E−03	.000	.000

$\epsilon_\infty = 1.000000$ $d\epsilon_\infty/dT = .0000000$
Allowed IR Modes: 4

Multiphonon model parameters:
$\alpha_1 = .5370$ $\nu_{max} = 914.0000$
$\alpha_2 = .1530$ $D_0 = 14000.0$
$\alpha_3 = .0520$ $K = 1.4630E+07$

Sellmeier parameters: Lower & upper wave number: 1818.000–50000.000

Mode	Location	Strength
1	137621.40	1.43135
2	83805.30	.650547
3	554.70	5.34140

Bandgap [eV]: 9.000000

Urbach tail model parameters:
Absorption constant [cm^{-1}]   : 130000.0
Exponential constant, σ_0 :   .7500000
Effective Phonon Energy, E_p [eV] :   .1000000E−07

Table A4.5 Solid-State Complex Index of Refraction Model Parameter—cont'd

				Oxides			

Material [Al_2O_3 *e*-ray]   Space group #: 167

Classical oscillator model parameters:

Mode	v_i	$a1_i$	$\Delta\epsilon_i$	$b1_i$	Γ_i/v_i	$c1_i$	$c2_i$
1	399.50	−.24E−01	6.78	.137E−02	.210E−01	.392E−04	.170E−07
2	584.0	−.25E−01	1.70	−.890E−04	.360E−01	.575E−04	.440E−07
3	750.0	−.59E−01	.200E−01	.890E−04	.150	.148E−03	.000
4	810.0	.0	.000	.000E+00	.100E−03	.000	.000
5	82201.10	.0	.551	.350E−04	.100E−03	.000	.000
6	135082.60	.0	1.50	.000E+00	.100E−03	.000	.000

$\epsilon_\infty = 1.000000$ $d\epsilon_\infty/dT = .0000000$
Allowed IR Modes: 2

Multiphonon model parameters:
$\alpha_1 = .5370$ $v_{max} = 871.0000$
$\alpha_2 = .1530$ $D_0 = 9800.000$
$\alpha_3 = .0520$ $K = 8.1640E+06$

Sellmeier parameters: Lower & upper wave number: 1818.000–50000.000

Mode	Location	Strength
1	135082.60	1.50398
2	82201.10	.550691
3	498.20	6.59274

Bandgap [eV]: 9.000000

Urbach tail model parameters:
Absorption constant [cm^{-1}]   : 130000.0
Exponential constant, σ_0 :   .7500000
Effective Phonon Energy, E_p [eV] :   .1000000E−05

Material [AlON poly]   Space group #: 227

Classical oscillator model parameters:

Mode	v_i	$a1_i$	$\Delta\epsilon_i$	$b1_i$	Γ_i/v_i	$c1_i$	$c2_i$
1	346.0	−.71E−02	1.0	.374E−03	.160	.357E−04	.000
2	395.0	−.71E−02	.400	.180E−03	.130	.714E−04	.000
3	495.0	−.71E−02	3.33	.251E−03	.200	.117E−03	.170E−06
4	634.0	−.11E−01	1.32	.293E−03	.150	.653E−04	.690E−07
5	768.0	−.22E−01	.160	.900E−04	.850E−01	.442E−04	.550E−07
6	920.0	−.36E−01	.300E−01	.208E−04	.500E−01	.542E−04	.000
7	97503.90	.0	2.14	.887E−04	.100E−03	.000	.000

$\epsilon_\infty = 1.000000$ $d\epsilon_\infty/dT = .0000000$
Allowed IR Modes: −1

Multiphonon model parameters:
$\alpha_1 = .5370$ $v_{max} = 969.0000$
$\alpha_2 = .1530$ $D_0 = 11500.0$
$\alpha_3 = .0520$ $K = 7.6670E+06$

Sellmeier parameters: Lower & upper wave number: 4350.000–25000.000

Mode	Location	Strength
1	97503.90	2.13750
2	530.0	4.58200

Bandgap [eV]: 6.500000

Table A4.5 Solid-State Complex Index of Refraction Model Parameter—cont'd

Oxides

Urbach tail model parameters:

Absorption constant [cm^{-1}]   : 9770.000

Exponential constant, σ_0 :   .1660000

Effective Phonon Energy, E_p [eV] :   .0000000

Scatter Model Parameters:

Rayleigh Coeff. (ν^4 Dependence)   : 0.0000E+00

Mie-like Coeff. (ν^A Dependence)   : 2.8900E–05

Mie-like Exponential Constant (A) : 1.01

Material [BeO *o*-ray]   Space group #: 186

Classical oscillator model parameters:

Mode	ν_i	$a1_i$	$\Delta\epsilon_i$	$b1_i$	Γ_i/ν_i	$c1_i$	$c2_i$
1	724.0	.0	4.02	.000E+00	.160E–01	.000	.000
2	126454.20	.0	1.92	.000E+00	.000	.000	.000

$\epsilon_\infty = 1.000000$ $d\epsilon_\infty/dT = $ .0000000

Allowed IR Modes: 1

Sellmeier parameters: Lower & upper wave number: 1429.000–22727.000

Mode	Location	Strength
1	126454.20	1.92274
2	1029.54	1.24209

Bandgap [eV]:   10.60000

Material [BeO *e*-ray]   Space group #: 186

Classical oscillator model parameters:

Mode	ν_i	$a1_i$	$\Delta\epsilon_i$	$b1_i$	Γ_i/ν_i	$c1_i$	$c2_i$
1	680.0	.0	4.68	.000E+00	.160	.000	.000
2	116414.40	.0	1.92	.000E+00	.000	.000	.000

$\epsilon_\infty = 1.000000$ $d\epsilon_\infty/dT = $ .0000000

Allowed IR Modes: 1

Sellmeier parameters: Lower & upper wave number: 1429.000–22727.000

Mode	Location	Strength
1	116414.40	1.96939
2	954.23	1.67389

Bandgap [eV]: 10.60000

Material [BeO poly]   Space group #: 186

Classical oscillator model parameters:

Mode	ν_i	$a1_i$	$\Delta\epsilon_i$	$b1_i$	Γ_i/ν_i	$c1_i$	$c2_i$
1	710.0	.0	3.70	.000E+00	.220E–01	.000	.000
2	790.0	.0	.450E–01	.000E+00	.900E–01	.000	.000
3	865.0	.0	.400E–01	.000E+00	.100	.000	.000
4	900.0	.0	.100E–01	.000E+00	.900E–01	.000	.000
5	955.0	.0	.250E–01	.000E+00	.900E–01	.000	.000

Table A4.5 Solid-State Complex Index of Refraction Model Parameter—cont'd

				Oxides			
6	1050.0	.0	.100E–02	.000E+00	.200E–01	.000	.000
7	116700.0	.0	1.84	.343E–04	.100E–03	.000	.000

$\epsilon_\infty = 1.000000$ $d\epsilon_\infty/dT = .0000000$
Allowed IR Modes: −1

Multiphonon model parameters:
$\alpha_1 = .5370$ $\nu_{max} = 1100.000$
$\alpha_2 = .1530$ $D_0 = 15000.0$
$\alpha_3 = .0520$ $K = 1.0000E+07$

Bandgap [eV]: 10.60000

Material [Cr_2O_3 o-ray]   Space group #: 167

Classical oscillator model parameters:

Mode	ν_i	$a1_i$	$\Delta\epsilon_i$	$b1_i$	Γ_i/ν_i	$c1_i$	$c2_i$
1	306.0	.0	.100	.000E+00	.327E–01	.000	.000
2	417.0	.0	.400	.000E+00	.192E–01	.000	.000
3	444.0	.0	.150	.000E+00	.158E–01	.000	.000
4	532.0	.0	5.35	.000E+00	.282E–01	.000	.000
5	613.0	.0	.500	.000E+00	.196E–01	.000	.000

$\epsilon_\infty = 6.200000$ $d\epsilon_\infty/dT = .0000000$
Allowed IR Modes: 4

Bandgap [eV]: .0000000

Material [Cr_2O_3 o-ray]   Space group #: 167

Classical oscillator model parameters:

Mode	ν_i	$a1_i$	$\Delta\epsilon_i$	$b1_i$	Γ_i/ν_i	$c1_i$	$c2_i$
1	303.0	.0	.100	.000E+00	.330E–01	.000	.000
2	419.0	.0	.500E–01	.000E+00	.120E–01	.000	.000
3	444.0	.0	.120	.000E+00	.135E–01	.000	.000
4	538.0	.0	4.90	.000E+00	.335E–01	.000	.000
5	613.0	.0	.430	.000E+00	.147E–01	.000	.000

$\epsilon_\infty = 6.100000$ $d\epsilon_\infty/dT = .0000000$
Allowed IR Modes: 2

Bandgap [eV]: .0000000

Material [GeO_2 o-ray]   Space group #: 136

Classical oscillator model parameters:

Mode	ν_i	$a1_i$	$\Delta\epsilon_i$	$b1_i$	Γ_i/ν_i	$c1_i$	$c2_i$
1	334.0	.0	8.70	.000E+00	.160E–01	.000	.000
2	655.0	.0	.850	.000E+00	.380E–01	.000	.000
3	708.0	.0	.790	.000E+00	.370E–01	.000	.000

$\epsilon_\infty = 4.600000$ $d\epsilon_\infty/dT = .0000000$
Allowed IR Modes: 3

Bandgap [eV]: 5.600000

Table A4.5 Solid-State Complex Index of Refraction Model Parameter—cont'd

Oxides

Material [GeO$_2$ *e*-ray]   Space group #: 136

Classical oscillator model parameters:

Mode	v_i	$a1_i$	$\Delta\epsilon_i$	$b1_i$	Γ_i/v_i	$c1_i$	$c2_i$
1	552.0	.0	5.80	.000E+00	.310E–01	.000	.000

$\epsilon_\infty = 4.100000$ $d\epsilon_\infty/dT = .0000000$
Allowed IR Modes: 1

Bandgap [eV]: 5.600000

Material [Y$_2$O$_3$:HfO$_2$]   Space group #: 225

Classical oscillator model parameters:

Mode	v_i	$a1_i$	$\Delta\epsilon_i$	$b1_i$	Γ_i/v_i	$c1_i$	$c2_i$
1	230.0	.0	2.50	.000E+00	.250	.000	.000
2	320.0	.0	2.50	.000E+00	.200	.000	.000
3	380.0	.0	2.0	.000E+00	.200	.000	.000
4	410.0	.0	3.50	.000E+00	.258	.000	.000
5	470.0	.0	.260	.000E+00	.140	.000	.000
6	530.0	.0	.400E–01	.000E+00	.100	.000	.000
7	580.0	.0	.400E–01	.000E+00	.100	.000	.000
8	64541.10	.0	1.96	.252E–04	.100E–03	.000	.000
9	157728.70	.0	1.35	.000E+00	.100E–03	.000	.000

$\epsilon_\infty = 1.000000$ $d\epsilon_\infty/dT = .0000000$
Allowed IR Modes: −1

Sellmeier parameters: Lower & upper wave number: 1800.000–27400.000

Mode	Location	Strength
0	368.70	10.4100
1	64541.10	1.95580
2	157728.70	1.34500

Bandgap [eV]: 4.500000

Material [Ice Type Ih[*]]   Space group #: 194

Classical oscillator model parameters:

Mode	v_i	$a1_i$	$\Delta\epsilon_i$	$b1_i$	Γ_i/v_i	$c1_i$	$c2_i$
1	63.66	.119	.1198	.195E–3	.568	.125E–2	.000
2	158.52	−.378E–1	.5977	−.992E–3	.342	−.415E–3	.000
3	203.37	.510E–1	.3879	−.128E–2	.196	−.353E–3	.000
4	234.59	−.109	.0000	.144E–2	−.094	.118E–2	.000
5	260.17	−.658E–2	.2053	−.364E–3	.316	−.104E–3	.000
6	670.14	.154	−.6474E–1	.878E–3	.340	−.267E–3	.000
7	794.87	.294E–1	.1072	−.138E–4	.147	−.100E–3	.000
8	867.63	.424E–1	.8906E–1	−.172E–3	.441E–1	.212E–3	.000
9	1237.98	−.402	.6920E–3	.437E–4	.191	−.225E–3	.000
10	1460.54	−.278	.3153E–1	−.436E–4	.417	−.136E–2	.000
11	1584.18	.224	.1565E–1	.287E–4	.260	−.485E–3	.000

[*] $T_0 = 0$ K in this case. Model is valid from 100 to 273 K in the infrared. In the visible and near-infrared it is valid at $T = 266$K. Ice Type Ih is uniaxial, but the distinction between the *o*-ray and *e*-ray hasn't been measured. Thus, only a single listing is given for both rays.

(continued)

Table A4.5 Solid-State Complex Index of Refraction Model Parameter—cont'd

			Oxides				
Mode	v_i	$a1_i$	$\Delta\epsilon_i$	$b1_i$	Γ_i/v_i	$c1_i$	$c2_i$
12	2242.86	−.117	.2006E−2	.174E−4	.556E−1	.819E−4	.000
13	3194.95	−.277	.1520E−2	.649E−4	.312	−.101E−2	.000
14	3134.50	.370	.1683	−.461E−3	.940E−1	−.250E−3	.000
15	3332.88	.479E−1	.2120E−2	.472E−4	.347E−1	−.402E−4	.000
16	3386.35	.221	−.5046E−2	.505E−4	.739E−2	.120E−2	.000
17	4201.36	−.718	.1064E−4	.648E−6	.478	−.184E−4	.000
18	4863.31	.395	.6746E−3	−.143E−5	.182	−.478E−3	.000
19	6092.93	.235	.1564E−3	−.374E−6	.122	−.222E−3	.000
20	6618.72	.144	.1130E−3	−.113E−6	.111	−.246E−3	.000
21	7800.0	—	.43EE−5	—	.115	—	
22	9700.0	—	.6E−6	—	.103	—	
23	11050.0	—	.92E−7	—	.109	—	
24	12700.0	—	.27E−7	—	.110	—	
25	15000.0	—	.55E−8	—	.113	—	
26	18000.0	—	.2E−8	—	.106	—	
27	65012.2	—	.0614147	—	.00001	—	
28	114396.97	—	.6391084	—	.00001	—	

$\epsilon_\infty = 1.000000$ $d\epsilon_\infty/dT = .0000000$

Sellmeier parameters: Lower & upper wave number: 10000–30000

Mode	Location	Strength
1	65012.2	.0614147
2	114396.97	.6391084

Bandgap [eV]: 8.1

Material [KDP *o*-ray]   Space group #: 122

Classical oscillator model parameters:

Mode	v_i	$a1_i$	$\Delta\epsilon_i$	$b1_i$	Γ_i/v_i	$c1_i$	$c2_i$
1	299.60	.0	33.9	.000E+00	.000	.000	.000
2	108800.0	.0	1.26	−.187E−03	.000	.000	.000

$\epsilon_\infty = 1.000000$ $d\epsilon_\infty/dT = .0000000$
Allowed IR Modes: 12

Sellmeier parameters: Lower & upper wave number: 9433.000–25000.000

Mode	Location	Strength
1	108800.0	1.25662
2	299.62	33.8991

Bandgap [eV]: 7.000000

Material [KDP *e*-ray]   Space group #: 122

Classical oscillator model parameters:

Mode	v_i	$a1_i$	$\Delta\epsilon_i$	$b1_i$	Γ_i/v_i	$c1_i$	$c2_i$
1	351.0	.0	5.76	.000E+00	.000	.000	.000
2	110797.10	.0	1.13	−.285E−03	.000	.000	.000

$\epsilon_\infty = 1.000000$ $d\epsilon_\infty/dT = .0000000$
Allowed IR Modes: 6

Table A4.5 Solid-State Complex Index of Refraction Model Parameter—cont'd

Oxides

Sellmeier parameters: Lower & upper wave number: 9434.000–25000.000

Mode	Location	Strength
1	110797.10	1.13109
2	350.98	5.75675

Bandgap [eV]: 7.000000

Material [KNbO$_3$ n_x]   Space group #: 38

Classical oscillator model parameters:

Mode	ν_i	$a1_i$	$\Delta\epsilon_i$	$b1_i$	Γ_i/ν_i	$c1_i$	$c2_i$
1	187.0	.0	1.96	.000E+00	.160E–01	.000	.000
2	243.0	.0	21.7	.000E+00	.193	.000	.000
3	270.0	.0	2.50	.000E+00	.148E–01	.000	.000
4	534.0	.0	3.65	.000E+00	.356E–01	.000	.000
5	47214.0	.0	3.93	.000E+00	.000	.000	.000

$\epsilon_\infty = 1.000000$ $d\epsilon_\infty/dT = .0000000$
Allowed IR Modes: 4

Sellmeier parameters: Lower & upper wave number: 9434.000–25000.000

Mode	Location	Strength
1	47214.0	3.93280

Bandgap [eV]: 3.300000

Material [KNbO$_3$ n_y]   Space group #: 38

Classical oscillator model parameters:

Mode	ν_i	$a1_i$	$\Delta\epsilon_i$	$b1_i$	Γ_i/ν_i	$c1_i$	$c2_i$
1	56.0	.0	713.	.000E+00	1.02	.000	.000
2	195.0	.0	3.84	.000E+00	.154E–01	.000	.000
3	511.0	.0	2.66	.000E+00	.607E–01	.000	.000
4	50787.0	.0	3.79	.000E+00	.000	.000	.000

$\epsilon_\infty = 1.000000$ $d\epsilon_\infty/dT = .0000000$
Allowed IR Modes: 3

Sellmeier parameters: Lower & upper wave number: 9434.000–25000.000

Mode	Location	Strength
1	50787.0	3.79360

Bandgap [eV]: 3.300000

Material [KNbO$_3$ n_z]   Space group #: 38

Classical oscillator model parameters:

Mode	ν_i	$a1_i$	$\Delta\epsilon_i$	$b1_i$	Γ_i/ν_i	$c1_i$	$c2_i$
1	190.0	.0	.900E–01	.000E+00	.158E–01	.000	.000
2	290.0	.0	10.8	.000E+00	.110	.000	.000
3	299.0	.0	.810	.000E+00	.134E–01	.000	.000
4	607.0	.0	2.53	.000E+00	.511E–01	.000	.000
5	53850.0	.0	3.38	.000E+00	.000	.000	.000

(continued)

Table A4.5 Solid-State Complex Index of Refraction Model Parameter—cont'd

		Oxides	

$\epsilon_\infty = 1.000000$ $d\epsilon_\infty/dT = .0000000$
Allowed IR Modes: 4

Sellmeier parameters: Lower & upper wave number: 9434.000–25000.000

Mode	Location	Strength
1	53850.0	3.38360

Bandgap [eV]: 3.300000

Material [KTP(KTiOPO$_4$) n_x]   Space group #: 33

Classical oscillator model parameters:

Mode	v_i	$a1_i$	$\Delta\epsilon_i$	$b1_i$	Γ_i/v_i	$c1_i$	$c2_i$
1	158.70	.0	.450	.000E+00	.252E–01	.000	.000
2	171.0	.0	.210	.000E+00	.117E–01	.000	.000
3	210.30	.0	.300E–01	.000E+00	.950E–02	.000	.000
4	221.0	.0	.250	.000E+00	.181E–01	.000	.000
5	250.0	.0	.300E–01	.000E+00	.360E–01	.000	.000
6	265.0	.0	.250	.000E+00	.377E–01	.000	.000
7	289.0	.0	1.40	.000E+00	.311E–01	.000	.000
8	301.0	.0	.380	.000E+00	.299E–01	.000	.000
9	318.50	.0	.550	.000E+00	.283E–01	.000	.000
10	342.0	.0	.320	.000E+00	.439E–01	.000	.000
11	363.70	.0	.690	.000E+00	.687E–01	.000	.000
12	404.0	.0	.800E–01	.000E+00	.198E–01	.000	.000
13	426.0	.0	.500E–01	.000E+00	.235E–01	.000	.000
14	467.0	.0	.800E–01	.000E+00	.257E–01	.000	.000
15	486.0	.0	.150	.000E+00	.267E–01	.000	.000
16	499.0	.0	.200E–01	.000E+00	.200E–01	.000	.000
17	556.50	.0	.500E–01	.000E+00	.270E–01	.000	.000
18	594.0	.0	.300E–01	.000E+00	.202E–01	.000	.000
19	639.0	.0	.100	.000E+00	.235E–01	.000	.000
20	781.0	.0	.160	.000E+00	.320E–01	.000	.000
21	812.0	.0	.400E–01	.000E+00	.185E–01	.000	.000
22	975.0	.0	.700E–01	.000E+00	.154E–01	.000	.000
23	987.0	.0	.180	.000E+00	.172E–01	.000	.000
24	46569.60	.0	.837	.000E+00	.000	.000	.000

$\epsilon_\infty = 2.167470$ $d\epsilon_\infty/dT = .0000000$
Allowed IR Modes: 47

Sellmeier parameters: Lower & upper wave number: 9434.000–25000.000

Mode	Location	Strength
0	Infinity	1.16747
1	46569.60	.837330
2	654.40	4.00000

Bandgap [eV]: 3.600000

Table A4.5 Solid-State Complex Index of Refraction Model Parameter—cont'd

				Oxides			

Material [KTP(KTiOPO$_4$) n_y]   Space group #: 33

Classical oscillator model parameters:

Mode	v_i	$a1_i$	$\Delta\epsilon_i$	$b1_i$	Γ_i/v_i	$c1_i$	$c2_i$
1	181.0	.0	.600E−01	.000E+00	.166E−01	.000	.000
2	202.0	.0	.400E−01	.000E+00	.500E−02	.000	.000
3	221.50	.0	.200	.000E+00	.158E−01	.000	.000
4	231.0	.0	.230	.000E+00	.195E−01	.000	.000
5	243.0	.0	.600E−01	.000E+00	.165E−01	.000	.000
6	268.70	.0	.350	.000E+00	.186E−01	.000	.000
7	291.20	.0	.600	.000E+00	.343E−01	.000	.000
8	331.50	.0	1.13	.000E+00	.241E−01	.000	.000
9	380.0	.0	.700	.000E+00	.395E−01	.000	.000
10	393.70	.0	.400	.000E+00	.356E−01	.000	.000
11	416.20	.0	.220	.000E+00	.601E−01	.000	.000
12	499.0	.0	.100E−01	.000E+00	.401E−01	.000	.000
13	553.70	.0	.800E−01	.000E+00	.217E−01	.000	.000
14	596.20	.0	.300E−01	.000E+00	.151E−01	.000	.000
15	631.20	.0	.130	.000E+00	.317E−01	.000	.000
16	673.70	.0	.400E−02	.000E+00	.450E−02	.000	.000
17	698.70	.0	.280	.000E+00	.286E−01	.000	.000
18	826.20	.0	.100E−01	.000E+00	.242E−01	.000	.000
19	863.70	.0	.200E−02	.000E+00	.289E−01	.000	.000
20	970.0	.0	.150	.000E+00	.820E−02	.000	.000
21	1019.0	.0	.200	.000E+00	.790E−02	.000	.000
22	1035.0	.0	.110	.000E+00	.155E−01	.000	.000
23	1119.0	.0	.100E−01	.000E+00	.890E−02	.000	.000
24	45175.40	.0	.836	.000E+00	.000	.000	.000

$\epsilon_\infty = 2.192290$ $d\epsilon_\infty/dT = .0000000$
Allowed IR Modes: 47

Sellmeier parameters: Lower & upper wave number: 9434.000–25000.000

Mode	Location	Strength
0	Infinity	1.19229
1	45175.40	.835470
2	636.60	4.00000

Bandgap [eV]: 3.600000

Material [KTP(KTiOPO$_4$) n_z]   Space group #: 33

Classical oscillator model parameters:

Mode	v_i	$a1_i$	$\Delta\epsilon_i$	$b1_i$	Γ_i/v_i	$c1_i$	$c2_i$
1	167.0	.0	.700E−01	.000E+00	.240E−01	.000	.000
2	178.70	.0	.110	.000E+00	.336E−01	.000	.000
3	203.70	.0	.200	.000E+00	.172E−01	.000	.000
4	213.0	.0	.400	.000E+00	.940E−02	.000	.000
5	235.0	.0	.500	.000E+00	.298E−01	.000	.000
6	260.0	.0	.450	.000E+00	.104E−01	.000	.000
7	268.0	.0	2.50	.000E+00	.168E−01	.000	.000
8	288.0	.0	.200	.000E+00	.347E−01	.000	.000
9	311.0	.0	1.40	.000E+00	.225E−01	.000	.000
10	326.0	.0	.400	.000E+00	.215E−01	.000	.000

Table A4.5 Solid-State Complex Index of Refraction Model Parameter—cont'd

<table>
<tr><td colspan="8" align="center">Oxides</td></tr>
<tr><td>Mode</td><td>v_i</td><td>$a1_i$</td><td>$\Delta\epsilon_i$</td><td>$b1_i$</td><td>Γ_i/v_i</td><td>$c1_i$</td><td>$c2_i$</td></tr>
<tr><td>11</td><td>385.0</td><td>.0</td><td>.700</td><td>.000E+00</td><td>.260E−01</td><td>.000</td><td>.000</td></tr>
<tr><td>12</td><td>400.0</td><td>.0</td><td>.140</td><td>.000E+00</td><td>.200E−01</td><td>.000</td><td>.000</td></tr>
<tr><td>13</td><td>428.70</td><td>.0</td><td>.150</td><td>.000E+00</td><td>.210E−01</td><td>.000</td><td>.000</td></tr>
<tr><td>14</td><td>458.70</td><td>.0</td><td>.190</td><td>.000E+00</td><td>.327E−01</td><td>.000</td><td>.000</td></tr>
<tr><td>15</td><td>540.0</td><td>.0</td><td>.300E−01</td><td>.000E+00</td><td>.352E−01</td><td>.000</td><td>.000</td></tr>
<tr><td>16</td><td>585.0</td><td>.0</td><td>.200E−01</td><td>.000E+00</td><td>.427E−01</td><td>.000</td><td>.000</td></tr>
<tr><td>17</td><td>622.50</td><td>.0</td><td>.130</td><td>.000E+00</td><td>.482E−01</td><td>.000</td><td>.000</td></tr>
<tr><td>18</td><td>687.50</td><td>.0</td><td>.740</td><td>.000E+00</td><td>.393E−01</td><td>.000</td><td>.000</td></tr>
<tr><td>19</td><td>958.70</td><td>.0</td><td>.370</td><td>.000E+00</td><td>.125E−01</td><td>.000</td><td>.000</td></tr>
<tr><td>20</td><td>991.20</td><td>.0</td><td>.300E−01</td><td>.000E+00</td><td>.910E−02</td><td>.000</td><td>.000</td></tr>
<tr><td>21</td><td>1023.70</td><td>.0</td><td>.200E−01</td><td>.000E+00</td><td>.780E−02</td><td>.000</td><td>.000</td></tr>
<tr><td>22</td><td>1043.70</td><td>.0</td><td>.900E−01</td><td>.000E+00</td><td>.960E−02</td><td>.000</td><td>.000</td></tr>
<tr><td>23</td><td>1096.20</td><td>.0</td><td>.100E−01</td><td>.000E+00</td><td>.820E−02</td><td>.000</td><td>.000</td></tr>
<tr><td>24</td><td>42694.50</td><td>.0</td><td>1.07</td><td>.000E+00</td><td>.000</td><td>.000</td><td>.000</td></tr>
</table>

$\epsilon_\infty = 2.254110$ $d\epsilon_\infty/dT = .0000000$
Allowed IR Modes: 47

Sellmeier parameters: Lower & upper wave number: 9434.000–25000.000

Mode	Location	Strength
0	Infinity	1.25411
1	42694.50	1.06543
2	731.44	4.00000

Bandgap [eV]: 3.600000

Material [LiNbO$_3$ o-ray]   Space group #: 161

Classical oscillator model parameters:

<table>
<tr><td>Mode</td><td>v_i</td><td>$a1_i$</td><td>$\Delta\epsilon_i$</td><td>$b1_i$</td><td>Γ_i/v_i</td><td>$c1_i$</td><td>$c2_i$</td></tr>
<tr><td>1</td><td>152.0</td><td>.0</td><td>22.0</td><td>.000E+00</td><td>.921E−01</td><td>.000</td><td>.000</td></tr>
<tr><td>2</td><td>236.0</td><td>.0</td><td>.800</td><td>.000E+00</td><td>.508E−01</td><td>.000</td><td>.000</td></tr>
<tr><td>3</td><td>265.0</td><td>.0</td><td>5.50</td><td>.000E+00</td><td>.453E−01</td><td>.000</td><td>.000</td></tr>
<tr><td>4</td><td>322.0</td><td>.0</td><td>2.20</td><td>.000E+00</td><td>.342E−01</td><td>.000</td><td>.000</td></tr>
<tr><td>5</td><td>363.0</td><td>.0</td><td>2.30</td><td>.000E+00</td><td>.909E−01</td><td>.000</td><td>.000</td></tr>
<tr><td>6</td><td>431.0</td><td>.0</td><td>.180</td><td>.000E+00</td><td>.278E−01</td><td>.000</td><td>.000</td></tr>
<tr><td>7</td><td>586.0</td><td>.0</td><td>3.30</td><td>.000E+00</td><td>.597E−01</td><td>.000</td><td>.000</td></tr>
<tr><td>8</td><td>670.0</td><td>.0</td><td>.200</td><td>.000E+00</td><td>.701E−01</td><td>.000</td><td>.000</td></tr>
<tr><td>9</td><td>46082.0</td><td>.0</td><td>2.51</td><td>.000E+00</td><td>.000</td><td>.000</td><td>.000</td></tr>
</table>

$\epsilon_\infty = 2.391980$ $d\epsilon_\infty/dT = .0000000$
Allowed IR Modes: 9

Sellmeier parameters: Lower & upper wave number: 3226.000–25000.000

Mode	Location	Strength
0	Infinity	1.39198
1	46082.0	2.51118
2	606.0	7.13330

Bandgap [eV]: 4.650000

Urbach tail model parameters:
Absorption constant [cm^{-1}]   : .6000000E+08
Exponential constant, σ_0 : .7500000
Effective Phonon Energy, E_p [eV] : .6000000E−01

Table A4.5 Solid-State Complex Index of Refraction Model Parameter—cont'd

Oxides

Material [LiNbO$_3$ *e*-ray]   Space group #: 161

Classical oscillator model parameters:

Mode	v_i	$a1_i$	$\Delta\epsilon_i$	$b1_i$	Γ_i/v_i	$c1_i$	$c2_i$
1	248.0	.0	16.0	.000E+00	.847E−01	.000	.000
2	274.0	.0	1.0	.000E+00	.511E−01	.000	.000
3	307.0	.0	.160	.000E+00	.814E−01	.000	.000
4	628.0	.0	2.55	.000E+00	.541E−01	.000	.000
5	692.0	.0	.130	.000E+00	.708E−01	.000	.000
6	47619.10	.0	2.26	.000E+00	.000	.000	.000

$\epsilon_\infty = 2.324680$ $d\epsilon_\infty/dT = .0000000$
Allowed IR Modes: 4

Sellmeier parameters: Lower & upper wave number: 3226.000–25000.000

Mode	Location	Strength
0	Infinity	1.32468
1	47619.10	2.25650
2	385.88	14.5030

Bandgap [eV]: 4.650000

Urbach tail model parameters:
Absorption constant [cm^{-1}]   : .6000000E+08
Exponential constant, σ_0 : .7500000
Effective Phonon Energy, E_p [eV] : .6000000E−01

Material [MgAl$_2$O$_4$ poly]   Space group #: 227

Classical oscillator model parameters:

Mode	v_i	$a1_i$	$\Delta\epsilon_i$	$b1_i$	Γ_i/v_i	$c1_i$	$c2_i$
1	307.0	−.10E−01	.400	.168E−03	.800E−01	.357E−04	.000
2	488.0	−.14E−01	2.70	.819E−03	.600E−01	.145E−03	.000
3	505.0	−.14E−01	1.20	−.345E−03	.800E−01	.101E−03	.000
4	585.0	−.10E−01	.900E−01	.355E−04	.100	.357E−04	.000
5	667.0	−.71E−02	.800	.416E−03	.700E−01	.357E−04	.000
6	818.0	−.10E−01	.200E−01	.867E−04	.110	.717E−04	.000
7	99980.0	.0	1.90	.307E−04	.100E−03	.000	.000

$\epsilon_\infty = 1.000000$ $d\epsilon_\infty/dT = .0000000$
Allowed IR Modes: 4

Multiphonon model parameters:
$\alpha_1 = .5370$ $v_{max} = 869.0000$
$\alpha_2 = .1530$ $D_0 = 15500.0$
$\alpha_3 = .0520$ $K = 1.7440E+07$

Sellmeier parameters: Lower & upper wave number: 4310.000–28571.000

Mode	Location	Strength
1	100080.0	1.89300
2	527.0	4.40200

Bandgap [eV]: 7.750000

Urbach tail model parameters:
Absorption constant [cm^{-1}]   : 10900.0
Exponential constant, σ_0 :   .1640000
Effective Phonon Energy, E_p [eV] :   .1000000E−07

Table A4.5 Solid-State Complex Index of Refraction Model Parameter—cont'd

<div align="center">Oxides</div>

Scatter Model Parameters:
Rayleigh Coeff. (ν^4 Dependence)   : 0.0000E+00
Mie-like Coeff. (ν^A Dependence)   : 8.7600E−07
Mie-like Exponential Constant (A)   : 1.35

Material [MgO]   Space group #: 225

Classical oscillator model parameters:

Mode	ν_i	$a1_i$	$\Delta\epsilon_i$	$b1_i$	Γ_i/ν_i	$c1_i$	$c2_i$
1	401.0	−.29E−01	6.60	.732E−03	.190E−01	.587E−04	.000
2	640.0	−.45E−01	.500E−01	.116E−03	.160	.564E−04	.000
3	72716.50	.0	.846	.000E+00	.100E−03	.000	.000
4	140358.0	.0	1.11	.000E+00	.100E−03	.000	.000

$\epsilon_\infty = 2.960000$ $d\epsilon_\infty/dT = .3790000E{-}04$
Allowed IR Modes: 1

Multiphonon model parameters:
$\alpha_1 = .5370$ $\nu_{max} = 725.0000$
$\alpha_2 = .1530$ $D_0 = 13000.0$
$\alpha_3 = .0520$ $K = 6.3860E{+}06$

Sellmeier parameters: Lower & upper wave number: 1850.000–29410.000

Mode	Location	Strength
0	140357.80	1.11103
1	72716.50	.846008
2	371.80	7.80853

Bandgap [eV]: 7.800000

Material [SiO$_2$ Quartz *o*-ray]   Space group #: 152

Classical Oscillator model parameters:

Mode	ν_i	$a1_i$	$\Delta\epsilon_i$	$b1_i$	Γ_i/ν_i	$c1_i$	$c2_i$
1	394.0	.0	.330	.000E+00	.700E−02	.000	.000
2	450.0	.0	.820	.000E+00	.900E−02	.000	.000
3	697.0	.0	.200E−01	.000E+00	.120E−01	.000	.000
4	797.0	.0	.110	.000E+00	.900E−02	.000	.000
5	1072.0	.0	.670	.000E+00	.710E−02	.000	.000
6	1163.0	.0	.100E−01	.000E+00	.600E−02	.000	.000
7	1227.0	.0	.940E−02	.000E+00	.110	.000	.000
8	128.0	.0	.600E−03	.000E+00	.390E−01	.000	.000
9	84034.0	.0	.176	.000E+00	.000	.000	.000
10	94340.0	.0	.518	.000E+00	.000	.000	.000
11	166666.0	.0	.663	.000E+00	.000	.000	.000

$\epsilon_\infty = 1.000000$ $d\epsilon_\infty/dT = .0000000$
Allowed IR Modes: 8

Sellmeier parameters: Lower & upper wave number: 14000.000–54000.000

Mode	Location	Strength
1	166666.0	.663044
2	94340.0	.517852
3	84034.0	.175912
4	1131.0	.565380
5	482.0	1.67530

Bandgap [eV]: 8.400000

Table A4.5 Solid-State Complex Index of Refraction Model Parameter—cont'd

Oxides

Material [SiO$_2$ Quartz *e*-ray]   Space group #: 152

Classical Oscillator model parameters:

Mode	v_i	$a1_i$	$\Delta\epsilon_i$	$b1_i$	Γ_i/v_i	$c1_i$	$c2_i$
1	364.0	.0	.680	.000E+00	.140E−01	.000	.000
2	495.0	.0	.660	.000E+00	.900E−02	.000	.000
3	509.0	.0	.500E−01	.000E+00	.140E−01	.000	.000
4	539.0	.0	.100E−01	.000E+00	.400E−01	.000	.000
5	778.0	.0	.100	.000E+00	.100E−01	.000	.000
6	1080.0	.0	.670	.000E+00	.690E−02	.000	.000
7	1220.0	.0	.110E−01	.000E+00	.150	.000	.000
8	84034.0	.0	.215	.000E+00	.000	.000	.000
9	94340.0	.0	.503	.000E+00	.000	.000	.000
10	166666.0	.0	.666	.000E+00	.000	.000	.000

$\epsilon_\infty = 1.000000$ $d\epsilon_\infty/dT = .0000000$
Allowed IR Modes: 4

Sellmeier parameters: Lower & upper wave number: 14000.000–54000.000

Mode	Location	Strength
1	166666.0	.665721
2	94340.0	.503511
3	84034.0	.214792
4	1137.40	.539173
5	507.60	1.80761

Bandgap [eV]: 8.400000

Material [TiO$_2$ *o*-ray]   Space group #: 136

Classical Oscillator model parameters:

Mode	v_i	$a1_i$	$\Delta\epsilon_i$	$b1_i$	Γ_i/v_i	$c1_i$	$c2_i$
1	189.0	.0	70.8	.000E+00	.135	.000	.000
2	381.50	.0	.995	.000E+00	.500E−01	.000	.000
3	508.0	.0	3.0	.000E+00	.700E−01	.000	.000
4	35285.80	.0	3.04	.000E+00	.000	.000	.000

$\epsilon_\infty = 2.873000$ $d\epsilon_\infty/dT = .0000000$
Allowed IR Modes: 3

Sellmeier parameters: Lower & upper wave number: 6666.000–23256.000

Mode	Location	Strength
0	Infinity	1.87300
1	35285.0	3.04000

Bandgap [eV]: 3.030000

Material [TiO$_2$ *e*-ray]   Space group #: 136

Classical Oscillator model parameters:

Mode	v_i	$a1_i$	$\Delta\epsilon_i$	$b1_i$	Γ_i/v_i	$c1_i$	$c2_i$
1	172.0	.0	148.	.000E+00	.340	.000	.000
2	34447.10	.0	3.94	.000E+00	.000	.000	.000

$\epsilon_\infty = 3.256000$ $d\epsilon_\infty/dT = .0000000$
Allowed IR Modes: 1

Table A4.5 Solid-State Complex Index of Refraction Model Parameter—cont'd

Oxides

Sellmeier parameters: Lower & upper wave number: 6666.000–23256.000

Mode	Location	Strength
0	Infinity	2.25600
1	34447.13	3.94100

Bandgap [eV]: 3.040000

Material [VO_2 poly (26C)]   Space group #: 14

Classical Oscillator model parameters:

Mode	ν_i	$a1_i$	$\Delta\epsilon_i$	$b1_i$	Γ_i/ν_i	$c1_i$	$c2_i$
1	227.50	.0	.100	.000E+00	.200E−01	.000	.000
2	285.0	.0	3.30	.000E+00	.600E−01	.000	.000
3	324.0	.0	1.95	.000E+00	.180E−01	.000	.000
4	355.0	.0	7.40	.000E+00	.800E−01	.000	.000
5	392.50	.0	1.0	.000E+00	.300E−01	.000	.000
6	478.0	.0	.200	.000E+00	.800E−01	.000	.000
7	530.0	.0	.650	.000E+00	.450E−01	.000	.000
8	700.0	.0	.250	.000E+00	.550E−01	.000	.000
9	6210.10	.0	1.99	.000E+00	.520	.000	.000
10	7742.90	.0	1.72	.000E+00	.480	.000	.000
11	9597.90	.0	1.27	.000E+00	.530	.000	.000
12	12178.90	.0	1.16	.000E+00	.550	.000	.000
13	23954.50	.0	.490	.000E+00	.150	.000	.000
14	27583.90	.0	.482	.000E+00	.260	.000	.000
15	30648.80	.0	.747	.000E+00	.365	.000	.000
16	34681.60	.0	.866	.000E+00	.390	.000	.000
17	46941.10	.0	.884	.000E+00	.560	.000	.000

$\epsilon_\infty = 5.600000$ $d\epsilon_\infty/dT = .0000000$
Allowed IR Modes: 8

Bandgap [eV]: .7500000

Material [Y_2O_3 poly]   Space group #: 206

Classical Oscillator model parameters:

Mode	ν_i	$a1_i$	$\Delta\epsilon_i$	$b1_i$	Γ_i/ν_i	$c1_i$	$c2_i$
1	120.0	−.10E−01	.200	.000E+00	.350E−01	.000	.000
2	172.0	−.10E−01	.100	.000E+00	.250E−01	.000	.000
3	182.0	−.10E−01	.150	.000E+00	.250E−01	.000	.000
4	241.0	−.72E−02	.200	.710E−04	.250E−01	.146E−04	.000
5	303.0	−.14E−01	2.60	.624E−03	.135E−01	.335E−04	.000
6	335.0	−.11E−01	1.75	−.355E−03	.115E−01	.238E−04	.000
7	371.0	−.11E−01	2.65	.638E−04	.210E−01	.251E−04	.000
8	415.0	−.11E−01	.400E−01	.355E−04	.110E−01	.324E−04	.000
9	461.0	−.14E−01	.500E−01	.355E−04	.150E−01	.180E−04	.000
10	490.0	−.18E−01	.500E−02	.355E−05	.180E−01	.212E−04	.000
11	555.0	−.21E−01	.950E−01	.936E−04	.250E−01	.121E−04	.000
12	72100.0	.0	2.58	.140E−03	.100E−03	.000	.000

$\epsilon_\infty = 1.000000$ $d\epsilon_\infty/dT = .0000000$
Allowed IR Modes: 16

Table A4.5 Solid-State Complex Index of Refraction Model Parameter—cont'd

<div align="center">Oxides</div>

Multiphonon model parameters:

$\alpha_1 = .5370$ $\nu_{max} = 620.0000$
$\alpha_2 = .1530$ $D_0 = 12000.0$
$\alpha_3 = .0520$ $K = 2.2500E{+}07$

Sellmeier parameters: Lower & upper wave number: 825.000–45000.000

Mode	Location	Strength
1	72100.0	2.57771
2	436.0	3.93485

Bandgap [eV]: 6.080000

Urbach tail model parameters:

Absorption constant [cm^{-1}]   : 8222000.
Exponential constant, σ_0 :   .6880000
Effective Phonon Energy, E_p [eV] :   .1870000E$-$01

Scatter Model Parameters:

Rayleigh Coeff. (nu^4 Dependence) : 0.0000E+00
Mie-like Coeff. (nu^A Dependence) : 2.0800E$-$08
Mie-like Exponential Constant (A) : 1.82

Material [La$_2$O$_3$:Y$_2$O$_3$ poly]   Space group #: 206

Classical Oscillator model parameters:

Mode	ν_i	$a1_i$	$\Delta\epsilon_i$	$b1_i$	Γ_i/ν_i	$c1_i$	$c2_i$
1	235.0	$-$.72E$-$02	.150	.723E$-$04	.400E$-$01	.529E$-$04	.000
2	294.0	$-$.52E$-$02	3.10	.208E$-$03	.400E$-$01	.831E$-$04	.000
3	327.0	$-$.63E$-$02	1.60	$-$.687E$-$03	.370E$-$01	.256E$-$04	.000
4	364.0	$-$.52E$-$02	2.80	.521E$-$03	.380E$-$01	.440E$-$04	.000
5	407.0	$-$.10E$-$01	.400E$-$01	.208E$-$04	.250E$-$01	.172E$-$04	.000
6	451.0	$-$.15E$-$01	.530E$-$01	.447E$-$04	.370E$-$01	.318E$-$04	.000
7	477.80	$-$.12E$-$01	.500E$-$02	.409E$-$05	.400E$-$01	.529E$-$04	.000
8	550.0	$-$.72E$-$02	.950E$-$01	.113E$-$03	.320E$-$01	.879E$-$04	.000
9	115.0	$-$.10E$-$01	.200	.000E+00	.350E$-$01	.000	.000
10	167.0	$-$.10E$-$01	.100	.000E+00	.250E$-$01	.000	.000
11	177.0	$-$.10E$-$01	.150	.000E+00	.250E$-$01	.000	.000
12	74711.60	.0	2.56	.165E$-$03	.000	.000	.000

$\epsilon_\infty = 1.000000$ $d\epsilon_\infty/dT = .0000000$
Allowed IR Modes: -1

Multiphonon model parameters:

$\alpha_1 = .5370$ $\nu_{max} = 612.0000$
$\alpha_2 = .1530$ $D_0 = 12000.0$
$\alpha_3 = .0520$ $K = 2.0900E{+}07$

Sellmeier parameters: Lower & upper wave number: 4100.000–25000.000

Mode	Location	Strength
1	.13	2.56446

Bandgap [eV]: 6.000000

Scatter Model Parameters:

Rayleigh Coeff. (ν^4 Dependence)   : 0.0000E+00
Mie-like Coeff. (ν^A Dependence)   : 4.4700E$-$05
Mie-like Exponential Constant (A) : .99

Table A4.5 Solid-State Complex Index of Refraction Model Parameter—cont'd

Oxides						

Material [YAG]   Space group #: 230

Classical Oscillator model parameters:

Mode	v_i	$a1_i$	$\Delta\epsilon_i$	$b1_i$	Γ_i/v_i	$c1_i$	$c2_i$
1	122.30	.0	.875E–01	.000E+00	.860E–02	.000	.000
2	163.40	.0	1.48	.000E+00	.172E–01	.000	.000
3	177.50	.0	.135	.000E+00	.400E–02	.000	.000
4	220.0	.0	.436	.000E+00	.150E–01	.000	.000
5	289.70	.0	.583	.000E+00	.157E–01	.000	.000
6	330.20	.0	.751	.000E+00	.190E–01	.000	.000
7	372.50	.0	.498	.000E+00	.150E–01	.000	.000
8	387.30	.0	.763E–01	.000E+00	.400E–02	.000	.000
9	394.50	.0	.515	.000E+00	.230E–01	.000	.000
10	429.0	.0	1.18	.000E+00	.600E–01	.000	.000
11	450.0	.0	.778	.000E+00	.750E–01	.000	.000
12	478.0	.0	.355E–01	.000E+00	.750E–01	.000	.000
13	516.50	.0	.653E–01	.000E+00	.400E–01	.000	.000
14	569.20	.0	.627E–01	.000E+00	.128E–01	.000	.000
15	692.0	.0	.416	.000E+00	.300E–01	.000	.000
16	728.0	.0	.170	.000E+00	.290E–01	.000	.000
17	785.0	.0	.792E–01	.000E+00	.250E–01	.000	.000
18	91324.0	.0	2.29	.000E+00	.100E–03	.000	.000

$\epsilon_\infty = 1.000000$ $d\epsilon_\infty/dT = .0000000$
Allowed IR Modes: 17

Sellmeier parameters: Lower & upper wave number: 2500.000–25000.000

Mode	Location	Strength
1	91324.0	2.29300
2	561.0	3.70500

Bandgap [eV]: 7.012000

Urbach tail model parameters:
Absorption constant [cm^{-1}]   : 212500.0
Exponential constant, σ_0 :   .5600000
Effective Phonon Energy, E_p [eV] :   .3720000E–01

Material [Y_2O_3 : ZrO_2]   Space group #: 225

Classical Oscillator model parameters:

Mode	v_i	$a1_i$	$\Delta\epsilon_i$	$b1_i$	Γ_i/v_i	$c1_i$	$c2_i$
1	411.0	.0	9.45	.000E+00	.100	.000	.000
2	59974.0	.0	2.12	.000E+00	.100E–03	.000	.000
3	159890.0	.0	1.35	.000E+00	.100E–03	.000	.000

$\epsilon_\infty = 1.000000$ $d\epsilon_\infty/dT = .0000000$
Allowed IR Modes: −1

Multiphonon model parameters:
$\alpha_1 = .5370$ $v_{max} = 668.0000$
$\alpha_2 = .1530$ $D_0 = 9700.000$
$\alpha_3 = .0520$ $K = 6.0000E+07$

Table A4.5 Solid-State Complex Index of Refraction Model Parameter—cont'd

Oxides

Sellmeier parameters: Lower & upper wave number: 2000.000–27700.000

Mode	Location	Strength
1	59974.0	2.11779
2	159890.0	1.34091
3	411.20	9.45294

Bandgap [eV]: 5.600000

Alkali-halides

Material [AgBr]   Space group #: 225

Classical Oscillator model parameters:

Mode	v_i	$a1_i$	$\Delta\epsilon_i$	$b1_i$	Γ_i/v_i	$c1_i$	$c2_i$
1	80.0	.0	9.27	.000E+00	.190	.000	.000
2	34264.20	.0	1.24	.000E+00	.000	.000	.000
3	999999.0	.0	2.45	.000E+00	.100E−03	.000	.000

$\epsilon_\infty = 1.000000$ $d\epsilon_\infty/dT = .0000000$
Allowed IR Modes: 1

Sellmeier parameters: Lower & upper wave number: 14925.000–20408.000

Mode	Location	Strength
0	Infinity	2.45000
1	34264.20	1.24168

Bandgap [eV]: 2.790000

Urbach tail model parameters:
Absorption constant [cm^{-1}]   : 15000.0
Exponential constant, σ_0 :   1.000000
Effective Phonon Energy, E_p [eV] :   .0000000

Material [AgCl]   Space group #: 225

Classical Oscillator model parameters:

Mode	v_i	$a1_i$	$\Delta\epsilon_i$	$b1_i$	Γ_i/v_i	$c1_i$	$c2_i$
1	105.0	.0	9.54	.000E+00	.135	.000	.000
2	41005.60	.0	.946	.000E+00	.000	.000	.000
3	96241.40	.0	2.06	.000E+00	.000	.000	.000

$\epsilon_\infty = 1.000000$ $d\epsilon_\infty/dT = .0000000$
Allowed IR Modes: 1

Sellmeier parameters: Lower & upper wave number: 476.000–18518.000

Mode	Location	Strength
1	96241.40	2.06251
2	41005.61	.946146
3	141.13	4.30079

Bandgap [eV]: 3.440000

Urbach tail model parameters:
Absorption constant [cm^{-1}]   : 1600000.
Exponential constant, σ_0 :   .8000000
Effective Phonon Energy, E_p [eV] :   .0000000

(continued)

Table A4.5 Solid-State Complex Index of Refraction Model Parameter—cont'd

Alkali-halides

Material [CsBr]   Space group #: 221

Classical Oscillator model parameters:

Mode	v_i	$a1_i$	$\Delta\epsilon_i$	$b1_i$	Γ_i/v_i	$c1_i$	$c2_i$
1	75.0	.0	3.57	.000E+00	.600E−01	.000	.000
2	103.0	.0	.113	.000E+00	.160	.000	.000
3	59825.90	.0	.830	.000E+00	.000	.000	.000
4	110418.80	.0	.953	.000E+00	.000	.000	.000

$\epsilon_\infty = 1.000000$ $d\epsilon_\infty/dT = .0000000$
Allowed IR Modes: 1

Sellmeier parameters: Lower & upper wave number: 256.000–27778.000

Mode	Location	Strength
1	84.02	2.84717
2	59825.89	.830381
3	110418.80	.953379

Bandgap [eV]: 6.900000

Material [CsI]   Space group #: 221

One-phonon model parameters:

Mode	v_i	$a1_i$	$\Delta\epsilon_i$	$b1_i$	Γ_i/v_i	$c1_i$	$c2_i$
1	62.0	.0	3.27	.000E+00	.700E−01	.000	.000
2	85.0	.0	.600E−01	.000E+00	.150	.000	.000
3	45872.0	.0	.192E−01	.000E+00	.100E−03	.000	.000
4	48544.0	.0	.518	.000E+00	.100E−03	.000	.000
5	54054.0	.0	.150	.000E+00	.100E−03	.000	.000
6	56497.0	.0	.653E−01	.000E+00	.100E−03	.000	.000
7	61350.0	.0	.626E−01	.000E+00	.100E−03	.000	.000
8	68027.0	.0	.261	.000E+00	.100E−03	.000	.000
9	76923.0	.0	.687	.000E+00	.100E−03	.000	.000

$\epsilon_\infty = 1.275870$ $d\epsilon_\infty/dT = .0000000$
Allowed IR Modes: 1

Multiphonon model parameters:

$\alpha_1 = .5300$ $v_{max} = 90.00000$
$\alpha_2 = .1450$ $D_0 = 1800.000$
$\alpha_3 = .0520$ $K = 2.0000E+05$

Sellmeier parameters: Lower & upper wave number: 200.000–34483.000

Mode	Location	Strength
1	435602.70	.346173
2	68212.80	1.0 809
3	55248.60	.285518
4	47169.80	.397432
5	62.10	3.36054

Bandgap [eV]: 6.300000

Table A4.5 Solid-State Complex Index of Refraction Model Parameter—cont'd

| Alkali-halides | | | | | | |

Material [KBr]   Space group #: 225

Classical Oscillator model parameters:

Mode	ν_i	$a1_i$	$\Delta\epsilon_i$	$b1_i$	Γ_i/ν_i	$c1_i$	$c2_i$
1	114.0	−.26E−01	2.27	.548E−03	.720E−01	.796E−04	.621E−06
2	146.50	−.34E−01	.400E−01	.606E−03	.160	.677E−03	.000
3	168.50	−.26E−01	.800E−01	.458E−03	.140	.397E−03	.000
4	53476.0	.0	.156	−.123E−03	.100E−03	.000	.000
5	57803.0	.0	.198E−01	.000E+00	.100E−03	.000	.000
6	68493.0	.0	.792	.000E+00	.100E−03	.000	.000

$\epsilon_\infty = 1.394080$ $d\epsilon_\infty/dT = .0000000$
Allowed IR Modes: 1

Multiphonon model parameters:
$\alpha_1 = .5300$ $\nu_{max} = 166.0000$
$\alpha_2 = .1450$ $D_0 = 2350.000$
$\alpha_3 = .0520$ $K = 2.1000E+05$

Sellmeier parameters: Lower & upper wave number: 385.000–25000.000

Mode	Location	Strength
1	126.70	1.95755
2	56385.07	.442023
3	99207.92	.919413

Bandgap [eV]: 6.840000

Urbach tail model parameters:
Absorption constant [cm^{-1}]   : .6000000E+10
Exponential constant, σ_0 : .7740000
Effective Phonon Energy, E_p [eV] : .1050000E−01

Material [KCl]   Space group #: 225

Classical Oscillator model parameters:

Mode	ν_i	$a1_i$	$\Delta\epsilon_i$	$b1_i$	Γ_i/ν_i	$c1_i$	$c2_i$
1	141.50	−.34E−01	2.34	.777E−03	.230E−01	.150E−04	.556E−06
2	189.50	−.29E−01	.900E−01	.371E−03	.170	.193E−03	.000
3	212.0	−.30E−01	.550E−01	.920E−04	.780E−01	.150E−03	.000
4	235.50	−.86E−02	.200E−01	.211E−03	.400E−01	.353E−03	.000
5	61728.0	.0	.189	−.103E−03	.100E−03	.000	.000
6	76336.0	.0	.416	.000E+00	.100E−03	.000	.000
7	100000.0	.0	.305	.000E+00	.100E−03	.000	.000

$\epsilon_\infty = 1.264860$ $d\epsilon_\infty/dT = .0000000$
Allowed IR Modes: 1

Multiphonon model parameters:
$\alpha_1 = .5300$ $\nu_{max} = 213.0000$
$\alpha_2 = .1450$ $D_0 = 2840.000$
$\alpha_3 = .0520$ $K = 6.3000E+05$

Sellmeier parameters: Lower & upper wave number: 695.000–45500.000

Mode	Location	Strength
1	119569.40	.747836
2	64977.30	.426266
3	105.20	4.68671

Bandgap [eV]: 7.834000

Table A4.5 Solid-State Complex Index of Refraction Model Parameter—cont'd

Alkali-halides

Urbach tail model parameters:
Absorption constant [cm^{-1}]   : .1260000E+11
Exponential constant, σ_0 : .7450000
Effective Phonon Energy, E_p [eV] : .1350000E−01

Material [KF]   Space group #: 225

Classical Oscillator model parameters:

Mode	ν_i	$a1_i$	$\Delta\epsilon_i$	$b1_i$	Γ_i/ν_i	$c1_i$	$c2_i$
1	194.0	.0	3.60	.000E+00	.000	.000	.000
2	79365.10	.0	.292	.000E+00	.000	.000	.000

$\epsilon_\infty = 1.550830$ $d\epsilon_\infty/dT = .0000000$
Allowed IR Modes: 1

Sellmeier parameters: Lower & upper wave number: 455.000–66666.000

Mode	Location	Strength
0	Infinity	.550830
1	79365.10	.291620
2	194.0	3.60000

Bandgap [eV]: 10.80000

Material [KI]   Space group #: 225

Classical Oscillator model parameters:

Mode	ν_i	$a1_i$	$\Delta\epsilon_i$	$b1_i$	Γ_i/ν_i	$c1_i$	$c2_i$
1	102.0	.0	2.14	.000E+00	.840E−01	.000	.000
2	144.0	.0	.280	.000E+00	.300	.000	.000
3	45662.0	.0	.161	.000E+00	.100E−03	.000	.000
4	53476.0	.0	.442	.000E+00	.100E−03	.000	.000
5	57143.0	.0	.412	.000E+00	.100E−03	.000	.000
6	77519.0	.0	.165	.000E+00	.100E−03	.000	.000

$\epsilon_\infty = 1.472850$ $d\epsilon_\infty/dT = .0000000$
Allowed IR Modes: 1

Multiphonon model parameters:
$\alpha_1 = .5300$ $\nu_{max} = 150.0000$
$\alpha_2 = .1450$ $D_0 = 2000.000$
$\alpha_3 = .0520$ $K = 2.0000E+05$

Sellmeier parameters: Lower & upper wave number: 200.000–40000.000

Mode	Location	Strength
0	Infinity	1.63797
1	57142.86	.412220
2	53475.94	.441630
3	45662.10	.160760
4	144.01	.335710
5	102.0	1.92474

Bandgap [eV]: 5.890000

Urbach tail model parameters:
Absorption constant [cm^{-1}]   : .6000000E+10
Exponential constant, σ_0 : .8300000
Effective Phonon Energy, E_p [eV] : .4500000E−02

Table A4.5 Solid-State Complex Index of Refraction Model Parameter—cont'd

Alkali-halides						

Material [KRS-5]   Space group #: 221
Classical Oscillator model parameters:

Mode	ν_i	$a1_i$	$\Delta\epsilon_i$	$b1_i$	Γ_i/ν_i	$c1_i$	$c2_i$
1	60.80	.0	12.4	.000E+00	.000	.000	.000
2	22222.0	.0	.451E−01	.000E+00	.000	.000	.000
3	28571.0	.0	1.12	.000E+00	.000	.000	.000
4	40000.0	.0	1.67	.000E+00	.000	.000	.000
5	66666.0	.0	1.83	.000E+00	.000	.000	.000

$\epsilon_\infty = 1.000000$ $d\epsilon_\infty/dT = .0000000$
Allowed IR Modes: 1

Sellmeier parameters: Lower & upper wave number: 200.000–17000.000

Mode	Location	Strength
1	60.76	12.3802
2	22222.0	.451337E−01
3	28571.0	1.12104
4	40000.0	1.66756
5	66666.60	1.82940

Bandgap [eV]: 2.600000

Scatter Model Parameters:
Rayleigh Coeff. (nu^4 Dependence) : 0.0000E+00
Mie-like Coeff. (nu^A Dependence) : 5.8300E−13
Mie-like Exponential Constant (A)   : 2.20

Material [LiF]   Space group #: 225

Classical Oscillator model parameters:

Mode	ν_i	$a1_i$	$\Delta\epsilon_i$	$b1_i$	Γ_i/ν_i	$c1_i$	$c2_i$
1	306.0	.0	6.80	.000E+00	.600E−01	.000	.000
2	503.0	.0	.110	.000E+00	.180	.000	.000
3	135575.0	.0	.930	.000E+00	.100E−03	.000	.000

$\epsilon_\infty = 1.000000$ $d\epsilon_\infty/dT = .0000000$
Allowed IR Modes: 1

Multiphonon model parameters:
$\alpha_1 = .5300$ $\nu_{max} = 673.0000$
$\alpha_2 = .1450$ $D_0 = 6500.000$
$\alpha_3 = .0520$ $K = 7.2000E+06$

Sellmeier parameters: Lower & upper wave number: 1667.000–25000.000

Mode	Location	Strength
1	137155.40	.925563
2	354.0	5.12820

Bandgap [eV]: 12.75000

Urbach tail model parameters:
Absorption constant [cm^{-1}]   : 90030.0
Exponential constant, σ_0 :   .2300000
Effective Phonon Energy, E_p [eV] :   .0000000

Table A4.5 Solid-State Complex Index of Refraction Model Parameter—cont'd

Alkali-halides

Material [NaBr]   Space group #: 225

Classical Oscillator model parameters:

Mode	v_i	$a1_i$	$\Delta\epsilon_i$	$b1_i$	Γ_i/v_i	$c1_i$	$c2_i$
1	134.0	.0	3.80	.000E+00	.000	.000	.000
2	53191.50	.0	.244	.000E+00	.000	.000	.000
3	56818.20	.0	.240E−02	.000E+00	.000	.000	.000
4	68965.50	.0	.188	.000E+00	.000	.000	.000
5	80000.0	.0	1.10	.000E+00	.000	.000	.000

$\epsilon_\infty = 1.067280$ $d\epsilon_\infty/dT = .0000000$
Allowed IR Modes: 1

Sellmeier parameters: Lower & upper wave number: 294.000–47619.000

Mode	Location	Strength
0	Infinity	.672800E−01
1	80000.0	1.10463
2	68965.50	.188160
3	56818.20	.243000E−02
4	53191.50	.244540
5	133.99	3.79600

Bandgap [eV]: 6.770000

Urbach tail model parameters:
Absorption constant [cm^{-1}]   : .6000000E+10
Exponential constant, σ_0 : .7650000
Effective Phonon Energy, E_p [eV] : .1070000E−01

Material [NaCl]   Space group #: 225

Classical Oscillator model parameters:

Mode	v_i	$a1_i$	$\Delta\epsilon_i$	$b1_i$	Γ_i/v_i	$c1_i$	$c2_i$
1	83.10	−.71E−02	.500E−01	.848E−03	.165	.164E−03	.000
2	163.60	−.39E−01	3.20	.665E−03	.520E−01	−2.77E−05	.690E−06
3	232.0	−.35E−01	.380E−01	.137E−03	.780E−01	.206E−03	.000
4	253.0	−.38E−01	.500E−01	.143E−03	.880E−01	.205E−03	.000
5	63291.0	.0	.260	−.108E−03	.100E−03	.000	.000
6	78125.0	.0	.387	.000E+00	.100E−03	.000	.000
7	100000.0	.0	.484	.000E+00	.100E−03	.000	.000
8	200000.0	.0	.198	.000E+00	.100E−03	.000	.000

$\epsilon_\infty = 1.000550$ $d\epsilon_\infty/dT = .0000000$
Allowed IR Modes: 1

Multiphonon model parameters:
$\alpha_1 = .5300$ $v_{max} = 268.0000$
$\alpha_2 = .1450$ $D_0 = 4000.000$
$\alpha_3 = .0520$ $K = 8.5000E+05$

Sellmeier parameters: Lower & upper wave number: 448.000–54054.000

Mode	Location	Strength
1	200000.0	.187895
2	100000.0	.497649
3	78125.0	.384897
4	63291.14	.259500
5	163.67	3.47400

Bandgap [eV]: 8.025000

Table A4.5 Solid-State Complex Index of Refraction Model Parameter—cont'd

Alkali-halides

Urbach tail model parameters:
Absorption constant [cm^{-1}]   : .1200000E+11
Exponential constant, σ_0 : .7570000
Effective Phonon Energy, E_p [eV] : .1003000E−01

Material [NaF]   Space group #: 225

Classical Oscillator model parameters:

Mode	v_i	$a1_i$	$\Delta\epsilon_i$	$b1_i$	Γ_i/v_i	$c1_i$	$c2_i$
1	246.0	.0	3.0	.000E+00	.190E−01	.000	.000
2	375.0	.0	.700E−01	.000E+00	.135	.000	.000
3	85470.10	.0	.328	.000E+00	.000	.000	.000

$\epsilon_\infty = 1.415720$ $d\epsilon_\infty/dT = .0000000$
Allowed IR Modes: 1

Sellmeier parameters: Lower & upper wave number: 600.000–66666.000

Mode	Location	Strength
0	Infinity	.415720
1	85470.10	.327850
2	246.50	3.18248

Bandgap [eV]: 10.70000

Urbach tail model parameters:
Absorption constant [cm^{-1}]   : .1000000E+11
Exponential constant, σ_0 : .6900000
Effective Phonon Energy, E_p [eV] : .1650000E−01

Material [NaI]   Space group #: 225
Classical Oscillator model parameters:

Mode	v_i	$a1_i$	$\Delta\epsilon_i$	$b1_i$	Γ_i/v_i	$c1_i$	$c2_i$
1	116.0	.0	4.27	.000E+00	.000	.000	.000
2	58823.50	.0	1.53	.000E+00	.000	.000	.000

$\epsilon_\infty = 1.478000$ $d\epsilon_\infty/dT = .0000000$
Allowed IR Modes: 1

Sellmeier parameters: Lower & upper wave number: 250.000–40000.000

Mode	Location	Strength
0	Infinity	.478000
1	58823.50	1.52300
2	116.0	4.27000

Bandgap [eV]: 5.666000

Urbach tail model parameters:
Absorption constant [cm^{-1}]   : .6000000E+10
Exponential constant, σ_0 : .8450000
Effective Phonon Energy, E_p [eV] : .8500000E−02

(continued)

Table A4.5 Solid-State Complex Index of Refraction Model Parameter—cont'd

	Alkali-halides						

Material [TlBr]   Space group #: 221

Classical Oscillator model parameters:

Mode	v_i	$a1_i$	$\Delta\epsilon_i$	$b1_i$	Γ_i/v_i	$c1_i$	$c2_i$
1	45.0	.0	26.3	.000E+00	.140	.000	.000
2	32645.60	.0	1.85	.000E+00	.000	.000	.000
3	999999.0	.0	2.31	.000E+00	.000	.000	.000

$\epsilon_\infty = 1.000000$ $d\epsilon_\infty/dT = .0000000$
Allowed IR Modes: 1

Sellmeier parameters: Lower & upper wave number: 12987.000–23256.000

Mode	Location	Strength
0	Infinity	2.31028
1	32645.60	1.84780

Bandgap [eV]: 3.100000

Material [TlCl]   Space group #: 221

Classical Oscillator model parameters:

Mode	v_i	$a1_i$	$\Delta\epsilon_i$	$b1_i$	Γ_i/v_i	$c1_i$	$c2_i$
1	60.0	.0	31.0	.000E+00	.150	.000	.000
2	35550.50	.0	1.65	.000E+00	.000	.000	.000
3	999999.0	.0	1.91	.000E+00	.000	.000	.000

$\epsilon_\infty = 1.000000$ $d\epsilon_\infty/dT = .0000000$
Allowed IR Modes: 1

Sellmeier parameters: Lower & upper wave number: 13514.000–23256.000

Mode	Location	Strength
0	Infinity	1.91159
1	35550.50	1.65125

Bandgap [eV]: 3.430000

Urbach tail model parameters:
Absorption constant [cm^{-1}]   : 40000.0
Exponential constant, σ_0 :   1.040000
Effective Phonon Energy, E_p [eV] :   .7000000E–02

	Fluorides						

Material [BaF$_2$]   Space group #: 225

Classical Oscillator model parameters:

Mode	v_i	$a1_i$	$\Delta\epsilon_i$	$b1_i$	Γ_i/v_i	$c1_i$	$c2_i$
1	188.0	−.12E–01	4.50	−.168E–02	.690E–01	−0.0141	.402E–06
2	236.0	−.44E–01	.960E–01	.395E–03	.210	.126E–03	.000
3	278.0	−.44E–01	.150E–01	.178E–03	.150	.168E–03	.000
4	328.0	−.47E–01	.140E–01	.129E–03	.125	.386E–03	.000
5	90117.0	.0	.507	−.481E–04	.100E–03	.000	.000
6	173042.0	.0	.634	.000E+00	.100E–03	.000	.000

$\epsilon_\infty = 1.000000$ $d\epsilon_\infty/dT = .0000000$
Allowed IR Modes: 1

Table A4.5 Solid-State Complex Index of Refraction Model Parameter—cont'd

Fluorides

Multiphonon model parameters:

$\alpha_1 = .5370$ $\nu_{max} = 338.0000$
$\alpha_2 = .1530$ $D_0 = 4300.000$
$\alpha_3 = .0520$ $K = 4.3390E+06$

Sellmeier parameters: Lower & upper wave number: 961.000–38461.000

Mode	Location	Strength
1	173043.30	.643356
2	91174.30	.506762
3	215.60	3.82610

Bandgap [eV]: 10.16200

Urbach tail model parameters:

Absorption constant [cm^{-1}]   : .4170000E+09
Exponential constant, σ_0 : .5800000
Effective Phonon Energy, E_p [eV] : .4000000E−01

Material [CaF$_2$]   Space group #: 225

Classical Oscillator model parameters:

Mode	ν_i	$a1_i$	$\Delta\epsilon_i$	$b1_i$	Γ_i/ν_i	$c1_i$	$c2_i$
1	259.40	−.25E−01	4.40	−.562E−03	.900E−02	−0.014	.355E−06
2	333.0	−.69E−01	.850E−01	.701E−03	.144	.267E−03	.000
3	368.0	−.68E−01	.780E−01	.151E−03	.210	.186E−03	.000
4	416.0	−.43E−01	.500E−02	.271E−04	.900E−01	.448E−03	.000
5	469.0	−.71E−01	.180E−01	−.355E−04	.250	.524E−03	.000
6	99610.60	.0	.471	−.374E−04	.100E−03	.000	.000
7	198951.10	.0	.568	.000E+00	.100E−03	.000	.000

$\epsilon_\infty = 1.000000$ $d\epsilon_\infty/dT = .0000000$
Allowed IR Modes: 1

Multiphonon model parameters:

$\alpha_1 = .5370$ $\nu_{max} = 479.0000$
$\alpha_2 = .1530$ $D_0 = 7500.000$
$\alpha_3 = .0520$ $K = 7.3500E+06$

Sellmeier parameters: Lower & upper wave number: 1020.000–45454.000

Mode	Location	Strength
1	198951.10	.567589
2	99610.60	.471091
3	288.60	3.84847

Bandgap [eV]: 11.22800

Urbach tail model parameters:

Absorption constant [cm^{-1}]   : .1330000E+11
Exponential constant, σ_0 : .6100000
Effective Phonon Energy, E_p [eV] : .4500000E−01

(continued)

Table A4.5 Solid-State Complex Index of Refraction Model Parameter—cont'd

Fluorides

Material [MgF$_2$ *o*-ray]   Space group #: 136

Classical Oscillator model parameters:

Mode	v_i	$a1_i$	$\Delta\epsilon_i$	$b1_i$	Γ_i/v_i	$c1_i$	$c2_i$
1	248.0	$-.54E-02$	2.23	.254E$-$03	.115E$-$01	.253E$-$05	.494E$-$07
2	408.50	$-.20E-01$	.220	.716E$-$04	.165E$-$01	.484E$-$04	.000
3	447.0	$-.40E-01$	1.10	.734E$-$04	.250E$-$01	.351E$-$04	.160E$-$06
4	535.0	$-.18E-01$	.500E$-$01	.716E$-$04	.300	.207E$-$03	.240E$-$06
5	105692.10	.0	.399	.122E$-$04	.100E$-$03	.000	.000
6	230499.30	.0	.488	.000E+00	.100E$-$03	.000	.000

$\epsilon_\infty = 1.000000$ $d\epsilon_\infty/dT = .0000000$
Allowed IR Modes: 3

Multiphonon model parameters:
$\alpha_1 = .5370$ $v_{max} = 621.0000$
$\alpha_2 = .1530$ $D_0 = 5750.000$
$\alpha_3 = .0520$ $K = 2.4420E+06$

Sellmeier parameters: Lower & upper wave number: 1430.000–50000.000

Mode	Location	Strength
1	230500.0	.487551
2	105692.20	.398750
3	420.30	2.31204

Bandgap [eV]: 11.80000

Urbach tail model parameters:
Absorption constant [cm^{-1}]   : .1144000E+09
Exponential constant, σ_0 : .2400000
Effective Phonon Energy, E_p [eV] : .0000000

Material [MgF$_2$ *e*-ray]   Space group #: 136

Classical Oscillator model parameters:

Mode	v_i	$a1_i$	$\Delta\epsilon_i$	$b1_i$	Γ_i/v_i	$c1_i$	$c2_i$
1	399.0	.0	2.70	.000E+00	.480E$-$01	.000	.000
2	556.0	.0	.100E$-$01	.000E+00	.800E$-$01	.000	.000
3	110178.70	.0	.505	.170E$-$05	.100E$-$03	.000	.000
4	271424.80	.0	.413	.000E+00	.100E$-$03	.000	.000

$\epsilon_\infty = 1.000000$ $d\epsilon_\infty/dT = .0000000$
Allowed IR Modes: 1

Sellmeier parameters: Lower & upper wave number: 1430.000–50000.000

Mode	Location	Strength
1	271425.0	.413440
2	110178.80	.504975
3	420.70	2.49049

Bandgap [eV]: 11.80000

Urbach tail model parameters:
Absorption constant [cm^{-1}]   : .2860000E+08
Exponential constant, σ_0 : .2400000
Effective Phonon Energy, E_p [eV] : .0000000

Table A4.5 Solid-State Complex Index of Refraction Model Parameter—cont'd

			Fluorides				

Material [PbF$_2$]   Space group #: 225

Classical Oscillator model parameters:

Mode	v_i	$a1_i$	$\Delta\epsilon_i$	$b1_i$	Γ_i/v_i	$c1_i$	$c2_i$
1	102.0	.0	24.4	.000E+00	.180	.000	.000
2	35555.0	.0	.167E−01	.000E+00	.000	.000	.000
3	58327.90	.0	1.31	.000E+00	.000	.000	.000
4	999999.0	.0	.670	.000E+00	.000	.000	.000

$\epsilon_\infty = 1.000000$ $d\epsilon_\infty/dT = .0000000$
Allowed IR Modes: 1

Sellmeier parameters: Lower & upper wave number: 840.000–33333.000

Mode	Location	Strength
1	999999.0	.669593
2	58327.91	1.30863
3	35554.91	.167064E−01
4	125.51	2007.89

Bandgap [eV]: 5.000000

Material [SrF$_2$]   Space group #: 225

Classical Oscillator model parameters:

Mode	v_i	$a1_i$	$\Delta\epsilon_i$	$b1_i$	Γ_i/v_i	$c1_i$	$c2_i$
1	217.0	.0	4.0	.000E+00	.170E−01	.000	.000
2	316.0	.0	.700E−01	.000E+00	.250	.000	.000
3	92583.80	.0	.371	−.290E−04	.100E−03	.000	.000
4	177651.80	.0	.678	.000E+00	.100E−03	.000	.000

$\epsilon_\infty = 1.000000$ $d\epsilon_\infty/dT = .0000000$
Allowed IR Modes: 1

Multiphonon model parameters:
$\alpha_1 = .5370$ $v_{max} = 389.0000$
$\alpha_2 = .1530$ $D_0 = 4750.000$
$\alpha_3 = .0520$ $K = 4.5000E+06$

Sellmeier parameters: Lower & upper wave number: 870.000–47620.000

Mode	Location	Strength
1	177651.80	.678059
2	92583.80	.371405
3	250.60	3.34853

Bandgap [eV]: 10.67000

Urbach tail model parameters:
Absorption constant [cm^{-1}]   : .1350000E+10
Exponential constant, σ_0 : .6000000
Effective Phonon Energy, E_p [eV] : .4400000E−01

Material [YLF *o*-ray]   Space group #: 88

Classical Oscillator model parameters:

Mode	v_i	$a1_i$	$\Delta\epsilon_i$	$b1_i$	Γ_i/v_i	$c1_i$	$c2_i$
1	143.0	.0	2.60	.000E+00	.133E−01	.000	.000
2	292.0	.0	.750	.000E+00	.750E−02	.000	.000

(continued)

Table A4.5 Solid-State Complex Index of Refraction Model Parameter—cont'd

				Fluorides			
Mode	v_i	$a1_i$	$\Delta\epsilon_i$	$b1_i$	Γ_i/v_i	$c1_i$	$c2_i$
3	326.0	.0	.960	.000E+00	.550E–02	.000	.000
4	424.0	.0	.850	.000E+00	.417E–01	.000	.000
5	103639.50	.0	.708	.000E+00	.000	.000	.000

$\epsilon_\infty = 1.387570$ $d\epsilon_\infty/dT = .0000000$
Allowed IR Modes: 4

Sellmeier parameters: Lower & upper wave number: 3846.000–44444.000

Mode	Location	Strength
0	Infinity	.387570
1	103639.50	.707570
2	1400.30	.188490

Bandgap [eV]: 7.000000

Material [YLF *e*-ray]   Space group #: 88

Classical Oscillator model parameters:

Mode	v_i	$a1_i$	$\Delta\epsilon_i$	$b1_i$	Γ_i/v_i	$c1_i$	$c2_i$
1	106843.50	.0	.849	.000E+00	.000	.000	.000

$\epsilon_\infty = 1.310210$ $d\epsilon_\infty/dT = .0000000$
Allowed IR Modes: 4

Sellmeier parameters: Lower & upper wave number: 3846.000–44444.000

Mode	Location	Strength
0	Infinity	.310210
1	106843.50	.849030
2	860.80	.536070

Bandgap [eV]: 7.000000

				Others			

Material [AlAs]   Space group #: 216

Classical Oscillator model parameters:

Mode	v_i	$a1_i$	$\Delta\epsilon_i$	$b1_i$	Γ_i/v_i	$c1_i$	$c2_i$
1	361.80	.0	1.90	.000E+00	.221E–01	.000	.000
2	31455.40	.0	3.02	.000E+00	.129	.000	.000
3	36617.30	.0	3.03	.000E+00	.463	.000	.000

$\epsilon_\infty = 2.114000$ $d\epsilon_\infty/dT = .0000000$
Allowed IR Modes: 1

Sellmeier parameters: Lower & upper wave number: 4545.000–17857.000

Mode	Location	Strength
0	Infinity	1.07920
1	35435.90	6.08400
2	362.10	1.90000

Bandgap [eV]: 2.950000

Table A4.5 Solid-State Complex Index of Refraction Model Parameter—cont'd

				Others			

Material [AlN *o*-ray]   Space group #: 186

Classical Oscillator model parameters:

Mode	v_i	$a1_i$	$\Delta\epsilon_i$	$b1_i$	Γ_i/v_i	$c1_i$	$c2_i$
1	671.60	.0	8.02	.000E+00	.000	.000	.000
2	58309.0	.0	1.38	.000E+00	.000	.000	.000

$\epsilon_\infty = 3.139900$ $d\epsilon_\infty/dT = .0000000$
Allowed IR Modes: 1

Sellmeier parameters: Lower & upper wave number: 2000.000–45454.000

Mode	Location	Strength
0	Infinity	2.13990
1	58309.0	1.37860
2	665.30	3.86100

Bandgap [eV]: 5.880000

Material [AlN *e*-ray]   Space group #: 186

Classical Oscillator model parameters:

Mode	v_i	$a1_i$	$\Delta\epsilon_i$	$b1_i$	Γ_i/v_i	$c1_i$	$c2_i$
1	659.30	.0	8.51	.000E+00	.000	.000	.000
2	57273.80	.0	1.62	.000E+00	.000	.000	.000

$\epsilon_\infty = 3.072900$ $d\epsilon_\infty/dT = .0000000$
Allowed IR Modes: 1

Sellmeier parameters: Lower & upper wave number: 2000.000–45454.000

Mode	Location	Strength
0	Infinity	2.07290
1	57273.80	1.61730
2	665.30	4.13900

Bandgap [eV]: 5.740000

Material [BN (cubic)]   Space group #: 216

Classical oscillator model parameters:

Mode	v_i	$a1_i$	$\Delta\epsilon_i$	$b1_i$	Γ_i/v_i	$c1_i$	$c2_i$
1	1065.0	.0	2.60	.000E+00	.380E–01	.000	.000

$\epsilon_\infty = 4.500000$ $d\epsilon_\infty/dT = .0000000$
Allowed IR Modes: 1

Bandgap [eV]: 8.000000

Material [BP]   Space group #: 216

Classical oscillator model parameters:

Mode	v_i	$a1_i$	$\Delta\epsilon_i$	$b1_i$	Γ_i/v_i	$c1_i$	$c2_i$
1	37453.20	.0	6.84	.000E+00	.000	.000	.000

$\epsilon_\infty = 1.000000$ $d\epsilon_\infty/dT = .0000000$
Allowed IR Modes: 1

(continued)

Table A4.5 Solid-State Complex Index of Refraction Model Parameter—cont'd

Others

Sellmeier parameters: Lower & upper wave number: 15873.000–22222.000

Mode	Location	Strength
1	37453.20	6.84100

Bandgap [eV]: 6.000000

Material [CaLa$_2$S$_4$]   Space group #: 220

$\epsilon_\infty = 1.000000$ $d\epsilon_\infty/dT = .0000000$
Allowed IR Modes: −1

Multiphonon model parameters:
$\alpha_1 = .5370$ $\nu_{max} = 314.0000$
$\alpha_2 = .1530$ $D_0 = 2200.000$
$\alpha_3 = .0520$ $K = 5.3400E+05$

Bandgap [eV]: 2.700000

Material [Diamond (C)]   Space group #: 227

Classical oscillator model parameters:

Mode	ν_i	$a1_i$	$\Delta\epsilon_i$	$b1_i$	Γ_i/ν_i	$c1_i$	$c2_i$
1	57142.0	.0	.331	.460E−04	.100E−03	.000	.000
2	94339.0	.0	4.34	.000E+00	.100E−03	.000	.000

$\epsilon_\infty = 1.000000$ $d\epsilon_\infty/dT = .0000000$
Allowed IR Modes: 0

Multiphonon model parameters:
$\alpha_1 = .8000$ $\nu_{max} = 1332.000$
$\alpha_2 = .1300$ $D_0 = 5300.000$
$\alpha_3 = .1500$ $K = 1.1430E+05$

Sellmeier parameters: Lower & upper wave number: .000–50000.000

Mode	Location	Strength
1	57142.0	.331000
2	94339.0	4.33600

Bandgap [eV]: 6.500000

Urbach tail model parameters:
Absorption constant [cm^{-1}]   : .4230000E+12
Exponential constant, σ_0 : .5850000
Effective Phonon Energy, E_p [eV] : .0000000

Material [GaN *o*-ray]   Space group #: 186

Classical oscillator model parameters:

Mode	ν_i	$a1_i$	$\Delta\epsilon_i$	$b1_i$	Γ_i/ν_i	$c1_i$	$c2_i$
1	560.0	.0	4.10	.000E+00	.300E−01	.000	.000
2	39062.0	.0	1.75	.000E+00	.000	.000	.000

$\epsilon_\infty = 3.600000$ $d\epsilon_\infty/dT = .0000000$
Allowed IR Modes: 1

Table A4.5 Solid-State Complex Index of Refraction Model Parameter—cont'd

Others

Sellmeier parameters: Lower & upper wave number: 1000.000–25000.000

Mode	Location	Strength
0	Infinity	2.60000
1	39062.50	1.75000
2	560.0	4.10000

Free carrier model parameters: (Carrier Density = 0.0 E+00)

Plasma Frequency [cm^{-1}]   : 4750.000
Temperature Derviative [cm^{-1}/K] :   .0000000
Relaxation Frequency [cm^{-1}]   :   600.0000
Temperature Derviative [cm^{-1}/K] :   .0000000

Bandgap [eV]: 3.700000

Material [GaN *e*-ray]   Space group #: 186

Classical oscillator model parameters:

Mode	v_i	$a1_i$	$\Delta\epsilon_i$	$b1_i$	Γ_i/v_i	$c1_i$	$c2_i$
1	533.0	.0	5.08	.000E+00	.320E–01	.000	.000

$\epsilon_\infty = 5.350000$ $d\epsilon_\infty/dT = .0000000$
Allowed IR Modes: 1

Sellmeier parameters: Lower & upper wave number: 1000.000–10000.000

Mode	Location	Strength
0	Infinity	4.35000
1	533.0	5.08000

Free carrier model parameters:: (Carrier Density = 0.0 E+00)

Plasma Frequency [cm^{-1}]   : 4750.000
Temperature Derviative [cm^{-1}/K] :   .0000000
Relaxation Frequency [cm^{-1}]   :   600.0000
Temperature Derviative [cm^{-1}/K] :   .0000000

Bandgap [eV]: 3.500000

Material [GaP]   Space group #: 216

Classical oscillator model parameters:

Mode	v_i	$a1_i$	$\Delta\epsilon_i$	$b1_i$	Γ_i/v_i	$c1_i$	$c2_i$
1	349.40	.0	.700E–03	.000E+00	.600E–01	.000	.000
2	358.40	.0	.300E–03	.000E+00	.335E–01	.000	.000
3	363.40	.0	2.06	.000E+00	.300E–02	.000	.000
4	29000.0	.0	2.57	.000E+00	.000	.000	.000
5	42700.0	.0	4.13	.000E+00	.000	.000	.000
6	58000.0	.0	1.39	.000E+00	.000	.000	.000

$\epsilon_\infty = 1.000000$ $d\epsilon_\infty/dT = .0000000$
Allowed IR Modes: 1

Sellmeier parameters: Lower & upper wave number: 800.000–12500.000

Mode	Location	Strength
1	58140.0	1.39000
2	42735.0	4.1310

(continued)

Table A4.5 Solid-State Complex Index of Refraction Model Parameter—cont'd

<div align="center">Others</div>

Material [ZnS (cubic)]   Space group #: 216

Classical oscillator model parameters:

Mode	v_i	$a1_i$	$\Delta\epsilon_i$	$b1_i$	Γ_i/v_i	$c1_i$	$c2_i$
1	274.0	.0	1.98	.000E+00	.300E–01	.000	.000
2	280.0	.0	.900	.000E+00	.550E–01	.000	.000
3	290.0	.0	.250	.000E+00	.550E–01	.000	.000
4	298.0	.0	.400E–01	.000E+00	.350E–01	.000	.000
5	305.0	.0	.300E–01	.000E+00	.250E–01	.000	.000
6	333.0	.0	.200E–02	.000E+00	.400E–01	.000	.000
7	31826.60	.0	.340	.543E–03	.100E–03	.000	.000
8	56837.0	.0	3.76	.000E+00	.100E–03	.000	.000

$\epsilon_\infty = 1.000000$ $d\epsilon_\infty/dT = .0000000$
Allowed IR Modes: 1

Sellmeier parameters: Lower & upper wave number: 952.000–18182.000

Mode	Location	Strength
1	31823.80	.339040
2	56837.0	3.76069
3	295.10	2.73124

Bandgap [eV]: 3.540000

<div align="center">Glasses</div>

Material [As$_2$S$_3$ glass]   Space group #: 0

Classical oscillator model parameters:

Mode	v_i	$a1_i$	$\Delta\epsilon_i$	$b1_i$	Γ_i/v_i	$c1_i$	$c2_i$
1	163.0	.0	.480	.000E+00	.150	.000	.000
2	309.0	.0	.980	.000E+00	.900E–01	.000	.000
3	340.0	.0	.440	.000E+00	.170	.000	.000
4	22222.20	.0	.119	.000E+00	.000	.000	.000
5	28571.40	.0	.877	.000E+00	.000	.000	.000
6	40000.0	.0	1.92	.000E+00	.000	.000	.000
7	66666.70	.0	1.90	.000E+00	.000	.000	.000

$\epsilon_\infty = 1.000000$ $d\epsilon_\infty/dT = .0000000$
Allowed IR Modes: −1

Sellmeier parameters: Lower & upper wave number: 833.000–17857.000

Mode	Location	Strength
1	66666.66	1.89837
2	40000.0	1.92230
3	28571.43	.876513
4	22222.22	.118870
5	365.15	.956990

Bandgap [eV]: .0000000

Table A4.5 Solid-State Complex Index of Refraction Model Parameter—cont'd

Glasses

Material [As$_2$S$_3$ glass]   Space group #: 0

Classical oscillator model parameters:

Mode	v_i	$a1_i$	$\Delta\epsilon_i$	$b1_i$	Γ_i/v_i	$c1_i$	$c2_i$
1	101.0	.0	.700	.000E+00	.190	.000	.000
2	218.0	.0	1.17	.000E+00	.110	.000	.000
3	246.0	.0	.380	.000E+00	.230	.000	.000
4	28835.10	.0	6.69	.000E+00	.000	.000	.000

$\epsilon_\infty = 1.000000$ $d\epsilon_\infty/dT = .0000000$
Allowed IR Modes: −1

Sellmeier parameters: Lower & upper wave number: 8700.000–12050.000

Mode	Location	Strength
1	28835.06	6.69060

Bandgap [eV]: .0000000

Material [BK-7 glass]   Space group #: 0

Classical oscillator model parameters:

Mode	v_i	$a1_i$	$\Delta\epsilon_i$	$b1_i$	Γ_i/v_i	$c1_i$	$c2_i$
1	218031.20	.0	.549	.000E+00	.000	.000	.000
2	86182.50	.0	.723	.000E+00	.000	.000	.000
3	993.20	.0	.983	.000E+00	.000	.000	.000

$\epsilon_\infty = 1.000000$ $d\epsilon_\infty/dT = .0000000$
Allowed IR Modes: −1

Sellmeier parameters: Lower & upper wave number: 4300.000–27400.000

Mode	Location	Strength
1	218031.20	.548753
2	86182.45	.722599
3	993.23	.982884

Bandgap [eV]: 7.700000

Urbach tail model parameters:
Absorption constant [cm^{-1}]   : .2940000E+13
Exponential constant, σ_0 : .2000000
Effective Phonon Energy, E_p [eV] : .0000000

Material [GeO$_2$ germainia glass]   Space group #: 0

Classical oscillator model parameters:

Mode	v_i	$a1_i$	$\Delta\epsilon_i$	$b1_i$	Γ_i/v_i	$c1_i$	$c2_i$
1	844.50	.0	.854	.000E+00	.000	.000	.000
2	64949.40	.0	.718	.000E+00	.000	.000	.000
3	144985.10	.0	.807	.000E+00	.000	.000	.000

$\epsilon_\infty = 1.000000$ $d\epsilon_\infty/dT = .0000000$
Allowed IR Modes: −1

(continued)

Table A4.5 Solid-State Complex Index of Refraction Model Parameter—cont'd

	Glasses	

Sellmeier parameters: Lower & upper wave number: 2326.000–27778.000

Mode	Location	Strength
0	844.46	.854168
1	64949.40	.718158
2	144985.10	.806866

Bandgap [eV]: 5.600000

Material [SiO$_2$ Fused silica (glass)]   Space group #: 0

Classical Oscillator model parameters:

Mode	ν_i	$a1_i$	$\Delta\epsilon_i$	$b1_i$	Γ_i/ν_i	$c1_i$	$c2_i$
1	460.0	.0	.780	.000E+00	.500E–01	.000	.000
2	797.0	.0	.840E–01	.000E+00	.700E–01	.000	.000
3	1046.0	.0	.170	.000E+00	.700E–01	.000	.000
4	1080.0	.0	.330	.000E+00	.170E–01	.000	.000
5	1105.0	.0	.050	.000E+00	.700E–01	.000	.000
6	1193.0	.0	.3300E–01	.000E+00	.80E–01	.000	.000
7	86028.0	.0	.408	.350E–04	.100E–04	.000	.000
8	146190.0	.0	.696	.000E+00	.100E–04	.000	.000

$\epsilon_\infty = 1.000000$ $d\epsilon_\infty/dT = .0000000$
Allowed IR Modes: −1

Multiphonon model parameters:
$\alpha_1 = .530$ $\nu_{max} = 1263.0$
$\alpha_2 = .160$ $D_0 = 13000.0$
$\alpha_3 = .0520$ $K = 5.0000E+06$

Sellmeier parameters: Lower & upper wave number: 2700.000–47620.000

Mode	Location	Strength
1	146189.60	.696166
2	86027.90	.407943
3	1010.50	.897479

Bandgap [eV]: 8.400000

Scatter Model Parameters:
Rayleigh Coeff. (ν^4 Dependence)   : 5.000E–21
Mie-like Coeff. (ν^A Dependence)   : 0.000E+00
Mie-like Exponential Constant (A) :   .0

Material [ZBL glass]   Space group #: 0

Sellmeier parameters: Lower & upper wave number: 2000–10000

Mode	Location	Strength
1	54945.05	0.265
2	483.09	1.22
3	263.85	1.97
0		
3	28986.0	2.57000
4	363.40	2.05600

Bandgap [eV]: 2.880000

Table A4.5 Solid-State Complex Index of Refraction Model Parameter—cont'd

Semiconductors

Material [CdS *o*-ray]   Space group #: 186

Classical oscillator model parameters:

Mode	v_i	$a1_i$	$\Delta\epsilon_i$	$b1_i$	Γ_i/v_i	$c1_i$	$c2_i$
1	241.0	.0	3.13	.000E+00	.230E–01	.000	.000
2	20710.30	.0	.181	.000E+00	.000	.000	.000
3	42332.0	.0	3.97	.000E+00	.000	.000	.000

$\epsilon_\infty = 1.000000$ $d\epsilon_\infty/dT = .0000000$
Allowed IR Modes: 1

Sellmeier parameters: Lower & upper wave number: 7143.000–19608.000

Mode	Location	Strength
0	Infinity	.000000
1	42331.98	3.96583
2	20710.28	.181139

Bandgap [eV]: 2.584000

Urbach tail model parameters:
Absorption constant [cm^{-1}]   : .2700000E+10
Exponential constant, σ_0 : 2.170000
Effective Phonon Energy, E_p [eV] : .0000000

Material [CdS *e*-ray]   Space group #: 186

Classical oscillator model parameters:

Mode	v_i	$a1_i$	$\Delta\epsilon_i$	$b1_i$	Γ_i/v_i	$c1_i$	$c2_i$
1	234.0	.0	3.51	.000E+00	.170E–01	.000	.000
2	19640.50	.0	.700E–03	.000E+00	.000	.000	.000
3	21416.10	.0	.267	.000E+00	.000	.000	.000
4	44589.10	.0	3.97	.000E+00	.000	.000	.000

$\epsilon_\infty = 1.000000$ $d\epsilon_\infty/dT = .0000000$
Allowed IR Modes: 1

Sellmeier parameters: Lower & upper wave number: 7143.000–19608.000

Mode	Location	Strength
1	44589.14	3.97479
2	21416.13	.266808
3	19640.52	.740800E–03

Bandgap [eV]: 2.584000

Urbach tail model parameters:
Absorption constant [cm^{-1}]   : .2700000E+10
Exponential constant, σ_0 : 2.170000
Effective Phonon Energy, E_p [eV] : .0000000

(continued)

Table A4.5 Solid-State Complex Index of Refraction Model Parameter—cont'd

				Semiconductors			

Material [CdSe *o*-ray]   Space group #: 186

Classical oscillator model parameters:

Mode	ν_i	$a1_i$	$\Delta\epsilon_i$	$b1_i$	Γ_i/ν_i	$c1_i$	$c2_i$
1	172.0	.0	3.09	.000E+00	.407E–01	.000	.000
2	20988.80	.0	1.77	.000E+00	.000	.000	.000

$\epsilon_\infty = 4.224300$ $d\epsilon_\infty/dT = .0000000$
Allowed IR Modes: 1

Sellmeier parameters: Lower & upper wave number: 454.000–10000.000

Mode	Location	Strength
0	Infinity	3.22430
1	20988.77	1.76800
2	172.01	3.12000

Bandgap [eV]: 1.887000

Urbach tail model parameters:
Absorption constant [cm^{-1}]   : .9000000E+09
Exponential constant, σ_0 : 2.200000
Effective Phonon Energy, E_p [eV] :   .2800000E–01

Material [CdSe *e*-ray]   Space group #: 186

Classical oscillator model parameters:

Mode	ν_i	$a1_i$	$\Delta\epsilon_i$	$b1_i$	Γ_i/ν_i	$c1_i$	$c2_i$
1	166.0	.0	3.86	.000E+00	.482	.000	.000
2	21462.0	.0	1.89	.000E+00	.000	.000	.000

$\epsilon_\infty = 4.200900$ $d\epsilon_\infty/dT = .0000000$
Allowed IR Modes: 1

Sellmeier parameters: Lower & upper wave number: 454.000–10000.000

Mode	Location	Strength
0	Infinity	3.20090
1	21461.99	1.88750
2	166.0	3.64610

Bandgap [eV]: 1.902000

Urbach tail model parameters:
Absorption constant [cm^{-1}]   : .5000000E–07
Exponential constant, σ_0 : 2.200000
Effective Phonon Energy, E_p [eV] :   .2800000E-01

Material [CdTe]   Space group #: 216

Classical oscillator model parameters:

Mode	ν_i	$a1_i$	$\Delta\epsilon_i$	$b1_i$	Γ_i/ν_i	$c1_i$	$c2_i$
1	141.0	.0	3.10	.000E+00	.468E-01	.000	.000
2	23149.60	.0	3.46	.000E+00	.000	.000	.000

$\epsilon_\infty = 3.758900$ $d\epsilon_\infty/dT = .0000000$
Allowed IR Modes: 1

Table A4.5 Solid-State Complex Index of Refraction Model Parameter—cont'd

	Semiconductors	

Sellmeier parameters: Lower & upper wave number: 333.000–5000.000

Mode	Location	Strength
0	Infinity	2.75890
1	23149.64	3.45918
2	102.97	6.34600

Bandgap [eV]: 1.650000

Urbach tail model parameters:

Absorption constant [cm^{-1}]	:	.3000000E+13
Exponential constant, σ_0	:	4.390000
Effective Phonon Energy, E_p [eV]	:	.0000000

Material [GaAs]   Space group #: 216

Classical oscillator model parameters:

Mode	ν_i	$a1_i$	$\Delta\epsilon_i$	$b1_i$	Γ_i/ν_i	$c1_i$	$c2_i$
1	268.70	.0	2.0	.000E+00	.890E-02	.000	.000
2	24497.80	.0	7.50	.000E+00	.000	.000	.000

$\epsilon_\infty = 3.360000$ $d\epsilon_\infty/dT = .0000000$
Allowed IR Modes: 1

Sellmeier parameters: Lower & upper wave number: 909.000–7143.000

Mode	Location	Strength
0	Infinity	2.36000
1	24500.0	7.49690
2	269.0	1.93470

Bandgap [eV]: 1.500000

Material [Germanium (Ge)]   Space group #: 227

Classical oscillator model parameters:

Mode	ν_i	$a1_i$	$\Delta\epsilon_i$	$b1_i$	Γ_i/ν_i	$c1_i$	$c2_i$
1	15076.10	9.2	6.75	.929E–02	.000	.000	.000
2	160.70	−.31E–01	.214	.415E–03	.000	.000	.000

$\epsilon_\infty = 9.269480$ $d\epsilon_\infty/dT = -.6040000E-02$
Allowed IR Modes: 0

Sellmeier parameters: Lower & upper wave number: 833.000–5000.000

Mode	Location	Strength
0	Infinity	8.26948
1	15076.08	6.74739
2	160.68	.213905

Free carrier model parameters: (Carrier Density = 7.5 E+13 cm^{-3})

Plasma Frequency [cm^{-1}]	: 1489.0
Relaxation Frequency [cm^{-1}] :	49.3

Bandgap [eV]: 0.664

Table A4.5 Solid-State Complex Index of Refraction Model Parameter—cont'd

			Semiconductors				

Material [InAs]   Space group #: 216

Classical oscillator model parameters:

Mode	ν_i	$a1_i$	$\Delta\epsilon_i$	$b1_i$	Γ_i/ν_i	$c1_i$	$c2_i$
1	218.0	.0	2.48	.000E+00	.183E−01	.000	.000
2	3920.0	.0	.710	.000E+00	.000	.000	.000

$\epsilon_\infty = 11.10000$ $d\epsilon_\infty/dT = .0000000$
Allowed IR Modes: 1

Sellmeier parameters: Lower & upper wave number: 320.000–2703.000

Mode	Location	Strength
0	Infinity	10.1000
1	3920.03	.710000
2	219.0	2.75000

Bandgap [eV]: .4100000

Material [InP]   Space group #: 216

Classical oscillator model parameters:

Mode	ν_i	$a1_i$	$\Delta\epsilon_i$	$b1_i$	Γ_i/ν_i	$c1_i$	$c2_i$
1	303.70	.0	2.79	.000E+00	.115E−01	.000	.000
2	15966.80	.0	2.32	.000E+00	.000	.000	.000

$\epsilon_\infty = 7.255000$ $d\epsilon_\infty/dT = .0000000$
Allowed IR Modes: 1

Sellmeier parameters: Lower & upper wave number: 4762.000–10526.000

Mode	Location	Strength
0	Infinity	6.25500
1	15966.79	2.31600
2	303.63	2.76500

Bandgap [eV]: 1.430000

Urbach tail model parameters:
Absorption constant [cm^{-1}]   :   .8000000E+08
Exponential constant, σ_0 : 1.350000
Effective Phonon Energy, E_p [eV] :   .0000000

Material [PbS]   Space group #: 225

Classical oscillator model parameters:

Mode	ν_i	$a1_i$	$\Delta\epsilon_i$	$b1_i$	Γ_i/ν_i	$c1_i$	$c2_i$
1	71.0	.0	133.	.000E+00	.211	.000	.000
2	12987.0	.0	15.9	.000E+00	.000	.000	.000

$\epsilon_\infty = 1.000000$ $d\epsilon_\infty/dT = .0000000$
Allowed IR Modes: 1

Sellmeier parameters: Lower & upper wave number: 1000.000–2860.000

Mode	Location	Strength
1	12987.0	15.9000
2	71.0	133.200

Bandgap [eV]: .4100000

Table A4.5 Solid-State Complex Index of Refraction Model Parameter—cont'd

Semiconductors

Material [PbSe]   Space group #: 225

Classical oscillator model parameters:

Mode	ν_i	$a1_i$	$\Delta\epsilon_i$	$b1_i$	Γ_i/ν_i	$c1_i$	$c2_i$
1	39.0	.0	180.	.000E+00	.615	.000	.000
2	7299.30	.0	21.1	.000E+00	.000	.000	.000

$\epsilon_\infty = 1.000000$ $d\epsilon_\infty/dT = .0000000$
Allowed IR Modes: 1

Sellmeier parameters: Lower & upper wave number: 1000.000–2000.000

Mode	Location	Strength
0	Infinity	.000000
1	7299.30	21.1000

Free carrier model parameters: (Carrier Density = 1.0 E+17)
Plasma Frequency [cm^{-1}]   : 419.0000
Temperature Derviative [cm^{-1}/K] :   .0000000
Relaxation Frequency [cm^{-1}]   :   20.00000
Temperature Derviative [cm^{-1}/K] : $-.2200000$E-01

Bandgap [eV]: .2700000

Material [PbTe]   Space group #: 225

Classical oscillator model parameters:

Mode	ν_i	$a1_i$	$\Delta\epsilon_i$	$b1_i$	Γ_i/ν_i	$c1_i$	$c2_i$
1	32.0	.0	370.	.000E+00	.313	.000	.000
2	6397.90	.0	30.0	.000E+00	.000	.000	.000

$\epsilon_\infty = 1.000000$ $d\epsilon_\infty/dT = .0000000$
Allowed IR Modes: 1

Sellmeier parameters: Lower & upper wave number: 800.000–2500.000

Mode	Location	Strength
1	6397.90	30.0460

Free carrier model parameters: (Carrier Density=1.0 E+01)
Plasma Frequency [cm^{-1}]   : 1320.000
Temperature Derviative [cm^{-1}/K] :   .0000000
Relaxation Frequency [cm^{-1}]   :   30.00000
Temperature Derviative [cm^{-1}/K] :   .0000000

Bandgap [eV]: .3100000

Material [Silicon (Si)]   Space group #: 227

Classical oscillator model parameters:

Mode	ν_i	$a1_i$	$\Delta\epsilon_i$	$b1_i$	Γ_i/ν_i	$c1_i$	$c2_i$
1	32701.10	1.3	10.7	.100E$-$02	.000	.000	.000

$\epsilon_\infty = 1.000000$ $d\epsilon_\infty/dT = .0000000$
Allowed IR Modes: 0

Table A4.5 Solid-State Complex Index of Refraction Model Parameter—cont'd

| | | *Semiconductors* | | | | | |

Sellmeier parameters: Lower & upper wave number: 900.000–7353.000

Mode	Location	Strength
1	33165.68	10.6684
2	8812.50	.304350E−02
3	9.06	1.54133

Free carrier model parameters: (Carrier Density = 1.0E+10 cm^{-3})
Plasma Frequency [cm^{-1}]:   270.8
Relaxation Frequency [cm^{-1}]:   62.4

Bandgap [eV]: 1.11

Material [β-SiC (cubic)]   Space group #: 216
Classical oscillator model parameters:

Mode	ν_i	$a1_i$	$\Delta\epsilon_i$	$b1_i$	Γ_i/ν_i	$c1_i$	$c2_i$
1	793.0	.0	3.30	.000E+00	.600E−02	.000	.000
2	61162.0	.0	5.57	.000E+00	.000	.000	.000

$\epsilon_\infty = 1.000000$ $d\epsilon_\infty/dT = .0000000$
Allowed IR Modes: 1

Sellmeier parameters: Lower & upper wave number: 14500.000–21275.000

Mode	Location	Strength
1	61162.0	5.57050

Bandgap [eV]: 2.400000

Material [VO$_2$ poly (80C)]   Space group #: 136

Classical oscillator model parameters:

Mode	ν_i	$a1_i$	$\Delta\epsilon_i$	$b1_i$	Γ_i/ν_i	$c1_i$	$c2_i$
1	23712.50	.0	.830	.000E+00	.290	.000	.000
2	29439.0	.0	1.20	.000E+00	.350	.000	.000
3	42747.0	.0	2.12	.000E+00	.300	.000	.000

$\epsilon_\infty = 4.170000$ $d\epsilon_\infty/dT = .0000000$
Allowed IR Modes: 1

Free carrier model parameters: (Carrier Density = 1.0E+01]
Plasma Frequency [cm^{-1}]:   33875.0
Temperature Derviative [cm^{-1}/K]:   .0000000
Relaxation Frequency [cm^{-1}]   : 10000.0
Temperature Derviative [cm^{-1}/K] :   .0000000
Bandgap [eV]   :   2.000000

Material [ZnSe]   Space group #: 216

Classical oscillator model parameters:

Mode	ν_i	$a1_i$	$\Delta\epsilon_i$	$b1_i$	Γ_i/ν_i	$c1_i$	$c2_i$
1	205.0	−.14E−01	3.0	.392E−03	.220E−01	.330E−04	.181E−06
2	218.0	−.36	.500E−01	.180E−03	.800E−01	.291E−03	.000
3	250.0	−.25E−01	.500E−02	.106E−03	.500E−01	.615E−03	.000

Table A4.5 Solid-State Complex Index of Refraction Model Parameter—cont'd

			Semiconductors				
Mode	v_i	$a1_i$	$\Delta\epsilon_i$	$b1_i$	Γ_i/v_i	$c1_i$	$c2_i$
4	26400.40	.0	.628	.908E−03	.100E−03	.000	.000
5	52066.20	.0	4.30	.000E+00	.100E−03	.000	.000

$\epsilon_\infty = 1.000000$ $d\epsilon_\infty/dT = .0000000$
Allowed IR Modes: 1

Sellmeier parameters: Lower & upper wave number: 556.000–18182.000

Mode	Location	Strength
1	52066.20	4.29802
2	26400.40	.627766
3	212.80	2.89556

Bandgap [eV]: 2.700000

Material [ZnTe]   Space group #: 216

Classical oscillator model parameters:

Mode	v_i	$a1_i$	$\Delta\epsilon_i$	$b1_i$	Γ_i/v_i	$c1_i$	$c2_i$
1	177.0	.0	2.32	.000E+00	.170E−01	.000	.000
2	26478.80	.0	2.98	.000E+00	.000	.000	.000

$\epsilon_\infty = 4.302300$ $d\epsilon_\infty/dT = .0000000$
Allowed IR Modes: 1

Sellmeier parameters: Lower & upper wave number: 333.000–18182.000

Mode	Location	Strength
0	Infinity	3.30230
1	26478.80	2.98190
2	177.0	2.63580

Bandgap [eV]: 2.556000

Urbach tail model parameters:
Absorption constant [cm^{-1}]   : .1000000E+16
Exponential constant, σ_0 : 2.800000
Effective Phonon Energy, E_p [eV] : .5000000E−01

	Metals	

Material [Aluminum (Al)]   Space group #: 225

$\epsilon_\infty = 1.000000$ $d\epsilon_\infty/dT = .0000000$
Allowed IR Modes: 0

Free carrier model parameters: (Carrier Density = 0.0E+00)
Plasma Frequency [cm^{-1}]   : 119000.0
Temperature Derviative [cm^{-1}/K] :   .0000000
Relaxation Frequency [cm^{-1}]   :   660.0000
Temperature Derviative [cm^{-1}/K] :   .0000000

Bandgap [eV]: .0000000

Table A4.5 Solid-State Complex Index of Refraction Model Parameter—cont'd

<div align="center">Metals</div>

Material [Cobalt (Co)]   Space group #: 194

$\epsilon_\infty = 1.000000$ $d\epsilon_\infty/dT = .0000000$
Allowed IR Modes: 0

Free carrier model parameters: (Carrier Density = 0.0E+00)
Plasma Frequency [cm^{-1}]   :   32000.0
Temperature Derviative [cm^{-1}/K] :   .0000000
Relaxation Frequency [cm^{-1}]   :   295.0000
Temperature Derviative [cm^{-1}/K] :   .0000000

Bandgap [eV]: .0000000

Material [Copper (Cu)]   6/1/92   Space group #: 225

$\epsilon_\infty = 1.000000$ $d\epsilon_\infty/dT = .0000000$
Allowed IR Modes: 0

Free carrier model parameters: (Carrier Density = 0.0E+00)
Plasma Frequency [cm^{-1}]   :   59600.0
Temperature Derviative [cm^{-1}/K] :   .0000000
Relaxation Frequency [cm^{-1}]   :   73.20000
Temperature Derviative [cm^{-1}/K] :   .0000000

Bandgap [eV]: .0000000

Material [Gold (Au)]   6/1/92   Space group #: 225

$\epsilon_\infty = 1.000000$ $d\epsilon_\infty/dT = .0000000$
Allowed IR Modes: 0

Free carrier model parameters: (Carrier Density = 0.0E+00)
Plasma Frequency [cm^{-1}]   :   72800.0
Temperature Derviative [cm^{-1}/K] :   .0000000
Relaxation Frequency [cm^{-1}]   :   215.0000
Temperature Derviative [cm^{-1}/K] :   .0000000

Bandgap [eV]: .0000000

Material [Iron (Fe)]   6/1/92   Space group #: 229

$\epsilon_\infty = 1.000000$ $d\epsilon_\infty/dT = .0000000$
Allowed IR Modes: 0

Free carrier model parameters: (Carrier Density = 0.0E+00)
Plasma Frequency [cm^{-1}]   :   33000.0
Temperature Derviative [cm^{-1}/K] :   .0000000
Relaxation Frequency [cm^{-1}]   :   147.0000
Temperature Derviative [cm^{-1}/K] :   .0000000

Bandgap [eV]: .0000000

Table A4.5 Solid-State Complex Index of Refraction Model Parameter—cont'd

Metals

Material [Lead (Pb)]   6/1/92   Space group #: 225

$\epsilon_\infty = 1.000000$ $d\epsilon_\infty/dT = .0000000$
Allowed IR Modes: 0

Free carrier model parameters: (Carrier Density = 0.0E+00)
Plasma Frequency [cm^{-1}]   : 59400.0
Temperature Derviative [cm^{-1}/K] :   .0000000
Relaxation Frequency [cm^{-1}]   :   1630.000
Temperature Derviative [cm^{-1}/K] :   .0000000

Bandgap [eV]: .0000000

Material [Molybdenum (Mo)]   6/1/92   Space group #: 229

$\epsilon_\infty = 1.000000$ $d\epsilon_\infty/dT = .0000000$
Allowed IR Modes: 0

Free carrier model parameters: (Carrier Density = 0.0E+00)
Plasma Frequency [cm^{-1}]   : 60200.0
Temperature Derviative [cm^{-1}/K] :   .0000000
Relaxation Frequency [cm^{-1}]   :   412.0000
Temperature Derviative [cm^{-1}/K] :   .0000000

Bandgap [eV]:   .0000000

Material [Nickel (Ni)]   6/1/92   Space group #: 225

$\epsilon_\infty = 1.000000$ $d\epsilon_\infty/dT = .0000000$
Allowed IR Modes: 0

Free carrier model parameters: (Carrier Density = 0.0E+00)
Plasma Frequency [cm^{-1}]   : 39400.0
Temperature Derviative [cm^{-1}/K] :   .0000000
Relaxation Frequency [cm^{-1}]   :   352.0000
Temperature Derviative [cm^{-1}/K] :   .0000000

Bandgap [eV]: .0000000

Material [Palladium (Pd)]   6/1/92   Space group #: 225

$\epsilon_\infty = 1.000000$ $d\epsilon_\infty/dT = .0000000$
Allowed IR Modes: 0

Free carrier model parameters: (Carrier Density = 0.0E+00)
Plasma Frequency [cm^{-1}]   : 44000.0
Temperature Derviative [cm^{-1}/K] :   .0000000
Relaxation Frequency [cm^{-1}]   :   124.0000
Temperature Derviative [cm^{-1}/K] :   .0000000

Bandgap [eV]: .0000000

(continued)

Table A4.5 Solid-State Complex Index of Refraction Model Parameter—cont'd

Metals

Material [Platinum (Pt)]   6/3/92   Space group #: 225

$\epsilon_\infty = 1.000000$ $d\epsilon_\infty/dT = .0000000$
Allowed IR Modes: 0

Free carrier model parameters: (Carrier Density = 0.0E+00)
Plasma Frequency [cm^{-1}]   : 41500.0
Temperature Derviative [cm^{-1}/K] :   .0000000
Relaxation Frequency [cm^{-1}]   :   558.0000
Temperature Derviative [cm^{-1}/K] :   .0000000

Bandgap [eV]: .0000000

Material [Silver (Ag)]   6/1/92   Space group #: 225

$\epsilon_\infty = 1.000000$ $d\epsilon_\infty/dT = .0000000$
Allowed IR Modes: 0

Free carrier model parameters: (Carrier Density = 0.0E+00)
Plasma Frequency [cm^{-1}]   : 72700.0
Temperature Derviative [cm^{-1}/K] :   .0000000
Relaxation Frequency [cm^{-1}]   :   145.0000
Temperature Derviative [cm^{-1}/K] :   .0000000

Bandgap [eV]: .0000000

Material [Titanium (Ti)]   6/1/92   Space group #: 194

$\epsilon_\infty = 1.000000$ $d\epsilon_\infty/dT = .0000000$
Allowed IR Modes: 0

Free carrier model parameters: (Carrier Density = 0.0E+00)
Plasma Frequency [cm^{-1}]   : 20300.0
Temperature Derviative [cm^{-1}/K] :   .0000000
Relaxation Frequency [cm^{-1}]   :   382.0000
Temperature Derviative [cm^{-1}/K] :   .0000000

Bandgap [eV]: .0000000

Material [Tungsten (W)]   Space group #: 229

$\epsilon_\infty = 1.000000$ $d\epsilon_\infty/dT = .0000000$
Allowed IR Modes: 0

Free carrier model parameters: (Carrier Density = 0.0E+00)
Plasma Frequency [cm^{-1}]   : 51700.0
Temperature Derviative [cm^{-1}/K] :   .0000000
Relaxation Frequency [cm^{-1}]   :   487.0000
Temperature Derviative [cm^{-1}/K] :   .0000000

Bandgap [eV]: .0000000

Table A4.5 Solid-State Complex Index of Refraction Model Parameter—cont'd

Metals

Material [Vanadium (V)]   Space group #: 229

$\epsilon_\infty = 1.000000$ $d\epsilon_\infty/dT = .0000000$
Allowed IR Modes: 0

Free carrier model parameters: (Carrier Density = 0.0E+00)
Plasma Frequency [cm^{-1}]   : 41600.0
Temperature Derviative [cm^{-1}/K] :   .0000000
Relaxation Frequency [cm^{-1}]   :   489.0000
Temperature Derviative [cm^{-1}/K] :   .0000000

Bandgap [eV]: .0000000

Adachi model parameters for semiconductors are listed in Tables A4.6–A4.8. The Adachi models represent the optical properties above the bandgap and are described in detail in Chapter 8.

Table A4.6 Adachi Model Parameters for GaAs that Are Least-Squares Fit to a Linear Function in Temperature Covering the Temperature Range from 22 to 754 K Where $T_0 = 0$ K

Parameter	T_0 Value	Slope [K^{-1}]	Units
E_0	1.543	−0.000440	eV
$E_0 + \Delta_0$	1.874	−0.000431	eV
A	4.259	−0.002425	eV$^{1.5}$
E_{x0}	0.0047		eV
A_{0x}	0.00235	0.0	eV
Γ_{0x}	0.0035	0.000073	eV
E_1	3.075	−0.000598	eV
$E_1 + \Delta_1$	3.296	−0.000583	eV
B_1	4.0	0.0	—
B_{01}^*	12.380	−0.000414	—
B_2	2.0	0.0	—
B_{02}^*	6.201	−0.000178	—
Γ	0.073	0.000138	eV
E_{x1}	0.05		eV
B_{1x}	1.1	0.0	eV
B_{2x}	0.55	0.0	eV
E_0'	4.511	−0.000412	eV
E_2	4.959	−0.000487	eV
C_2	1.014	−0.001408	—
γ_2	0.080	4.18×10^{-5}	—
C_0	0.739	0.0093	—
γ_0	0.043	0.00228	—
E_g^{ID}	1.73		eV
D	24.2		—
$\epsilon_{1\infty}$	1.388	−0.00786	—

Table A4.7 Room Temperature Adachi Model Parameters for a Variety of Binary Semiconductor Compounds

Parameter	GaP	GaSb	InP	InAs	InSb	Units
E_0	2.74	0.72	1.35	0.36	0.18	eV
$E_0 + \Delta_0$	2.84	1.46	1.45	0.76	0.99	eV
A	13.76	0.71	6.57	0.61	0.19	eV$^{1.5}$
E_1	3.70	2.05	3.10	2.50	1.80	eV
$E_1 + \Delta_1$	3.71	2.50	3.25	2.78	2.30	eV
B_1	6.36	6.68	4.93	6.59	6.37	—
B_{11}	9.49	14.29	10.43	13.76	12.26	—
Γ	0.06	0.09	0.10	0.20	0.16	eV
E_2	5.0	4.0	4.7	4.45	3.9	eV
C_2	2.08	5.69	1.49	1.78	1.78	—
γ_2	0.132	0.290	0.092	0.108	0.318	—
E_g^{1D}	2.26	0.76	2.05	1.07	0.93	eV
D	4.6	7.4	60.4	20.8	19.5	—
$\epsilon_{1\infty}$	0.1	1.0	1.6	2.8	3.1	—

To find out how to apply the B_{11} coefficient see Ref. A4.38 in the reference section concerning this table.

Table A4.8 Room Temperature Adachi Model Parameters for Ternary Semiconductor Alloy $Al_xGa_{1-x}As$

					x					
Parameter	0.00	0.099	0.198	0.315	0.419	0.491	0.590	0.700	0.804	Unit
E_0	1.42	1.54	1.67	1.83	1.97	2.08	2.24	2.42	2.59	eV
$E_0 + \Delta_0$	1.77	1.88	2.00	2.15	2.30	2.40	2.55	2.73	2.90	eV
A	3.45	4.21	4.58	8.80	8.96	12.55	15.40	23.20	30.63	eV$^{1.5}$
E_1	2.90	2.90	3.06	3.13	3.19	3.24	3.32	3.43	3.56	eV
B_1	6.37	6.37	6.37	6.05	5.73	5.73	5.41	5.41	5.09	—
B_{11}	13.08	9.99	11.27	11.05	10.89	10.22	10.41	9.55	10.21	—
Γ	0.10	0.10	0.10	0.11	0.11	0.12	0.12	0.12	0.12	eV
E_2	4.70	4.70	4.70	4.70	4.70	4.70	4.70	4.70	4.70	eV
C_2	2.39	2.31	2.09	2.30	2.45	2.22	2.32	1.76	1.35	—
γ_2	0.146	0.129	0.127	0.135	0.138	0.127	0.131	0.103	0.08	—
E_g^{1D}	1.73	1.79	1.85	1.92	1.96	1.97	2.00	2.03	2.07	eV
D	24.2	21.3	19.0	16.1	13.8	10.0	9.2	8.1	7.0	—
$\epsilon_{1\infty}$	1.6	1.4	1.2	0.6	0.5	0.3	0.0	−0.3	−0.4	—

To find out how to apply the B_{11} coefficient see Ref. A4.35 in the reference section concerning this table.

Table A4.9 Room-Temperature Adachi Model Parameters for Quaternary
Semiconductor Alloy $In_{1-x}Ga_xAs_yP_{1-y}$

Parameter	Unit
$E_0(y) = 1.35 - 0.72y + 0.12y^2$	eV
$E_0 + \Delta_0(y) = 1.466 - 0.557y + 0.129y^2$	eV
$A(y) = 5.4 - 4.2y$	$eV^{1.5}$
$E_1(y) = 3.163 - 0.590y + 0.33y^2$	eV
$E_1 + \Delta_1(y) = 3.296 - 0.466y + 0.26y^2$	eV
$B_1(y) = 4.91 - 3.85y + 2.78y^2$	—
$B_2(y) = 0.09 + 2.65y - 1.26y^2$	—
$\Gamma(y) = 0.14 - 0.10y + 0.10y^2$	eV
$E_2(y) = 4.72 - 0.31y - 0.01y^2$	eV
$C_2(y) = 1.30 + 3.70y - 2.10y^2$	—
$\gamma_2(y) = 0.093 + 0.256y - 0.124y^2$	—
$E_g^{1D}(y) = 2.05 - 0.85y$	eV
$D(y) = 60.4 - 83.9y + 44.2y^2$	—
$\epsilon_{1\infty} = 2.1(y < 1)$	—

$x = 0.1896y/(0.4176 - 0.0125y)$ for lattice matching to InP.

Bibliograpy

Tables A4.1 A4.2, and A4.3

A4.1 E.W. Washburn (Ed.), *International Critical Tables of Numerical Data Physics, Chemistry, and Technology*, Vol. VII, McGraw-Hill (1930).

A4.2 L. Cauchy, *Bull. des. sc. math.* **14**, 9 (1830), and "Sur la dispersion de la lumière," *Nouv. exerc. de math* (1836).

A4.3 R. Coulon, G. Montixi, and R. Occelli, "Determination experimentale des coefficients du viriel de la réfractivité des gaz: étude de l'argon," *Can. J. Phys.* **59**, 1555 (1981).

A4.4 R. Coulon, G. Montixi, and R. Occelli, "Coefficients du viriel de la réfractivité de l'azote à 25°C," *Can. J. Phys.* **61**, 473 (1983).

A4.5 J.M. St.-Arnaud and T.K. Bose, "Direct determination of the intermolecular interaction contribution to the refractive index of carbon dioxide and sulfur hexafluoride," *J. Chem. Phys.* **71**, 4951 (1979).

Table A4.5

A4.6 A.S. Barker, Jr., "Infrared Lattice Vibrations and Dielectric Dispersion in Corundum," *Phys. Rev.* **132**, pp. 1474–1481 (1963).

A4.7 J.R. Jasperse, A. Kahan, and J.N. Plendly, "Temperature Dependence of Infrared Dispersion in Ionic Crystals LiF and MgO," *Phys. Rev.* **146**, No. 2, 526–542 (1966).

A4.8 W.G. Spitzer and D.A. Kleinman, "Infrared Lattice Bands of Quartz," *Phys. Rev.* **121**, No. 5, 1324–1335 (1961).

A4.9 A. Kahan, J.W. Goodrum, R.S. Singh, and S.S. Mitra, "Polarized Reflectivity Spectra of Tetragonal GeO_2," *J. Appl. Phys.* **42**, No. 11, 4444–4446 (1971).

A4.10 I.H. Malitson, "Interspecimen Comparison of the Refractive Index of Fused Silica," *J. Opt. Soc.* of *Am.* **55**, No. 10, 1205–1209 (1965).

A4.11 W. Kaiser, W.G. Spitzer, R.H. Kaiser, and L.E. Howarth, "Infrared Properties of CaF_2, SrF_2, and BaF_2," *Phys. Rev.* **127**, No. 6, (1950–1954).

A4.12 G.R. Hunt, C.H. Perry, and J. Ferguson, "Far-Infrared Reflectance and Transmittance of Potassium Magnesium Fluoride and Magnesium Fluoride," *Phys. Rev.* **134**, No. 3A, A688–A691 (1964).

A4.13 M.J. Dodge, "Refractive Properties of Magnesium Fluoride," *Appl. Opt.* **23**, No. 12, 1980–1985 (1984).

A4.14 S.S. Mitra, "Optical Properties of Nonmetallic Solids," in *Handbook of Optical Constants of Solids*, E.D. Palik (ed.), Academic Press Handbook Series (1985).

A4.15 C. Kittel, *Introduction to Solid State Physics*, 4th Ed. John Wiley, p. 190 (1971).

A4.16 W.W. Ho, "Millimeter-Wave Dielectric Properties of Infrared Window Materials," in *Proceedings of the Second DOD Electromagnetic Windows Symposium*, Vol. 1, AEDC-TR-87-21, Arnold Air Force Station, Tennessee, October 1987.

A4.17 H.H. Genzel and R. Weber, "Dispersion Measurement on NaCl, KCl and KBr Between 0.3 and 3 mm Wavelength," *Z. Phys.* **154**, 13–18 (1959).

A4.18 H.H. Li, "Refractive Index of Alkali Halides and Its Wavelength and Temperature Derivatives," *J. Phys. Chem. Ref. Data* **5**, No. 2, 329–528 (1976).

A4.19 A. Hadni, J. Claudel, D. Chanal, P. Strimer, and P. Vergnat, "Optical Constants of Potassium Bromide in the Far Infrared," *Phys. Rev.* **163**, No. 3, 836–843 (1967).

A4.20 A. Hadni, J. Claudel, G. Morlot, and P. Strimer, "Transmission and Reflection Spectra of Pure and Doped Potassium Iodide at Low Temperatures," *Appl. Opt.* **7**, No. 1, 161–165 (1968).

A4.21 P. Vergnat, J. Claudel, A. Hadni, P. Strimer, and F. Vermillard, "Far Infrared Optical Constants of Cesium Halides at Low Temperatures," *J. Phys.* **30**, No. 8–9, 723–735 (1969).

A4.22 T.F. Deutsch, "Absorption Coefficient of Infrared Laser Window Materials," *J. Phys. Chem. Solids* **14**, 2091–2104 (1973).

A4.23 I.H. Malitson, "Refraction and Dispersion of Synthetic Sapphire," *J. Opt. Soc. Am.* **52**, 1377–1379 (1962).

A4.24 I. H. Malitson, "Refractive Properties of Barium Fluoride," *J. Opt. Soc. Am.* **54**, 628 (1964).

A4.25 Y. Nigara, "Measurement of the Optical Constants of Yttrium Oxide," *Japan. J. Appl. Phys.* **7**, 404–408 (1968).

A4.26 S. Roberts and D.D. Coon, "Far-Infrared Properties of Quartz and Sapphire," *J. Opt. Soc. Am.* **52**, 1023–1029 (1962).

A4.27 G.J. Simonis, *Handbook of Optical Constants of Solids*, Chapter 8, E.D. Palik (ed.), Academic Press (1985).

A4.28 I.H. Malitson, "A Redetermination of Some Optical Properties of Calcium Fluoride," *Appl. Opt.* **2**, 1103–1107 (1963).

A4.29 M.J. Dodge, "Refractive Index of Strontium Fluoride," in *Laser Induced Damage in Optical Materials: 1978*, A.J. Glass and A.H. Guenther (eds.) NBS (U.S.) Spec. Publ. No. 541, 55 (1978).

A4.30 M.J. Dodge, "Refractive Properties of CVD Zinc Sulfide" in *Laser Induced Damage in Optical Materials: 1977*, A.J. Glass and A.H. Guenther (eds.), NBS (U.S.) Spec. Publ. No. 509, 83 (1977).

A4.31 M.J. Dodge, "Refractive Index and Temperature Coefficient of Refractive Index of CVD Zinc Selenide," in *Laser Induced Damage in Optical Materials: 1975*, A.J. Glass and A.H. Guenther (eds.), NBS (U.S.) Spec. Publ. No. 435, 170 (1976).

A4.32 I.H. Malitson and M.J. Dodge, "Refractive Index and Birefringence of Synthetic Sapphire," *J. Opt. Soc. Am.* **62**, 1405A (1972).

A4.33 I.F. Chang and S.S. Mitra, "Temperature Dependence of Long-Wavelength Optic Phonons of NaF Single Crystals," *Phys. Rev.* B **5**, 4094–4100 (1972).

Tables A4.6–A4.8

A4.34 S. Adachi, "Excitonic effects in the Optical Spectrum Of GaAs," *Phys. Rev.* B **41**, 1003–1013 (1990).

A4.35 S. Adachi, "Optical properties of $Al_xGa_{1-x}As$ Alloys," *Phys. Rev.* B **38**, 12345–12352 (1988).

A4.36 S. Adachi, "Optical properties of $In_{1-x}Ga_xAs_yP_{1-y}$ Alloys," *Phys. Rev.* B **39**, 12612–12621 (1989).

A4.37 S. Adachi, "Effects of the indirect transitions on optical dispersion relations," *Phys. Rev.* B **41**, 3504–3508 (1990).

A4.38 S. Adachi, "Model dielectric constants of GaP, GaAs, GaSb, InSb, InAs, and InSb," *Phys. Rev.* B **35**, 7454–7463 (1987).

A4.39 S. Adachi, *Physical Properties of III-V Semiconductor Compounds*, Wiley-Interscience (1992).

This page intentionally left blank

Appendix 5

Electromagnetic Field Quantization

The quantization of the electromagnetic field is essential for a complete understanding of light–matter interactions. This appendix presents the essential elements of the derivation, without too much detail, leading to the general result. The important lessons from this development concern spontaneous emission and mode replication by stimulated emission. More complete derivations can be found in the references (Goldin, Ref. A5.1; Marcuse, Ref. A5.2).

Free-space electromagnetic field propagation can also be described by the magnetic vector potential, $\mathbf{a}(t)$, as defined by

$$\mathbf{b}(\mathbf{r},t) = \nabla \times \mathbf{a}(\mathbf{r},t). \tag{A5.1}$$

where $\mathbf{b}$ is the magnetic flux density. This definition ensures that the $\mathbf{b}$-field is solenoidal by the vector identity

$$\nabla \cdot \nabla \times \mathbf{a}(\mathbf{r},t) = \nabla \cdot \mathbf{b}(\mathbf{r},t) = 0. \tag{A5.2}$$

The electric field is related to the magnetic vector potential through Faraday's law. Thus, in point form

$$\nabla \times \mathbf{e}(t) = -\frac{\partial \mathbf{b}(t)}{\partial t} = -\nabla \times \frac{\partial \mathbf{a}(t)}{\partial t}. \tag{A5.3}$$

$\mathbf{e}(\mathbf{r},t)$ is uniquely determined within an arbitrary scalar potential function, $\phi(\mathbf{r},t)$, by the above equation. Therefore, the electric field can be written as

$$\mathbf{e}(t) = -\frac{\partial \mathbf{a}(t)}{\partial t} - \nabla \phi(t). \tag{A5.4}$$

In free space, the **e**-field is also solenoidal, and this leads to the following condition;

$$\nabla \cdot \mathbf{e}(t) = 0 = -\frac{\partial}{\partial t} \nabla \cdot \mathbf{a}(t) - \nabla^2 \phi(t). \tag{A5.5}$$

The Coulomb gauge condition is applied, which requires

$$\nabla \cdot \mathbf{a}(\mathbf{r},t) = 0. \tag{A5.6}$$

Therefore, the scalar function satisfies Laplace's equation,

$$\nabla^2 \phi(\mathbf{r},t) = 0, \tag{A5.7}$$

with the solution $\phi(\mathbf{r}) = 0$ in a source-free region, since ϕ must go to zero at $r = \pm\infty$. Thus the **b**- and **e**-fields can be described in terms of a single vector potential, as given by

$$\mathbf{b}(\mathbf{r},t) = \nabla \times \mathbf{a}(\mathbf{r},t) \tag{A5.8}$$

and

$$\mathbf{e}(\mathbf{r},t) = \frac{-\partial \mathbf{a}(\mathbf{r},t)}{\partial t}. \tag{A5.9}$$

Consider a TEM electromagnetic field in a one-dimensional cavity of length L. Assume the **e**-field is polarized in the x-direction and propagating in the z-direction, and is given by

$$e_x(t) = e_{x0} \sin k'z \sin \omega t. \tag{A5.10}$$

The corresponding magnetic vector potential has the same polarization as the **e**-field and the mathematical form can be compared with Eq. 1.15a for no y dependence and $l = 0$; the result is

$$a_x(t) = -a_{x0} \sin k'z \cos \omega t, \tag{A5.11}$$

where $\omega a_{x0} = e_{x0}$. Based on Eq. 5.71, the magnetic flux density is

$$b_y(t) = -k'a_{x0} \cos k'z \cos \omega t. \tag{A5.12}$$

The total energy stored within the cavity volume, E_x, for this x-polarized field is

$$E_x = \frac{1}{2} \int_V d^3r \left(\epsilon_0 e_x^2 + \frac{1}{\mu_0} b_y^2 \right). \tag{A5.13}$$

Letting the cavity have a cross-sectional area of A and substituting the results of Eqs. A5.10 and A5.12, we obtain

$$E_x = \frac{A}{2}\epsilon_0 \left(e_{x0}^2 \sin^2 \omega t \int\limits_0^L dz \sin^2 k'z + \omega^2 a_{x0}^2 \cos^2 \omega t \int\limits_0^L dz \cos^2 k'z \right), \quad \text{(A5.14)}$$

since $\omega = k'/\sqrt{\epsilon_0\mu_0}$. The boundary conditions within the cavity require that the **e**-field go to zero at $z = 0$ and $z = L$, thus (recall Eq. 1.15e)

$$k' = k'_m = \frac{\pi m}{L}, \quad \text{(A5.15)}$$

where $m = 0, \pm1, \pm2, \pm3, \dots$. The following result for single mth mode energy is obtained after integration of Eq. A5.14:

$$E_{mx} = \left(\frac{V\epsilon_0}{4}\right)(e_{x0m}^2 \sin^2 \omega_m t + \omega_m^2 a_{x0m}^2 \cos^2 \omega_m t), \quad \text{(A5.16)}$$

where $V = AL$ is the cavity volume. The total energy is obtained by summing over all modes and polarizations. This result is similar in form to Eq. 3.77 for the total energy in a vibrating system. This suggests that the electromagnetic field can be quantized in a similar fashion. To see this, define the following quantities:

$$P_{mx}(t) = -e_{x0m}\left(\frac{V\epsilon_o}{2}\right)^{1/2} \sin \omega_m t \quad \text{(A5.17)}$$

and

$$Q_{mx}(t) = a_{x0m}\left(\frac{V\epsilon_o}{2}\right)^{1/2} \cos \omega_m t. \quad \text{(A5.18)}$$

Then, Eq. A5.16 becomes

$$E_{mx} = \frac{1}{2}\left[P_{mx}^2(t) + \omega_m^2 Q_{mx}^2(t)\right]. \quad \text{(A5.19)}$$

Note that $P_{mx}(t) = dQ_{mx}(t)/dt$, as is the case for vibrating systems. This form of the total energy of the electromagnetic field is analogous to the result for the simple harmonic oscillator Hamiltonian. Thus, this TEM wave propagating in a bounded region described in terms of harmonic oscillations, can be quantized by enforcing the commutation relation

$$[P_{mx}, Q_{lx}] = j\hbar\delta_{ml}. \quad \text{(A5.20)}$$

The conjugate pair field operators, the magnetic vector potential and the electric field, are now expressible in terms of the raising and lowering operators $\hat{a}_{m\sigma}(t)$ and $\hat{a}_{m\sigma}^\dagger(t)$,

respectively, where σ is an index for the two possible polarization directions. Based on Eqs. 3.79 and 3.80, $P_{m\sigma}$ and $Q_{m\sigma}$ can be expressed as

$$P_{m\sigma}(t) = j \left(\frac{\hbar \omega_m}{2} \right)^{1/2} \left[\hat{a}_{m\sigma}(t) - \hat{a}_{m\sigma}^{\dagger}(t) \right] \qquad (A5.21)$$

and

$$Q_{m\sigma}(t) = \left(\frac{\hbar}{2\omega_m} \right)^{1/2} \left[\hat{a}_{m\sigma}(t) + \hat{a}_{m\sigma}^{\dagger}(t) \right]. \qquad (A5.22)$$

Thus, equating Eqs. A5.17–A5.21 and Eqs. A5.18–A5.22, the conjugate pair electromagnetic field operators become

$$\hat{e}_{m\sigma}(t) = \hat{\boldsymbol{\varepsilon}}_{\sigma} \frac{\hat{e}_{\sigma 0 m}}{2j} \left(e^{j\omega_m t} - e^{-j\omega_m t} \right) = \left(\frac{\hbar \omega_m}{V \epsilon_0} \right)^{1/2} \frac{1}{j} \left[\hat{a}_{m\sigma}(t) - \hat{a}_{m\sigma}^{\dagger}(t) \right] \quad (A5.23)$$

and

$$\hat{a}_m(t) = \hat{\boldsymbol{\varepsilon}}_{\sigma} \frac{\hat{a}_{\sigma 0 m}}{2} \left(e^{j\omega_m t} + e^{-j\omega_m t} \right) = \left(\frac{\hbar}{\omega_m V \epsilon_0} \right)^{1/2} \left[\hat{a}_{m\sigma}(t) + \hat{a}_{m\sigma}^{\dagger}(t) \right]. \quad (A5.24)$$

$\hat{\boldsymbol{\varepsilon}}_{\sigma}$ is a unit vector and indicates the direction of polarization. This suggests that the time dependences of the lowering and raising operators are

$$\hat{a}_{m\sigma}(t) = \hat{\boldsymbol{\varepsilon}}_{\sigma} \, \hat{a}_{m\sigma} \, e^{j\omega_m t} \text{ and } \hat{a}_{m\sigma}^{\dagger}(t) = \hat{\boldsymbol{\varepsilon}}_{\sigma} \, \hat{a}_{m\sigma}^{\dagger} e^{-j\omega_m t}. \qquad (A5.25)$$

A raising operator, $\hat{a}_{m\sigma}^{\dagger}$, represents the emission of a photon at frequency ω_m and shall be called a creation operator. A lowering operator, $\hat{a}_{m\sigma}$, represents the absorption of a photon at frequency ω_m and shall be called an annihilation operator.

Recall the above results are for a single-dimension cavity mode. In general, a three-dimensional cavity must be considered. A Comparison of Eqs. A5.10, A5.11, A5.23, and A5.24 with Eqs. 1.15a–e suggests the following spatially dependent field operators summed over all the cavity modes and polarizations, as given by

$$\hat{e}(\mathbf{r}, t) = \sum_{m=-\infty}^{\infty} \sum_{\sigma=1}^{2} \hat{\boldsymbol{\varepsilon}}_{\sigma} \hat{e}_{m\sigma}(\mathbf{r}, t)$$

$$= \sum_{m,\sigma} \frac{1}{j} \left[\frac{\hbar \omega_m}{2V \epsilon_0} \right]^{1/2} \left(\hat{\boldsymbol{\varepsilon}}_{\sigma} \hat{a}_{m\sigma} \, e^{j(\omega_m t - \mathbf{k}_m' \cdot \mathbf{r})} - \hat{\boldsymbol{\varepsilon}}_{\sigma}^{*} \hat{a}_{m\sigma}^{\dagger} \, e^{-j(\omega_m t - \mathbf{k}_m' \cdot \mathbf{r})} \right) \qquad (A5.26)$$

and

$$\hat{a}(\mathbf{r}, t) = \sum_{m=-\infty}^{\infty} \sum_{\sigma=1}^{2} \hat{\boldsymbol{\varepsilon}}_{\sigma} \hat{a}_{m\sigma}(\mathbf{r}, t)$$

$$= \sum_{m,\sigma} \left[\frac{\hbar}{2\omega_m V \epsilon_0} \right]^{1/2} \left(\hat{\boldsymbol{\varepsilon}}_{\sigma} \hat{a}_{m\sigma} \, e^{j(\omega_m t - \mathbf{k}_m' \cdot \mathbf{r})} + \hat{\boldsymbol{\varepsilon}}_{\sigma}^{*} \hat{a}_{m\sigma}^{\dagger} \, e^{-j(\omega_m t - \mathbf{k}_m' \cdot \mathbf{r})} \right) \qquad (A5.27)$$

â and **ê** are the conjugate pair operators for the electromagnetic field just as **r̂** and **p̂** are for a particle. The sum on m is for all positive and negative values, thus forward- and backward-propagating solutions are included. The first term in the field operator represents photon annihilation (or photon absorption by a molecule) and the second term represents photon creation (or photon creation by a molecule). The general results for the quantized electromagnetic field can be obtained in a more rigorous fashion. This is also a more tedious approach, which does not offer any needed additional insight. For more information, the interested reader is referred to the bibliography at the end of this chapter concerning textbooks on quantum optics.

The net eigenstate for the electromagnetic field is the product of all eigenstates for each mode. It is

$$|N_{0\sigma}, N_{1\sigma}, N_{2\sigma}, N_{3\sigma}, \ldots, N_{m\sigma}, \ldots\rangle \tag{A5.28}$$

where $N_{m\sigma}$ is the photon occupation number and represents the number of photons in the mode m with polarization σ. When all the photon occupation numbers are zero, the eigenstate is called the vacuum state. In terms of this formalism for the quantized electromagnetic field, the net energy stored in a TEM electromagnetic wave is given by the following elegantly simple equation:

$$E = \sum_{m,\sigma} \hbar\omega_m \left(N_{m\sigma} + \frac{1}{2} \right). \tag{A5.29}$$

Based on the similar development of the molecular harmonic oscillator, this is not a surprising result. In the vacuum state a zero point energy exists. This is caused by random matter–antimatter reactions, which create photons and random photon reactions, which create matter and antimatter. Thus, the net number of photons is always fluctuating and the probable photon energy can never be zero, even in vacuum. This fluctuation level is small, but does have some important consequences. For example, these vacuum fluctuations are regarded as the cause of spontaneous emission, the most common source of photon radiation. The photon occupation number in Eq. A5.29 represents stimulated processes. Thus, a stimulated emission photon is a exact copy of the incident photon in polarization, frequency, and direction. This explains the high coherence observed in laser sources.

Bibliography

A5.1 E. Goldin, *Waves and Photons: An Introduction to Quantum Optics*, Wiley (1982).

A5.2 D. Marcuse, *Principles of Quantum Electronics*, Academic Press (1980).

This page intentionally left blank

Index